

The Pennsylvania State University

The Graduate School

Department of Physics

AT THE INTERFACE:

GRAVITATIONAL WAVES AS TOOLS TO TEST QUANTUM  
GRAVITY AND PROBE THE ASTROPHYSICAL UNIVERSE

A Dissertation in

Physics

by

Nicolás Yunes

© 2008 Nicolás Yunes

Submitted in Partial Fulfillment  
of the Requirements  
for the Degree of

Doctor of Philosophy

August 2008

The dissertation of Nicolás Yunes was read and approved\* by the following:

Benjamin J. Owen  
Assistant Professor of Physics  
Dissertation Adviser  
Chair of Committee

Stephon H. S. Alexander  
Assistant Professor of Physics

Pablo Laguna  
Professor of Astronomy and Astrophysics  
Professor of Physics

Steinn Sigurdsson  
Associate Professor of Astronomy and Astrophysics

Jayanth Banavar  
Professor of Physics  
Head of the Department of Physics

---

\*Signatures on file in the Graduate School.

## Abstract

This thesis discusses gravitational waves from binary systems of compact objects and their role as probes of quantum gravity and the astrophysical universe.

Part A deals with the modeling of the merger phase of binary systems through numerical relativity, concentrating on the initial data problem. In particular, Chapters 2 and 3 present an improved method to construct such data for non-spinning black hole binaries by combining post-Newtonian and black hole perturbation theory via matched asymptotic expansions. Chapter 4 studies a class of transition functions that allow such gluing of asymptotically-matched approximate 4-metrics. Chapter 5 discusses how to extend the analysis of the previous chapters to spinning black holes, by studying vacuum perturbations of the Kerr metric via the modified Chrzanowski procedure.

Part B focuses on astrophysical applications of gravitational waves from binary black hole inspirals and mergers. Chapters 6 and 7 construct estimates of the recoil velocity a merger remnant acquires for circular and eccentric inspirals of non-spinning black holes. These estimates are calculated by combining techniques from black hole perturbation theory in the close-limit approximation and post-Newtonian theory. Chapter 8 studies relativistic burst signals, namely relativistic sling-shot orbits of massive compact objects around supermassive black holes. In particular, this chapter deals with the possibility of extracting the spin parameter of the central object through a gravitational wave detection of such gravitational wave bursts.

Part C concentrates on tests of string theory and loop quantum gravity with gravitational experiments. Chapter 9 considers the possibility of using solar-system experiments to test Chern-Simons gravity – an ubiquitous correction to general relativity that emerges as the low-energy limit of string theory and possibly loop quantum gravity. Chapter 10 studies spinning black holes in Chern-Simons gravity, while Chapter 11 is concerned with perturbations of non-spinning black holes in this theory. These chapters suggest that a gravitational wave detection could be used to test the Chern-Simons correction, which is discussed in Chapter 12.

## Table of Contents

List of Tables . . . . .	ix
List of Figures . . . . .	x
Preface . . . . .	xii
Acknowledgments . . . . .	xiii
Chapter 1. Introduction . . . . .	1
1.1 Modeling black hole binaries . . . . .	2
1.1.1 Background . . . . .	2
1.1.2 Initial data via matched asymptotic expansions . . . . .	4
1.1.3 Beyond the first-order matching for non-spinning binaries . . . . .	6
1.2 Astrophysical applications of gravitational-wave theory . . . . .	7
1.2.1 Background . . . . .	7
1.2.2 Recoil via the close-limit approximation . . . . .	9
1.2.3 Relativistic gravitational wave bursts . . . . .	11
1.3 Testing quantum gravity with gravitational waves . . . . .	12
1.3.1 Background . . . . .	12
1.3.2 Chern-Simons gravity . . . . .	13
1.3.3 Can we probe quantum gravity? . . . . .	14
PART A: Modeling of compact object binary systems . . . . .	17
Chapter 2. Binary black hole initial data from matched asymptotic expansions . . . . .	18
2.1 Introduction . . . . .	18
2.2 Approximation regions and precision . . . . .	21
2.3 Near zone metric . . . . .	25
2.4 Inner zone metric . . . . .	27
2.5 Asymptotic matching . . . . .	31
2.6 An approximate metric for binary black holes . . . . .	39
2.6.1 Global character of the asymptotic metric . . . . .	41
2.6.2 Transition Functions . . . . .	46
2.7 Initial data for numerical relativity . . . . .	51
2.8 Conclusions . . . . .	60
Chapter 3. Improved initial data for black hole binaries . . . . .	62
3.1 Introduction . . . . .	62
3.2 Division of spacetime into zones and matching in GR . . . . .	66
3.3 Near Zone: An ADMTT post-Newtonian metric . . . . .	68
3.4 Inner Zone: A Black Hole Perturbative Metric . . . . .	71

3.5	Matching Conditions and Coordinate Transformations . . . . .	74
3.6	Constructing a Global Metric . . . . .	77
3.7	Constraint Violations . . . . .	91
3.8	Horizon penetrating coordinates . . . . .	95
3.9	Conclusions . . . . .	102
Chapter 4.	Frankenstein's Glue: Transition functions for approximate solutions .	106
4.1	Introduction . . . . .	106
4.2	Junction Conditions at a Hypersurface . . . . .	109
4.3	Pure joined solutions . . . . .	110
4.3.1	Asymptotically matched metrics . . . . .	111
4.3.2	Asymptotic Junction Conditions . . . . .	114
4.3.3	Projection to a Cauchy Hypersurface . . . . .	119
4.4	A simple example . . . . .	122
4.5	Conclusion . . . . .	133
Chapter 5.	Metric of a tidally perturbed spinning black hole . . . . .	135
5.1	Introduction . . . . .	135
5.2	The slow-motion approximation and the NP scalar . . . . .	138
5.3	The potential . . . . .	144
5.4	The metric perturbation . . . . .	148
5.4.1	Action of the Differential Operators . . . . .	151
5.4.2	Decomposition into real and imaginary parts . . . . .	153
5.5	Conclusions . . . . .	160
PART B:	Gravitational waves as probes of the astrophysical universe . . . . .	163
Chapter 6.	Gravitational Recoil from the Close-limit . . . . .	164
6.1	Introduction . . . . .	164
6.2	Description of our Calculation . . . . .	167
6.3	Initial Data . . . . .	168
6.4	The Close Limit Approximation . . . . .	175
6.4.1	Black hole perturbation theory . . . . .	176
6.4.2	Relation between ADM variables and metric perturbation . .	180
6.4.3	Initial data for the metric perturbations . . . . .	182
6.4.4	Initial data for the master functions . . . . .	186
6.5	Results from the CLA . . . . .	187
6.5.1	Determining the parameters of the initial data . . . . .	188
6.5.2	Results from the numerical evolution of the master equations	190
6.6	Estimating the total recoil . . . . .	197
6.7	Conclusions and Discussion . . . . .	204
Chapter 7.	Gravitational recoil for eccentric binaries . . . . .	206
7.1	Introduction . . . . .	206
7.2	Recoil velocities and the Close Limit approximation . . . . .	207
7.3	Estimating the total recoil . . . . .	210

7.4	Summary and Discussion . . . . .	212
Chapter 8.	Relativistic Effects in Extreme Mass Ratio Gravitational Wave Bursts	215
8.1	Introduction . . . . .	215
8.2	EMRB Dynamics . . . . .	218
8.3	EMRB Waveforms . . . . .	220
8.4	Numerical Simulations . . . . .	221
8.5	Comparison of Trajectories and Waveforms . . . . .	223
8.5.1	Orbital Trajectories . . . . .	225
8.5.2	Waveforms . . . . .	226
8.5.3	Data Analysis . . . . .	231
8.6	Conclusions . . . . .	235
PART C:	Gravitational waves as probes of the quantum gravity . . . . .	238
Chapter 9.	PPN expansion of Chern-Simons gravity . . . . .	239
9.1	Introduction . . . . .	239
9.2	The ABC of PPN . . . . .	242
9.3	CS Gravity in a Nutshell . . . . .	244
9.4	PN expansion of CS Gravity . . . . .	249
9.5	PPN Solution of CS gravity . . . . .	250
9.5.1	$h_{00}$ and $h_{ij}$ to $\mathcal{O}(2)$ . . . . .	251
9.5.2	$h_{0i}$ to $\mathcal{O}(3)$ . . . . .	252
9.5.3	$h_{00}$ to $\mathcal{O}(4)$ . . . . .	253
9.5.4	PPN Parameters for CS Gravity . . . . .	254
9.6	Astrophysical Implications . . . . .	255
9.7	Conclusion . . . . .	259
Chapter 10.	How do Black Holes Spin in Chern-Simons Modified Gravity? . . . . .	261
10.1	Introduction . . . . .	261
10.2	CS modified gravity . . . . .	265
10.2.1	ABC of CS . . . . .	265
10.2.2	Pontryagin Constraint . . . . .	267
10.2.3	Space of Solutions . . . . .	270
10.3	Persistence of GR solutions . . . . .	271
10.3.1	Schwarzschild Solution . . . . .	271
10.3.2	Spherically symmetric metrics . . . . .	273
10.3.3	Losing the Kerr solution . . . . .	274
10.4	Static, axisymmetric solutions . . . . .	274
10.5	Stationary, axisymmetric solutions . . . . .	278
10.5.1	General line elements . . . . .	278
10.5.2	Van Stockum line element . . . . .	281
10.6	Beyond the canon . . . . .	283
10.6.1	Killing embedding . . . . .	283
10.6.2	pp-waves and boosted black holes . . . . .	284
10.6.3	Weakening axisymmetry/stationarity . . . . .	287

10.6.4 Adding matter . . . . .	288
10.7 Conclusions and discussion . . . . .	289
Chapter 11. Perturbations of Schwarzschild black holes in Chern-Simons gravity . . . . .	295
11.1 Introduction . . . . .	295
11.2 Introduction to Chern-Simons Modified Gravity . . . . .	298
11.3 Birkhoff's Theorem in Chern-Simons Modified Gravity . . . . .	299
11.4 Perturbations of a Schwarzschild Black Hole . . . . .	300
11.4.1 Basics . . . . .	300
11.4.2 Pontryagin Constraint . . . . .	303
11.4.3 Structure of the Modified Field Equations . . . . .	304
11.5 Black Hole Perturbation Theory with a Canonical Embedding . . . . .	305
11.5.1 One-handed Perturbations . . . . .	305
11.5.1.1 Pure Axial Perturbations . . . . .	306
11.5.1.2 Pure Polar Perturbations . . . . .	306
11.5.1.3 General Perturbations . . . . .	308
11.6 Beyond the Cannon . . . . .	309
11.6.1 Extended CS Modified Gravity . . . . .	309
11.6.2 Birkhoff's Theorem in the Extended Theory . . . . .	310
11.6.3 BH perturbations in the extended theory . . . . .	311
11.7 Conclusions . . . . .	313
Chapter 12. A gravitational-wave probe of effective quantum gravity . . . . .	315
12.1 Introduction . . . . .	315
12.2 Chern-Simons Modified Gravity . . . . .	317
12.2.1 Brief Review . . . . .	317
12.2.2 Linearized Chern-Simons gravitational waves . . . . .	318
12.3 Observational consequences . . . . .	321
12.3.1 Birefringence in a Matter-Dominated Cosmology . . . . .	321
12.3.2 Binary Inspiral at Cosmological Distances . . . . .	324
12.4 Discussion . . . . .	327
12.4.1 What can be measured? . . . . .	327
12.4.2 How accurately can $\xi$ be measured? . . . . .	328
12.4.3 How large might $\xi$ be? . . . . .	331
12.5 Conclusions . . . . .	333
Appendix A. Coordinate transformation from Kerr to Kerr-Schild . . . . .	335
Appendix B. Conventions for special functions . . . . .	338
B.1 Special polynomials . . . . .	338
B.2 Spherical harmonics . . . . .	339
B.3 Spin-weighted scalar spherical harmonics . . . . .	340
Appendix C. Regge-Wheeler parameterization . . . . .	341
Appendix D. Derivation of the linear momentum flux . . . . .	342

Appendix E. Extremal surfaces in Brill-Lindquist data . . . . .	344
Appendix F. PPN Potentials . . . . .	346
Appendix G. Linearization of the Cotton Tensor . . . . .	347
Appendix H. Proof of ${}^*RR = {}^*CC$ . . . . .	350
Appendix I. Pontryagin constraint . . . . .	351
Appendix J. Explicit expressions for the perturbed C- and Einstein tensors . .	353
Appendix K. Equations of the extended CS theory in the Regge-Wheeler gauge	356
Bibliography . . . . .	357

## List of Tables

3.1	Spacetime Regions . . . . .	67
6.1	Parameters of the non-linear fit for circular orbits . . . . .	201
7.1	Parameters of the non-linear fit for eccentric orbits . . . . .	211
8.1	SNR and overlap of different burst waveforms . . . . .	229
8.2	Comparison of quadrupole and octopole burst waveforms . . . . .	232

## List of Figures

2.1	Diagram of regions . . . . .	22
2.2	Near zone coordinate system . . . . .	26
2.3	Inner zone coordinate system . . . . .	28
2.4	Bare $g_{xx}$ . . . . .	44
2.5	Bare $g_{tt}$ . . . . .	45
2.6	Bare $g_{xx}/\psi^4$ . . . . .	45
2.7	Matched $g_{xx}$ . . . . .	47
2.8	Matched $g_{tt}$ . . . . .	48
2.9	Global $g_{xx}$ . . . . .	50
2.10	Global $g_{tt}$ . . . . .	50
2.11	Bare $K_{xy}$ . . . . .	56
2.12	Bare lapse . . . . .	57
2.13	Global lapse . . . . .	58
2.14	Global shift . . . . .	58
2.15	Global $K_{xy}$ . . . . .	59
3.1	Diagram of regions . . . . .	66
3.2	Bare $g_{xx}$ . . . . .	79
3.3	Bare lapse . . . . .	80
3.4	Bare shift . . . . .	81
3.5	Bare $g_{xx}$ for unequal masses . . . . .	82
3.6	Bare $K_{xy}$ . . . . .	83
3.7	Bare $K_{xy}$ for unequal masses . . . . .	84
3.8	Transition functions . . . . .	86
3.9	Transition of $g_{xx}$ . . . . .	87
3.10	Bare $g_{xx}/\Psi^4$ . . . . .	88
3.11	Transition of $g_{xx}$ for unequal masses . . . . .	89
3.12	Global $g_{xx}$ . . . . .	90
3.13	Global $K_{xy}$ . . . . .	90
3.14	Bare hamiltonian constraint violations . . . . .	92
3.15	Transitioning hamiltonian constraint violation . . . . .	93
3.16	Global hamiltonian constraint violations . . . . .	94
3.17	Bare momentum constraint . . . . .	94
3.18	Global lapse . . . . .	95
3.19	Transitioning regions . . . . .	101
3.20	New $g_{xx}$ . . . . .	102
3.21	New momentum constraint violations . . . . .	103
3.22	Ricci scalar . . . . .	103
4.1	Transition functions . . . . .	127
4.2	Derivatives of transition functions . . . . .	128

4.3	Determinant of spatial metric . . . . .	129
4.4	Ricci scalar . . . . .	130
4.5	Global $K_{xy}$ . . . . .	132
5.1	Newman-Penrose scalar . . . . .	144
5.2	Potential . . . . .	147
5.3	Perturbed metric component . . . . .	159
6.1	Physical configuration . . . . .	170
6.2	Coordinate distance . . . . .	191
6.3	Bare distance . . . . .	192
6.4	Energy flux . . . . .	193
6.5	Angular momentum flux . . . . .	194
6.6	Plus-polarized waveform . . . . .	195
6.7	Master functions . . . . .	196
6.8	Linear momentum flux . . . . .	197
6.9	Close-limit estimates of the Recoil velocity . . . . .	198
6.10	Upper and Lower limits for recoil velocity . . . . .	200
6.11	Recoil comparison . . . . .	202
7.1	Recoil velocity as a function of mass ratio . . . . .	210
7.2	Recoil velocity for eccentric binaries . . . . .	212
7.3	Bounds on recoil from eccentric binaries . . . . .	213
8.1	Possible burst orbits . . . . .	224
8.2	Trajectory of particle around black hole . . . . .	225
8.3	Newtonian and Schwarzschild burst waveforms . . . . .	227
8.4	Schwarzschild and Kerr burst waveforms . . . . .	228
8.5	Overlap of Newtonian and Kerr burst waveforms . . . . .	230
8.6	Overlap of Schwarzschild and Kerr burst waveforms . . . . .	231
8.7	Difference in quadrupole and octopole waveforms . . . . .	232
8.8	Extreme burst waveform . . . . .	235
10.1	Space of solutions for Chern-Simons gravity . . . . .	271

## Preface

The work presented in this thesis has been carried out in collaboration with a number of researchers at different institutions and it has been either accepted or submitted for publication in refereed journals.

Part A is based on work published in the *Physical Review D* (Chapters 2, 3 and 5) and *Classical and Quantum Gravity* (Chapter 4). This work was carried out in collaboration with Wolfgang Tichy (Chapters 2 and 3), Benjamin J. Owen and Bernd Brügmann (Chapter 2), and José González (Chapter 5).

Part B is rooted in research published in the *Astrophysical Journal* (Chapters 6 and 8) and the *Astrophysical Journal Letters* (Chapter 7). This research was carried out in collaboration with Pablo Laguna (Chapters 6 and 7), Louis Rubbo and Kelly Holley-Bockelmann (Chapter 8) and Carlos Sopena (Chapters 6, 7 and 8).

Part C consists of work either accepted for publication or submitted to the *Physical Review D*. These papers were written in collaboration with Stephon Alexander (Chapter 9 and 12), Daniel Grümiller (Chapter 10), Carlos Sopena (Chapter 11) and Sam Finn (Chapter 12).

My participation in all of these projects has been extensive. I am first author in the papers derived from Chapters 2, 3, 5, 8 and 11, while I am the sole author of the paper derived from Chapter 4. The remaining chapters are derived from papers that were collaborative efforts and where I contributed at least equally relative to my collaborators. I have carried out most analytical calculations, all of which have been double-checked by collaborators. Some analytical calculations, such as the initial data computed in Chapter 6, were originally carried out by collaborators, while I performed the double-check. I also carried out all the numerical computations in this thesis, except for some in Chapter 3, which were carried out by Wolfgang Tichy, and some in Chapters 6 and 7, which were carried out by Carlos Sopena.

## Acknowledgments

This thesis would not have been possible without the support of a large number of people. First, I would like to thank the Physics Department at Washington University in Saint Louis and the Pennsylvania State University, whose undergraduate and graduate classes taught me everything I know about physics. I would also like to thank the Institute for Gravitational Physics and Geometry, the Center for Gravitational Wave Physics and the Institute for Gravity and the Cosmos at Penn State for both holding educational workshops, invited seminars, and advanced gravity courses, as well as sponsoring me to attend several conferences.

Beyond the Centers and Institutions, it is the people that work in them that have made the real difference to me. Let me begin with those people that were essential to me during my undergraduate days. First, I want to thank Jan Snow for believing in me and giving me the opportunity to study at Washington University. I would also like to thank Washington University for providing financial support during the Argentine economic crisis of 2001. Academically, I would like to thank Christopher Aubin, Carl Bender, Mark Conradi, Michael Ogilvie and Matt Visser for teaching me the pillars this thesis rests on and continue to be good friends and give good advice. In particular, I would like to thank Maria Cristina Capelo, Sarah Jordan, Olga Pechenaya, Alison Verbeck, and Randi and Gretchen Wolfmeyer for putting up with me and offering me the gift of their friendship.

The people that helped me during my graduate days have also been essential for the completion of this thesis. Along these lines, I would like to thank Randi Neshteruk, Megan Meinecke, Richard Robinett and Kathy Smith, whose help has been invaluable to understand the mysterious web of university policy. Moreover, I would like to thank Abhay Ashtekar, Martin Bojowald, Mike Eraclous, Sam Finn and Deirdre Shoemaker for patiently discussing research with me and pointing me always in the right direction when I went astray. Special thanks must go to those who were post-docs at Penn State and Washington University while this thesis was being developed. In particular, Emanuele Berti, José González, Frank Herrmann, Ian Hinder, Kelly Holley-Bockelmann, Louis Rubbo, Hanno Sahlmann, Carlos Sopena, Uli Sperhake and Wolfgang Tichy, have taught me the real research and computational techniques that cannot be found in textbooks.

During my doctoral studies I have also been extremely fortunate to interact with several professors that in one way or another have also served as advisors. First, I would like to thank Clifford Will, who has not only taught me about all that is post-Newtonian and PPN, but has also continued to give me advice and shown me how to become a successful and ethical physicist and human being. I am also indebted to Bernd Brügmann for convincing me to come to Penn State and giving me the initial push to start research in the right direction. Moreover, I am grateful to Pablo Laguna for many research discussions, as well as career advice and friendship that both him and Maria Laura and Jorge Sofo provided. Discussions and collaborations with Stephon Alexander have been extremely stimulating, driving me always to think out of my (classical) box,

teaching me to not be afraid of quantum gravity, and giving me invaluable career advice. Perhaps most importantly, I am most indebted to Ben Owen, my Ph. D. advisor, whose constant support and encouragement has helped me move forward and adjust my route the many times I took wrong turns. Not only has he taught me about gravitational waves, but he has also shown me how to be patient with students, thoughtful about research and a honorable physicist as a whole.

Last but not least, I want to thank my friends and family, without whom none of this would have been possible. In particular, I want to thank my Argentinian friends Pablo Truchi, Peto Augustovski and Nano Cao for always putting up with Yust Yuns. I would also like to thank my Penn State friends Jeff Fraser, Chrysta Goto, Andrew Knapp, Lissette Szwydky, Victor Taveras, Shannon Walters and Shaun Wood for sharing with me some of the thrills and pains of the doctoral road. Finally, I want to thank my parents, Roberto and Lita Yunes, and my wife-to-be, Jessica Lorien Raley, whose continuous financial, emotional and moral support has helped me through the easy and the not-so-easy Ph. D. times.

All of the work described in this thesis was supported by the Center for Gravitational Wave Physics, funded by the National Science Foundation under Cooperative Agreement PHY-01-14375. I would also like to thank the University of Jena and the University of Guelph for their hospitality, where parts of this thesis were written, as well as to acknowledge support from the DFG grant “SFP Transregio 7: Gravitationswellenastronomie.” Support was also received from National Science Foundation grants PHY-02-18-750, PHY-02-44-788, PHY-02-45-649, PHY-05-55-628, as well as the Braddock, Duncan and Mebus Fellowships. Finally, I would like to thank the Information Technology Services at Penn State University for the use of the LION-XO and LION-XM computer clusters in some of the calculations presented in this thesis. Other calculations used computer algebra systems MATHEMATICA and MAPLE (in combination with the GRTensorII package [1]).

“The triumphant vindication of bold theories – are these not the pride and justification of our life’s work?”

–Sherlock Holmes, *The Valley of Fear*, Sir Arthur Conan Doyle.

## Chapter 1

### Introduction

The main body of this thesis consists of an introduction and three distinct parts, each of which contains several chapters. Each chapter is based on a paper that has either been published or submitted to a refereed journal, and thus, it is written for experts in the field. This introduction is then essential to present some background information and explain how different parts of this thesis are interconnected. In view of this, this chapter is written for a general audience of physicists, who may or may not be experts in the fields of numerical relativity, post-Newtonian theory or gravitational-wave analysis. Due to the long and complicated history of these fields, the background information presented here shall be *minimal* instead of comprehensive, *i.e.* I shall only describe some aspects of the history and background that I believe are necessary for the understanding of the remaining chapters.

The principal topic of this thesis is the study of gravitational waves from inspiraling and merging compact binaries to probe the quantum gravitational regime of spacetime and to obtain a better understanding of the astrophysical universe. Part A of this thesis focuses on the numerical modeling of the merger phase of black hole binaries, and in particular, on the initial data problem. Chapters 2 and 3 introduce an improved method to build initial data for numerical simulations of non-spinning black hole binaries by “gluing” information from post-Newtonian and black hole perturbation theory. The gluing procedure is rooted in the theory of matched asymptotic expansions and the use of well-behaved transition functions, which are discussed in Chapter 4. This method can be extended to spinning black hole binaries, by considering the modified Chrzanowski procedure in black hole perturbation theory, developed in Chapter 5.

Part B discusses some examples of the interplay between gravitational-wave physics and astronomy. On the one hand, Chapters 6 and 7 estimate the recoil velocity a merger remnant obtains after the circular and eccentric inspiral and merger of non-spinning black holes binaries respectively. On the other hand, Chapter 8 focuses on sling-shot orbits of small black holes around a supermassive one and the possibility of extracting relativistic astrophysical parameters from gravitational wave observations of such systems.

Part C proposes the use of gravitational waves to test a generic low-energy correction to general relativity derived from string theory and loop quantum gravity: Chern-Simons gravity. Chapter 9 performs a parametrized post-Newtonian expansion of the theory and concentrates on solar-system experiments. Chapter 10 and 11 study spinning black holes in the modified theory and black hole perturbation theory about a non-spinning black hole background respectively. These two chapters suggest that gravitational wave emission and propagation are modified in Chern-Simons gravity. Chapter 12 pushes this idea further and proposes a gravitational wave test of Chern-Simons gravity with LISA.

## 1.1 Modeling black hole binaries

### 1.1.1 Background

According to Einstein’s theory of general relativity, all spatial dimensions and time form a “spacetime continuum” that is dynamically determined by matter/energy distributions. Gravitational waves are generated when these distributions possess a non-vanishing quadrupole moment – that is, when matter undergoes acceleration. The term “gravitational waves” then can be thought of as the oscillatory features of spacetime that arise when matter/energy distributions accelerate.

One of the staple sources of gravitational radiation is binary systems of compact objects or simply “compact binaries.” These sources are important to the gravitational wave community for several reasons. First, such systems are expected to be ubiquitous in nature, with detection event rates that could go up to thousands of events per year out to  $z = 1$  with advanced LIGO<sup>1</sup>. Moreover, such systems produce strong gravitational waves because these scale with the mass of the system, and black holes can have a total mass that is a million times that of the Sun. Finally, gravitational waves from compact binaries can be modeled extremely well and they lead to a large accumulation of gravitational wave cycles [3]. A strong, well-modeled signal with many cycles renders compact binaries ideal for gravitational wave detection through matched filtering techniques [4] at interferometers, such as LIGO [5], VIRGO [6], GEO [7] and TAMA [8].

The evolution of black hole binaries have been traditionally thought of as having three distinct phases [2]: the inspiral phase; the plunge and merger phase; and the ringdown phase. During the inspiral phase, the binary components are well-separated, such that gravity is weak and the orbital velocities and tidal effects are small. In this phase, the system can be modeled extremely well by post-Newtonian theory [3], where one assumes the orbit is quasicircular and its radius shrinks adiabatically on a much longer timescale than the orbital one. Therefore, all binaries spend most of their lifetimes in this phase, possibly producing tens of thousands of gravitational wave cycles.

The plunge and merger phase was thought to begin when the binary components break circular orbit and plunge toward each other. The precise radius where this happens is fuzzy, but it was traditionally believed to be near the innermost stable circular orbit. Therefore, during this phase, gravity is not weak and non-linear gravitational radiation is expected to be produced. Numerical relativity [9] was expected to be the only avenue to model this phase, due to the breakage of all other approximation schemes.

The ringdown phase begins roughly when a common apparent horizon forms and the system rings down all excess energy and momentum to return to equilibrium in an isolated, spinning black hole configuration. During this phase, the binary can be approximated as a single, perturbed black hole and modeled via perturbation theory [10], where one finds that it vibrates at certain quasi-normal frequencies, like a ringing bell. Eventually, the black hole settles down to a spinning configuration with constant angular velocity, where it ceases to emit gravitational waves.

---

<sup>1</sup>These event rate estimates are quite uncertain, depending on the details of black hole population synthesis. The quoted rate corresponds to that presented in [2].

When I entered the graduate doctoral program at Penn State, one of the remaining standing problems in gravitational wave physics concerned the plunge and merger phase of black hole binaries. The inspiral could be modeled extremely well with post-Newtonian techniques, since soon after I arrived Blanchet, Damour, Esposito-Farese and Iyer [11, 12] finished the so-called 3 PN expansion of the equations of motion. Such an expansion entails the calculation of iterative corrections to Newton’s law to  $\mathcal{O}(v/c)^6$ , where  $v$  is the orbital velocity and  $c$  is the speed of light. Similarly, Price and Pullin [13] had recently developed the close-limit approximation, which used black hole perturbation theory to model the ringdown phase and yielded results that matched certain numerical simulations incredibly well [14, 15]. The plunge and merger phase, however, remained a mystery because approximation schemes could not be used consistently and numerical relativity was still struggling with the black hole head-on collision problem.

Numerical relativity deals essentially with the evolution of the Einstein equations on supercomputers. This task of course appears quixotic due to the complexity of the Einstein equations – a system of ten coupled, non-linear, partial differential equations. This system can be classified into two subsystems: a set of four constraint equations and a set of six evolution equations. In order to evolve the equations numerically, one of the standard procedures<sup>2</sup> is to “foliate” spacetime with spatial hypersurface. Then, once initial data is prescribed on one such hypersurface (that is, a spatial metric and its first derivative or extrinsic curvature at one instant of time), the evolution equations describe how that data evolves to other hypersurfaces. The constraint equations, analogous to the divergence-free condition of the electric field in Maxwell’s equations, determine which initial data is acceptable on each hypersurface.

The choice of initial data characterizes the system that one evolves, but finding data that represents a closely-separated, binary black hole system is quite difficult. This is because no exact solution is known for the two-body problem in general relativity and approximation schemes break down when the system is closely-separated. One could, in principle, begin with a system that is widely separated, such that data could be prescribed via post-Newtonian theory. This approach, however, is and will remain to be too numerically expensive in the near future<sup>3</sup>.

Several techniques have been proposed to prescribe initial data for closely-separated black hole binaries. One of the most popular methods was developed by Brandt and Brügmann [17] and goes by the name of “puncture data” (*c.f.*, *e.g.* [18] for a review of initial data in numerical relativity). Puncture data begins by assuming the spatial metric is conformally flat and the initial spatial hypersurface is maximally sliced (vanishing trace of the extrinsic curvature), such that the momentum constraint can be solved exactly to yield the Bowen-York solution [19, 20, 21]. The conformal factor is then determined by approximately solving the Hamiltonian constraint in the small-momentum limit, yielding the so-called Brill-Lindquist solution [22]. The uncontrolled remainder

---

<sup>2</sup>There are other formulations, such as those that use a characteristic approach, but I shall not discuss those here [9].

<sup>3</sup>Other complications also plague the use of post-Newtonian theory as initial data, which are discussed further in [16]

in the conformal factor can then be obtained by numerically solving the Hamiltonian constraint again.

Puncture data, like all other data currently in use in numerical relativity, does represent *approximately* a binary black hole system. However, certain assumptions are always made that limit both the accuracy of this data and our ability to improve on it<sup>4</sup>. In the case of puncture data, the assumption of conformal flatness is greatly limiting, since binary black hole systems are known to break conformal flatness at second post-Newtonian order. Moreover, the use of a hybrid analytical-numerical or a purely numerical approach to solve the constraint equations forces us to surrender analytic control. That is, the data produced numerically contains unknown errors, for example due to the conformal flatness assumption, that cannot be *a priori* modeled analytically and whose accuracy cannot be improved straightforwardly in an iterative way.

For these reasons, in 2003-2004 Bernd Brügmann and Ben Owen suggested that I look at the initial data problem for binary black hole system, through the combination of post-Newtonian and black hole perturbation theory, which I shall discuss next.

### 1.1.2 Initial data via matched asymptotic expansions

Our attempts to construct more “astrophysically realistic<sup>5</sup>” initial data were not new at that time. That is, initial data built from approximate solutions to the Einstein equations already existed. For example, Hu, Matzner and Shoemaker [23, 24, 25] proposed combining the spatial metric and extrinsic curvature of two isolated spinning black holes in a certain way, such that the Newtonian limit could be recovered. This data, however, is known to deviate from post-Newtonian theory at second order in the far field. Another approach was simply to push post-Newtonian theory to close separations and construct initial data with it [16, 26, 27]. This data had the advantage that it identically reproduced post-Newtonian theory by construction and its uncontrolled remainders were analytically fully under control. However, post-Newtonian theory breaks down not only dynamically for closely separated black holes, but also near singularities on every hypersurface. A consequence of these problems is that this data possesses the incorrect tidal horizon deformations relative to black hole perturbation theory.

A procedure to incorporate both post-Newtonian and black hole perturbation theory had already been proposed by Alvi [28, 29], following the theory of matched asymptotic expansions [30, 31]. Essentially, the idea was to construct three approximate spacetime metrics: one with post-Newtonian theory that represented a non-spinning black hole binary; and two others with black hole perturbation theory that represented two non-spinning perturbed black holes. The post-Newtonian metric was formally valid

---

<sup>4</sup>In the past four years, several different numerical relativity groups have succeeded in evolving binary black hole systems with puncture data. These groups have observed that this data produces an undesired burst of initial radiation, which is believed to arise due to some of the incorrect assumptions discussed here.

<sup>5</sup>The term “astrophysical realism” is a very controversial one, which is why I present it here between quotation marks. By realistic data I here mean that which incorporates deviations from conformal flatness and maximal slicing that match both: the deviations predicted by post-Newtonian theory far away from the black holes; and the deviations predicted by black hole perturbation theory close to the horizons of the black holes.

for sufficiently separated binaries and sufficiently far from the singularities, while the perturbed black hole metrics were valid sufficiently close to the singularities. One could then asymptotically expand each approximate metric near the edge of their regions of validity, thus forcing these regions to *overlap*. Inside the overlap regions, one could then asymptotically match asymptotically-expanded, approximate metrics – that is, one could relate the coordinate systems and the parameters used by each approximation by comparing their invariant intervals. A global metric thus arises as a piecewise function, where each piece corresponds to different approximate metrics that have undergone asymptotic matching.

This problem was ideal for me since I had studied asymptotic analysis extensively under Carl Bender (one of the world experts on the subject) during my undergraduate days at Washington University. As I began to read Alvi’s papers I found a major inconsistency relative to the standard way one carries out asymptotic matching. Essentially, the inconsistency was rooted in the difference between *matching* and *patching*. In asymptotic matching, one obtains a parameter and coordinate map in a *region* of spacetime, while in patching one chooses only one *point* in this region. This is a subtle difference but an important one, because patching could in principle lead to solutions with large discontinuities in its derivatives. My suspicion was that Alvi had carried out patching instead of matching, which explained why Brügmann and Jansenn [32] had found large discontinuities in spatial derivatives of his data.

Another problem with Alvi’s analysis was rooted in the ordering of the terms computed. In order to prescribe initial data with post-Newtonian theory to some order in  $v/c$ , one requires that the spatial metric and its time derivative be accurate to that same order or higher. However, in post-Newtonian theory time derivatives are smaller by a factor of  $v/c$  relative to spatial derivatives. Wolfgang Tichy thus realized that the extrinsic curvature had to be calculated to a slightly higher order (one factor of  $v/c$  higher) relative to the spatial metric. This implied that certain components of the spacetime metrics (*i.e.*, the shifts) had to be matched to higher order than all other components. Alvi performed matching to the same order in  $v/c$  for all components of the spacetime metric, thus making his result useless for the construction of initial data to a consistent order.

Chapter 2 (written with Tichy, Brügmann and Owen) repeats and corrects Alvi’s analysis. First, asymptotic matching is performed in a region of space, never restricting attention to a single point – that is, we perform matching instead of patching. Moreover, the calculation is carried out to  $\mathcal{O}(v/c)^2$  in the spatial and temporal-temporal components of the metric and to  $\mathcal{O}(v/c)^3$  in the shift, thus allowing for the construction of initial data to a consistent order. Chapter 3 (written with Tichy) improves on this data by repeating the calculation in a coordinate system much better adapted to asymptotic matching and to numerical relativity. Furthermore, the constraint violations of the data are computed and shown to be indeed of the expected order.

The results of asymptotic matching is a global metric, composed of several different approximate solutions, but its piece-wise nature renders the data formally discontinuous in the overlap regions. This behavior can be removed by joining the pieces together with transition functions, thus leading to smooth global data. Such a procedure is carried out in Chapters 2 and 3, but it is not until Chapter 4 that I study in

detail these transition functions. In this chapter, I calculate a set of sufficient conditions for this transition functions that guarantee that the smooth global data, produced via asymptotic matching, remains accurate to the desired order, *i.e.*, to the same order as the approximate solutions.

The problem of prescribing initial data using approximation schemes that correctly prescribe both the far field behavior of the gravitational field, as well as its behavior near the black hole horizons, has then been formally solved. The use of post-Newtonian theory guarantees that the data has the expected far field behavior, while the use of black hole perturbation theory guarantees that the black hole horizons possess the expected tides. Moreover, the errors in the data can be modeled analytically because they are directly related to the uncontrolled remainders in each approximation. Last but not least, this method of prescribing initial data can formally be extended to higher orders and to other physical systems straightforwardly, which I shall discuss next.

### 1.1.3 Beyond the first-order matching for non-spinning binaries

The method described above to construct initial data from approximate solutions to the Einstein equations can in principle be extended to other physical systems, provided the corresponding approximate solutions exist. After tackling the non-spinning black hole binary problem, I decided to look into spinning black holes. The post-Newtonian metric for a spinning black hole binary already existed [33] in 2004, but a perturbed spinning black hole solution did not.

I was ideal for tackling the problem of constructing a perturbed spinning black hole metric because I had already used perturbed black hole solutions and I was very familiar with perturbation theory as applied in post-Newtonian expansions and asymptotic analysis. As I began to work on this problem, I realized that new techniques would have to be employed, since a simple generalization of non-spinning black hole perturbation theory would not work. The main problem is that in the non-spinning case, the metric can be expanded in tensor spherical harmonics, which automatically satisfy the angular sector of the Einstein equations. One is then left only with the radial and temporal sectors of these equations, which can then be solved analytically in the framework of black hole perturbation theory. In the spinning case, however, a tensor harmonic decomposition does not solve the angular sector of the Einstein equations and a spin-weighted generalization of these harmonics does not exist.

Since I was stuck, I decided to ask Eric Poisson for advice, since he is an expert in the construction of perturbed black hole metrics and we had already discussed how to tackle this problem at GR 17. He pointed me to the work of Chrzanowski, Cohen and Kegeles, and Wald, who had worked on similar problems in the 1970s. After going through the literature, I arrived at the modified Chrzanowski procedure, which I realized one could use to construct an approximate metric for a perturbed spinning black hole. The general idea is to express the perturbed metric in terms of derivatives of a certain potential. This potential satisfies a certain differential equation, where the source is given by one of the Newman-Penrose scalars, which itself satisfies the Teukolsky equation – a certain version of the linearized Einstein equations. Thus, if one could obtain an approximate form of the Newman-Penrose scalars for a perturbed spinning black hole,

one could then turn the crank and compute the potential and from that the perturbed metric.

I came to the problem with the missing ingredient: Poisson’s 2004 work [34], where he perturbatively computes precisely the Newman-Penrose scalar that I needed in terms of tidal tensors. In 2005, then, I used Poisson’s results to compute the perturbed metric of a spinning black hole. Chapter 5 (written with Jose González) deals with this calculation, which was in fact finished at the University of Jena, where Brüggmann invited me to spend one semester. With these results, one can now in principle perform asymptotic matching between the post-Newtonian metric of a spinning black hole binary and the perturbed spinning black hole metric discussed here.

After these papers were written, however, numerical relativity went through a scientific revolution, where essentially three methods were developed to fully solve the Einstein equations numerically. The first method was developed by Frans Pretorius [35], while the second one was proposed by the then University of Brownsville numerical relativity group [36] and the NASA Goddard group [37]. Recently, a third method has also been successful, proposed by the Caltech group. I shall not describe each of these methods here, but instead I would like to concentrate on the results they obtained regarding the initial data problem. All of these groups have used different initial data (*i.e.*, a collapsing scalar field, puncture data and effective potential data), but the general result is the same: initially there is a burst of “unphysical” radiation, which propagates out of the numerical domain<sup>6</sup>. Little work has been carried out to fully understand this initial data burst, but it is believed to be due to the incorrect assumptions discussed earlier in the initial data construction.

Initial data via matched asymptotic expansions is probably just as accurate as puncture data, which means that if evolved it would probably contain approximately the same burst of unphysical radiation. Thus, it is worthwhile to complete the analysis to next order in the matching scheme to investigate whether the initial burst of radiation is diminished. Currently, Nathan Johnson-McDaniel, together with Owen, Tichy and myself, are carrying out the second order matching calculation [39], with results expected soon.

## 1.2 Astrophysical applications of gravitational-wave theory

### 1.2.1 Background

After the numerical relativity revolution, there was a push to connect gravitational wave theory to astrophysics. In the past, the gravitational wave community had already pointed out that astrophysical intrinsic and orbital parameters, such as the intrinsic spin of black holes or the period of binary systems, could be extracted from gravitational wave detections. But now that the merger phase was under numerical control, the community

---

<sup>6</sup>There are some claims that this unphysical radiation does not really disappear, but it bounces off the edge of the numerical grid and continues to contaminate the simulations. This statement, however, depends on the boundary conditions used and one seems to require a very large resolution to observe it [38]

wanted to determine whether this new knowledge would play a role in astrophysics and if so how.

One of the most dramatic consequences of binary black hole mergers is the recoil of the system’s center of mass. Essentially, as the black holes orbit, the system radiates energy, angular and linear momentum through gravitational waves. For a system with a certain degree of asymmetry, the linear momentum radiated does not completely cancel out, and after merger, the center of mass of the system acquires a certain velocity due to momentum conservation. This simple picture was put forth by Alan Wiseman [40] in 1992, and although it is not formally correct (*e.g.* there is no formal, exact definition of the “center of mass” of a binary system in full general relativity), it does provide the correct physical picture.

The recoil problem is of great interest to astrophysics because, if this “kick” is large enough, the remnant could be expelled from its host galaxy. Of course, for this to happen the recoil velocity has to exceed the escape velocity of the host, or otherwise the remnant is displaced but it eventually returns to the host’s center via dynamical friction (for more details on this see [41]). These kicks also have a strong effect on black hole merger scenarios, specially in globular clusters. In these systems, the escape velocities are not very high (*i.e.*, on the order of tens of  $\text{km s}^{-1}$ ), and recoil velocities can easily exceed them. Traditionally, black hole formation scenarios have either neglected recoil velocities or modeled them via quasi-Newtonian estimates, which are now known to be inaccurate. The inclusion of the correct recoil estimates put in jeopardy many of these formation scenarios, especially for intermediate-mass black holes [42], unless a mechanism is found to suppress such kicks. The recoil velocity is then an example where gravitational wave theory has forced astrophysics to rethink parts of its standard model.

The recoil velocity calculation has a long history that is worth recapitulating. The first analytical studies of this effect were carried out in the 1980s by Fitchett [43], followed quickly by several others [44, 45, 46, 47, 40]. The general consensus in the 1990s was that Fitchett’s quasi-Newtonian estimates were sufficient, because its first post-Newtonian corrections only altered his estimates by a few  $\text{km s}^{-1}$ . However, in the 2000s Favata, *et. al.* [48] performed a black hole perturbation theory calculation in the extreme-mass ratio limit and found results in disagreement with Fitchett’s calculation. A few years later, Blanchet, *et. al.* [49] performed a second-order post-Newtonian calculation and found that Fitchett’s estimates overestimated the kick for non-spinning binaries by roughly a factor of ten.

In 2004, Pablo Laguna realized that Blanchet’s estimates were dominated by the last few orbits of the binary system, which also coincided with the regime where their approximations were least accurate. He then suggested to Carlos Sopuerta and myself that we estimate the recoil with black hole perturbation theory, since this approximation scheme is extremely well-suited to model the final stage of the merger and the ringdown phase. This calculation is described in Chapters 6 and 7 (written with Sopuerta and Laguna) and I shall describe it further in the next subsection.

The merger phase, however, is not the only phase in a binary’s lifetime that can be of use to the astrophysics community. As already pointed out, gravitational wave detection could in the future provide information on the distribution of spins, masses and velocities in our and other galaxies. Given a gravitational wave detection, this

can be achieved by extracting the orbital and intrinsic parameters that are used to model the gravitational wave via matched filtering. This technique, however, assumes the accumulation of a large number of cycles, which thus renders the inspiral phase of roughly equal mass binaries ideal for such studies. With the advent of space-borne gravitational wave detectors, such as LISA [50, 51], soon attention shifted to a different kind of inspiraling binary: extreme-mass ratio systems.

Extreme-mass ratio inspirals consist of a small compact object orbiting a supermassive black hole, which can be modeled with black hole perturbation theory techniques. The beauty of such systems is that their orbital period is assumed to be very small, which implies the small object spends a large amount of time (and gravitational wave cycles) near the supermassive black hole. Since the period is short, the small object’s orbital radius must be reasonable small as well, thus allowing this object to sample and map the spacetime curvature produced by the supermassive black hole. A large amount of literature exists on the estimation of orbital parameters from such systems [52, 53, 54], but we shall not discuss this here.

In 2006, Louis Rubbo, *et. al.* [55] proposed a new possible source of gravitational waves that could be detected with LISA. This source consisted of a small black hole slingshotting around a supermassive black hole<sup>7</sup>, thus reaching rather high orbital velocities but possessing long period. As the small black hole swings by the supermassive one, the system emits a strong burst of gravitational wave radiation that could potentially be observed by LISA, which is why these systems were labeled “extreme-mass ratio burst signals.”

An interesting debate arose as to whether these new sources would be interesting for LISA. Although highly uncertain, the calculated event rate is expected to be rather high, roughly 1 – 15 events per year, for events with signal-to-noise ratio greater than five out to the Virgo cluster [55, 56]. Each event, however, probably bursts only once in the LISA lifetime, thus limiting the power of matched-filtering techniques. This is why I suggested to Rubbo, Holley-Bockelmann and Sopena to revisit the problem, and this time, to include relativistic corrections. The idea was to determine whether such relativistic corrections could be extracted given a hypothetical gravitational wave detection. I had recently finished studying geodesic motion in an advanced general relativity class taught by Owen, so I had the necessary tools to carry out this analysis. Chapter 8 (written with Rubbo, Holley-Bockelmann and Sopena) describes this calculation in detail and I shall summarize its results in Subsection 1.2.3.

### 1.2.2 Recoil via the close-limit approximation

Laguna’s suggestion to compute the recoil velocity with black hole perturbation theory techniques was a good one, but also a challenging one. The main idea was to consider the merger phase, right after a common apparent horizon had formed, and treat the system as a perturbed or deformed single black hole spacetime. This is in essence the spirit of black hole perturbation theory, which I knew little about. The calculation

---

<sup>7</sup> In fact, the proposed systems are similar to those observed at the center of the Milky Way, where several stars are seen to orbit Sgr\*A.

of the perturbed metric of a spinning black hole discussed earlier is intrinsically different from the modeling of the merger phase with black hole perturbation theory. The main difference is that in the former one assumes the perturbations are slowly varying in time, such that we can essentially ignore the time evolution of the metric perturbations. In the latter case, one is precisely after this time evolution, which has to be solved for numerically. Sopuerta, however, is an expert on the subject and we thus tackled the project together.

The calculation begins by assuming the spacetime can be modeled by a background metric (in this case, a non-spinning black hole) plus an arbitrary perturbation. One then expands the perturbations in tensor spherical harmonics of axial and polar parity, such that the angular sector of the linearized Einstein equations is automatically satisfied. The temporal-radial sector of the field equations can be further decoupled harmonically to obtain two master equations (one for polar and one for axial modes) in terms of a master function, composed of the metric perturbation and its derivatives. These master equations, also known as the Regge-Wheeler and Zerilli-Moncrief equations, are wave-like partial differential equations on a non-flat background with a certain potential that is also background dependent.

Once the master equations are posed one must solve them numerically, provided some initial data is given. The numerical solution to these equations was carried out with a finite-element code that Sopuerta had previously developed. The numerical solution to the master equations can then be used to reconstruct the emitted waveforms, as well as the energy, angular and linear momentum radiated. The recoil velocity is then simply computed by integrating the momentum flux.

The most challenging part of this calculation was the prescription of initial data. We chose to prescribe this data in the so-called *close-limit* approximation, where the 3-metric is given by the Brill-Lindquist solution and the extrinsic curvature is of Bowen-York form (see Sec. 1.1.1). In the close-limit, however, one re-expands this data for small separations, so as to enforce the concept that the system can be described by a single perturbed black hole with a perturbed, common apparent horizon. Once one obtains close-limit expanded initial data, one must map this to initial conditions for the master equations, which among other steps involves a harmonic decomposition. With this initial data, one can then evolve the master equations numerically.

The method described above is appropriate to model the merger phase of a black hole binary, but it cannot model the inspiral phase. In order to remedy this, we used post-Newtonian theory to model the inspiral and its associated accumulated recoil, which was then added to the close-limit estimate. Unfortunately, the results were rather sensitive to where the merger phase was assumed to begin, which forced us to present only upper and lower limits on the possible value of the recoil. These limits, however, improved all of the then current bounds on the recoil velocity and narrowed the answer to a maximum between  $80 - 225 \text{ km s}^{-1}$ . Our results also suggested that Blanchet, *et. al.* overestimated the recoil, while Damour and Gopakumar [57] severely underestimated it. The suggested reason for this was that during the ringdown phase an *anti-kick* was present that damped down the final recoil velocity.

Numerical relativity followed shortly after, with several groups presenting accurate results of the kick velocity for several different systems, including non-spinning

black hole binaries [58]. Their results verified that our estimates were indeed correct: the maximum kick velocity was on the order of  $160 \text{ km s}^{-1}$ . Moreover, they verified that an anti-kick was indeed present in the ringdown phase.

The next step after modeling non-spinning mergers could have been to either model spinning black hole binaries or eccentric mergers. We decided to concentrate on the latter since the generalization to eccentric systems was much simpler than including spin in the merger phase. This generalization consists essentially of a rescaling of the initial momentum parameters to include eccentricity, which then simply rescales the final recoil velocity by a similar factor. We showed that the general effect of including eccentricity in the merger is to increase the recoil velocity by roughly a factor of order  $1+e$ , where  $e$  is the eccentricity of the system before merger. This is because the inclusion of eccentricity essentially increases the plunge velocity, forcing the binary components to merge more rapidly.

The next step could have been to model spinning binary black hole mergers, but this step proved dramatically more difficult. One of the main complications was the need to consider perturbations about a spinning black hole background. Such a study would then have required the use of the Teukolsky formalism, which has not been as developed in the close-limit approximation as the Regge-Wheeler/Zerilli-Moncrief scheme. Unfortunately, as we were beginning to think about this problem, the numerical relativity community produced several papers where the recoil velocity for spinning black hole binaries was presented for several different spin arrangements and mass ratios. Work on this topic then ceased and we concentrated on other astrophysical applications, one of which I shall discuss next.

### 1.2.3 Relativistic gravitational wave bursts

After our adventures in the calculation of the recoil velocity in the merger of binary black hole systems, I decided to investigate the prospect of other relativistic signatures in binary inspirals. By then Rubbo, Holley-Bockelmann and Finn had already proposed the existence of a new source of gravitational waves that could be detected by LISA: gravitational wave bursts. I then suggested to Rubbo and Holley-Bockelmann to revisit the problem but this time to include relativistic effects both in the orbital description as well as in the gravitational wave generation formalism, the results of which are presented in Chapter 10. The goal of this project was to investigate whether relativistic corrections could be observable if LISA detected a series of such gravitational wave bursts.

The first relativistic effect that we wished to include was that induced by the black hole nature of the central potential. In their first paper, Rubbo, *et. al.* modeled the central potential with purely Newtonian theory. Such a description, of course, not only neglects the steeper relativistic potential but also any possible spin effects. I thus proposed using the geodesic equations of motion to model the trajectories of the small particles around the central potential. These equations neglect radiation-reaction effects – that is, the effect of the small object’s self gravity on its own trajectory – but they do allow for the modeling of rotating and non-rotating black hole central potentials. We thus assumed that the geometry could be well-approximated by the metric of the supermassive black hole and pretended the smaller object was moving on this fixed

geometry. The result were trajectories that significantly deviated from that considered by Rubbo, *et. al.* , particularly when the central potential was allowed to spin. In all cases we found that orbital precession seemed to be the dominant difference relative to Newtonian orbits, and this precession effects depended strongly on the mass and spin parameter of the supermassive black hole.

The second relativistic effect we considered was the inclusion of higher multipole moments in the gravitational wave generation formalism. Rubbo, *et. al.* used the quadrupole formula to model gravitational waves, but in general relativity, these waves are given by an infinite sum over mass and current multipole moments [59]. We thus included the next order terms in the series, namely the current quadrupole and the mass octopole moments. We found that the inclusion of these corrections made a small difference in the waveforms for most orbits, except for those with very small pericenter distance (on the order of microparsecs).

Both the modeling of the orbital motion and the gravitational waves were carried out numerically. We used Sopena's geodesic integrator, which we modified to include the mass octopole and the current quadrupole in the wave generation. I then carried out a back of the envelope data analysis calculation investigating the Fourier transform of the waveforms and their cross-correlation assuming a nominal LISA spectral noise density. We found a significant dephasing between the Newtonian and relativistic models, related to precession. We thus, concluded that those astrophysical parameters that determine this precession and dephasing might be extractable from LISA data given a sufficiently high signal-to-noise ratio.

The analysis we presented, however, contains a large number of uncertainties that are difficult to model. The main problem was the fact that other parameters could mimic the dephasing effect that we observed. If this were the case, then it might not be possible to disentangle the spin from the effect of these other parameters, especially if only a few bursts are observed. A more formal and complete Fisher analysis would be required to determine whether relativistic astrophysical parameters can be extracted, given a gravitational wave burst observation with LISA.

## 1.3 Testing quantum gravity with gravitational waves

### 1.3.1 Background

Perhaps the most interesting application of gravitational wave theory to other areas of physics is that of testing alternative theories of gravity. This area has a long history, which I shall only summarize briefly (for a more complete review see [60]).

The first gravitational-wave tests concerned metric theories of gravity and were proposed by Eardley, *et. al.* [61, 62]. Roughly a decade later, this topic was revisited by Finn [63], and more recently by Cutler and Lindblom [64], who suggested a way to perform these measurements with observations of solar oscillations via space-borne detectors. Another decade went by until Ryan [65] proposed using the phase information from compact binary inspirals to test alternative theories of gravity in the strong field regime. Since then, there have been several proposals to place bounds on the graviton

Compton wavelength [66, 67, 68, 69, 70, 71] and the Brans-Dicke coupling parameter [72, 69, 70, 71], given a gravitational wave observation from inspiraling compact binaries.

Until now, however, no gravitational wave test of string theory or loop quantum gravity had been suggested. The main reason for this is that these theories are not formally complete, in the sense that their full action has not yet been calculated and agreed upon. Another reason is perhaps that the corrections these theories pose on the Einstein equations are expected to be Planck-suppressed, and thus, unobservable through weak-field manifestations of gravity. Gravitational waves, however, can be used to map the strong field regime of gravitational interactions, such as in binary black hole mergers. Thus, although in principle quantum gravitational corrections could be suppressed, there is an enhancement effect due to the non-linearity of spacetime that could push these corrections to the observable.

In 2006 Stephon Alexander joined the Penn State Physics faculty, bringing with him knowledge about string theory and anomalies in quantum field theories. In particular, he was excited about a new effective gravity theory: Chern-Simons gravity. This theory was proposed by Jackiw and Pi and it corrects the Einstein equations in a parity-violating way. Much of Alexander's excitement came from the fact that this theory had already been used to propose an explanation to the leptogenesis problem in the early universe [73, 74], as well as the polarization of the cosmic microwave background [75, 76, 77].

Due to my undergraduate background, it seemed I was the perfect candidate to work on tests of Chern-Simons gravity. During my undergraduate days, I had studied under Clifford Will, one of the world experts in tests of alternative theories of gravity. In fact, as part of my undergraduate studies I had worked with Will on tests of massive graviton theories and Brans-Dicke theory through gravitational wave observations with LISA. I decided then to collaborate with Alexander, a collaboration that eventually led to the publication of four different papers, which are discussed in the last four chapters of this thesis.

### 1.3.2 Chern-Simons gravity

One of the problems with tests of string theory is that there is not just one string theory but actually several different flavors, each of which advocates a slightly different form for the action. In recent years, however, Alexander and Gates [74] have shown that all flavors of string theory *require* a certain correction to the Einstein-Hilbert action in the low-energy limit. This correction consists of the addition of the product of a scalar field with a Pontryagin term, which is essentially the wedge product of Riemann tensors. The sum of the Einstein-Hilbert action and this product of scalar field and Pontryagin term define Chern-Simons gravity.

The Chern-Simons term arises naturally in quantum gravity. In the string theoretical framework, this correction is required as an anomaly-canceling term through the Green-Schwarz mechanism. Without it, string theory loses unitarity, and thus, would be mathematically ill-defined (in the sense that probabilities associated with observables would not necessarily be positive definite). In loop quantum gravity, the Chern-Simons correction encodes information about the so-called Immirzi parameter, which is related to

area quantization. Within this framework, the Chern-Simons correction is also *required* to guarantee invariance under large gauge transformations [78].

The main physical effect of this correction is to introduce parity-violation in the solutions to the modified field equations. This violation arises due to the appearance of the Levi-Civita tensor through the wedge product operator in the action. It is then not too surprising that Chern-Simons gravity leads to a polarization of the cosmic microwave background and to an asymmetry in the propagation of left- and right-polarized gravitational waves (an asymmetry that was in fact used to propose an explanation to the leptogenesis problem in the early universe).

Chern-Simons gravity has a long and complicated history as well. The modern formulation of this effective gravity theory was proposed by Jackiw and Pi [79]. Not only did they propose this generalization of general relativity (without actually knowing that it represented the low-energy limit of quantum gravity), but they also investigated some of its consequences, such as the persistence of certain black hole solutions and the propagation of gravitational waves. Jackiw and Pi found that indeed left- and right-polarized waves obey different wave equations in the modified theory that forces them to have different amplitudes, although their velocities remain that of light<sup>8</sup>.

Until 2006 nobody had investigated whether this extension of general relativity could be detected with gravitational experiments. When I first looked at the action, the Levi-Civita tensor and the Riemann squared term immediately told me that strong amplitude birefringence would plague gravitational wave generation and propagation in the modified theory. Moreover, due to my recent experience with the merger of binary black hole systems, it seemed natural that such systems would be excellent probes. I thus embarked on a journey across everything that was Chern-Simons, as I shall describe in the next subsection.

### 1.3.3 Can we probe quantum gravity?

The first obvious step toward investigating the testability of Chern-Simons gravity was the use of current gravitational experiments: solar system tests. Although these tests sample the weak gravitational regime of the theory, I had hopes that certain gravitomagnetic experiments would be able to bound, at least weakly, the modified theory.

Solar system tests were familiar to me from my experience at Washington University, where Will lectured us on several occasions about the parameterized post-Newtonian framework. This framework was developed in the 1970s, when several alternative theories of gravity had been proposed, including scalar-tensor theories and vector-tensor theories. Will and Nordtvedt [80, 81] developed this framework in such a way so as to facilitate the testing of all available alternative theories simultaneously with solar system experiments (for a complete review of parameterized post-Newtonian theory see [82]).

The parameterized post-Newtonian scheme consists of two parts, which can be briefly described as follows. Given a certain alternative theory of gravity, the first part

---

<sup>8</sup>In fact, the term “birefringence” is technically incorrect in this context since it implies that different polarizations possess different group velocities. In Chern-Simons gravity, however, it is the imaginary part of the dispersion relation that is modified, thus leading to a different amplitude for left- and right-polarized modes.

consists of expanding the modified field equations in the weak field and in the slow-motion approximation (thus, the name post-Newtonian). One then solves the linearized, modified field equations in terms of certain potentials, that consist of Green function-like integrals. The second part consists of constructing a family of metrics in terms of these potentials, but parameterized by certain constants. These parameters modify the traditional predictions of general relativity, such as the bending of light and the precession of the perihelium of Mercury, and thus, they can be used to distinguish between general relativity and other alternative theories. One then compares this family of metrics to the weak-field solution found and determines the parameters of the theory under consideration. Experiments can then simply measure these parameters, thus testing several theories simultaneously.

Chapter 9 (written with Alexander) applies this procedure to Chern-Simons gravity and finds that the modified theory introduces a correction to precession in the weak field. This correction requires a new parameterized post-Newtonian parameter that had not been previously considered. The immediate consequence of such a correction is the modification of Lense-Thirring precession. Thus, experiments, that measure the angular velocity of precession of gyroscopes in Earth's orbit, such as Gravity Probe B, would be able to test Chern-Simons gravity. Our work constitutes the first proposal to experimentally test Chern-Simons gravity through solar system experiments. In fact, shortly after the publication of our work, Smith, *et. al.* [83] extended our analysis and compared their results to experimental data, indeed placing the first bounds on the Chern-Simons coupling parameter.

Solar system experiments, however, cannot be the best probes of Chern-Simons gravity, since they only sample the weak field. My interests then shifted to strong field tests of the theory, through gravitational wave observations. Before carrying out this analysis, however, I wished to study two missing components of the modified theory: the absence of a spinning black hole solution and the issue of perturbations of non-spinning black holes.

From the work of Jackiw and Pi, it was known that the Kerr metric, which represents the exterior gravitational field of spinning black holes in general relativity, is not a solution to the modified field equations in Chern-Simons gravity. Chapter 10 (written with Daniel Grumiller) studies this issue further, finding that stationary and axisymmetric line elements cannot generally solve the modified field equations. Such a result is consistent with the previous weak-field analysis, where we found that Chern-Simons gravity naturally induces a gravitomagnetic metric component that modifies Lense-Thirring precession. Our results suggest that Chern-Simons gravity requires a non-vanishing gravitomagnetic component, which would then imply that the spinning black hole does not rotate about a fixed axis, but precesses about some other axis probably defined by some combination of the black hole's spin angular momentum and a Chern-Simons contribution.

While carrying out this analysis of exact solutions in Chern-Simons gravity, I also studied perturbed black hole in the modified theory. This problem was suggested to me by Poisson and later by Pullin, while visiting Sopena at the University of Guelph. In particular, Pullin seemed interested in what the Chern-Simons correction would do to the merger and ringdown of black hole binaries in the close-limit approximation.

Clearly, during the merger phase the Chern-Simons correction should dominate over the Einstein-Hilbert term, since it is quadratic in the Riemann tensor. Chapter 11 (written with Sopuerta) describes black hole perturbation theory on a non-spinning black hole background for Chern-Simons gravity. We found that perturbation theory in canonical Chern-Simons gravity (when the scalar field is treated as a background field) is not mathematically consistent. In other words, perturbation theory demands that Chern-Simons gravity accounts for the dynamical behavior of the scalar field coupling. In that case, we find that certain parity modes are greatly suppressed, possibly leading to a signature in the gravitational waves produced during the ringdown phase of a binary merger.

Once this projects were completed, I focused all my attention in gravitational wave tests of Chern-Simons gravity, discussed in Chapter 11 (written with Alexander and Finn). As expected, gravitational waves are corrected in the modified theory, leading to left- and right-polarized waves with different amplitudes. This amplitude difference is proportional to the frequency of the wave and to some power of the redshift, thus possibly rendering it detectable with LISA for binary black hole inspirals. We performed a back-of-the-envelope calculation to determine the level to which the modified theory could be tested through gravitational wave observations. Our conservative estimates suggest that such tests could lead to at least an order of magnitude enhancement on the bound on the Chern-Simons coupling parameter relative to solar systems bounds.

The analysis presented here, however, completely neglects the merger phase of the binary, where the Chern-Simons correction should be the largest. Such a phase can only be accurately modeled through numerical simulations. I plan to continue studying these systems in the merger regime, in the hopes of determining whether gravitational wave tests could lead to even stronger tests. Another avenue of possible future research concerns tests of Chern-Simons gravity with earth-based detectors. Until now, such tests have been neglected, because the data analysis problem for neutron star-black hole inspirals could possibly be more difficult. Earth-based detectors, however, operate in a higher frequency band, thus leading to a stronger correction during gravitational wave propagation. Hopefully, the efforts presented here to test quantum gravity, and those which will follow, will aid in the construction of full quantum gravitational framework.

**PART A:**  
**MODELING OF COMPACT BINARIES**

## Chapter 2

# Binary black hole initial data from matched asymptotic expansions

We present an approximate metric for a binary black hole spacetime to construct initial data for numerical relativity. This metric is obtained by asymptotically matching a post-Newtonian metric for a binary system to a perturbed Schwarzschild metric for each hole. In the *inner zone* near each hole, the metric is given by the Schwarzschild solution plus a quadrupolar perturbation corresponding to an external tidal gravitational field. In the *near zone*, well outside each black hole but less than a reduced wavelength from the center of mass of the binary, the metric is given by a post-Newtonian expansion including the lowest-order deviations from flat spacetime. When the near zone overlaps each inner zone in a *buffer zone*, the post-Newtonian and perturbed Schwarzschild metrics can be asymptotically matched to each other. By demanding matching (over a 4-volume in the buffer zone) rather than patching (choosing a particular 2-surface in the buffer zone), we guarantee that the errors are small in all zones. The resulting piecewise metric is made formally  $C^\infty$  with smooth transition functions so as to obtain the finite extrinsic curvature of a 3-slice. In addition to the metric and extrinsic curvature, we present explicit results for the lapse and the shift, which can be used as initial data for numerical simulations. This initial data is not accurate all the way to the asymptotically flat ends inside each hole, and therefore must be used with evolution codes which employ black hole excision rather than puncture methods. This paper lays the foundations of a method that can be straightforwardly iterated to obtain initial data to higher perturbative order.

### 2.1 Introduction

The simulation of binary black-hole systems is of fundamental physical interest as the purely general relativistic two-body problem<sup>1</sup>. It is also of astrophysical interest, since accurate simulations of the late inspiral and merger phases of such binaries will considerably help the effort to detect the gravitational-wave signals and extract information from them [9]. Simulation reduces to the numerical solution of the Cauchy problem: take some initial data and evolve it. The evolution is difficult for many reasons, although

---

<sup>1</sup>This chapter is based on the following paper: N. Yunes, W. Tichy, B. J. Owen and B. Bruegmann, Phys. Rev. D **74**, 104011 (2006)

in recent years there has been much progress. Still, any evolution is only as good as its initial data.

A key issue of initial data is astrophysical realism. The goal is to compute data on a hypersurface that represents one moment in time of an astrophysical inspiral of two black holes. If such an inspiral is defined by initial conditions in the distant past for widely separated black holes, then the only way to obtain the exact data at a later time would be to perform the actual evolution using the full Einstein equations. This procedure, however, is computationally expensive and thus impractical. On the other hand, several schemes have been developed to pose initial data that approximates the astrophysical situation at a given time. These schemes are typically either based on post-Newtonian (PN) methods or on the numerical solution of the constraint equations of relativity.

For example, the literature provides many types of initial data for black holes in approximately circular orbits [84, 23, 85, 24, 18, 86, 87, 88, 16, 89, 90, 91, 92] that satisfy the constraints of the Einstein equations. To obtain such data, certain assumptions are made, such as conformal flatness and quasi-circularity. These assumptions are expected to be good approximations within a certain error, although the astrophysical metric after a long inspiral is known to be not exactly conformally flat and the orbit not perfectly circular.

In this paper we consider a post-Newtonian method combined with black hole perturbation theory to construct approximate inspiral initial data. For large to intermediate separations of compact objects, an astrophysically relevant approximate spacetime can be obtained far from the black holes by analytical post-Newtonian and post-Minkowskian methods [3]. One advantage of such methods is that they allow systematic improvements through higher order expansions (compared to numerical constraint solving schemes which typically include only the correct lowest order PN behavior). In their regime of validity, PN methods do result in appropriate deviations from conformal flatness and in non-circular inspiral orbits. The main disadvantage of PN methods is that, by construction, they are generally believed to fail in the final phase of the inspiral for fast moving objects, and also close to non-pointlike objects with horizons. On the other hand, black hole perturbation theory provides an accurate spacetime in a region of the manifold sufficiently close to the background black hole. The main disadvantage of this theory is that it fails sufficiently far from the background hole and, thus, cannot provide information about the dynamics of the entire spacetime.

In what follows, we take a concrete step toward combining PN theory with black hole perturbation theory using the mathematical machinery of asymptotic matching. The method maintains the potential for systematic improvement through higher order expansions, although we only work at low order here [93, 39]. From the PN approach the method inherits its astrophysical justification, *i.e.* that for sufficient separation between the holes the method will yield metric components that are correct up to uncontrolled remainders of certain orders. The uncontrolled remainders in the metric components have different effects on different quantities, and it is of interest to see how other quantities such as the binding energy compare to those of other initial data sets in the literature. This question is beyond the scope of this article, but should be addressed in the future.

Concretely, we have to discuss how black holes are incorporated in our approach. While formally PN methods assume slow motion and weak internal gravity of the sources, it has been shown that the results hold as well for objects such as black holes with strong internal gravity [94] as long as one is not too close to these objects. Near each black hole, a tidally perturbed Schwarzschild or Kerr spacetime provides another analytical approximation. Given that different approximate metrics can be constructed from different scale expansions, it is natural to try the method of matched asymptotic expansions [30]. If there is an overlap region (also known as a buffer zone) where both approximations (post-Newtonian and tidal perturbation) are valid, a diffeomorphism can be constructed between charts used in different regions of the manifold by different approximation schemes. Matching—demanding that both approximation schemes have the same asymptotic form in the overlap region—relates physical observables in the different regions, *i.e.* ensures that both expansions represent the same physical system.

The first attempt to construct initial data in such a way was by Alvi [28]. By construction, there are discontinuities in the data, which were found to be too large for numerical experiments [32]. Alvi’s fundamental problem was that, in the terminology of textbooks such as Bender’s [30], he did not *match* (construct expansions asymptotic to each other everywhere in the overlap region) but rather *patched* (set approximate solutions to the Einstein equations equal to each other on specified 2-surfaces) so that large errors in the extrinsic curvature were possible. Alvi’s Table I shows that his spatial metric near the black holes is discontinuous apart from the Minkowski terms (independent of  $G$ ) in either region. Such discontinuities are problematic for numerical relativity, since part of the initial data is the extrinsic curvature which includes derivatives of the spacetime metric. Smoothing can be attempted, for example with transition functions as in Alvi’s next paper [29], but it is not trivial to implement—especially with such large discontinuities—without adding unphysical content to the initial data. There is also the issue of making sure that the initial data slicing is treated consistently in the various expansions, which Alvi addressed to some extent but did not always make explicit his assumptions. Finally, there was a problem with the accuracy to which Alvi calculated metric components. Construction of the extrinsic curvature requires terms in the expansions that Alvi did not calculate because he assumed (incorrectly) that the counting of orders follows the standard pattern used in deriving post-Newtonian equations of motion.

The main point of this paper is that we are able to correct the mathematical problems with Alvi’s approach, and that we provide initial data for actual numerical evolutions. We use true asymptotic matching to construct a piecewise metric for two black holes in circular orbit, including terms of order the gravitational constant  $G$  on the diagonal of the metric and  $O(G)^{3/2}$  off the diagonal. We then remove the piecewise nature of the approximate metric by “merging” or “smoothing” the solutions in the buffer zones, thus generating a uniform approximate metric. We do this by constructing smooth transition functions so that the uniform approximate solution is in principle  $C^\infty$ , although in practice higher-order derivatives will be less accurate than lower-order ones. These transition functions are carefully constructed to avoid introducing errors in the smoothed global metric larger than those already contained in the approximate solutions. This metric allows for the calculation of the lapse to  $O(G)$ , the shift to  $O(G)^{3/2}$ , and the extrinsic curvature to  $O(G)^{3/2}$ . Although this data contains only the first order

deviations from flat spacetime, our approach does include the tidal perturbations near the black holes. Strictly speaking, these tidal perturbations are valid only near the horizons—our approach cannot model the asymptotically flat ends inside the holes and therefore must be used in numerical evolutions with excision rather than punctures. Our formalism can be extended to higher order by including more precise post-Newtonian [12] and black hole perturbation theory results [95] already in the literature.

By construction, our initial data satisfies the constraints only up to uncontrolled remainders of a certain order. Therefore, this data may still need to be projected to the constraint hypersurface via a conformal decomposition. One avenue worth exploring is that since the constraint violations are  $O(G)^{3/2}$  or smaller, it may be possible to find a constraint projection algorithm that changes the physical content of our initial data only at a comparably small order. In this manner, the formalism presented here can potentially be used to construct extremely accurate background data for constraint solving. This hybrid combination of an accurate background 4-metric plus constraint solving might potentially lead to very astrophysically realistic initial data, which then could be compared and tested against other sets already in the literature.

This paper is organized as follows: Sec. 2.2 describes the method of asymptotic matching as applicable to this problem. Sec. 2.3 discusses the near zone expansion of the metric and determines its asymptotic expansion in the overlap region. Sec. 2.4 concentrates on the inner zone expansion of the metric and expands it asymptotically in the overlap region. Sec. 2.5 applies asymptotic matching to the metrics to obtain matching relations between expansion coefficients and a map that relates the charts used in the different regions. Sec. 2.6 constructs the global metric, discusses its properties, and builds transition functions to eliminate discontinuities between local approximations. Sec. 2.7 computes the extrinsic curvature, lapse and shift. Sec. 2.8 concludes and points toward future research.

Throughout this paper we use geometrized units ( $G = c = 1$ ) and we have relied heavily on symbolic manipulation software, such as MAPLE and MATHEMATICA. We use the tilde as a relational symbol such that  $a \sim b$  means “ $a$  is asymptotic to  $b$ ” [30]. When we refer to our results as “global,” we mean that they cover the region of most interest to numerical relativity. Strictly speaking, our results do not cover the radiation zone (further from the binary than a reduced wavelength) or the asymptotically flat ends inside the holes. However, obtaining the radiation-zone solution and matching it to the near-zone solution is a solved problem [3] and the asymptotic ends inside the holes can be removed with excision before numerically evolving the initial data.

## 2.2 Approximation regions and precision

Let us now consider a binary black hole spacetime, with holes of mass  $m_1$  and  $m_2$ , total mass  $m = m_1 + m_2$  and spatial coordinate separation  $b$ . The manifold (Fig. 2.1) can be divided into 4 submanifolds, the boundaries of which cannot be determined precisely due to the presence of uncontrolled remainders in black hole perturbation theory (BHPT) and post-Newtonian (PN) asymptotic series. Nonetheless, an approximate subdivision is possible and we make one as follows:

1. **The inner zone of Black Hole 1**, (submanifold  $\mathcal{C}_1$ ):  $R_1 \ll b$ , where  $R_A$  is the distance from the  $A$ th black hole in isotropic coordinates. In this region, the metric is obtained via black hole perturbation theory as an expansion in  $\epsilon_{(1)} = R_1/b$ . [28, 94].
2. **The inner zone of Black hole 2**, (submanifold  $\mathcal{C}_2$ ):  $R_2 \ll b$ , where the metric is obtained in the same manner as in region  $\mathcal{C}_1$  but with labels 1 and 2 swapped.
3. **The near zone**, (submanifold  $\mathcal{C}_3$ ):  $r_A \gg m_A$  and  $r \leq \lambda/2\pi$ , where  $\lambda$  is the wavelength of gravitational radiation,  $r$  is the distance from the binary center of mass in harmonic coordinates, and  $r_A - m_A$  is the separation in harmonic coordinates from the horizon of the  $A$ th black hole. In this region, a post-Newtonian approximation is used for the metric with an expansion parameter  $\epsilon_{(3)} = m_A/r_A$  [3] which is formally treated as the same order for both values of  $A$ .
4. **The far zone**, (submanifold  $\mathcal{C}_4$ ):  $r \geq \lambda/2\pi$ , where the metric is obtained from a post-Minkowski calculation [96].

These zones are shown schematically in Fig. 2.1, projected onto the orbital plane. In these figures, the near zone is shown in dark gray, the inner zones in light gray and the buffer zones in a checkered pattern. The holes' horizons are denoted by black solid lines, while the dashed black lines are the excision boundaries.

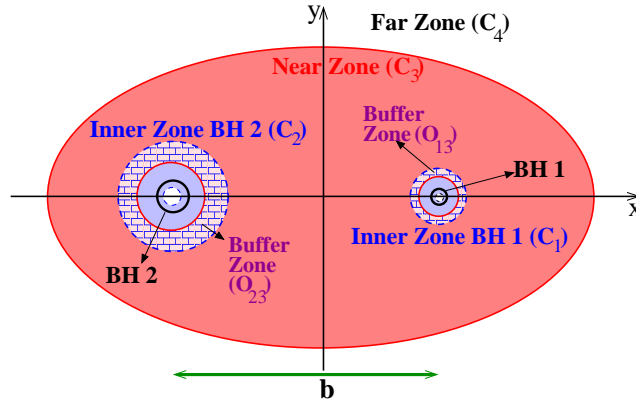


Fig. 2.1. Schematic diagram of the near zone (dark gray), inner zones (light gray) and buffer zones (checkered) projected onto the orbital plane. The black holes' horizons are shown by solid black lines, while the excision boundaries are shown by dashed black lines. The near zone overlaps the inner zone of each black hole, and these overlap regions are the buffer zones (checkered patterns.) The boundaries of all zones are somewhat imprecise since they are based on power series approximations, but the buffer zones are roughly spherical shells shown in this Figure as annuli.

The manifold is subdivided in such a way so that approximate solutions to the Einstein equations can be found in each region. These approximate solutions will depend on certain coordinates and parameters local only to that region. The near zone metric,  $g_{\mu\nu}^{(3)}$ , is an expansion in  $\epsilon_{(3)} \equiv m/r \ll 1$ , which depends on harmonic coordinates  $x^\mu$  and parameters, such as the masses  $m_A$  of the holes and the angular velocity  $\omega$  of the system. Similarly, the metric in inner zone 1 (or 2),  $h_{\bar{\mu}\bar{\nu}}^{(1)}$  (or  $h_{\bar{\mu}\bar{\nu}}^{(2)}$ ), is an expansion in  $\epsilon_{(1)} \equiv r_1/b \ll 1$  (or  $\epsilon_{(2)} \equiv r_2/b \ll 1$ ), which depends on isotropic coordinates  $x^{\bar{\mu}}$  and certain parameters, such as the mass of the background hole  $M$  and the angular velocity  $\Omega$  of the tidal perturbation. The parameters and the coordinates used in different regions are not identical and are valid only inside their respective regions, although those regions overlap.

A global metric can be obtained by relating the different approximate solutions through asymptotic matching. The theory of matched asymptotic expansions was first developed to perform multiple scale analysis on non-linear partial differential equations and to obtain global approximate solutions [30]. In general relativity, this method was first applied by Burke and Thorne [97], Burke [98], and D'Eath [99, 100] in the 1970s to derive corrections to the laws of motion due to coupling of the body's motion to the geometry of the surrounding spacetime. Based on these ideas, in this paper we will develop a version of the theory of matched asymptotics that is useful to obtain initial data for numerical relativity simulations.

Asymptotic matching consists of relating different approximate solutions inside a common region of validity. This region is usually called the buffer zone by relativists, but is called the overlap region by others. For a binary there exists three such regions, which are 4-volumes: Two buffer zones ( $\mathcal{O}_{13}$  and  $\mathcal{O}_{23}$ ) are defined by the intersection of the near zone and the inner zones of black hole 1 and 2; the third one is defined by the intersection of the near zone and the radiation zone ( $\mathcal{O}_{34}$ ). The former two, shown in Fig. 2.1 in a checkered pattern, are defined by the asymptotic condition  $m_A \ll r_A \ll b$ . The latter has been analyzed in Ref. [3] and will not be discussed here. In this paper we perform asymptotic matching in the former two buffer zones  $\mathcal{O}_{13}$  and  $\mathcal{O}_{23}$ . In order for our tidal perturbations in the inner zones to be valid, the inner zones  $\mathcal{C}_1$  and  $\mathcal{C}_2$  cannot overlap.

Once a buffer zone has been found, asymptotic matching can be used to relate adjacent approximate solutions. The first step is to find the asymptotic expansions of the approximate solutions inside the buffer zones. These approximate solutions depend on the expansion parameters,  $\epsilon_{(1)}$ ,  $\epsilon_{(2)}$  and  $\epsilon_{(3)}$ , which are small only in their respective regions of validity  $\mathcal{C}_1$ ,  $\mathcal{C}_2$ , and  $\mathcal{C}_3$ . By definition, in each overlap region both expansion parameters are small, specifically  $\epsilon_{(1)} \ll 1$  and  $\epsilon_{(3)} \ll 1$  in  $\mathcal{O}_{13}$ , while  $\epsilon_{(2)} \ll 1$  and  $\epsilon_{(3)} \ll 1$  in  $\mathcal{O}_{23}$ . Inside buffer zone 1, for example, we can then asymptotically expand the near zone solution in  $\epsilon_{(1)} \ll 1$  to obtain  $\tilde{g}_{\mu\nu}^{(3)}$  and the inner zone solution in  $\epsilon_{(3)} \ll 1$  to obtain  $\tilde{h}_{\bar{\mu}\bar{\nu}}^{(1)}$ . These asymptotic expansions of approximate solutions are naturally bivariate since they depend on two *independent* expansion parameters. When working with these bivariate expansions, we use the symbol  $O(p, q)$  both to denote terms of order  $(m/b)^p (r_A/b)^q$  and uncontrolled remainders of order  $(m/b)^p$  or  $(r_A/b)^q$ . Relating

adjacent approximations then reduces to imposing the asymptotic matching condition

$$\tilde{g}_{\mu\nu}^{(3)} \sim \tilde{h}_{\bar{\mu}\bar{\nu}} \frac{\partial x^{\bar{\mu}}}{\partial x^\mu} \frac{\partial x^{\bar{\nu}}}{\partial x^\nu}. \quad (2.1)$$

This expression means not that the two approximate solutions are equated, which is correctly called “patching,” but rather that all coefficients of all controlled terms in the bivariate expansions are equated.

After imposing the asymptotic matching condition, one obtains a coordinate and parameter transformation between the near zone and the inner zone 1 in  $\mathcal{O}_{13}$  (and similarly in  $\mathcal{O}_{23}$ .) These transformations allow for the construction of a global piecewise metric, which is guaranteed to be asymptotically smooth in the buffer zone up to uncontrolled remainders in the matching scheme. Asymptotic smoothness here means that adjacent pieces of the piecewise global metric and all of their derivatives are asymptotic to each other inside the buffer zones. This asymptotic smoothness, however, does not rule out small discontinuities on the order of the uncontrolled remainders in the approximations, when we pass from one approximation to the other. The global metric can be made formally  $C^\infty$  by smoothing over these discontinuities, which introduces a new error into the solution. Asymptotic smoothness, however, guarantees that this error will be smaller than or equal to that already contained in the uncontrolled remainders of the approximations, provided the smoothing functions are sufficiently well-behaved.

Finally, we enumerate the orders of approximation used in the near zone. The Einstein equations are guaranteed to generate a well-posed initial value problem for globally hyperbolic spacetimes [9], where the initial data could consist of the extrinsic curvature  $K_{ij}$  and the spatial 3-metric  $\gamma_{ij} = g_{ij}$ . We can write the extrinsic curvature in the form

$$K_{ij} = \frac{1}{2\alpha} \left( 2D_{(i}\beta_{j)} - \partial_t \gamma_{ij} \right), \quad (2.2)$$

where  $\beta_i = g_{0i}$  is the shift vector and  $\alpha$  is the lapse. Time derivatives are smaller than spatial derivatives by a characteristic velocity, which by the virial theorem is  $O(m/b)^{1/2}$ . Therefore to compute  $K_{ij}$  consistently to a given order in  $m/b$ , the 4-metric components  $g_{0i}$  are needed to  $O(m/b)^{1/2}$  beyond the highest order in  $g_{ij}$  (and  $g_{00}$ , which appears in  $\alpha$ ). In this paper we compute the first two nonzero contributions to the 3-metric and extrinsic curvature, *i.e.* the leading order terms and the lowest-order corrections. This means that we need the 4-metric components  $g_{00}$  and  $g_{ij}$  to  $O(m/b)$ , but we need  $g_{0i}$  to  $O(m/b)^{3/2}$ . Note that this does not correspond to any standard post-Newtonian order counting or nomenclature, which is why we quote precisions and remainders precisely in terms of expansion parameters rather than in ambiguous terms such as “*n*th PN”. The standard post-Newtonian order counting corresponds to the calculation of the equations of motion for spinless bodies, but the counting must be altered when studying other problems, such as the bending of light or the equations of motion for bodies with spin [33].

### 2.3 Near zone metric

In this section, we present the post-Newtonian (PN) metric in the near zone  $\mathcal{C}_3$  and expand it in the overlap region  $\mathcal{O}_{13}$ , the buffer zone where the inner zone  $\mathcal{C}_1$  of BH1 and the near zone overlap. When performing the matching in Sec. 2.5, we will obtain the corresponding expansion in the other overlap region  $\mathcal{O}_{23}$  by a simple symmetry transformation.

We use harmonic corotating coordinates  $(t, x, y, z)$  rotating around the center of mass such that

$$\begin{aligned} t' &= t, \\ x' &= x \cos \omega t - y \sin \omega t, \\ y' &= x \sin \omega t + y \cos \omega t, \\ z' &= z, \end{aligned} \tag{2.3}$$

where primed coordinates are nonrotating. The near-zone metric takes the form [101]

$$\begin{aligned} g_{00}^{(3)} &\approx -1 + \frac{2m_1}{r_1} + \frac{2m_2}{r_2} + \omega^2(x^2 + y^2), \\ g_{01}^{(3)} &\approx -y \omega \left(1 + \frac{2m_1}{r_1}\right), \\ g_{02}^{(3)} &\approx x \omega \left(1 + \frac{2m_1}{r_1}\right) - 4\mu b \omega \left(\frac{1}{r_1} - \frac{1}{r_2}\right), \\ g_{ij}^{(3)} &\approx \delta_{ij} \left(1 + \frac{2m_1}{r_1} + \frac{2m_2}{r_2}\right), \end{aligned} \tag{2.4}$$

where all remainders are at least  $O(m/r)^2$  and the superscript reminds us we are working on submanifold  $\mathcal{C}_3$ . Here

$$\begin{aligned} r_1 &= \sqrt{x_1^2 + y^2 + z^2} = \sqrt{(x - m_2 b/m)^2 + y^2 + z^2}, \\ r_2 &= \sqrt{x_2^2 + y^2 + z^2} = \sqrt{(x + m_1 b/m)^2 + y^2 + z^2} \end{aligned} \tag{2.5}$$

are the usual harmonic radial coordinates centered on black holes 1 and 2 and  $b$  is the separation between holes. Implicit in this metric is the assumption that  $r_A$  (for  $A = 1, 2$ ) is of order  $b$ , or in other words that the field point is not too close to one of the holes. (Recall that, in harmonic coordinates, the horizons are at  $r_A = m_A$  if we neglect tidal deformations.) We do not include the  $O(m/r)^2$  terms in  $g_{00}$  in what is commonly called the first post-Newtonian (1PN) metric and we do include  $O(m/r)^{3/2}$  terms in  $g_{0i}$  for reasons discussed at the end of Sec. 2.2. In Eq. (2.4) it is sufficient to use the first post-Newtonian approximation

$$\omega = \sqrt{\frac{m}{b^3}} \left[ 1 - \frac{1}{2} \left( 3 - \frac{\mu}{m} \right) \frac{m}{b} + O\left(\frac{m}{b}\right)^2 \right], \tag{2.6}$$

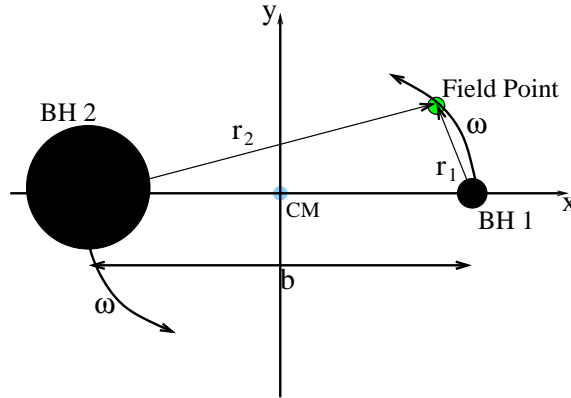


Fig. 2.2. Diagram of the near zone coordinate system used for the post-Newtonian metric in harmonic coordinates. The  $z$  axis is chosen parallel to the orbital angular momentum of the binary, so that the black holes orbit counter-clockwise here with angular velocity  $\omega$ . The origin is chosen to be the center of mass, while  $r_1$  and  $r_2$  denote the coordinate separations of the field point from hole 1 and 2 respectively. The coordinate separation between the holes is  $b$ .

to the angular velocity, where  $\mu = m_1 m_2 / (m_1 + m_2)$  is the reduced mass of the binary. Our choice of sign corresponds to coordinates in which the orbital angular momentum is in the positive  $z$  direction, as shown in Fig. 2.2.

We now concentrate on the overlap region (buffer zone)  $\mathcal{O}_{13}$ . Inside  $\mathcal{O}_{13}$  we expand  $1/r_2$  as a power series in  $r_1$  as

$$\frac{1}{r_2} = \frac{1}{b} \sum_{n=0}^{\infty} (-1)^n \left(\frac{r_1}{b}\right)^n P_n\left(\frac{x_1}{r_1}\right), \quad (2.7)$$

where the  $P_n$  are Legendre polynomials. Substituting into Eq. (2.4), we obtain

$$\begin{aligned}
\tilde{g}_{00}^{(3)} &\sim -1 + \frac{2m_1}{r_1} + \frac{2m_2}{b} \left[ 1 - \frac{r_1}{b} P_1 \left( \frac{x_1}{r_1} \right) + \left( \frac{r_1}{b} \right)^2 P_2 \left( \frac{x_1}{r_1} \right) \right] + \omega^2 (x^2 + y^2), \\
\tilde{g}_{01}^{(3)} &\sim -y \omega \left\{ 1 + \frac{2m_1}{r_1} + \frac{2m_2}{b} \left[ 1 - \frac{r_1}{b} P_1 \left( \frac{x_1}{r_1} \right) \right] \right\}, \\
\tilde{g}_{02}^{(3)} &\sim x \omega \left\{ 1 + \frac{2m_1}{r_1} + \frac{2m_2}{b} \left[ 1 - \frac{r_1}{b} P_1 \left( \frac{x_1}{r_1} \right) \right] \right\} - 4\mu b \omega \left\{ \frac{1}{r_1} - \frac{1}{b} \left[ 1 - \frac{r_1}{b} P_1 \left( \frac{x_1}{r_1} \right) \right. \right. \\
&\quad \left. \left. + \left( \frac{r_1}{b} \right)^2 P_2 \left( \frac{x_1}{r_1} \right) \right] \right\}, \\
\tilde{g}_{03}^{(3)} &\sim O(2, 3), \\
\tilde{g}_{ij}^{(3)} &\sim \delta_{ij} \left\{ 1 + \frac{2m_1}{r_1} + \frac{2m_2}{b} \left[ 1 - \frac{r_1}{b} P_1 \left( \frac{x_1}{r_1} \right) + \left( \frac{r_1}{b} \right)^2 P_2 \left( \frac{x_1}{r_1} \right) \right] \right\}, \tag{2.8}
\end{aligned}$$

where all errors are of order  $O(2, 3)$  and where  $m_1 \ll r_1 \ll b$ . The metric (2.8), denoted with a tilde, is the asymptotic expansion in the inner zone of BH1 of the PN metric, which is already an asymptotic expansion in the near zone.

Observe that these expansions constitute a series within a series (bivariate series). In order to see this more clearly, we can rearrange the spatial metric to get

$$\tilde{g}_{ij}^{(3)} \sim \delta_{ij} \left( 1 + \frac{2m_1}{r_1} \left\{ 1 + \frac{m_2 r_1}{m_1 b} \left[ 1 - \frac{r_1}{b} P_1 \left( \frac{x_1}{r_1} \right) + \left( \frac{r_1}{b} \right)^2 P_2 \left( \frac{x_1}{r_1} \right) \right] \right\} \right). \tag{2.9}$$

Equation (2.9) is a generalized Frobenius series [102], where the expansion is about the regular singular points  $r_1 = 0$  and  $r_1 = \infty$ . There are clearly two independent perturbation parameters, namely  $\epsilon_{(3)} = m_1/r_1$  (the usual PN expansion parameter used in  $\mathcal{C}_3$ ) and  $\epsilon_{(1)} = r_1/b$  (a tidal perturbation parameter used in  $\mathcal{C}_\infty$ ). In the overlap region  $\mathcal{O}_{13}$  we can expand in both.

## 2.4 Inner zone metric

In this section we discuss the metric in the inner zone  $\mathcal{C}_1$  of BH1 and its asymptotic expansion in the overlap region  $\mathcal{O}_{13}$ .

Physically, we expect the spacetime in the inner zone of BH1 to be Schwarzschild with mass  $M_1$  plus a tidal perturbation due to BH2. Thorne and Hartle [94] argue that, in the local asymptotic rest frame (LARF) of BH1, the metric can be expanded in powers of  $M_1$  outside the horizon of BH1. The first term, independent of  $M_1$ , can be taken to represent the external universe and thus can be computed by placing a test particle in the spacetime of BH2 as done by Alvi [28]. This is the tidal perturbation due to BH2. Terms of higher order in  $M_1$  describe BH1 itself (the Schwarzschild metric) and interactions between BH1 and BH2 (tidally-induced quadrupole, etc). At the level of approximation of this paper, we can neglect the interaction terms because they are  $O(2, 1)$  or higher.

Alvi identifies LARF coordinates, in terms of which the tidal perturbation is obtained, with isotropic coordinates (Fig. 2.3). Observe that this coordinate system is

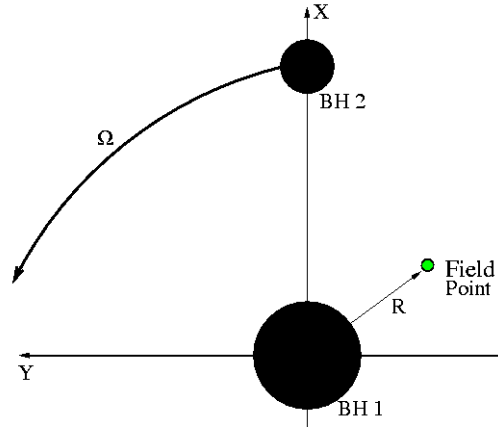


Fig. 2.3. ]

Coordinate system used in inner zone 1. The isotropic coordinates are centered on black hole 1 and the other hole orbits with angular velocity  $\Omega$ . The matching parameters  $M_1$  and  $\Omega$  and the coordinates  $X^\mu$  need not be equal to those used in the near zone.

centered on BH1 and is inertial. The asymptotic form of the inner-zone tidally perturbed metric valid in the buffer zone is given by Eq. (3.14) of Alvi [28], who derives it by extending Thorne-Hartle type arguments. But to serve as initial data the perturbation is needed throughout all the inner zone including the strong-field region, not just in the buffer zone where the field is weak. Alvi derives a form of the perturbation valid everywhere in the inner zone and presents it in Eq. (3.23) of Ref. [28]. The result depends on parameters  $M_1$  and  $\Omega$  which will be related to the near-zone parameters  $m_1$  and  $\omega$  when we perform the matching.

We write Eq. (3.23) of Ref. [28] as

$$\begin{aligned}
h_{00}^{IC,(1)} &\approx - \left[ \frac{1 - M_1/(2R_1)}{1 + M_1/(2R_1)} \right]^2 + \frac{m_2}{b^3} \left( 1 - \frac{M_1}{2R_1} \right)^4 \left[ 3(X \cos \Omega T + Y \sin \Omega T)^2 - R_1^2 \right], \\
h_{01}^{IC,(1)} &\approx \frac{2m_2}{b^3} \sqrt{\frac{m}{b}} \left( 1 - \frac{M_1}{2R_1} \right)^2 \left( 1 + \frac{M_1}{2R_1} \right)^4 \left[ (Z^2 - Y^2) \sin \Omega T - XY \cos \Omega T \right], \\
h_{02}^{IC,(1)} &\approx \frac{2m_2}{b^3} \sqrt{\frac{m}{b}} \left( 1 - \frac{M_1}{2R_1} \right)^2 \left( 1 + \frac{M_1}{2R_1} \right)^4 \left[ (X^2 - Z^2) \cos \Omega T + XY \sin \Omega T \right], \\
h_{03}^{IC,(1)} &\approx \frac{2m_2}{b^3} \sqrt{\frac{m}{b}} \left( 1 - \frac{M_1}{2R_1} \right)^2 \left( 1 + \frac{M_1}{2R_1} \right)^4 (Y \cos \Omega T - X \sin \Omega T) Z, \\
h_{ij}^{IC,(1)} &\approx \left( 1 + \frac{M_1}{2R_1} \right)^4 \left( \delta_{ij} + \frac{m_2}{b^3} \left[ 3(X \cos \Omega T + Y \sin \Omega T)^2 - R_1^2 \right] \right. \\
&\quad \times \left. \left\{ \left[ \left( 1 + \frac{M_1}{2R_1} \right)^4 - \frac{2M_1^2}{R_1^2} \right] \delta_{ij} - \frac{2M_1}{R_1} \left( 1 + \frac{M_1^2}{4R_1^2} \right) \frac{X^i X^j}{R_1^2} \right\} \right), \tag{2.10}
\end{aligned}$$

where once more the superscript (1) is to remind us that this metric is valid in submanifold  $\mathcal{C}_1$ , while the *IC* superscript refers to isotropic coordinates. The uncontrolled remainders in all components of Eq. (2.10) are  $O(R_1/b)^3$ .

Inspection of Eq. (2.10) shows that the perturbed metric diverges as  $R_1 \rightarrow 0$  faster than  $(1/R_1)^4$ , which prevents the use of puncture methods [16]. Physically, this is because the tidal perturbation tacitly assumes a small spacelike separation from the event horizon. Of course this assumption is violated as  $R_1 \rightarrow \infty$ , the asymptotically flat spatial infinity we call the “outside” of hole 1; but it is also violated as  $R_1 \rightarrow 0$  since, in isotropic coordinates, that is the other asymptotically flat spatial infinity “inside” hole 1. Outside the hole we match to the near zone metric which is well behaved, but inside we have nothing to match to. Thus numerical evolutions using our initial data will need to excise the black holes. Excision in practice still requires a slice that extends somewhat inside each horizon, which raises the question of how far inside our data can be considered valid. Outside hole A the tidal perturbation is valid for  $R_A \ll (m_A/m)b$ . The corresponding limit inside the hole is approximated by the transformation  $R_A \rightarrow (m_A/2)^2/R_A$ , which is an isometry for an unperturbed Schwarzschild hole, where we have used  $m_A \approx M_A$ . Thus the tidal perturbation is good roughly for

$$\frac{m_A}{2} \frac{m}{2b} \ll R_A \ll \frac{m_A}{m} b, \tag{2.11}$$

and the excision radius can be chosen anywhere between the lower limit of this expression and the horizon.

Since matching will be simpler if performed between two coordinate systems that live in charts that are similar to each other, we choose to corotate first. We define inner

isotropic corotating coordinates (ICC)

$$\begin{aligned}
\bar{X} &= X \cos \Omega T + Y \sin \Omega T, \\
\bar{Y} &= -X \sin \Omega T + Y \cos \Omega T, \\
\bar{Z} &= Z, \\
\bar{T} &= T.
\end{aligned} \tag{2.12}$$

Using these equations, we can obtain the inner metric in isotropic corotating coordinates, given by

$$\begin{aligned}
h_{00}^{(1)} &\approx H_t + H_{s1} \Omega^2 (\bar{X}^2 + \bar{Y}^2) + 2H_{st} \bar{X} \frac{\Omega}{b^2} (\bar{X}^2 + \bar{Y}^2 - \bar{Z}^2), \\
h_{11}^{(1)} &\approx H_{s1} - H_{s2} \frac{\bar{X}^2}{b^2}, \\
h_{01}^{(1)} &\approx -H_{s1} \bar{Y} \Omega - H_{st} \frac{\bar{Y} \bar{X}}{b^2}, \\
h_{22}^{(1)} &\approx H_{s1} - H_{s2} \frac{\bar{Y}^2}{b^2}, \\
h_{02}^{(1)} &\approx H_{s1} \bar{X} \Omega + \frac{H_{st}}{b^2} (\bar{X}^2 - \bar{Z}^2), \\
h_{33}^{(1)} &\approx H_{s1} - H_{s2} \frac{\bar{Z}^2}{b^2}, \\
h_{03}^{(1)} &\approx H_{st} \frac{\bar{Y} \bar{Z}}{b^2}, \\
h_{12}^{(1)} &\approx -H_{s2} \frac{\bar{Y} \bar{X}}{b^2}, \\
h_{23}^{(1)} &\approx -H_{s2} \frac{\bar{Z} \bar{Y}}{b^2}, \\
h_{13}^{(1)} &\approx -H_{s2} \frac{\bar{Z} \bar{X}}{b^2},
\end{aligned} \tag{2.13}$$

where we use the shorthand

$$\begin{aligned}
H_{st} &= 2m_2 \sqrt{\frac{m}{b^3}} \left(1 - \frac{M_1}{2R_1}\right)^2 \left(1 + \frac{M_1}{2R_1}\right)^4, \\
H_{s1} &= \left(1 + \frac{M_1}{2R_1}\right)^4 \left\{ 1 + 2\frac{m_2}{b^3} R_1^2 P_2 \left(\frac{\bar{X}}{R_1}\right) \left[ \left(1 + \frac{M_1}{2R_1}\right)^4 - 2\frac{M_1^2}{R_1^2} \right] \right\}, \\
H_{s2} &= \left(1 + \frac{M_1}{2R_1}\right)^4 \left(1 + \frac{M_1^2}{4R_1^2}\right) \frac{4m_2 M_1}{bR_1} P_2 \left(\frac{\bar{X}}{R_1}\right), \\
H_t &= -\left(\frac{1 - M_1/2R_1}{1 + M_1/2R_1}\right)^2 + 2\left(1 - \frac{M_1}{2R_1}\right)^4 \\
&\quad \frac{m_2}{b^3} R_1^2 P_2 \left(\frac{\bar{X}}{R_1}\right), \tag{2.14}
\end{aligned}$$

and the errors are still  $O(R_1/b)^3$ . In Eq. (2.13) we have dropped the superscript ICC in favor of (1), which refers to submanifold  $\mathcal{C}_1$ .

By expanding Eq. (2.13) in powers of  $M_1/R_1$ , which is permissible in overlap region  $\mathcal{O}_{13}$ , we obtain

$$\begin{aligned}
\tilde{h}_{00}^{(1)} &\sim -1 + \frac{2M_1}{R_1} + \frac{2m_2}{b^3} R_1^2 P_2 \left(\frac{\bar{X}}{R_1}\right) + \Omega^2 (\bar{X}^2 + \bar{Y}^2), \\
\tilde{h}_{01}^{(1)} &\sim \frac{-2m_2}{b^3} \sqrt{\frac{m}{b}} \bar{Y} \bar{X} - \bar{Y} \Omega \left(1 + \frac{2M_1}{R_1}\right), \\
\tilde{h}_{02}^{(1)} &\sim \frac{2m_2}{b^3} \sqrt{\frac{m}{b}} (\bar{X}^2 - \bar{Z}^2) + \bar{X} \Omega \left(1 + \frac{2M_1}{R_1}\right), \\
\tilde{h}_{03}^{(1)} &\sim \frac{2m_2}{b^3} \sqrt{\frac{m}{b}} \bar{Z} \bar{Y}, \\
\tilde{h}_{ij}^{(1)} &\sim \delta_{ij} \left[ 1 + \frac{2M_1}{R_1} + \frac{2m_2}{b^3} R_1^2 P_2 \left(\frac{\bar{X}}{R_1}\right) \right] \tag{2.15}
\end{aligned}$$

where the errors are  $O(2,3)$ . Like Eq. (2.8),  $\tilde{h}^{(1)}$  is a bivariate expansion in both  $\epsilon_{(1)} = R_1/b$  (valid in the inner zone  $\mathcal{C}_1$ ) and  $\epsilon_{(3)} = \frac{M_1}{R_1}$  (valid in the buffer zone  $\mathcal{O}_{13}$ ). In other words, it is the asymptotic expansion in the buffer zone to the asymptotic expansion in the inner zone.

## 2.5 Asymptotic matching

In this section, we concentrate on finding a matching condition ( $\psi_{13}$ ) and a coordinate transformation ( $\phi_{13}$ ) that maps points in  $\mathcal{C}_1$  labeled with isotropic corotating coordinates (ICC)  $\bar{X}^\mu$  to points in  $\mathcal{C}_3$  labeled with harmonic corotating coordinates (HCC)  $x^\mu$ . As already discussed, we concentrate on buffer zone  $\mathcal{O}_{13}$ , while the matching

condition  $\psi_{23}$  and the coordinate transformation  $\phi_{23}$  in  $\mathcal{O}_{23}$  will be given later by a symmetry transformation.

We assume that the coordinates are asymptotic to each other and that they can be expanded in an implicit bivariate series. That is, we assume that the map  $\phi_{13} : \bar{X}^\mu \rightarrow x^\mu$  has the form

$$\begin{aligned}\bar{X} &\approx \left(x - \frac{m_2 b}{m}\right) + x \left[ \left(\frac{m_2}{b}\right)^{1/2} \chi_1(x^\mu) + \left(\frac{m_2}{b}\right) \chi_2(x^\mu) + \left(\frac{m_2}{b}\right)^{3/2} \chi_3(x^\mu) \right], \\ \bar{Y} &\approx y \left[ 1 + \left(\frac{m_2}{b}\right)^{1/2} \gamma_1(x^\mu) + \left(\frac{m_2}{b}\right) \gamma_2(x^\mu) + \left(\frac{m_2}{b}\right)^{3/2} \gamma_3(x^\mu) \right], \\ \bar{Z} &\approx z \left[ 1 + \left(\frac{m_2}{b}\right)^{1/2} \zeta_1(x^\mu) + \left(\frac{m_2}{b}\right) \zeta_2(x^\mu) + \left(\frac{m_2}{b}\right)^{3/2} \zeta_3(x^\mu) \right], \\ \bar{T} &\approx t \left[ 1 + \left(\frac{m_2}{b}\right)^{1/2} \tau_1(x^\mu) + \left(\frac{m_2}{b}\right) \tau_2(x^\mu) + \left(\frac{m_2}{b}\right)^{3/2} \tau_3(x^\mu) \right],\end{aligned}\tag{2.16}$$

where  $\chi$ ,  $\gamma$ ,  $\zeta$  and  $\tau$  are functions of the harmonic corotating coordinates which do not depend on  $m/b$  (or equivalently  $\omega$ ), but are power series in  $r_1/b$ . We continue these power series only to  $O(r_1/b)^2$  so that the errors here in  $\phi_{13}$  are  $O(2, 3)$  as in Eqs. (2.8) and (2.15) which are linked by  $\phi_{13}$ . The first term in the  $\bar{X}$  equation above is chosen so that both coordinate systems have their origins at the center of mass of the binary.

Like the coordinates, the matching parameters in the two coordinate systems must be identical to lowest order in  $m_2/b$ . (They must also be independent of coordinates.) Then  $\psi_{13}$  is given by

$$\begin{aligned}M_1 &\approx m_1 \left[ 1 + \left(\frac{m_2}{b}\right)^{1/2} \eta_1 + \frac{m_2}{b} \eta_2 + \left(\frac{m_2}{b}\right)^{3/2} \eta_3 \right], \\ \Omega &\approx \omega \left[ 1 + \left(\frac{m_2}{b}\right)^{1/2} \kappa_1 + \frac{m_2}{b} \kappa_2 + \left(\frac{m_2}{b}\right)^{3/2} \kappa_3 \right],\end{aligned}\tag{2.17}$$

where the errors are  $O(m/b)^2$ .

Before moving on with the calculation, let us discuss the physical meaning of the assumptions we have just made. Equation (2.16) implies that inner and near zone metrics are identical in the buffer zone up to a change in coordinates. For a single black hole, in the buffer zone (which is outside the horizon), the only difference between isotropic and harmonic coordinates is the radial transformation

$$r = R \left( 1 + \frac{M^2}{4R^2} \right),\tag{2.18}$$

where  $r$  is in harmonic coordinates and  $R$  is in isotropic coordinates. This has the asymptotic form posited in Eq. (2.16). Thus the assumption of Eq. (2.16) is only needed in the buffer zone for the matching in this section. However, we will want to write our final results in a global coordinate system which goes inside the horizons (though not all the way to the asymptotically flat ends). For this purpose we assume that the form of

Eq. (2.16) holds for all values of  $r_1 > 0$ . This has the effect of defining a new coordinate system which is asymptotic to harmonic coordinates in the near zone and to isotropic coordinates in the inner zone.

Now let us return to the asymptotic matching. Using Eq. (2.17) we can transform Eq. (2.15) to harmonic corotating coordinates and impose the matching condition of Eq. (2.1),

$$\tilde{g}_{\mu\nu}^{(3)}(x^\gamma) \sim \tilde{h}_{\alpha\beta}^{(1)}(\bar{X}^\gamma(x^\gamma)) \frac{\partial \bar{X}^\alpha}{\partial x^\mu} \frac{\partial \bar{X}^\beta}{\partial x^\nu}. \quad (2.19)$$

Equation (2.19) provides 10 independent asymptotic relations per order, all of which must be satisfied simultaneously. Each asymptotic relation results in a first-order partial differential equation for the coordinate transformation, leading to 10 integration constants per order. As we shall see, these constants correspond to boosts, rotations, and translations of the origin.

Equation (2.19) must be solved iteratively in orders of  $(m/b)^{1/2}$ . Evaluating the nonzero components (the diagonals) of Eq. (2.19) at zeroth order in  $m/b$ , *i.e.* comparing Eqs. (2.8) and (2.15), provides no information, since it only asserts that at lowest order both metrics represent Minkowski spacetime. This is true for any matching formulation involving metrics of objects that would have asymptotically flat spacetimes in isolation.

The asymptotic relations given by evaluating Eqs. (2.8), (2.15), and (2.19) at  $O(m/b)^{1/2}$  are

$$\begin{aligned} \chi_1 &\sim -x\chi_{1,x}, & \zeta_1 &\sim -z\zeta_{1,z} \\ \gamma_1 &\sim -y\gamma_{1,y}, & \tau_1 &\sim -t\tau_{1,t}, \\ t\tau_{1,x} &\sim x\chi_{1,t}, & y\gamma_{1,t} - t\tau_{1,y} &\sim \left(\frac{m_2}{m}\right)^{1/2}, \\ t\tau_{1,z} &\sim z\zeta_{1,t}, & x\chi_{1,y} &\sim -y\gamma_{1,x}, \\ z\zeta_{1,x} &\sim -x\chi_{1,z}, & y\gamma_{1,z} &\sim -z\zeta_{1,y}, \end{aligned} \quad (2.20)$$

where commas stand for partial differentiation. The solution in terms of integration constants  $C_i$  is

$$\begin{aligned} t\tau_1(x, y, z, t) &= C_4x + C_5y - \sqrt{m_2/m}y + C_8z + C_9, \\ x\chi_1(x, y, z, t) &= -C_1y + C_2z + C_4t + C_3, \\ y\gamma_1(x, y, z, t) &= -C_1x + C_7z + C_5t + C_6, \\ z\zeta_1(x, y, z, t) &= -C_2x - C_7y + C_8t + C_{10}. \end{aligned} \quad (2.21)$$

For simplicity, we choose all  $C_i = 0$  except  $C_5 = \sqrt{m_2/m}$ . Thus the coordinate systems are identical at  $O(m/b)^{1/2}$ . The coordinate transformation then becomes

$$\begin{aligned}
\bar{X} &\approx \left(x - \frac{m_2 b}{m}\right) + x \left[ \left(\frac{m_2}{b}\right) \chi_2(x^\mu) + \left(\frac{m_2}{b}\right)^{3/2} \chi_3(x^\mu) \right], \\
\bar{Y} &\approx y \left[ 1 + \left(\frac{m_2}{b}\right) \gamma_2(x^\mu) + \left(\frac{m_2}{b}\right)^{3/2} \gamma_3(x^\mu) \right] + \sqrt{\frac{m_2}{b}} \sqrt{\frac{m_2}{m}} t, \\
\bar{Z} &\approx z \left[ 1 + \left(\frac{m_2}{b}\right) \zeta_2(x^\mu) + \left(\frac{m_2}{b}\right)^{3/2} \zeta_3(x^\mu) \right], \\
\bar{T} &\approx t \left[ 1 + \left(\frac{m_2}{b}\right) \tau_2(x^\mu) + \left(\frac{m_2}{b}\right)^{3/2} \tau_3(x^\mu) \right],
\end{aligned} \tag{2.22}$$

where the errors are still  $O(2, 3)$ .

Applying asymptotic matching to  $O(m/b)$ , we obtain

$$\begin{aligned}
-\left(\tau_2 + t\tau_{2,t}\right) &\sim 1 - \frac{(x - m_2 b/m)}{b} = 1 - \frac{x_1}{b}, \\
\chi_2 + x\chi_{2,x} &\sim 1 - \frac{(x - m_2 b/m)}{b} = 1 - \frac{x_1}{b}, \\
\gamma_2 + y\gamma_{2,y} &\sim 1 - \frac{(x - m_2 b/m)}{b} = 1 - \frac{x_1}{b}, \\
\zeta_2 + z\zeta_{2,z} &\sim 1 - \frac{(x - m_2 b/m)}{b} = 1 - \frac{x_1}{b}, \\
x\chi_{2,t} - t\tau_{2,x} &\sim \frac{t}{b} + \left(\frac{m}{m_2}\right)^{1/2} \frac{y}{b} \kappa_1, \\
y\gamma_{2,t} - t\tau_{2,y} &\sim -\left(\frac{m}{m_2}\right)^{1/2} \frac{x - m_2 b/m}{b} \kappa_1, \\
z\zeta_{2,t} &\sim t\tau_{2,z}, \\
x\chi_{2,y} &\sim -y\gamma_{2,x}, \\
x\chi_{2,z} &\sim -z\zeta_{2,x}, \\
\gamma_{2,z} &\sim -z\zeta_{2,y}.
\end{aligned} \tag{2.23}$$

Once more we have a system of 10 coupled partial differential equations that now depends on  $\kappa_1$ , which is a parameter that relates  $\Omega$  and  $\omega$ . For simplicity, we choose  $\kappa_1 = 0$ , so that the  $\Omega = \omega$  to this order. The solution to this system is then given by

$$\begin{aligned}
\tau_2 &= -\left[1 - \frac{x}{b} + \frac{m_2}{m}\right] + D_5 \frac{y}{t} + D_4 \frac{x}{t} + D_8 \frac{z}{t} + \frac{D_9}{t}, \\
\chi_2 &= 1 - \frac{x}{2b} + \frac{m_2}{m} + \frac{1}{2xb} (2t^2 + y^2 + z^2) + D_1 \frac{y}{x} + D_4 \frac{t}{x} + D_2 \frac{z}{x} + \frac{D_3}{x}, \\
\gamma_2 &= 1 - \frac{x}{b} + \frac{m_2}{m} - D_1 \frac{x}{y} + D_7 \frac{z}{y} + D_5 \frac{t}{y} + \frac{D_6}{y}, \\
\zeta_2 &= 1 - \frac{x}{b} + \frac{m_2}{m} + D_8 \frac{t}{z} - D_7 \frac{y}{z} - D_2 \frac{x}{z} + \frac{D_{10}}{z},
\end{aligned} \tag{2.24}$$

where the  $D_i$  are 10 more integration constants. For simplicity we set them to zero, and the coordinate transformation becomes

$$\begin{aligned}
\bar{X} &\approx \left(x - \frac{m_2 b}{m}\right) + x \left\{ \left(\frac{m_2}{b}\right) \left[1 - \frac{(x - 2m_2 b/m)}{2b}\right] + \left(\frac{m_2}{b}\right)^{3/2} \chi_3(x^\mu) \right\} \\
&\quad + \frac{m_2}{2b^2} (2t^2 + y^2 + z^2), \\
\bar{Y} &\approx y \left\{ 1 + \left(\frac{m_2}{b}\right) \left[1 - \frac{(x - m_2 b/m)}{b}\right] + \left(\frac{m_2}{b}\right)^{3/2} \gamma_3(x^\mu) \right\} + \sqrt{\frac{m_2}{b}} \sqrt{\frac{m_2}{m}} t, \\
\bar{Z} &\approx z \left\{ 1 + \left(\frac{m_2}{b}\right) \left[1 - \frac{(x - m_2 b/m)}{b}\right] + \left(\frac{m_2}{b}\right)^{3/2} \zeta_3(x^\mu) \right\}, \\
\bar{T} &\approx t \left\{ 1 - \left(\frac{m_2}{b}\right) \left[1 - \frac{(x - m_2 b/m)}{b}\right] + \left(\frac{m_2}{b}\right)^{3/2} \tau_3(x^\mu) \right\},
\end{aligned} \tag{2.25}$$

with errors of  $O(2, 3)$ .

Now that matching has been completed to  $O(m/b)^0$ ,  $O(m/b)^{1/2}$  and  $O(m/b)$ , we can proceed with matching at  $O(m/b)^{3/2}$ . However, keeping in mind our discussion in Sec. 2.2 of the orders needed, we will only use the spatial-temporal part of the asymptotic

relations matrix (2.19),

$$\begin{aligned}
x\chi_{3,t} - t\tau_{3,x} &\sim -\left(\frac{m}{m_2}\right)^{1/2} \left[ \frac{y}{b} \left( 1 - \kappa_2 - \frac{4x}{b} + 3\frac{m_2}{m} \right) \right], \\
t\tau_{3,y} - y\gamma_{3,t} &\sim \left(\frac{m}{m_2}\right)^{1/2} \left( \frac{x}{b} \left[ \kappa_2 - 1 + \frac{4m_1 - 6m_2}{m} - 4\left(\frac{m_2}{m}\right)^2 + 8\frac{\mu}{m} \right] + \left(\frac{x}{b}\right)^2 \right. \\
&\quad \times \left( \frac{7}{2} - \frac{4m_1}{m} + \frac{2m_2}{m} \right) + \left(\frac{y}{b}\right)^2 \left( -\frac{1}{2} - \frac{m_2}{m} + \frac{2m_1}{m} \right) + \left(\frac{z}{b}\right)^2 \\
&\quad \times \left( -\frac{3}{2} - \frac{m_2}{m} + \frac{2m_1}{m} \right) + \left(\frac{t}{b}\right)^2 + \frac{4\mu b}{m_2 r_1} + \left\{ \frac{m_2}{m} \left[ 1 - \kappa_2 + 2\left(\frac{m_2}{m}\right)^2 \right. \right. \\
&\quad \left. \left. + \frac{3m_2 - 4\mu}{m} \right] - \frac{9\mu + 8m_1}{2m} + \frac{3}{2} \right\} \Bigg), \\
t\tau_{3,z} - z\zeta_{3,t} &\sim \left(\frac{m}{m_2}\right)^{1/2} \frac{zy}{b^2}. \tag{2.26}
\end{aligned}$$

For simplicity, we choose  $\kappa_2 = 1 + 3m_2/m$ . This completes the derivation of the matching parameters, since  $\eta_i$  and  $\kappa_3$  did not appear in the differential equations at all, and hence, we can neglect them to this order. Note that this choice of parameter matching is different from Alvi's choice, and thus our coordinate transformation is also different. Up to  $O(m/b)^2$ , the corresponding parameter matching condition  $\psi_{13}$  is

$$\Omega \approx \omega \left[ 1 + \frac{m_2}{b} \left( 1 + 3\frac{m_2}{m} \right) \right], \quad M_1 \approx m_1. \tag{2.27}$$

This choice of  $\psi_{13}$  simplifies Eq. (2.26), which now becomes

$$\begin{aligned}
t\tau_{3,x} - x\chi_{3,t} &\sim -\left(\frac{m}{m_2}\right)^{1/2} \frac{4yx}{b^2}, \\
t\tau_{3,z} - z\zeta_{3,t} &\sim \left(\frac{m}{m_2}\right)^{1/2} \frac{zy}{b^2}, \\
t\tau_{3,y} - y\gamma_{3,t} &\sim \left(\frac{m}{m_2}\right)^{1/2} \left( \frac{x}{b} \left[ \frac{4m_1 - 3m_2}{m} - 4\left(\frac{m_2}{m}\right)^2 + 8\frac{\mu}{m} \right] + \left(\frac{x}{b}\right)^2 \left( \frac{7}{2} - \frac{4m_1}{m} \right. \right. \\
&\quad \left. \left. + \frac{2m_2}{m} \right) + \left(\frac{y}{b}\right)^2 \left( -\frac{1}{2} - \frac{m_2}{m} + \frac{2m_1}{m} \right) + \left(\frac{z}{b}\right)^2 \left( -\frac{3}{2} - \frac{m_2}{m} + \frac{2m_1}{m} \right) \right. \\
&\quad \left. + \left(\frac{t}{b}\right)^2 + \frac{4\mu b}{m_2 r_1} + \left\{ \frac{m_2}{m} \left[ 2\left(\frac{m_2}{m}\right)^2 - \frac{4\mu}{m} \right] - \frac{9\mu + 8m_1}{2m} + \frac{3}{2} \right\} \right). \tag{2.28}
\end{aligned}$$

As before, we choose the integration constants for simplicity (and to keep the slicings close to each other), resulting in the following solution:

$$\begin{aligned}
\tau_3(x, y, z, t) &= 0, \\
\chi_3(x, y, z, t) &= \left(\frac{m}{m_2}\right)^{1/2} \frac{4yt}{b^2}, \\
\zeta_3(x, y, z, t) &= -\left(\frac{m}{m_2}\right)^{1/2} \frac{yt}{b^2}, \\
\gamma_3(x, y, z, t) &= -\left(\frac{m}{m_2}\right)^{1/2} \frac{t}{y} \left( \frac{x}{b} \left[ \frac{4m_1 - 3m_2}{m} - 4\left(\frac{m_2}{m}\right)^2 + 8\frac{\mu}{m} \right] + \left(\frac{x}{b}\right)^2 \left( \frac{7}{2} - \frac{4m_1}{m} \right) \right. \\
&\quad + \left. \frac{2m_2}{m} \right) + \left(\frac{y}{b}\right)^2 \left( -\frac{1}{2} - \frac{m_2}{m} + \frac{2m_1}{m} \right) + \left(\frac{z}{b}\right)^2 \left( -\frac{3}{2} - \frac{m_2}{m} + \frac{2m_1}{m} \right) \\
&\quad + \left. \frac{1}{3} \left(\frac{t}{b}\right)^2 + \frac{4\mu b}{m_2 r_1} + \left\{ \frac{m_2}{m} \left[ 2\left(\frac{m_2}{m}\right)^2 - \frac{4\mu}{m} \right] - \frac{9\mu + 8m_1}{2m} + \frac{3}{2} \right\} \right). \quad (2.29)
\end{aligned}$$

To summarize, we have found a coordinate transformation  $\phi_{13}$  and a set of parameter relations  $\psi_{13}$  that produce asymptotic matching to  $O(3/2, 3)$  in the  $00$  and  $ij$  components of the 4-metric and to  $O(2, 3)$  in the  $0i$  components.

Note however that the  $\gamma_3$  piece of the coordinate transformation becomes singular at  $r_1 = 0$ . Also recall that the point  $r_1 = 0$  is not identical to the point  $R_1 = 0$ , where the inner zone metric perturbation diverges. Hence if we excise the inner zone metric close to  $R_1 = 0$ , the point  $r_1 = 0$  might be outside the excised region, in which case our coordinate transformation would introduce a coordinate singularity outside the excised region. To get rid of this singularity we will replace  $r_1$  by

$$\tilde{r}_1 = \sqrt{r_1^2 + 6m^2}. \quad (2.30)$$

This change amounts to adding a higher order term to the coordinate transformation, which has no effect in the buffer zone at the current order of approximation, but it has the advantage that the resulting coordinate transformation is now regular at  $r_1 = 0$ .

With this replacement the coordinate transformation is given by

$$\begin{aligned}
\bar{X} &\approx \left(x - \frac{m_2 b}{m}\right) + x \left\{ \left(\frac{m_2}{b}\right) \left[1 - \frac{(x - 2m_2 b/m)}{2b}\right] + \frac{m_2}{b} \sqrt{\frac{m}{b}} \frac{4yt}{b^2} \right\} \\
&\quad + \frac{m_2}{2b^2} (2t^2 + y^2 + z^2), \\
\bar{Y} &\approx y \left\{ 1 + \left(\frac{m_2}{b}\right) \left[1 - \frac{x - m_2 b/m}{b}\right] \right\} - \frac{m_2}{b} \sqrt{\frac{m}{b}} t \left( \frac{x}{b} \left[ \frac{4m_1 - 3m_2}{m} - 4 \left(\frac{m_2}{m}\right)^2 \right. \right. \\
&\quad + \left. \left. 8 \frac{\mu}{m} \right] + \left(\frac{x}{b}\right)^2 \left(\frac{7}{2} - \frac{4m_1}{m} + \frac{2m_2}{m}\right) + \left(\frac{y}{b}\right)^2 \left(-\frac{1}{2} - \frac{m_2}{m} + \frac{2m_1}{m}\right) \right. \\
&\quad + \left(\frac{z}{b}\right)^2 \left(-\frac{3}{2} - \frac{m_2}{m} + \frac{2m_1}{m}\right) + \frac{1}{3} \left(\frac{t}{b}\right)^2 + \frac{4\mu b}{m_2 \tilde{r}_1} + \left\{ \frac{m_2}{m} \left[ 2 \left(\frac{m_2}{m}\right)^2 - \frac{4\mu}{m} \right] \right. \\
&\quad \left. \left. - \frac{9\mu + 8m_1}{2m} + \frac{3}{2} \right\} \right) + \sqrt{\frac{m_2}{m}} \sqrt{\frac{m_2}{b}} t, \\
\bar{Z} &\approx z \left\{ 1 + \left(\frac{m_2}{b}\right) \left[1 - \frac{x - m_2 b/m}{b}\right] - \frac{m_2}{b} \sqrt{\frac{m}{b}} \frac{yt}{b^2} \right\}, \\
\bar{T} &\approx t \left\{ 1 - \left(\frac{m_2}{b}\right) \left[1 - \frac{x - m_2 b/m}{b}\right] \right\}, \\
\Omega &\approx \omega \left[ 1 + \frac{m_2}{b} \left( 1 + 3 \frac{m_2}{m} \right) \right], \\
M_1 &\approx m_1.
\end{aligned} \tag{2.31}$$

The coordinate transformation for matching in the other overlap region  $\mathcal{O}_{23}$  is obtained by the following symmetry transformation:

$$1 \leftrightarrow 2, \quad x \rightarrow -x, \quad y \rightarrow -y, \quad z \rightarrow z. \tag{2.32}$$

In Eq. (2.31),  $t$  should be considered small just as  $x$ ,  $y$ , and  $z$  are. Recall that fundamentally the overlap regions are 4-volumes, although when we choose a time slicing we have to deal with their projections on a spatial hypersurface ( $m_A \ll r_A \ll b$ ). Just as the overlap regions span a limited range of  $r_A$ , so they span a limited range of  $t$ . The post-Newtonian metric and the perturbed Schwarzschild metric are formally stationary, but the true physical system includes gravitational waves (not modeled here) which for example change the orbital frequency on a radiation reaction timescale. While this timescale is longer than an orbital period, which must be of order  $b$ , rotation and boosts mix space and time terms and to be consistent with  $r_A \ll b$  we must keep  $t \ll b$ . Therefore we choose the  $t = 0 = T$  slice when discussing the approximate metric in the next section, which restricts our overlap region to the intersection of this 3-surface with the overlap 4-volume.

## 2.6 An approximate metric for binary black holes

In this section we transform the inner zone metric in isotropic corotating coordinates to harmonic corotating coordinates via Eq. (2.31). The metric in the inner zone of black hole 1 is given by

$$g_{\mu\nu}^{(1)} = h_{\bar{\delta}\bar{\rho}}^{(1)} J^{\bar{\delta}}_{\mu} J^{\bar{\rho}}_{\nu}, \quad (2.33)$$

where in the buffer zone the  $g_{00}$  and  $g_{ij}$  components have errors of  $O(2, 3)$  and  $g_{0i}$  has errors of  $O(5/2, 3)$ . In the above equation the Jacobian  $J^{\bar{\mu}}_{\nu} = \partial_{\nu} \bar{X}^{\bar{\mu}}$  can be expanded

as

$$\begin{aligned}
J^{\bar{T}}_t &= 1 - \frac{m_2}{b} \left( 1 - \frac{x - m_2 b/m}{b} \right), \\
J^{\bar{T}}_x &= \frac{m_2 t}{b^2}, \\
J^{\bar{X}}_t &= \frac{m_2}{b} \left( \frac{2t}{b} + 4 \frac{xy\omega}{b} \right), \\
J^{\bar{X}}_x &= 1 + \frac{m_2}{b} \left( 1 - \frac{x - m_2 b/m}{b} + \frac{4\omega yt}{b} \right), \\
J^{\bar{X}}_y &= \frac{m_2}{b} \left( \frac{y}{b} + 4 \frac{x\omega t}{b} \right), \\
J^{\bar{X}}_z &= \frac{m_2 z}{b^2}, \\
J^{\bar{Y}}_t &= \sqrt{\frac{m_2}{m}} \sqrt{\frac{m_2}{b}} - \frac{m_2}{b} \sqrt{\frac{m}{b}} \left\{ \frac{x}{b} \left[ \frac{4m_1 - 3m_2}{m} - 4 \left( \frac{m_2}{m} \right)^2 + 8 \frac{\mu}{m} \right] + \left( \frac{x}{b} \right)^2 \left( \frac{7}{2} \right. \right. \\
&\quad \left. \left. - \frac{4m_1}{m} + \frac{2m_2}{m} \right) + \left( \frac{y}{b} \right)^2 \left( -\frac{1}{2} - \frac{m_2}{m} + \frac{2m_1}{m} \right) \left( \frac{z}{b} \right)^2 \left( -\frac{3}{2} - \frac{m_2}{m} + \frac{2m_1}{m} \right) + \left( \frac{t}{b} \right)^2 \right. \\
&\quad \left. + \frac{4\mu b}{m_2 \tilde{r}_1} + \frac{m_2}{m} \left[ 2 \left( \frac{m_2}{m} \right)^2 - 4 \frac{\mu}{m} \right] - \frac{9\mu + 8m_1}{2m} - \frac{3}{2} \right\}, \\
J^{\bar{Y}}_x &= \frac{-m_2 y}{b} \frac{1}{b} - \frac{m_2}{b} \sqrt{\frac{m}{b}} \frac{t}{b} \left\{ \left[ \frac{4m_1 - 3m_2}{m} - 4 \left( \frac{m_2}{m} \right)^2 + 8 \frac{\mu}{m} \right] + \frac{2x}{b} \left( \frac{7}{2} - \frac{4m_1}{m} + \frac{2m_2}{m} \right) \right. \\
&\quad \left. - 4 \frac{\mu b^2 x - m_2 b/m}{m_2 \tilde{r}_1^3} \right\}, \\
J^{\bar{Y}}_y &= 1 + \frac{m_2}{b} \left( 1 - \frac{x - m_2 b/m}{b} \right) - \frac{m_2}{b} \sqrt{\frac{m}{b}} t \left[ \frac{2y}{b^2} \left( -\frac{1}{2} - \frac{m_2}{m} + \frac{2m_1}{m} \right) - 4 \frac{\mu b}{m_2 \tilde{r}_1^3} \frac{y}{b} \right], \\
J^{\bar{Y}}_z &= -\frac{m_2}{b} \sqrt{\frac{m}{b}} t \left[ \frac{2z}{b^2} \left( -\frac{3}{2} - \frac{m_2}{m} + \frac{2m_1}{m} \right) - 4 \frac{\mu b}{m_2 \tilde{r}_1^3} \frac{z}{b} \right], \\
J^{\bar{Z}}_t &= -\frac{m_2}{b} \sqrt{\frac{m}{b}} \frac{zy}{b^2}, \\
J^{\bar{Z}}_x &= -m_2 \frac{z}{b^2}, \\
J^{\bar{Z}}_y &= -\frac{m_2}{b} \sqrt{\frac{m}{b}} \frac{zt}{b^2}, \\
J^{\bar{Z}}_z &= 1 + \frac{m_2}{b} \left( 1 - \frac{x - m_2 b/m}{b} \right) - \frac{m_2}{b} \sqrt{\frac{m}{b}} \frac{yt}{b^2}. \tag{2.34}
\end{aligned}$$

Furthermore,  $h_{\mu\nu}^{(1)}$  refers to the inner metric presented in Eq. (2.13), where we substitute the coordinate transformation given by Eq. (2.31) and

$$R_1 = \left( \bar{X}^2 + \bar{Y}^2 + \bar{Z}^2 \right)^{1/2}. \quad (2.35)$$

The metric in the inner zone of black hole 2 ( $\mathcal{C}_2$ ) is given by the symmetry transformation (2.32) applied to Eq. (2.33).

We now have all the ingredients to construct an approximate piecewise metric, for example

$$g_{\mu\nu}^{piece} \approx \begin{cases} g_{\mu\nu}^{(1)}, & r_1 < r_1^T \\ g_{\mu\nu}^{(2)}, & r_2 < r_2^T \\ g_{\mu\nu}^{(3)}, & r_1 > r_1^T, r_2 > r_2^T, r < \lambda/2\pi \end{cases} \quad (2.36)$$

for some transition radii  $r_A^T$  which are chosen to be inside  $\mathcal{O}_{A3}$  for  $A = \{1, 2\}$ . In Eq. (2.36),  $g_{\mu\nu}^{(3)}$  is given in Eq. (2.4),  $g_{\mu\nu}^{(1)}$  is given in Eq. (2.33) and  $g_{\mu\nu}^{(2)}$  is the symmetry transformed version of Eq. (2.33). The inner zone pieces of this metric are accurate to  $O(R_1/b)^2$ , while the post-Newtonian near zone pieces are accurate to  $O(m/r)^{3/2}$ . In the overlap region, the inner and near zone  $0i$  components asymptotically match up to  $O(3/2, 2)$  as required for the extrinsic curvature, while all other components asymptotically match only up to  $O(1, 2)$ .

Note that when we applied the coordinate transformation of Eq. (2.31) to the inner zone metric we kept terms up to  $O(m/b)^5$ , which at first glance seems too high. These terms are needed because the inner zone metric represents a tidally perturbed black hole with errors in the physics of  $O[(m/b)(R_1/b)^3]$ . Close to BH1 ( $R_1 \sim m$ ), the error in the physics is only of order  $O(m/b)^4$  and hence we should keep terms to at least order  $O(m/b)^3$ . However, recall that the perturbed black hole metric satisfies the Einstein equations up to errors of only  $O[(m/b)^{5/2}(R_1/b)^2]$  even though its astrophysical resemblance to a binary black hole has errors already at  $O[(m/b)(R_1/b)^3]$ . If we want to obtain a metric which is close to the constraint hypersurface, we should keep terms larger than  $O[(m/b)(R_1/b)^3]$ , but not larger than  $O[(m/b)^{5/2}(R_1/b)^2]$ . In particular, close to the black hole we have constraint violations of  $O(m/b)^{9/2}$ . For example, if we had dropped terms of order  $O(m/b)^4$  in the inner zone metric we would have introduced additional constraint violations at this order.

### 2.6.1 Global character of the asymptotic metric

In this subsection we plot Eq. (2.36) to describe some features of the approximate piecewise metric. We choose a system of equal-mass black holes  $m_1 = m_2 = m/2$  separated by  $b = 10m$ , so that both holes are located on the  $x$  axis with BH1 at  $x \approx 5m$  and BH2 at  $x \approx -5m$ . Figures 2.4 and 2.5 show the  $xx$  and  $00$  components of the metric along the  $x$  axis for this system. (Other components of the piecewise 4-metric

exhibit similar behavior.) In all plots we use a dashed line to denote the near zone metric ( $g_{\mu\nu}^{(3)}$ ) and dotted lines to denote the inner zone metrics ( $g_{\mu\nu}^{(1,2)}$ ). We choose the separation  $b = 10m$  because it is near the minimum for which our formalism makes sense, and we plot on the  $x$ -axis because it is where the worst behavior occurs. The idea is to (i) show some practical features of matching which have not been presented in the literature and (ii) demonstrate the limits of the method, particularly regarding the minimum separation.

In these plots, we also include error bars that estimate the uncontrolled remainders in the approximations. These remainders can be approximated by

$$2[(m_1/r_1)^2 + (m_2/r_2)^2] \quad (2.37)$$

in the near zone,

$$2(m_2/b)(R_1/b)^3 \quad (2.38)$$

in inner zone 1, and the same with  $1 \leftrightarrow 2$  for inner zone 2. The error in the near zone metric was estimated by looking at the next order (2PN) term in the metric components [101]. [That term is much more complicated than Eq. (2.37), but is numerically about equal to it in the region plotted.] The error in the inner zone metric comes about because the next tidal correction for a single black hole of mass  $m$  in perturbation theory will be roughly proportional to  $\frac{1}{3}R_{i0j0,k}$ . The error bars of the approximations are position-dependent, and thus provide a useful sign of where each approximation is breaking down. The PN error bars are larger near the holes than far away, and the BHPT error bars exhibit the opposite behavior. The error bars also provide an indicator of where both approximations are comparably good: Neglecting angular factors (as is typical in the literature), the error bars for the near zone and inner zone  $A$  are comparable at

$$r_A^T \approx \left(b^4 m_A^2 / m\right)^{1/5}, \quad (2.39)$$

which takes a value of about  $4.8m$  for the system plotted here. This radius is a good candidate for the “transition radius” of Eq. (2.36), but note that, in principle, there is an infinite number of possible candidates, as long as they are in the buffer zone. Furthermore, note that this is not a “matching radius,” since there is no such thing. Matching asymptotic expansions, as opposed to patching them as done by Alvi [28], does not happen at any particular place in the buffer zone. Rather, it makes two expansions comparable throughout the buffer zone up to the uncontrolled remainders.

In Figs. 2.4 and 2.5 we plot the  $xx$  and  $00$  metric components along the  $x$ -axis for the PN approximation as well as for the two perturbed black hole approximations. In Fig. 2.1 the buffer zones around each black hole were sketched as spherical shells around the holes, formally defined by  $m_1 \ll r_1 \ll b$  and  $m_2 \ll r_2 \ll b$ . It is important to recall that this definition, which is ubiquitous in the literature, is imprecise because of the  $\ll$  symbols and one cannot simply substitute  $<$  symbols. (For one thing, there is angular dependence of the uncontrolled remainders.) Inserting the parameters of our system into these definitions, in Fig. 2.4 the intersection of buffer zone 1 with the  $x$ -axis is given by  $5.5 \ll x/m \ll 15$  (to the right of BH1) and  $-5 \ll x/m \ll 4.5$  (to the left, between

the holes). In the part of the buffer zone to the right, away from BH2, we see a clean example of the behavior expected of matched asymptotic expansions: The near-zone curve and the BH1 inner-zone curve do not intersect, but the difference between them is comparable to the estimated error bars everywhere within this part of the buffer zone, even if we replace the  $\ll$  operator in the definition of the buffer zone by the precise  $<$  operator.

Between the holes, to the left in Fig. 2.4, the interpretation of the curves is not so simple. We cannot replace  $\ll$  by  $<$  in the definition of buffer zone 1 because to the left of  $x/m \approx 0$  ( $r_1 \approx b/2$ ) the near-zone metric component resembles that of BH2 rather than BH1. This is because  $m_1 \ll r_1 \ll b$  is a rough criterion obtained by ignoring (among other things) the angular dependence of the expansion coefficients in Eq. (2.8), inspection of which shows about a factor of two variation as the angle is changed. This angular dependence means that if one tries to redefine the buffer zone heuristically as “the region where the error bars on two curves overlap and are not too large,” it is significantly aspherical and can be squeezed out entirely. Even at the origin (where they are smallest), the error bars from the PN approximation in the near zone are visibly larger than they are for most of the right-hand part of buffer zone 1. These error bars, however, are what is expected: At the origin in Fig. 2.4 the  $O(m/r)$  term which is kept in the PN metric has a value of 0.4, for a total metric component of  $g_{xx}^{(3)} = 1.4$ . The uncontrolled  $O(m/r)^2$  term we use for the error bar is 0.04, which is precisely 10% of the  $m/b$  correction and about twice the value at  $x/m = \pm 10$ , a comparable distance on the other side of each hole. The fact that the error bars are worst in between the holes does not depend on  $m/b$  or the mass ratio, but rather is a reflection of the physical assumptions on which matching is based. The near-zone metric is matched in buffer zone 1 to the metric of inner zone 1, and in buffer zone 2 it is matched to the metric of inner zone 2, but inner zone 1 is never matched to inner zone 2. It is the intervening near zone that ensures that each black hole’s tidal perturbation is the appropriate one (up to uncontrolled remainders) for the other black hole, because each tidal perturbation is derived for a black hole without a nearby body. (See, for example, the discussion in Sec. II.B of Thorne and Hartle [94].)

Since the inner-zone and near-zone metric components diverge as  $r_A \rightarrow 0$ , Fig. 2.4 might seem to imply that the solutions approach each other near the horizons. This misconception can be rectified by scaling the solutions to the Brill-Lindquist factor  $\psi^4$ , where

$$\psi = 1 + \frac{m_1}{2r_1} + \frac{m_2}{2r_2}. \quad (2.40)$$

This removes most of the divergent behavior of the solutions, as shown in Fig. 2.6. In this figure, we only plot the region near BH 1 to show the difference in divergence better, but the region near BH 2 is very similar. To the right, away from the other black hole, we see that the near-zone and inner-zone solutions are indeed quite similar near BH1 and that there is a wide region where both sets of error bars are comparable and overlap. The transition radius  $r_1^T \approx 4.8m$  ( $x/m \approx 10$ ) discussed above is seen to be a good approximation of where the error bars are equal. To the left, between the holes, there is

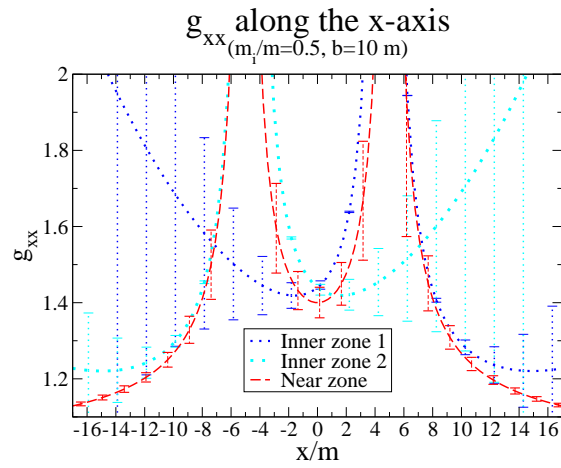


Fig. 2.4. This figure shows the  $xx$  component of the near zone metric (PN), denoted by a dashed line, and the inner zone metrics (BHPT), denoted by dotted lines, along the (harmonic)  $x$  axis for a perturbative parameter  $m/b = 1/10$ , with the black holes located at  $x/m = \pm 5$ . The buffer zones cannot be precisely defined, but most of the region plotted is within one or the other (see text). Matching does not guarantee that two curves which are asymptotically matched intersect anywhere in the buffer zone, but rather that they are comparable at the level of the uncontrolled remainders. The error bars estimate these remainders as described in the text.

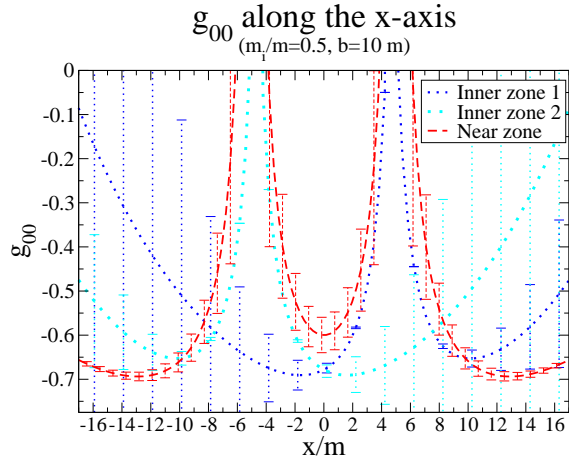


Fig. 2.5. This figure is similar to Fig. 2.4, but it shows the 00 component of the metric. Observe that in this component the differences between the different approximations are more pronounced, although the general features of asymptotic matching are still discernible.

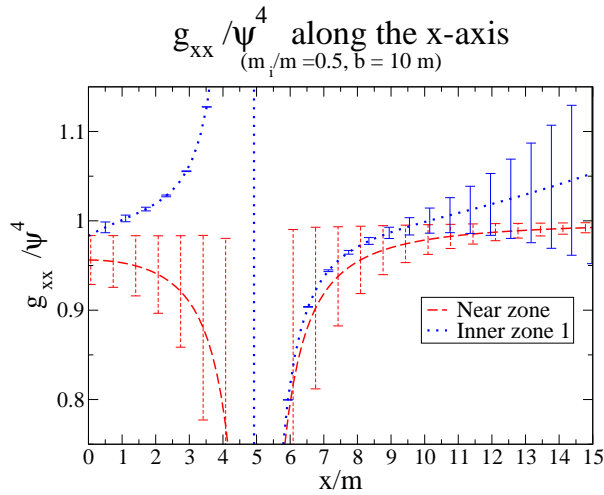


Fig. 2.6. In this figure we plot the  $xx$  component of the near zone (PN - dashed line) and inner zone 1 (BHPT - dotted line) metrics divided by the Brill-Lindquist factor  $\psi^4$ . The behavior of the solutions is clearly different as we approach the event horizon from the left (the direction of the other hole).

only a small region (about  $|x|/m < 1$ ) where the error bars overlap, and they are never equal.

The smallness of the region where the error bars overlap is an indication that  $b = 10m$  is approaching the minimum separation for which our approximation method makes sense. The disappearance of such a region could be used as a criterion for the failure of matching, although this is not a standard test and several different approximate criteria could be used (and this region is not the formal definition of a buffer zone anyway.) In Fig. 2.5 the error bars never do quite overlap at  $x/m \approx 0$ , but they do overlap at  $x/m \approx \pm 1$ , although we must keep in mind that they are rough estimates. As discussed above, the error bars cannot be made equal at the origin by changing  $m/b$ , although the overlap can be made better by increasing the separation. The fact that the rescaled metric components in Fig. 2.6 take off in different directions as they approach BH1 from between the holes is partly because the two metrics blow up at different coordinate locations. This small relative translation is due to the coordinate system used in the matching.

### 2.6.2 Transition Functions

The fact that matched curves do not strictly overlap even in the buffer zone means that a piecewise metric such as Eq. (2.36) possesses discontinuities at the transition radii  $r_A^T$ , wherever they are chosen to be. These discontinuities can be problematic for numerical evolutions of the spacetime and thus it is desirable to smooth them. We now construct transition functions that smooth these discontinuities out, by letting

$$g_{\mu\nu}^{(1,3)} = [1 - F_1(R_1)] g_{\mu\nu}^{(1)} + F_1(R_1) g_{\mu\nu}^{(3)}, \quad (2.41)$$

where  $F_1$  has the properties that  $F_1(R_1 \gtrsim b) = 1$ ,  $F_1(R_1 \lesssim m_1) = 0$ ,  $F_1(R_1 \approx r_1^T) \approx 1/2$ . This ansatz yields a metric that is equal to the inner zone metric near black hole 1, while it is equal to the near zone metric far away from black hole 1. In between (i.e. in the buffer zone) we obtain a weighted average of these two solutions. Since the Einstein equations are nonlinear, the sum of two solutions is in general not another solution. But since both solutions are valid in the buffer zone, and since both have been matched, these two solutions are equal to each other in the buffer zone up to uncontrolled remainders of  $O(2,3)$ , corresponding to higher order post-Newtonian and tidal perturbation terms. Hence any weighted average of these two solutions in the buffer zone will yield the same correct solution up to uncontrolled remainders of  $O(2,3)$ . This justifies the use of smoothing to merge the two solutions in the buffer zone. A similar solution can be obtained for the other black hole by replacing  $1 \rightarrow 2$ .

We choose transition functions of the form

$$f(r) = \begin{cases} 0, & r \leq r_0 \\ \frac{1}{2} \left\{ 1 + \tanh \left[ \frac{s}{\pi} \left( \tan \left( \frac{\pi}{2w} (r - r_0) \right) - \frac{q^2}{\tan \left( \frac{\pi}{2w} (r - r_0) \right)} \right) \right] \right\}, & r_0 < r < r_0 + w \\ 1, & r \geq r_0 + w. \end{cases} \quad (2.42)$$

This function transitions from zero to one in a transition window which starts at  $r_0$  and has a width  $w$ . The parameter  $q$  controls the location at which  $f$  reaches  $1/2$ , and  $s$  controls the slope at that location. Note that this transition function is  $C^\infty$ , a property which is useful for numerics. In Eq. (2.41) we set

$$F_A(R_A) = f(R_A), \quad (2.43)$$

with parameters

$$r_0 = 1.5m, \quad w = 5r_A^T, \quad q = 1/4, \quad s = 10, \quad (2.44)$$

where  $r_A^T$  is given by Eq. (2.39). With these parameters the transition functions reach the value  $1/2$  at  $R_A \approx 1.5m + 0.16w \approx 5.2m$ , very close to  $r_A^T \approx 4.8m$ . We could have used something more sophisticated such as a transition with the same anisotropic behavior as the buffer zones, but several trials show that such details do not matter as long as the transition function has the right asymptotic properties. (Trials also showed that the results were not too sensitive to the precise parameter values.)

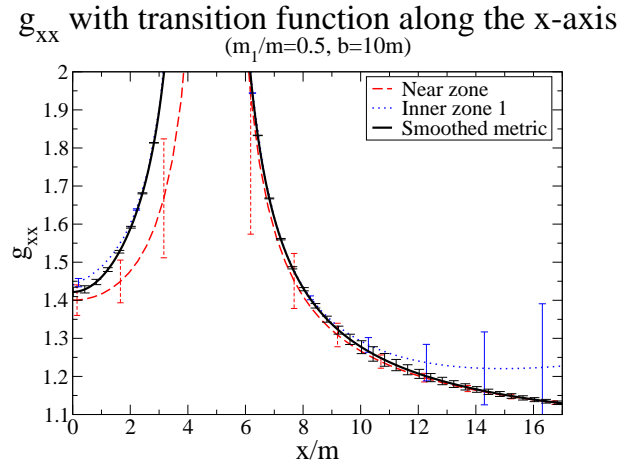


Fig. 2.7. In this figure we show the  $xx$  component of the global metric compared to the near-zone PN metric and the inner-zone BHPT metric around BH1. Observe that the transition function takes the global metric smoothly from one to the other. Error bars in the global metric are the same as the error bars of whichever local approximation is better at that point.

We can see the effect of this transition function in Fig. 2.7 and 2.8. In these figures we only show the region near BH 1, but similar behavior is observed near the other hole. The transition function effectively takes one solution into the other smoothly

in the buffer zone. The size of the transition window can be modified by changing the “thickness”  $w$ , but if  $w$  is made too small the derivatives of the metric (which include  $1/w$  terms) develop artificial peaks inside the transition window.

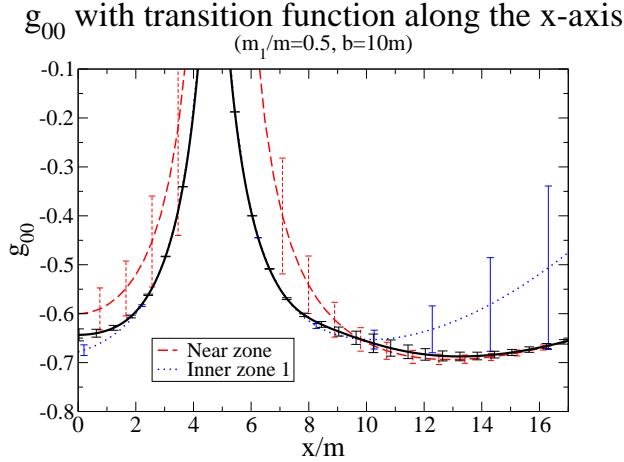


Fig. 2.8. Same as the previous Figure, but for the 00 metric component.

If the separation of the black holes is large enough so that the two transition windows of width  $w$  do not intersect, the transition functions given in Eq. (2.42) will suffice to generate a global metric of the form

$$g_{\mu\nu}^{(global)} = F_2(R_2)F_1(R_1)g_{\mu\nu}^{(3)} + [1 - F_1(R_1)]g_{\mu\nu}^{(1)} + [1 - F_2(R_2)]g_{\mu\nu}^{(2)}, \quad (2.45)$$

However, if the separation is small enough that the two transition windows of width  $w$  start to overlap, we must construct a third function  $G(x)$  to allow for a smooth transition between the two black holes while not contaminating the global solution near BH1 with a piece of the solution from inner zone 2 and vice versa. (In essence, this is an after the fact way of handling the fact that the buffer zones are not really spherically symmetric as often implied in the literature. When the holes are too close, a good transition function should not be spherically symmetric either.) For the system considered here,  $b = 10m$  is a sufficiently small separation that such a third transition function is necessary. The global metric then becomes

$$g_{\mu\nu}^{(global)} = G(x) \left\{ F_1(R_1)g_{\mu\nu}^{(3)} + [1 - F_1(R_1)]g_{\mu\nu}^{(1)} \right\} + [1 - G(x)] \left\{ F_2(R_2)g_{\mu\nu}^{(3)} + [1 - F_2(R_2)]g_{\mu\nu}^{(2)} \right\}. \quad (2.46)$$

(Recall that  $x$  is the distance along the axis between the holes with the origin at the center of mass.) The function  $G(x)$  will be chosen such that it is equal to unity near black hole 1 and zero near black hole 2. In between the two black holes,  $G(x)$  will range from zero to one, so that non-trivial averaging will occur only in this region. Again, this averaging is allowed because the two solutions in the curly brackets are both valid (and equal up to uncontrolled remainders) in between the two black holes. Near each black hole we obtain the appropriate inner zone solution, while far away  $F_1(R_1) = F_2(R_2) = 1$ , so that we obtain the near zone solution  $g_{\mu\nu}^{(3)}$ . We choose the transition function  $G(x)$  between  $\mathcal{C}_1 \cup \mathcal{C}_3$  and  $\mathcal{C}_2 \cup \mathcal{C}_3$  to be of the same form as the function in Eq. (2.42), *i.e.*

$$G(x) = f(x), \quad (2.47)$$

but with different parameter values

$$r_0 = \frac{b(m_2 - m_1)}{2m} - \frac{b - m}{2}, \quad w = b - m, \quad q = 1, \quad s = 5/2. \quad (2.48)$$

(The more complicated form of  $r_0$  is to account for the origin of the  $x$  coordinate being at the binary center of mass rather than on either hole.)

The reader might worry that the use of transition functions could introduce large artificial gradients. However, with a reasonable choice of transition functions this is not the case. In order to understand why, let us look at the derivatives of the smoothed metric in more detail. Consider for example the overlap region  $\mathcal{O}_{13}$  in which  $F_2 = 1$  and the smoothed metric is thus  $F_1 g_{\mu\nu}^{(3)} + [1 - F_1] g_{\mu\nu}^{(1)}$ . A derivative of this smoothed metric takes the form

$$F_1 g_{\mu\nu}^{(3)'} + [1 - F_1] g_{\mu\nu}^{(1)'} + F_1' [g_{\mu\nu}^{(3)} - g_{\mu\nu}^{(1)}]. \quad (2.49)$$

The last term is the worrying one since it involves a derivative of the transition function. But note that the coefficient multiplying this term is the difference between the inner-zone and near-zone metrics in the buffer zone, and therefore is by definition of the order of the uncontrolled remainders in the expansions of the first two terms. Therefore the third (unphysical) term will be safely absorbed into the small uncontrolled remainders unless we make a pathological choice of transition function—for example, one that has an inverse power of a small expansion parameter built into it. Our transition functions are chosen to avoid this. Their maximum slope is roughly  $1/r_A^T$ , comparable to the slopes of  $g_{\mu\nu}^{(1)}$  and  $g_{\mu\nu}^{(3)}$  in the vicinity of  $r_A^T$  where the maximum occurs. Thus the unphysical third term in Eq. (2.49) is always formally small. (We demonstrate that it is also small in practice in Sec. 2.7.) The errors introduced into the constraint equations are found by differentiating (2.49). Again, all terms involving derivatives of the transition functions are multiplied by the differences between expanded metrics in the buffer zone, which are of the same order as the uncontrolled remainders and therefore can be neglected.

In Figs. 2.9 and 2.10, we demonstrate the good behavior of the smoothed solution.

Observe that as  $x$  increases, the global metric with the transition function becomes identical to the near zone metric, while as  $r_A$  approaches zero (near each hole,  $x/m \rightarrow$

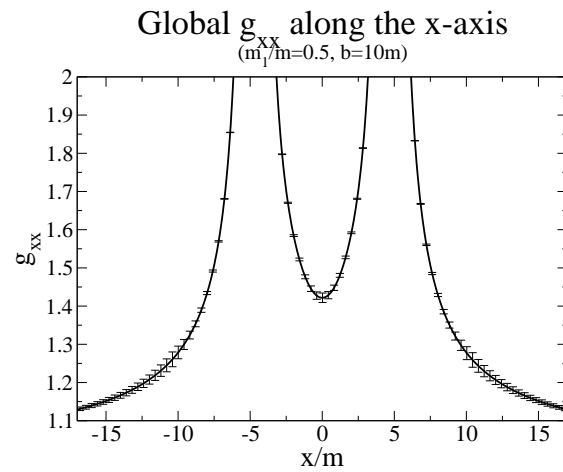


Fig. 2.9. This figure shows the  $xx$  component of the global approximation of the metric across both holes.

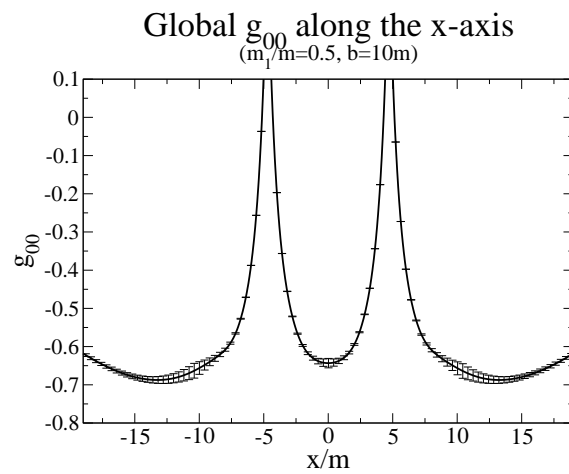


Fig. 2.10. Same as the previous Figure, but for the 00 metric component.

$\pm 5$ ) it becomes equal to the inner zone metric. Since the holes are close to each other, in the region between the holes the global metric never becomes identical to the near zone metric but rather always contains a contribution from the inner zone metrics. This linear combination is valid in that region because there the asymptotic expansions of both approximate metrics are comparable to each other. In Figs. 2.7 and 2.8, the error bars of the global metric with the transition function overlap the error bars of the inner and near zone metrics in the regions where the former are valid. This criterion would not be satisfied if the near zone and inner zone curves were farther from each other, which would occur if the holes were closer, and thus could be taken as another indicator that the holes are still (barely) far enough apart for matching.

## 2.7 Initial data for numerical relativity

The approximate metric (2.46) could be used as initial data for binary black hole simulations. To facilitate this task we now present this metric in the 3+1 decomposition, by providing explicit analytic expressions for the extrinsic curvature, lapse and shift on the  $\bar{T} = t = 0$  slice. If the normal vector to this slice is denoted by  $n^a$ , then the intrinsic metric in the slice is given by

$$q_{ab} = g_{ab} + n_a n_b, \quad (2.50)$$

and the extrinsic curvature is

$$K_{ab} = -\frac{1}{2} \mathcal{L}_n q_{ab}, \quad (2.51)$$

where  $\mathcal{L}_n$  is the Lie derivative in the direction normal to the  $t = 0$ -slice. Below we compute  $K_{ab}$  using the explicit expression

$$K_{ab} = -\frac{1}{2} n^c (\partial_c q_{ab} - \partial_a q_{cb} - \partial_b q_{ac}), \quad (2.52)$$

which has been obtained using the ordinary derivative operator and the fact that  $q_{ab} n^b = 0$ . The evolution vector

$$(\partial_t)^a = \alpha n^a + \beta^a \quad (2.53)$$

is split into pieces perpendicular and parallel to the  $t = 0$  slice, where  $\alpha$  denotes the lapse and  $\beta^a$  the shift. Note that  $n^a n_a = -1$  and  $\beta^a n_a = 0$ .

The near zone extrinsic curvature computed from the PN metric [101] in corotating harmonic coordinates on the  $t = 0$  slice is given by

$$K_{ij}^{(3)} = \sum_{A=1}^2 m_A \frac{4v_A^{(i} n^{j)} - v_A^k n_A^A \delta_{ij}}{r_A^2}, \quad (2.54)$$

where the error is of  $O(m/b)^{5/2}$ , the superscript 3 is to remind us that this expression is only valid in  $\mathcal{C}_3$ , and where the parentheses on the indices stand for symmetrization. In the previous equation,  $v_A^i$  and  $n_A^i$  denotes the particle velocities and directional vectors given by

$$v_1^2 = \omega \frac{m_2}{m} b, \quad v_2^2 = -\omega \frac{m_1}{m} b, \quad v_A^1 = v_A^3 = 0 \quad (2.55)$$

and

$$n_A^k = \frac{x^k - x_A^k}{r_A}, \quad x_1^1 = \frac{m_2}{m}b, \quad x_2^1 = -\frac{m_1}{m}b, \quad x_A^2 = x_A^3 = 0. \quad (2.56)$$

The corresponding near zone lapse and shift on the  $t = 0$  slice are

$$\alpha_{(3)} = 1 - \sum_{A=1}^2 \frac{m_A}{r_A} \quad (2.57)$$

and

$$\beta_{(3)}^i = - \sum_{A=1}^2 \frac{4m_A v_A^i}{r_A} - \epsilon_{ij3} \omega x^j, \quad (2.58)$$

where once more this is valid on  $\mathcal{C}_3$ .

The extrinsic curvature of the  $\bar{T} = 0$  slice valid in the inner zone of black hole 1 ( $\mathcal{C}_1$ ) and computed from the metric given in the previous section in isotropic corotating coordinates is

$$\begin{aligned} K_{00}^{(1),ICC} &= -\frac{m_2}{b^3} \Omega^2 \bar{Y} (\bar{X}^2 + \bar{Y}^2) \frac{\Psi^5}{\Psi - \frac{M_1}{R_1}} \left[ 2 \left( \Psi - \frac{M_1}{R_1} \right)^2 b\omega + 3\Omega \bar{X} \left( \Psi^4 - \frac{2M_1^2}{R_1^2} \right) \right], \\ K_{01}^{(1),ICC} &= \frac{m_2}{b} \Omega \frac{\Psi^5}{\Psi - \frac{M_1}{R_1}} \left[ 3\Omega \bar{X} \frac{\bar{Y}^2}{b^2} \left( \Psi^4 - \frac{2M_1^2}{R_1^2} \right) + \left( \Psi - \frac{M_1}{R_1} \right)^2 \frac{\omega}{b} (\bar{X}^2 + 2\bar{Y}^2) \right. \\ &\quad \left. + \left( \Psi - \frac{M_1}{R_1} \right) M_1 \omega \frac{\bar{X}^2}{R_1^3 b} (\bar{X}^2 + \bar{Y}^2 - \bar{Z}^2) \right], \\ K_{02}^{(1),ICC} &= -\frac{m_2 \bar{X} \bar{Y}}{b^3} \Omega \frac{\Psi^5}{\Psi - \frac{M_1}{R_1}} \left[ \left( \Psi - \frac{M_1}{R_1} \right)^2 b\omega + 3\Omega \bar{X} \left( \Psi^4 - \frac{2M_1^2}{R_1^2} \right) \right. \\ &\quad \left. - \left( \Psi - \frac{M_1}{R_1} \right) \frac{bM_1}{R_1^3} \omega (\bar{X}^2 + \bar{Y}^2 - \bar{Z}^2) \right], \\ K_{03}^{(1),ICC} &= \frac{m_2}{b^2} \omega \Omega \bar{X} \bar{Z} \Psi^5 \left[ \frac{M_1}{R_1^3} (\bar{X}^2 + \bar{Y}^2 - \bar{Z}^2) - \Psi + \frac{M_1}{R_1} \right], \end{aligned} \quad (2.59)$$

$$\begin{aligned}
K_{11}^{(1),ICC} &= -\frac{m_2 \bar{Y}}{2b^3} \frac{\Psi^5}{\Psi - \frac{M_1}{R_1}} \left[ 4 \left( \Psi - \frac{M_1}{R_1} \right)^2 b\omega + 4 \left( \Psi - \frac{M_1}{R_1} \right) b \frac{M_1}{R_1^3} \omega \bar{X}^2 \right. \\
&\quad \left. - 3\Omega \bar{X} \left( 4 \frac{M_1^2}{R_1^2} - 2\Psi^4 + \frac{M_1^3 \bar{X}^2}{R_1^5} + \frac{4M_1 \bar{X}^2}{R_1^3} \right) \right], \\
K_{12}^{(1),ICC} &= \frac{m_2 \bar{X}}{2b^3} \frac{\Psi^5}{\Psi - \frac{M_1}{R_1}} \left[ 2 \left( \Psi - \frac{M_1}{R_1} \right)^2 b\omega + 12M_1 \Omega \frac{\bar{X} \bar{Y}^2}{R_1^3} \left( 1 + \frac{M_1^2}{\left( \Psi - \frac{M_1}{R_1} \right) R_1^2} \right) \right. \\
&\quad \left. + 2 \left( \Psi - \frac{M_1}{R_1} \right) b\omega \frac{M_1}{R_1^3} (\bar{X}^2 - \bar{Y}^2 - \bar{Z}^2) \right], \tag{2.60} \\
K_{13}^{(1),ICC} &= \frac{6M_1 m_2 \Omega \bar{X}^2 \bar{Y} \bar{Z}}{b^3 R_1^3} \frac{\Psi^5}{\Psi - \frac{M_1}{R_1}} \left( 1 + \frac{M_1^2}{4R_1^2} \right), \\
K_{22}^{(1),ICC} &= \frac{m_2 \bar{Y}}{2b^3} \frac{\Psi^5}{\Psi - \frac{M_1}{R_1}} \left\{ 12 \frac{M_1^2}{R_1^2} \Omega \bar{X} - 6\Omega \Psi^4 \bar{X} + 3 \frac{M_1^3 \bar{Y}^2}{R_1^5} \Omega \bar{X} + 4 \frac{M_1}{R_1^3} \left[ 3\Omega \bar{X} \bar{Y}^2 \right. \right. \\
&\quad \left. \left. + \left( \Psi - \frac{M_1}{R_1} \right) b\omega (\bar{X}^2 - \bar{Z}^2) \right] \right\}, \\
K_{23}^{(1),ICC} &= -\frac{m_2 \bar{Z}}{2b^3} \frac{\Psi^5}{\Psi - \frac{M_1}{R_1}} \left[ 2 \left( \Psi - \frac{M_1}{R_1} \right)^2 b\omega - 12M_1 \Omega \frac{\bar{X} \bar{Y}^2}{R_1^3} \left( 1 + \frac{M_1^2}{4R_1^2} \right) \right. \\
&\quad \left. - 2 \left( \Psi - \frac{M_1}{R_1} \right) \frac{bM_1 \omega}{R_1^3} (\bar{X}^2 + \bar{Y}^2 - \bar{Z}^2) \right], \\
K_{33}^{(1),ICC} &= \frac{m_2 \bar{Y}}{2b^3} \frac{\Psi^5}{\Psi - \frac{M_1}{R_1}} \left[ 4 \left( \Psi - \frac{M_1}{R_1} \right)^2 b\omega + 4 \left( \Psi - \frac{M_1}{R_1} \right) b\omega \frac{M_1 \bar{Z}^2}{R_1^3} \right. \\
&\quad \left. + 3\Omega \bar{X} \left( 4 \frac{M_1^2}{R_1^2} - 2\Psi^4 + \frac{M_1^3 \bar{Z}^2}{R_1^5} + 4 \frac{M_1 \bar{Z}^2}{R_1^3} \right) \right], \tag{2.61}
\end{aligned}$$

where the error is of  $O(\bar{R}_1/b)^3$ , and where the superscript *ICC* is to remind that that this is calculated in isotropic corotating coordinates. Later on, we will transform this metric to harmonic corotating coordinates with the map  $\phi_{13}$  found in Eq. (2.31), and we will drop this superscript. In the above equations,  $\Psi$  is the Brill-Lindquist factor for black hole 1 in isotropic coordinates, *i.e.*

$$\Psi = 1 + \frac{M_1}{2R_1}. \tag{2.62}$$

The  $K_{0\mu}^{(1),ICC}$  components will be needed later in the coordinate transformation and are obtained from the purely spatial components  $K_{kl}^{(1),ICC}$  using

$$K_{0\nu}^{(1),ICC} = q_0^k q_\nu^l K_{kl}^{(1),ICC}, \quad (2.63)$$

where the projection tensor  $q_\mu^\nu$  is given by

$$q_\mu^\nu = \delta_\mu^\nu + n_\mu^{(1),ICC} n_{(1),ICC}^\nu. \quad (2.64)$$

Here, the normal vector to the slice computed with

$$n_a^{(1),ICC} = -\sqrt{-1/h_{(1)}^{00}} (d\bar{T})_a \quad (2.65)$$

is given by

$$\begin{aligned} n_0^{(1),ICC} &= -\frac{1 - \frac{M_1}{2R_1}}{\Psi} \left[ 1 - \frac{m_2}{b} \left( 1 - \frac{M_1}{2R_1} \right)^2 \Psi^2 \frac{R_1^2}{b^2} P_2\left(\frac{\bar{X}}{R_1}\right) \right], \\ n_i^{(1),ICC} &= 0, \end{aligned} \quad (2.66)$$

where  $P_2$  stands for the second Legendre polynomial.

The upper components are then

$$\begin{aligned} n_{(1),ICC}^0 &= \frac{\Psi}{1 - \frac{M_1}{2R_1}} \left[ 1 + \frac{m_2}{b} \left( 1 - \frac{M_1}{2R_1} \right)^2 \Psi^2 \frac{R_1^2}{b^2} P_2(\bar{X}/R_1) \right], \\ n_{(1),ICC}^1 &= \frac{\Psi}{1 - \frac{M_1}{2R_1}} \bar{Y} \left[ \Omega + 2\frac{m_2}{b}\omega \left( 1 - \frac{M_1}{2R_1} \right)^2 \frac{\bar{X}}{b} \right. \\ &\quad \left. + \frac{m_2}{b}\Omega \left( 1 - \frac{M_1}{2R_1} \right)^2 \Psi^2 \frac{R_1^2}{b^2} P_2(\bar{X}/R_1) \right], \\ n_{(1),ICC}^2 &= -\frac{\Psi}{1 - \frac{M_1}{2R_1}} \left[ \Omega\bar{X} + 2\frac{m_2}{b}\omega \left( 1 - \frac{M_1}{2R_1} \right)^2 \frac{\bar{X}^2 - \bar{Z}^2}{b} \right. \\ &\quad \left. + \frac{m_2}{b}\Omega \left( 1 - \frac{M_1}{2R_1} \right)^2 \Psi^2 \frac{R_1^2}{b^2} \bar{X} P_2(\bar{X}/R_1) \right], \\ n_{(1),ICC}^3 &= -2\frac{m_2}{b}\omega \left( 1 - \frac{M_1}{2R_1} \right) \Psi \frac{\bar{Y}\bar{Z}}{b}. \end{aligned} \quad (2.67)$$

This means that the lapse and shift of the  $\bar{T} = 0$  slice in the inner zone ( $\mathcal{C}_1$ ) and in inner corotating coordinates are given by

$$\begin{aligned}\alpha_{(1),ICC} &= -n_0^{(1),ICC} = \frac{1 - \frac{M_1}{2R_1}}{\Psi} \left[ 1 - \frac{m_2}{b} \left( 1 - \frac{M_1}{2R_1} \right)^2 \Psi^2 \frac{R_1^2}{b^2} P_2(\bar{X}/R_1) \right], \\ \beta_{(1),ICC}^i &= -\alpha_{(1),ICC} n_{(1),ICC}^i.\end{aligned}\quad (2.68)$$

Observe that the lapse of Eq. (2.68) goes through zero at  $R_1 = M/2$ . Apart from a small perturbation it closely resembles the standard Schwarzschild lapse in isotropic coordinates.

Note that the extrinsic curvature, lapse and shift given up to this point are expressed in two different coordinate systems. The post-Newtonian quantities valid in the near zone ( $\mathcal{C}_3$ ) are given in harmonic corotating coordinates, while the black hole perturbation theory results valid in the inner zones ( $\mathcal{C}_{1,2}$ ) are given in isotropic corotating coordinates. We will now apply the coordinate transformation found in Sec. 2.5, namely Eq. (2.31), to transform the inner zone expressions to harmonic corotating coordinates, thus dropping the label ICC in favor of the superscript (1). The result for the inner extrinsic curvature of black hole 1 is given by

$$K_{ij}^{(1)} = K_{\bar{l}\bar{m}}^{(1)} J_{\bar{l}}^i J_{\bar{m}}^j, \quad (2.69)$$

where all components still have errors of  $O(5/2, 3)$ . The extrinsic curvature in harmonic corotating coordinates in submanifold  $\mathcal{C}_2$  can be obtained from the above equation by the symmetry transformation discussed in Eq. (2.32). In Fig. 2.11 we have plotted the  $xy$  component of the extrinsic curvature along the  $x$ -axis. Observe that the behavior of the post-Newtonian solution (dashed line) is different from that of the black hole perturbation solution close to the black hole, where the latter diverges more abruptly. In Figs. 2.11–2.15, the error bars have been estimated by inserting Eqs. (2.37) and (2.38) into the definition of the quantity plotted and using  $\partial_t r_A \approx b\omega$  and  $\partial_t R_A \approx b\Omega$ .

Similarly, the lapse and shift in harmonic corotating coordinates corresponding to the inner zone of black hole 1 are given by

$$\begin{aligned}\alpha_{(1)} &= \frac{1}{n_{(1)}^0} = -n_0^{(1)} = J^{\bar{T}}_t \alpha_{(1),ICC}, \\ \beta_{(1)}^i &= -\alpha_1 n_1^i,\end{aligned}\quad (2.70)$$

where again the lapse and shift for the inner zone around black hole 2 ( $\mathcal{C}_2$ ) can be obtained by the symmetry transformation (2.32). In these equations, the normal vector is given by

$$n_{(1)}^\mu = J^{\bar{\nu}}_\nu n_{(1),ICC}^\nu, \quad (2.71)$$

where the matrix  $J^{\bar{\mu}}_\nu$  has been defined in Eq. (2.34). Note that  $\alpha_{(1)}$  in Eq. (2.70) has the same zeros as  $\alpha_{(1),ICC}$  and, thus,  $\alpha_{(1)}$  also changes sign at  $R_1 = M/2$ . Furthermore,

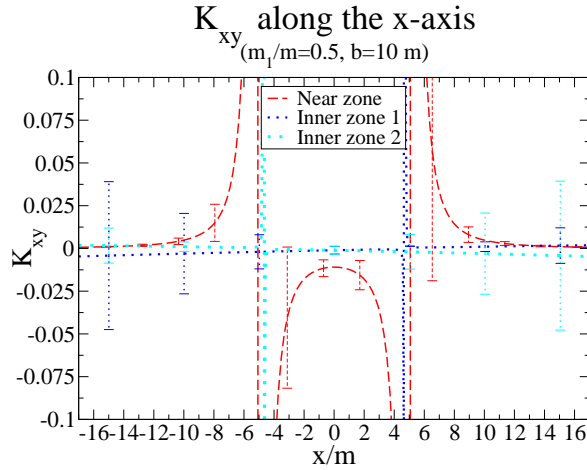


Fig. 2.11. This figure shows the  $xy$  component of the near zone (PN - dashed line) extrinsic curvature, as well as the inner zone curvatures (BHPT - dotted lines) obtained via black hole perturbation theory. This figure uses the same test case as previous figures, with equal mass black holes and  $m/b = 1/10$ .

since  $J^{\bar{T}}_t = 1 + O(m/b)$  the inner zone lapse  $\alpha_{(1)}$  equals  $\alpha_{(1),ICC}$  up to a perturbation of  $O(m/b)$  and thus  $\alpha_{(1)}$  is equal to the standard lapse of Schwarzschild in isotropic coordinates plus a perturbation of  $O(m/b)$ . These features are borne out by the plot in Fig. 2.12 which shows the global lapse along the  $x$ -axis. We can also see from the figure that while the inner zone lapse goes to  $-1$  as  $r_1 \rightarrow 0$ , the near zone one diverges to negative infinity.

With these equations, we can construct an approximate piecewise global extrinsic curvature, lapse and shift by substituting the metric for these quantities in Eq. (2.36). By the theorems of asymptotic matching, the derivatives of adjacent pieces of the piecewise metric will be asymptotic to each other inside their respective buffer zones. This asymptotic similarity is, thus, also observed in the extrinsic curvature, as well as the lapse and the shift. Due to the piecewise nature of these solutions, there will be discontinuities on a 2-sphere located at some transition radius inside of the buffer zone. In order to eliminate these discontinuities, we use the same transition functions used for the metric in Eq. (2.42) with the same parameters. In this manner, we obtain a smooth

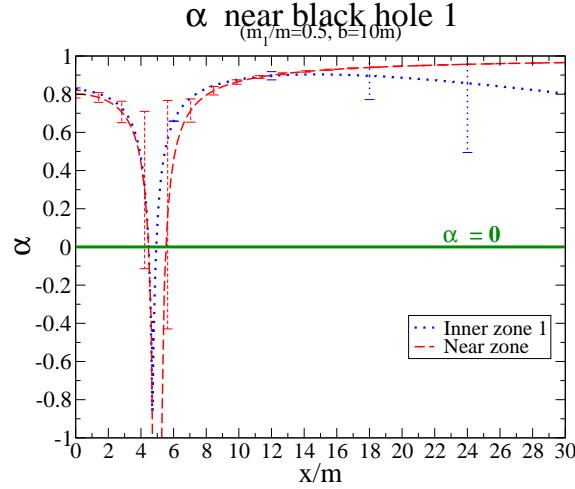


Fig. 2.12. This figure shows the near zone (PN - dashed line) and the inner zone lapse (BHPT - dotted line) along the  $x$ -axis. Observe that the near zone lapse crosses zero at  $x/m = 5.5$  and  $x/m = 4.5$ , which is the location of the event horizon in harmonic coordinates.

global extrinsic curvature, lapse and shift given by

$$\begin{aligned}
 K_{ij}^{(global)} &= G(x) \left\{ F_1(R_1) K_{ij}^{(3)} + [1 - F_1(R_1)] K_{ij}^{(1)} \right\} \\
 &+ [1 - G(x)] \left\{ F_2(R_2) K_{ij}^{(3)} + [1 - F_2(R_2)] K_{ij}^{(2)} \right\}, \\
 \alpha_{(global)} &= G(x) \left\{ F_1(R_1) \alpha_{(3)} + [1 - F_1(R_1)] \alpha_{(1)} \right\} \\
 &+ [1 - G(x)] \left\{ F_2(R_2) \alpha_{(3)} + [1 - F_2(R_2)] \alpha_{(2)} \right\}, \\
 \beta_{(global)}^i &= G(x) \left\{ F_1(R_1) \beta_{(3)}^i + [1 - F_1(R_1)] \beta_{(1)}^i \right\} \\
 &+ [1 - G(x)] \left\{ F_2(R_2) \beta_{(3)}^i + [1 - F_2(R_2)] \beta_{(2)}^i \right\}. \tag{2.72}
 \end{aligned}$$

Figs. 2.13, 2.14 and 2.15 show the global lapse, shift and extrinsic curvature with the transition functions.

We also could have computed the extrinsic curvature directly from Eq. (2.46). This would add terms involving derivatives of the transition functions. The parameters of the transition functions were chosen so that these derivatives are of the same order as the uncontrolled remainders in the buffer zone, and thus formally do not affect the accuracy of the extrinsic curvature. Since the two methods are equivalent, we took the one which was simpler to compute (had fewer terms).

The initial data constructed by the methods above [Eqs. (2.46) and (2.72)] is only an approximate solution to the Einstein equations. Therefore, this data leads to

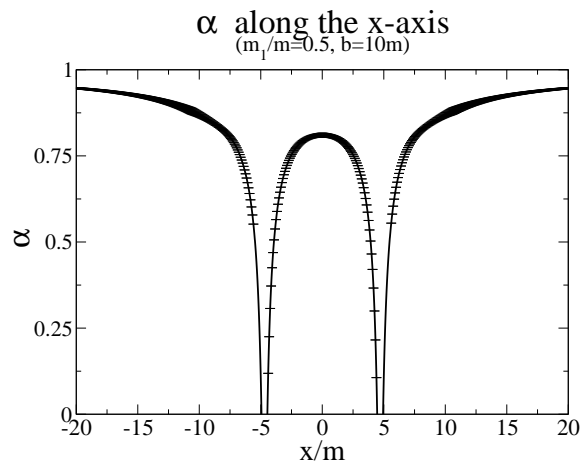


Fig. 2.13. This figure shows the global lapse along the x-axis with the transition function.

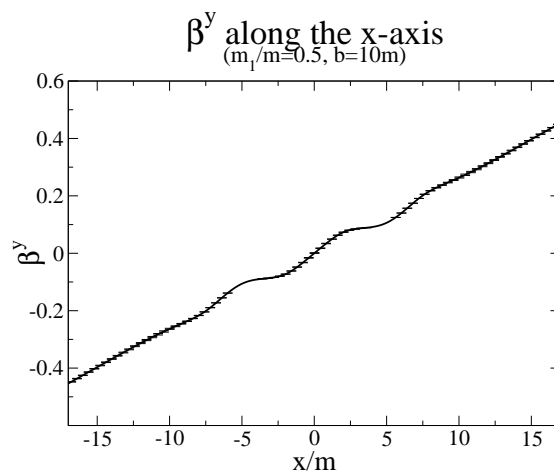


Fig. 2.14. This figure shows the global shift vector along the x-axis with the transition function.

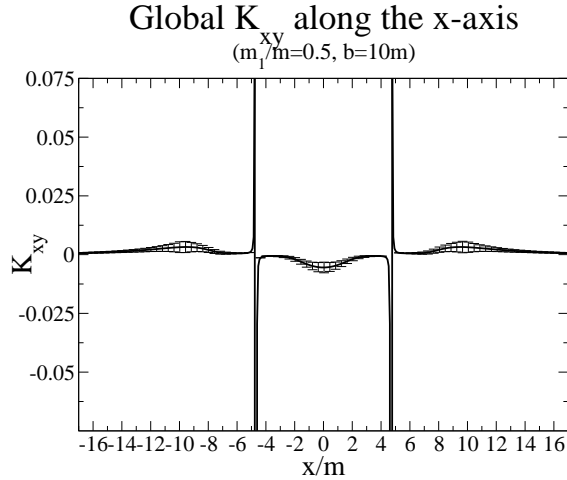


Fig. 2.15. This figure shows the global  $xy$  component of the extrinsic curvature along the  $x$ -axis with the transition function. Note that the bumps due to the transition function are comparable to the error bars which estimate uncontrolled remainders in the expansions.

an error in the constraints of the full theory of order  $O(m/b)^{9/2}$  near the horizons and  $O(m/r)^2$  in the near zone. This error can be sufficiently small compared to other sources of numerical error such that solving the constraints more accurately is not required. However, perhaps the optimal approach would be to use this solution as input to York's conformal method [18] and compute a numerical solution to the full constraints. Since this data is already significantly close to the constraint hypersurface, there might be some hope that appropriate projection methods will *not* alter much the astrophysical content of the initial data. Somewhat surprisingly, standard PN data (without matching) has not yet been used for the generation of numerical black hole initial data except in Ref. [16], which is based on the PN data of Ref. [103]. We leave it to future work to explore similar techniques for the data set presented here.

If this data is to be evolved, it is necessary to choose a lapse and a shift. The choice presented in this section is natural in the sense that it is close to quasi-equilibrium. In other words, with the lapse and shift presented in this section, the 3-metric and extrinsic curvature should evolve slowly. However, since our lapse is not everywhere positive, some evolution codes may have trouble evolving with it. If this is the case, one can simply replace the above lapse with a positive function at the cost of losing manifest quasi-equilibrium, but without changing the physical content of the initial data or the results of the evolution.

## 2.8 Conclusions

We have constructed initial data for binary black hole evolutions by calculating a uniform global approximation to the spacetime via asymptotic matching of locally good approximations. The manifold was first divided into three submanifolds: two inner zones (one for each hole),  $\mathcal{C}_1$  and  $\mathcal{C}_2$  ( $r_A \ll b$ ) equipped with isotropic coordinates; and one near zone,  $\mathcal{C}_3$  ( $r_A \gg m_A$  and  $r \ll \lambda/2\pi$ ), equipped with harmonic coordinates. In the near zone, the metric was approximated with a post-Newtonian expansion, while in each inner zone the metric was approximated with a perturbative tidal expansion of Schwarzschild geometry. Each approximate solution depends on small parameters locally defined on each submanifold. These submanifolds overlap in two buffer zones,  $\mathcal{O}_{13}$  and  $\mathcal{O}_{23}$  (4-volumes), given by the intersection of the inner zones with the near zone, *i.e.* on an initial spatial hypersurface the buffer zones becomes 3-volumes given by  $m_A \ll r_A \ll b$ . Inside each buffer zone, two different approximations for the metric were simultaneously valid and hence we were allowed to asymptotically match them inside this zone.

The matching procedure consisted of first expanding both adjacent approximate metrics asymptotically inside the buffer zones. After transforming to the same gauge, these asymptotic expansions were then set asymptotic to each other—equating their expansion coefficients, which does not in general set the functions equal to each other anywhere in the buffer zone. After solving the differential systems given by equating expansion coefficients, asymptotic matching returned a coordinate transformation ( $\phi_{13}$  and  $\phi_{23}$ ) between submanifolds and matching conditions ( $\psi_{13}$  and  $\psi_{23}$ ) that relate parameters native to different charts. A piecewise global metric was then obtained by transforming all metrics with the set  $\{\phi_{nm}; \psi_{nm}\}$ , resulting in coordinates which resemble harmonic coordinates in the near zone but isotropic coordinates in each inner zone.

Once a piecewise global metric was found, the spatial metric and extrinsic curvature were calculated in each zone by choosing a spatial hypersurface, with the standard  $3 + 1$  decomposition. This initial data was then transformed in the same manner as the 4 metric. Due to the inherent piecewise nature of asymptotic matching, this data was found to have discontinuities of order  $O(3/2, 3)$  or smaller inside the buffer zone. We constructed transition functions to remove the remaining discontinuities in metric components and spikes in derivatives. These transition functions were carefully built to avoid introducing errors larger than the uncontrolled remainders of the approximations in the buffer zones. With these functions, we constructed a global uniform approximation to the metric valid everywhere in the manifold with errors  $O(m/b)^{9/2}$  near the black holes and  $O(m/r)^2$  far away from either of them.

This uniform global approximation of the metric can be used as long as the black holes are sufficiently far apart. When the two black holes are too close, there is no intervening post-Newtonian near zone in which to match. However, since there is no precise knowledge of the region of convergence of the PN series, it is unknown precisely at what separation the near zone vanishes. We have experimented with separations  $b \geq 10m$  and we have found that, in these cases, a region does exist between the holes where the post-Newtonian metric is reasonably close to the perturbed black hole metrics and thus matching is still possible. For separations of  $b < 10m$ , this region shrinks

rapidly and matching is not guaranteed to be successful. Also, the “global” metric is not valid all the way to the asymptotically flat ends inside the holes, implying that our initial data must be evolved with excision techniques rather than punctures.

We then constructed a lapse, shift, and extrinsic curvature, all of which are needed for numerical evolutions. The lapse was found to possess the expected feature that it becomes negative inside the horizon of either black hole. Some numerical codes might find this feature undesirable, in which case the lapse can be replaced by some positive function at the cost of losing approximate quasi-stationarity. These 3+1 quantities were then smoothed with transition functions of the same type as those used in the 4-metric.

In conclusion, we have constructed initial data for an inspiraling black hole binary that satisfies the constraints to order  $O[(m/b)^{5/2}(R_1/b)^2]$  in the inner zone, and to order  $O(m/r)^2$  in the near zone. This data is a concrete step toward using PN and perturbation methods to construct such initial data, and it should be compared to other numerical methods with respect to its ability to approximate the astrophysical situation. We should note that the data presented here makes use of perturbative expansions of low order (*e.g.*, the near zone metric is built from a 1 PN expansion), but this paper firms up a method introduced by Alvi [28] that could be repeated to higher order at the cost of more algebra [93, 39]. The post-Newtonian metric needed for the next order in  $m/r$  (and beyond) is available [101], as is the octopole perturbation  $(r/b)^3$  of a Schwarzschild black hole [95]. Our method might also be extended to spinning black holes, which are more astrophysically realistic, with the available post-Newtonian near-zone metric [33] and tidal perturbation [104].

## Acknowledgments

We thank Thomas Baumgarte, Carl Bender, Lee Lindblom, Eric Poisson, Kip Thorne, Qinghai Wang, and Clifford Will for useful discussions and insightful comments.

We acknowledge the support of the Institute for Gravitational Physics and Geometry and the Center for Gravitational Wave Physics, funded by the National Science Foundation under Cooperative Agreement PHY-01-14375. This work was also supported by NSF grants PHY-02-18750, PHY-02-44788, PHY-02-45649, PHY-05-55628, PHY-05-55644, and by DFG grant “SFB Transregio 7: Gravitational Wave Astronomy”.

## Chapter 3

# Improved initial data for black hole binaries by asymptotic matching of post-Newtonian and perturbed black hole solutions

We construct approximate initial data for non-spinning black hole binary systems by asymptotically matching the 4-metrics of two tidally perturbed Schwarzschild solutions in isotropic coordinates to a resummed post-Newtonian 4-metric in ADMTT coordinates. The specific matching procedure used here closely follows the calculation in [105], and is performed in the so-called buffer zone where both the post-Newtonian and the perturbed Schwarzschild approximations hold. The result is that both metrics agree in the buffer zone, up to the errors in the approximations. However, since isotropic coordinates are very similar to ADMTT coordinates, matching yields better results than in the previous calculation [105], where harmonic coordinates were used for the post-Newtonian 4-metric. In particular, not only does matching improve in the buffer zone, but due to the similarity between ADMTT and isotropic coordinates the two metrics are also close to each other near the black hole horizons. With the help of a transition function we also obtain a global smooth 4-metric which has errors on the order of the error introduced by the more accurate of the two approximations we match. This global smoothed out 4-metric is obtained in ADMTT coordinates which are not horizon penetrating. In addition, we construct a further coordinate transformation that takes the 4-metric from global ADMTT coordinates to new coordinates which are similar to Kerr-Schild coordinates near each black hole, but which remain ADMTT further away from the black holes. These new coordinates are horizon penetrating and lead, for example, to a lapse which is everywhere positive on the  $t = 0$  slice. Such coordinates may be more useful in numerical simulations.

### 3.1 Introduction

The modeling of binary black hole systems is essential for the detection of gravitational waves both by space and earth-based interferometers <sup>1</sup> [106, 5, 7, 6, 8]. Often

---

<sup>1</sup>This chapter is based on the following paper: N. Yunes and W. Tichy, Phys. Rev. D **74**, 064013 (2006)

this detection relies on matched filtering, which consists of comparing accurate waveform templates to the signal. In the strong field regime, these templates can be modeled accurately enough only by numerical simulations [107], where one solves the Einstein equations subject to initial conditions that determine the physical character of the system. The astrophysical accuracy of the template generated via a numerical evolution will depend on two main factors: the numerical error introduced by the evolution and gravitational wave extraction codes; and the astrophysical accuracy of the initial data set. In this paper we study one particular approach to solve the initial data problem. This approach was developed in Ref. [105] (henceforth paper 1) and is based on matching several approximate solutions of the Einstein equations.

There have been numerous efforts to find astrophysically accurate initial data for binary systems [84, 108, 23, 85, 24, 109, 18, 110, 88, 16, 87, 89, 90, 111, 25, 112, 113, 91, 92, 114], which usually consist of the 3-metric and extrinsic curvature. Most methods rely on performing decompositions of the data to separate the so-called physical degrees of freedom from those constrained by the Einstein equations and those associated with diffeomorphisms. These physical degrees of freedom carry the gravitational wave content of the data, and thus should be chosen to represent the astrophysical scenario that is being described. However, the exact solution to the Einstein equations for the 2-body scenario remains elusive. Therefore, the gravitational wave content of the data is not known exactly.

One commonly used cure to this problem is to give an ansatz for these physical degrees of freedom, which usually does not satisfy the constraints. This ansatz is then projected onto the constraint-satisfying hypersurface by solving the constraint equations for the quantities introduced by the decomposition. The projected data will now satisfy the constraints, but it is unclear whether such data are astrophysically accurate. First, some of the assumptions that are used in the construction of the initial ansatz are known to be physically inaccurate. For example, the spatial metric is often assumed to be conformally flat, which is known to be incorrect at 2 post-Newtonian (PN) order [3], and which also does not contain realistic tidal deformations near the black holes. Furthermore, after projecting onto the constraint hypersurface, the data will be physically different from the initial ansatz [115, 87, 16]. It is thus unclear exactly what physical scenario these projected data represent and whether or not they will be realistic.

Recent efforts have concentrated on using physical approximations to construct initial data sets. One such effort can be called the quasiequilibrium approach [110, 90, 92] where one assumes that the quantities describing the initial data evolve on a time scale much longer than the orbital timescale, when appropriate coordinates are used. There are also approaches built entirely from second post-Newtonian approximations [16, 27]. Even though [16] also develops a complete method to project onto the constraint hypersurface, both [16] and [27] are not guaranteed to be realistic close to the black holes, since post-Newtonian theory is in principle not valid close to black holes. Another recent effort, which will be the subject of this work, involves several analytic approximations that are both physically accurate and close to the constraint hypersurface far and close to the holes (see paper 1). Such initial data coming from analytic approximations can then be evolved without solving the constraints, provided that constraint violations are everywhere smaller than numerical error. A perhaps more appealing alternative is to

project these data onto the constraint hypersurface. If these data are close enough to the hypersurface, then any sensible projection algorithm should produce constraint-satisfying data that are close to the original approximate solution.

Regardless of how such data are implemented, there are reasons to believe that such an approach will produce astrophysically realistic initial data. First, since the data are built from physical approximations, there are no assumptions that are unrealistic. The only limit to the accuracy is given by the order to which the approximations are taken. Moreover, the analytic control provided by these physical approximations allows for the tracking of errors in the physics, thus providing a means to measure the distance to the exact initial data set. Note however, that our work described below will only be accurate up to leading order in both the post-Newtonian and the tidal perturbation expansions used. This means that at the currently achieved expansion order, our initial data are by no means guaranteed to be superior to the other approaches discussed above. Nevertheless, our approach can be systematically extended to higher order.

Data that use analytic approximations valid on the entire hypersurface are difficult to find because such approximations are usually valid only in certain regions of the hypersurface. One method to construct such data is by asymptotically matching two different physical approximations in a region where they overlap. Asymptotic matching, which for general relativity was developed in [98, 97, 100, 99, 94], consists of comparing the asymptotic approximations of two adjacent solutions inside of an overlap 4-volume. By comparing these asymptotic approximations, matching returns a map between coordinates and parameters local to different regions, which forces adjacent solutions to be asymptotic to each other inside the overlap region called the buffer zone. Since these solutions are close to each other in the buffer zone, it is possible to construct transition functions that merge these solutions, thus generating a smooth global metric.

Alvi [28] attempted to apply matching to binary systems, but instead of matching he actually performed patching, because he set the physical approximations equal to each other at a 2-surface. As a result, Jansen and Brüggmann [32] found that Alvi's 4-metric, and in particular his extrinsic curvature, was hard to smooth with transition functions in the buffer zone, since the solutions were not sufficiently close to each other. Jansen and Brüggmann thus concluded that these large discontinuities in Alvi's data renders them impractical for numerical implementation. In paper 1, binary systems were studied once more, but this time true asymptotic matching was implemented, thus successfully generating solutions that approach each other in the buffer zone. It was possible to smooth these solutions and thus to create useful initial data. The approach we used in paper 1 was to match a PN metric in harmonic gauge [3], valid far from both black holes but less than a gravitational wavelength from the center of mass (near zone), to a perturbed Schwarzschild metric in isotropic coordinates, valid close to the holes (inner zone).

In this paper, we study the method developed in paper 1 in more detail and we investigate and improve the resulting data. This improvement is mainly due to using different coordinates in the PN approximation. Instead of employing harmonic gauge, we now use a post-Newtonian metric in ADMTT gauge [116, 117, 103]. We will see that this leads to better matching. The reason for this improvement is that the 4-metric in ADMTT coordinates can be brought into a form that is very close to

Schwarzschild in isotropic coordinates near each black hole. Therefore, we obtain a much smoother match between this near zone metric and the inner zone one, which is also given in isotropic coordinates (see Fig. 3.2). The results presented in Sec. 3.6 indeed show that matching with the ADMTT PN near zone metric works better than with the harmonic PN near zone metric. In addition, the ADMTT PN near zone metric is very similar to the perturbed Schwarzschild metric even near the black hole horizon, where PN approximations in principle break down. This similarity is due to the fact that, we use a resummed version of the ADMTT metric, obtained by adding higher order post-Newtonian terms.

Another piece of evidence that suggests that matching works better between ADMTT and isotropic coordinates comes from looking at Hamiltonian and momentum constraint violations. In Sec. 3.7 we compare the Hamiltonian and momentum constraint violations for the data of this paper and of paper 1. We find that the use of the ADMTT PN near zone metric leads to smaller constraint violations than in paper 1. With the help of a transition function we can also obtain a global smooth 4-metric which has errors on the order of the error introduced by the more accurate of the two approximations we match.

By computing the constraint violations, we discover that both the data set of this paper and that presented in paper 1 might not be easily implemented in numerical simulations. In particular, we observe that the momentum constraint diverges near the apparent horizon of each black hole. This makes it difficult or impossible to excise a region inside each black hole, which contains all points where divergences occur. This divergence arises due to the choice of coordinates in the inner zone. Since we use the  $t = \text{const}$  slices of isotropic coordinates as spatial slices, the lapse goes through zero near the horizon. This zero in the lapse in turn leads to a blowup of some components of the extrinsic curvature and the momentum constraint. In order to circumvent this problem, we construct a map from isotropic coordinates to new horizon-penetrating coordinates. A similar idea was presented in Ref. [29], but here we extend those ideas and provide explicit expressions for the transformed inner zone metric in a ready-to-implement form. These new coordinates are identical Kerr-Schild coordinates inside the horizon and become isotropic in the buffer zone. When this transformation is applied to either the data set presented in this paper or that presented in paper 1, the lapse of the new  $t = \text{const}$  slices is positive through the horizon, eliminating the divergence in the extrinsic curvature. This new coordinate system will make excision easier, without changing the physical content of the data.

The paper is organized as follows. Sec. 3.2 explains how the spacetime is divided into zones and how matching will be implemented. Sec. 3.3 describes the near zone post-Newtonian metric, while Sec. 3.4 focuses on the inner zone metric. Sec. 3.5 performs the matching and provides a map between coordinates and parameters local to the near and inner zones. Sec. 3.6 gives explicit formulas for the global metric, introduces the smoothing functions and also decomposes this 4-metric into initial data for numerical relativity. Sec. 3.7 compares the constraint violations of the initial data presented in this paper to those of paper 1. In Sec. 3.8 we present an additional coordinate transformation which can be used to construct horizon penetrating coordinates. Sec. 3.9 concludes and points to future work. Throughout we use geometrized units, where  $G = c = 1$ .

### 3.2 Division of spacetime into zones and matching in GR

Consider a binary black hole spacetime and divide it into 4 zones. First, there are the so-called inner zones  $\mathcal{C}_1$  and  $\mathcal{C}_2$  close to each black hole, where we can use black hole perturbation theory to obtain an approximate solution to the Einstein equations. These solutions are obtained under the assumption that the black holes are separated far enough that the influence of black hole 2 is only a small perturbation near black hole 1. Second, there is the near zone  $\mathcal{C}_3$  where PN theory should provide a good approximation as long as the black holes do not move too fast. Finally  $\mathcal{C}_4$  denotes the far zone where retardation effects matter. These zones are shown in Fig. 3.1 and we summarize them in Table I. The quantities introduced in this table are defined as follows:  $r_{in}$  and  $r_{out}$

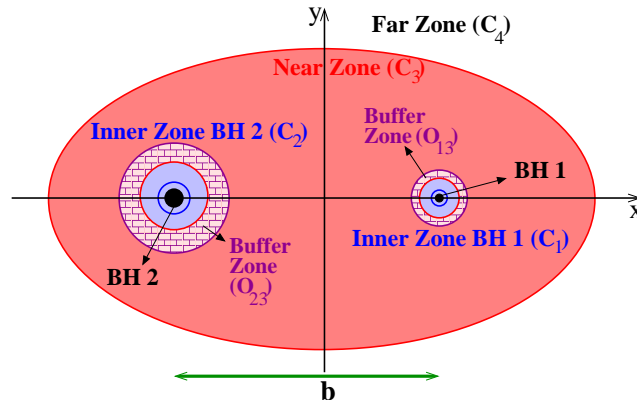


Fig. 3.1. Schematic diagram of the near zone (dark gray), inner zones (light gray) and buffer zones (checkered). The near zone extends up to the inner boundary of the buffer zone, while the inner zone extends from the outer boundary of the buffer zone up to the black hole. Therefore, the buffer zones are spherical shells where the near zone and inner zones overlap. BH 1 and BH 2 (black) are separated by distance  $b$ .

are the approximate inner and outer boundary of each zone respectively, as measured from the  $A$ th black hole ( $A = 1$  or  $2$ ) in the coordinate system local to it;  $\epsilon_{(n)}$  is the expansion parameter used to find an approximate solution to the Einstein equations in that zone;  $m_A$  is the mass parameter of the  $A$ th black hole in the near and far zones;  $r_A$  and  $\bar{r}_A$  are the radial distances as measured from the  $A$ th hole in the near and inner zones respectively;  $\lambda$  is the typical gravitational wavelength; and  $b$  is the coordinate separation of the black holes.

Inside of each zone we approximate the 4-metric with an monovariate expansion in  $\epsilon_{(n)}$ , which is defined in some coordinate system, and which depends on parameters, like the mass of the black holes or the orbital angular velocity. The inner zones are both

Zone	$r_{in}$	$r_{out}$	$\epsilon_{(n)}$
Inner zone BH 1 ( $\mathcal{C}_1$ )	0	$\ll b$	$\bar{r}_1/b$
Inner zone BH 2 ( $\mathcal{C}_2$ )	0	$\ll b$	$\bar{r}_2/b$
Near zone ( $\mathcal{C}_3$ )	$\gg m_A$	$\ll \lambda/2\pi$	$m_A/r_A$
Far zone ( $\mathcal{C}_4$ )	$\gg b$	$\infty$	$m_A/r_A$

Table 3.1. Description of the division of the spacetime into zones [28].

equipped with isotropic coordinates and have parameters  $(M_A, \Omega)$ , where the approximate solutions to the Einstein equations are given by a perturbed Schwarzschild metric. On the other hand, the near zone is equipped with ADMTT coordinates (ADMTT gauge), where the approximate solution to the Einstein equations is a PN approximation with parameters  $m_A$  and  $\omega$ . This PN approximation is valid in both  $\mathcal{C}_3$  and  $\mathcal{C}_4$  up to the order treated in this paper.

As explained in paper 1, asymptotic matching consists of comparing the asymptotic expansions of adjacent approximate metrics in an overlap region or buffer zone. These buffer zones are defined by the intersection of the regions of validity of two adjacent metrics. The 2 buffer zones are delimited by the intersection of the inner zones  $\mathcal{C}_1$  and  $\mathcal{C}_2$  (of BHs 1 and 2), and the near zone  $\mathcal{C}_3$ . These buffer zones  $\mathcal{O}_{12} = \mathcal{C}_1 \cap \mathcal{C}_2$  and  $\mathcal{O}_{13} = \mathcal{C}_1 \cap \mathcal{C}_3$  can only be defined in the asymptotic sense [30] via  $m_A \ll r_A \ll b$  and are the regions in which asymptotic matching will be performed. Formally, there is a third buffer zone ( $\mathcal{O}_{34}$ ), given by the intersection of the near and far zone, but since the ADMTT PN metric at the order considered here is valid in both  $\mathcal{C}_3$  and  $\mathcal{C}_4$ , it is unnecessary to perform any matching there. The asymptotic expansions of the approximate metrics in the buffer zones  $\mathcal{O}_{A3}$  are bivariate, because they will depend on 2 independent parameters:  $m_A/r_A$  and  $r_A/b$ . Thus, the errors in the asymptotic expansions valid in the buffer zones will be denoted as  $O(p, q)$ , which stands for errors of  $O(m/b)^p$  or errors of  $O(r_A/b)^q$ .

Asymptotic matching then produces a coordinate and parameter mapping between adjacent regions. In this paper, these maps will consist of a transformation between isotropic and ADMTT coordinates, as well as a set of conditions to relate  $M_A$  and  $\Omega$  to  $m_A$  and  $\omega$ . With these maps, we can construct a piecewise global metric by choosing a 3-surface inside the buffer zone, where we join the approximate solutions to the Einstein equations together. Small discontinuities will be present in the global metric at the chosen 3-surface, due to its inherent piecewise nature, but they are of the same order as the errors in the physical approximations, and thus controllable by the size of the perturbation parameters. Furthermore, if such parameters are chosen sufficiently small, these errors could, in particular, become smaller than numerical discretization errors. Ultimately, a  $C^\infty$  metric is sought after, so, since these discontinuities are small, the global metric can be smoothed by introducing transition functions.

### 3.3 Near Zone: An ADMTT post-Newtonian metric

In this section, we present the near zone metric in ADMTT gauge valid in  $\mathcal{C}_3$  and  $\mathcal{C}_4$  and expand it in the buffer zone  $\mathcal{O}_{13}$ . Analyzing matching in  $\mathcal{O}_{13}$  will suffice due to the symmetry of the problem. The coordinate-parameter map for the overlap region  $\mathcal{O}_{23}$  will later be given by a simple symmetry transformation.

The ADMTT PN metric is obtained by solving the equations of motion for a binary black hole system with Hamiltonian dynamics [116]. The Hamiltonian is expanded in a slow-motion, weak-field approximation (PN) in ADMTT coordinates. This approach is similar to the standard Lagrangian PN expansion implemented in paper 1 and there exists a mapping between the two methods [3]. However, they differ in that the Hamiltonian formulation introduces a 3 + 1 decomposition of the 4-metric from the start, and thus it provides PN expressions for the lapse, shift, 3-metric and the conjugate momentum.

We follow the conventions of Ref. [116] where the black hole trajectories from the center of mass of the system is given by

$$\vec{\xi}_1(t'') = \frac{m_2}{m} \vec{b}(t''), \quad \vec{\xi}_2(t'') = -\frac{m_1}{m} \vec{b}(t''). \quad (3.1)$$

In Eq. (3.1),  $m_A$  and  $m = m_1 + m_2$  stand for the mass of BH A and the combined mass of the system in the ADMTT gauge, whereas the separation vector  $\vec{b}(t)$  is given by

$$\vec{b}(t'') = b \left( \cos \omega t'', \sin \omega t'', 0 \right). \quad (3.2)$$

Note that Eq. (3.2) assumes the black holes are initially in a circular orbit, which is a sensible approximation in the late stages of inspiral, since gravitational radiation will have circularized the orbit. The angular velocity of this orbit is given by Eq. (60) in Ref. [16]:

$$\omega = \sqrt{m/b^3} \left[ 1 + \frac{1}{2} \left( \frac{\mu}{m} - 3 \right) \frac{m}{b} \right], \quad (3.3)$$

with errors of  $O(m/b)^{5/2}$ . In Eq. (3.3),  $\mu = m_1 m_2 / m$  is the reduced mass of the system and  $b$  is the norm of the separation vector. This angular velocity is valid in the ADMTT gauge, which is different from the PN velocity used in paper 1, since the latter is valid only in harmonic coordinates.

We further define the radial vector pointing from either black hole to a field point by

$$\vec{r}_A'' = (x'' - \xi_A^x, y'' - \xi_A^y, z'' - \xi_A^z), \quad (3.4)$$

where the double primed variables  $(t'', x'', y'', z'')$  are inertial ADMTT coordinates measured from the center of mass. With these definitions, it is clear that  $\vec{r}_1'' = \vec{r}_2'' + \vec{b}$ , where  $\vec{b}$  points from black hole 1 to 2. We also introduce the unit vector

$$\vec{n}_A'' = \vec{r}_A'' / r_A''. \quad (3.5)$$

and the radial vector pointing from the center of mass to a field point  $r'' = (x'', y'', z'')$ .

The particle's velocity vector is given by

$$\vec{v}_A'' = \partial_t \vec{r}_A'' = (-1)^{A+1} \frac{\mu}{m_A} b\omega \left( -\sin \omega t'', \cos \omega t'', 0 \right). \quad (3.6)$$

The post-Newtonian near zone metric in inertial ADMTT coordinates (Eqs. (5.4)-(5.6) in Ref. [116]) can then be written as

$$\begin{aligned} g_{i''j''}^{(3)} &= \Psi^4 \delta_{ij}, \\ g_{0''i''}^{(3)} &= g_{i''j''}^{(3)} \beta^{(3)j''}, \\ g_{0''0''}^{(3)} &= g_{0''i''}^{(3)} \beta^{(3)i''} - (\alpha^{(3)})^2, \end{aligned} \quad (3.7)$$

where we introduced a post-Newtonian conformal factor

$$\Psi = 1 + \frac{m_1}{2r_1''} + \frac{m_2}{2r_2''}. \quad (3.8)$$

and where the post-Newtonian lapse and shift (Eqs.(5.4)-(5.6) in Ref. [116]) are written as

$$\alpha^{(3)} = \frac{2 - \Psi}{\Psi} \quad (3.9)$$

and

$$\beta^{(3)i''} = \frac{m_1}{r_1''} \left[ \frac{1}{2} \left( v_1^{i''} - \vec{v}_1'' \cdot \vec{n}_1'' n_1^{i''} \right) - 4v_1^{i''} \right] + \frac{m_2}{r_2''} \left[ \frac{1}{2} \left( v_2^{i''} - \vec{v}_2'' \cdot \vec{n}_2'' n_2^{i''} \right) - 4v_2^{i''} \right]. \quad (3.10)$$

These expressions are accurate up to errors of  $O(m/r_A)^2$ . The 3-metric is conformally flat and in the vicinity of each black hole (near  $r_A = 0$ ) the metric is very similar to the metric of a black hole in isotropic coordinates. Note that Ref. [116] uses units where  $16\pi G = 1$ , but in Eq. (3.7) we use units where  $G = 1$  instead.

Also note that the PN expressions above are not pure Taylor expansions in  $m/r$  or  $v/c$ . Instead, certain higher order PN terms have been added to make the metric similar to the Schwarzschild metric in isotropic coordinates near each black hole. This resummation formally does not change the PN accuracy of the metric, but in practice it improves the PN metric since it yields a metric that is very similar to the inner zone black hole metric. The PN metric written in this form above even has apparent horizons near  $r_A = m_A/2$ . Later when we plot our results we will use this resummed form of the metric. The reader may worry that there is a certain arbitrariness in adding higher order terms. However, we have used the following two criteria to minimize this arbitrariness: i) We only add terms that would actually be present at higher PN order (compare [116, 117, 103, 16]). ii) The terms added have coefficients of order unity, and thus do not affect the usual PN order counting. Notice that point i) of course only means that we have added some higher order terms, not all higher order terms.

The lapse and the spatial metric are similar to what was used in paper 1, when we expand them in the buffer zone. However, the shift given here is different from that in paper 1 and, thus, the maps returned by asymptotic matching will also be different.

Now that we have the 4-metric in the near zone it is convenient to remove the frame rotation by performing the transformation

$$\begin{aligned} t'' &= t, \\ x'' &= x \cos \omega t - y \sin \omega t, \\ y'' &= x \sin \omega t + y \cos \omega t, \\ z'' &= z, \end{aligned} \tag{3.11}$$

where unprimed symbols stand for corotating ADMTT coordinates and double primed symbols correspond to the inertial ADMTT frame. After doing this coordinate change, the form of the near zone metric (3.7) as well as the lapse and conformal factor remain unchanged, with only the shift picking up an additional  $\omega \times r$  term and now becomes

$$\beta^{(3)i} = \frac{m_1}{r_1} \left[ \frac{1}{2} \left( v_1^i - \vec{v}_1 \cdot \vec{n}_1 n_1^i \right) - 4v_1^i \right] + \frac{m_2}{r_2} \left[ \frac{1}{2} \left( v_2^i - \vec{v}_2 \cdot \vec{n}_2 n_2^i \right) - 4v_2^i \right] - \epsilon_{ik3} \omega x^k, \tag{3.12}$$

where  $\vec{v}_A$  and  $\vec{n}_A$  are now time independent and equal to the double primed versions at  $t = 0$ . In these coordinates, the magnitude of the radial vectors become

$$r_A'' = r_A = \left( x_A^2 + y^2 + z^2 \right)^{1/2}, \tag{3.13}$$

where  $x_1 = x - bm_2/m$  and  $x_2 = x + bm_1/m$ .

Let us now make one final coordinate transformation where we will shift the origin to the center of BH 1, i.e.,

$$\begin{aligned} x' &= x_1 = x - \frac{m_2 b}{m}, \\ y' &= y, \quad z' = z, \quad t' = t, \end{aligned} \tag{3.14}$$

and  $r_A' = r_A$ . The single-primed coordinates then stand for the shifted corotating ADMTT coordinate system. This coordinate change is useful because we will later concentrate on matching in  $\mathcal{O}_{13}$ . We will usually make explicit reference to  $x_1$  instead of  $x'$  to remind us that this distance should be measured from BH 1. This shift of the origin was not performed in paper 1 and, thus, the coordinate transformations that we will find will look slightly different. However, to  $O(m/b)$  this transformation should reduce to the results of paper 1 when the shift is undone.

We now concentrate on the overlap region (buffer zone)  $\mathcal{O}_{13}$ . Inside  $\mathcal{O}_{13}$  we can expand all terms proportional to  $1/r_2$  in Legendre polynomials of the form

$$\frac{1}{r'_2} = \frac{1}{b} \sum_{n=0}^{\infty} \left(-\frac{r'_1}{b}\right)^n P_n\left(\frac{x_1}{r'_1}\right). \quad (3.15)$$

Substituting Eq. (3.15) into Eq. (3.7), we obtain

$$\begin{aligned} \tilde{g}_{0'0'}^{(3)} &\sim -1 + \frac{2m_1}{r'_1} + \frac{2m_2}{b} \left[ 1 + \frac{r'_1}{b} P_1\left(\frac{x_1}{r'_1}\right) + \left(\frac{r'_1}{b}\right)^2 P_2\left(\frac{x_1}{r'_1}\right) \right] \\ &\quad + \omega^2 \left[ \left(x_1 + \frac{m_2 b}{m}\right)^2 + y'^2 \right], \\ \tilde{g}_{0'1'}^{(3)} &\sim -y' \omega \left\{ 1 + \frac{2m_1}{r'_1} + \frac{2m_2}{b} \left[ 1 + \frac{r'_1}{b} P_1\left(\frac{x_1}{r'_1}\right) \right] \right\} - \frac{1}{2} \frac{\mu}{r'_1} b \omega \frac{y' \left(x_1 + \frac{m_2 b}{m}\right)}{r_1'^2} \left( 1 - \frac{r_1'^3}{b^3} \right) \\ &\quad + \frac{\mu}{2m} b \omega \frac{b y}{r_1'^2} \left[ \frac{m_2}{r'_1} + \frac{m_1}{b} \frac{r_1'^2}{b^2} \left( 1 + 3 \frac{r'_1}{b} P_1\left(\frac{x_1}{r'_1}\right) \right) \right], \\ \tilde{g}_{0'2'}^{(3)} &\sim \left(x_1 + \frac{m_2 b}{m}\right) \omega \left\{ 1 + \frac{2m_1}{r'_1} + \frac{2m_2}{b} \left[ 1 + \frac{r'_1}{b} P_1\left(\frac{x_1}{r'_1}\right) \right] \right\} - \frac{7}{2} \frac{\mu}{r'_1} b \omega \left\{ 1 - \frac{r_1'}{b} \right. \\ &\quad \left. + \left[ 1 + \frac{r'_1}{b} P_1\left(\frac{x_1}{r'_1}\right) + \left(\frac{r'_1}{b}\right)^2 P_2\left(\frac{x_1}{r'_1}\right) \right] \right\} - \frac{1}{2} \frac{\mu}{r'_1} b \omega \frac{y'^2}{r_1'^2} \left( 1 - \frac{r_1'^3}{b^3} \right), \\ \tilde{g}_{0'3'}^{(3)} &\sim -\frac{1}{2} \frac{\mu}{r'_1} b \omega \frac{y z}{r_1'^2} \left( 1 - \frac{r_1'}{b^3} \right), \\ \tilde{g}_{i'j'}^{(3)} &\sim \delta_{ij} \left\{ 1 + \frac{2m_1}{r'_1} + \frac{2m_2}{b} \left[ 1 + \frac{r'_1}{b} P_1\left(\frac{x_1}{r'_1}\right) + \left(\frac{r'_1}{b}\right)^2 P_2\left(\frac{x_1}{r'_1}\right) \right] \right\}, \end{aligned} \quad (3.16)$$

where all errors are of order  $O(2,3)$  and where  $m_1 \ll r_1 \ll b$ . Eq. (3.16) is denoted with a tilde because it is the asymptotic expansion in the buffer zone around BH 1 of the ADMTT metric. This metric has now been expressed entirely in terms of the shifted corotating ADMTT coordinate system  $(x', y', z', t')$ .

Note that Eq. (3.16) is a bivariate series, since it depends on two *independent* expansion parameters  $m_1/r'_1$  and  $r'_1/b$ . Since both expansion parameters must be small independently, Eq.(3.16) is valid in a 4-volume defined by the size of the buffer zone.

### 3.4 Inner Zone: A Black Hole Perturbative Metric

In this section we discuss the metric in the inner zone  $\mathcal{C}_1$  of BH 1 and its asymptotic expansion in the overlap region  $\mathcal{O}_{13}$ . Since this metric will be the same as that used in

the inner zone in paper 1, we will minimize its discussion and mostly refer to that paper. However, since we are using different notation than that used in paper 1, we will summarize here the principal formulas.

In the inner zone 1, let us use inertial isotropic coordinates, labeled by  $x^{i'} = (\bar{x}', \bar{y}', \bar{z}', \bar{t}')$ , which are centered at BH 1. Note that these coordinate are identical to the shifted corotated harmonic coordinates used in the near zone to zeroth order. Let us further denote the inner zone metric by  $g_{\bar{\mu}'\bar{\nu}'}^{(1)}$ , which will be given by a tidally perturbed Schwarzschild solution as

$$\begin{aligned}
g_{\bar{0}'\bar{0}'}^{(1)} &\approx - \left[ \frac{1 - M_1/(2\bar{r}'_1)}{1 + M_1/(2\bar{r}'_1)} \right]^2 + \frac{m_2}{b^3} \left( 1 - \frac{M_1}{2\bar{r}'_1} \right)^4 \left[ 3 \left( \bar{x}' \cos \Omega \bar{t}' + \bar{y}' \sin \Omega \bar{t}' \right)^2 - \bar{r}'_1{}^2 \right], \\
g_{\bar{0}'\bar{1}'}^{(1)} &\approx \frac{2m_2}{b^3} \sqrt{\frac{m}{b}} \left( 1 - \frac{M_1}{2\bar{r}'_1} \right)^2 \left( 1 + \frac{M_1}{2\bar{r}'_1} \right)^4 \left[ (\bar{z}'^2 - \bar{y}'^2) \sin \Omega \bar{t}' - \bar{x}' \bar{y}' \cos \Omega \bar{t}' \right], \\
g_{\bar{0}'\bar{2}'}^{(1)} &\approx \frac{2m_2}{b^3} \sqrt{\frac{m}{b}} \left( 1 - \frac{M_1}{2\bar{r}'_1} \right)^2 \left( 1 + \frac{M_1}{2\bar{r}'_1} \right)^4 \left[ (\bar{x}'^2 - \bar{z}'^2) \cos \Omega \bar{t}' + \bar{x}' \bar{y}' \sin \Omega \bar{t}' \right], \\
g_{\bar{0}'\bar{3}'}^{(1)} &\approx \frac{2m_2}{b^3} \sqrt{\frac{m}{b}} \left( 1 - \frac{M_1}{2\bar{r}'_1} \right)^2 \left( 1 + \frac{M_1}{2\bar{r}'_1} \right)^4 \left( \bar{y}' \cos \Omega \bar{t}' - \bar{x}' \sin \Omega \bar{t}' \right) \bar{z}', \\
g_{\bar{i}'\bar{j}'}^{(1)} &\approx \left( 1 + \frac{M_1}{2\bar{r}'_1} \right)^4 \left( \delta_{ij} + \frac{m_2}{b^3} \left[ 3 \left( \bar{x}' \cos \Omega \bar{t}' + \bar{y}' \sin \Omega \bar{t}' \right)^2 - \bar{r}'_1{}^2 \right] \left\{ \left[ \left( 1 + \frac{M_1}{2\bar{r}'_1} \right)^4 \right. \right. \right. \\
&\quad \left. \left. \left. - \frac{2M_1^2}{\bar{r}'_1{}^2} \right] \delta_{ij} - \frac{2M_1}{\bar{r}'_1} \left( 1 + \frac{M_1}{4\bar{r}'_1} \right) \frac{\bar{x}'^i \bar{x}'^j}{\bar{r}'_1{}^2} \right\} \right), \tag{3.17}
\end{aligned}$$

where  $\bar{r}'_1 = (\bar{x}'^2 + \bar{y}'^2 + \bar{z}'^2)^{1/2}$ . This equation is identical to that used in the inner zone of paper 1 or Eq. (3.23) of Ref. [28]. This metric was first computed by Alvi [28] by linearly superposing a Schwarzschild metric to a tidal perturbation near BH 1. This perturbation is computed as an expansion in  $\epsilon_{1,2} = \bar{r}'_{1,2}/b$  and it represents the tidal effects of the external universe on BH 1. Since a simple linear superposition would not solve the Einstein equations, multiplicative scalar functions are introduced into the metric perturbation, which in turn are determined by solving the linearized Einstein equations. With these scalar functions, the metric then solves the linearized Einstein equations and it represents a tidally perturbed Schwarzschild black hole. This metrics has been found to be isomorphic to that computed by Poisson [95] in advanced Eddington-Finkelstein coordinates.

Asymptotic matching will be easier when performed between metrics in similar coordinate systems. We, thus, choose to make a coordinate transformation to corotating isotropic coordinates  $x^i = (\bar{x}, \bar{y}, \bar{z}, \bar{t})$ . The inner zone metric in corotating isotropic

coordinates will be denoted by  $g_{\bar{\mu}\bar{\nu}}^{(1)}$  and is given by

$$\begin{aligned}
g_{\bar{0}\bar{0}}^{(1)} &\approx H_t + H_{s1}\Omega^2(\bar{x}^2 + \bar{y}^2) + 2H_{st}\bar{x}\frac{\Omega}{b^2}(\bar{x}^2 + \bar{y}^2 - \bar{z}^2), \\
g_{\bar{0}\bar{i}}^{(1)} &\approx -H_{s1}\Omega\epsilon_{\bar{i}\bar{j}\bar{3}}x^{\bar{j}} + \frac{H_{st}}{b^2}\left[\bar{y}\left(\delta_{\bar{i}}^{\bar{3}}\bar{z} - \delta_{\bar{i}}^{\bar{1}}\bar{x}\right) + (\bar{x}^2 - \bar{z}^2)\delta_{\bar{i}}^{\bar{2}}\right], \\
g_{\bar{i}\bar{j}}^{(1)} &\approx \delta_{\bar{i}\bar{j}}H_{s1} - H_{s2}\frac{x^{\bar{i}}x^{\bar{j}}}{b^2},
\end{aligned} \tag{3.18}$$

where  $\epsilon_{\bar{i}\bar{j}\bar{k}}$  is the standard Levi-Civita symbol with convention  $\epsilon_{\bar{1}\bar{2}\bar{3}} = 1$  and where  $\delta_{\bar{i}}^{\bar{a}}$  is the Kronecker delta. In Eq. (3.18) we use the shorthand

$$\begin{aligned}
H_{st} &= 2m_2\sqrt{\frac{m}{b^3}}\left(1 - \frac{M_1}{2\bar{r}_1}\right)^2\left(1 + \frac{M_1}{2\bar{r}_1}\right)^4, \\
H_{s1} &= \left(1 + \frac{M_1}{2\bar{r}_1}\right)^4\left\{1 + 2\frac{m_2}{b^3}\bar{r}_1^2P_2\left(\frac{\bar{x}}{\bar{r}_1}\right)\left[\left(1 + \frac{M_1}{2\bar{r}_1}\right)^4 - 2\frac{M_1^2}{\bar{r}_1^2}\right]\right\}, \\
H_{s2} &= \left(1 + \frac{M_1}{2\bar{r}_1}\right)^4\left(1 + \frac{M_1^2}{4\bar{r}_1^2}\right)\frac{4m_2M_1}{b\bar{r}_1}P_2\left(\frac{\bar{x}}{\bar{r}_1}\right), \\
H_t &= -\left(\frac{1 - M_1/2\bar{r}_1}{1 + M_1/2\bar{r}_1}\right)^2 + 2\left(1 - \frac{M_1}{2\bar{r}_1}\right)^4\frac{m_2}{b^3}\bar{r}_1^2P_2\left(\frac{\bar{x}}{\bar{r}_1}\right),
\end{aligned} \tag{3.19}$$

where  $\bar{r}_1 = \bar{r}'_1$  and the errors are still of  $O(\bar{r}_1/b)^3$ . These shorthands for the different components of the metric are identical to those used in paper 1.

We now need to asymptotically expand the inner zone metric in the buffer zone, *i.e.*, as  $M_1/\bar{r}_1 \ll 1$ . Doing so we obtain

$$\begin{aligned}
\tilde{g}_{\bar{0}\bar{0}}^{(1)} &\sim -1 + \frac{2M_1}{\bar{r}_1} + \frac{2m_2}{b^3}\bar{r}_1^2P_2\left(\frac{\bar{x}}{\bar{r}_1}\right) \\
&\quad + \Omega^2(\bar{x}^2 + \bar{y}^2), \\
\tilde{g}_{\bar{0}\bar{1}}^{(1)} &\sim \frac{-2m_2}{b^3}\sqrt{\frac{m}{b}}\bar{y}\bar{x} - \bar{y}\Omega\left(1 + \frac{2M_1}{\bar{r}_1}\right), \\
\tilde{g}_{\bar{0}\bar{2}}^{(1)} &\sim \frac{2m_2}{b^3}\sqrt{\frac{m}{b}}(\bar{x}^2 - \bar{z}^2) + \bar{x}\Omega\left(1 + \frac{2M_1}{\bar{r}_1}\right), \\
\tilde{g}_{\bar{0}\bar{3}}^{(1)} &\sim \frac{2m_2}{b^3}\sqrt{\frac{m}{b}}\bar{z}\bar{y}, \\
\tilde{g}_{\bar{i}\bar{j}}^{(1)} &\sim \delta_{\bar{i}\bar{j}}\left[1 + \frac{2M_1}{\bar{r}_1} + \frac{2m_2}{b^3}\bar{r}_1^2P_2\left(\frac{\bar{x}}{\bar{r}_1}\right)\right]
\end{aligned} \tag{3.20}$$

The asymptotic expansion of  $g_{\bar{\mu}\bar{\nu}}^{(1)}$  will be denoted by  $\tilde{g}_{\bar{\mu}\bar{\nu}}^{(1)}$ . Note that this asymptotic expansion is a bivariate expansion in both  $\bar{r}_1/b$  and  $M_1/\bar{r}_1$ . In other words, it is the asymptotic expansion in the buffer zone to the approximate solution in the inner zone.

### 3.5 Matching Conditions and Coordinate Transformations

In this section, we find the coordinate and parameter maps that relate adjacent solutions. Since the coordinate systems are similar to each other in the buffer zone, we make the following ansatz for the transformation between coordinates and parameters

$$\begin{aligned}
\bar{x} &\approx x' \left[ 1 + \left(\frac{m_2}{b}\right)^{1/2} \chi_1(x^{\mu'}) + \left(\frac{m_2}{b}\right) \chi_2(x^{\mu'}) + \left(\frac{m_2}{b}\right)^{3/2} \chi_3(x^{\mu'}) \right], \\
\bar{y} &\approx y' \left[ 1 + \left(\frac{m_2}{b}\right)^{1/2} \gamma_1(x^{\mu'}) + \left(\frac{m_2}{b}\right) \gamma_2(x^{\mu'}) + \left(\frac{m_2}{b}\right)^{3/2} \gamma_3(x^{\mu'}) \right], \\
\bar{z} &\approx z' \left[ 1 + \left(\frac{m_2}{b}\right)^{1/2} \zeta_1(x^{\mu'}) + \left(\frac{m_2}{b}\right) \zeta_2(x^{\mu'}) + \left(\frac{m_2}{b}\right)^{3/2} \zeta_3(x^{\mu'}) \right], \\
\bar{t} &\approx t' \left[ 1 + \left(\frac{m_2}{b}\right)^{1/2} \tau_1(x^{\mu'}) + \left(\frac{m_2}{b}\right) \tau_2(x^{\mu'}) + \left(\frac{m_2}{b}\right)^{3/2} \tau_3(x^{\mu'}) \right], \\
M_1 &\approx m_1 \left[ 1 + \left(\frac{m_2}{b}\right)^{1/2} \eta_1 + \frac{m_2}{b} \eta_2 + \left(\frac{m_2}{b}\right)^{3/2} \eta_3 \right], \\
\Omega &\approx \omega \left[ 1 + \left(\frac{m_2}{b}\right)^{1/2} \kappa_1 + \frac{m_2}{b} \kappa_2 + \left(\frac{m_2}{b}\right)^{3/2} \kappa_3 \right], \tag{3.21}
\end{aligned}$$

where, as in paper 1,  $\chi_{1,2,3}$ ,  $\gamma_{1,2,3}$ ,  $\zeta_{1,2,3}$  and  $\tau_{1,2,3}$  are functions of the coordinates, whereas  $\eta_{1,2,3}$  and  $\kappa_{1,2,3}$  are coordinate independent. Note that this ansatz is slightly different from the one made in paper 1, because here we have shifted the origin of the near zone coordinate system, so that to zeroth order it agrees with the coordinates used in the inner zone. In order to determine these maps, we enforce the matching condition, *i.e.*

$$\tilde{g}_{\bar{\mu}'\bar{\nu}'}^{(3)}(x^{\lambda'}) \sim \tilde{g}_{\bar{\rho}\bar{\sigma}}^{(1)} \left( \bar{x}^{\lambda} \left( x^{\lambda'} \right) \right) \frac{\partial \bar{x}^{\rho}}{\partial x^{\mu'}} \frac{\partial \bar{x}^{\sigma}}{\partial x^{\nu'}}, \tag{3.22}$$

which leads to a system of first-order coupled partial differential equations, which we solve order by order.

The system to  $O(m/b)^0$  provides no information because both metrics are asymptotic to Minkowski spacetime to lowest order. The first nontrivial matching, occurs at  $O(m/b)^{1/2}$ . The differential system at this order and at order  $O(m/b)$  are similar to those obtain in paper 1 and we, thus, omit them here. The solution up to  $O(m/b)$  is

given by

$$\begin{aligned}
\bar{x} &\approx x' \left[ 1 + \frac{m_2}{b} \left( 1 - \frac{x'}{2b} \right) + \left( \frac{m_2}{b} \right)^{3/2} \chi_3(x^{\mu'}) \right] + \frac{m_2}{2b^2} (2t'^2 + y'^2 + z'^2), \\
\bar{y} &\approx y' \left[ 1 + \left( \frac{m_2}{b} \right) \left( 1 - \frac{x'}{b} \right) + \left( \frac{m_2}{b} \right)^{3/2} \gamma_3(x^{\mu'}) \right] + \sqrt{\frac{m_2}{b}} \sqrt{\frac{m_2}{m}} t', \\
\bar{z} &\approx z' \left[ 1 + \left( \frac{m_2}{b} \right) \left( 1 - \frac{x'}{b} \right) + \left( \frac{m_2}{b} \right)^{3/2} \zeta_3(x^{\mu'}) \right], \\
\bar{t} &\approx t' \left[ 1 - \left( \frac{m_2}{b} \right) \left( 1 - \frac{x'}{b} \right) + \left( \frac{m_2}{b} \right)^{3/2} \tau_3(x^{\mu'}) \right], \tag{3.23}
\end{aligned}$$

with  $\eta_1 = 0$  and  $\kappa_1 = 0$ . We should note that in solving the differential system to  $O(m/b)^{1/2}$  and  $O(m/b)$  we have explicitly required that the coordinate system be not boosted or rotating with respect to each other. Furthermore, we found the particular solution where the  $t' = 0$  and the  $\bar{t} = 0$  slices coincide, since  $t' = 0$  implies  $\bar{t} = 0$ . We should also note that Eq. (3.23) of this paper is different from the transformation found in paper 1 because in this paper we have shifted the origin of the near zone coordinate system, which simplifies the transformation.

Matching at  $O(m/b)^{3/2}$  needs to be performed only on the  $0i$  components of the metric to get the first nontrivial correction to the extrinsic curvature. This order counting does not follow the standard post-Newtonian scheme and it is explained in more detail in paper 1. Since the near zone shift is different from that used in paper 1, the differential system obtained by imposing the matching condition of Eq. (3.22) is also different. This system is given by

$$\begin{aligned}
t' \tau_{3,x'} - x' \chi_{3,t'} &\sim \sqrt{\frac{m}{m_2}} \left\{ \frac{y' x'}{b^2} \left[ \frac{m_1}{2m} \left( \frac{b^3}{r_1'^3} - 1 + 3 \frac{m_1}{m} \right) - 4 \right] \right. \\
&\quad \left. + \frac{y'}{b} \left[ -\frac{m_2}{m} - \kappa_2 + 1 - \frac{m_1}{2m} \right] \right\}, \\
t' \tau_{3,y'} - y' \gamma_{3,t'} &\sim \sqrt{\frac{m}{m_2}} \left\{ \frac{z'^2}{b^2} \left( \frac{7m_1}{4m} - \frac{3}{2} - \frac{m_2}{m} \right) + \frac{y'^2}{b^2} \left[ \frac{m_1}{2m} \left( \frac{b^3}{r_1'^3} + \frac{5}{2} \right) - \frac{m_2}{m} - \frac{1}{2} \right] \right. \\
&\quad + \frac{t'^2}{b^2} + \frac{x'^2}{b^2} \left( \frac{7}{2} + 2 \frac{m_2}{m} - \frac{7m_1}{2m} \right) + \frac{x'}{b} \left( \kappa_2 - 1 + \frac{m_2}{m} + \frac{7m_1}{2m} \right) + \frac{3}{2} \\
&\quad \left. - \frac{m_2}{m} + \frac{7m_1}{2m} \left( -1 + \frac{b}{r_1'} \right) - \frac{\mu}{2m} \right\}, \\
t' \tau_{3,z'} - z' \zeta_{3,t'} &\sim \sqrt{\frac{m}{m_2}} \frac{y' z'}{b^2} \left[ \frac{m_1}{2m} \left( \frac{b^3}{r_1'^3} - 1 \right) + 1 \right]. \tag{3.24}
\end{aligned}$$

Note that  $\kappa_2$  represents the degree of freedom associated with the angular velocity. For simplicity, we now set  $\kappa_2 = 0$ . Also note that  $\eta_2, \eta_3$  and  $\kappa_3$  never enter the matching conditions to this order, so we set those quantities to zero. All the matching relations between the parameters local to different approximation have now been specified to  $O(m/b)^2$ , *i.e.*

$$\Omega \approx \omega, \quad M_1 \approx m_1. \quad (3.25)$$

With these matching relations, we can now find a particular solution to Eqs. (3.24) and this set will produce matching. Once more, we choose constants of integration such that the  $t' = 0$  and the  $\bar{t} = 0$  slices coincide. Doing so we obtain the solution

$$\begin{aligned} \bar{x} &\approx x_1 \left( 1 + \frac{m_2}{b} \left( 1 - \frac{x_1}{2b} \right) - \left( \frac{m_2}{b} \right)^{3/2} \sqrt{\frac{m}{m_2}} \left\{ \frac{yt}{b^2} \left[ \frac{m_1}{2m} \left( \frac{b^3}{r_1^3} - 1 + \frac{3m_1}{m} \right) - 4 \right] \right. \right. \\ &\quad \left. \left. + \frac{y}{b} \left( 1 - \frac{m_2}{m} - \frac{m_1}{2m} \right) \right\} \right) + \frac{m_2}{2b^2} (2t^2 + y^2 + z^2), \\ \bar{y} &\approx y \left[ 1 + \left( \frac{m_2}{b} \right) \left( 1 - \frac{x_1}{b} \right) \right] - \left( \frac{m_2}{b} \right)^{3/2} t \sqrt{\frac{m}{m_2}} \left\{ \frac{z^2}{b^2} \left( \frac{7m_1}{4m} - \frac{3}{2} - \frac{m_2}{m} \right) \right. \\ &\quad \left. + \frac{y^2}{b^2} \left[ \frac{m_1}{2m} \left( \frac{b^3}{r_1^3} + \frac{5}{2} \right) - \frac{m_2}{m} - \frac{1}{2} \right] + \frac{t^2}{3b^2} + \frac{x_1^2}{b^2} \left( \frac{7}{2} + 2\frac{m_2}{m} - \frac{7m_1}{2m} \right) \right. \\ &\quad \left. + \frac{x_1}{b} \left( -1 + \frac{m_2}{m} + \frac{7m_1}{2m} \right) + \frac{3}{2} - \frac{m_2}{m} + \frac{7m_1}{2m} \left( -1 + \frac{b}{r_1} \right) - \frac{\mu}{2m} \right\} + \sqrt{\frac{m_2}{b}} \sqrt{\frac{m_2}{m}} t, \\ \bar{z} &\approx z \left\{ 1 + \left( \frac{m_2}{b} \right) \left( 1 - \frac{x_1}{b} \right) - \left( \frac{m_2}{b} \right)^{3/2} \sqrt{\frac{m}{m_2}} \frac{yt}{b^2} \left[ \frac{m_1}{2m} \left( \frac{b^3}{r_1^3} - 1 \right) + 1 \right] \right\}, \\ \bar{t} &\approx t \left[ 1 - \left( \frac{m_2}{b} \right) \left( 1 - \frac{x_1}{b} \right) \right], \end{aligned} \quad (3.26)$$

where errors are of  $O(2, 3)$ .

As in paper 1, this coordinate transformation is singular at  $r'_1 = 0$ . Note, however, that in Eq. (3.26) we have replaced  $r'_1$  by

$$r_1 = \sqrt{r_1'^2 + 6m^2}. \quad (3.27)$$

This replacement amounts to adding higher order terms to the coordinate transformation, which have no effect in the buffer zone at the current level of accuracy. Yet it has the advantage that the resulting coordinate transformation is now regular at  $r'_1 = 0$ . Thus, the replacement does not affect asymptotic matching (in the buffer zone). It merely leads to an inner zone metric expressed in a better coordinate system.

In paper 1 there was one term in the coordinate transformation that was singular at the location of the holes, whereas here there are 3 such singular terms. This increase in singular behavior is due to the ADMTT shift having more poles than the shift of paper 1. The shift of the origin into the complex plane, as introduced in Eq. (3.27), removes this singular behavior from the real line, while only introducing uncontrolled remainders

at a higher order. We should also note that in Eq. (3.26), we undid the shift given by Eq. (3.14), so that we measure distances from the center of mass of the system.

The coordinate transformations presented in Eq. (3.26) are only valid in  $\mathcal{O}_{13}$ , but we can find the transformation in  $\mathcal{O}_{23}$  by a simple symmetry transformation. This transformation is given by the following rules: substitute  $1 \leftrightarrow 2$  and

$$x \rightarrow -x, \quad y \rightarrow -y, \quad z \rightarrow z. \quad (3.28)$$

The set of matching conditions plus the coordinate transformation presented in Eqs. (3.25) and (3.26) are the end result of the matching scheme. Now that we have an approximate global metric, we can decompose it to provide initial data for numerical simulations. This decomposition consists of a foliation of the manifold with spacelike hypersurfaces, where we choose the slicing given by  $t = 0 = \bar{t}$ . Notice that we have found a coordinate transformation that is consistent both with this foliation and with the condition  $m_A \ll r_A \ll b$ , valid in the buffer zone.

Note that there is some freedom in the matching scheme at the order of accuracy of this paper. This freedom is rooted in that a different choice for the matching parameters ( $M$  and  $\Omega$ ) could be made. However, except for the  $\kappa_2$  term in  $\Omega$ , this would have no effect on the coordinate transformation or the 4-metric at the orders considered here. Furthermore, one can show that the value of  $\kappa_2$  does not affect the physics of the initial data we will construct below. Above, the choice of  $\kappa_2 = 0$  was made in order to simplify the relation between the parameters of the two approximations. Specifically, it was chosen such that the angular velocity parameters of the two approximations are equal. This is, however, not the only possible choice. Fortunately, the choice of  $\kappa_2$  will not affect the initial data we will construct later, since both the 3-metric and the extrinsic curvature will change only by uncontrolled remainders of higher order. This happens for the following reasons. A non-zero  $\kappa_2$  would only change the spatial part of the coordinate transformation at  $O(m/b)^{3/2}$ , and thus would have no effect on the slicing. Since the leading order non-zero piece in the extrinsic curvature is already of  $O(m/b)^{3/2}$  and proportional to  $\Omega$ , any change due to spatial coordinate transformations or parameter changes at  $O(m/b)^{3/2}$  will cause changes only at even higher order. For the 3-metric, coordinate transformations or parameter changes at  $O(m/b)^{3/2}$  will make a difference at order  $O(m/b)^{3/2}$  in the metric. We can, however, again neglect these changes, since the 3-metric was only matched up to  $O(m/b)$ . In conclusion, this means that any allowed change in the matching parameters will not affect the physics of the initial data sets constructed below.

### 3.6 Constructing a Global Metric

In this section, we present the global metric, by performing the coordinate transformation found in the previous section on the inner zone metric. The piecewise metric

in corotating ADMTT coordinates is given by

$$g_{\mu\nu}^{(global)} \approx \begin{cases} g_{\mu\nu}^{(1)}, & \text{in } \mathcal{C}_1, \\ g_{\mu\nu}^{(2)}, & \text{in } \mathcal{C}_2, \\ g_{\mu\nu}^{(3)}, & \text{in } \mathcal{C}_3. \end{cases} \quad (3.29)$$

In Eq. (3.29),  $g_{\mu\nu}^{(3)}$  denotes the near zone metric given in Eq. (3.7), but in unprimed corotating ADMTT coordinates, whereas  $g_{\mu\nu}^{(1)}$  and  $g_{\mu\nu}^{(2)}$  stand for the inner zone metrics of BH 1 and 2 transformed to corotating ADMTT coordinates via Eq. (3.26). Explicitly, the inner zone metric is given by

$$g_{\mu\nu}^{(1,2)} = g_{\bar{\mu}\bar{\nu}}^{(1,2)} J_{\mu}^{\bar{\mu}} J_{\nu}^{\bar{\nu}}, \quad (3.30)$$

where  $J_{\nu}^{\bar{\mu}}$  is the Jacobian of Eq. (3.26), namely

$$J_{\nu}^{\bar{\mu}} = \frac{\partial x^{\bar{\mu}}}{\partial x^{\nu}}. \quad (3.31)$$

In Eq. (3.30),  $g_{\bar{\mu}\bar{\nu}}^{(1)}$  is the inner zone metric in corotating isotropic coordinates given by Eqs. (3.18), while  $g_{\bar{\mu}\bar{\nu}}^{(2)}$  can be obtained by applying Eq. (3.28) to  $g_{\bar{\mu}\bar{\nu}}^{(1)}$ . Eq. (3.30) is also expanded in paper 1 with the substitution  $h_{\mu\nu}^{(1)} = g_{\bar{\mu}\bar{\nu}}^{(1)}$ . Note that the Jacobian given in the Appendix of [93] will be different from that presented in paper 1 because the coordinate transformation is different.

In the following we present plots of different metric components at time  $\bar{t} = t' = 0$ . These plots are representative samples of the initial data and will show how well the matching procedure works. In most of these figures we choose to plot along the axis that connects the holes (the  $x$ -axis). We have checked that the behavior along other axis is qualitatively similar to that along the  $x$ -axis, as evidenced by the contour plots included in the section. Furthermore, we plot only the relevant components because either the other components vanish along the  $x$ -axis or they present similar behavior. Thus the components and axis chosen present the general behavior of the data.

For these plots, we choose two different physical systems. The first system consists of equal mass black holes separated by  $b = 10m$ . The two black holes are located at  $x = \pm 5m$  and are surrounded by apparent horizons, which approximately are coordinate spheres of radius  $m/4$ . For this system, some quantities, like the  $xx$ -component of the metric, are reflection symmetric under  $x \rightarrow -x$  and we then plot only the positive  $x$ -axis, omitting the inner zone 2 data. The second system consists of two holes with mass ratio  $m_2/m_1 = 0.25$  separated by  $b = 20m$ . Here the holes are located at  $x = 4m$  and  $x = -16m$ , and surrounded by apparent horizons with radii of approximately  $m_1/2$  and  $m_2/2$  for holes 1 and 2 respectively. In general, a dashed line corresponds to the post-Newtonian near zone metric, while the dotted or dot-dot-dashed lines represent the perturbed Schwarzschild inner zone metrics.

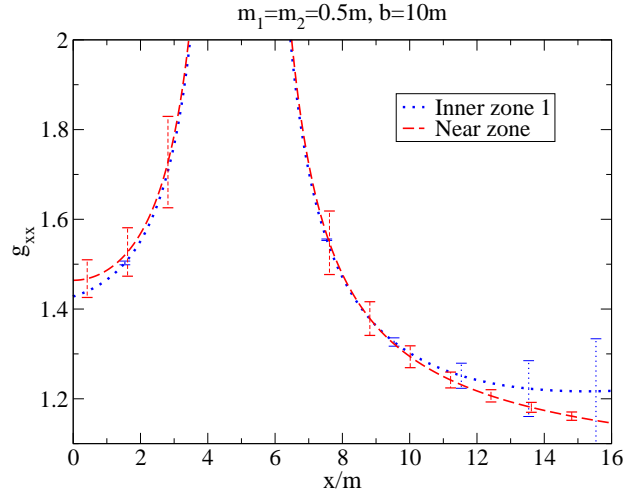


Fig. 3.2. This figure shows the  $xx$ -component of the near zone (dashed line) and inner zone 1 metric (dotted line) along the positive  $x$ -axis in ADMTT coordinates. The black holes are located at  $x/m \approx \pm 5$  and the perturbative parameter is  $m/b = 1/10$ . Observe that the metrics become asymptotic to each other in the buffer zone, whose approximate center is roughly  $4m$  away from each black hole. Also plotted are estimates of the error in the approximations. Note that the off-diagonal components of the 3-metric vanish along the  $x$ -axis for symmetry reasons, and that the  $yy$ - and  $zz$ -components are very similar to the  $xx$ -component.

Most figures will contain error bars, which in the case of the metric are given by

$$\begin{aligned}
 E_{near} &= \frac{3}{2} \left( \frac{m_1^2}{r_1^2} + \frac{m_2^2}{r_2^2} \right) + \frac{5}{4} \frac{m_1 m_2}{b} \left( \frac{1}{r_1} + \frac{1}{r_2} \right) - 2 \frac{m_1 m_2}{S^2}, \\
 E_{inner,A} &= 2 \frac{m}{b} \left( \frac{r_A}{b} \right)^3,
 \end{aligned} \tag{3.32}$$

where  $S = r_1 + r_2 + b$ . These error bars were obtained by analyzing the next order term in the ADMTT PN metric and in the black hole perturbation approximation. In particular, the PN error is different from that used in paper 1. Here the first term comes from the expansion of the conformal factor and the last two from the 2 PN part of the transverse-traceless term in the ADMTT metric. The full PN error, given by the 3.5 ADMTT PN metric, is much more complex than the simplified approximation used in  $E_{near}$ , where the former contains some terms that scale for example as  $m_A^2/r_A^3$  and  $m_A^3/(S r_A^2)$ . However, here we have neglected those terms and we have checked that  $E_{near}$  models well both the magnitude and functional behavior of the full error in the regions plotted in all figures with fractional errors of less than 1% everywhere.

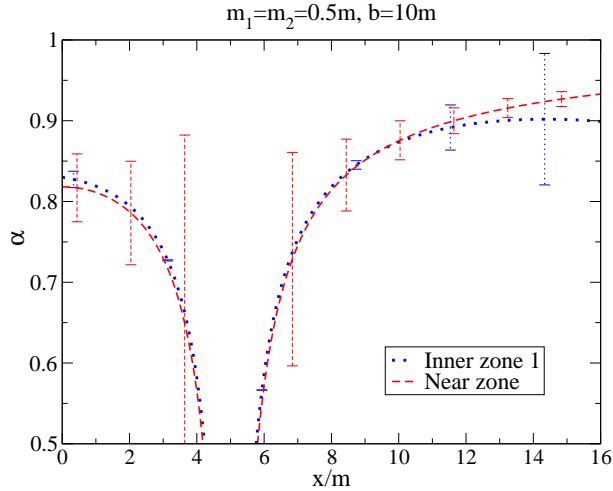


Fig. 3.3. Plot of the lapse along the positive  $x$ -axis for the inner zone and near zone metrics. Note that the lapses are similar to each other not only in the buffer zone, but also near the hole.

In Fig. 3.2, we plot the  $xx$ -component of the piecewise metric along the positive  $x$ -axis. Observe that the inner zone metric of black hole 1 (dotted line) is close to the post-Newtonian near zone metric (dashed line) in the buffer zone of black hole 1 given by  $m_1 \ll \bar{r}_1 \ll b$ . Recall that the definition of the buffer zone in the theory of asymptotic matching is inherently imprecise in the sense that as one approaches either the inner or outer radius of the buffer zone shell, one of the two approximations (i.e. near zone or inner zone metric) has much larger errors than the other. In our case we need both  $\bar{r}_A/b$  and  $m_A/\bar{r}_A$  to be small, which will not be the case at either end of the interval  $m_A \ll \bar{r}_A \ll b$ . Hence we expect the best agreement between the two approximations to occur somewhere in the middle of each buffer zone shell. In fact the best agreement should occur where each of the two approximations have roughly the same error. From Fig. 3.2 we see that the inner zone metric of each black hole agrees with the near zone metric within error bars in the middle of each of the two buffer zones, where both have comparable errors. This agreement means that we have performed successful matching. However, our result in Fig. 3.2 is even better than this, since the near zone 3-metric is close to each of the inner zone 3-metrics even near the black holes, where post-Newtonian theory has large errors and is expected to fail. The reason for this somewhat surprising success near the black holes is that we have used resummed post-Newtonian expressions [Eqs. (3.7), (3.8), (3.9) and (3.10)] in the ADMTT gauge, which are very close to the isotropic Schwarzschild metric used in the inner zone. Note that the off-diagonal components of the 3-metric vanish along the  $x$ -axis for symmetry reasons, and that the  $yy$ - and  $zz$ -components are very similar to the  $xx$  component.

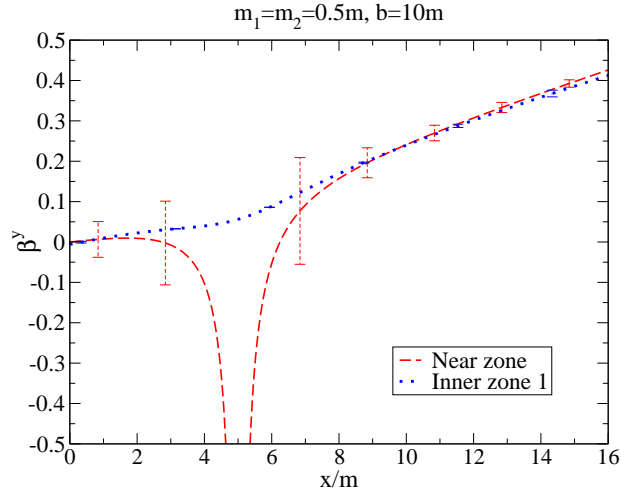


Fig. 3.4. Plot of the  $y$ -component of the shift along the positive  $x$ -axis for the inner zone and near zone metrics. Observe that although the inner zone and near zone curves are similar in the buffer zones, in this case they differ near the black holes. Also note that the  $x$ - and  $z$ -components of the shift vanish along the  $x$ -axis.

The quality of the asymptotic matching (in the buffer zone) is equally good for all other components of the 4-metric. This is evidenced in Figs. 3.3 and 3.4 which show the near and inner zone lapse and  $y$ -component of the shift, computed from the 4-metric (3.29) via

$$\begin{aligned}\beta^i &= g^{ij} g_{oj}, \\ \alpha &= \left( g_{ok} \beta^k - g_{00} \right)^{1/2}.\end{aligned}\tag{3.33}$$

As one can see from Fig. 3.3 the near (dashed line) and inner zone 1 lapse (dotted line) agree well in the buffer zone, located about  $4m$  away from each black hole. Furthermore, the resummed expression [Eq. (3.9)] we use for the near zone lapse also is very close to the inner zone lapse near each black hole, where post-Newtonian theory has large error bars. In Fig. 3.4 we see that the near zone shift (dashed line) is close to the inner zone 1 shift (dotted line) in the buffer zone as expected after matching there. However, in the inner zone the post-Newtonian near zone shift is not valid anymore and deviates strongly from the inner zone shift.

Thus in summary asymptotic matching works well for all components of the 4-metric in the buffer zone. In addition, for most components (except the shift) the resummed post-Newtonian expressions [Eqs. (3.7), (3.8), (3.9) and (3.10)] we use in the near zone, follow the inner zone behavior even near the black holes, where this is not necessarily expected.

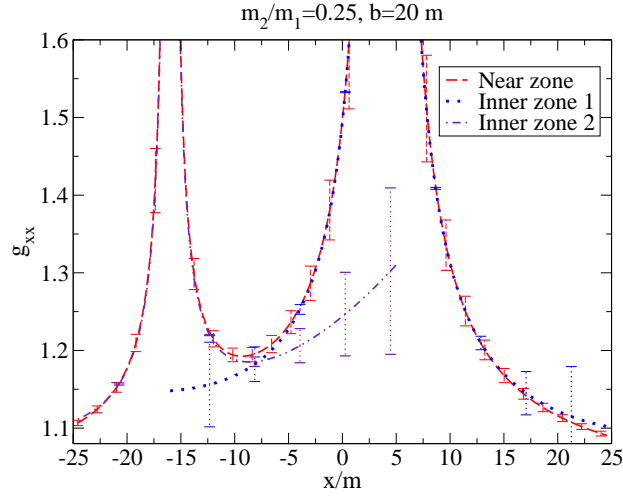


Fig. 3.5. This figure shows the  $xx$  component of the piecewise metric for a system of unequal masses and at larger separations. In particular, we have used  $m_2/m_1 = 0.25$  and  $b = 20m$ . Note that the matching improves since the perturbation parameter  $m/b$  is smaller.

We have also tested the coordinate and parameter maps for system with unequal masses and found that matching is still valid. Figure 3.5 shows the  $xx$ -component of the piecewise metric along the entire  $x$ -axis for the case of  $m_2/m_1 = 0.25$  and  $b = 20m$ . Observe that the matching improves in this case because the perturbation parameter  $m/b$  has become smaller. Also note that the general features of the matching are the same as those presented in the equal mass case. We have plotted along the entire  $x$ -axis and show both the metrics of inner zone 1 (dotted line) and 2 (dot-dot-dashed line).

Since we are interested in initial data on the  $\bar{t} = t' = 0$  slice we also have to discuss the extrinsic curvature given by

$$K_{ij} = -\frac{1}{2\alpha} \left( \partial_t g_{ij} - \mathcal{L}_\beta g_{ij} \right). \quad (3.34)$$

In the inner zones we use this equation to numerically compute  $K_{ij}^{(1)}$  and  $K_{ij}^{(2)}$ . Note however, that the inner zone extrinsic curvature in corotating isotropic coordinates can also be found in paper 1, where  $K_{ij}^{(1),ICC} = K_{ij}^{(1)}$  in the new notation.

The near zone extrinsic curvature can easily be computed analytically from the near zone post-Newtonian 4-metric in ADMTT coordinates. The result [16]

$$K_{ij}^{(3)} = \Psi^{-2} \sum_{A=1}^2 \frac{3}{2r_A^2} \left[ p_A^i n_A^j + p_A^j n_A^i - p_A^m n_A^n \delta_{mn} (\delta_{ij} - n_A^i n_A^j) \right]. \quad (3.35)$$

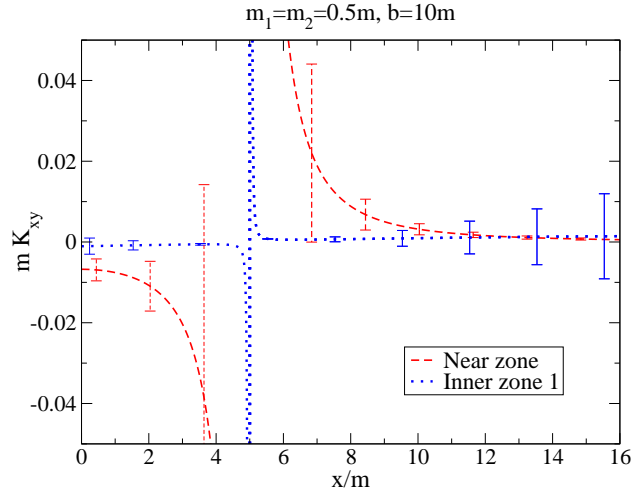


Fig. 3.6. This figure shows the  $xy$  component of the near zone (dashed line) extrinsic curvature, as well as the inner zone curvature (dotted line) obtained via black hole perturbation theory. The plot is for equal mass black holes with  $m/b = 1/10$ . In the buffer zones, where the near and inner zone approximations have comparable error bars, the two approximations agree within error bars. All other components vanish along the  $x$ -axis.

is of Bowen-York form, and  $v_A^i$  and  $n_A^i$  denote the particle velocities and directional vectors already introduced in Sec. 3.3. On the  $t' = 0$  slice these quantities become

$$v_1^2 = \omega \frac{m_2}{m} b, \quad v_2^2 = -\omega \frac{m_1}{m} b, \quad v_A^1 = v_A^3 = 0, \quad (3.36)$$

and

$$\begin{aligned} n_A^k &= \frac{x^k - \xi_A^k}{r_A}, \quad \xi_1^1 = \frac{m_2}{m} b, \quad \xi_2^1 = -\frac{m_1}{m} b, \\ \xi_A^2 &= \xi_A^3 = 0. \end{aligned} \quad (3.37)$$

In Fig. 3.6 we plot the  $xy$  component of the extrinsic curvature along the positive  $x$ -axis in the equal mass case. For reasons of symmetry all other components vanish along the  $x$ -axis. Observe that the near zone solution (dashed line) diverges faster than the inner zone solution (dotted line). From this figure we see that even though the resummed ADMTT post-Newtonian expansion models well the 3-metric of a perturbed Schwarzschild hole, the ADMTT and inner extrinsic curvatures do not agree well in the inner zone, just like in the case of the shift. However, in the buffer zone where both inner and near zone results have similar errors, both approximations roughly agree. On the side away from the companion black hole this agreement is within error bars, while

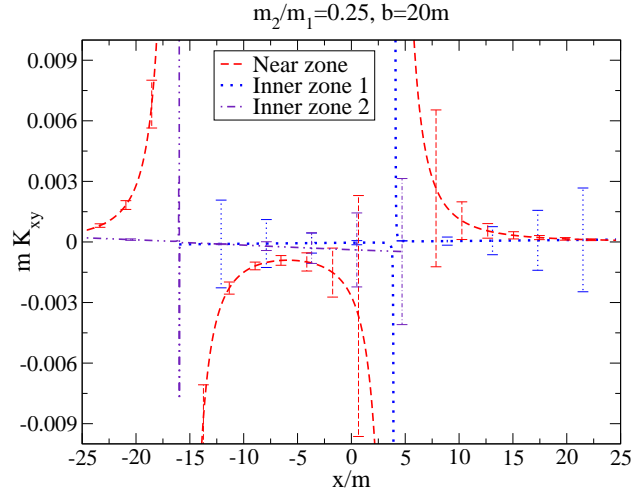


Fig. 3.7. This figure shows the  $xy$  component of the piecewise extrinsic curvature for a system of unequal masses ( $m_2/m_1 = 0.25$ ) at separation  $b = 20m$ . Note that the scale of the  $y$ -axis has been reduced. The curves are closer to each other in this case because the perturbation parameter  $m/b$  has decreased by the choice of parameters.

between the holes the two error bars do not quite overlap. This suggests that a separation of  $b = 10m$  is at the edge of validity of the matching scheme employed here. Notice, however, that the error bars

$$\begin{aligned}
 E_{KPN} &= \frac{3}{2}v \left( \frac{m_1^2}{r_1^3} + \frac{m_2^2}{r_2^3} \right) + \frac{5}{4}v \frac{m_1 m_2}{b} \left( \frac{1}{r_1^2} + \frac{1}{r_2^2} \right) - 8v \frac{m_1 m_2}{S^3}, \\
 E_{KBHPT,A} &= 6 \frac{m}{b} \left( \frac{r_A}{b} \right)^3 \frac{v}{r_A},
 \end{aligned} \tag{3.38}$$

plotted here (for  $v = (m/b)^{1/2}$ ) are only approximations of the true errors. These approximate errors were obtained by differentiating the error bars for the metric in Eq. (3.32) with respect to time. Note that the absolute error in the extrinsic curvature is  $O(m/b)^{1/2}$  smaller than that of the metric because the first nontrivial term in the extrinsic curvature appears at  $O(m/b)^{3/2}$ .

Similar results for the extrinsic curvature are also obtained for different separations and mass ratios. Figure 3.7 shows the  $xy$  component of the piecewise extrinsic curvature along the  $x$ -axis for the case of  $m_2/m_1 = 0.25$  and  $b = 20m$ . The near zone curvature (dashed line) agrees within error bars with the inner zone 1 curvature (dotted line) and the inner zone 2 curvature (dot-dot-dashed line) in buffer zones 1 and 2 respectively. Observe however, that the agreement worsens outside the buffer zone, e.g. as we approach either hole.

### Transition Functions

In this subsection, we construct transition functions that allow us to remove the piecewise nature of Eq. (3.29) and merge the approximate solutions smoothly in the buffer zone. This smoothing is performed by taking weighted averages of the two approximations. This procedure is justified by the fact that both approximations are equal to each other in the buffer zone up to uncontrolled remainders (asymptotic matching theorem [30]) which were neglected in the approximations used.

In the following we assume that the middle of each buffer zone is located around

$$r_A^M = \left(b^4 m_A^2 / m\right)^{1/5}, \quad (3.39)$$

which corresponds to the distance from the black holes where the error bars of the adjacent approximations are comparable.

The transition functions we use are all of the form

$$f(r) = \begin{cases} 0, & r \leq r_0 \\ \frac{1}{2} \left\{ 1 + \tanh \left[ \frac{s}{\pi} \left( \tan \left( \frac{\pi}{2w} (r - r_0) \right) - \frac{q^2}{\tan \left( \frac{\pi}{2w} (r - r_0) \right)} \right) \right] \right\}, & r_0 < r < r_0 + w \\ 1, & r \geq r_0 + w, \end{cases} \quad (3.40)$$

which is a function which smoothly transitions from zero to one in the region  $r_0 < r < r_0 + w$ . The parameters used here are as follows:  $r_0$  defines where the transition begins;  $w$  gives the width of the transition window;  $q$  determines the point where the transition function is equal to 1/2 (this happens at  $r_{1/2} = r_0 + (2w/\pi) \arctan q$ ); the slope of the transition function at this point is  $s(1+q^2)/(2w)$  and thus can be influenced by choosing  $s$  (and of course  $w$ ).

The global merged 4-metric is then given by

$$g_{\mu\nu}^{(global)} = G(x) \left\{ F_1(\bar{r}_1) g_{\mu\nu}^{(3)} + [1 - F_1(\bar{r}_1)] g_{\mu\nu}^{(1)} \right\} + [1 - G(x)] \left\{ F_2(\bar{r}_2) g_{\mu\nu}^{(3)} + [1 - F_2(\bar{r}_2)] g_{\mu\nu}^{(2)} \right\}, \quad (3.41)$$

where we have introduced

$$F_A(\bar{r}_A) = f(\bar{r}_A), \quad (3.42)$$

with

$$r_0 = 0.4r_A^M, \quad w = 3.5r_A^M, \quad q = 0.2, \quad s = b/m, \quad (3.43)$$

and also

$$G(x) = f(x), \quad (3.44)$$

but with

$$\begin{aligned} r_0 &= \frac{b(m_2 - m_1)}{2m} - \frac{b}{2} + 2.2m_2, \quad w = b - 2.2m, \\ q &= 1, \quad s = 2.5. \end{aligned} \quad (3.45)$$

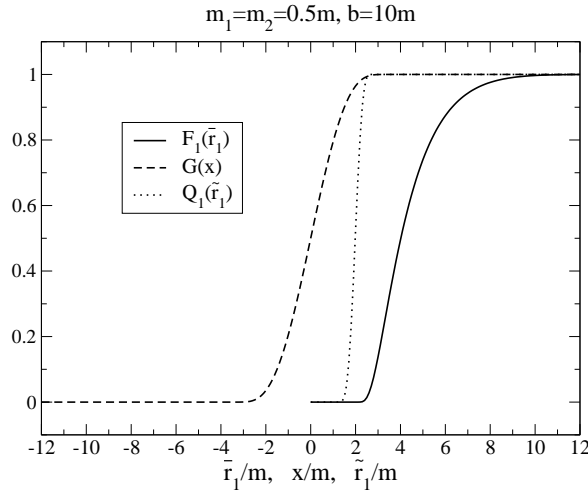


Fig. 3.8. This figure shows the transition functions used to merge the different pieces of the 4-metric. The transition function  $F_1(\bar{r}_1)$  with the transition parameters of Eq. (3.43) is shown as a solid line, while the function  $G(x)$  with the parameters of Eq. (3.45) is shown with a dashed line. The transition function  $Q_1(\bar{r}_1)$  (dotted line) defined in Eqs. (3.57) and (3.58) is used in Sec. 3.8 to construct horizon penetrating coordinates via the coordinate transformation (3.55).

The transition functions  $F_1(\bar{r}_1)$  and  $G(x)$  are shown in Fig. 3.8 for  $m_A = m/2$ ,  $b = 10m$  and the parameters of Eqs. (3.43) and (3.45), respectively.

The global lapse, shift and extrinsic curvature are merged using the same transition functions as for the 4-metric above. With these transition functions, the global metric is a mixture of inner zone and near zone metric in a transition region given by  $0.4r_A^M < \bar{r}_A < 3.9r_A^M$ . On the other hand, the global metric becomes identical to the inner zone metric in the region  $\bar{r}_A < 0.4r_A^M$ , while it becomes equal to the near zone metric in the region  $\bar{r}_A > 3.9r_A^M$ . Note that although the transition functions are identical to those used in paper 1, the transition parameters chosen here are slightly different. This change is because the inner zone metric is very similar to the near zone metric close to the black holes in ADMTT coordinates, so that the transition region has been moved closer to the black holes.

The exact choice of a transition function is to a certain degree arbitrary and could in principle be changed. However, the resulting global metrics generated by any other reasonable transition function should look very similar, and in fact be identical up to uncontrolled higher order post-Newtonian and tidal perturbation terms. Also note that the functions presented in this section are general enough to perform a smooth merge for systems with different masses and separations.

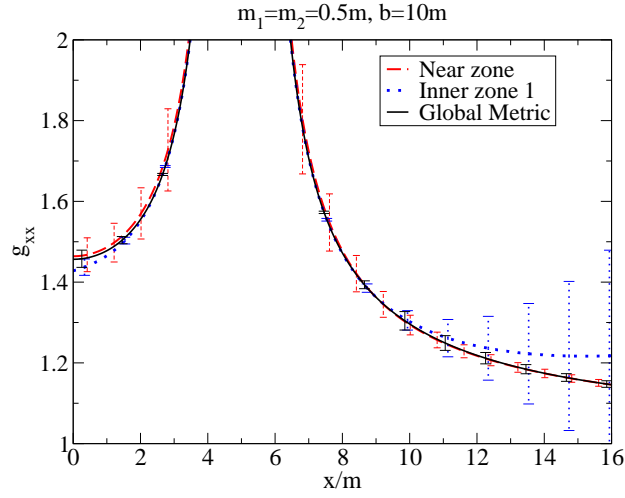


Fig. 3.9. In this figure we show how the transition function takes the  $xx$  component of the near zone metric to the inner zone solution around BH 1. Observe that the transition function is smooth and does not introduce kinks into the global solution.

In Fig. (3.9), we present the  $xx$ -component of the metric around BH 1. In this figure, the dotted curve corresponds to the inner zone metric, the dashed line is the near zone metric and the solid line is the merged global metric. The error bar in the global metric is given by the smallest of the error bars of the respective approximations. The purpose of this figure is to show explicitly that the transition function effectively merges the different approximations in the buffer zone, where the errors are comparable.

Even though the near zone 3-metric models the inner zone 3-metric well near the black hole horizons, the two metrics diverge differently at  $r_A = 0$ . In Fig. 3.10, we plot the  $xx$ -component of the metric divided by  $\Psi^4$ . This denominator removes the divergence of the near zone metric, which now becomes identically unity, while showing that the inner zone metric differs by an amount equal to the size of the tidal perturbation near the horizon. The reason that the inner zone metric still diverges after dividing by  $\Psi^4$  is due to the fact that the tidal perturbation piece of the inner zone metric is divergent at  $r_A = 0$ . This happens because the tidal perturbation piece is valid only for finite spacelike separations from the horizon, while  $r_A = 0$  which is located at the inner asymptotically flat end inside the black hole, is infinitely far from the horizon. This means that the tidal perturbation piece of the inner zone metric is not valid near  $r_A = 0$ . Yet, if this spurious tidal perturbation is removed, the resulting 3-metric of the Schwarzschild background will again agree well with the resummed post-Newtonian near zone 3-metric.

The same analysis can be performed for systems of unequal masses and at different separations. In Fig. 3.11 we plot the  $xx$  component of the metric along the  $x$ -axis for a binary with mass ratio  $m_2/m_1 = 0.25$  and at a separation  $b = 20m$ . The transition is now easier than before (note the scale of the  $y$ -axis), because the perturbation parameter

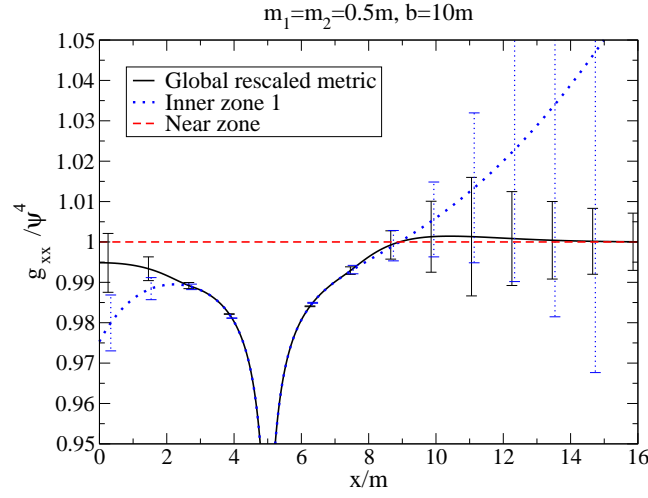


Fig. 3.10. In this figure we show the  $x$ -component of the metric, divided by  $\Psi^4$ . The dashed line is the near zone metric, the dotted line is the inner zone metric and the black solid line is the global metric with transition functions.

has become smaller. Also note that we have used the same parameters in the transition function as those used in the equal mass case and the transition is still smooth.

With these transition functions we can construct a smooth global metric, as shown in Fig. 3.12. There are no discontinuous features in the global metric. Just as in the case of the metric, to generate a global extrinsic curvature we will use the same transition function of the previous section with the same parameters. Figure 3.13 shows the global extrinsic curvature with the transition functions. Note that we could have computed the extrinsic curvature directly from Eq. (3.41), but this curvature would have been very similar to the curvature merged with transition functions. The difference between these two curvatures lies in the derivatives of the transition functions, but these terms will be of the same order or smaller than the uncontrolled remainders in either approximation in the buffer zone because of the parameter choice in Eqs. (3.43) and (3.45).

The 3-metric  $g_{ij}^{(global)}$  and the extrinsic curvature given in this section can now be used as initial data for black hole binaries. Recall, however, that these data are solutions to the Einstein equations only approximately and, thus, they only approximately satisfy the constraints. An analytic estimate of the constraint violation and physical accuracy of this data is given in Table II. Note that in the near zone, both the errors in the physics and the constraint violations are given by the neglected terms in the post-Newtonian approximation, which scale as  $O(m/r_A)^2$ . On the other hand, in the inner zone, the leading error in the physics is due to the terms neglected in the perturbation, which scales as  $O[(m/b)(r/b)^3]$ . The inner zone constraint violations, however, are smaller, because the perturbed Schwarzschild metric used here, satisfies the Einstein Equations up to order  $O[(m/b)^{5/2}(r/b)^2]$ .

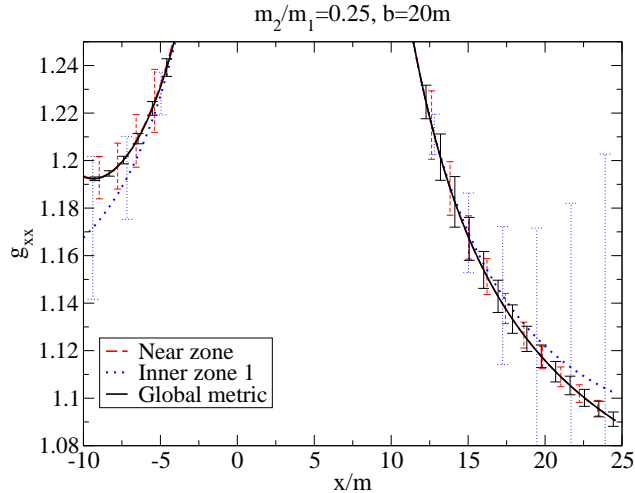


Fig. 3.11. In this figure we plot a system of unequal masses ( $m_2/m_1 = 0.25$ ) and a larger separation ( $b = 20m$ ). We use the same parameters in the transition function as in the equal mass case.

In order to obtain initial data that satisfy the constraints exactly, it will be necessary to project the data given in this paper to the constraint hypersurface. However, since these data are already significantly close to this hypersurface, sensible projection methods should *not* alter much the astrophysical content of the initial data. Furthermore, as stressed earlier, if this constraint violation is smaller than discretization error, these data could be evolved without any projection.

There are a couple of caveats that need to be discussed in more detail. First, as in paper 1, asymptotic matching will break down when the separation of the bodies is small enough that the near zone disappears between the two black holes. An approximate criterion for when this happens, corresponds to the separation where the middles of the two buffer zone shells touch for the first time. If we define the middle of each buffer zone as in Eq. (3.39), this happens when the two spheres of radius  $r_1^M$  and  $r_2^M$  centered on each of the black holes, touch for the first time (roughly  $b \approx 8m$  for an equal mass system). Furthermore, the tidal perturbation used in the inner zone metric is only valid for small spacelike separation from the horizon. This criterion implies that the tidal perturbation is good roughly for

$$\frac{m_A}{2} \frac{m}{2b} \ll \bar{r}_A \ll \frac{m_A}{m} b. \quad (3.46)$$

Therefore, numerical simulations will need to excise the data somewhere inside the apparent horizons of the black holes before evolving it, since the inner zone metric is not valid all the way up to  $\bar{r}_A = 0$ . Notice, however, that these limitations are due to the approximations and coordinates used and not due to asymptotic matching.

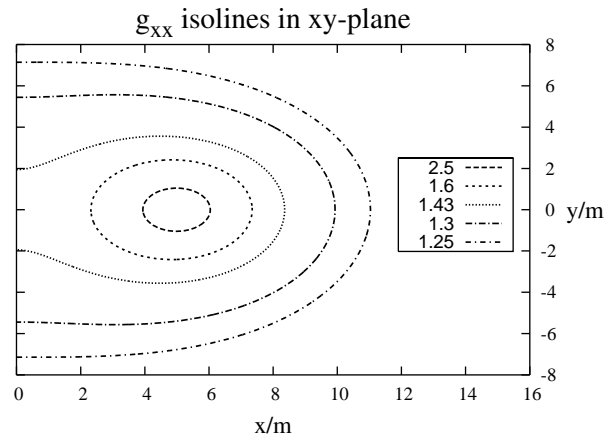


Fig. 3.12. Contour plot of the  $xx$ -component of the global metric in the  $xy$ -plane around black hole 1 for the equal mass system. Apart from the singularity at  $x = \pm 5m$ ,  $y = 0$  the 3-metric is everywhere smooth. The different line styles correspond to different isolines of constant metric value.

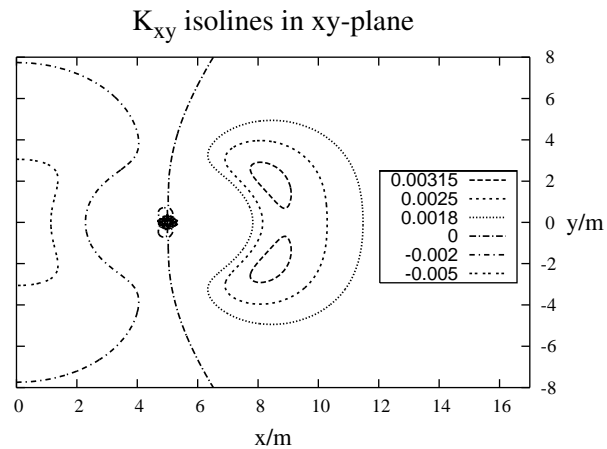


Fig. 3.13. Contour plot of the  $xy$  component of the global extrinsic curvature in the  $xy$ -plane around hole 1 for the equal mass system. The different line styles correspond to different isolines of constant extrinsic curvature.

Zone	Constraint Viol.	Physical Error
Inner zone BH1 ( $\mathcal{C}_1$ )	$O[(m/b)^{5/2}(\bar{r}_1/b)^2]$	$O[(m/b)(\bar{r}_1/b)^3]$
Inner zone BH2 ( $\mathcal{C}_2$ )	$O[(m/b)^{5/2}(\bar{r}_2/b)^2]$	$O[(m/b)(\bar{r}_2/b)^3]$
Near zone ( $\mathcal{C}_3$ )	$O(m/r_A)^2$	$O(m/r_A)^2$

Table II: This table shows an order of magnitude estimate of the constraint violation of this data, together with the error in the physics.

### 3.7 Constraint Violations

The initial data constructed here are based on approximate solutions and, thus, they do not solve the Einstein equations exactly. We have estimated that the largest error in the constraints of the full theory occurs in the buffer zone and is at most  $O(m_A/b)^2$ . This error can be sufficiently small compared to other sources of numerical error such that solving the constraints more accurately may not be required. On the other hand, the initial data could be used as input in one of the many conformal decompositions [18] to compute a numerical solution to the full constraints. In this section, we study the constraint violations of the data presented in this paper and we compare them to what was obtained in paper 1.

In Fig. 3.14 we show the Hamiltonian constraint violation along the positive  $x$ -axis for both data sets. The solid line is the constraint violation produced by the data presented in this paper, while the dot-dashed line is that produced by the data of paper 1. Observe that far away from both holes, both data sets (paper 1 and this paper's) have a constraint violation that approaches zero. This feature arises because both global metrics are given by a 1 PN solution in the near zone, which has a constraint violation that decays when the expansion parameter  $m_A/r_A$  becomes smaller. Note, however, that the constraint violation in ADMTT gauge is much smaller than in harmonic gauge. The reason for this difference is that our resummed PN expressions satisfy the Hamiltonian constraint up to errors of  $O(m_A/r_A)^3$  in ADMTT gauge, while the harmonic gauge expressions have errors of  $O(m_A/r_A)^2$ .

Also in Fig. 3.14, observe that close to the holes, the violation is given by that of the inner zone solution, which is small near the horizon, but increases as we move away from the holes. The largest constraint violation occurs in the buffer zone, where we transition from inner to near zone expressions. Note that this maximum in the violation is mainly caused by the transition functions. As can be seen in Fig. 3.15, both the inner and near zone solutions individually have smaller constraint violations in the buffer zone than the global curve. This, however, is not an indication of a bad choice of transition functions. Rather the inner and near zone solutions have smaller constraint violations than expected, because we have kept some extra higher order terms. Recall that matching in the buffer zone was only performed up to errors of  $O(m_A/r_A)^2$ . Hence the two solutions differ by this amount, and thus the error in the physics is of the same order as well. Nevertheless, the inner zone solution has constraint violations of

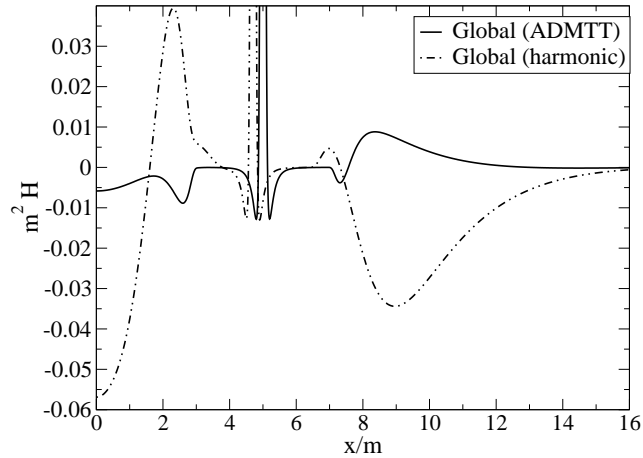


Fig. 3.14. This figure shows the violation of the Hamiltonian constraint for the equal mass system along the positive  $x$ -axis for both the data presented in this paper (solid black line) and that of paper 1 (dot-dashed black line).

$O(m_A/r_A)^{5/2}$  only, and the errors in the Hamiltonian constraint in the ADMTT near zone solution are only of  $O(m_A/r_A)^3$ . When these two solutions (which are equal to up to order  $O(m_A/r_A)$ ) are averaged with a transition function we obtain a new solution which differs from both inner and near zone solution by  $O(m_A/r_A)^2$ . Therefore, we expect the error in the constraints of the averaged solution to be of  $O(m_A/r_A)^2$  as well, and thus larger than the error in the individual solutions.

From Fig. 3.14 we see that the Hamiltonian constraint for the data of this paper is smaller than the data of paper 1. This decrease in the constraint violation is an indication that the matching performed in this paper produces near and inner zone solutions that are closer to each other in the buffer zone. Thus, the transition function has to do less work to join the solutions together, therefore introducing less of a constraint violation. We should point out that while the functional form of the transition function in paper 1 and in this paper is identical, the parameters used are different. The biggest difference is that here we use a smaller transition window  $w$ . Thus stronger artificial gradients and larger constraint violations might be expected in this work. This however, does not happen because matching works so much better in ADMTT coordinates that the inner and near zone solutions are substantially closer. Also note that the singularities in the constraint violations of the data in ADMTT and harmonic gauge (see Figs. 3.14 and 3.17) occur at different coordinate locations. This is simply because the inner zone metric, which is relevant in this region, is expressed in different coordinates.

One obtains qualitatively similar plots if the constraints are plotted along different directions. Evidence for this behavior can be seen in Fig. 3.16, which shows a contour plot of Hamiltonian constraint violation for the global metric in ADMTT coordinates in the  $xy$ -plane. We see that there is ring of radius  $3m$  of negative constraint violation

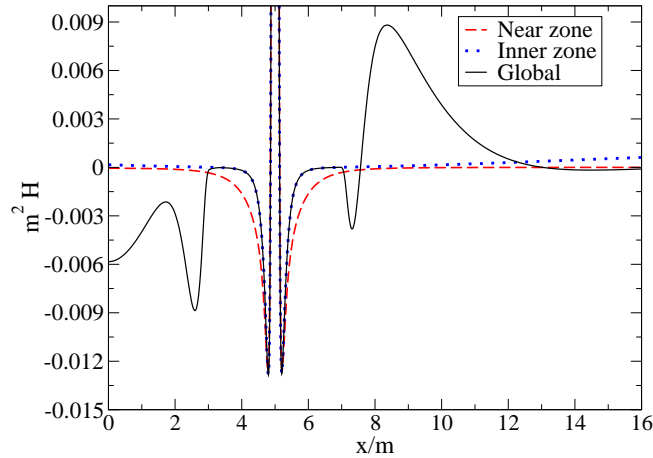


Fig. 3.15. This figure shows the violation of the Hamiltonian constraint for the equal mass system along the positive  $x$ -axis for the near zone (dashed line), the inner zone (dotted line) and the global (solid line) data with transition functions.

around the black hole. Outside this ring, about  $4.5m$  away from the hole, there are three maxima. The largest of these occurs on the  $x$ -axis. Note that these minima and maxima are all located in the buffer zone. In addition, there is a blowup inside the horizon at  $r_A = 0$ .

In Fig. 3.17, we plot the  $y$ -component of the momentum constraint along the positive  $x$ -axis close to black hole 1 for both data sets. For reasons of symmetry all other components vanish along this axis. Observe that the violation is everywhere small, reaching a maximum in the buffer zone. As expected, in the near zone the violation decays as we move away from the black holes and becomes identically post-Newtonian. Note however, that the resummed PN data in ADMTT gauge satisfy the momentum constraint exactly, while in harmonic gauge it has an error of  $O(m_A/r_A)^2$ . On the other hand, in the inner zone, the violation is close to zero outside the horizon (which is located at  $r_A \approx m_A/2$ ) and it grows as  $r_A$  becomes larger. As in the case of the Hamiltonian constraint the largest violation occurs in the region where the transition function leads to nontrivial averaging of the two approximations. The violation is once more smaller for the data presented in this paper relative to that of paper 1, which is one more indication that the matching is smoother here. Finally, observe that close to the holes, and in particular close to the horizons, the violation due to the inner zone data diverges. This divergence can be traced back to the choice of slicing, which forces the lapse to be zero at the horizon.

The vanishing of the lapse can be observed in Fig. 3.18, where we plot the inner zone, near zone and global lapse along the positive  $x$ -axis. This figure shows how the inner zone lapse goes through zero near the horizon. The vanishing of the lapse translates into a divergence of the momentum constraint, which renders excision difficult and the

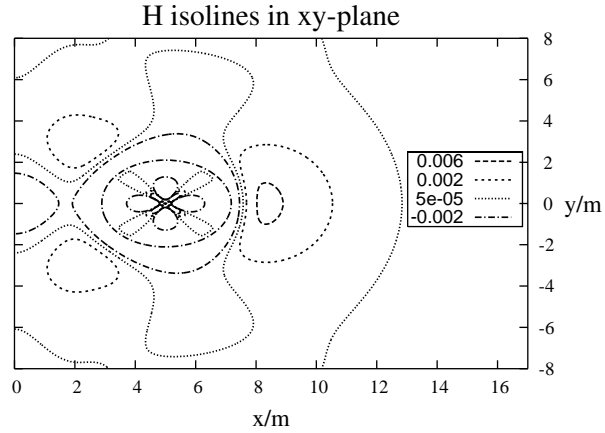


Fig. 3.16. Hamiltonian constraint violation of the global metric in ADMTT coordinates in the  $xy$ -plane for the equal mass system. The different line styles corresponds to isolines of constant constraint violation.

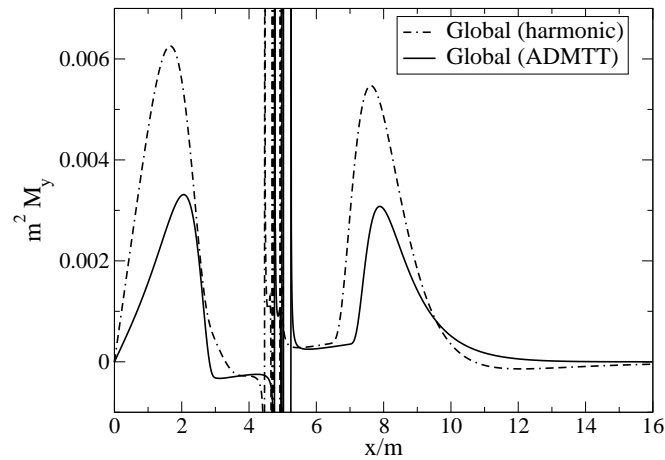


Fig. 3.17. This figure shows the  $y$ -component of the momentum constraint violation along the positive  $x$ -axis for the data computed in this paper (solid black line) and in paper 1 (dot-dashed black line), assuming the parameters of the equal mass system. Note that all other components vanish along this axis.

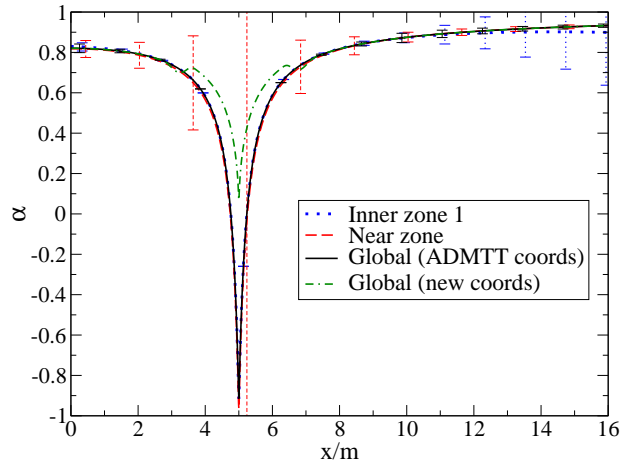


Fig. 3.18. This figure shows the near zone (dashed line), the inner zone (dotted line) and the global lapse (solid line) along the positive  $x$ -axis in ADMTT coordinates for the equal mass system. Observe that the global ADMTT lapse crosses zero near the horizon. Also shown is the lapse (dash-dash-dotted line) in the new horizon-penetrating coordinates of Sec. 3.8.

data difficult to implement numerically. However, this is a failure of the coordinate system used in the inner zone and not of the method of asymptotic matching. In the next section, we construct a new coordinate system in which the lapse remains non-zero across the horizon, and approaches an isotropic Schwarzschild lapse in the buffer zone to allow for matching.

In Figs. 3.14 and 3.17 we have compared the constraint violation of the data set presented here to that presented in paper 1. Technically this comparison suffers from the problem that the constraints were computed in different coordinate systems. Note however, that both coordinate systems are identical to leading order. Yet instead of comparing the violations point by point, we can study their global average. Figs. 3.14 and 3.17 favor the data of this paper because the humps are consistently smaller. As explained earlier, this is an indication that after performing the matching, the inner and near zone solutions are very close to each other, making the transition smoother.

### 3.8 Horizon penetrating coordinates

Recall that the global coordinate system constructed in Sec. 3.5 was based on matching the tidally perturbed black hole metric of the inner zone in isotropic coordinates to a post-Newtonian metric in ADMTT coordinates in the near zone. We have chosen to match in these coordinates because they are already very similar to each other. Hence, the coordinate transformation [Eq. (3.26)] that leads to matching is close to the identity, and thus facilitates computations. However, the fact that the global coordinate system

remains very close to isotropic coordinates is also a disadvantage, since the  $t = 0$  slice is not horizon penetrating in isotropic coordinates. The lapse goes through zero very close to the horizon and in addition, the extrinsic curvature has a coordinate singularity at the point where the lapse goes through zero. Initial data on such a slice may not be suitable for numerical evolutions. In this section we present a remedy for this problem. By constructing a further coordinate transformation, we obtain coordinates which are close to horizon penetrating Kerr-Schild coordinates near each black hole.

The basic strategy we will use is the following. We first determine the perturbed black hole metric valid in the inner zone in Kerr-Schild coordinates. We then transform this metric into a coordinate system which remains Kerr-Schild near the black hole horizons, but which is corotating isotropic in the buffer zone. In this manner, the transformed inner zone metric components in the buffer zone will remain identical to those in Sec. 3.5, so that we can use the same matching coordinate transformation [Eq. (3.26)] as in Sec. 3.5.

The standard transformation between spherical Kerr-Schild  $(\hat{t}', \hat{r}'_1)$  and spherical isotropic coordinates  $(\bar{t}, \bar{r}_1)$  centered at hole 1 and its inverse are given by [118]

$$\begin{aligned}\hat{t}' &= \bar{t} + 2M_1 \ln \left[ \frac{\bar{r}_1}{2M_1} \psi(\bar{r}_1)^2 - 1 \right], & \hat{r}'_1 &= \bar{r}_1 \psi(\bar{r}_1)^2, \\ \bar{t} &= \hat{t}' - 2M_1 \ln \left[ \frac{\hat{r}'_1}{2M_1} - 1 \right], & \bar{r}_1 &= \frac{\hat{r}'_1}{\psi(\hat{r}'_1)^2}, \\ \bar{\theta} &= \hat{\theta}', & \bar{\phi} &= \hat{\phi}',\end{aligned}\tag{3.47}$$

where the radius is measured from the center of a black hole with mass  $M_1$  and where the conformal factor and its inverse are given by

$$\begin{aligned}\psi(\bar{r}_1) &= 1 + \frac{M_1}{2\bar{r}_1}, \\ \psi(\hat{r}'_1) &= \frac{\hat{r}'_1}{M_1} \left[ 1 - \left( 1 - \frac{2M_1}{\hat{r}'_1} \right)^{1/2} \right].\end{aligned}\tag{3.48}$$

Note that the inverse transformation contains a square root in the conformal factor, which becomes complex inside the horizon. For this reason, it is simpler to first transform the inner zone metric to Kerr-Schild coordinates analytically. Then, we can construct a new coordinate system that is the identity map near the horizon, but that brings back the metric to isotropic coordinates outside the horizon in the buffer zone.

Let us first transform the inner zone metric of hole 1 to Kerr-Schild coordinates. By applying Eqs. (3.47) to the inner zone metric in spherical isotropic coordinates

[Eq. (3.22) of Ref. [28]] we obtain

$$\begin{aligned}
g_{\hat{0}'\hat{0}'}^{(1)} &= -f + \frac{m_2}{b^3} \hat{r}_1'^2 f^2 \left[ 3 \sin^2 \hat{\theta}' \left( \cos \hat{\phi}' \cos \Omega \bar{t} + \sin \hat{\phi}' \sin \Omega \bar{t} \right)^2 - 1 \right], \\
g_{\hat{1}'\hat{1}'}^{(1)} &= (2-f) + \frac{m_2}{b^3} \hat{r}_1'^2 \left( 1 + \frac{4M_1^2}{\hat{r}_1'^2} \right) \left[ 3 \sin^2 \hat{\theta}' \left( \cos \hat{\phi}' \cos \Omega \bar{t} + \sin \hat{\phi}' \sin \Omega \bar{t} \right)^2 - 1 \right], \\
g_{\hat{2}'\hat{2}'}^{(1)} &= \hat{r}_1'^2 + \frac{m_2}{b^3} \hat{r}_1'^2 f^2 \left[ 3 \sin^2 \hat{\theta}' \left( \cos \hat{\phi}' \cos \Omega \bar{t} + \sin \hat{\phi}' \sin \Omega \bar{t} \right)^2 - 1 \right], \\
g_{\hat{3}'\hat{3}'}^{(1)} &= g_{\hat{2}'\hat{2}'}^{(1)} \sin^2 \hat{\theta}', \\
g_{\hat{0}'\hat{1}'}^{(1)} &= \frac{2M_1}{\hat{r}_1'} - \frac{m_2}{b^3} \hat{r}_1'^2 f \frac{2M_1}{\hat{r}_1'} \left[ 3 \sin^2 \hat{\theta}' \left( \cos \hat{\phi}' \cos \Omega \bar{t} + \sin \hat{\phi}' \sin \Omega \bar{t} \right)^2 - 1 \right], \\
g_{\hat{0}'\hat{2}'}^{(1)} &= -\frac{2m_2}{b^3} \sqrt{\frac{m}{b}} \hat{r}_1'^3 f \cos \hat{\theta}' \left( \sin \hat{\phi}' \cos \Omega \bar{t} - \cos \hat{\phi}' \sin \Omega \bar{t} \right), \\
g_{\hat{0}'\hat{3}'}^{(1)} &= -\frac{2m_2}{b^3} \sqrt{\frac{m}{b}} \hat{r}_1'^3 f \sin \hat{\theta}' \cos 2\hat{\theta}' \left( \cos \hat{\phi}' \cos \Omega \bar{t} + \sin \hat{\phi}' \sin \Omega \bar{t} \right), \\
g_{\hat{1}'\hat{2}'}^{(1)} &= \frac{1}{f} g_{\hat{0}'\hat{2}'}^{(1)}, \quad g_{\hat{1}'\hat{3}'}^{(1)} = \frac{1}{f} g_{\hat{0}'\hat{3}'}^{(1)},
\end{aligned} \tag{3.49}$$

where all coordinates are centered on BH 1 and where we used the abbreviation

$$f = \left( 1 - \frac{2M_1}{\hat{r}_1'} \right). \tag{3.50}$$

In Eq. (3.49),  $\bar{t}$  stands for the isotropic time coordinate, given in Eq. (3.47). Recall that this metric was derived under the assumption that the second black hole responsible for the tidal perturbation is moving slowly. In particular Alvi obtained the perturbation from a stationary perturbation by replacing  $\bar{\phi}$  by  $\bar{\phi} - \Omega \bar{t}$ . This means the largest error in this perturbation is of order  $O(m/b)^{5/2} O(r_A/b)^2$ . In the following we will replace Schwarzschild time  $\bar{t}$  by Kerr-Schild time  $\hat{t}$  to simplify our expressions. This replacement will change the tidal perturbation only at order  $O(m/b)^{5/2} O(r_A/b)^2$  and thus not introduce any extra errors.

We now go one step further and transform Eq. (3.49) to Cartesian Kerr-Schild coordinates via the standard map

$$\begin{aligned}
\hat{t}' &= \hat{t}, \quad \hat{r}_1' = \left( \hat{x}^2 + \hat{y}^2 + \hat{z}^2 \right)^{1/2}, \\
\hat{\theta}' &= \cos^{-1} \left[ \frac{\hat{z}}{\left( \hat{x}^2 + \hat{y}^2 + \hat{z}^2 \right)^{1/2}} \right], \\
\hat{\phi}' &= \tan^{-1} \left( \frac{\hat{y}}{\hat{x}} \right).
\end{aligned} \tag{3.51}$$

We then obtain

$$\begin{aligned}
g_{\hat{0}\hat{0}}^{(1)} - g_{\hat{0}\hat{0}}^{(KS)} &= \frac{m_2}{b^3} f^2 d, \\
g_{\hat{1}\hat{1}}^{(1)} - g_{\hat{1}\hat{1}}^{(KS)} &= \frac{m_2}{b^3} d \left[ 1 + \frac{2M_1^2}{\hat{r}_1^2} \left( \frac{3\hat{x}^2}{\hat{r}_1^2} - 1 \right) \right] \\
&\quad - \frac{4M_1 m_2}{\hat{r}_1 b^3} \sqrt{\frac{m}{b}} \frac{\hat{x}}{\hat{r}_1} \left[ (\hat{z}^2 - \hat{y}^2) \sin \Omega \hat{t} - \hat{y} \hat{x} \cos \Omega \hat{t} \right], \\
g_{\hat{2}\hat{2}}^{(1)} - g_{\hat{2}\hat{2}}^{(KS)} &= \frac{m_2}{b^3} d \left[ 1 + \frac{2M_1^2}{\hat{r}_1^2} \left( \frac{3\hat{y}^2}{\hat{r}_1^2} - 1 \right) \right] \\
&\quad - \frac{4M_1 m_2}{\hat{r}_1 b^3} \sqrt{\frac{m}{b}} \frac{\hat{y}}{\hat{r}_1} \left[ (\hat{x}^2 - \hat{z}^2) \cos \Omega \hat{t} + \hat{y} \hat{x} \sin \Omega \hat{t} \right], \\
g_{\hat{3}\hat{3}}^{(1)} - g_{\hat{3}\hat{3}}^{(KS)} &= \frac{m_2}{b^3} d \left[ 1 + \frac{2M_1^2}{\hat{r}_1^2} \left( \frac{3\hat{z}^2}{\hat{r}_1^2} - 1 \right) \right] - \frac{4M_1 m_2}{\hat{r}_1 b^3} \sqrt{\frac{m}{b}} \frac{\hat{z}^2}{\hat{r}_1} (\hat{y} \cos \Omega \hat{t} - \hat{x} \sin \Omega \hat{t}), \\
g_{\hat{0}\hat{1}}^{(1)} - g_{\hat{0}\hat{1}}^{(KS)} &= -\frac{2M_1}{\hat{r}_1} \frac{\hat{x}}{\hat{r}_1} \frac{m_2}{b^3} f d + \frac{2m_2}{b^3} \sqrt{\frac{m}{b}} f \left[ (\hat{z}^2 - \hat{y}^2) \sin \Omega \hat{t} - \hat{x} \hat{y} \cos \Omega \hat{t} \right], \\
g_{\hat{0}\hat{2}}^{(1)} - g_{\hat{0}\hat{2}}^{(KS)} &= -\frac{2M_1}{\hat{r}_1} \frac{\hat{y}}{\hat{r}_1} \frac{m_2}{b^3} f d + \frac{2m_2}{b^3} \sqrt{\frac{m}{b}} f \left[ (\hat{x}^2 - \hat{z}^2) \cos \Omega \hat{t} + \hat{x} \hat{y} \sin \Omega \hat{t} \right], \\
g_{\hat{0}\hat{3}}^{(1)} - g_{\hat{0}\hat{3}}^{(KS)} &= -\frac{2M_1}{\hat{r}_1} \frac{\hat{z}}{\hat{r}_1} \frac{m_2}{b^3} f d + \frac{2m_2}{b^3} \sqrt{\frac{m}{b}} f \hat{z} (\hat{y} \cos \Omega \hat{t} - \hat{x} \sin \Omega \hat{t}), \\
g_{\hat{1}\hat{2}}^{(1)} - g_{\hat{1}\hat{2}}^{(KS)} &= \frac{\hat{x} \hat{y}}{\hat{r}_1^2} \frac{6m_2}{b^3} \frac{M_1}{\hat{r}_1^2} d + \frac{4m_2}{b^3} \frac{M_1}{\hat{r}_1} \sqrt{\frac{m}{b}} \frac{1}{\hat{r}_1^3} \left[ (\hat{y} \sin \Omega \hat{t} + \hat{x} \cos \Omega \hat{t}) (\hat{y}^4 - \hat{x}^4) \right. \\
&\quad \left. + (\hat{x} \cos \Omega \hat{t} - \hat{y} \sin \Omega \hat{t}) \hat{z}^2 (2\hat{y}^2 + \hat{z}^2) \right], \\
g_{\hat{1}\hat{3}}^{(1)} - g_{\hat{1}\hat{3}}^{(KS)} &= \frac{\hat{x} \hat{z}}{\hat{r}_1^2} \frac{6m_2}{b^3} \frac{M_1^2}{\hat{r}_1^2} d + \frac{4m_2 M_1}{b^3} \sqrt{\frac{m}{b}} \left( 1 - \frac{2\hat{z}^2}{\hat{r}_1^2} \right) \hat{z} \sin \Omega \hat{t}, \\
g_{\hat{2}\hat{3}}^{(1)} - g_{\hat{2}\hat{3}}^{(KS)} &= \frac{\hat{y} \hat{z}}{\hat{r}_1^2} \frac{6m_2}{b^3} \frac{M_1^2}{\hat{r}_1^2} d - \frac{4m_2 M_1}{b^3} \sqrt{\frac{m}{b}} \left( 1 - \frac{2\hat{z}^2}{\hat{r}_1^2} \right) \hat{z} \cos \Omega \hat{t}, \tag{3.52}
\end{aligned}$$

where  $\hat{r}_1 = \hat{r}'_1$ . This is the inner zone metric for hole 1 in Cartesian Kerr-Schild coordinates, where the standard metric in Cartesian Kerr-Schild form is

$$g_{\hat{a}\hat{b}}^{(KS)} = \eta_{\hat{a}\hat{b}} + \frac{2M_1}{\hat{r}_1} l_{\hat{a}} l_{\hat{b}}, \tag{3.53}$$

with null vectors  $l_{\hat{a}} = \{1, x^{\hat{i}}/\hat{r}_1\}$  and where we have introduced the shorthand

$$d = \left[ 3 (\hat{x} \cos \Omega \hat{t} + \hat{y} \sin \Omega \hat{t})^2 - \hat{r}_1^2 \right]. \tag{3.54}$$

The lapse in this coordinate system is now a positive definite function.

The matching of Sec. 3.5, however, is performed in the buffer zone in Cartesian corotating isotropic coordinates. We thus need a coordinate transformation that leaves Eq. (3.52) unchanged near the horizon, but takes the metric to isotropic corotating coordinates in the buffer zone. For black hole A, the transformation we use is given by

$$\begin{aligned}\hat{t} &= (1 - Q_A) \tilde{t} + Q_A \left[ \tilde{t} + 2m_A \ln \left| \frac{\tilde{r}_A \psi_A^2}{2m_A} - 1 \right| \right], \\ \hat{x} &= (1 - Q_A) \tilde{x} + Q_A (\tilde{x} \cos \Omega \tilde{t} - \tilde{y} \sin \Omega \tilde{t}) \psi_A^2, \\ \hat{y} &= (1 - Q_A) \tilde{y} + Q_A (\tilde{x} \sin \Omega \tilde{t} + \tilde{y} \cos \Omega \tilde{t}) \psi_A^2, \\ \hat{z} &= (1 - Q_A) \tilde{z} + Q_A \tilde{z} \psi_A^2,\end{aligned}\tag{3.55}$$

where

$$\psi_A = 1 + \frac{m_A}{2\tilde{r}_A}, \quad \tilde{r}_A = \sqrt{\tilde{x}^2 + \tilde{y}^2 + \tilde{z}^2}\tag{3.56}$$

and the transition function

$$Q_A = f(\tilde{r}_A)\tag{3.57}$$

with

$$\begin{aligned}r_0 &= 2.2m_A, & w &= 0.6r_A^M - 2.2m_A, \\ q &= 1, & s &= 2.8,\end{aligned}\tag{3.58}$$

is designed such that  $Q_A$  is unity in the buffer zone and zero near black hole A (see Fig. 3.8). This means that using Eq. (3.55) we can transform from Kerr-Schild coordinates (labeled by a hat), to coordinates (labeled by a tilde) which are corotating isotropic coordinates in the buffer zone (where  $Q_A = 1$ ), but which are equal to Kerr-Schild coordinates at the black hole horizons (where  $Q_A = 0$ ). The function  $Q_A$  is chosen carefully so that the transformed coordinate system is identically Kerr-Schild at the horizon ( $\tilde{r}_A = 2m_A$ ), while it is equal to isotropic coordinates in the buffer zone where we perform the matching. We can adjust, as usual, how fast we transition by changing the parameters of  $Q_A$ , but we are constrained to having the metric completely in isotropic coordinates in the buffer zone, in order for the matching to be valid.

The inner zone metric then becomes

$$g_{\hat{\mu}\hat{\nu}}^{(1)} = g_{\hat{\alpha}\hat{\beta}}^{(1)} J_{\hat{\mu}}^{\hat{\alpha}} J_{\hat{\nu}}^{\hat{\beta}},\tag{3.59}$$

where, in analogy to Eq. (3.31), the Jacobian matrix is given by

$$J_{\hat{\mu}}^{\hat{\alpha}} = \frac{\partial x^{\hat{\alpha}}}{\partial x^{\hat{\mu}}}.\tag{3.60}$$

This Jacobian can be computed by taking derivatives of Eq. (3.55).

With this new coordinate transformation, the global metric contains several transition functions. A schematic drawing of these transitions is presented in Fig. 3.19. In this drawing, the black dot represents BH 1 and the solid black line is the radial direction, where the horizon, for example, is located at  $\tilde{r}_1 = 2m_1$ . Fig. 3.19 also shows the different coordinate systems used, where KS stands for Kerr-Schild, ISO for isotropic coordinates and ADMTT for the PN near zone. The dotted line shows the region where the transitions take place:  $T1$  is the transition between KS to ISO and  $T2$  is the transition produced by the matching coordinate transformation. Observe that  $T1$  is chosen so that the 4-metric is in KS coordinates everywhere near and inside the horizon, while it is completely in ISO coordinates where  $T2$  begins. This restriction makes the transition window of  $T1$  narrow. On the other hand, the transition window of  $T2$  is restricted only by the size of the buffer zone and, thus, is chosen to be wider.

### Effect of the new coordinates

In this subsection, we describe the advantages of the new coordinate system. In these coordinates, the new global 4-metric is much better behaved close to the horizons, where it is of Kerr-Schild form. Thus, the lapse remains positive definite through the horizon. The lapse for an equal mass system along the positive x-axis in the new coordinates is shown in Fig. 3.18 (dash-dash-dotted line) together with the lapse in the old ADMTT coordinates (solid line). The inner zone lapse in new coordinates is approximately equal to the Kerr-Schild lapse inside the horizon, while it smoothly approaches the lapse of isotropic coordinates in the buffer zone and the ADMTT lapse in the near zone.

Another quantity that changes in the new coordinates is the spatial metric. Fig. 3.20 shows the  $xx$ -component of the new global metric along the  $x$ -axis for an equal mass system. The large humps on either side of each black hole in Fig. 3.20 are produced by derivatives of the coordinate transformation (3.55), which contains the transition function  $Q_A$  that changes rapidly from zero to unity in a small region of width  $w = 0.6r_A^M - 2.2m_A$ . Had we chosen a wider transition window  $w$  to transition, this derivative would become smaller and the hump would be smoothed out. However, we need the metric to be completely in isotropic coordinates in the buffer zone where we perform the matching (approximately at  $\bar{r}_A = 6m_A$ ). Therefore, we are constrained to have a narrow transition window  $w$ , which then produces large derivatives of the transition functions and humps in the metric. Note, however, that these humps are *not* spurious gravitational radiation. They simply arise because of performing a coordinate transformation. Therefore, due to the inherent diffeomorphism invariance of General Relativity, the physical content of the data will not be altered by the coordinate transformation. In addition, if we choose a larger black hole separation,  $r_A^M$  increases and we obtain a wider transition window to transition, and hence the humps become smaller.

Since the inner zone lapse in this new coordinates is now a positive definite function, we expect the extrinsic curvature and the momentum constraint violation to be small and well-behaved across the horizon. In Fig. 3.21 we compare the  $y$ -component of the momentum constraint violation for an equal mass binary in this new coordinate system to that in the old ADMTT coordinates near BH 1. Observe that the constraint

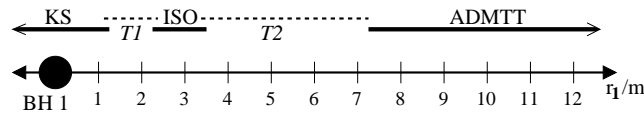


Fig. 3.19. Schematic drawing of the different metrics, coordinate systems and transition windows. The solid line represents the distance  $r_1$  (in ADMTT coordinates) from BH 1. The thick solid line labeled by ADMTT delineates the region where we use the PN near zone solution in ADMTT coordinates. The other two thick solid lines labeled by ISO and KS, show the region in which we use the inner zone solution. The labels here stand for the isotropic (ISO) and Kerr-Schild (KS) coordinates we have used in the inner zone before applying the matching coordinate transformation (3.26). The dotted line  $T1$  corresponds to the region where the transition function  $Q_1$  (see Fig. 3.8) of Eqs. (3.57) and (3.58) is between zero and one, so that the coordinate transformation of Eq. (3.55) yields nontrivial results. I.e. in that region the inner zone metric is given in coordinates that are a mixture of Kerr-Schild and isotropic coordinates, while to the left and right of  $T1$  it is given in Kerr-Schild and isotropic coordinates, respectively. Using the definitions (3.57) and (3.58) for the transition function  $Q_1$ , we find that the inner and outer radii of  $T1$  are  $2.2m_A$  and  $0.6r_A^M$ , where  $r_A^M$  given in Eq. (3.39). The dotted line labeled  $T2$  indicates the transition window of the transition function  $F_1$  (see Fig. 3.8) of Eq. (3.42) with parameters given by Eqs. (3.43) and (3.39). In  $T2$  we use a weighted average of both the inner zone metric (transformed into ADMTT coordinates using Eq. (3.26)) and the near zone ADMTT metric. From Eq. (3.43) we see that the inner and outer radii of  $T2$  are  $0.4r_A^M$  and  $3.9r_A^M$ .

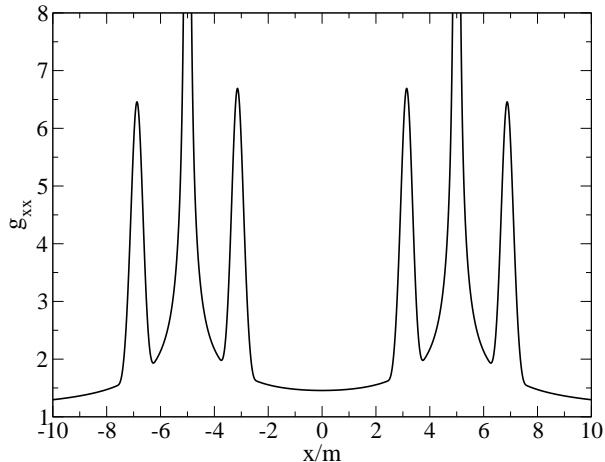


Fig. 3.20. This figure shows the  $xx$ -component of the global metric in new coordinates for an equal-mass system along the  $x$ -axis.

violation is finite everywhere, except near the singularity. With this new coordinate system, excision is now possible, since the curvature does not blow up until close to the physical singularity. We have zoomed to a region  $0.5m$  away from the singularity of BH 1 to distinguish the behavior of the violation better. As we can observe from the figure, the ADMTT constraint violation is identical to the violation in the new coordinates away from the horizon. However, near the horizon there are spikes when we use the old coordinates. These spikes are poorly resolved in this figure, but we have checked that they are indeed divergences. Observe that these spikes are not present in the new coordinates.

Since our method really yields a 4-metric we can also compute the Ricci tensor. This tensor should be close to zero for an approximate vacuum metric. Figure 3.22 shows the Ricci scalar along the  $x$ -axis at  $t = 0$ . One can see that it has the same qualitative features as the Hamiltonian and momentum constraints. I.e. apart from the singularity at the center of the black hole, the largest violations occur in the buffer zone. Notice however, that unlike in the case of metric (see Fig. 3.20) the coordinate transformation (3.55), with the transition function  $Q_A$  does not produce large humps in the Ricci scalar. This confirms that the large humps in the metric are a pure coordinate effect, that has no influence on coordinate invariant quantities such as the Ricci scalar.

### 3.9 Conclusions

We have constructed approximate initial data for non-spinning black hole binaries by asymptotically matching the 4-metrics of two tidally perturbed Schwarzschild solutions in isotropic coordinates to a post-Newtonian metric in ADMTT coordinates. The two perturbed Schwarzschild metrics are valid only close to each black hole (in the inner

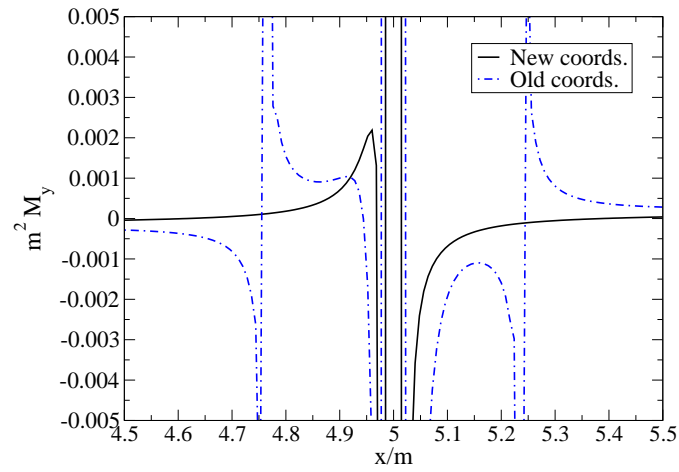


Fig. 3.21. Plot of the y-component of the momentum constraint violation for an equal mass binary near BH 1 in new coordinates (black solid line) and in ADMTT coordinates (dot-dashed line). Observe that in new coordinates there is no divergence until the singularity.

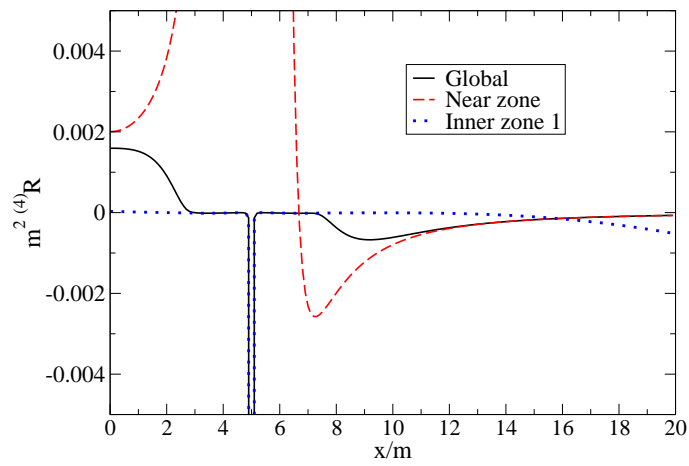


Fig. 3.22. This figure shows the Ricci scalar at  $t = 0$  along the  $x$ -axis for the inner (dotted line), near (dashed line) and global (solid line) 4-metrics.

zones) and contain tidal deformations which are correct up to  $O(r_A/b)^2$ . The ADMTT post-Newtonian metric we use is formally correct only up to  $O(m/b)^{3/2}$  and valid only in the near zone, and not close to the black holes. However, by adding certain higher order terms to the ADMTT metric we bring it into a form that is close to the Schwarzschild metric plus some artificial perturbation. This means that instead of blowing up in an uncontrolled way, the ADMTT metric approaches the Schwarzschild metric in isotropic coordinates when we approach one of the black holes. Since the two tidally perturbed Schwarzschild solutions, which are actually valid close to each black hole are also given in isotropic coordinates, both metrics agree at leading order even before asymptotic matching is performed.

The procedure we have used to achieve asymptotic matching closely follows the calculation of paper 1, and is performed in the so called buffer zone where both the post-Newtonian and the perturbed Schwarzschild approximations hold. The result is that both metrics agree in the buffer zone, up to the errors in the approximations. However, since both approximations are similar to Schwarzschild in isotropic coordinates, matching yields much better results than in paper 1, where harmonic coordinates were used for the post-Newtonian 4-metric. In addition, after matching in the buffer zone the two metrics are also very similar near the black hole horizons, even though the post-Newtonian metric is formally not valid there. The biggest deviation of the post-Newtonian 4-metric from the correct perturbed Schwarzschild solution near the horizon occurs in the  $g_{0i}$  or shift components at  $O(m/b)^{3/2}$ . At this same order similar deviations are also observable in the extrinsic curvature of the  $t = 0$  slice.

The resulting global piecewise 4-metric is made formally  $C^\infty$  by the use of smoothing functions. These functions are chosen such that the smoothed global metric has errors on the order of the error introduced by the more accurate of the two approximations we match. This smoothing procedure works much better than in paper 1, because the tidally perturbed Schwarzschild solutions and the post-Newtonian metric are much closer to each other and diverge at similar locations. The smoothed global metric is obtained in ADMTT coordinates, and thus very similar to isotropic coordinates near each black hole. Hence our coordinates are not horizon penetrating and, for example, result in a lapse that goes through zero close to the horizons. Since such coordinates may be problematic for certain numerical simulations, we construct an additional coordinate map. With this map one can transform the 4-metric from global ADMTT coordinates, obtained through asymptotic matching, to new coordinates which are similar to Kerr-Schild coordinates near each black hole, but which remain ADMTT further away from the black holes. These new coordinates are horizon penetrating and lead to a lapse which is everywhere positive on the  $t' = 0$  slice. The same map can in principle also be applied to the data computed in paper 1.

For both, global ADMTT and new coordinates we have constructed initial data sets on the respective  $t' = 0$  slices. These initial data are then used to compute Hamiltonian and momentum constraint violations. We find that the initial data found in this paper is closer to the constraint hypersurface than the data presented in paper 1, making it perhaps more amenable to numerical simulations.

In conclusion, we have used the method of asymptotic matching to construct improved approximate initial data for non-spinning black hole binaries. Future work will concentrate on applying this method to spinning binary systems. This problem is of fundamental importance to astrophysics and gravitational wave detection, since most black holes are believed to be rotating. Using the results of [104] the matching of a tidally perturbed Kerr black hole to a post-Newtonian metric should be possible. Other work will concentrate on repeating this analysis to higher post-Newtonian order to explicitly incorporate the effect of gravitational waves.

## Acknowledgments

We would like to thank the University of Jena for their hospitality. We would also like to thank Ben Owen and Bernd Brügmann for useful discussion and comments. Nicolas Yunes acknowledges the support of the Institute for Gravitational Physics and Geometry and the Center for Gravitational Wave Physics, funded by the National Science Foundation under Cooperative Agreement PHY-01-14375. This work was also supported by NSF grants PHY-02-18750, PHY-02-44788, and PHY-02-45649. Wolfgang Tichy acknowledges partial support by the National Computational Science Alliance under Grants PHY050012T, PHY050015N, and PHY050016N.

## Chapter 4

# Frankenstein's Glue: Transition functions for approximate solutions

Approximations are commonly employed to find approximate solutions to the Einstein equations. These solutions, however, are usually only valid in some specific spacetime region. A global solution can be constructed by gluing approximate solutions together, but this procedure is difficult because discontinuities can arise, leading to large violations of the Einstein equations. In this paper, we provide an attempt to formalize this gluing scheme by studying transition functions that join approximate analytic solutions together. In particular, we propose certain sufficient conditions on these functions and prove that these conditions guarantee that the joined solution still satisfies the Einstein equations analytically to the same order as the approximate ones. An example is also provided for a binary system of non-spinning black holes, where the approximate solutions are taken to be given by a post-Newtonian expansion and a perturbed Schwarzschild solution. For this specific case, we show that if the transition functions satisfy the proposed conditions, the joined solution does not contain any violations to the Einstein equations larger than those already inherent in the approximations. We further show that if these functions violate the proposed conditions, then the matter content of the spacetime is modified by the introduction of a matter-shell, whose stress-energy tensor depends on derivatives of these functions.

### 4.1 Introduction

The detection and modeling of gravitational radiation is currently one of the primary driving forces in classical general relativity due to the advent of ground-based [119, 120, 121, 122] and space-born detectors <sup>1</sup> [123, 124]. This radiation is generated in highly dynamical spacetimes, whose exact metric has not yet been found. Approximate solutions to the Einstein equations, both analytical (such as post-Newtonian solutions [3]) and numerical, have served to provide insight on the dynamics of such spacetimes and the character of the radiation produced. These approximations, however, have inherent uncontrolled remainders, or errors, due to truncation of certain higher order terms in the analytical case, or discretization error in the numerical case. An approximate global

---

<sup>1</sup>This chapter is based on the following paper: N. Yunes, *Class. Quant. Grav.* **245**, 4313-4336 (2007)

solution, then, could be constructed by joining several approximate solutions together in some overlap region [105, 93].

Before proceeding, we must distinguish between two different kinds of joined solutions: mixed ones, where one joins an analytical solution to a numerical one; and pure ones, where one joins two analytical solutions that have different but overlapping regions of validity. A special kind of mixed joined solutions have been created in the context of the effective-one-body formalism [125, 126], with the motivation of providing accurate waveform templates to gravitational wave interferometers. Pure joined solutions have been discussed in the context of asymptotic matching, where one of the motivations is to use the joined solution as initial data for relativistic simulations [105, 93]. In this paper, we concentrate on pure joined solutions, although the methods and conditions we find can be straightforwardly extended to mixed joined solutions.

The construction of pure joined solutions is not always simple because approximation methods tend to break down in highly dynamical spacetimes. The main difficulty lies in that approximate solutions usually depend on the existence of a background about which to perturb the solution. However, in highly dynamical spacetimes, such a background cannot usually be constructed. Thus, in those scenarios, the region of validity of the different approximations tends not to overlap. In slightly less dynamical cases, the regions of validity can overlap, but the different approximate metrics usually describe the spacetime in different coordinates and parameters. Patching [30] could be used to relate the different approximate solutions, but this method usually leads to an overdetermined system if we require the patched metric to be differentiable at the junction. A better alternative is to relate the approximate solutions via asymptotic matching, which guarantees that adjacent metrics and their derivatives be asymptotic to each other in some overlap region.

Asymptotic matching was developed as a technique of multiple-scale analysis to solve non-linear partial differential equations [30, 31]. In general relativity, this method was first studied in [98, 97, 100, 99, 94] and it has recently had important applications to post-Newtonian theory [3], black hole perturbation theory [127] and initial data constructions [105, 93]. Asymptotic matching requires that we compare the asymptotic expansions of the approximate solutions inside the region of the manifold where the regions of validity of the approximations overlap (the buffer zone.) This method then provides a coordinate and parameter transformation that relates the approximate metrics, such that adjacent metrics and their derivatives become asymptotic to each other inside the buffer zone. In essence, asymptotically matched approximations are guaranteed to represent the same metric components in the same coordinate system inside the buffer zone.

After matching has been carried out, there is still freedom as to how to join the matched approximate solutions together. The simplest way to do so is through a weighted linear combination of approximate solutions with transition functions. This method was first considered in depth in [105, 93], where a binary black hole system was studied to construct initial data for numerical simulations (the so-called Frankenstein approach). In that work, only broad comments were made as to the type of allowed transition functions, requiring only that the functions be “differentiable enough,” and the the properties and conditions these functions must satisfy were not studied. A priori, it might not be clear

which functions are allowed such that the global metric still approximately solves the Einstein equations. For instance, it might seem natural to use Heaviside functions to join the metrics together at a hypersurface, as is done in the standard junction conditions of general relativity [128, 129, 130, 131, 132, 133, 134, 118, 135]. These joining procedure works well when dealing with exact solutions to the Einstein equations, in the sense that the joined solution is itself also a solution. As we show in this paper, however, when working with approximate solutions better transition functions need to be found.

The purpose of this paper is to study whether a global approximate solution to the Einstein equations, be it pure or mixed, can be constructed directly from a weighted linear superposition of approximate solutions with transition functions. We thus refine, prove and verify many of the broad statements made in [105, 93] regarding transition functions. This goal is achieved by constraining the family of allowed transition functions for pure joined solutions via certain sufficient asymptotic differentiability conditions. These conditions are independent of the perturbative order to which asymptotic matching is carried out and the location in which the transition occurs, as long as it is inside the buffer zone. We then derive and prove theorems that guarantee that pure joined solutions constructed with this restricted family of transition functions satisfy the Einstein equations to the same order as the approximations. Moreover, we also show that if the transition functions do not satisfy the proposed conditions, their derivatives modify the energy-matter content of the spacetime by introducing a non-negligible stress-energy tensor. Finally, we extend these theorems to solutions projected onto spatial hypersurfaces, so that they can be directly applied to initial data construction schemes. These theorems then allow for the systematic construction of pure joined solutions and they can be straightforwardly extended to mixed joined solutions.

An example of the proposed theorems and allowed transition functions is then provided by studying a binary system of non-spinning black holes, where the approximate solutions are taken to be given by a post-Newtonian expansion and a linearly perturbed Schwarzschild solution. We shall not perform a systematic study of transition functions here, but instead we pick functions that are variations of those chosen in [105, 93] in order to illustrate how the gluing procedure works and how it breaks down. We explicitly show that if the transition functions satisfy the proposed conditions, the 4-Ricci scalar calculated with the pure joined solution vanishes to the same order as the uncontrolled remainders in the approximations. In particular, we explicitly show that derivatives of the pure joined approximate solution built with appropriate transition functions are equal to derivatives of both original approximate solutions up to the uncontrolled remainders in the approximations. We also numerically show that if the transition functions violate the proposed conditions, their derivatives modify the matter content of the spacetime by introducing a shell of matter. In this manner, we explicitly verify, both analytically and numerically, that a pure joined solution does represent the same spacetime as that of the original approximate solutions in their respective regions of validity up to the accuracy of the approximations used.

This paper is divided as follows: in Sec. 4.2 we review the standard junction conditions at a hypersurface, so that we can extend them to the case where the solutions used are approximate instead of exact, provided the existence of a buffer zone; in Sec. 4.3 we study how to join approximate solutions with transition function and derive conditions

such that a pure joined solution satisfies the Einstein equations to the same order as the approximations used; in this section, we also study projections of these pure joined solutions to a Cauchy hypersurface in order to develop conditions for transition functions that can be used in initial data construction schemes; in Sec. 4.4 we study an example of the theorems formulated by considering a binary system of non-spinning black hole, constructing approximate global metrics with different transition function, and explicitly calculating the 4-Ricci scalar; in Sec. 4.5 we conclude and point to future research.

The notation of this paper is as follows: Greek indices range over all spacetime indices, while Latin indices range only over spatial indices; the symbol  $\mathcal{O}(A)$  stands for terms of order  $A$  at most, while the symbol  $\mathcal{O}(A, B)$  stands for remainders of order  $A$  or  $B$  at most, where  $A$  and  $B$  are dimensionless; a tilde superscript  $\tilde{A}$  stands for the asymptotic expansion of  $A$  as defined in [30, 31]; the relation  $A = B + \mathcal{O}(C)$  means that  $A$  is asymptotic to  $B$  with uncontrolled remainders of order  $C$  (the so-called Landau or asymptotic notation); we use units where  $c = G = 1$ . Symbolic calculations are performed with either Mathematica or Maple.

## 4.2 Junction Conditions at a Hypersurface

In this section, we review a variation of the standard junction conditions of general relativity. These conditions have been discussed extensively in the literature (see [128, 129, 130, 131, 132, 133, 134, 118, 135] and references therein.) Here, we review only those concepts important to the understanding of this paper, following in particular [135]. Certain departures from the notation of [135] are so that the generalization to the case of approximate solutions in the next section becomes easier.

Let us first set up the problem. Consider a spatial (or timelike) hypersurface  $\mathcal{J}$  that divides spacetime into two regions:  $\mathcal{C}_1$  and  $\mathcal{C}_2$ . Each of these regions possesses an associated metric and coordinates,  $\{g_{\mu\nu}^{(1)}, x_{(1)}^\alpha\}$  and  $\{g_{\mu\nu}^{(2)}, x_{(2)}^\alpha\}$ , such that these metrics solve the Einstein equations exactly in their respective regions. In the literature, this exact solutions and coordinate systems are also sometimes referred to as  $\{g_{\mu\mu}^\pm, x_\pm^\alpha\}$ . Let us further assume that an overlapping coordinate system  $x^\alpha$  exists in a neighbourhood of  $\mathcal{J}$ . The problem is to formulate junction conditions on  $\mathcal{J}$  that guarantee that the joined 4-metric satisfies the Einstein equations.

Let us make these statements more precise by considering a congruence of geodesics piercing  $\mathcal{J}$  defined with respect to first metric in  $\mathcal{C}_1$  and the second metric in  $\mathcal{C}_2$  (see [135] for a detailed definition of such congruence.) Let then  $\ell$  denote the proper time (or proper distance) along the geodesics, such that  $\ell = 0$  corresponds to when the geodesics reach  $\mathcal{J}$ . The joined solution then takes the following form [135]:

$$g_{\mu\nu} = \Theta(\ell)g_{\mu\nu}^{(1)} + \Theta(-\ell)g_{\mu\nu}^{(2)}, \quad (4.1)$$

where  $\Theta(\cdot)$  is the Heaviside function. Equation (4.1) implicitly uses coordinates  $x^\alpha$  that overlap both the coordinates local to  $\mathcal{C}_1$  and  $\mathcal{C}_2$  in a neighbourhood of  $\mathcal{J}$ .

We now proceed to formulate the junction conditions. The first junction condition arises by requiring that the 4-metric be continuous across  $\mathcal{J}$ , in a coordinate system  $x^\alpha$

that overlaps both  $x_1^\alpha$  and  $x_2^\alpha$  in an open region that contains this hypersurface. This condition can be expressed in a coordinate-independent way by projecting it to  $\mathcal{J}$ . Then, in terms of 3-tensors this condition becomes

$$h_{ab}^{(1)} \Big|_{\mathcal{J}} = h_{ab}^{(2)} \Big|_{\mathcal{J}}, \quad (4.2)$$

where here  $h_{ab}$  is the 3-metric associated with the junction hypersurface, *i.e.*

$$h_{\mu\nu} = g_{\mu\nu} + e_{\pm} n_{\mu} n_{\nu}, \quad (4.3)$$

with  $n_a$  normal to  $\mathcal{J}$  and  $e_{\pm} = \pm 1$  depending on whether  $\mathcal{J}$  is spatial (−) or timelike (+). Equation 4.2 guarantees that the hypersurface  $\mathcal{J}$  has a well-defined geometry. These equations also imply that the metric is differentiable across  $\mathcal{J}$ , except for its normal derivative to  $\mathcal{J}$  that in general is discontinuous.

The second junction condition arises by requiring that this normal derivative does not lead to violations of the Einstein equations across  $\mathcal{J}$ . In terms of 3-tensors on  $\mathcal{J}$ , this condition becomes

$$K_{ab}^{(1)} \Big|_{\mathcal{J}} = K_{ab}^{(2)} \Big|_{\mathcal{J}}. \quad (4.4)$$

One can show that the failure of these equations to be satisfied changes the distribution of energy-momentum tensor of the spacetime and gives raise to a shell of matter with stress-energy tensor [135]

$$S_{ab} = -\frac{\epsilon}{8\pi} \left[ K_{ab}^{(1)} \Big|_{\mathcal{J}} - K_{ab}^{(2)} \Big|_{\mathcal{J}} - h_{ab} \left( K^{(1)} \Big|_{\mathcal{J}} - K^{(2)} \Big|_{\mathcal{J}} \right) \right]. \quad (4.5)$$

In the next section, we shall be mostly interested in vacuum spacetimes, for which such a stress-energy tensor should vanish.

The satisfaction of the Einstein equations out of  $\mathcal{J}$  by Eq. 4.1 and the absence of a stress-energy tensor as in Eq. 4.5 then guarantees that the junction conditions [Eq. 4.2 and Eq. 4.4] are also satisfied. Exact solutions, however, are rarely available for astrophysically realistic scenarios. In that case, one must rely on approximate solutions, for which similar conditions to those discussed here can be found, as we shall study in the next section.

### 4.3 Pure joined solutions

In this section we build a pure joined solution by extending the standard junction conditions to the case where the metrics  $g_{\mu\nu}^{(1,2)}$  are only approximate solutions to the Einstein equations. For simplicity, we assume a vacuum spacetime and that there exists analytic approximate expressions for  $g_{\mu\nu}^{(1,2)}$ , such that pure joined solutions are sought. The conclusions of this section, however, can straightforwardly be extended to other cases, where numerical solutions are available instead of analytical ones, provided information about first and second derivatives of the numerical solutions is also available (note that for numerical solutions the continuum derivative operator must be replaced by its

finite counterpart.) As shown in [105, 93], the first step in joining approximate solutions is to apply asymptotic matching inside some overlap region. Once this has been done, one can search for conditions such that the pure joined metric tensor satisfies the Einstein equations to the same order as  $g_{\mu\nu}^{(1,2)}$ . We here first present the basics of asymptotic matching as applicable to this problem [3, 105]. We then search for asymptotic junction conditions (or buffer zone conditions), which are asymptotic in the sense of [30, 31] and, thus, are to be understood only approximately to within some uncontrolled remainder.

### 4.3.1 Asymptotically matched metrics

Consider then a manifold  $\mathcal{M}$  that can be divided into two submanifolds with boundary  $C_1$  and  $C_2$ , each equipped with a approximate metrics  $g_{\mu\nu}^{(1)}$  and  $g_{\bar{\mu}\bar{\nu}}^{(2)}$  and a coordinate system  $x^\alpha$  and  $x^{\bar{\alpha}}$  respectively. These metrics are approximate in the sense that they solve the Einstein equations to  $\mathcal{O}(\epsilon_n^{\ell_n})$  for some  $l \in \mathbb{N}$  in their respective submanifolds, *e.g.* in vacuum

$$G_{\mu\nu}[g_{\mu\nu}^{(n)}] = \mathcal{O}(\epsilon_n^{\ell_n+1}), \quad (4.6)$$

where  $n = \{1, 2\}$ ,  $(\ell_1, \ell_2)$  are real numbers greater than zero, and  $\epsilon_n \ll 1$  is some dimensionless combination of parameters and coordinates relative to the  $n$ -th submanifold. The symbol  $\mathcal{O}(\epsilon_n^{\ell_n+1})$  refers to terms of *relative* order  $\epsilon_n^{\ell_n+1}$  with respect to the leading order term in the approximate solution  $g_{\mu\nu}^{(n)}$ . In principle, there could be logarithms of  $\epsilon_n$  present in the remainders, such as in high-order post-Newtonian expansions, but we neglect such terms here because they shall not affect the analysis of this paper. Notice that we use here bars to denote the different coordinate systems (as opposed to numbers, as in the previous section) because we must be more careful about the coordinates used in these approximate metric components. For concreteness, let the region of validity of  $g_{\mu\nu}^{(1)}(x^\alpha)$  be defined by  $x^\alpha \gg x_{in}^\alpha$  and that of  $g_{\bar{\mu}\bar{\nu}}^{(2)}(x^{\bar{\alpha}})$  by  $x^{\bar{\alpha}} \ll x_{out}^{\bar{\alpha}}$ . These inequalities define a *spacetime* region of validity, since the approximate metric might not be valid for all times. For example, such is the case for the post-Newtonian metric of two point particles in quasi-circular orbit, which is valid only for times  $t \ll t_c$ , where  $t_c$  is the time of coalescence.

Let us further assume that these submanifolds overlap in some 4-volume, defined by the intersection  $\mathcal{B} = C_1 \cap C_2$ , and sometimes referred to as the overlap region or buffer zone. The boundary of the buffer zone,  $\partial\mathcal{B}$ , cannot be determined exactly, because it is inherently tied to the regions of validity of the approximate solutions, which themselves are only defined approximately. With this in mind, let us further assume that the charts  $\{x^\alpha\}$  and  $\{x^{\bar{\alpha}}\}$  are defined in the neighbourhood of any field point in the buffer zone and that they satisfy  $x^{\bar{\alpha}} = x^\alpha + \mathcal{O}(\epsilon_1^{\ell_1+1}, \epsilon_2^{\ell_2+1})$ . The buffer zone can then be asymptotically defined by the following condition:  $(x_{in}^\alpha x_{\alpha}^{in})^{1/2} \ll (x^\alpha x_\alpha)^{1/2} \ll (x_{out}^\alpha x_{\alpha}^{out})^{1/2}$ , where indices are raised or lowered with the local metric to  $\mathcal{C}_{1,2}$ . Wherever possible, we use the Landau notation, which specifically specifies the behavior of the remainder. The definition of the boundary of the buffer zone should be understood only in an asymptotic

sense, as defined in [30, 31]. This boundary is made up of two disconnected pieces,  $\partial\mathcal{B}_-$  and  $\partial\mathcal{B}_+$ , defined via  $x^\alpha = x_{in}^\alpha + \mathcal{O}(\epsilon_1^{\ell_1+1}, \epsilon_2^{\ell_2+1})$  and  $x^\alpha = x_{out}^\alpha + \mathcal{O}(\epsilon_1^{\ell_1+1}, \epsilon_2^{\ell_2+1})$  respectively. The definition of the buffer zone can be thought of in terms of a simplistic spherically symmetric static example, where  $x^\alpha \rightarrow r$ ,  $\partial\mathcal{B}$  is a spherical shell and  $\partial\mathcal{B}_\pm$  are 2-spheres. However, in practical examples, such as binary black hole spacetimes, the boundary of the buffer zone is not simply a spherical shell, but instead it acquires some deformation in accordance with the deformation of the spacetime that is being modeled.

Before proceeding with the description of asymptotic matching, let us make some comments on the approach adopted in this paper. In the previous paragraphs and in what shall follow, we have not adopted a rigorous geometrical approach in the description of asymptotic matching, the definition of the buffer zone and the submanifolds. A rigorous geometrical approach, for example, would impose other constraints on  $\mathcal{B}$ , such that it is properly embedded in  $\mathcal{C}_1$  and  $\mathcal{C}_2$ . Furthermore, such an approach would describe the conditions under which asymptotic matching can be performed, since in general this method is valid only locally. Instead of such an approach, in this paper we adopt an *analytical* one, where we only provide a minimal amount of details in order to make the presentation simpler. For example, we shall restrict our attention to coordinate grids that coincide when both  $\epsilon_1 \rightarrow 0$  and  $\epsilon_2 \rightarrow 0$  and, henceforth, we shall call  $\mathcal{C}_{1,2}$  regions instead of submanifolds. Such an approach is adopted because the aim of this paper is not to provide a detailed geometrical account of asymptotic matching, but instead to study transition functions and approximate joined solutions (see [136] and references therein for a more detailed and rigorous geometric account of asymptotic matching.)

The approximate metrics live in different regions and depend on different coordinates  $(x^\alpha, x^{\bar{\alpha}})$  and local parameters  $(\theta^\alpha, \theta^{\bar{\alpha}})$ . Examples of these parameters are the mass of the system and its velocity. However, since both  $g_{\mu\nu}^{(n)}$  are valid in  $\mathcal{B}$ , both coordinate systems must be valid in the buffer zone (*i.e.*, the charts of  $\mathcal{C}_n$  overlap in  $\mathcal{B}$ .) Using the uniqueness theorems of asymptotic expansions [30, 31], one can find a coordinate and parameter transformation to relate adjacent regions inside  $\mathcal{B}$ . In order to achieve this, one must first compute the asymptotic expansions of the approximate line elements,  $\tilde{d}s_{(n)}^2$ , near the boundaries of the buffer zone,  $\partial\mathcal{B}$ , and then compare them inside  $\mathcal{B}$  but yet away from  $\partial\mathcal{B}$ , *i.e.*

$$\tilde{d}s_{(1)}^2 - \tilde{d}s_{(2)}^2 = \mathcal{O}(\epsilon_1^{\ell_1+1}, \epsilon_2^{\ell_2+1}), \quad \text{in } \mathcal{B} \setminus \partial\mathcal{B}, \quad (4.7)$$

where the  $\setminus$  symbol is the standard exclusion symbol of set theory and where  $\mathcal{O}(\epsilon_1^{\ell_1+1}, \epsilon_2^{\ell_2+1})$  stands for uncontrolled remainders of order  $\epsilon_1^{\ell_1+1}$  or  $\epsilon_2^{\ell_2+1}$  as defined at the end of Sec. 1. Using Eq. 4.7, a coordinate transformation  $\psi : x^{\bar{\alpha}} \rightarrow x^\alpha$  and a parameter transformation  $\phi : \theta^{\bar{\alpha}} \rightarrow \theta^\alpha$  can be found inside  $\mathcal{B}$ . We have written (4.7) in terms of the line element, but we could have easily written it in terms of the metric components. In fact, depending on the calculation, it might be necessary to asymptotically match different components of the metric to different order. For example, for the construction of initial data, the  $g_{00}$  and  $g_{ij}$  components of the metric need to be matched to lower order than the  $g_{0i}$  components [105, 93]. In what follows, we will assume that all metric components

have been asymptotically matched to the same order. When this is not the case, the conditions that we shall propose on transition functions can be adapted by noting that one must use the highest order to which metric components have been asymptotically matched.

These transformations guarantee that all components of adjacent 4-metrics are asymptotic to each other inside the buffer zone [30, 31]. This fact implies that the derivatives of adjacent metrics are also asymptotic to each other

$$\frac{\partial^m}{\partial x^{\alpha_1} \dots \partial x^{\alpha_m}} g_{\mu\nu}^{(1)} - \frac{\partial^m}{\partial x^{\alpha_1} \dots \partial x^{\alpha_m}} g_{\mu\nu}^{(2)} = \mathcal{O}(\epsilon_1^{\ell_1+1-m}, \epsilon_2^{\ell_2+1-m}), \quad (4.8)$$

for all  $m < l$ . However, the relative order to which the derivatives of adjacent metrics are asymptotic to each other is in general not the same as the relative order to which the adjacent metrics themselves are asymptotic to each other. This reduction in *matching accuracy* is due to the implicit assumption that asymptotic matching is carried out to some finite order. In (4.8), we have assumed that this decrease in accuracy occurs in single powers of  $\epsilon_{1,2}$ , but if this is not the case the results of this paper can be rescaled appropriately.

Let us provide a general example of such matching accuracy reduction, without specifying a particular spacetime (for a more detailed example see [105, 93].) Consider a post-Newtonian expression that is known to  $\mathcal{O}(1/c^4)$  and that is asymptotically matched to a perturbed black hole solution in some buffer zone to  $\mathcal{O}(1/c^4, \epsilon^2)$ , where  $c$  is here the speed of light and  $\epsilon$  is the black hole perturbation theory expansion parameter. Let us now take the time derivative of the post-Newtonian expression, which results in a term of  $\mathcal{O}(1/c^5)$ . In post-Newtonian theory, one would never truncate the differentiated term at  $\mathcal{O}(1/c^4)$ . However, in the theory of asymptotic matching to a finite order, the time derivative of the post-Newtonian quantity remains matched only to  $\mathcal{O}(1/c^4, \epsilon^2)$ , and thus it will disagree with the perturbed black hole quantity at  $\mathcal{O}(1/c^5)$ . It is in this sense that differentiation usually decreases the relative order to which two expressions have been asymptotically matched (we should note that when asymptotic matching is carried out to all orders, then this reduction in matching accuracy disappears [136].)

Let us provide a more explicit example that, although similar in spirit to the one described above, does not require general relativity. Consider two functions

$$f(t) = \left[ f_0^2 + 2f_1^2 \epsilon_1 x(\omega t) \right]^{1/2}, \quad g(t) = \frac{9}{9 + \epsilon_2 y(\Omega t)}, \quad (4.9)$$

where  $f_{0,1}$  are constants and  $x(\omega t)$  and  $y(\Omega t)$  are periodic functions of time with period  $1/\omega$  and  $1/\Omega$  respectively. Let us pretend that  $f(t)$  and  $g(t)$  are approximate solutions to the same differential equation in the limits  $\epsilon_1 \ll 1$  and  $\epsilon_2 \ll 1$  respectively. If we asymptotically match these functions in a buffer zone where both  $\epsilon_1 \ll 1$  and  $\epsilon_2 \ll 1$  up to uncontrolled remainders of  $\mathcal{O}(\epsilon_1^2, \epsilon_2^2)$ , we discover that at  $t = 0$  the constants are  $f_0 = 1$  and  $f_1 = y(0)/[9x(0)]$ . If we now study their time derivatives, we find that at  $t = 0$

$$\frac{\partial f}{\partial t} = \epsilon_1 \frac{y(0)}{9x(0)} \omega \left( \frac{\partial x}{\partial t} \right)_{t=0}, \quad \frac{\partial g}{\partial t} = \frac{\epsilon_2}{9} \Omega \left( \frac{\partial y}{\partial t} \right)_{t=0}, \quad (4.10)$$

with uncontrolled remainders of  $\mathcal{O}(\epsilon_1^2, \epsilon_2^2)$ . Note that the derivatives are not equal to each other to this order because the velocities  $\omega$  and  $\Omega$  have not yet been determined via asymptotic matching. The reduction in matching accuracy is here explicit since, while  $f(t)$  and  $g(t)$  have been asymptotically matched up to uncontrolled remainders of  $\mathcal{O}(\epsilon_1^2, \epsilon_2^2)$ , their time derivatives match only up to uncontrolled remainders of  $\mathcal{O}(\epsilon_1, \epsilon_2)$ .

Henceforth, we assume that asymptotic matching has been carried out and that one of the metrics has been transformed according to  $\{\psi, \phi\}$  such that Eq. 4.7 holds. We refer the reader to [30, 31] for more details on the theory of asymptotic analysis and [3, 105, 98, 97, 100, 99, 94] for a more detailed discussion on asymptotic expansions in general relativity.

### 4.3.2 Asymptotic Junction Conditions

Let us now return to the buffer zone and note that it can be foliated by a family of junction hypersurfaces  $\mathcal{J}_i$ , where  $i$  labels the member of the family. For simplicity, we choose these hypersurfaces to be timelike, since in the next section we project the 4-metric to a Cauchy (spatial) hypersurface  $\Sigma$  and it is convenient then that  $\mathcal{J}_i$  be orthogonal to  $\Sigma$ . Asymptotic matching has provided a coordinate transformation to relate the charts inside  $\mathcal{B}$ , so, in particular, these matched coordinates are valid in an open region containing every  $\mathcal{J}_i$  as long as this is not close to  $\partial\mathcal{B}$ . We look for asymptotic junction conditions in this subregion of  $\mathcal{B}$  (*i.e.* away from  $\partial\mathcal{B}$ ), in terms of differentiability conditions of  $g_{\mu\nu}^{(n)}$ .

Furthermore, let us also consider a family of geodesic congruences  $\gamma_i$  that pierce  $\mathcal{J}_i$ . The  $i$ th member of the family is parameterized by proper distance  $\ell_i$  to the  $i$ th hypersurface  $\mathcal{J}_i$ , such that  $\ell_i = 0$  occurs when that member reaches that hypersurface. Such a family of geodesic congruences is defined with respect to the approximate metrics  $g_{\mu\nu}^{(n)}$  since these metrics are equal to each other up to uncontrolled remainders in the asymptotic matching scheme. Even though these geodesics are not strictly necessary for the construction of asymptotic junction conditions, we find them useful to define a measure of distance to  $\mathcal{J}_i$ , which shall later become important in the definition of transition functions.

We can now begin to look for asymptotic junction conditions by considering the following 4-metric tensor:

$$g_{\mu\nu} = F(\ell_i) g_{\mu\nu}^{(1)} + [1 - F(\ell_i)] g_{\mu\nu}^{(2)}, \quad (4.11)$$

where  $F(\cdot)$  is a (proper) transition function that smoothly ranges from zero to unity inside  $\mathcal{B}$  and which will be defined more rigorously later. Equation 4.11 is motivated by the fact that any tensor  $E^{a_1 a_2 \dots a_i}_{b_1 b_2 \dots b_j}$  can always be split into

$$E^{a_1 a_2 \dots a_i}_{b_1 b_2 \dots b_j} = G^{a_1 a_2 \dots a_i}_{b_1 b_2 \dots b_j} F(\ell_i) + [1 - F(\ell_i)] H^{a_1 a_2 \dots a_i}_{b_1 b_2 \dots b_j}, \quad (4.12)$$

provided that

$$E^{a_1 a_2 \dots a_i}_{b_1 b_2 \dots b_j} = G^{a_1 a_2 \dots a_i}_{b_1 b_2 \dots b_j} = H^{a_1 a_2 \dots a_i}_{b_1 b_2 \dots b_j} \quad (4.13)$$

inside the transition region and that the proper transition function is sufficiently regular. The regularity requirement is to guarantee that both terms of Eq. 4.12 are differentiable. In Eq. 4.11 this split is valid because  $g_{\mu\nu}^{(1)}$  is asymptotic to  $g_{\mu\nu}^{(2)}$  in  $\mathcal{B}$  up to uncontrolled remainders once the maps  $\{\psi, \phi\}$  have been applied. As we will see below, however, care must be taken when constructing such proper transition functions  $F(\cdot)$  to avoid ruining the differentiability properties of the joined metric.

Let us now define proper transition functions in order to clarify how to merge the metrics via Eq. 4.11. A proper transition function is a smooth real map  $\mathcal{F} : \mathfrak{R} \rightarrow [0, 1]$  that ranges from zero to unity inside some transition window  $w$ , while it acquires the value of  $1/2$  as  $\ell_i \rightarrow 0$ , and that satisfies the following conditions:

$$\begin{aligned} F(\ell_i) &\rightarrow 1 & \text{as } \ell_i &\rightarrow \ell_+, \\ F(\ell_i) &\rightarrow 0 & \text{as } \ell_i &\rightarrow \ell_-, \end{aligned} \quad (4.14)$$

where here  $\ell_{\pm}$  is the proper distance to  $\partial\mathcal{B}_{\pm}$ . Note that the point  $\ell_i = 0$  is where the global approximate metric of Eq. 4.11 contains equal contributions from  $g_{\mu\nu}^{(1)}$  and  $g_{\mu\nu}^{(2)}$ . The transition window will be studied later in Sec. 4, but we can think of it qualitatively as a parameter of a proper transition function that determines the region where these functions are significantly different from unity or zero. The requirement that a proper transition function vanishes or tends to unity at  $\partial\mathcal{B}_{\pm}$  is necessary to avoid contamination of  $g_{\mu\nu}^{(1)}$  in  $\mathcal{C}_2$  and vice versa, since in general  $g_{\mu\nu}^{(n)}$  has large uncontrolled remainders and could diverge outside its region of validity. In fact, the speed at which a proper transition function must tend to unity or zero will depend on the speed of the growth of the uncontrolled remainders of the approximations outside their region of validity, as we shall study later. This definition does not constrain how the transition function behaves inside the transition region. Also note that this family of functions tends to the Heaviside function of the previous section as  $w \rightarrow 0$  and that it does not need to be analytic. We shall not constrain this family further for now, but instead we search for conditions on this family such that Eq. 4.11 satisfies the Einstein equations to the same order as  $g_{\mu\nu}^{(n)}$ .

With these proper transition functions, we immediately see that the joined metric itself also satisfies the following set of asymptotic conditions:

$$\begin{aligned} g_{\mu\nu} &= g_{\mu\nu}^{(1)} + \mathcal{O}(\epsilon_1^{\ell_1+1}, \epsilon_2^{\ell_2+1}), & \text{in } \mathcal{C}_1 \setminus \mathcal{B}, \\ g_{\mu\nu} &= g_{\mu\nu}^{(2)} + \mathcal{O}(\epsilon_1^{\ell_1+1}, \epsilon_2^{\ell_2+1}), & \text{in } \mathcal{C}_2 \setminus \mathcal{B}, \end{aligned} \quad (4.15)$$

while in the buffer zone the metric is some weighted linear superposition of both approximate solutions. Thanks to asymptotic matching, the approximate metrics are identical

inside the buffer zone up to uncontrolled remainders [see Eq. 4.8] and, thus, this linear superposition is valid there, in spite of the non-linearity of the Einstein field equations. Also note that we are free to choose any junction hypersurface  $\mathcal{J}_i$  to join the metrics as long as it is inside  $\mathcal{B}$  but away from  $\partial\mathcal{B}$ . However, there is usually a typical choice of  $\mathcal{J}_i$ , given by the surface where the error bars of the approximate metrics become comparable. Such a choice is not unique, but has previously proved to be close to optimal in certain scenarios [105, 93]. Asymptotic matching then seems to be a good technique for the construction of a pure joined 4-metric as given in Eq. 4.11, as long as we find transition functions that are sufficiently well-behaved so that their derivatives do not introduce errors larger than those contained in the approximations.

We now proceed to determine the asymptotic junction conditions by analogy with the standard junction conditions discussed in the previous section. The first junction condition of the previous section is automatically satisfied asymptotically in  $\mathcal{B}$  via Eq. 4.7 with uncontrolled remainders of  $\mathcal{O}(\epsilon_1^{\ell_1+1}, \epsilon_2^{\ell_2+1})$ . However, the second junction condition is not necessarily satisfied because Eq. 4.7 does not guarantee differentiability across  $\mathcal{J}_i$  to the same order as continuity. Differentiating Eq. 4.11 we obtain

$$g_{\mu\nu,\alpha} = F(\ell_i) g_{\mu\nu,\alpha}^{(1)} + [1 - F(\ell_i)] g_{\mu\nu,\alpha}^{(2)} + F_{,\alpha} \{g_{\mu\nu}\}, \quad (4.16)$$

where we have defined the operation  $\{E\} \equiv E^{(1)} - E^{(2)}$  for any function  $E$ . In order for Eq. 4.11 to be a solution to the Einstein equations, we should require that the third term be as small as the uncontrolled remainders of the first two terms. By Eq. 4.8, we know that the last piece of the third term is of  $\mathcal{O}(\epsilon_1^{\ell_1+1}, \epsilon_2^{\ell_2+1})$ . On the other hand, the first two terms are bounded below by their smallest size, which is of  $\mathcal{O}(\epsilon_1^{\ell_1}, \epsilon_2^{\ell_2})$ . We, thus, arrive at the condition

$$F_{,\alpha} = \mathcal{O}(\epsilon_1^0, \epsilon_2^0), \quad \text{in } \mathcal{B}. \quad (4.17)$$

One can show that this condition is sufficient, since it excludes cases where  $F_{,\alpha} = \mathcal{O}(\ln(\epsilon_1, \epsilon_2))$ . With this condition, Eq. 4.16 becomes

$$g_{\mu\nu,\alpha} = F(\ell_i) g_{\mu\nu,\alpha}^{(1)} + [1 - F(\ell_i)] g_{\mu\nu,\alpha}^{(2)} + \mathcal{O}(\epsilon_1^{\ell_1+1}, \epsilon_2^{\ell_2+1}). \quad (4.18)$$

In vacuum, another condition must be imposed on the 4-metric in order for the Einstein equations to be asymptotically satisfied inside  $\mathcal{B}$ . This condition can be enforced by requiring that the 4-metric tensor be asymptotically  $C^2$  in  $\mathcal{B}$ . Differentiating Eq. 4.16 we obtain

$$g_{\mu\nu,\alpha\beta} = F(\ell_i) g_{\mu\nu,\alpha\beta}^{(1)} + [1 - F(\ell_i)] g_{\mu\nu,\alpha\beta}^{(2)} + 2F_{,(\alpha} \{g_{\mu\nu,|\beta)}\} + F_{,\alpha\beta} \{g_{\mu\nu}\}. \quad (4.19)$$

Here the parenthesis on the indices represent the standard symmetry operation  $g_{(a|b,|c)} = 1/2 (g_{ab,c} + g_{cb,a})$ . In order for the metric to be asymptotically  $C^2$  in  $\mathcal{B}$ , we must require that the last two terms be much smaller than the first two. This requirement can be

enforced by requiring that

$$\begin{aligned} F_{,\alpha} &= \mathcal{O}(\epsilon_1, \epsilon_2), \quad \text{in } \mathcal{B}, \\ F_{,\alpha\beta} &= \mathcal{O}(\epsilon_1^0, \epsilon_2^0), \quad \text{in } \mathcal{B}. \end{aligned} \quad (4.20)$$

The first condition in Eq. 4.20 is a refinement of Eq. 4.17, while the second condition is new. These equations are also compatible with  $F_{,\alpha} \ll F_{,\alpha\beta}$ , which is a consequence of the fact that  $\{g_{\mu\nu,\alpha}\} = \mathcal{O}(\epsilon_1^{\ell_1}, \epsilon_2^{\ell_2})$ . As one can show, the decrease in matching accuracy of the derivatives of matched expressions has led to different conditions for the first and second derivatives of the transition functions. In this way, the last two terms of Eq. 4.19 become of  $\mathcal{O}(\epsilon_1^{\ell_1+1}, \epsilon_2^{\ell_2+1})$  or smaller, because by Eq. 4.8,  $\{g_{\mu\nu}\} = \mathcal{O}(\epsilon_1^{\ell_1+1}, \epsilon_2^{\ell_2+1})$  and  $\{g_{\mu\nu,\alpha}\} = \mathcal{O}(\epsilon_1^{\ell_1}, \epsilon_2^{\ell_2})$ . With these conditions, Eq. 4.19 becomes

$$g_{\mu\nu,\alpha\beta} = F(\ell_i) g_{\mu\nu,\alpha\beta}^{(1)} + [1 - F(\ell_i)] g_{\mu\nu,\alpha\beta}^{(2)} + \mathcal{O}(\epsilon_1^{\ell_1+1}, \epsilon_2^{\ell_2+1}). \quad (4.21)$$

Transition functions that satisfy Eq. 4.20 are enough to guarantee a  $C^2$  global metric in  $\mathcal{B}$ , irrespective of the matching order or the junction hypersurface chosen. Requiring the joined solution to be  $C^2$  in  $\mathcal{B}$  guarantees that the Einstein tensor is also continuous across any  $\mathcal{J}_i$ . Since we are dealing with a vacuum spacetime, the junction hypersurfaces do not represent any physical boundary, such as a shell of matter, and can thus be chosen arbitrarily as long as they are inside  $\mathcal{B}$  and away from  $\partial\mathcal{B}$ , so that the approximations are still valid.

We have then derived conditions on the 4-metric and, thus, on the transition functions, that guarantee that the Einstein tensor is continuous in  $\mathcal{B}$ . The standard junction conditions in the presence of matter do not necessarily require the metric to be  $C^1$  across  $\mathcal{J}$ , whereas here we must require it to be at least asymptotically  $C^2$  in  $\mathcal{B}$ , so that no artificial features are introduced at the boundary. We can now formulate the following theorem:

**THEOREM 4.1 (BUFFER ZONE JUNCTION CONDITION).** *Consider a spacetime manifold  $\mathcal{M}$  that can be divided into two submanifolds with boundary  $C_1$  and  $C_2$ , inside which  $g_{\mu\nu}^{(1,2)}$  are approximate solutions to the vacuum Einstein equations up to uncontrolled remainders of  $\mathcal{O}(\epsilon_1^{\ell_1+1}, \epsilon_2^{\ell_2+1})$ . Let the boundaries of the submanifolds be defined asymptotically by the approximate boundary of the region of validity of  $g_{\mu\nu}^{(1,2)}$  and let the intersection of these submanifolds,  $\mathcal{B} = C_1 \cap C_2$ , be called the buffer zone. Let us foliate the buffer zone with a family of timelike hypersurfaces  $\mathcal{J}_i$  and consider a family of geodesic congruences  $\gamma_i$ , such that the  $i$ th member is parametrized by proper distance  $\ell_i$  to the  $i$ th hypersurface  $\mathcal{J}_i$ . Consider the family of joined 4-metric tensor parameterized by  $\ell_i$ , namely*

$$g_{\mu\nu} = F(\ell_i) g_{\mu\nu}^{(1)} + [1 - F(\ell_i)] g_{\mu\nu}^{(2)}, \quad (4.22)$$

where  $F(\cdot)$  is a proper transition function as defined by Eq. 4.14. Then, equation (4.22) is also an  $\ell_i$ -independent approximate solution to the Einstein equations up to uncontrolled remainders of  $\mathcal{O}(\epsilon_1^{\ell_1+1}, \epsilon_2^{\ell_2+1})$  if and only if the following conditions hold:

- (i) The metrics  $g_{\mu\nu}^{(1,2)}$  have been asymptotically matched in  $\mathcal{B}$  up to uncontrolled remainders of  $\mathcal{O}(\epsilon_1^{\ell_1+1}, \epsilon_2^{\ell_2+1})$ ,
- (ii)  $F_{,\alpha} = \mathcal{O}(\epsilon_1, \epsilon_2)$ , in  $\mathcal{B}$ ,
- (iii)  $F_{,\alpha\beta} = \mathcal{O}(\epsilon_1^0, \epsilon_2^0)$ , in  $\mathcal{B}$ .

The proof follows directly from the calculation of the Ricci tensor, which should vanish in vacuum. Let us then use the joined metric to calculate the Christoffel connection. Doing so we obtain

$$\Gamma_{\beta\gamma}^{\alpha} = \Gamma_{\beta\gamma}^{\alpha(1)} F(\ell_i) + \Gamma_{\beta\gamma}^{\alpha(2)} [1 - F(\ell_i)] + \frac{1}{2} g^{\alpha\delta} \left( F_{,\gamma} \{g_{\beta\delta}\} + F_{,\beta} \{g_{\gamma\delta}\} - F_{,\delta} \{g_{\beta\gamma}\} \right), \quad (4.23)$$

where the  $\{\cdot\}$  operator was defined in Eq. 4.16. We have here used the fact that the inverse metric can be written as  $g^{\alpha\beta} = F g_{(1)}^{\alpha\beta} + (1 - F) g_{(2)}^{\alpha\beta}$ , neglecting terms that are proportional to  $F(1 - F)$  because they are of  $\mathcal{O}(\epsilon_1^{2\ell_1}, \epsilon_2^{2\ell_2})$ . Outside the buffer zone the terms in parenthesis clearly vanish, but inside this region they could be large. However, note that by condition (i),  $\{g_{\mu\nu}\} = \mathcal{O}(\epsilon_1^{\ell_1+1}, \epsilon_2^{\ell_2+1})$ , while by condition (ii) the derivative of the transition function satisfies  $F_{,\alpha} = \mathcal{O}(\epsilon_1, \epsilon_2)$ . Thus, the term in parenthesis satisfies

$$\left( F_{,\gamma} \{g_{\beta\delta}\} + F_{,\beta} \{g_{\gamma\delta}\} - F_{,\delta} \{g_{\beta\gamma}\} \right) \ll \mathcal{O}(\epsilon_1^{\ell_1+1}, \epsilon_2^{\ell_2+1}). \quad (4.24)$$

Due to the precision of the Christoffel symbols, namely that  $\Gamma_{\beta\gamma}^{\alpha(1)} = \Gamma_{\beta\gamma}^{\alpha(2)}$  in  $\mathcal{B}$  up to uncontrolled remainders of  $\mathcal{O}(\epsilon_1^{\ell_1+1}, \epsilon_2^{\ell_2+1})$ , combined with conditions (i) and (ii), we are allowed to write the connection as

$$\Gamma_{\beta\gamma}^{\alpha} = \Gamma_{\beta\gamma}^{\alpha(1)} F(\ell_i) + \Gamma_{\beta\gamma}^{\alpha(2)} [1 - F(\ell_i)] + \mathcal{O}(\epsilon_1^{\ell_1+1}, \epsilon_2^{\ell_2+1}). \quad (4.25)$$

However, in order to compute the 4-Riemann tensor, we need the derivative of the connection. This quantity is given by

$$\begin{aligned} \Gamma_{\beta\gamma,\sigma}^{\alpha} &= \Gamma_{\beta\gamma,\sigma}^{\alpha(1)} F(\ell_i) + \Gamma_{\beta\gamma,\sigma}^{\alpha(2)} [1 - F(\ell_i)] + F_{,\sigma} \left\{ \Gamma_{\beta\gamma}^{\alpha} \right\} \\ &+ \frac{1}{2} g^{\alpha\delta} \left( F_{,\gamma\sigma} \{g_{\beta\delta}\} + F_{,\sigma\beta} \{g_{\gamma\delta}\} - F_{,\delta\sigma} \{g_{\beta\gamma}\} \right) \\ &+ \frac{1}{2} g^{\alpha\delta} \left( F_{,\gamma} \{g_{\beta\delta,\sigma}\} + F_{,\beta} \{g_{\gamma\delta,\sigma}\} - F_{,\delta} \{g_{\beta\gamma,\sigma}\} \right), \end{aligned} \quad (4.26)$$

where other terms either vanish by Eq. 4.24 or are negligible. Equation 4.26 must be obtained by differentiating Eq. 4.23, rather than Eq. 4.25, because otherwise we would miss the second derivatives of the transition functions. The third and fourth terms of Eq. 4.26 are already of  $\mathcal{O}(\epsilon_1^{\ell_1+1}, \epsilon_2^{\ell_2+1})$  by Eq. 4.8, condition (i), (ii) and (iii). The last term is finally also of  $\mathcal{O}(\epsilon_1^{\ell_1+1}, \epsilon_2^{\ell_2+1})$  because although  $\{g_{\mu\nu,\sigma}\} = \mathcal{O}(\epsilon_1^{\ell_1}, \epsilon_2^{\ell_2})$ , by condition (ii)  $F_{,\alpha} = \mathcal{O}(\epsilon_1, \epsilon_2)$ . We are therefore left with

$$\Gamma_{\beta\gamma,\sigma}^\alpha = \Gamma_{\beta\gamma,\sigma}^{\alpha(1)} F(\ell_i) + \Gamma_{\beta\gamma,\sigma}^{\alpha(2)} [1 - F(\ell_i)] + \mathcal{O}(\epsilon_1^{\ell_1+1}, \epsilon_2^{\ell_2+1}), \quad (4.27)$$

which again leads to the asymptotic condition  $\Gamma_{\beta\gamma,\sigma}^{\alpha(1)} - \Gamma_{\beta\gamma,\sigma}^{\alpha(2)} = \mathcal{O}(\epsilon_1^{\ell_1+1}, \epsilon_2^{\ell_2+1})$  in  $\mathcal{B}$ .

We are now ready to compute the Ricci tensor. Once more, using Eq. 4.25 and Eq. 4.27 we can write

$$R_{\alpha\beta} = R_{\alpha\beta}^{(1)} F(\ell_i) + R_{\alpha\beta}^{(2)} [1 - F(\ell_i)] + \mathcal{O}(\epsilon_1^{\ell_1+1}, \epsilon_2^{\ell_2+1}), \quad (4.28)$$

where the third term groups all the cross terms that are  $\mathcal{O}(\epsilon_1^{\ell_1+1}, \epsilon_2^{\ell_2+1})$  in  $\mathcal{B}$ . Furthermore, we know that the approximate solutions  $g_{\mu\nu}^{(1,2)}$  satisfy the Einstein equations to  $\mathcal{O}(\epsilon_n^{\ell_n})$ , which then implies that

$$R_{\alpha\beta}^{(n)} = \mathcal{O}(\epsilon_n^{\ell_n+1}). \quad (4.29)$$

We thus arrive at the conclusion that

$$R_{\alpha\beta} = \mathcal{O}(\epsilon_1^{\ell_1+1}, \epsilon_2^{\ell_2+1}), \quad (4.30)$$

which then proves the theorem. q. e. d.

This theorem allows for the construction of pure joined solutions, with a restricted class of transition functions. Although the theorem has been formulated for vacuum spacetimes, it also holds for non-vacuum scenarios as discussed above. The proof for the non-vacuum case can be established simply by following the above proof and realizing that now  $R_{\alpha\beta}^{(n)} - 8\pi T_{\alpha\beta}^{(n)} = \mathcal{O}(\epsilon_n^{\ell_n+1})$ . Also note that the ideas of this section can be extended to mixed joined solutions, by replacing condition (i) by some other condition that guarantees that the approximate solutions represent the same spacetime in  $\mathcal{B}$ . Finally, note that the conditions we impose on the transition functions are not very stringent, thus allowing for a wide range of possible functions.

### 4.3.3 Projection to a Cauchy Hypersurface

Let us now specialize the pure joined solution of Eq. 4.11 to joined initial data on a Cauchy hypersurface. Since this hypersurface is by definition spacelike, it is convenient to have a foliation of the buffer zone that is timelike as given in the previous section. The data constructed in this section consists of an induced 3-metric on the Cauchy hypersurface and its extrinsic curvature.

Consider then a Cauchy hypersurface  $\Sigma \in \mathcal{M}$ , on which the 4-dimensional regions  $(C_1, C_2, \mathcal{B})$  become 3-dimensional surfaces. We still have a foliation of the buffer zone by an infinite number of timelike junction hypersurfaces  $\mathcal{J}_i$  of  $\Sigma$ . These hypersurfaces are now actually submanifolds with boundary of co-dimension 1 with respect to  $\Sigma$  but co-dimension 2 with respect to  $\mathcal{M}$ .

In either  $C_n$  we can now define the 3-metric  $(h_{ab}^{(n)})$  and the extrinsic curvature  $(K_{ab}^{(n)})$  of  $\Sigma$  by projecting the asymptotically matched approximate metrics  $g_{\mu\nu}^{(n)}$  to this hypersurface [9]. In analogy with the previous section, let us then define these objects via

$$\begin{aligned} h_{ab} &= F(\ell_i) h_{ab}^{(1)} + [1 - F(\ell_i)] h_{ab}^{(2)}, \\ K_{ab} &= F(\ell_i) K_{ab}^{(1)} + [1 - F(\ell_i)] K_{ab}^{(2)}. \end{aligned} \quad (4.31)$$

In Eq. 4.31,  $F(\cdot)$  is a proper transition function as defined by Eq. 4.14. Provided this transition function satisfies conditions (ii) and (iii) of Theorem 1, then Eq. 4.31 satisfies the constraint equations of general relativity.

There might be some concern that the extrinsic curvature of Eq. 4.31 does not correspond to the same hypersurface  $\Sigma$  as that described by the 3-metric because derivatives of the transition functions have been neglected. However, if the transition functions satisfy the conditions of Theorem 1, then these derivatives are of the same order as the uncontrolled remainders. In order to show this, we can compute the extrinsic curvature from the spatial metric of Eq. 4.31 directly, *i.e.*

$$K_{ab} = F(\ell_i) K_{ab}^{(1)} + [1 - F(\ell_i)] K_{ab}^{(2)} - \frac{1}{2} \{h_{ab}\} \mathcal{L}_{\vec{n}} F(\ell_i), \quad (4.32)$$

where  $\mathcal{L}_{\vec{n}}$  is the Lie derivative along the normal vector to  $\Sigma$ . Clearly, since  $F(\cdot)$  is a scalar function, the Lie derivative reduces to the directional partial derivative of this function along the normal vector, *i.e.*  $\mathcal{L}_{\vec{n}} = n^\alpha F_{,\alpha}$ . Here  $n^\alpha$  could be that associated with either of the approximate solutions, since in the buffer zone  $n_{(1)}^\alpha - n_{(2)}^\alpha = \mathcal{O}(\epsilon_1^{\ell_1+1}, \epsilon_2^{\ell_2+1})$ . Since the 3-metrics are already asymptotic to each other up to uncontrolled remainders of  $\mathcal{O}(\epsilon_1^{\ell_1+1}, \epsilon_2^{\ell_2+1})$  by Eq. 4.8, we must only require that the Lie derivative be of  $\mathcal{O}(\epsilon_1, \epsilon_2)$ . This condition is consistent with the conditions of the asymptotic junction theorem.

We see then that the global 3-metric and extrinsic curvature of Eq. 4.31 represent the same data as that obtained from Eq. 4.11 directly up to the uncontrolled remainders in the approximations. We can then formulate the following theorem, which can be viewed as a corollary of Theorem 1:

**THEOREM 4.2.** *Consider a spacetime manifold  $\mathcal{M}$  with approximate metrics  $g_{\mu\nu}^{(1)}$  and  $g_{\mu\nu}^{(2)}$  that satisfy the vacuum Einstein equations up to uncontrolled remainders of  $\mathcal{O}(\epsilon_1^{\ell_1+1})$  and  $\mathcal{O}(\epsilon_2^{\ell_2+1})$  on submanifolds with boundary  $C_1$  and  $C_2$  respectively. Let these submanifolds intersect on a 4-volume  $\mathcal{B} = C_1 \cap C_2$  and foliate the 3-dimensional projection of  $\mathcal{B}$  onto a Cauchy hypersurface  $\Sigma$  with timelike junction hypersurfaces  $\mathcal{J}_i$ . Consider the 3-metric*

and extrinsic curvature of  $\Sigma$  constructed via

$$\begin{aligned} h_{ab} &= F(\ell_i) h_{ab}^{(1)} + [1 - F(\ell_i)] h_{ab}^{(2)}, \\ K_{ab} &= F(\ell_i) K_{ab}^{(1)} + [1 - F(\ell_i)] K_{ab}^{(2)}, \end{aligned} \quad (4.33)$$

where  $F(\cdot)$  is a proper transition function as defined via Eq. 4.14,  $\ell_i$  is the proper distance to  $\mathcal{J}_i$  on  $\Sigma$ , and  $\{h_{ab}^{(1,2)}, K_{ab}^{(1,2)}\}$  are the 3-metric and extrinsic curvature of  $\Sigma$  associated with  $g_{\mu\nu}^{(1,2)}$ . Then, the 3-metric and extrinsic curvature Eq. 4.33 satisfy the constraint equations of General Relativity on  $\Sigma$  to the same order as  $g_{\mu\nu}^{(1,2)}$  if and only if the following conditions are satisfied:

$$\begin{aligned} (i) \quad & \text{The metrics } g_{\mu\nu}^{(1,2)} \text{ have been asymptotically matched} \\ & \text{in } \mathcal{B} \text{ up to uncontrolled remainders of } \mathcal{O}(\epsilon_1^{\ell_1+1}, \epsilon_2^{\ell_2+1}), \\ (ii) \quad & F_{,\alpha} = \mathcal{O}(\epsilon_1, \epsilon_2), \quad \text{in } \mathcal{B}, \\ (iii) \quad & F_{,\alpha\beta} = \mathcal{O}(\epsilon_1^0, \epsilon_2^0), \quad \text{in } \mathcal{B}. \end{aligned} \quad (4.34)$$

The proof of this theorem is established by projecting the 4-metric onto  $\Sigma$ . The 3-metric is given by

$$h_{\alpha\beta} = g_{\alpha\beta} + n_\alpha n_\beta, \quad (4.35)$$

where  $n_\alpha$  is the covariant normal vector to  $\Sigma$ . Using Eq. 4.11 and the fact that any smooth tensor can be decomposed with transition functions via Eq. 4.12, we rewrite the spatial part of the 3-metric as

$$h_{ab} = h_{ab}^{(1)} F(\ell_i) + [1 - F(\ell_i)] h_{ab}^{(2)}. \quad (4.36)$$

The extrinsic curvature is given by

$$K_{ab} = \mathcal{L}_{\vec{n}} h_{ab}. \quad (4.37)$$

Inserting Eq. 4.36 into Eq. 4.37 we can rewrite the extrinsic curvature as given in Eq. 4.32. However, since the transition function satisfies  $F_{,\alpha} = \mathcal{O}(\epsilon_1, \epsilon_2)$ , the last term of that equation can be neglected and we obtain

$$K_{ab} = K_{ab}^{(1)} F(\ell_i) + [1 - F(\ell_i)] K_{ab}^{(2)}. \quad (4.38)$$

Now, recall that the 4-metric satisfies the vacuum Einstein equations up to uncontrolled remainders of  $\mathcal{O}(\epsilon_1^{\ell_1+1}, \epsilon_2^{\ell_2+1})$  by Theorem 1. Therefore, this metric also satisfies the constraint equations, since these are related to the temporal components of the Einstein tensor and the normal vector to  $\Sigma$ . Recall here that the normal can be that associated with either approximate solution, since these vectors are asymptotic to

each other inside the buffer zone. Since the 3-metric and extrinsic curvature come directly from a projection of this 4-metric, it follows that this data must also satisfy the constraints to the same order. q. e. d.

#### 4.4 A simple example

In this section, we investigate the impact of different transition functions on the satisfaction of the Einstein equations. For this purpose, we pick a metric that has already been matched in [93], henceforth paper I. This metric represents a binary system of Schwarzschild black holes in a quasicircular orbit. We here show explicitly that as long as the transition functions satisfy the conditions of Theorems 1 and 2, the joined metric satisfies the vacuum Einstein equations and, thus, also the constraint equations.

As explained in paper I, the manifold can be divided into 3 regions (Table 3.1). The symbols of Table 3.1 represent the following quantities:  $C_n$  labels the  $n$ th regions, where  $n = \{1, 2, 3\}$ ;  $A$  labels the black hole, with  $A = \{1, 2\}$ ;  $r_{in}$  and  $r_{out}$  are the approximate inner and outer boundary radius of each  $C_n$  regions as measured from the  $A$ th black hole;  $r_A$  and  $\bar{r}_A$  are the radial distances as measured from the  $A$ th black hole in near and inner zone coordinates;  $\epsilon_n$  is the perturbation parameter used in the approximate solution  $g_{\mu\nu}^{(n)}$  in  $C_n$ ;  $m_A$  is the mass of the  $A$ th black hole;  $b$  is the orbital separation on  $\Sigma$ ;  $\lambda$  is the gravitational wavelength. The quantity  $b$  is usually defined as the black hole separation in the near zone, which we shall see coincides with the black hole separation in the inner zone up to uncontrolled remainders, namely  $b = \bar{b} + \mathcal{O}(\epsilon_1, \epsilon_2)$ . Technically, there is a fourth region beyond the near zone, but we neglect this here since it does not affect the study of transition functions. For a detailed description of this subdivision and a pictorial representation of these zones refer to [105, 93].

These regions overlap clearly in two buffer zones, which on the  $t = \bar{t} = 0$  slice can be defined by the following inequalities:  $O_{13} = C_1 \cap C_3$  ( $m_1 \ll r_1 \ll b$ ) and  $O_{23} = C_2 \cap C_3$  ( $m_2 \ll r_2 \ll b$ ), where  $r_A$  is the radial distance from the  $n$ th black hole to a field point. Asymptotic matching and the transition functions act in these buffer zones, which can only be defined asymptotically and, thus, any statement regarding them must be interpreted in that sense. In particular, this implies that any quantity that is valid in the buffer zone need not be valid near the boundary of the buffer zone (*i.e.*, as  $r_A \rightarrow b$  or  $r_A \rightarrow m_A$ .) Also note that these buffer zones are actually 4-volumes and can be foliated by an infinite number of timelike junction hypersurfaces.

Different approximations are used in each zone to solve the Einstein equation. In either inner zone, black hole perturbation theory allows us to obtain a tidally perturbed metric. Let us concentrate on inner zone 1 near black hole 1, since the metric in the other inner zone can be obtained via a symmetry transformation. In  $C_1$ , the perturbed

metric is given in isotropic corotating coordinates  $x^{\bar{a}} = \{\bar{t}, \bar{x}, \bar{y}, \bar{z}\}$  by

$$\begin{aligned}
g_{\bar{0}\bar{0}}^{(1)} &\approx H_t + H_{s1}\Omega^2(\bar{x}^2 + \bar{y}^2) + 2H_{st}\bar{x}\frac{\Omega}{b^2}(\bar{x}^2 + \bar{y}^2 - \bar{z}^2), \\
g_{\bar{0}\bar{a}}^{(1)} &\approx -H_{s1}\Omega\epsilon_{\bar{a}\bar{b}\bar{c}}x^{\bar{b}} + \frac{H_{st}}{b^2}\left[\bar{y}\left(\delta_{\bar{a}}^{\bar{3}}\bar{z} - \delta_{\bar{a}}^{\bar{1}}\bar{x}\right) + (\bar{x}^2 - \bar{z}^2)\delta_{\bar{a}}^{\bar{2}}\right], \\
g_{\bar{a}\bar{b}}^{(1)} &\approx \delta_{\bar{a}\bar{b}}H_{s1} - H_{s2}\frac{x^{\bar{a}}x^{\bar{b}}}{b^2},
\end{aligned} \tag{4.39}$$

where  $\Omega$  is the angular velocity of the perturbation,  $\epsilon_{\bar{a}\bar{b}\bar{c}}$  is the standard Levi-Civita symbol with convention  $\epsilon_{\bar{1}\bar{2}\bar{3}} = 1$  and where  $\delta_{\bar{b}}^{\bar{a}}$  is the Kronecker delta. In Eq. 4.39 we used the shorthand

$$\begin{aligned}
H_{st} &= 2m_2\sqrt{\frac{m}{b^3}}\left(1 - \frac{M_1}{2\bar{r}}\right)^2\left(1 + \frac{M_1}{2\bar{r}}\right)^4, \\
H_{s1} &= \left(1 + \frac{M_1}{2\bar{r}}\right)^4\left\{1 + 2\frac{m_2}{b^3}\bar{r}^2P_2\left(\frac{\bar{x}}{\bar{r}}\right)\left[\left(1 + \frac{M_1}{2\bar{r}}\right)^4 - 2\frac{M_1^2}{\bar{r}^2}\right]\right\}, \\
H_{s2} &= \left(1 + \frac{M_1}{2\bar{r}}\right)^4\left(1 + \frac{M_1^2}{4\bar{r}^2}\right)\frac{4m_2M_1}{b\bar{r}}P_2\left(\frac{\bar{x}}{\bar{r}}\right), \\
H_t &= -\left(\frac{1 - M_1/2\bar{r}}{1 + M_1/2\bar{r}}\right)^2 + 2\left(1 - \frac{M_1}{2\bar{r}}\right)^4\frac{m_2}{b^3}\bar{r}^2P_2\left(\frac{\bar{x}}{\bar{r}}\right),
\end{aligned} \tag{4.40}$$

where  $M_1$  is the mass of the background black hole,  $m_2$  is the mass of the binary companion that is causing the perturbation,  $m = M_1 + m_2$  is the total mass,  $\bar{r} = (\bar{x}^2 + \bar{y}^2 + \bar{z}^2)^{1/2}$  and  $P_2(\cdot)$  is the second Legendre polynomial. Equation 4.39 then satisfies the linearized Einstein equations in  $C_1$ . These equations are identical to (18) and (19) of paper I and solve the Einstein equations up to uncontrolled remainders of  $\mathcal{O}(\bar{r}_1/b)^3$ . We refer the reader to that paper for an explanation of the derivation of this metric.

In the near zone, a post-Minkowskian expansion is used to find an approximate solution. This solution in corotating ADMTT coordinates  $x^a = \{t, x, y, z\}$  [(7)-(12) in paper I] is given by

$$\begin{aligned}
g_{ab}^{(3)} &= \Psi^4\delta_{ab}, \\
g_{0a}^{(3)} &= g_{ab}^{(3)}\beta^{(3)b}, \\
g_{00}^{(3)} &= g_{0a}^{(3)}\beta^{(3)a} - (\alpha^{(3)})^2,
\end{aligned} \tag{4.41}$$

where we introduced a post-Newtonian conformal factor

$$\Psi = 1 + \frac{m_1}{2r_1} + \frac{m_2}{2r_2}, \tag{4.42}$$

and where the post-Newtonian lapse and shift are given by

$$\begin{aligned}\alpha^{(3)} &= \frac{2 - \Psi}{\Psi} \\ \beta^{(3)i} &= \frac{m_1}{r_1} \left[ \frac{1}{2} \left( v_1^i - \vec{v}_1 \cdot \vec{n}_1 n_1^i \right) - 4v_1^i \right] \\ &+ \frac{m_2}{r_2} \left[ \frac{1}{2} \left( v_2^i - \vec{v}_2 \cdot \vec{n}_2 n_2^i \right) - 4v_2^i \right] - \epsilon_{ik3} \omega x^k.\end{aligned}\quad (4.43)$$

In these equations, the radial distance to the  $A$ th black hole is given by  $r_A = (x_A^2 + y^2 + x^2)^{1/2}$ , where  $x_1 = x - m_2 b/m$  and  $x_2 = x + m_1 b/m$ . These equations solve the Einstein equations in  $C_3$  up to uncontrolled remainders of  $\mathcal{O}(m_A/r_A)^2$ . Once more, we refer the reader to that paper for an explanation of the derivation of such a metric. In these equations, the non-zero components of the velocities  $\vec{v}_A$  and the unit vectors  $\vec{n}_A$  are given in the  $t = 0$  slice by

$$\begin{aligned}v_1^2 &= \omega \frac{m_2}{m} b, & v_2^2 &= -\omega \frac{m_1}{m} b, \\ n_A^k &= \frac{x^k - \xi_A^k}{r_A}, & \xi_1^1 &= \frac{m_2}{m} b, & \xi_2^1 &= -\frac{m_1}{m} b,\end{aligned}\quad (4.44)$$

where  $\omega$  is the post-Newtonian angular velocity given by

$$\omega = \sqrt{\frac{m}{b^3}} \left[ 1 + \frac{1}{2} \left( \frac{\mu}{m} - 3 \right) \frac{m}{b} \right], \quad (4.45)$$

with errors of  $\mathcal{O}(m/b)^{5/2}$ . Equation 4.45 appears also in paper I and in (60) of [16], where  $\mu = m_1 m_2/m$  is the reduced mass of the system.

Asymptotic matching was performed in paper I and a coordinate and parameter transformation was found such that Eq. 4.7 is satisfied. For buffer zone 1,  $O_{13}$ , such a transformation to  $\mathcal{O}[m_A/r_A, (\bar{r}_A/b)^2]$  is given by

$$\begin{aligned}x^{\bar{\mu}} &= x^\sigma \left[ \delta_\sigma^{\bar{\mu}} + \eta_\sigma^{\bar{\mu}} \frac{m_2}{b} \left( 1 - \frac{x}{b} \right) \right] + \delta_y^{\bar{\mu}} t \frac{m_2}{\sqrt{mb}}, \\ M_A &= m_A, & \Omega &= \omega,\end{aligned}\quad (4.46)$$

where  $\eta_{\mu\nu}$  is the Minkowski metric and  $\delta_{\mu\nu}$  is the 4-Euclidean metric. Note that  $x^{\bar{\mu}} = x^\mu$  to zeroth order as previously mentioned and, when describing certain figures, we will sometimes use them interchangeably. One might worry that Eq. 4.46 is not bounded above, since  $x^{\bar{\sigma}} \rightarrow \infty$  as  $t \rightarrow \infty$ . However, recall that the buffer zone is technically a 4-volume delimited by the boundaries of the regions of validity of the approximations. In this sense, time cannot go to infinity, because then the post-Newtonian metric would break down as  $t$  approaches the time of coalescence. Furthermore, when constructing initial data,  $t = 0$  and  $\bar{t} = 0$ , and it is clear that  $t \rightarrow \infty$  is not allowed. In paper I, asymptotic matching is carried out to slightly higher order, but since the purpose of this

section is to study transition functions we use Eq. 4.46 instead. The metric in inner zone 2 and the matching coordinate and parameter transformations in buffer zone 2,  $\mathcal{O}_{23}$ , can be obtained by applying the following transformation to Eq. 4.39 and Eq. 4.46:

$$1 \rightarrow 2, \quad x \rightarrow -x, \quad y \rightarrow -y, \quad z \rightarrow z. \quad (4.47)$$

In order to study these transition functions, we pick a particular physical system. We choose a system of equal mass black holes  $m_1 = m_2 = 0.5m$  separated by an orbital distance  $b = 20m$ . The black holes are non-spinning and located on the  $x$ -axis at  $x = 10m$  and  $x = -10m$  for the first and second black hole respectively. The black holes are orbiting in the counter-clockwise direction about the  $z$ -axis. The buffer zones are then given by  $O_{A3} : 20 \gg r_A/m \gg 0.5$ . This system is used to study different transition functions, but we should note that the asymptotically matched metric of paper I is valid for a wide range of systems.

We here keep the physical system fixed and pick several different transition functions to investigate how these functions change the satisfaction of the Einstein equations. We consider the following type of transition functions:

- **Transition function 1 (TF 1)**

$$f_1(r) = \begin{cases} 0 & , r \leq r_- \\ \frac{1}{2} \left\{ 1 + \tanh \left[ \frac{s}{\pi} \left( \tan \left( \frac{2m\pi}{bw} (r - r_-) \right) - \frac{q^2}{\tan \left( \frac{2m\pi}{bw} (r - r_-) \right)} \right) \right] \right\} & , r_- < r < r_+ \\ 1 & , r \geq r_+, \end{cases} \quad (4.48)$$

where  $r_-$  and  $r_+$  determine where the transition begins and ends,  $w$  determines the size of the region, and  $s$  and  $q$  determine the slope of the transition function roughly when  $f_1 \approx 1/2$ . This function is similar to that used in paper I and we use similar parameters, *i.e.*

$$\begin{aligned} r_- &= m, & r_+ &= b - m, \\ w &= 9m, & q &= 0.2, & s &= b/m. \end{aligned} \quad (4.49)$$

- **Transition function 2 (TF 2) and 3 (TF 3)**

$$f_2(r) = \exp \left( \frac{b}{2m} \frac{r - d}{w} \right) \left[ 1 + \exp \left( \frac{b}{2m} \frac{r - d}{w} \right) \right]^{-1}, \quad (4.50)$$

where  $w$  is approximately the size of the transition window and  $d$  is approximately the distance from the  $A$ th black hole at which the derivative of the transition function peaks. For TF 2 we choose the following parameters

$$w = 7m, \quad d = 6m, \quad (4.51)$$

while for TF 3 we choose

$$w = m, \quad d = 8m. \quad (4.52)$$

For all these transition functions, the transition window  $w$  is defined approximately as the size of the region inside which the function ranges from 0.01 to 0.99.

The purpose of this paper is not to perform a systematic study of the properties of transition functions, but to illustrate the theorems discussed in earlier sections with a practical example. In fact, as discussed in the introduction, transition functions were first introduced in [105, 93], but the properties and conditions that these functions must satisfy were not explored. In this paper, we are in essence following up on previous work and providing further details that might be relevant to future investigations. In particular, we shall investigate how the gluing of asymptotically matched approximate solutions breaks down if improper transition functions are chosen.

The transition functions that we have chosen clearly have different properties. First, notice that the region where functions are significantly different from zero or unity varies, because the size of their respective transition windows  $w$  is different. In particular, TF 3 has the smallest transition window, followed by TF 2 and then TF 1. Second, notice that the transition functions become roughly equal to 1/2 at different radii:  $r \approx 7m$  for TF 1,  $r \approx 6m$  for TF 2 and  $r \approx 8m$  for TF 3. Third, notice that the speed at which the transition functions tend to zero and unity is also different. In particular, note that TF 3 tends to zero the fastest, followed by TF 1 and finally TF 2. This speed is important in the definition of proper transition functions in Eq. 4.14, because it prevents contamination of possibly divergent uncontrolled remainders outside the buffer zone. Finally, notice that not all functions are analytic, since TF 1 does not have a Taylor expansion about  $r = r_{\pm}$  (recall, however, that analyticity was not required.)

These different features of the transition functions can be observed in Figures 4.1 and 4.2. Figure 4.1 shows the behaviour of the different transition functions as a function of radius, while Fig. 4.2 shows their first and second derivatives. Observe in Fig. 4.1 that the transition occurs at different radii and that they transition at different speeds. In Fig. 4.2 we can observe the difference in the transitioning speed better. We can clearly see in this figure that the derivatives of TF 1 are the smallest, followed by TF 2 and then TF 3. However, both TF 1 and TF 2 have derivatives that are consistently of order much less than  $\mathcal{O}(1)$ , while TF 3 has first derivatives of  $\mathcal{O}(1)$  or larger. The inset in this figure shows the large derivatives of TF 3. Also note that the second derivatives of the first and second transition functions are consistently smaller than their first derivatives. This is a consequence of the size of the transition window. If such a window were chosen to be smaller, as in the case of TF 3, then the second derivative would become larger than the first.

With these transition functions we can now construct pure joined solutions via

$$g_{\mu\nu} = f(\bar{r}_1)f(\bar{r}_2)g_{\mu\nu}^{(3)} + [1 - f(\bar{r}_1)]g_{\mu\nu}^{(1)} + [1 - f(\bar{r}_2)]g_{\mu\nu}^{(2)}, \quad (4.53)$$

where we assume  $g_{\mu\nu}^{(1,2)}$  has been transformed with the coordinate and parameter transformation of Eq. 4.46 and where  $f(\cdot)$  can be any of TF 1, TF 2 or TF 3. Equation 4.53 is an extension of Eq. 4.11 applicable to two buffer zones. Extensions to more than 2 buffer zones are also straightforward.

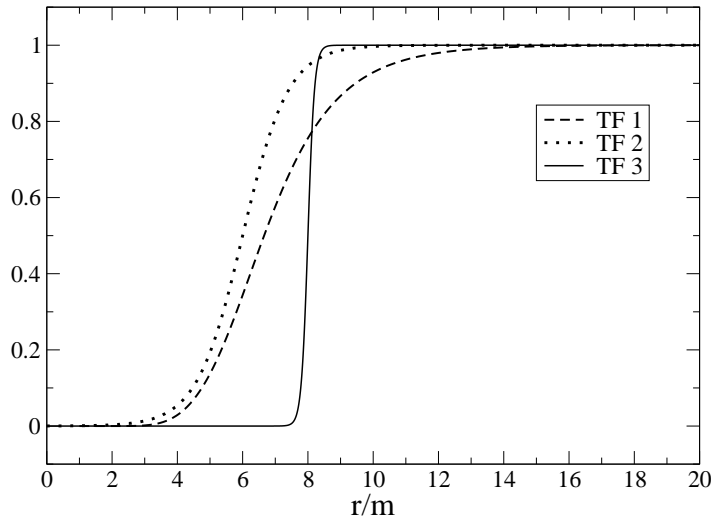


Fig. 4.1. This figure shows the first (TF 1), second (TF 2) and third (TF 3) transition functions as a dashed, dotted and solid lines respectively. Observe that these functions transition at different radii and at different speeds.

Whether the joined metric of Eq. 4.53 satisfies the Einstein equations to the same order as the approximate solution depends on the transition function used. We expect the metric constructed with TF 1 to generate small violations because it is a proper transition function that clearly satisfies the differentiability conditions required in Theorems 1 and 2. On the other hand, TF 2 and 3 do not satisfy these conditions because TF 2 is not a proper transition function and TF 3 violates condition (ii) and (iii) of Theorem 1. This behaviour, however, is not clear by simply looking at metric components. In Fig. 4.3 we plot the determinant of the spatial metric along the  $x$ -axis, corresponding to the  $x$  harmonic (near zone) coordinate, with  $t = 0$ ,  $y = 0$  and  $z = 0$ . This axis is where joined metrics are glued together with different transition functions. This determinant gives a measure of the volume element on  $\Sigma$  and, as one can see in the figure, the difference when different transition function are used is small. This behaviour is not unique to the  $x$ -axis, but is actually observed along the other axis as well. When this is the case, we only show the behaviour along the  $x$ -axis in order to avoid redundancy.

Although the volume element computed with different transition functions is similar, metrics joined with different transition functions do not satisfy the Einstein equations to the same order. In Fig. 4.4, we plot the 4-Ricci scalar calculated with the global metrics joined with different transition functions. This plot is representative of the behaviour of the 4-Ricci scalar in the entire domain, although here we plot it only along the  $x$ -axis. We also plot only the region  $x/m > 10$ , to the right of where BH 1 is located at  $t = 0$ , because the behaviour of the 4-Ricci scalar is symmetric about  $x = 0$  and the transition functions are symmetric about  $\bar{r}_A = 0$ . Thus, the behaviour of the 4-Ricci scalar in other

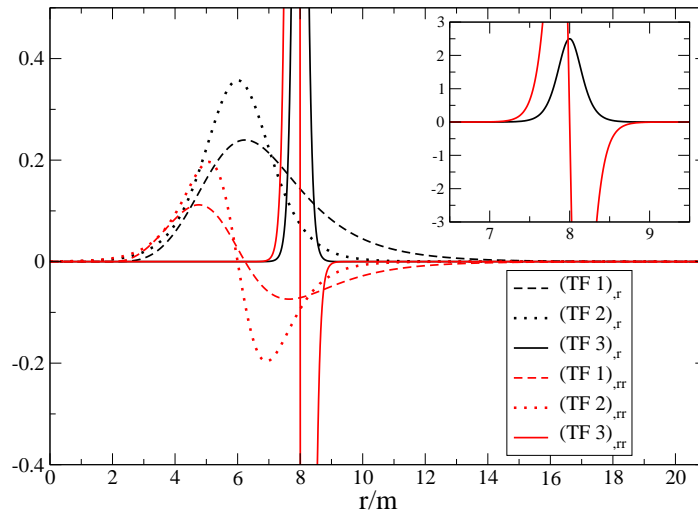


Fig. 4.2. This figure shows the first and second derivatives of the transition functions. The first derivative of the first  $[(TF 1)_{,r}]$ , second  $[(TF 2)_{,r}]$  and third  $[(TF 3)_{,r}]$  transition functions are denoted with a dashed, dotted and solid black line respectively. The second derivative of the first  $[(TF 1)_{,rr}]$ , second  $[(TF 2)_{,rr}]$  and third  $[(TF 3)_{,rr}]$  transition functions are denoted with a dashed, dotted and solid cyan (or light gray on black and white print) line respectively. In the inset we zoomed out to show better the derivatives of the third transition function.

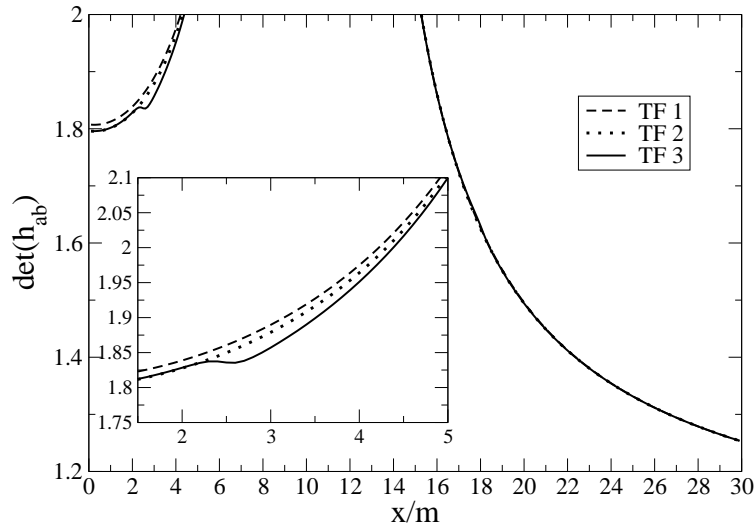


Fig. 4.3. This figure shows the determinant of the spatial metric along the  $x$ -axis with TF 1 (dashed line), TF 2 (dotted line) and TF 3 (solid line.) Observe that the differences in the global metrics are small if at all visible. In the inset we zoom to the region where the curves look the most different.

regions of the domain is similar to that shown in Fig. 4.4 (see paper I for contour plots of some of these quantities.)

There are several features in Fig. 4.4 that we should comment on. First, observe that the  ${}^{(4)}R$  is everywhere smaller than the uncontrolled remainder in the approximate solutions (roughly  $\mathcal{O}(m/b)^2 \approx 0.0025$  in the buffer zone for the system considered) when the joined metric is constructed with TF 1. However, this is not the case for the metrics constructed with TF 2 and 3. For those metrics,  ${}^{(4)}R$  has spikes close to  $r_A = 0$  ( $x \approx 10m$ ) and  $r_A = 8m$  ( $x \approx 18m$ ) for TF 2 and 3 respectively. The spike resulting from the metric constructed with TF 3 is associated with the small size of its transition window, which forces large derivatives in the transition function, thus violating conditions (ii) and (iii) of Theorems 1 and 2. The spike in the metric built with TF 2 is related to the fact that this function does not tend to zero faster than the uncontrolled remainders of the post-Newtonian near zone metric close to BH A. As we discussed earlier, the rate at which transition functions tend to zero and unity is important to avoid contamination from divergent uncontrolled remainders in the approximations. In this case, TF 2 is of  $\mathcal{O}(m/b)^3$  as  $r/m \rightarrow m/b$ , while the post-Newtonian Ricci scalar diverges as  $m/r^3$  as  $r \rightarrow 0$  and is in fact of  $\mathcal{O}(b/m)^3$  as  $r/m \rightarrow m/b$ . Since the transition function is not able to eliminate this contamination from the near zone metric, the Einstein equations are violated near either black hole for the metric constructed with TF 2. From a physical standpoint, the failure to use appropriate transition functions to create a pure joined solution introduces a modification in the matter-sector of the Einstein equations, namely

the artificial creation of a shell of matter. One can straightforwardly see from Eq. 4.5 and Eq. 4.32 that the stress-energy tensor of this shell depends on the non-vanishing derivatives of the transition function.

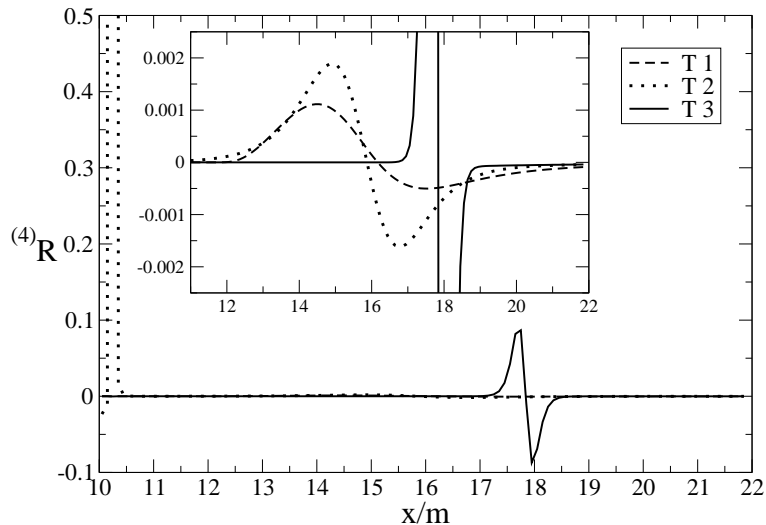


Fig. 4.4. 4-Ricci scalar along the  $x$ -axis for the global metrics joined with TF 1 (dashed line), TF 2 (dotted line) and TF 3 (solid line.) Observe that the 4-Ricci scalar is small everywhere for the metric constructed with TF 1, but it has spikes for that built with TF 2 and 3. The inset zooms to the region  $x \in [11, 22]$  so that the difference between the 4-Ricci scalar calculated with TF 1 and 2 are more noticeable.

A deeper analysis of the spike in  ${}^{(4)}R$  due to the joined metric with TF 2 reveals that the conditions found are sufficient but formally not necessary. The 4-Ricci scalar constructed with the post-Newtonian metric ( ${}^{(4)}R_{PN}$ ) diverges close to BH A, since this approximation breaks down in that region. Therefore, if the transition function does not vanish identically, or faster than the divergence in  ${}^{(4)}R_{PN}$ , then  ${}^{(4)}R$  will present a spike. This spike, however, would disappear if the transition function decayed to zero faster than the divergence in  ${}^{(4)}R_{PN}$ . In this sense, even though the conditions discussed here are not necessary since the definition of a proper transition function could be weakened, they are certainly sufficient and universal.

The second feature we should comment on is the behaviour of  ${}^{(4)}R$  in the region  $x/m \in [11, 17]$ . As one can observe in the inset, the transition functions indeed introduce some error in this region. However, note that this error for the metric constructed with TF 1 is smaller than the uncontrolled remainders in the approximate solutions. Also note that this error is independent of the location of the center of the transition window. In other words, asymptotic matching is performed inside of a buffer zone and not on a

patching surface, which means that approximate solutions can be glued with transition functions anywhere in the buffer zone away from the boundaries and not just at a specific 2-surface. As one can see from the figure, the metric constructed with TF 1 has the smallest error in this region, followed by that built with TF 2 and 3. This fact is not too surprising because, as shown in the proof of Theorem 1, the error introduced by the transition functions in the calculation of the Ricci tensor scales with the first and second derivatives of these functions. Finally, note that the error introduced by these functions seems to be correlated to both the size and functional form of the second derivative of the transition functions, as one can see by comparing the inset of Fig. 4.2 to Fig. 4.4. The reason for such similarity, however, is beyond the scope of this paper.

Once an approximate global 4-metric has been found, we can use it to construct initial data. These data could be given for example by

$$\begin{aligned} h_{ab} &= f(\bar{r}_1)f(\bar{r}_2)h_{ab}^{(3)} + [1 - f(\bar{r}_1)] h_{ab}^{(1)} + [1 - f(\bar{r}_2)] h_{ab}^{(2)}, \\ K_{ab} &= f(\bar{r}_1)f(\bar{r}_2)K_{ab}^{(3)} + [1 - f(\bar{r}_1)] K_{ab}^{(1)} + [1 - f(\bar{r}_2)] K_{ab}^{(2)}. \end{aligned} \quad (4.54)$$

Equation 4.54 is simply a generalization of Eq. 4.31 for 2 buffer zones. The extrinsic curvatures for the inner zones and near zone are provided explicitly in paper I.

Are we allowed to construct data with transition functions in this way? There might be some doubt as to whether this is valid, since the fact that the joined metric satisfies the Einstein equations does not necessarily guarantee that we can use transition function to construct the data itself. In particular, there might be some worry that the extrinsic curvature calculated from Eq. 4.53 generally contains derivatives of the transition functions that Eq. 4.54 neglects. Theorem 2, however, ensures that this construction is indeed valid, provided the transition functions satisfy the same differentiability conditions proposed in Theorem 1. This is because the derivatives of these functions are then small and, in particular, the terms that are proportional to them are of the same order as the uncontrolled remainders in the approximations.

These expectations can be verified in Fig. 4.5, where we plot the  $xy$ -component of the extrinsic curvature along the  $x$ -axis constructed both via Eq. 4.54 (referred to as glued T 1, 2 and 3 in the figure) and by direct differentiation of Eq. 4.53 (referred to as full T 1, 2 and 3 in the figure.) We plot only the  $xy$ -component because this is the dominant term of this tensor along the  $x$ -axis for the system considered and it shows the main differences in using different transition functions. We have checked that other quantities, like the trace of the extrinsic curvature, behaves similarly. For contour plots of the extrinsic curvature refer to paper I.

As in the case of the Ricci scalar, there are several features of Fig. 4.5 that we should discuss. First, observe that that the extrinsic curvatures constructed with TF 1 agree in the buffer zone up to uncontrolled remainders. These remainders are of  $\mathcal{O}(m/b)^{3/2} \approx 0.01$  in the buffer zone, because here we have used a coordinate transformation from the matching scheme that is valid only up to  $\mathcal{O}(m/b)$ . The inset zooms to a region close to the outer boundary of the buffer zone in order to show this agreement better. The humps in this region are produced by the non-vanishing Lie derivatives of the transition functions. Observe that, as expected, these humps are smallest for TF 1,

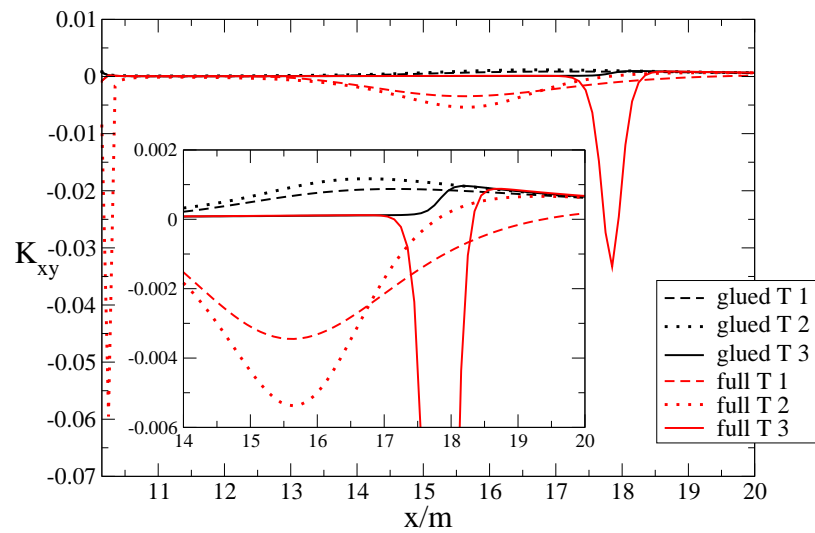


Fig. 4.5.  $xy$ -component of the extrinsic curvature along the  $x$ -axis, constructed via Eq. 4.54 (black) for TF 1 (dashed line), TF 2 (dotted line) and TF 3 (solid line.) We also plot this component constructed by direct differentiation of Eq. 4.53 (cyan, or light gray on black and white print) for TF 1 (dashed line), TF 2 (dotted line) and TF 3 (solid line.) The inset zooms to the region  $x \in \{15, 22\}$  so that the differences are more noticeable.

followed by TF 2 and 3. Our analysis suggests that if we performed matching to higher order, the agreement would be better and the size of the humps would decrease. The agreement is good for the curvatures constructed with TF 1, but the curvatures built with TF 2 and 3 have strong spikes roughly near the boundary of the buffer zone. These spikes arise because TF 2 violates the definition of a proper transition function, while TF 3 violates conditions (ii) and (iii) of Theorem 2.

We have then seen in this section how Theorems 1 and 2 can aid us in constructing transition functions. Even though we have not shown the error in the constraints, we have checked that this error presents the same features as those shown in Fig. 4.4. We have also seen the importance of restricting the family of transition functions to those that satisfy conditions (ii) and (iii) of Theorems 1 and 2, as well as the definition of a proper transition function. The construction of pure, or mixed, joined solutions can then be carried out with ease as long as transition functions are chosen that satisfy the conditions suggested here.

## 4.5 Conclusion

We studied the construction of joined solutions via transition functions. In particular, we focused on pure joined solutions, constructed by gluing analytical approximate solutions inside some buffer zone where they were both valid. The gluing process was accomplished via a weighted-linear combination of approximate solutions with certain transition functions. We constrained the family of allowed transition functions by imposing certain sufficient conditions that guarantee that the pure joined solution satisfies the Einstein equations to the same order as the approximations. With these conditions, we formulated and proved a theorem that ensures that the joined solution is indeed an approximate solution to the Einstein equations. We extended these conditions to projections of the joined solution onto a Cauchy hypersurface. We verified that the data on this hypersurface can itself be constructed as a weighted-linear combination with the same transition functions as those used for the joined solution. We proved that if these functions satisfy the same sufficient conditions, the data is guaranteed to solve the constraints of the Einstein equations to the same order as the approximations.

We explicitly verified these theorems numerically by considering a binary system of non-spinning black holes. The approximate solutions used were a post-Newtonian expansion in the far field and a perturbed Schwarzschild solution close to the black holes. We considered three different kinds of transition functions, two of which violated the conditions proposed in the theorems. The joined solutions constructed with these transition functions were shown to produce large violations to the Einstein equations. These violations were interpreted as the introduction of a matter-shell, whose stress-energy tensor was shown to be related to derivatives of the transition functions. The joined solution constructed with the transition function that did satisfy the conditions of the theorems was seen to introduce error comparable to that already contained in the approximate solutions. We further verified that projections of this joined solution to a Cauchy hypersurface can also be constructed as a weighted-linear combination of projections of approximate solutions with transition function. These joined projected solutions were seen to still satisfy the constraints of the theory to the same order as the

approximate solutions provided the transition functions satisfied the conditions of the theorems.

The glue proposed here to join approximate solutions has several applications to different areas of relativistic gravitation. Initial data for numerical simulations could, for example, be constructed once approximate solutions to the system have been found and asymptotically matched inside some buffer zone. In particular, initial data for a binary system of spinning black holes could be generated by asymptotically matching and gluing a tidally perturbed Kerr metric [104] to a post-Newtonian expansion (see [137].) One could also study the absorption of energy and angular momentum [34], as well as the motion of test particles [138], in the spacetime described by such pure joined solutions. Finally, one could extend the scheme developed here to formalize the construction of mixed joined solutions. Such solutions could, for example, be composed of a post-Newtonian metric glued to a numerically simulated metric or a semi-analytical approximate metric [125, 126, 139, 140]. Such mixed joined solutions could then be used to construct reliable waveform templates for extremely non-linear physical scenarios.

## Acknowledgments

We would like to thank Ben Owen for his continuous support and encouragement. We would also like to thank Martin Bojowald, Victor Taveras, Carlos Sopena and Ben Owen for reading this manuscript and providing useful comments. Finally, we would like to acknowledge the support of the Institute for Gravitational Physics and Geometry and the Center for Gravitational Wave Physics, funded by the National Science Foundation under Cooperative Agreement PHY-01-14375. This work was also supported by NSF grants PHY-02-18750, PHY-02-44788, PHY-02-45649, PHY-05-55628.

## Chapter 5

### Metric of a tidally perturbed spinning black hole

We explicitly construct the metric of a Kerr black hole that is tidally perturbed by the external universe in the slow-motion approximation. This approximation assumes that the external universe changes slowly relative to the rotation rate of the hole, thus allowing the parameterization of the Newman-Penrose scalar  $\psi_0$  by time-dependent electric and magnetic tidal tensors. This approximation, however, does not constrain how big the spin of the background hole can be and, in principle, the perturbed metric can model rapidly spinning holes. We first generate a potential by acting with a differential operator on  $\psi_0$ . From this potential we arrive at the metric perturbation by use of the Chrzanowski procedure in the ingoing radiation gauge. We provide explicit analytic formulae for this metric perturbation in Kerr coordinates, where the perturbation is finite at the horizon. This perturbation is parametrized by the mass and Kerr spin parameter of the background hole together with the electric and magnetic tidal tensors that describe the time evolution of the perturbation produced by the external universe. In order to make the metric accurate far away from the hole, these tidal tensors should be determined by asymptotically matching this metric to another one valid far from the hole. The tidally perturbed metric constructed here could be useful in initial data constructions to describe the metric near the horizons of a binary system of spinning holes. This perturbed metric could also be used to construct waveforms and study the absorption of mass and angular momentum by a Kerr black hole when external processes generate gravitational radiation.

#### 5.1 Introduction

Gravitational wave observatories, such as LIGO and VIRGO, have the potential to study black holes in the strong field regime<sup>1</sup> [2]. These black holes are expected to be immersed in a sea of gravitational perturbations that will alter the gravitational field of the background hole. Even though tidal perturbations are expected to be small relative to the background, they will be important in some astrophysical scenarios when attempting to provide an accurate description of the non-linear dynamical orbital evolution of

---

<sup>1</sup>This chapter is based on the following paper: N. Yunes and J. González, Phys. Rev. D **73**, 024010 (2006)

bodies around this background. The need for high accuracy in the description of the orbital evolution derives from the fact that gravitational wave observatories are extremely sensitive to the phase of the gravitational waves emitted by the system. Therefore, since this phase is directly related to the orbital evolution, in some astrophysical scenarios it is necessary to take these tidal effects into consideration.

The study of gravitational perturbations around Kerr black holes is important for several reasons. First, it is of astrophysical interest to study the flux of mass and angular momentum across a perturbed Kerr horizon [34, 141, 142, 143], which can be calculated through manipulations of the tidally perturbed metric computed in this paper. Although this flux might be small for equal-mass binaries, in extreme-mass ratio inspirals (EMRI) up to 5% of the total energy might be absorbed by the background hole. This absorption might slow down the orbital evolution increasing the duration of the gravitational wave signal [144, 138]. Space-based detectors, such as LISA, will be able to observe and measure the gravitational waveforms of EMRIs, since they have particularly low noise in the low frequency band where such inspirals are common. Therefore, precise knowledge of the gravitational waveform including the tidal perturbations effects might be important in data analysis [145]. Finally, the explicit formulae of this paper might be useful to compute initial data near the horizons of a binary system of spinning holes. For example, Refs. [28, 105] make use of such explicit formulae for the non-spinning case to construct initial data via asymptotic matching. This data might be useful to the numerical relativity community because it derives from an approximate solution to the Einstein equation and, thus, we expect it to accurately describe the gravitational field of the system up to uncontrolled remainders.

In this paper, we analytically construct explicit formulae for the metric of a tidally perturbed Kerr hole, where the perturbations of the external universe are assumed to vary slowly in a well-defined sense. Metric perturbations for non-spinning holes have been studied in Refs. [100, 99, 146, 28, 95] using the Regge-Wheeler formalism [147]. However, this method is difficult to implement for spinning holes because the metric will now depend on both radius and angle  $\theta$  in a non-trivial way, rendering the Einstein equations very difficult to solve. For this reason, we use the Chrzanowski procedure [148, 149] to construct the metric perturbation from the Newman-Penrose (NP) scalar  $\psi_0$ . This procedure allows us to calculate the metric in the so-called ingoing radiation gauge (IRG), which is suitable to study gravitational perturbations near the outer horizon ( $r_+$ ), since there the metric is transverse and traceless.

We will work in the slow-motion approximation, described in detail in Refs. [97, 98, 100, 99, 94, 146, 34, 95], where we assume that the rate of change of the curvature of the external universe is small relative to the rotation rate of the background black hole, which in principle could be extremal. The external universe is completely arbitrary in that sense, as long as it respects the slow-motion approximation. For example, in the case where the external universe is given by a second black hole in a quasicircular orbit around the background hole, this approximation is valid as long as their orbital separation is sufficiently large. In particular, this separation must be at least greater than the inner most stable circular orbit (ISCO)[85, 110], so that the binary is still in a quasicircular orbit. In that case, the curvature generated by the second hole would correspond to the external universe, which will change slowly as long as the orbital

velocity is sufficiently small. In this sense, the slow-motion approximation will hold for astrophysically realistic binaries as long as they are sufficiently separated.

Assuming this approximation to be valid, Poisson [34] has computed  $\psi_0$  in the neighborhood of a spinning hole. First, the Weyl tensor of the spacetime is re-expressed in terms of the electric and magnetic tidal tensors of the external universe. Using the slow-motion approximation, Poisson argues that these tensors will be spatially coordinate independent if evaluated at sufficiently large distances from the worldline of the hole. With this tensor, the asymptotic form of  $\psi_0$ , denoted by  $\tilde{\psi}_0$ , is computed far from the hole by projecting the Weyl tensor onto the Kinnersly tetrad. This scalar will be a combination of slowly varying functions of time, which will be parametrized via the electric and magnetic tidal tensors, and scalar functions of the spatial coordinates, which will be given by the tetrad. The asymptotic form of  $\psi_0$  now allows for the construction of an ansatz for  $\psi_0$ , which consists of its asymptotic form  $\tilde{\psi}_0$  multiplied by a set of undetermined function of radius  $R_m(r)$ . These functions must satisfy the asymptotic condition  $R_m \rightarrow 1$  as  $r \gg r_+$ , as well as the Teukolsky equation. This last condition is a differential constraint on  $R_m(r)$  which can be solved for explicitly, thus allowing for the full determination of  $\psi_0$ . In this manner, the final expression for  $\psi_0$  is obtained and is now valid close to the horizon as well, in particular, approaching the perturbations generated by the external universe sufficiently far from the hole's worldline.

Once  $\psi_0$  has been calculated, we can apply the Chrzanowski procedure to compute the metric perturbation, still in the slow-motion approximation. This calculation contains two parts: the computation of a potential ( $\Psi$ ) and the determination of the metric perturbation ( $h_{ab}$ ) from  $\Psi$ . In principle, one might think that it would be easier to try to compute  $h_{ab}$  directly from  $\psi_0$ . Chrzanowski [148] attempted this by applying a differential operator onto  $\psi_0$ . However, Wald [150] discovered that doing this leads to a physically different gravitational perturbation from that represented by  $\psi_0$ . Cohen and Kegeles [151] showed that by constructing a Hertz-like potential  $\Psi$  from  $\psi_0$  first and then applying Chrzanowski's differential operator to  $\Psi$  instead leads to the real metric perturbation. This is the procedure we will follow to construct the metric perturbation in this paper.

The construction of  $\Psi$  requires the action of a fourth order differential operator on  $\psi_0$ , where here we follow Ori [149]. This potential is simplified by the use of the slow-motion approximation that allows us to neglect any time derivatives of the electric and magnetic tidal tensors. Once  $\Psi$  is calculated, we can apply Chrzanowski's differential operator to this potential [151, 152]. In this manner, we compute the metric of a perturbed spinning hole from a tidal perturbation described by  $\psi_0$  in terms of tidal tensors. These tensors are unknown functions of time that represent the external universe and which should be determined by asymptotically matching this metric to another approximation valid far from the holes [28, 105].

The metric computed here, however, has a limited applicability given by the validity of the slow-motion approximation and the Chrzanowski procedure. The slow-motion approximation implies that we can neglect all derivatives of the tidal tensors. Furthermore, since we are working only to first non-vanishing order in this approximation, it suffices to consider only the quadrupolar perturbation of the metric, since the monopolar and dipolar perturbations are identically zero. In perturbation theory, any  $l$  mode in the

decomposition of the perturbation is one order larger than the  $l + 1$  mode. Therefore, any higher modes or couplings of the quadrupole to other modes will be of higher order. The Chrzanowski procedure also possesses a limited region of validity, given by a region sufficiently close to the event horizon so that the spatial distance from the horizon to the radius of curvature of the external universe is small. This restriction is because the Chrzanowski procedure builds the metric as a linear perturbation of the background and neglects any non-linear interactions with the external universe. In particular, this restriction implies that this metric cannot provide valid information on the dynamics of the entire spacetime. However, if this metric is asymptotically matched to another approximation that is valid far from the background hole, then the combined global metric will describe the the 3-manifold accurately.

We verify the validity of our calculations in several ways. First, we check that  $\psi_0$  indeed satisfies the Teukolsky equation. After computing  $\Psi$ , we also check that it satisfies the Teukolsky equation and the differential constraint that relates  $\Psi$  to  $\psi_0$ . Finally, we check that the metric perturbation constructed with this potential satisfies all of the Einstein equations to the given order. We further check that this perturbation is indeed transverse and traceless in the tetrad frame so that it is suitable for the study of gravitational perturbations near the horizon.

This paper is divided as follows. Sec. 5.2 describes the slow-motion approximation in detail, summarizes some relevant results from Ref. [34] and establishes some notation. Sec. 5.3 computes  $\Psi$  from  $\psi_0$  while Sec. 5.4 calculates  $h_{ab}$  from  $\Psi$ . Finally, Sec. 5.5 presents some conclusions and points toward future work. In the appendix, we provide an explicit transformation to Kerr-Schild coordinates that might be more amenable to numerical implementation.

In the remaining of the paper, we use geometrized units ( $G = 1, c = 1$ ) and the symbol  $O(a)$  stands for terms of order  $a$ , where  $a$  is dimensionless. Latin indices range from 0 to 3, where 0 is the time coordinate. The Einstein summation convention is assumed all throughout the paper, where repeated indices are to be summed over unless otherwise specified. Tetrad notation will be used, where indices with parenthesis refer to the tetrad and those without parenthesis to the components of the tensor. The relational symbol  $\sim$  stands for “asymptotic to” as defined in [30], while the symbols  $\ll$  and  $\gg$  are also to be understood in the asymptotic sense. In particular, note that if  $f(r)$  is valid for  $r \ll b$ , then this function is not valid as  $r \rightarrow b$ . In this paper we have relied heavily on the use of symbolic manipulation software, such as MAPLE and MATHEMATICA.

## 5.2 The slow-motion approximation and the NP scalar

In this section we will describe the slow-motion approximation in more detail and discuss the construction of  $\psi_0$  due to perturbations of the external universe. Both the slow-motion approximation and  $\psi_0$  have already been explained in detail and computed by Poisson in Ref. [34]. Therefore, here we follow this reference and summarize the most relevant results for this paper while establishing some notation.

Let us begin by discussing the slow-motion approximation. Consider a non-spinning black hole of mass  $m_1$  immersed in an external universe, with radius of curvature  $\mathcal{R}$ . This external universe could be given by any object that lives in the exterior of the

hole's horizon, such as a scalar field or another black hole. The slow-motion approximation requires that the external universe's length scales be much larger than the hole's scales. In other words, for the non-spinning case we must have  $m_1/\mathcal{R} \ll 1$ , since these are the only scales available.

For concreteness, let us assume that the external universe can be described by another object of mass  $M_{ext}$  and that our hole is in a quasicircular orbit around it. Then, we have

$$\frac{m_1}{\mathcal{R}} \sim \frac{m_1}{m_1 + M_{ext}} V^2, \quad V = \sqrt{\frac{m_1 + M_{ext}}{b}}, \quad (5.1)$$

where  $V$  is the orbital velocity and  $b$  is the orbital separation. There are two ways of enforcing  $m_1/\mathcal{R} \ll 1$ : the small-body approximation, where we let  $m_1/M_{ext} \ll 1$ ; and the slow-motion approximation, where  $V \ll 1$ . However, in a future paper we might want to asymptotically match the metric perturbation computed in this paper to a post-Newtonian (PN) expansion [3], which requires small velocities. For this reason, we will restrict our attention to the slow-motion approximation, which implies that we can only investigate systems that are sufficiently separated. The ISCO is not a well-defined concept for black hole binaries, but it has been estimated for non-spinning binary numerically [85, 110] to be given approximately by  $\omega_{ISCO}M/10$ , where  $M$  and  $\omega_{ISCO}$  are the total mass of the system and its angular velocity at the ISCO respectively. For spinning binaries the holes can get closer without plunging, where the value of the ISCO becomes a function of the spin parameter of the holes. Regardless of the type of binary system, the slow-motion approximation will hold as long as we consider systems that are separated by at least more than their ISCO so that they are still in a quasicircular orbit.

The above considerations suffice for non-spinning holes because there is only one length scale associated with it,  $m_1$ . However, for spinning ones we must also take into account the time scale associated with the intrinsic spin of the hole. The slow motion approximation does not constraint how large the spin of the background hole could be. However, in the standard theory, it is usually assumed that isolated holes will obey  $a < m_1$ , where  $a$  is the rotation parameter of the hole and  $m_1$  is its mass. If the previous inequality did not hold, then the hole would be tidally disrupted by centrifugal forces. When the background hole is surrounded by an accretion disk, however, some configuration might lead to a violation of the previous condition [153], but we will not consider those in this paper. Let us then define a dimensionless rotation parameter  $\chi = a/m_1$ , which is now restricted to  $0 < \chi < 1$ . The mass of the hole and this rotation parameter now define a new timescale, related to the rotation rate of the horizon and given by

$$\tau_H = \frac{1}{\Omega_H} = \frac{2m_1}{\chi} (1 + \sqrt{1 - \chi^2}), \quad (5.2)$$

where  $\Omega_H$  is the angular velocity of the hole's horizon [135]. The slow-motion approximation then requires this time scale to be much smaller than the time scale associated with the change of the radius of curvature of the external universe,  $\tau_{ext}$ , *i.e.*  $\tau_H/\tau_{ext} \ll 1$ . This condition then becomes

$$m_1/\mathcal{R} \ll \chi, \quad (5.3)$$

since  $\tau_{ext} \approx \mathcal{R}$ . We take the above relation as the precise definition of the slow-motion approximation for spinning black holes. Following the reasoning that lead to Eq. (5.1), we must then have  $V^2 \ll \chi$ , which, for a binary system, means that the orbital velocity of the system cannot exceed the rotation rate of the background hole. Thus, the slow-motion approximation implies that, to this order and for spinning holes, we can also only consider systems that are sufficiently separated and where the black holes have relatively rapid spins. This reasoning does not imply that the Schwarzschild limit is incompatible with the slow motion approximation. Actually, Poisson [34] showed that when computing certain quantities, such as  $\psi_0$ , this limit can be recovered if we work to higher order in the slow-motion approximation. The precise radius of convergence of the slow-motion approximation to first order remains unknown, but an approximate measure of how small a separation the approximation can tolerate will be studied in a later section.

Now that the slow-motion approximation has been explained in detail, let us proceed with the construction of  $\psi_0$ , which is defined by

$$\psi_0 = C_{abcd} l^a m^b l^c m^d, \quad (5.4)$$

where  $C_{abcd}$  is the Weyl tensor of the spacetime and  $l^a$  and  $m^a$  are the first and third tetrad vectors. This null vector  $m^a$  is not to be confused with the  $m$  that we will introduce later in this section to denote the angular mode of the perturbation. Poisson works with the Kinnersly tetrad in advanced Eddington-Finkelstein (EF) coordinates, also known as Kerr coordinates, which are well-behaved at the outer horizon, given by  $r_+ = m_1 + (m_1^2 - a^2)^{1/2}$ .

The calculation of  $\psi_0$  is based on making an ansatz guided by its asymptotic form far from the worldline of the hole but less than the radius of curvature of the external universe, *i.e.*  $r_+ \ll r \ll \mathcal{R}$ . In this region, the Weyl tensor can be decomposed into electric  $\mathcal{E}_{ab}$  and magnetic  $\mathcal{B}_{ab}$  tidal fields, which are slowly varying functions of advanced time  $v$  only. Thus, in this region, the only spatial coordinate dependence in  $\psi_0$  is given by the tetrad, namely

$$\tilde{\psi}_0 \sim - \sum_m z_m(v) {}_2Y_2^m(\theta, \phi), \quad (5.5)$$

where the tilde is to remind us that this quantity is the asymptotic form of  $\psi_0$  and where  ${}_2Y_2^m(\theta, \phi)$  are spin-weighted spherical harmonics, given by

$$\begin{aligned} {}_2Y_2^0(\theta, \phi) &= -\frac{3}{2} \sin^2 \theta, \\ {}_2Y_2^{\pm 1}(\theta, \phi) &= -\sin \theta (\cos \theta \mp 1) e^{\pm i\phi}, \\ {}_2Y_2^{\pm 2}(\theta, \phi) &= \frac{1}{4} (1 \mp 2 \cos \theta + \cos^2 \theta) e^{\pm 2i\phi}. \end{aligned} \quad (5.6)$$

In Eq. (5.5), the quantities  $z_m(v)$  are complex combinations of the tidal fields given by  $z_m(v) = \alpha_m(v) + i\beta_m(v)$ , where

$$\begin{aligned}
\alpha_0(v) &= \mathcal{E}_{11}(v) + \mathcal{E}_{22}(v), \\
\alpha_{\pm 1}(v) &= \mathcal{E}_{13}(v) \mp i\mathcal{E}_{23}(v), \\
\alpha_{\pm 2}(v) &= \mathcal{E}_{11}(v) - \mathcal{E}_{22}(v) \mp 2i\mathcal{E}_{12}(v), \\
\beta_0(v) &= \mathcal{B}_{11}(v) + \mathcal{B}_{22}(v), \\
\beta_{\pm 1}(v) &= \mathcal{B}_{13}(v) \mp i\mathcal{B}_{23}(v), \\
\beta_{\pm 2}(v) &= \mathcal{B}_{11}(v) - \mathcal{B}_{22}(v) \mp 2i\mathcal{B}_{12}(v).
\end{aligned} \tag{5.7}$$

Note that in this region,  $\psi_0$  is independent of radial coordinate.

With Eq. (5.5) at hand, Poisson makes an ansatz for the functional form of  $\psi_0$ , namely

$$\psi_0 = - \sum_m z_m(v) R_m(r) {}_2Y_2^m(\theta, \phi), \tag{5.8}$$

where  $R_m(r)$  is an undetermined function of radius that must satisfy  $R_m(r) \rightarrow 1$  as  $r \gg r_+$ . If Eq. (5.8) is inserted into the Teukolsky equation, one obtains a differential equation for  $R_m(r)$ . The angular part of the Teukolsky equation is automatically satisfied by the angular decomposition of  $\psi_0$  in spin-weighted spherical harmonics with eigenvalue  $E = 4$  (Eq. 2.10 in Ref. [154]). The spatial part of the Teukolsky equation yields a differential constraint for  $R_m(r)$  namely,

$$\left\{ x(1+x) \frac{d^2}{dx^2} + [3(2x+1) + 2im\gamma] \frac{d}{dx} + 4im\gamma \frac{2x+1}{x(1+x)} \right\} R_m(x) = 0, \tag{5.9}$$

where  $x$  is a rescaled version of the radial coordinate given by

$$x = \frac{r - r_+}{r_+ - r_-}, \tag{5.10}$$

and where the inner and outer horizons are given, respectively, by  $r_{\pm} = m_1^2 \pm (m_1^2 - a^2)^{1/2}$ . We should note that  $r_+$  is an event horizon, while  $r_-$  is actually an apparent horizon. Solving this equation [34] one obtains

$$R_m(r) = A_m x^{-2} (1+x)^{-2} F(-4, 1, -1 + 2im\gamma; -x), \tag{5.11}$$

where  $A_m$  is a normalization constant given by

$$A_m = -\frac{i}{6} m\gamma (1 + im\gamma) (1 + 4m^2 \gamma^2). \tag{5.12}$$

In Eq. (5.11), the function  $F(a, b, c; x)$  is the hypergeometric function

$$F(a, b, c; x) = \sum_{n=0}^{\infty} \frac{(a)_n (b)_n}{(c)_n} \frac{x^n}{n!}, \tag{5.13}$$

where  $(a)_n$  is the Pochhammer symbol defined as

$$\begin{aligned} (a)_n &= a(a+1)(a+2)\dots(a+n-1) = \frac{(a+n-1)!}{(a-1)!}, \\ (a)_0 &= 1. \end{aligned} \tag{5.14}$$

For the present case, the series gets truncated at the fourth power and we obtain

$$\begin{aligned} F(-4, 1, -1 + 2im\gamma; -x) &= \left( 1 + \frac{4}{2im\gamma - 1}x \right. \\ &+ \frac{6}{(2im\gamma - 1)im\gamma}x^2 + \frac{12}{(2im\gamma - 1)im\gamma(2im\gamma + 1)}x^3 \\ &\left. + \frac{12}{(2im\gamma - 1)im\gamma(2im\gamma + 1)(2im\gamma + 2)}x^4 \right), \end{aligned} \tag{5.15}$$

where  $\gamma$  is a constant given by

$$\gamma = \frac{a}{r_+ - r_-}. \tag{5.16}$$

In this manner, Poisson calculates  $\psi_0$ , which encodes the gravitational perturbations of the external universe on a spinning hole in the slow-motion approximation. The full expression for  $\psi_0$  is then given by

$$\begin{aligned} \psi_0 &= - \sum_{m \neq 0} B_m x^{-2} (1+x)^{-2} \left( 1 + \frac{4}{2im\gamma - 1}x + \frac{6}{(2im\gamma - 1)im\gamma}x^2 \right. \\ &+ \frac{12}{(2im\gamma - 1)im\gamma(2im\gamma + 1)}x^3 + \frac{12}{(2im\gamma - 1)im\gamma(2im\gamma + 1)(2im\gamma + 2)}x^4 \left. \right) \\ &\times {}_2Y_2^m(\theta, \phi), \end{aligned} \tag{5.17}$$

where we have used the final abbreviation

$$B_m = A_m z_m(v), \tag{5.18}$$

without summing over repeated indices here, to group all terms that are spatially coordinate independent. We have checked that Eq. (5.17) indeed satisfies the Teukolsky equation [154] for the  $s = 2$  mode that corresponds to this scalar. Note that, in this final expression, summation over the  $m = 0$  mode is removed because Poisson [34] has shown that it corresponds to the Schwarzschild limit and, thus, it contributes at a relative  $O(m_1/\mathcal{R})$  higher than all other modes. Also note that the final expression for  $\psi_0$  only contains the quadrupolar  $l = 2$  mode, once more because higher multipoles will be smaller by a relative factor of  $m_1/\mathcal{R}$  in the slow-motion approximation. For this reason, there are no mode couplings in the  $\psi_0$  presented above.

The time-evolution of the tidal perturbation will be exclusively governed by the electric and magnetic tidal fields. These tensors should be determined by asymptotically matching the metric perturbation generated by this  $\psi_0$  to another approximation valid far from the hole. However, in Refs. [94, 28, 105, 95] it has been shown that when the

external universe is given by another non-spinning black hole in a quasicircular orbit, these tensors scale approximately as

$$z_m \approx \frac{m_2}{b^3}, \quad (5.19)$$

where  $m_2$  is the mass of the other hole (the external universe) and  $b$  is the orbital separation (approximately equal to the radius of curvature of the external universe). Note that the factor of  $b^3$  in the denominator is necessary to make the tidal tensors dimensionally correct. Also note that in Eq. (5.19) we have neglected the time dependence of the tidal fields, which generally is given by a trigonometric function, since we are interested in a spatial hypersurface of constant time. For the case where the other hole is spinning, Eq. (5.19) will contain corrections proportional to  $\chi$ , but these terms will not change the overall scale of the tidal tensors.

Throughout the rest of the paper we will generate plots of physical quantities, such as  $\psi_0$ ,  $\Psi$  and  $h_{ab}$ . For the purpose of plotting, we will have to make two choices: one regarding the physical scenario that produces the perturbation of the external universe; and another regarding the parameters of the background black hole. As for the physical scenario, we will choose the external universe to be given by another orbiting black hole in a quasicircular orbit. This choice allows us to represent the tidal fields with the scaling given in Eq. (5.19). This scaling is not the exact functional form of the tidal fields and, therefore, the plots generated will not be exact. However, this scaling will allow us to provide plots accurate enough to study the general features of the global structure of the quantities plotted, as well as some local features near the horizons. Regarding the parameter choice, we will assume  $m_1 = m_2$ ,  $a = 0.99m_1$ , and  $b = 10m_1$ , where  $M = m_1 + m_2 = 1$  is the total mass. These choices are made in accordance with the slow-motion approximation, while making sure the system is not inside its ISCO. However, the formulae presented in this paper should apply to other choices of physical scenarios and background parameters as well, as long as these do not conflict with the slow motion approximation.

Given the chosen physical scenario, the formulae in this paper should apply to other mass ratios and separations, as long as the orbital velocity does not become too large. For the background parameters chosen, the orbital velocity is approximately  $V \approx 0.3$ , which indicates that, for fixed masses, we cannot reduce the orbital separation by much more without breaking the slow-motion approximation. However, since we provide explicit analytic formulae for all relevant physical quantities, we can estimate their error by considering the uncontrolled remainders, *i.e.* the neglected terms in the approximation. In particular, in a later section, we will see that the uncontrolled remainders are still much smaller than the perturbation itself even at  $b = 10M$  as long as we restrict ourselves to field points sufficiently near the outer horizon of the background hole.

In Fig.5.1 we plot the real part of  $\psi_0$  with the plotting choices described earlier. Observe that as  $r$  becomes large the scalar asymptotes to a constant given by  $\tilde{\psi}_0$ . Also observe that the functional behavior of the scalar is drastically different as  $r$  becomes small. In this figure, as well as in future figures, we have chosen to include an inset where we zoom to a region close to the horizons, so that we can observe its local and global

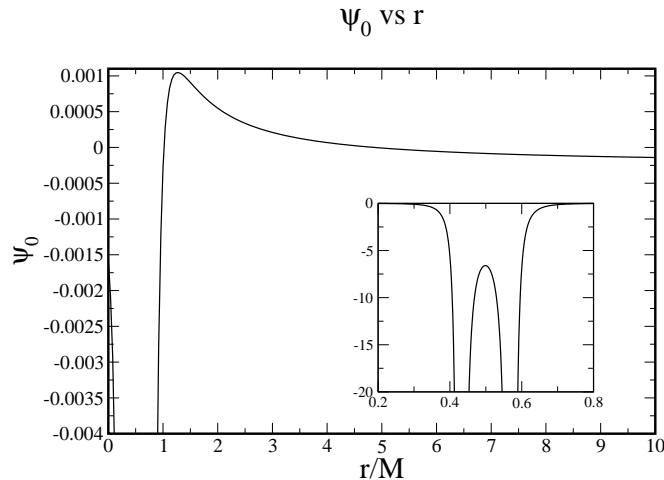


Fig. 5.1. Plot of the real part of the NP scalar  $\psi_0$  along the  $x$ -axis with the plotting parameters described in Sec. 5.2.

behavior. For the orbital parameter chosen, the inner and outer horizons are given by  $r_- \approx 0.43M$  and  $r_+ \approx 0.57M$ . Observe from the inset in Fig. 5.1 that the scalar diverges at the horizons and as  $r \rightarrow 0$ , which is due to the choice of tetrad. Finally, observe that, except for where it diverges, the real part of  $\psi_0$  is of  $O(V^2)$  in the entire 3-manifold.

### 5.3 The potential

In this section we will use  $\psi_0$  to construct the potential  $\Psi$  by acting some differential operators on the NP scalar. This potential must satisfy the vacuum Teukolsky equation for the  $s = -2$  mode together with the differential equation

$$\psi_0 = D^4[\bar{\Psi}], \quad (5.20)$$

where the overbar stands for complex conjugation and where the differential operator is given by  $D = l^a \partial_a$  [150, 155, 149].

Ori [149] has shown that the above differential equations can be inverted with use of the Teukolsky-Starobinsky relation to obtain

$$\Psi = \frac{1}{p} \Delta^2 (D^\dagger)^4 [\Delta^2 \bar{\psi}_0], \quad (5.21)$$

where here  $\Delta$  is given by

$$\Delta = r^2 - 2m_1 r + a^2, \quad (5.22)$$

while  $p$  is a constant that for the time-independent case reduces to

$$p = \left[ l(l+1) - s^2 + |s| \right]^2 \left[ l(l+1) - s^2 + |s| + 2 \right]^2. \quad (5.23)$$

In our case, since  $s$  and  $l$  refer to  $\psi_0$ ,  $s = 2$  and  $l = 2$  so that this constant becomes  $p = 576$ .

The differential operator  $D^\dagger$  is given in spherical Brill-Lindquist (BL) coordinates  $(t_{BL}, r, \theta, \phi_{BL})$  by

$$D_{BL}^\dagger = \partial_r - \frac{a}{\Delta} \partial_{\phi_{BL}}, \quad (5.24)$$

neglecting any time dependence, since time derivatives will only contribute at a higher order. In order to compute  $\Psi$  in Kerr coordinates, we must transform the above differential operator. The transformation between Kerr and BL coordinates is given by

$$\begin{aligned} dv &= dt_{BL} + dr_{BL} \left( \frac{2m_1 r}{\Delta} + 1 \right), \\ dr &= dr_{BL}, \\ d\theta &= d\theta_{BL}, \\ d\phi &= d\phi_{BL} + dr_{BL} \frac{a}{\Delta}. \end{aligned} \quad (5.25)$$

After transforming the differential operator  $D_{BL}^\dagger$  we obtain

$$D^\dagger = \partial_r, \quad (5.26)$$

because the  $dr_{BL}/d\phi$  term in the transformation cancels the  $\phi$  dependence. Note that  $r$  and  $\theta$  do not change in this transformation and, thus,  $\Delta$  remains unchanged. Also note that  $\Psi$  is a scalar constructed from differential operators on  $\psi_0$  and, since the latter is a scalar,  $\Psi$  will also be gauge invariant.

Before plugging in Eq. (5.17) into Eq. (5.21) to compute  $\Psi$ , let us try to simplify these expressions. In the previous section, we defined the inner and outer horizons  $r_+$  and  $r_-$ , as well as the new variable  $x$ . We can invert the definition of  $x$  so that it becomes a definition for  $r$  as a function of  $x$  and then insert this into Eq. (5.22). We then obtain

$$\Delta = 4\eta x(1+x), \quad (5.27)$$

where we have defined  $\eta = m_1^2 - a^2$ . It is clear now that when we combine the square of this expression with Eq. (5.17) some cancellations will occur that will simplify all future calculations.

We are now ready to compute  $\Psi$ , but first let us rewrite the function we want to differentiate, namely

$$\Delta^2 \bar{\psi}_0 = \sum_{m \neq 0} \bar{C}_m \bar{F}(x) {}_2\bar{Y}_2^m(\theta, \phi_{BL}), \quad (5.28)$$

where  $F(x)$  is shorthand for the aforementioned hypergeometric function and where  $C_m$  is a new function of advanced time only given by

$$C_m = -16B_m\eta^2 = -16A_m\eta^2 z_m(v). \quad (5.29)$$

Note that the angular dependence occurs in the spherical harmonics, while the only  $x$  dependence is in the hypergeometric function. We can transform the  $D^\dagger$  operator to  $x$  space to obtain

$$D^\dagger = \partial_r = \frac{1}{2\eta^{1/2}}\partial_x. \quad (5.30)$$

Applying all these simplifications,  $\Psi$  becomes

$$\Psi = \frac{\Delta^2}{576} \sum_{m \neq 0} \bar{C}_m {}_2\bar{Y}_2^m(\theta, \phi) \frac{1}{16\eta^2} \partial_x^4 [\bar{F}(x)]. \quad (5.31)$$

We can now apply all derivatives to obtain

$$\Psi = \frac{\Delta^2}{576} \sum_{m \neq 0} \bar{C}_m {}_2\bar{Y}_2^m(\theta, \phi) \frac{\bar{F}^{(4)}}{16\eta^2}, \quad (5.32)$$

where we have used the shorthand  $\bar{F}^{(n)}$  which stands for the  $n$ th derivative of the complex conjugate of the hypergeometric function. This derivative is given by

$$\bar{F}^{(4)} = \frac{288}{(2im\gamma + 1)im\gamma(-2im\gamma + 1)(-2im\gamma + 2)}, \quad (5.33)$$

Note that we can reexpress the constant  $\gamma$  in terms of  $\eta$  as  $\gamma = a/(2\eta^{1/2})$ . Interestingly this constant combines with  $\bar{C}_m$  to return an overall constant that is purely real so that  $\Psi$  is given by

$$\Psi = -\frac{1}{24}\Delta^2 \sum_{m \neq 0} Y^m(\theta) e^{-im\phi} \bar{z}_m(v), \quad (5.34)$$

where here  $Y^m$  stands for the  $l = 2$  spherical harmonics with zero  $\phi$  dependence. We have checked that the potential of Eq. (5.34) indeed satisfies the definition of Eq. (5.20) as well as the Teukolsky equation for the  $s = -2$  mode with angular eigenvalue  $E = 10$ . Note that  $\Psi$  has units of mass squared because the electric and magnetic tidal fields scale as the inverse of the mass squared. Furthermore, note that eventhough  $\psi_0$  is singular at the horizon,  $\Psi$  is finite and actually vanishes there.

Next, we proceed to decompose  $\Psi$  into real and imaginary parts. The potential contains 2 complex terms, namely the  $\phi$  part of the spherical harmonics and the electric

and magnetic tidal tensors. Decomposing  $\Psi$  we obtain

$$\begin{aligned}\Psi_R &= -\frac{\Delta^2}{24} \sum_{m \neq 0} Y^m (\alpha_m(v) \cos m\phi - \beta_m(v) \sin m\phi), \\ \Psi_I &= \frac{\Delta^2}{24} \sum_{m \neq 0} Y^m (\alpha_m(v) \sin m\phi + \beta_m(v) \cos m\phi).\end{aligned}\tag{5.35}$$

Note that the entire radial dependence is encoded in  $\Delta^2$ , whereas the angular dependence is hidden in the spherical harmonics. The time dependence occurs only in the tidal fields that should be determined via asymptotic matching, as mentioned previously. This is the potential in Kerr coordinates associated with the  $\psi_0$  calculated in the previous section in the slow-motion approximation.

In Fig. 5.2 we plot  $\Psi_R$  with the plotting choices described in Sec. 5.2. Observe from

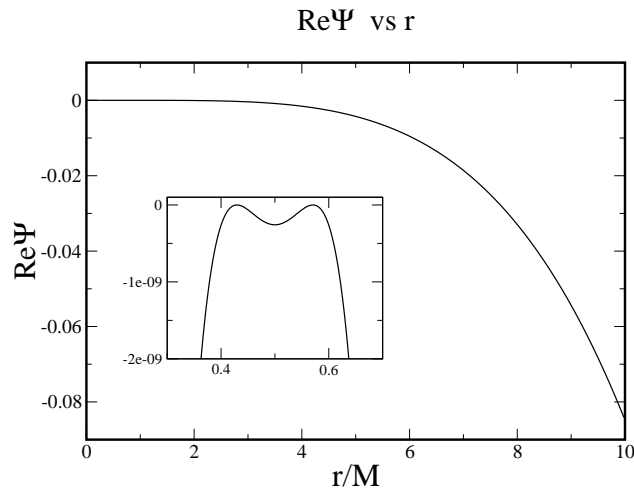


Fig. 5.2. Plot of the potential  $\Psi_R$  along the  $x$ -axis with the plotting parameters described in Sec. 5.2.

the inset that the potential has nodes at both horizons. Also observe that the potential does not asymptote to a constant, but instead it grows quartically. This growth is due to the factor of  $\Delta^2$  that dominates at large radius. Finally, note that the potential is still of  $O(V^2)$  for radii sufficiently close to the hole (roughly for  $r < 8m$ ).

## 5.4 The metric perturbation

In this section we compute the metric perturbation by applying Chrzanowski's differential operator to the potential calculated in the previous section. The full metric of the spacetime is given by

$$g_{ab} = g_{ab}^B + h_{ab}, \quad (5.36)$$

where  $g_{ab}^B$  is the background metric and  $h_{ab}$  is the perturbation. Since  $\psi_0$  and  $\Psi$  were computed in Kerr coordinates, the background should also be in this coordinate system. This background is given then by

$$\begin{aligned} g_{00}^B &= - \left( 1 - \frac{2m_1 r}{\Sigma} \right), \\ g_{01}^B &= 1, \\ g_{03}^B &= - \frac{m_1 r}{\Sigma} (2a \sin^2 \theta), \\ g_{13}^B &= -a \sin^2 \theta, \\ g_{22}^B &= \Sigma, \\ g_{33}^B &= (r^2 + a^2) \sin^2 \theta + \frac{2m_1 r}{\Sigma} (a^2 \sin^4 \theta), \end{aligned} \quad (5.37)$$

where  $m_1$  is the mass of the background black hole,  $a$  is its spin parameter, related to the angular momentum vector by  $\vec{S} = m\vec{a}$ , and where  $\Sigma = r^2 + a^2 \cos^2 \theta$ .

Let us now construct the metric perturbation. We will work with the form of the differential operator presented in Ref. [152], namely

$$\begin{aligned} h_{ab} &= 2\Re \left( \left\{ -l_a l_b (\delta + \bar{\alpha} + 3\beta - \tau)(\delta + 4\beta + 3\tau) \right. \right. \\ &\quad \left. \left. - m_a m_b (D - \rho)(D + 3\rho) + l_{(a} m_{b)} [(D - 2i\rho_I) \right. \right. \\ &\quad \left. \left. (\delta + 4\beta + 3\tau) + (\delta + 3\beta - \bar{\alpha} - \bar{\pi} - \tau) \right. \right. \\ &\quad \left. \left. (D + 3\rho) \right] \right\} \Psi \right), \end{aligned} \quad (5.38)$$

where we have replaced  $\bar{\rho} - \rho = -2i\rho_I$ . The metric perturbation constructed in this fashion will be in the ingoing radiation gauge (IRG), which is defined by the conditions

$$h_{ll} = h_{ln} = h_{lm} = h_{l\bar{m}} = h_{m\bar{m}} = 0. \quad (5.39)$$

In Eq. (5.38) there are terms that depend on the differential operators  $D = l^a \partial_a$  and  $\delta = m^a \partial_a$ , which in turn depends on the tetrad. To be consistent, we will continue

to work with the Kinnersly tetrad in Kerr coordinates given by

$$\begin{aligned}
e_{(1)}^a &= l^a = \left( 2\frac{r^2 + a^2}{\Delta}, 1, 0, \frac{2a}{\Delta} \right), \\
e_{(2)}^a &= n^a = \left( 0, -\frac{\Delta}{2\Sigma}, 0, 0 \right). \\
e_{(3)}^a &= m^a = \frac{1}{\sqrt{2}(r + ia \cos \theta)} \left[ ia \sin \theta, 0, 1, \frac{i}{\sin \theta} \right], \\
e_{(4)}^a &= \bar{m}^a,
\end{aligned} \tag{5.40}$$

where the overbar stands for complex conjugation. Note that the  $m^a$  vector is the same as the one in BL coordinates, but  $l^a$  and  $n^a$  are different. The differential operators associated with this tetrad in Kerr coordinates are

$$\begin{aligned}
D &= \partial_r + \frac{2a}{\Delta} \partial_\phi \\
\delta &= \frac{1}{\sqrt{2}(r + ia \cos \theta)} \left( \partial_\theta + \frac{i}{\sin \theta} \partial_\phi \right),
\end{aligned} \tag{5.41}$$

where once more we neglect the time derivatives by use of the slow motion approximation. The covariant form of the tetrad in these coordinates is given by

$$\begin{aligned}
l_a &= l_a^R = \left( 1, -\frac{2\Sigma}{\Delta}, 0, -a \sin^2 \theta \right), \\
n_a &= n_a^R = \frac{1}{2\Sigma} \left( \Delta, 0, 0, -a\Delta \sin^2 \theta \right), \\
m_a^R &= \frac{a \sin \theta}{\sqrt{2}\Sigma} \left[ a \cos \theta, 0, -\frac{r\Sigma}{a \sin \theta}, -\cos \theta (r^2 + a^2) \right], \\
m_a^I &= \frac{1}{\sqrt{2}\Sigma} \left[ ar \sin \theta, 0, a\Sigma \cos \theta, -r \sin \theta (r^2 + a^2) \right],
\end{aligned} \tag{5.42}$$

where the superscript  $I$  and  $R$  stand for the imaginary and real parts respectively. One can show that if this tetrad is used we can recover the background metric  $g_{ab}^B$  with the formula  $g_{ab}^B = 2l_{(a}n_{b)} + 2m_{(a}\bar{m}_{b)}$ .

Eq. (5.38) contains terms that depend on the spin coefficients of the background [156]. These coefficients, also called Ricci rotation coefficients for the case where the tetrad is non-null, are simply contraction of the tetrad with its derivatives. In the tetrad formalism, these quantities can also be related to the Riemann tensor. Let us decompose

the spin coefficients into real and imaginary parts, *i.e.*

$$\begin{aligned}
\rho_R &= -\frac{r}{\Sigma}, & \rho_I &= -\frac{a}{\Sigma} \cos \theta, \\
\beta_R &= \frac{\sqrt{2}}{4} \frac{r}{\Sigma} \cot \theta, & \beta_I &= -\frac{\sqrt{2}}{4} \frac{a}{\Sigma} \cot \theta \cos \theta, \\
\pi_R &= -\sqrt{2} \frac{a^2}{\Sigma^2} r \sin \theta \cos \theta, \\
\pi_I &= \frac{\sqrt{2}}{2} \frac{a}{\Sigma^2} (r^2 - a^2 \cos^2 \theta) \sin \theta, & \tau_I &= -\frac{\sqrt{2}}{2} \frac{a}{\Sigma} \sin \theta, \\
\alpha_R &= -\sqrt{2} \frac{a^2}{\Sigma^2} r \sin \theta \cos \theta - \frac{\sqrt{2}}{4} \frac{r}{\Sigma} \cot \theta, \\
\alpha_I &= \frac{\sqrt{2}}{2} \frac{a}{\Sigma^2} \sin \theta (r^2 - a^2 \cos^2 \theta) - \frac{\sqrt{2}}{4} \frac{a}{\Sigma} \cot \theta \cos \theta.
\end{aligned} \tag{5.43}$$

These spin coefficients are the same as those obtained with the Kinnersly tetrad in BL coordinates. This invariance is due to the fact that the spin coefficients are only tetrad dependent but still gauge invariant.

We will split Eq. (5.38) into 4 terms in order to make calculations more tractable. The split is as follows: the term proportional to  $l_a l_b$  will be denoted term *A*; the term proportional to  $m_a m_b$  will be referred to as term *B*; the first half of the term proportional to  $l_{(a} m_{b)}$  will be denoted term *C*; and the remaining of this term will be referred to as term *D*. In this manner we have

$$\begin{aligned}
h_{ab}^A &= [-l_a l_b (\delta + \bar{\alpha} + 3\beta - \tau)(\delta + 4\beta + 3\tau)] \Psi, \\
h_{ab}^B &= [-m_a m_b (D - \rho)(D + 3\rho)] \Psi, \\
h_{ab}^C &= [l_{(a} m_{b)} (D - 2i\rho_I)(\delta + 4\beta + 3\tau)] \Psi, \\
h_{ab}^D &= [l_{(a} m_{b)} (\delta + 3\beta - \bar{\alpha} - \bar{\pi} - \tau)(D + 3\rho)] \Psi,
\end{aligned} \tag{5.44}$$

and the full metric perturbation is given by

$$h_{ab} = 2\Re(h_{ab}^A + h_{ab}^B + h_{ab}^C + h_{ab}^D). \tag{5.45}$$

With this split we can now proceed to simplify each expression more easily. One such simplification is to operate with the differential operators. Expanding all terms we

obtain

$$\begin{aligned}
h_{ab}^A &= -l_a l_b \left[ \delta^2 \Psi + \Psi (4\delta\beta + 3\delta\tau) + (7\beta + 2\tau + \bar{\alpha}) \delta\Psi + (\bar{\alpha} + 3\beta - \tau) (4\beta + 3\tau) \Psi \right], \\
h_{ab}^B &= -m_a m_b \left[ D^2 \Psi + 2\rho D\Psi + 3\Psi D\rho - 3\rho^2 \Psi \right], \\
h_{ab}^C &= l_{(a} m_{b)} \left[ D\delta\Psi + 4\Psi D\beta + 3\Psi D\tau + (4\beta + 3\tau) D\Psi - 2i\rho_I (4\beta + 3\tau) \Psi - 2i\rho_I \delta\Psi \right], \\
h_{ab}^D &= l_{(a} m_{b)} \left[ \delta D\Psi + 3\Psi \delta\rho + 3\rho \delta\Psi + (3\beta - \bar{\pi} - \tau - \bar{\alpha}) D\Psi + (3\beta - \bar{\pi} - \tau - \bar{\alpha}) \Psi \right].
\end{aligned}
\tag{5.46}$$

These expressions give the metric perturbation in terms of the action of the differential operators on the spin coefficients and the potential.

#### 5.4.1 Action of the Differential Operators

In order to provide explicit formulae for the metric perturbation we must investigate how the differential operators act on the spin coefficients and on the potential. Let us first concentrate on the action of the differential operators on the spin coefficients. After taking the necessary derivatives and decomposing the result into imaginary and real parts, we obtain

$$\begin{aligned}
D\rho &= D_{\rho,R} + iD_{\rho,I} = \frac{r^2 - a^2 \cos^2 \theta}{\Sigma^2} + i \left[ 2 \frac{ra}{\Sigma^2} \cos \theta \right], \\
D\tau &= iD_{\tau,I} = i\sqrt{2} \frac{ar}{\Sigma^2} \sin \theta, \\
D\beta &= D_{\beta,R} + iD_{\beta,I} = -\frac{\sqrt{2} \cot \theta (r^2 - a^2 \cos^2 \theta)}{4 \Sigma^2} + i \left[ \frac{\sqrt{2} ra}{2 \Sigma^2} \cot \theta \cos \theta \right], \\
\delta\rho &= \delta_{\rho,R} + i\delta_{\rho,I} = -\frac{\sqrt{2} a^2}{2 \Sigma^2} \sin \theta \cos \theta \\
&\quad + i \left[ \frac{\sqrt{2} ar}{2 \Sigma^2} \sin \theta \right], \\
\delta\beta &= \delta_{\beta,R} + i\delta_{\beta,I} \\
&= \frac{a^4 \cos^6 \theta - r^4 + 3r^2 a^2 \cos^2 \theta - 3 \cos^4 \theta r^2 a^2}{4 \Sigma^3 \sin^2 \theta} \\
&\quad + i \left[ ra \cos \theta \frac{3a^2 \cos^4 \theta - r^2 \cos^2 \theta + 3r^2}{4 \sin^2 \theta \Sigma^3} - ra \cos \theta \frac{a^2 \cos^2 \theta}{4 \sin^2 \theta \Sigma^3} \right], \\
\delta\tau &= \delta_{\tau,R} + i\delta_{\tau,I} \\
&= \frac{1}{2} a^2 \cos^2 \theta \frac{-r^2 + a^2 \cos^2 \theta - 2a^2}{\Sigma^3} + i \left[ \frac{1}{2} ra \cos \theta \frac{-r^2 + a^2 \cos^2 \theta - 2a^2}{\Sigma^3} \right].
\end{aligned}
\tag{5.47}$$

We now need to act with the differential operators on the potential itself. We can separate the  $\phi$  dependence from these operators to obtain

$$\begin{aligned}
D\Psi &= D_m \Psi, \\
\delta\Psi &= \delta_m \Psi, \\
(D\delta)\Psi &= (D\delta)_m \Psi, \\
(\delta D)\Psi &= (\delta D)_m \Psi
\end{aligned} \tag{5.48}$$

where

$$\begin{aligned}
D_m &= \partial_r - 2i\frac{ma}{\Delta} = \frac{1}{2\eta^{1/2}}\partial_x - \frac{ima}{2\eta} \frac{1}{x(1+x)}, \\
\delta_m &= \delta_0 \left( \partial_\theta + \frac{m}{\sin\theta} \right), \\
\delta_0 &= \frac{-\bar{\rho}}{\sqrt{2}}, \quad \delta_{0,r} = -\sqrt{2}\delta_0^2.
\end{aligned} \tag{5.49}$$

We can also compute the square of these operators acting on  $\Delta^2 Y^m$ , where  $Y^m$  stands for the spherical harmonics with no  $\phi$  dependence. Doing so we obtain

$$\begin{aligned}
D_m^2 [\Delta^2] &= 8(r - m_1)^2 + 4\Delta - 4m^2 a^2 - 12ima(r - m_1), \\
\delta_m^2 [Y^m] &= \delta_0^2 Y_{,\theta\theta}^m + \left[ \delta_0 \left( \frac{ia \sin\theta}{\sqrt{2}\Sigma} + \frac{\delta_0}{\Sigma} a^2 \sin 2\theta \right) + 2\delta_0^2 \frac{m}{\sin\theta} \right] Y_{,\theta}^m \\
&\quad + \left[ \frac{\delta_0 m}{\sin\theta} \left( \frac{ia \sin\theta}{\sqrt{2}\Sigma} + \frac{\delta_0}{\Sigma} a^2 \sin 2\theta \right) + \frac{\delta_0^2 m}{\sin^2\theta} (m - \cos\theta) \right] Y^m, \\
(\delta D)_m [\Delta^2 Y^m] &= \delta_0 \left( Y_{,\theta}^m + \frac{m}{\sin\theta} Y^m \right) [4\Delta(r - m_1) - 2ima\Delta], \\
(D\delta)_m [\Delta^2 Y^m] &= -\sqrt{2}\delta_0^2 \Delta^2 \left( Y_{,\theta}^m + \frac{m}{\sin\theta} Y^m \right) + (\delta D)_m [\Delta^2 Y^m],
\end{aligned} \tag{5.50}$$

where the commas stand for partial differentiation.

We now have all the ingredients to compute the action of the differential operators on the potential. Doing so we obtain

$$\begin{aligned}
D_m \Psi &= -\frac{\Delta}{12} \sum_{m \neq 0} Y^m \bar{z}_m e^{-im\phi} [2(r - m_1) - ima], \\
\delta_m \Psi &= -\frac{\Delta^2}{24} \sum_{m \neq 0} \left( Y_{,\theta}^m + \frac{m}{\sin \theta} Y^m \right) e^{-im\phi} \bar{z}_m \delta_0, \\
(D_m)^2 \Psi &= -\frac{1}{6} \sum_{m \neq 0} Y^m e^{-im\phi} \bar{z}_m \left[ 2(r - m_1)^2 + \Delta - m^2 a^2 - 3ima(r - m_1) \right], \\
(\delta_m)^2 \Psi &= -\frac{\Delta^2}{24} \sum_{m \neq 0} e^{-im\phi} \bar{z}_m \left\{ \delta_0^2 Y_{,\theta\theta}^m + \left[ \delta_0 \frac{ia \sin \theta}{\sqrt{2}\Sigma} \right. \right. \\
&\quad \left. \left. + \delta_0^2 \left( \frac{a^2 \sin 2\theta}{\Sigma} + 2 \frac{m}{\sin \theta} \right) \right] Y_{,\theta}^m + \left[ \frac{\delta_0 m}{\sin \theta} \right. \right. \\
&\quad \left. \left. \left( \frac{ia \sin \theta}{\sqrt{2}\Sigma} + \frac{\delta_0}{\Sigma} a^2 \sin 2\theta \right) + \frac{\delta_0^2 m}{\sin^2 \theta} (m - \cos \theta) \right] Y^m \right\}, \\
(\delta D)_m \Psi &= -\frac{\Delta}{12} \sum_{m \neq 0} \left( Y_{,\theta}^m + \frac{m}{\sin \theta} Y^m \right) e^{-im\phi} \bar{z}_m [2\delta_0(r - m_1) - \delta_0 ima], \\
(D\delta)_m \Psi &= (\delta D)_m \Psi + \frac{\sqrt{2}}{24} \Delta^2 \sum_{m \neq 0} \left( Y_{,\theta}^m + \frac{m}{\sin \theta} Y^m \right) e^{-im\phi} \bar{z}_m \delta_0^2, \tag{5.51}
\end{aligned}$$

In order to complete the calculation, we need to provide explicit formulae for the first and second derivatives of the spherical harmonics. These derivatives are given by

$$\begin{aligned}
Y_{,\theta}^{\pm 1} &= -2 \cos^2 \theta + 1 \pm \cos \theta, \\
Y_{,\theta\theta}^{\pm 1} &= \sin \theta (4 \cos \theta \mp 1), \\
Y_{,\theta}^{\pm 2} &= -\frac{1}{2} \sin \theta (\cos \theta \mp 1), \\
Y_{,\theta\theta}^{\pm 2} &= -\cos^2 \theta \pm \frac{1}{2} \cos \theta + \frac{1}{2}. \tag{5.52}
\end{aligned}$$

Note that the spherical harmonics and all of its derivatives are purely real.

#### 5.4.2 Decomposition into real and imaginary parts

We will conclude this section by explicitly taking the real part of the metric perturbation, so as to have explicit formulae for the metric in terms of only the real and imaginary parts of the spin coefficients, the potential and the action of the differential operators on these quantities.

Before decomposing Eq. (5.46), however, we must decompose the action of the differential operators on the potential, *i.e.* Eq. (5.51). Let us first note that the action

of any differential operator on the potential always contains the product of 3 complex terms, the first 2 of which are always  $e^{-im\phi}$  and  $\bar{z}_m$ . The third term varies depending on the differential operator. Let us define the third term with superscripts as

$$\begin{aligned}
c^{(D)} &= -\frac{\Delta}{12} \sum_{m \neq 0} Y^m [2(r - m_1) - ima], \\
c^{(\delta)} &= -\frac{\Delta^2}{24} \sum_{m \neq 0} \left( Y_{,\theta}^m + \frac{m}{\sin \theta} Y^m \right) \delta_0, \\
c^{(D^2)} &= -\frac{1}{6} \sum_{m \neq 0} Y^m \left[ 2(r - m_1)^2 + \Delta - m^2 a^2 - 3ima(r - m_1) \right], \\
c^{(\delta)^2} &= -\frac{\Delta^2}{24} \sum_{m \neq 0} \left\{ \delta_0^2 Y_{,\theta\theta}^m + \left[ \delta_0 \frac{ia \sin \theta}{\sqrt{2}\Sigma} \right. \right. \\
&\quad \left. \left. + \delta_0^2 \left( \frac{a^2 \sin 2\theta}{\Sigma} + 2 \frac{m}{\sin \theta} \right) \right] Y_{,\theta}^m + \left[ \frac{\delta_0 m}{\sin \theta} \right. \right. \\
&\quad \left. \left. \left( \frac{ia \sin \theta}{\sqrt{2}\Sigma} + \frac{\delta_0}{\Sigma} a^2 \sin 2\theta \right) + \frac{\delta_0^2 m}{\sin^2 \theta} (m - \cos \theta) \right] Y^m \right\}, \\
c^{(\delta D)} &= -\frac{\Delta}{12} \sum_{m \neq 0} \left( Y_{,\theta}^m + \frac{m}{\sin \theta} Y^m \right) [2\delta_0(r - m_1) - \delta_0 ima], \\
c^{(D\delta)} &= c^{(\delta D)} + \frac{\sqrt{2}}{24} \Delta^2 \sum_{m \neq 0} \left( Y_{,\theta}^m + \frac{m}{\sin \theta} Y^m \right) \delta_0^2, \tag{5.53}
\end{aligned}$$

In general, if we want to decompose the product of 3 complex quantities  $a$ ,  $b$  and  $c$  we will obtain

$$\begin{aligned}
(abc)_R &= c_R (a_R b_R - a_I b_I) - c_I (a_R b_I + a_I b_R), \\
(abc)_I &= c_R (a_R b_I + a_I b_R) + c_I (a_R b_R - a_I b_I). \tag{5.54}
\end{aligned}$$

Since we have identified  $a = e^{-im\phi}$  and  $b = \bar{z}_m$ , their real and imaginary parts are  $a_R = \cos m\phi$ ,  $a_I = -\sin m\phi$ ,  $b_R = \alpha_m$  and  $b_I = -\beta_m$ . Finally, if we further decompose

$c$  we obtain

$$\begin{aligned}
c_R^{(D)} &= -\frac{\Delta}{6} \sum_{m \neq 0} Y^m (r - m_1), \\
c_I^{(D)} &= \frac{\Delta}{12} \sum_{m \neq 0} Y^m m a, \\
c_R^{(\delta)} &= -\frac{\Delta^2}{24} \sum_{m \neq 0} \left( Y_{,\theta}^m + \frac{m}{\sin \theta} Y^m \right) \delta_{0,R}, \\
c_I^{(\delta)} &= -\frac{\Delta^2}{24} \sum_{m \neq 0} \left( Y_{,\theta}^m + \frac{m}{\sin \theta} Y^m \right) \delta_{0,I}, \\
c_R^{(D^2)} &= -\frac{1}{6} \sum_{m \neq 0} Y^m \left[ 2(r - m_1) + \Delta - m^2 a^2 \right], \\
c_I^{(D^2)} &= \frac{1}{2} \sum_{m \neq 0} Y^m m a (r - m_1), \\
c_R^{(\delta D)} &= -\frac{\Delta}{12} \sum_{m \neq 0} \left( Y_{,\theta}^m + \frac{m}{\sin \theta} Y^m \right) \left[ 2\delta_{0,R}(r - m_1) + \delta_{0,I} m a \right], \\
c_I^{(\delta D)} &= -\frac{\Delta}{12} \sum_{m \neq 0} \left( Y_{,\theta}^m + \frac{m}{\sin \theta} Y^m \right) \left[ 2\delta_{0,I}(r - m_1) - \delta_{0,R} m a \right], \\
c_R^{(D\delta)} &= c_R^{(\delta D)} + \frac{\sqrt{2}}{24} \Delta^2 \sum_{m \neq 0} \left( Y_{,\theta}^m + \frac{m}{\sin \theta} Y^m \right) \left( \delta_{0,R}^2 - \delta_{0,I}^2 \right), \\
c_I^{(D\delta)} &= c_I^{(\delta D)} + \frac{\sqrt{2}}{12} \Delta^2 \sum_{m \neq 0} \left( Y_{,\theta}^m + \frac{m}{\sin \theta} Y^m \right) \delta_{0,R} \delta_{0,I}
\end{aligned}$$

$$\begin{aligned}
c_R^{(\delta^2)} &= -\frac{\Delta^2}{24} \sum_{m \neq 0} \left\{ Y_{,\theta\theta}^m (\delta_{0,R}^2 - \delta_{0,I}^2) + \left[ -\delta_{0,I} \frac{a \sin \theta}{\sqrt{2\Sigma}} \right. \right. \\
&\quad \left. \left. + (\delta_{0,R}^2 - \delta_{0,I}^2) \left( \frac{a^2 \sin 2\theta}{\Sigma} + \frac{2m}{\sin \theta} \right) \right] Y_{,\theta}^m \right. \\
&\quad \left. + \left[ (\delta_{0,R}^2 - \delta_{0,I}^2) \left( \frac{ma^2 \sin 2\theta}{\sin \theta \Sigma} + \frac{m}{\sin \theta^2} (m \right. \right. \right. \\
&\quad \left. \left. \left. - \cos \theta) \right) - \delta_{0,I} \frac{ma}{\sqrt{2\Sigma}} \right] Y^m \right\} \\
c_I^{(\delta^2)} &= -\frac{\Delta^2}{24} \sum_{m \neq 0} \left\{ Y_{,\theta\theta}^m 2\delta_{0,R} \delta_{0,I} + \left[ \delta_{0,R} \frac{a \sin \theta}{\sqrt{2\Sigma}} \right. \right. \\
&\quad \left. \left. + 2\delta_{0,R} \delta_{0,I} \left( \frac{a^2 \sin 2\theta}{\Sigma} + \frac{2m}{\sin \theta} \right) \right] Y_{,\theta}^m \right. \\
&\quad \left. + \left[ 2\delta_{0,R} \delta_{0,I} \left( \frac{ma^2 \sin 2\theta}{\sin \theta \Sigma} + \frac{m}{\sin \theta^2} (m \right. \right. \right. \\
&\quad \left. \left. \left. - \cos \theta) \right) + \delta_{0,R} \frac{ma}{\sqrt{2\Sigma}} \right] Y^m \right\} \tag{5.55}
\end{aligned}$$

and where

$$\delta_{0,R} = \frac{r}{\sqrt{2\Sigma}} \quad \delta_{0,I} = \frac{-a}{\sqrt{2\Sigma}} \cos \theta. \tag{5.56}$$

From these equations it is simple to reconstruct the real and imaginary parts of the action of the differential operators on the potential by combining Eq. (5.55) and (5.54). For example, the real part of  $D_m \Psi$  is then given by

$$\begin{aligned}
(D_m \Psi)_R &= c_R^{(D)} (a_R b_R - a_I b_I) - c_I^{(D)} (a_R b_I + a_I b_R) \\
&= \frac{\Delta}{12} \sum_{m \neq 0} Y^m [-2(r - m_1) (\alpha_m(v) \cos m\phi \\
&\quad - \beta_m(v) \sin m\phi) + ma (\alpha_m(v) \sin m\phi + \beta_m(v) \cos m\phi)]. \tag{5.57}
\end{aligned}$$

We are now finally ready to get a final expression for the metric perturbation by taking the real part of Eq. (5.46). Doing so we obtain

$$\begin{aligned}
\Re[h_{ab}^{(A)}] &= -l_a l_b \left[ \Psi_R \left( 4\delta_{\beta,R} + 4\alpha_R \beta_R + 3\alpha_I \tau_I + 3\tau_I^2 + 12\beta_R^2 - 5\beta_I \tau_I + 3\delta_{\tau,R} + 4\alpha_I \beta_I \right. \right. \\
&\quad \left. \left. - 12\beta_I^2 \right) + \Psi_I \left( -24\beta_R \beta_I - 4\delta_{\beta,I} - 3\delta_{\tau,I} - 5\tau_I \beta_R + 4\alpha_I \beta_R - 3\alpha_R \tau_I - 4\alpha_R \beta_I \right) \right. \\
&\quad \left. + (\delta_m \Psi)_R (7\beta_R + \alpha_R) (\delta_m \Psi)_I (-7\beta_I - 2\tau_I + \alpha_I) + [(\delta_m)^2 \Psi]_R \right], \\
\Re[h_{ab}^{(B)}] &= 2[(D_m)^2 \Psi]_I m_a^R m_b^I + [(D_m)^2 \Psi]_R (m_a^I m_b^I - m_a^R m_b^R) + (D_m \Psi)_R \left[ 2(m_a^I m_b^I \right. \\
&\quad \left. - m_a^R m_b^R) \rho_R + 4m_a^R m_b^I \rho_I \right] + (D_m \Psi)_I \left[ 4m_a^R m_b^I \rho_R + 2(m_a^R m_b^R - m_a^I m_b^I) \rho_I \right] \\
&\quad + 3\Psi_R \left[ (m_a^I m_b^I - m_a^R m_b^R) (\rho_I^2 - \rho_R^2) - 4m_a^R m_b^I \rho_R \rho_I + D_{\rho,R} (m_a^I m_b^I - m_a^R m_b^R) \right. \\
&\quad \left. + 2m_a^R m_b^I D_{\rho,I} \right] + 6\Psi_I \left[ (m_a^I m_b^I - m_a^R m_b^R) \rho_R \rho_I + m_a^R m_b^I (\rho_I^2 - \rho_R^2) \right. \\
&\quad \left. + \frac{1}{2} (m_a^R m_b^R - m_a^I m_b^I) D_{\rho,I} + m_a^R m_b^I D_{\rho,R} \right], \\
\Re[h_{ab}^{(C)}] &= l_{(a} \left( m_b^R \{ [(D\delta)_m \Psi]_R + 2(\delta_m \Psi)_I \rho_I \} - m_b^I \{ [(D\delta)_m \Psi]_I - 2(\delta_m \Psi)_R \rho_I \} \right. \\
&\quad \left. + (D_m \Psi)_R [4\beta_R m_b^R - (4\beta_I + 3\tau_I) m_b^I] - (D_m \Psi)_I [4\beta_R m_b^I + (4\beta_I + 3\tau_I) m_b^R] \right. \\
&\quad \left. + \Psi_R \left\{ [3D_{\tau,R} + (8\beta_I + 6\tau_I) \rho_I + 4D_{\beta,R}] m_b^R + (-3D_{\tau,I} - 4D_{\beta,I} + 8\rho_I \beta_R) m_b^I \right\} \right. \\
&\quad \left. + \Psi_I \left[ (-3D_{\tau,I} - 4D_{\beta,I} + 8\rho_I \beta_R) m_b^R - [3D_{\tau,R} + (8\beta_I + 6\tau_I) \rho_I + 4D_{\beta,R}] m_b^I \right] \right) \\
\Re[h_{ab}^{(D)}] &= l_{(a} \left\{ 3(\delta_m \Psi)_R (-m_b^I \rho_I + m_b^R \rho_R) - 3(\delta_m \Psi)_I (m_b^I \rho_R + m_b^R \rho_I) + (D_m \Psi)_R \right. \\
&\quad \times \left[ m_b^I (-\alpha_I - \pi_I + \tau_I - 3\beta_I) + m_b^R (-\alpha_R + 3\beta_R - \pi_R) \right] + (D_m \Psi)_I \left[ m_b^I (-3\beta_R \right. \\
&\quad \left. + \pi_R + \alpha_R) + m_b^R (-3\beta_I - \alpha_I + \tau_I - \pi_I) \right] + 3\Psi_R \left[ m_b^R (-\pi_R \rho_R + \delta_{\rho,R} - \alpha_R \rho_R \right. \\
&\quad \left. - \alpha_I \rho_I + 3\rho_R \beta_R - \pi_I \rho_I + \rho_I \tau_I - 3\rho_I \beta_I) + m_b^I (\alpha_R \rho_I - \delta_{\rho,I} - 3\beta_I \rho_R + \pi_R \rho_I \right. \\
&\quad \left. - \pi_I \rho_R - 3\rho_I \beta_R + \tau_I \rho_R - \alpha_I \rho_R) \right] + 3\Psi_I \left[ m_b^R (-\alpha_I \rho_R + \pi_R \rho_I - \delta_{\rho,I} - \pi_I \rho_R \right. \\
&\quad \left. + \tau_I \rho_R - 3\beta_I \rho_R + \alpha_R \rho_I - 3\rho_I \beta_R) + m_b^I (-\delta_{\rho,R} + \alpha_I \rho_I + \alpha_R \rho_R + \pi_R \rho_R - 3\beta_R \rho_R \right. \\
&\quad \left. + 3\rho_I \beta_I - \rho_I \tau_I + \pi_I \rho_I) \right] - m_b^I [(\delta D)_m \Psi]_I + m_b^R [(\delta D)_m \Psi]_R \left. \right\}. \tag{5.58}
\end{aligned}$$

The full metric perturbation is then given by

$$h_{ab} = 2 \left[ \Re[h_{ab}^{(A)}] + \Re[h_{ab}^{(B)}] + \Re[h_{ab}^{(C)}] + \Re[h_{ab}^{(D)}] \right]. \tag{5.59}$$

This is the metric of a tidally perturbed Kerr black hole in Kerr coordinates. We can transform this metric to Kerr-Schild coordinates, but this is left to the Appendix. We

have checked that this metric indeed satisfies the Einstein equations by linearizing the Ricci tensor and verifying that all components vanish to first order. We have further checked that the metric perturbation is transverse and traceless ( $h^a_a = 0$  and  $h_{ab}l^a = 0$ ) in the tetrad frame making it suitable to study gravitational perturbations near the horizon. Furthermore, we have checked that the conditions that define the IRG [Eq. (5.39)] are also satisfied. Another feature of this metric is that its determinant is zero, which renders it non-invertible. However, the full metric  $g_{ab} = g_{ab}^B + h_{ab}$  is invertible and, thus, the calculation of the Einstein tensor is straightforward.

The metric perturbation has now been expressed entirely in terms of quantities explicitly defined in this paper. These quantities are the real and imaginary parts of the spin coefficients, the potential and the action of the differential operators on the spin coefficients and the potential. The spin coefficients were decomposed in Eq. (5.43); the potential was decomposed in Eq. (5.35); the action of the differential operators on the spin coefficients is given in Eq. (5.47); and the action of these operators on the potential is decomposed in Eq. (5.54) and (5.55).

The metric perturbation possesses the general global features that it diverges as  $r \rightarrow \infty$  and it either diverges or converges to a finite value as  $r \rightarrow 0$ . The behavior as  $r \rightarrow \infty$  is to be expected because the Chrzanowski procedure ceases to be valid far from the hole. On the other hand, the behavior as  $r \rightarrow 0$  is a bit more surprising. In this region there are two different types of behavior: either the perturbation remains finite or it diverges. These different types of behavior depend on the component and axis we are investigating. On the one hand, there are some components that either are finite and of  $O(V^2)$  or vanish as  $r \rightarrow 0$  for all angles, such as  $h_{01}$ ,  $h_{11}$ ,  $h_{12}$ ,  $h_{13}$  and  $h_{22}$ . On the other hand, there are other components that diverge along certain axis as  $r \rightarrow 0$ . For example,  $h_{00}$ ,  $h_{03}$  and  $h_{33}$  diverge along the  $x$ -axis, the  $y$ -axis and the  $x$ - $y$  diagonal, while  $h_{02}$  and  $h_{23}$  diverge along the  $y$ -axis and  $x$ - $y$  diagonal. This divergence is due to the choice of tetrad, since the fourth Kinnersly tetrad vector clearly diverges as  $r \rightarrow 0$ . Note, however, that since the divergences occur well inside the inner horizon they will be causally disconnected with all physical processes occurring outside the outer horizon and, thus, these divergences are irrelevant to most physical applications. This divergent behavior could nonetheless be avoided if a different tetrad, such as the Hawking-Hartle one, is used to compute the perturbation, but this will not be discussed here further.

In order to illustrate this global behavior, we have plotted  $h_{00}$  in Fig. 5.3 with the plotting choices described in Sec. 5.2 along the  $x$ -axis and the  $y$ - $z$  diagonal ( $\theta = \pi/4$  and  $\phi = \pi/2$ ). Observe that the perturbation diverges as  $r \rightarrow \infty$  and as  $r \rightarrow 0$  along the  $x$ -axis, but it remains finite as  $r \rightarrow 0$  along the  $y$ - $z$  diagonal. Everywhere else, and in particular near the outer horizon, the perturbation is of  $O(V^2)$ , where  $V = (M/b)^{1/2}$  is the orbital velocity. Finally, observe that the perturbation vanishes close but not really at either horizon, remaining finite through them.

The divergence of the perturbation can be used to approximately determine the region of validity of the approximation. As we have discussed previously and seen in Fig. 5.3, the perturbation will be valid inside a shell centered at the background hole. The inner radius of this shell can be approximately determined by graphically studying the radius where  $h_{ab} > O(V^2)$ , approximately given by  $r_{inner} \approx 0.01M$ . This value for

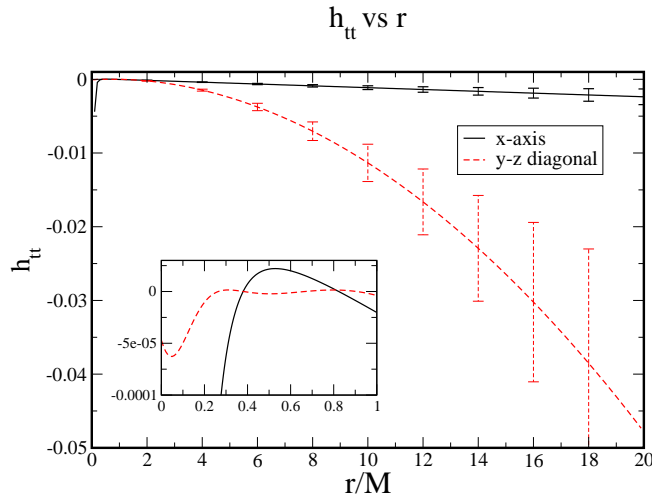


Fig. 5.3. Plot of the 00 component of the metric perturbation along the  $x$ -axis (solid line) and along the  $y$ - $z$  diagonal (dashed line) with the plotting parameters described in Sec. 5.2.

the inner radius of the shell is only an order of magnitude estimate, but it suffices to see that  $r_{inner} \ll r_-$ . The causal structure of the region  $r < r_-$  is extremely complex and many of its features are known to be unstable under small perturbations that destroy the symmetries of the spacetime [135]. However, note that the perturbation is well behaved for  $r - r_- \ll M$  and in particular it is of the order predicted by the approximation [ $O(V^2)$ ]. In any case, the region  $r < r_-$  is hidden inside the event horizon and most astrophysical applications will be concerned with regions of small spacelike separations from the outer horizon, and not the inner one.

The outer radius of the shell can be estimated by studying the fractional error in the perturbation, which is determined by comparing the perturbation to the uncontrolled remainders in the approximation. The approximate error bars in Fig. 5.3 are given by an estimate of these uncontrolled remainders,  $\delta h_{ab}$ , which are due to truncating the formal series solution at a finite order. In the present case, this truncation is done at  $O(V^2)$ , where the tidal fields provide this scaling. The uncontrolled remainders then will be of  $O(V^3)$  and should come from time derivatives of the tidal tensors, *i.e.*  $\delta h_{ab} \propto \dot{h}_{ab}$ . The argument of the tidal tensors is  $\omega v$ , where  $\omega = V/b$  is the angular velocity and where  $v$  is the advanced time coordinate. Any time derivative will pull out a factor of  $\omega$ , which will in turn increase the order of that term. However, in order for the uncontrolled remainders to be dimensionally consistent ( $\delta h_{ab}$  must have the same dimensions as  $h_{ab}$ ), we need to multiply the time derivatives of the tidal tensors by  $r$ , so that

$$\delta h_{ab} \approx r \dot{h}_{ab} \approx r(V/b)h_{ab}. \quad (5.60)$$

This line of reasoning, however, only leads to an order of magnitude estimate of the uncontrolled remainder. In principle, any dimensionless scalar function could be multiplying this estimate as long as it does not change the scaling. For the case of non-spinning holes, the metric perturbation has been computed to  $O(V^3)$  [95], which allows us to compare these terms to Eq. (5.60). This comparison suggests that the multiplicative scalar function is roughly unity and, thus, unnecessary so that Eq. (5.60) is indeed a good approximation to the scaling of the uncontrolled remainders. Clearly, this estimate is not the exact error in the approximation, which can formally only be determined if we know the exact functional form of the next order term. This estimate, however, is a physically well-motivated approximation for the uncontrolled remainders.

The outer radius of the region of validity of this approximation can be approximately determined by studying the behavior of these error bars. From Fig. 5.3 we see that the error bars become considerable large (approximately 50% as big as the perturbation itself) roughly at  $r = 13M$ . However, for  $r < 4M$  the estimated error bars are less than 10% relative to the perturbation. This seems to indicate that, even at  $b = 10M$  where the slow-motion approximation begins to become inaccurate, the approximate solution is still valid sufficiently close to the outer horizon. This estimation of the fractional errors is by no means a formal proof of the existence or size of the region of validity of the approximation. However, this estimation does provide a strong argument that the approximation is indeed valid sufficiently close to the outer horizon. If 10% fractional error is tolerable, which would correspond to neglecting terms of  $O(V^3)$ , then the outer radius of the shell is approximately given by  $r_{outer} \approx 4M$ . Clearly, as  $b$  is increased, the slow-motion approximation will become more accurate and, thus, the perturbation will be valid inside a bigger shell with larger outer radii.

The results of this paper are clearly valid close to the outer horizon of the background hole, thus allowing the study of physical processes of interest to the relativity community. For instance, we can use the perturbation presented here to construct initial data for a binary system near either hole. In this case, we are not interested in the behavior of the perturbation inside the inner horizon because that region can be excised and does not belong to the computational domain. Furthermore, the calculations of angular momentum and mass flux across the horizon can still be performed because they only depend on the behavior of the perturbation near or at the outer horizon.

## 5.5 Conclusions

We have computed a tidally perturbed metric for a spinning black hole in the slow-motion approximation. This approximation allows us to parameterize the NP scalar  $\psi_0$  [Eq. (5.17)] in terms of the electric and magnetic tidal tensors of the external universe. With this scalar we can then construct a potential  $\Psi$  [Eq. (5.34)], by applying certain differential operators to it. From this potential, we can then apply the Chrzanowski procedure to construct a metric perturbation [Eqs. (5.35), (5.43), (5.47), (5.54), (5.55), (5.58), (5.59)].

The metric is naturally computed in the ingoing radiation gauge and in Kerr coordinates, which are suitable to study perturbation near the horizon due to its horizon penetrating properties. This metric is given explicitly in terms of scalar functions of the coordinates and is parametrized by the mass of the background hole, its Kerr spin

parameter and electric and magnetic tidal tensors. The mass and the spin parameters of the background hole do not have to be small relative to each other, so in principle the metric presented here is capable of representing tidally perturbed extremal Kerr holes. The tidal tensors describe the time-evolution of the perturbation produced by the external universe and, thus, are functions of time that should be determined by matching the metric to another approximation valid far from the holes.

The slow motion approximation constrains what kind of perturbations are allowed, thus limiting the external universe that is producing them. In this approximation, the radius of curvature of the external universe must be changing sufficiently slowly relative to the scales of the background hole. One consequence of this restriction is that the tidal fields must be slowly-varying functions of time, thus allowing us to neglect their time derivatives. In this sense, this approximation leads to a quasi-static limit, where in this paper we have calculated the first non-vanishing deviations from staticity. Another consequence of this approximation is that we can parametrize the perturbation in terms of multipole moments, where here we have only considered the first non-vanishing one (the quadrupolar perturbation). In perturbation theory, the  $l+1$  mode will be one order smaller than the  $l$  mode, which allows us to neglect the octopole and any other higher modes, as well as any mode beating between the quadrupole and higher modes.

Due to these restrictions, if we allow the external universe to be given by another hole in a quasicircular orbit around the background (a binary system), we are limited to those whose separation is sufficiently large. In this case, we must have sufficiently large orbital separations so that the Riemann curvature produced by the companion is large relative to the scales of the background hole. In other words, this approximation will break if we consider systems that are close to their innermost stable orbit and ready to plunge. We have seen, however, that for a separation of  $b = 10M$ , the metric presented here is valid inside a shell given approximately by  $0.01M < r < 4M$ .

The reason why the region of validity of the approximation is a shell can be traced back to the choice of tetrad and to the limitations of the Chrzanowski procedure. The perturbation cannot be valid too close to the background hole because in that region the Kinnersly tetrad, from which the perturbation was constructed, is also divergent. This perturbation is also divergent as  $r \rightarrow \infty$  because the Chrzanowski procedure builds the perturbation as a linear expansion of the metric. In other words, we cannot analyze the dynamics of the entire spacetime with this metric, since its validity is limited to field points sufficiently close to the outer horizon of the background hole. However, if this metric were to be asymptotically matched to another metric valid far from the background hole, then the resultant metric would be accurate on the entire 3-manifold up to uncontrolled remainders thus, capable of reproducing the dynamics of the entire spacetime.

This metric might be useful to different areas in general relativity. On the one hand it might be useful in the construction of astrophysically realistic initial data for binary systems of spinning black holes. Its importance relies in that it could accurately represent the metric field in the neighborhood of a black hole tidally disrupted by a companion. These tides are analytic and arise as a true approximate solution to the Einstein equations in the slow-motion approximation. Initial data, however, requires a metric that is valid in the entire 3-manifold. Therefore, in order to use these results as

initial data they will first have to be asymptotically matched [28, 105] to a PN expansion valid far from the background holes [3]. In this manner, initial data could be constructed that satisfies the full set of the Einstein equation, including the constraints, to a high order of accuracy.

Another use for the metric computed in this paper relates to the flux of mass and angular momentum through a perturbed Kerr horizon. This flux will be important for EMRIs, where the effect of tidal perturbations could be large enough to lead to large fluxes, which in turn could affect the gravitational wave signal emitted by the system [144, 138]. Recent investigations [34] have used a curvature formalism to compute this flux directly from  $\psi_0$ . However, there exists a metric formalism to obtain this flux directly from the metric itself. An interesting research direction would be to compute this flux and compare to the results obtained with the curvature formalism.

Finally, the perturbed metric computed here can also be of use to the data analysis community to construct gravitational waveforms. EMRIs are particularly good candidates to be observed by LISA, but such observations require extremely accurate formulae for the phasing of the gravitational waves due to the use of matched filtering. Recently, Ref. [145] studied how to use and implement a quasi-Kerr metric (a perturbed Kerr metric in the limit of slow rotation of the background hole) to detect EMRIs with LISA. A similar study could be performed with the perturbed metric computed in this paper, which can also describe rapidly rotating black holes.

Future work will concentrate on performing the necessary asymptotic matching to shape this metric into useful initial data for numerical relativity applications. The matching procedure will provide expressions for the tidal tensors in terms of PN quantities, as well as a coordinate transformation between Kerr coordinates and the coordinate system used in the PN approximation. In this manner, a piece-wise global solution can be computed, which will contain small discontinuities inside the matching region that could be eliminated by the introduction of transition function. Since these discontinuities will be small due to the matching, the transition functions will not alter the content of the data to the order of the approximation used. After the matching is completed, we will have obtained an approximate analytic global metric that will contain the tidal fields of one hole on the other near the outer horizon of the former, where these fields come directly from solutions to the Einstein equations.

## Acknowledgments

We are indebted to Eric Poisson, whose good suggestions and clear explanations contributed greatly to this work. We are also grateful to Bernd Brügmann, Amos Ori, Ben Owen and Gerhard Schäfer for useful discussions and comments. Finally, we thank Bernd Brügmann and Ben Owen for their continuous support and encouragement. N.Y would also like to thank the University of Jena for their hospitality.

This work was supported by the Institute for Gravitational Physics and Geometry and the Center for Gravitational Wave Physics, funded by the National Science Foundation under Cooperative Agreement PHY-01-14375. This work was also supported by NSF grants PHY-02-18750, PHY-02-44788, and PHY-02-45649, as well as the DFG grant “SFB Transregio 7: Gravitationswellenastronomie.”

**PART B:**  
**GRAVITATIONAL WAVES AS PROBES**  
**OF THE ASTROPHYSICAL UNIVERSE**

## Chapter 6

# Gravitational Recoil from Binary Black Hole Mergers: the Close-Limit Approximation

The coalescence of a binary black hole system is one of the main sources of gravitational waves that present and future detectors will study. Apart from the energy and angular momentum that these waves carry, for unequal-mass binaries there is also a net flux of linear momentum that implies a recoil velocity of the resulting final black hole in the opposite direction. Due to the relevance of this phenomenon in astrophysics, in particular for galaxy merger scenarios, there have been several attempts to estimate the magnitude of this velocity. Since the main contribution to the recoil comes from the last orbit and plunge, an approximation valid at the last stage of coalescence is well motivated for this type of calculation. In this paper, we present a computation of the recoil velocity based on the close-limit approximation scheme, which gives excellent results for head-on and grazing collisions of black holes when compared to full numerical relativistic calculations. We obtain a maximum recoil velocity of  $\sim 64$  km/s for a symmetric mass ratio  $\eta = M_1 M_2 / (M_1 + M_2)^2 \sim 0.19$  and an initial proper separation of  $4M$ , where  $M$  is the total ADM mass of the system. This separation is the maximum at which the close-limit approximation is expected to provide accurate results. Therefore, it cannot account for the contributions due to inspiral and initial merger. If we supplement this estimate with PN calculations up to the innermost stable circular orbit, we obtain a lower bound for the recoil velocity, with a maximum around 84 km/s. This is a lower bound because it neglects the initial merger phase. We can however obtain a rough estimate by using PN methods or the close-limit approximation. Since both methods are known to overestimate the amount of radiation, we obtain in this way an upper bound for the recoil with maxima in the range of 220 – 265 km/s. We also provide non-linear fits to these estimated upper and lower bounds. These estimates are subject to uncertainties related to issues such as the choice of initial data and higher effects in perturbation theory. Nonetheless, our estimates are consistent with previous results in the literature and suggest a narrower range of possible recoil velocities.

### 6.1 Introduction

The inspiral and merger of binary black holes systems is one of the most interesting sources of gravitational waves that both earth-based interferometric antennas (LIGO [5],

VIRGO [6], GEO600 [7] and TAMA [8]) and space-based ones (LISA [124]) will detect <sup>1</sup>. These waves carry both energy and momentum away from the system, leading to the adiabatic shrinking of the orbit, due to the former, and a recoil of the merged object by conservation of momentum, due to the latter. The magnitude of this recoil is of astrophysical importance because it determines whether the merged hole will be ejected from its host galaxy.

Possible observational evidence for such a recoil may be the observations of faint galaxies [157, 158] where the lack of a dense nucleus has been associated with the central black hole being ejected after merger [41]. There is also evidence of an ejection of a supermassive black hole in ongoing galaxy mergers, either because of recoil or because of slingshot due to the presence of 3 or more supermassive black holes in the merger [159]. The gravitational recoil has also been shown to have important consequences in hierarchical merging scenarios and the observable structure of galaxy nuclei. Recoil velocities of a few hundred km/s could be large when compared to escape velocities of dwarf galaxies, globular clusters and dark matter halos [160, 41]. For super-massive black holes at the centers of galaxies, a kick of this magnitude could potentially transfer energy to the stars in the nucleus [41]. There are thus very important astrophysical aspects that can be refined or clarified with a better understanding of the black hole kicking process.

Mass distributions without symmetries that undergo gravitational collapse of any sort will exhibit momentum ejection and recoil of the center of mass of the remnant due to the strong emission of gravitational radiation [161, 162, 163, 164, 47]. Of particular interest is the case of unequal-mass black-hole binary systems. An intuitive picture of how the system gets a *kick* after the merger is the following [40, 48]: From the *center of mass* point of view, the lighter black hole will move faster than the heavier one, and hence it will beam forward gravitational radiation stronger. Then, there will be a net flux of linear momentum carried by the gravitational radiation in the direction of the lighter black hole, and this will cause a recoil of the *center of mass* in the opposite direction. The first analytic studies of this subject were carried out by Fitchett and Detweiler [43, 46]; Oohara and Nakamura [44]; Nakamura and Haugan [45]; and Wiseman [40]. Due to the strong non-linearity of the merger phase, analytic studies have difficulties in obtaining an accurate estimate of the recoil velocity. The first quasi-Newtonian analytic calculations were presented in [43, 46], while a post-Newtonian (PN) analysis have been carried out in [40, 49, 57]. Estimates using black-hole perturbation theory have been given in [48, 165], and a estimate that combines full numerical relativity and perturbation theory, the *Lazarus* approach, is given in [166].

Full numerical relativistic simulations are a natural approach to this problem since they can in principle handle the non-linearities of the gravitational field during the merger. The challenge is the resolution that the computational resources impose. Some calculations have already been carried out in different scenarios to estimate recoil velocities. The first one was done by Anninos and Brandt [167] for the case of the head-on collision of two unequal-mass black holes. Their numerical calculations were effectively 2-dimensional since they made use of the axisymmetry of the configuration. Using the same

---

<sup>1</sup>This chapter is based on the following paper: C. F. Sopuerta, N. Yunes and P. Laguna, Phys. Rev. D **74**, 124010 (2006)

type of numerical calculations they also estimated the gravitational radiation recoil from highly distorted black holes [168]. More recently, and due to the significant advances in 3-dimensional numerical relativity in the binary black hole problem [35, 36, 169], estimates of the radiation recoil velocity have also appeared [170, 171].

Each of the approaches described above has its own limitations. Analytic approaches are able to provide accurate estimates in their region of validity. However, the largest contribution to the recoil velocity occurs during merger, precisely where the approximation methods break down. Numerical simulations, in principle, have the opportunity of producing estimates with a minimal number of assumptions. However, as we have mentioned, these calculations have also limitations and use initial data that is only an approximation to the actual astrophysical configurations. Therefore, the error bars on the computed distribution of recoil velocities relative to the distribution present in nature are believed to be large and, even worse, are difficult to estimate. It is then not surprising to find disagreements on the estimated recoil velocity as calculated with different methods.

In this paper, we present estimates of the recoil velocity using an approach not used before, the close-limit approximation (CLA), which combines both analytical and numerical techniques. The CLA was introduced by Price and Pullin [13], who showed that this approximation method provides accurate results compared to those obtained from numerical relativity [14] for head-on collisions of two black holes (see also [15]). The CLA scheme is based on the assumption that in the last stage of coalescence, when the black holes are sufficiently *close* to each other, the system behaves, up to a certain degree of approximation, as a single distorted hole. Then, the CLA scheme consists of establishing an appropriate correspondence between the binary black hole system and a single perturbed hole. Once this correspondence is made, one can extract initial data that can be evolved by the perturbative relativistic equations. From the outcome of the evolution, one can estimate the fluxes of energy, angular momentum, and linear momentum carried away to spatial infinity by the gravitational radiation emitted. The CLA scheme has been developed and applied by a number of authors [172, 173, 174, 175, 176, 177, 178, 179]. In particular, Andrade and Price [180] used the CLA to estimate the recoil velocity of a head-on collision of unequal-mass black holes starting from rest.

Since the CLA applies to the last stage of the merger of two black holes, it is very appealing to use it to estimate the recoil velocity of the merger of an unequal-mass black hole binary system. With this scheme, we obtain a maximum recoil velocity of  $\sim \{17, 33, 64\}$  km/s for a symmetric mass ratio  $\eta = M_1 M_2 / (M_1 + M_2)^2 \sim 0.19$  and initial proper separations of  $\{3, 3.5, 4\} M$ , with  $M$  the total ADM mass. Beyond a proper separation of  $4M$  the CLA is not expected to provide accurate results [180]. Therefore, this method cannot account for the contributions during the inspiral and initial merger phase. Supplementing this estimate with PN calculations up to the innermost stable circular orbit (ISCO), we obtain a lower bound for the recoil velocity, with a maximum of  $\sim 84$  km/s. This lower bound neglects the initial merger phase, for which we can obtain an approximate estimate by using either PN methods or the CLA. Since both methods are known to overestimate the amount of radiation during the early merger phase, we obtain, thus, an upper limit for the recoil with maxima in the range of 220 – 265 km/s.

We also perform non-linear fits to these bounds and obtain

$$v_{\text{fit}} = a\eta^2 \sqrt{1 - 4\eta} \left(1 + b\eta + c\eta^2\right), \quad (6.1)$$

where  $a = 7782$  km/s,  $b = -2.507$  and  $c = 2.727$  for the lower bound and  $a = 14802$  km/s,  $b = -1.1339$  and  $c = 1.4766$  for the upper bound.

The plan of this paper is as follows: Sec. 6.2 describes the main procedure of our calculation; Sec. 6.3 constructs initial data for a quasicircular binary black hole system in the 3 + 1-formalism; Sec. 6.4 maps these initial data to a single perturbed black hole spacetime, such that it is suitable for a CLA evolution; Sec. 6.5 describes the numerical implementation and presents results from the evolution within the CLA scheme; Sec. 6.6 estimates the lower and upper bounds, as well as constructing the non-linear fits to these bounds; we finish in Sec. 6.7 with a summary and discussion of the main results and points to future research to obtain improved estimates.

The conventions that we use throughout this work are the following: For the 4-dimensional spacetime, we use Greek letters for the indices and a semicolon for the covariant derivative. The Schwarzschild metric admits a 2+2 decomposition consisting of the warped product of a Lorentzian 2-dimensional manifold with the 2-sphere (see [181, 182]). On the 2-dimensional Lorentzian manifold indices are denoted by capital Latin letters, the covariant derivative associated with the 2-dimensional metric is represented by a vertical bar, and the Levi-Civita antisymmetric tensor by  $\epsilon_{AB}$ . On the 2-sphere indices are denoted by the lower-case Latin letters  $a, b, \dots, h$ , the covariant derivative by a colon, and the Levi-Civita antisymmetric tensor by  $\epsilon_{ab}$ . When using the 3 + 1 decomposition of spacetime quantities, spatial indices are denoted by the lower-case Latin letters  $i, j, k, \dots$ . Uncontrolled remainders are denoted with  $\mathcal{O}(A)$  or  $\mathcal{O}(A, B)$ , which stands for terms of order  $A$  and terms of order  $A$  or  $B$  respectively. Although usually, when dealing with order symbols,  $A$  and  $B$  must be dimensionless, here they will not be, but can be made to be dimensionless through division by the appropriate factor. We also use physical units in which  $G = c = 1$ .

## 6.2 Description of our Calculation

In this paper, we use the CLA scheme to calculate the recoil velocities after the merger of an unequal-mass binary black hole system. Due to the complexity of the calculation, we discuss here the different steps involved, while getting a glimpse of the general scheme. First, we need to construct initial data corresponding to a non-spinning binary black hole system in quasicircular orbital motion. The method employed to construct the data is the standard one: we solve the constraints on an initial slice using the York-Lichnerowicz conformal decomposition. Then, the solution needs to be expanded in two parameters: the separation of the two black holes, based on the main assumption of the CLA, that is, small separation between the holes; and their linear momenta, rooted in an additional *slow motion* approximation [183].

The second step is to establish a map between this initial data and the generic initial data corresponding to a perturbed single black hole. In this work we only consider the case in which the single black hole is a non-rotating Schwarzschild hole. There

is also the possibility of considering a Kerr black hole (see [183] for details), but the CLA machinery in that case is more intricate. After expanding the initial data in the separation and linear momenta, it is straightforward, after some coordinate changes, to identify a Schwarzschild background and its perturbations.

Once the perturbations have been identified, we need to calculate initial data suitable for evolving the linearized (around the Schwarzschild background) Einstein equations. The spherical symmetry of the background allows us to separate the linearized equations. Then, by decomposing the perturbations in spherical harmonics we obtain decoupled equations for each mode. Moreover, by appropriately reparameterizing the perturbations, we can decouple the equations for each individual mode, so that the problem reduces to solving a master equation for a complex combination of the metric perturbations. These master equations (usually known as the Regge-Wheeler and Zerilli-Moncrief equations) are 1-dimensional wave-type equations containing a potential that accounts for the effect of the background spacetime curvature. Therefore, the problem of providing initial data reduces to finding initial conditions for these master functions.

The initial data contains three parameters that we need to specify. These parameters are associated with the initial distance between the holes, the mass ratio, and the initial linear momentum. The mass ratio is an independent parameter that will be used to study the functional behavior of the recoil velocity. The distance and linear momentum parameters determine the dynamical character of the binary and, therefore, they must be chosen carefully. To that end, we use the standard method of minimizing the binding energy of the system, so that the binary is in a quasi-circular orbit. The expressions that we obtain are formally the same as in Newtonian theory, although they cannot be assigned the same interpretation, since they are expressed in terms of *bare* parameters. In order to relate these parameters to meaningful physical ones, we must introduce a proper separation and a physical mass ratio. The proper separation can be calculated by evaluating the minimum proper distance between the marginally trapped surfaces surrounding each individual hole.

The final step is to solve the master equations and evaluate the different physical quantities of interest. The metric waveforms  $h_+$  and  $h_\times$ , together with the fluxes of energy, angular and linear momentum carried away by gravitational waves can be computed in terms of the master functions and their first time derivatives. In this paper, we include the general formulae for the linear momentum fluxes in terms of the perturbation master functions. We present several plots of these quantities, together with plots of the recoil velocities for different initial separations.

### 6.3 Initial Data

In this section, we begin the initial data construction for an unequal-mass binary black hole system suitable to the CLA scheme. To that end, we extend the results of Andrade and Price [180], who carried out the calculation for unboosted head-on collisions, and also extend the results of Khanna *et al* [183], who constructed data for equal-mass black holes in a quasicircular orbit. Our calculation not only allows for arbitrary mass ratios, but it also includes higher-order terms in the expansion of the initial data, which are essential in the calculation of the recoil.

In order to solve the Hamiltonian and momentum constraints, we use the conformal transverse-traceless method of Lichnerowicz, York and others [184, 19, 185, 20, 18]. The 3-metric  $\gamma_{ij}$  is decomposed in terms of a conformal factor  $\Phi$  and an auxiliary metric  $\hat{\gamma}_{ij}$ ,  $\gamma_{ij} = \Phi^4 \hat{\gamma}_{ij}$ , which here we assume to be conformally flat:

$$ds^2 = \gamma_{ij} dx^i dx^j = \Phi^4 (dR^2 + R^2 d\Omega^2), \quad (6.2)$$

where  $d\Omega^2 = d\theta^2 + \sin^2\theta d\varphi^2$  is the line element of the 2-sphere. For the extrinsic curvature  $K_{ij}$ , we choose a *maximal* initial slice, that is,  $K_{ij}$  is trace free:  $\gamma^{ij} K_{ij} = 0$ . Then, we also conformally decompose the trace-free extrinsic curvature  $K_{ij}$  as

$$K_{ij} = \Phi^{-2} \hat{K}_{ij}, \quad (6.3)$$

and we further make the choice that the longitudinal part of  $\hat{K}_{ij}$  vanishes, so that  $\hat{K}_{ij}$  is a symmetric transverse traceless tensor. Then, the momentum and Hamiltonian constraints reduce to

$$\hat{\nabla}^j \hat{K}_{ji} = 0, \quad (6.4)$$

$$\hat{\nabla}^2 \Phi = -\frac{1}{8} \Phi^{-7} \hat{K}_{ij} \hat{K}^{ij}, \quad (6.5)$$

where  $\hat{\nabla}_i$  and  $\hat{\nabla}^2$  denote the covariant derivative and Laplacian associated with the flat 3-metric  $\hat{\gamma}_{ij}$ . The momentum constraint [Eq. (6.4)] can be exactly solved using the method of Bowen and York [21]. For a single black hole located at  $\mathbf{R} = \mathbf{R}_o$  with linear momentum  $\mathbf{P}$  it can be written as follows:

$$\hat{K}_{ij}^{one} = \frac{3}{2|\mathbf{R} - \mathbf{R}_o|^2} \left[ 2P_{(i} n_{j)} - (\hat{\gamma}_{ij} - n_i n_j) P^k n_k \right], \quad (6.6)$$

$P^i$  is the ADM momentum of a single hole, while  $n^i$  is a unit vector in flat three-dimensional space directed from the location of the single hole to an arbitrary point, namely

$$n^i = \frac{R^i - R_o^i}{|\mathbf{R} - \mathbf{R}_o|}, \quad (6.7)$$

and the vertical bars,  $|\cdot|$ , denote the norm of vector in the flat 3-dimensional space. In order to construct a solution for two holes, we can simply superpose two solutions of the type of Eq. (6.6).

Before constructing the extrinsic curvature, it will be useful to first describe the initial physical configuration. The system we are modeling consists of two black holes with masses  $M_1$  and  $M_2$  located on the  $X$ -axis, a coordinate distance  $d$  apart, as shown in Figure 6.1. In this figure,  $\mathbf{R}_1$ ,  $\mathbf{R}_2$ , and  $\mathbf{R}$  are radial vectors that point from the origin to hole 1, hole 2, and an arbitrary point, respectively. Moreover,  $\mathbf{R}_{12} = \mathbf{R}_2 - \mathbf{R}_1$  is also

a vector that points from hole 1 to 2, and  $\mathbf{P}$  and  $-\mathbf{P}$  are the linear momenta associated with holes 1 and 2 respectively. Since the linear momenta are parallel to the  $Y$ -axis, the orbital angular momentum is directed along the  $Z$ -axis. With such physical scenario,

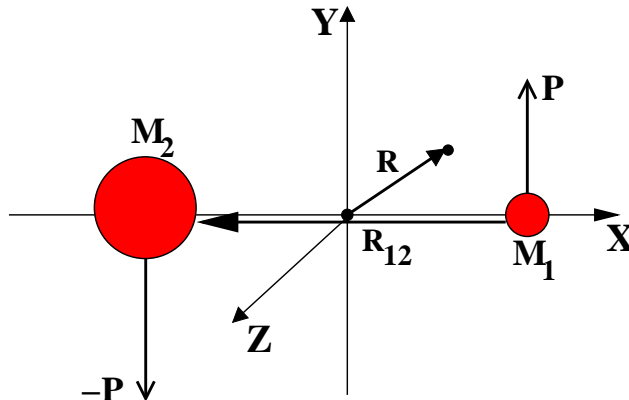


Fig. 6.1. Schematic diagram of the initial physical configuration. The linear momenta are parallel to the  $Y$ -axis and span the  $X$ - $Y$  plane, so that the angular momentum is aligned with the  $Z$ -axis.

the solution of Eq. (6.4) can be written as (see also [183]):

$$\hat{K}_{ij} = \hat{K}_{ij}^{one}[\mathbf{R}_o = \mathbf{R}_1, \mathbf{P}] + \hat{K}_{ij}^{one}[\mathbf{R}_o = \mathbf{R}_2, -\mathbf{P}], \quad (6.8)$$

where we have defined  $\mathbf{P} = P \hat{\mathbf{y}}$ . The ADM momentum corresponding to  $\hat{K}_{ij}^{one}$  is simply  $\mathbf{P}$  and the one associated with  $\hat{K}_{ij}$  is zero.

Let us now concentrate on the solution to the Hamiltonian constraint. Using Eq. (6.8) in the Hamiltonian constraint leads to a source term quadratic in  $P$ . We now introduce a *slow-motion* approximation, where we assume that the linear momentum  $P$  is *small*, in the sense that terms of  $\mathcal{O}(v^2)$  are much smaller than terms of  $\mathcal{O}(v)$ , where  $v$  is a measure of the orbital velocity. We, thus, neglect terms of  $\mathcal{O}(P^2)$ , so that the Hamiltonian constraint reduces to the Laplace equation

$$\nabla^2 \Phi = 0. \quad (6.9)$$

The solution of this equation depends on our choice of topology. If we choose the initial slice to have a single asymptotically flat region, the solution to the conformal factor is the Misner solution [186], but if one chooses the slice to have three asymptotically-flat regions, the solution is the Brill-Lindquist [22] one. In this paper, we adopt the latter

and the conformal factor takes the form of the Newtonian potential:

$$\Phi = 1 + \frac{m_1}{2|\mathbf{R} - \mathbf{R}_1|} + \frac{m_2}{2|\mathbf{R} - \mathbf{R}_2|}, \quad (6.10)$$

where  $m_1$  and  $m_2$  denote the *bare* masses of each individual hole. One reason for choosing the Brill-Lindquist (BL) solution is that it is simpler to manipulate, while it has also been shown [180] to lead to essentially the same results when calculating recoil velocities for head-on collisions. We remark that, although terms of  $\mathcal{O}(P^2)$  have been neglected, they can be straightforwardly added in a perturbative fashion, but this will be studied elsewhere.

Let us comment further on the topology of the initial slice associated with the BL solution, as it is important in some calculations. As we have already mentioned, this solution has three asymptotically-flat regions: one of them,  $\Sigma_0$ , corresponds to the region far from the two holes,  $R = |\mathbf{R}| \gg |\mathbf{R}_1| = R_1$  and  $R \gg |\mathbf{R}_2| = R_2$ ; the other two,  $\Sigma_1$  and  $\Sigma_2$ , are associated with hole 1 and 2 respectively. By simple inspection of the conformal factor [Eq. (6.10)], the solution seems ill-behaved at the location of the holes,  $\mathbf{R} = \mathbf{R}_1$  and  $\mathbf{R} = \mathbf{R}_2$ , although it is actually not. Near each hole, the geometry is invariant under the transformation:  $|\mathbf{R} - \mathbf{R}_\Lambda| \rightarrow m_\Lambda^2/(4R'_\Lambda)$  ( $\Lambda = 1, 2$ ). The value  $m_\Lambda/2$  coincides with the intersection of the event horizon with the initial slice for a single hole and it is a fixed point in the transformation. This value is sometimes referred to as the *throat*, joining two asymptotically-flat regions. Therefore, the points  $\mathbf{R} = \mathbf{R}_1$  and  $\mathbf{R} = \mathbf{R}_2$  are just an *image* of the infinities of  $\Sigma_1$  and  $\Sigma_2$ . For a single hole, there are two asymptotically-flat regions, and its mass, equal to  $m$ , is the same independent of which region we evaluate it on. In the case of a binary system, the gravitational interaction between the holes will change the value of the individual masses. Actually, there is not an invariant measure of them in  $\Sigma_0$ , but such a measure does exist on  $\Sigma_1$  and  $\Sigma_2$ . Doing the calculation yields the following result [22]

$$M_1 = m_1 \left( 1 + \frac{m_2}{2d} \right), \quad M_2 = m_2 \left( 1 + \frac{m_1}{2d} \right), \quad (6.11)$$

where  $d = |\mathbf{R}_{12}|$ . In  $\Sigma_0$ , we can compute the total mass of the binary system, the ADM mass of the system. We call the result  $M$  and it is given by

$$M = m_1 + m_2. \quad (6.12)$$

Eqs. (6.8), (6.10), and (6.3) are the initial data. We should note that, apart from our choice of initial data (BL conformal factor and Bowen-York extrinsic curvature), there are other possible choices that can be used in the CLA scheme. Some examples of other possible data sets are the following: a Misner conformal factor with a Bowen-York extrinsic curvature with inversion symmetry through the throats; Kerr-Schild initial data [178].

The next step in the construction of the initial data is to put it in a form suitable for the CLA scheme. Before doing so, however, it is convenient to study the parameters

that determine the configuration described by the data. To begin with, let us introduce the *bare* mass ratio

$$q = \frac{m_2}{m_1}. \quad (6.13)$$

The initial configuration can then be fully specified in terms of the parameters  $(q, d, P)$ . Since  $q$  and  $d$  are *bare* parameters, in the sense that we cannot give them a physical meaning, we are going to introduce analogous parameters, which can be given a physical interpretation. First, we introduce the mass ratio between the individual masses of the holes as computed in their respective asymptotically-flat regions:

$$Q = \frac{M_2}{M_1}. \quad (6.14)$$

The quantities  $q$  and  $Q$  are related through  $d$  via [180]:

$$Q = q \frac{1 + [(1+q)/2](M/d)}{1 + [(1+q)q/2](M/d)}, \quad (6.15)$$

$$q = \frac{Q-1}{2} \left(1 + \frac{M}{2d}\right) + \sqrt{Q + \left[\frac{Q-1}{2} \left(1 + \frac{M}{2d}\right)\right]^2}. \quad (6.16)$$

Defining a useful distance is a more difficult matter. In this paper, we use the same distance as Andrade and Price [180], which is the proper distance between the points where the marginally trapped surfaces, surrounding each individual hole, cross the  $X$ -axis (we obviously refer to crossing points closer to the opposite hole). When the initial configuration does not present a common apparent horizon, these marginally trapped surfaces are the individual components of the apparent horizon. If  $x_1$  and  $x_2$  stand for these crossing points, the distance we have just defined is given by  $D = \int_{x_2}^{x_1} \Phi^2 dx$ , which yields

$$D = \Delta x \left\{ 1 + \frac{m_1^2}{4(X_1 - x_1)(X_1 - x_2)} + \frac{m_2^2}{4(x_1 - X_2)(x_2 - X_2)} \right\} - M_1 \ln \left( \frac{X_1 - x_1}{X_1 - x_2} \right) + M_2 \ln \left( \frac{x_1 - X_2}{x_2 - X_2} \right), \quad (6.17)$$

where  $\Delta x = x_1 - x_2 > 0$ , and  $X_1 (= R_1)$  and  $X_2 (= -R_2)$  are the  $x$ -coordinate locations of holes 1 and 2 respectively in the conformal space. In summary, we can determine our initial configuration either by specifying the set  $(q, d, P)$  or the set  $(Q, D, P)$ .

The CLA scheme assumes that the black holes are sufficiently close enough, which allows us to expand the initial data in  $R \gg R_1$  and  $R \gg R_2$ . In this sense, it is useful to choose the coordinate origin,  $\mathbf{R} = 0$ , in such a way that it coincides with the *bare* center

of mass of the binary black hole, that is:

$$m_1 \mathbf{R}_1 + m_2 \mathbf{R}_2 = 0. \quad (6.18)$$

We can write then  $\mathbf{R}_1$  and  $\mathbf{R}_2$  in terms of the separation vector  $\mathbf{R}_{12}$  via

$$\mathbf{R}_1 = \chi_1 \mathbf{R}_{12}, \quad \mathbf{R}_2 = \chi_2 \mathbf{R}_{12}, \quad (6.19)$$

where we have defined

$$\chi_1 = -\frac{q}{1+q}, \quad \chi_2 = \frac{1}{1+q}. \quad (6.20)$$

Then, it is natural to expand the initial data in the following dimensionless parameter  $\epsilon$

$$\epsilon = |\epsilon| = \frac{d}{R}, \quad \epsilon = \frac{\mathbf{R}_{12}}{R}. \quad (6.21)$$

A key formula for performing these expansions is the following:

$$\frac{1}{|\mathbf{R} - \mathbf{R}_A|^N} = \frac{1}{R^N} \sum_{\ell=0}^{\infty} C_{\ell}^{(N/2)}(\hat{\epsilon} \cdot \hat{\mathbf{R}}) \left(\chi_A \epsilon\right)^{\ell}, \quad (6.22)$$

where we have introduced the following unit vectors

$$\hat{\mathbf{R}} = \frac{\mathbf{R}}{R}, \quad \hat{\epsilon} = \frac{\epsilon}{\epsilon}, \quad (6.23)$$

and where  $C_{\ell}^{(N/2)}$  denote the Gegenbauer polynomials. These polynomials, also known as ultra-spherical polynomials, are a generalization of the Legendre polynomials to  $(N/2 + 2)$ -dimensional spaces, which are common in angular momentum theory [187, 188]. For the special cases of  $N = 0, 1, 2$ , these polynomials reduce to Legendre polynomials and Chebyshev polynomials of type 1 and 2 respectively. We refer to Appendix B for more details on these polynomials.

We now use all these definitions and results to expand the conformal extrinsic curvature given by Eq. (6.8) in  $\epsilon$  to arbitrary order. The result we obtain can be written as follows:

$$\begin{aligned} \hat{K}_{ij} &= \frac{3}{2R^2} \sum_{\ell=0}^{\infty} \left(\frac{d}{R}\right)^{\ell+1} \left(\chi_1^{\ell+1} - \chi_2^{\ell+1}\right) \left\{ C_{\ell+1}^{(3/2)} \left[ 2P_{(i j)}^{\hat{\mathbf{R}}} - (\mathbf{P} \cdot \hat{\mathbf{R}}) \hat{\gamma}_{ij} \right] + C_{\ell+1}^{(5/2)} (\mathbf{P} \cdot \hat{\mathbf{R}}) \right. \\ &\times \hat{R}_i \hat{R}_j + C_{\ell}^{(3/2)} \left[ (\mathbf{P} \cdot \hat{\epsilon}) \hat{\gamma}_{ij} - 2P_{(i j)}^{\hat{\epsilon}} \right] - C_{\ell}^{(5/2)} \left[ (\mathbf{P} \cdot \hat{\epsilon}) \hat{R}_i \hat{R}_j + 2(\mathbf{P} \cdot \hat{\mathbf{R}}) \hat{R}_{(i j)}^{\hat{\epsilon}} \right] \left. \right\} \\ &+ \left(\frac{d}{R}\right)^{\ell+2} \left(\chi_1^{\ell+2} - \chi_2^{\ell+2}\right) C_{\ell}^{(5/2)} \left[ (\mathbf{P} \cdot \hat{\mathbf{R}}) \hat{\epsilon}_i \hat{\epsilon}_j + 2(\mathbf{P} \cdot \hat{\epsilon}) \hat{R}_{(i j)}^{\hat{\epsilon}} \right] \\ &- \left(\frac{d}{R}\right)^{\ell+3} \left(\chi_1^{\ell+3} - \chi_2^{\ell+3}\right) C_{\ell}^{(5/2)} (\mathbf{P} \cdot \hat{\epsilon}) \hat{\epsilon}_i \hat{\epsilon}_j, \end{aligned} \quad (6.24)$$

where for simplicity we have omitted the argument of the Gegenbauer polynomials, which still is  $\hat{\epsilon} \cdot \hat{\mathbf{R}}$ . It is worth noting that the  $\epsilon^0$  term has identically vanished due to the choice

of coordinate origin, which coincides with the *bare* center of mass. Another interesting fact is that only combinations of the (3/2)- and (5/2)-Gegenbauer polynomials appear due to the combination of odd powers in the denominators of the extrinsic curvature.

In this paper we are going to consider terms up to  $\mathcal{O}(\epsilon^3)$ , which is enough to get a gravitational recoil effect and actually the dominant part of it (see, e.g. [180]). Extensions of our calculations to higher order are in principle straightforward, but we are not going to present them here. Then, up to this order of approximation we can rewrite Eq. (6.24) as follows:

$$\begin{aligned}
\hat{K}_{ij} &= \frac{9}{2} \frac{d}{R^3} \left\{ \hat{\mathbf{R}} \cdot \hat{\boldsymbol{\epsilon}} + \frac{1}{2} \frac{d}{R} \frac{1-q}{1+q} [5(\hat{\mathbf{R}} \cdot \hat{\boldsymbol{\epsilon}})^2 - 1] \right\} \left[ (\mathbf{P} \cdot \hat{\mathbf{R}}) \hat{\gamma}_{ij} - 2P_{(i} \hat{R}_{j)} \right] \\
&- \frac{3}{2} \frac{d}{R^3} \left\{ 1 + 3 \frac{d}{R} \frac{1-q}{1+q} \hat{\mathbf{R}} \cdot \hat{\boldsymbol{\epsilon}} \right\} \left[ (\mathbf{P} \cdot \hat{\boldsymbol{\epsilon}}) \hat{\gamma}_{ij} - 2P_{(i} \hat{\boldsymbol{\epsilon}}_{j)} \right] \\
&- \frac{15}{2} \frac{d}{R^3} \left\{ \hat{\mathbf{R}} \cdot \hat{\boldsymbol{\epsilon}} + \frac{1}{2} \frac{d}{R} \frac{1-q}{1+q} [7(\hat{\mathbf{R}} \cdot \hat{\boldsymbol{\epsilon}})^2 - 1] \right\} (\mathbf{P} \cdot \hat{\mathbf{R}}) \hat{R}_i \hat{R}_j \\
&+ \frac{3}{2} \frac{d}{R^3} \left\{ 1 + 5 \frac{d}{R} \frac{1-q}{1+q} \hat{\mathbf{R}} \cdot \hat{\boldsymbol{\epsilon}} \right\} \left[ (\mathbf{P} \cdot \hat{\boldsymbol{\epsilon}}) \hat{R}_i \hat{R}_j + 2(\mathbf{P} \cdot \hat{\mathbf{R}}) \hat{R}_{(i} \hat{\boldsymbol{\epsilon}}_{j)} \right] \\
&- \frac{3}{2} \frac{d^2}{R^4} \frac{1-q}{1+q} \left[ (\mathbf{P} \cdot \hat{\mathbf{R}}) \hat{\boldsymbol{\epsilon}}_i \hat{\boldsymbol{\epsilon}}_j + 2(\mathbf{P} \cdot \hat{\boldsymbol{\epsilon}}) \hat{R}_{(i} \hat{\boldsymbol{\epsilon}}_{j)} \right] + \mathcal{O}(Pd^3). \tag{6.25}
\end{aligned}$$

The lowest-order contribution is of  $\mathcal{O}(Pd)$  and it is the only contribution used by Khanna *et al* [183] for grazing collisions of equal-mass black holes. The next contribution is of  $\mathcal{O}(Pd^2)$  and, as far as we know, this is the first time it has been considered.

Let us now look at the conformal factor [Eq. (6.10)]. Using Eq. (6.22), we can also expand  $\Phi$  in Gegenbauer polynomials to obtain

$$\Phi = 1 + \frac{M}{2R} + \sum_{\ell \geq 2}^{\infty} C_{\ell}^{(1/2)}(\hat{\mathbf{R}} \cdot \hat{\boldsymbol{\epsilon}}) \epsilon^{\ell} (m_1 \chi_1^{\ell} + m_2 \chi_2^{\ell}). \tag{6.26}$$

It is important to recall that in solving the Hamiltonian constraint we have used a *slow-motion* approximation, neglecting terms of  $\mathcal{O}(P^2)$ . The terms we are, thus, neglecting are of  $\mathcal{O}(P^2 d^2)$ . This expression can also be written in terms of the parameters  $(q, d)$  and  $M$ , and in terms of Legendre polynomials. In this way we obtain

$$\Phi = 1 + \frac{M}{2R} + \sum_{\ell \geq 2}^{\infty} \phi_{\ell} \left( \frac{M}{R} \right)^{\ell+1} P_{\ell}(\hat{\mathbf{R}} \cdot \hat{\boldsymbol{\epsilon}}) + \mathcal{O}(P^2 d^2), \tag{6.27}$$

where  $P_{\ell}$  denotes the Legendre polynomials and where the coefficients  $\phi_{\ell}$  are given by

$$\phi_{\ell} = \frac{1}{2} \left\{ (-1)^{\ell} + q^{\ell-1} \right\} \frac{q}{(1+q)^{\ell+1}} \left( \frac{d}{M} \right)^{\ell}. \tag{6.28}$$

The  $\ell = 1$ -term vanishes due to the choice of the origin of coordinates in Eq. (6.18). Finally, the expansion of the conformal factor up to third order in  $d$  is given by

$$\begin{aligned} \Phi &= 1 + \frac{M}{2R} + \frac{1}{2} \frac{q}{(1+q)^2} \frac{Md^2}{R^3} P_2(\hat{\mathbf{R}} \cdot \hat{\boldsymbol{\epsilon}}) \\ &\quad - \frac{1}{2} \frac{q(1-q)}{(1+q)^3} \frac{Md^3}{R^4} P_3(\hat{\mathbf{R}} \cdot \hat{\boldsymbol{\epsilon}}) + \mathcal{O}(P^2 d^2, d^4). \end{aligned} \quad (6.29)$$

With this, we finish the construction of initial data to be used in the CLA scheme. To summarize, we remark that this construction is based on expansions on two different parameters:  $P$  (related to the *slow-motion* approximation) and  $d$  (related to the assumption that the holes are close to each other). Since  $P$  and  $d$  have dimensions, the meaning of these expansions is that terms of order  $d^N$  and/or  $P^M$  are smaller than terms of order  $d^{N-1}$  and/or  $P^{M-1}$ . As we are going to see later, these expansions will provide the leading contribution of the multipoles  $\ell = 2$  and  $\ell = 3$ .

## 6.4 The Close Limit Approximation

The next stage in our computation is to recast the initial data just constructed into data for a perturbed Schwarzschild black hole, which is the essence of the CLA scheme. In this way we can extract initial data to be evolved by the corresponding perturbation equations. Thanks to the expansions performed in the previous section, the main task now becomes the extraction of the different multipoles from the data.

The 3-metric on the initial slice is conformally flat and hence determined by the conformal factor  $\Phi$ . If we look at the lowest-order contribution [see Eq. (6.29)] we realize that it coincides with the 3-metric of Schwarzschild spacetime associated with the  $\{t = \text{const.}\}$ -slicing in isotropic coordinates, being  $t$  the Schwarzschild time coordinate. However, in order to make the connection with perturbation theory, it is very convenient to reexpress the initial data in Schwarzschild coordinates:

$$ds^2 = f^{-1} dr^2 + r^2 d\Omega^2, \quad f = 1 - \frac{2M}{r}, \quad (6.30)$$

where we recall that  $M$  is the total ADM mass. The transformation from isotropic coordinates to Schwarzschild coordinates is given by the following relations:

$$R = \frac{1}{4}(\sqrt{r} + \sqrt{r - 2M})^2, \quad r = R \left(1 + \frac{M}{2R}\right)^2, \quad (6.31)$$

Applying this transformation to the 3-metric of our initial data we obtain:

$$ds^2 = \mathcal{F}^4 \left( f^{-1} dr^2 + r^2 d\Omega^2 \right), \quad (6.32)$$

where

$$\mathcal{F} = \frac{\Phi}{1 + \frac{M}{2R}}. \quad (6.33)$$

In order to construct initial data for the perturbations, evolve it, and compute from the result all the relevant physical information, in the next subsections we give a summary of (non-rotating) black-hole perturbation theory and the main tools needed for the application of the CLA scheme. Afterwards, we apply this machinery to the construction of the initial data and describe how the energy, angular momentum, and linear momentum fluxes carried away by the gravitational waves are evaluated.

### 6.4.1 Black hole perturbation theory

The CLA is based on the fact that, in the last stages of coalescence, the gravitational field can be modeled, to a good degree of approximation, as the gravitational field of a single perturbed black hole. Thus, perturbation theory plays a key role in our calculations and it is worth reviewing its main concepts and tools. The starting point is the assumption that the spacetime metric,  $g_{\mu\nu}$ , can be written as:  $g_{\mu\nu} = g_{\mu\nu}^{\text{Sch}} + h_{\mu\nu}$ , where  $g_{\mu\nu}^{\text{Sch}}$  denotes the background Schwarzschild metric and  $h_{\mu\nu}$  the first-order perturbations. Then, we can take advantage of the spherical symmetry of the Schwarzschild metric to simplify the structure of the perturbations and of the equations that govern them. We can do this by expanding the perturbations in tensor spherical harmonics. It turns out that the linearized Einstein equations (in this case, around the Schwarzschild background) decouple for each harmonic. Not only this, we can distinguish between the perturbative modes with polar parity, which pick up a factor of  $(-1)^l$  under parity transformations, and the ones that have axial parity, which pick up a factor of  $(-1)^{l+1}$ . This distinction is important because polar and axial modes also decouple.

Following this discussion, we split the metric perturbations  $h_{\mu\nu}$  into polar and axial perturbations,  $h_{\mu\nu} = h_{\mu\nu}^{\text{a}} + h_{\mu\nu}^{\text{p}}$ . And these perturbations can be expanded in tensor spherical harmonics as

$$h_{\mu\nu}^{\text{a}} = \sum_{\ell,m} h_{\mu\nu}^{\text{a},\ell m}, \quad h_{\mu\nu}^{\text{p}} = \sum_{\ell,m} h_{\mu\nu}^{\text{p},\ell m}, \quad (6.34)$$

where

$$h_{\mu\nu}^{\text{a},\ell m} = \begin{pmatrix} 0 & h_A^{\ell m} S_a^{\ell m} \\ * & H^{\ell m} S_{ab}^{\ell m} \end{pmatrix}, \quad (6.35)$$

$$h_{\mu\nu}^{\text{p},\ell m} = \begin{pmatrix} h_{AB}^{\ell m} Y^{\ell m} & p_A^{\ell m} Y_a^{\ell m} \\ * & r^2 (K^{\ell m} Y_{ab}^{\ell m} + G^{\ell m} Z_{ab}^{\ell m}) \end{pmatrix}, \quad (6.36)$$

where asterisks are used to denote components that are given by the symmetry of these tensors.  $Y^{\ell m}$  are the scalar spherical harmonics [see Appendix B.2 for the conventions that we use and other details].  $Y_a^{\ell m}$  and  $S_a^{\ell m}$  are vector spherical harmonics and are

defined (for  $l \geq 1$ ) in terms of the scalar spherical harmonics by

$$Y_a^{\ell m} \equiv Y_{:a}^{\ell m}, \quad S_a^{\ell m} \equiv \epsilon_a^b Y_b^{\ell m}. \quad (6.37)$$

Finally,  $Y_{ab}^{\ell m}$ ,  $Z_{ab}^{\ell m}$ , and  $S_{ab}^{\ell m}$  are (symmetric) tensor spherical harmonics, which can also be defined ( $Z_{ab}^{\ell m}$  and  $S_{ab}^{\ell m}$  only for  $l \geq 2$ ) in terms of the scalar spherical harmonics by

$$Y_{ab}^{\ell m} \equiv Y^{\ell m} \Omega_{ab}, \quad Z_{ab}^{\ell m} \equiv Y_{:ab}^{\ell m} + \frac{\ell(\ell+1)}{2} Y^{\ell m} \Omega_{ab}, \quad (6.38)$$

$$S_{ab}^{\ell m} \equiv S_{(a;b)}^{\ell m}. \quad (6.39)$$

Here, the sign convention for the Levi-Civita tensor associated with the metric of the 2-sphere is:  $\epsilon_{\theta\varphi} = \sin\theta$ . In Appendix B.2, we give the orthogonality relations for the different harmonic objects. All perturbative quantities, scalar ( $h_{AB}^{\ell m}$ ), vectorial ( $p_A^{\ell m}$  and  $q_A^{\ell m}$ ), and tensorial ( $K^{\ell m}$ ,  $G^{\ell m}$ , and  $q_2^{\ell m}$ ), are functions of  $t$  and  $r$  only.

The metric perturbations are in general not invariant under transformations of the mapping between the background and perturbed spacetimes, or in other words, they are in general not invariant under gauge transformations. However, for the case of a spherically-symmetric background, like the Schwarzschild metric, there is a complete set of perturbative quantities that are gauge invariant. For polar modes this set can be chosen as follows

$$\tilde{h}_{AB}^{\ell m} = h_{AB}^{\ell m} - 2v_{A|B}^{\ell m}, \quad (6.40)$$

$$\tilde{K}^{\ell m} = K^{\ell m} + \frac{\ell(\ell+1)}{2} G^{\ell m} - 2\frac{r^{;A}}{r} v_A^{\ell m}, \quad (6.41)$$

where  $v_A^{\ell m} = p_A^{\ell m} - (r^2/2)G_{|A}^{\ell m}$ . And for axial modes

$$\tilde{h}_A^{\ell m} = h_A^{\ell m} - \frac{1}{2} H_{|A}^{\ell m} + \frac{r_{|A}}{r} H^{\ell m}, \quad (6.42)$$

The equations for the metric perturbations decouple in terms of complex master functions, so that once we solve the decoupled equations for these master functions all the metric perturbations can be reconstructed from them. In the case of axial modes, it was first done by Regge and Wheeler [189], and for polar modes by Zerilli [190] and later by Moncrief [191]. These functions are made out of metric perturbations and their first derivatives and they are gauge invariant. It is also possible to express them in a covariant form. In the case of polar modes, the Zerilli-Moncrief function can be written as follows [192]

$$\Psi_{\text{ZM}}^{\ell m} = \frac{r}{1 + \lambda_\ell} \left\{ \tilde{K}^{\ell m} + \frac{1}{\Lambda_\ell} \left[ r^{;A} r^{;B} \tilde{h}_{AB}^{\ell m} - r r^{;A} \tilde{K}_{|A}^{\ell m} \right] \right\}, \quad (6.43)$$

where  $\lambda_\ell = (\ell + 2)(\ell - 1)/2$  and  $\Lambda_\ell = \lambda_\ell + 3M/r$ . For axial modes, instead of using the well-known Regge-Wheeler master function

$$\Psi_{\text{RW}}^{\ell m} = -\frac{f}{r} r^{|A} \tilde{h}_{|A}^{\ell m}, \quad (6.44)$$

we are going to use the master function introduced by Cunningham, Price and Moncrief [193], in the form used in [194, 192]. The main reason for this choice is that it is simpler to evaluate the fluxes of energy, angular momentum, and linear momentum. Moreover, the contributions of axial modes to these physical quantities have the same form as the one of polar modes. Nevertheless, for the sake of completeness, we provide formulae for both master functions. The Cunningham-Price-Moncrief master function can be written in covariant form as [192]

$$\Psi_{\text{CPM}}^{\ell m} = \frac{r}{\lambda_\ell} \epsilon^{AB} \left( \tilde{h}_{B|A}^{\ell m} - \frac{2}{r} r_{|A} \tilde{h}_{|B}^{\ell m} \right). \quad (6.45)$$

In Schwarzschild coordinates these functions take the following form (the connection with the Regge-Wheeler parameterization of the perturbations is given Appendix C)

$$\begin{aligned} \Psi_{\text{ZM}}^{\ell m} &= \frac{r}{1 + \lambda_\ell} \left\{ K^{\ell m} + (1 + \lambda_\ell) G^{\ell m} \right. \\ &\quad \left. + \frac{f}{\Lambda_\ell} \left[ f h_{rr}^{\ell m} - r \partial_r K^{\ell m} - \frac{2}{r} (1 + \lambda_\ell) p_r^{\ell m} \right] \right\}, \end{aligned} \quad (6.46)$$

$$\Psi_{\text{RW}}^{\ell m} = -\frac{f}{r} \left( h_r^{\ell m} - \frac{1}{2} \partial_r H^{\ell m} + \frac{1}{r} H^{\ell m} \right), \quad (6.47)$$

$$\Psi_{\text{CPM}}^{\ell m} = -\frac{r}{\lambda_\ell} \left\{ \dot{h}_r^{\ell m} - \partial_r h_t^{\ell m} + \frac{2}{r} h_t^{\ell m} \right\}. \quad (6.48)$$

These master functions obey the following wave-type equation with a potential:

$$\left[ -\partial_t^2 + \partial_{r_*}^2 - V_\ell^{\text{RW/ZM}}(r) \right] \Psi_{\text{CPM/ZM}}^{\ell m} = 0, \quad (6.49)$$

where  $r_*$  is the so-called *tortoise* coordinate ( $r_* = r + 2M \ln(r/(2M) - 1)$ ). The potential for the axial modes is the Regge-Wheeler potential

$$V_\ell^{\text{RW}}(r) = \frac{f}{r^2} \left( \ell(\ell + 1) - \frac{6M}{r} \right), \quad (6.50)$$

and the one for polar modes is the Zerilli potential

$$V_\ell^{\text{ZM}}(r) = \frac{f}{r^2 \Lambda_\ell^2} \left[ 2\lambda_\ell^2 \left( 1 + \lambda_\ell + \frac{3M}{r} \right) + 18 \frac{M^2}{r^2} \left( \lambda_\ell + \frac{M}{r} \right) \right], \quad (6.51)$$

Once the different master functions have been computed we can estimate the energy and angular momentum carried out by the radiation field to infinity. We can do this by using the expressions of the energy and angular momentum fluxes at infinity obtained from the Isaacson's averaged energy-momentum tensor for gravitational waves [195, 196] (see also [197, 59]). In terms of the axial and polar master functions the expressions are

$$\dot{E}_{\text{GW}} = \frac{1}{64\pi} \sum_{\ell \geq 2, m} \frac{(\ell+2)!}{(\ell-2)!} \left( |\dot{\Psi}_{\text{CPM}}^{\ell m}|^2 + |\dot{\Psi}_{\text{ZM}}^{\ell m}|^2 \right), \quad (6.52)$$

$$\dot{L}_{\text{GW}} = \frac{1}{64\pi} \sum_{\ell \geq 2, m} im \frac{(\ell+2)!}{(\ell-2)!} \left( \bar{\Psi}_{\text{CPM}}^{\ell m} \dot{\Psi}_{\text{CPM}}^{\ell m} + \bar{\Psi}_{\text{ZM}}^{\ell m} \dot{\Psi}_{\text{ZM}}^{\ell m} \right). \quad (6.53)$$

We can also construct the metric *waveforms* by using

$$h_+ - ih_\times = \frac{1}{2r} \sum_{\ell \geq 2, m} \sqrt{\frac{(\ell+2)!}{(\ell-2)!}} \left( \Psi_{\text{ZM}}^{\ell m} + i\Psi_{\text{CPM}}^{\ell m} \right) {}_{-2}Y^{\ell m}, \quad (6.54)$$

where  ${}_{-2}Y^{\ell m}$  denotes the spherical harmonics of spin weight  $-2$  (see, e.g. [198] and Appendix B.3 for details). In this work we are interested in studying the gravitational recoil due to the merger of unequal-mass black-hole binary systems and therefore, we want to evaluate the flux of linear momentum emitted in gravitational waves. This quantity can also be computed from the Isaacson's energy-momentum tensor and can be written in terms of the metric waveforms as follows:

$$\dot{P}_{\text{GW}}^k = \frac{r^2}{16\pi} \int d\Omega \hat{r}_{\text{obs}}^k \left( \dot{h}_+^2 + \dot{h}_\times^2 \right), \quad (6.55)$$

where  $\hat{r}_{\text{obs}}^k$  is a unit vector that points from the source to the observer. We can then express the components of  $\hat{r}_{\text{obs}}^k$  in terms of scalar spherical harmonics as

$$\hat{r}_{\text{obs}}^k = -2\sqrt{\frac{2\pi}{3}} \left( \Re(Y^{1,1}), \Im(Y^{1,1}), -\frac{Y^{1,0}}{\sqrt{2}} \right), \quad (6.56)$$

where  $\Re$  and  $\Im$  denote the real and imaginary parts of a complex number. By simple inspection of the linear momentum flux in Eq. (6.55), and taking into account the harmonic structure of the metric waveforms in Eq. (6.54) and of  $\hat{r}_{\text{obs}}^k$  in Eq. (6.56), we realize that all terms in the flux contain the product of three spherical harmonic objects. Therefore, in order to obtain a practical expression for  $\dot{P}_{\text{GW}}^k$  we need to use the machinery for studying coupled angular momenta common in quantum physics [187, 188]. The calculation goes along the lines described in [59], and some details are given in Appendix D.

The result can be written in the following form

$$\begin{aligned}
\dot{P}_{\text{GW}}^x &= -\frac{1}{64\pi} \sum_{\ell \geq 2, m} \frac{(\ell+3)!}{(\ell-2)!} \frac{1}{(\ell+1)\sqrt{(2\ell+3)(2\ell+1)}} \left\{ \sqrt{(\ell+m+2)(\ell+m+1)} \right. \\
&\times \left( \dot{\Psi}_{\text{ZM}}^{\ell m} \dot{\Psi}_{\text{ZM}}^{\ell+1, m+1} + \dot{\Psi}_{\text{CPM}}^{\ell m} \dot{\Psi}_{\text{CPM}}^{\ell+1, m+1} \right) \\
&- \sqrt{(\ell-m+2)(\ell-m+1)} \left( \dot{\Psi}_{\text{ZM}}^{\ell m} \dot{\Psi}_{\text{ZM}}^{\ell+1, m-1} + \dot{\Psi}_{\text{CPM}}^{\ell m} \dot{\Psi}_{\text{CPM}}^{\ell+1, m-1} \right) \left. \right\} \\
&- \frac{i}{64\pi} \sum_{\ell \geq 2, m} (\ell+2)(\ell-1) \left\{ \sqrt{(\ell-m)(\ell+m+1)} \left( \dot{\Psi}_{\text{ZM}}^{\ell m} \dot{\Psi}_{\text{CPM}}^{\ell, m+1} - \dot{\Psi}_{\text{CPM}}^{\ell m} \dot{\Psi}_{\text{ZM}}^{\ell, m+1} \right) \right. \\
&+ \left. \sqrt{(\ell+m)(\ell-m+1)} \left( \dot{\Psi}_{\text{ZM}}^{\ell m} \dot{\Psi}_{\text{CPM}}^{\ell, m-1} - \dot{\Psi}_{\text{CPM}}^{\ell m} \dot{\Psi}_{\text{ZM}}^{\ell, m-1} \right) \right\}, \tag{6.57}
\end{aligned}$$

$$\begin{aligned}
\dot{P}_{\text{GW}}^y &= \frac{i}{64\pi} \sum_{\ell \geq 2, m} \frac{(\ell+3)!}{(\ell-2)!} \frac{1}{(\ell+1)\sqrt{(2\ell+3)(2\ell+1)}} \left\{ \sqrt{(\ell+m+2)(\ell+m+1)} \right. \\
&\times \left( \dot{\Psi}_{\text{ZM}}^{\ell m} \dot{\Psi}_{\text{ZM}}^{\ell+1, m+1} + \dot{\Psi}_{\text{CPM}}^{\ell m} \dot{\Psi}_{\text{CPM}}^{\ell+1, m+1} \right) \\
&+ \sqrt{(\ell-m+2)(\ell-m+1)} \left( \dot{\Psi}_{\text{ZM}}^{\ell m} \dot{\Psi}_{\text{ZM}}^{\ell+1, m-1} + \dot{\Psi}_{\text{CPM}}^{\ell m} \dot{\Psi}_{\text{CPM}}^{\ell+1, m-1} \right) \left. \right\} \\
&- \frac{1}{64\pi} \sum_{\ell \geq 2, m} (\ell+2)(\ell-1) \left\{ \sqrt{(\ell-m)(\ell+m+1)} \left( \dot{\Psi}_{\text{ZM}}^{\ell m} \dot{\Psi}_{\text{CPM}}^{\ell, m+1} - \dot{\Psi}_{\text{CPM}}^{\ell m} \dot{\Psi}_{\text{ZM}}^{\ell, m+1} \right) \right. \\
&- \left. \sqrt{(\ell+m)(\ell-m+1)} \left( \dot{\Psi}_{\text{ZM}}^{\ell m} \dot{\Psi}_{\text{CPM}}^{\ell, m-1} - \dot{\Psi}_{\text{CPM}}^{\ell m} \dot{\Psi}_{\text{ZM}}^{\ell, m-1} \right) \right\}, \tag{6.58}
\end{aligned}$$

$$\begin{aligned}
\dot{P}_{\text{GW}}^z &= \frac{1}{32\pi} \sum_{\ell \geq 2, m} \frac{(\ell+3)!}{(\ell-2)!} \sqrt{\frac{(\ell+m+1)(\ell-m+1)}{(2\ell+3)(2\ell+1)(\ell+1)^2}} \left( \dot{\Psi}_{\text{ZM}}^{\ell m} \dot{\Psi}_{\text{ZM}}^{\ell+1, m} + \dot{\Psi}_{\text{CPM}}^{\ell m} \dot{\Psi}_{\text{CPM}}^{\ell+1, m} \right) \\
&- \frac{i}{32\pi} \sum_{\ell \geq 2, m} m(\ell+2)(\ell-1) \left( \dot{\Psi}_{\text{ZM}}^{\ell m} \dot{\Psi}_{\text{CPM}}^{\ell, m} - \dot{\Psi}_{\text{CPM}}^{\ell m} \dot{\Psi}_{\text{ZM}}^{\ell, m} \right). \tag{6.59}
\end{aligned}$$

In conclusion, all we need to extract relevant physical information is the master functions. In the next subsections, we extract initial data for these master functions.

#### 6.4.2 Relation between ADM variables and metric perturbation

In section 6.3, we constructed initial data for a binary black hole system in coalescence. The procedure used for this construction was based on the 3+1 ADM formalism [199] and, hence, the initial data is given in terms of ADM variables [Eqs. (6.29), (6.25) and (6.3)]. Then, in order to build initial data for the evolution of the master functions, we need to first find the relation between the ADM variables and the metric perturbations (see, e.g. [200]). This means that we need to use the relations between the components of the 3-metric  $\gamma_{ij}$  and the metric perturbations, and also the relations between the metric perturbations and their first derivatives and the components of the extrinsic curvature  $K_{ij}$ . For the former, we use the fact that the components of

the 3-metric are the spatial components of the orthogonal projection operator on the hypersurfaces of the spacetime slicing, described by a normal  $n_\mu$  :

$$\gamma_{\mu\nu} = g_{\mu\nu} + n_\mu n_\nu . \quad (6.60)$$

Then, the different modes of the harmonically decomposed 3-metric are related to the metric perturbations via

$$\gamma_{tt}^{\ell m} = -f \delta^{0,0} , \quad (6.61)$$

$$\gamma_{tr}^{\ell m} = h_{tr}^{\ell m} Y^{\ell m} , \quad (6.62)$$

$$\gamma_{ta}^{\ell m} = p_t^{\ell m} Y_a^{\ell m} + h_t^{\ell m} S_a^{\ell m} , \quad (6.63)$$

$$\gamma_{rr}^{\ell m} = f^{-1} \delta^{0,0} + h_{rr}^{\ell m} Y^{\ell m} , \quad (6.64)$$

$$\gamma_{ra}^{\ell m} = p_r^{\ell m} Y_a^{\ell m} + h_r^{\ell m} S_a^{\ell m} , \quad (6.65)$$

$$\begin{aligned} \gamma_{ab}^{\ell m} &= r^2 \Omega_{ab} \delta^{0,0} + r^2 \left( K^{\ell m} Y_{ab}^{\ell m} + G^{\ell m} Z_{ab}^{\ell m} \right) \\ &+ H^{\ell m} S_{ab}^{\ell m} . \end{aligned} \quad (6.66)$$

The first three equations are related to the choice of slicing, that is, to the choice of shift vector  $\beta^i$  and lapse  $\alpha$ . Actually, the lapse and shift at first order are given by

$$\alpha^2 = f(1 - fh^{tt}) = f - h_{tt} + \mathcal{O}(h^2) , \quad (6.67)$$

$$\beta^i = h_t^i + \mathcal{O}(h^2) . \quad (6.68)$$

The relation between the extrinsic curvature and the metric perturbations can be found through the relation between the 3-metric and the extrinsic curvature

$$K_{\mu\nu} = -\frac{1}{2} \mathcal{L}_{\mathbf{n}} \gamma_{\mu\nu} , \quad (6.69)$$

where the symbol  $\mathcal{L}$  denotes Lie differentiation, and Eq. (6.60) between the 3-metric and the spacetime metric. In this way, we find that the different modes of the harmonically decomposed extrinsic curvature are related to the metric perturbations by the following expressions:

$$K_{rr}^{\ell m} = \frac{1}{2\sqrt{f}} \left[ \dot{h}_{rr}^{\ell m} - 2h_{tr}^{\ell m'} - \frac{f'}{f} h_{tr}^{\ell m} \right] Y^{\ell m} , \quad (6.70)$$

$$K_{ra}^{\ell m} = \frac{1}{2\sqrt{f}} \left\{ \left[ \dot{p}_r^{\ell m} - p_t^{\ell m'} + \frac{2}{r} p_t^{\ell m} - h_{tr}^{\ell m} \right] Y_a^{\ell m} + \left[ \dot{h}_r^{\ell m} - h_t^{\ell m'} + \frac{2}{r} h_t^{\ell m} \right] S_a^{\ell m} \right\} , \quad (6.71)$$

$$\begin{aligned} K_{ab}^{\ell m} &= \frac{r^2}{2\sqrt{f}} \left\{ \left[ \dot{K}^{\ell m} + \frac{\ell(\ell+1)}{r^2} p_t^{\ell m} - \frac{2f}{r} h_{tr}^{\ell m} \right] Y_{ab}^{\ell m} + \left[ \dot{G}^{\ell m} - \frac{2}{r^2} p_t^{\ell m} \right] Z_{ab}^{\ell m} \right. \\ &+ \left. \frac{1}{r^2} \left[ \dot{H}^{\ell m} - 2h_t^{\ell m} \right] S_{ab}^{\ell m} \right\} , \end{aligned} \quad (6.72)$$

where the dots and primes denote partial differentiation with respect to time  $t$  and radial coordinate  $r$  respectively.

### 6.4.3 Initial data for the metric perturbations

Before computing initial data for the master functions, we must find data for the metric perturbations, that is, find  $(h_{\mu\nu}, \dot{h}_{\mu\nu})$ , in the parameterization given in Eqs. (6.35) and (6.36) on the initial slice  $t = t_o$ . To begin with, since our 3-metric is conformally flat, the following metric perturbations vanish on the initial slice:

$$p_r^{\ell m} = G^{\ell m} = 0, \quad h_r^{\ell m} = H^{\ell m} = 0. \quad (6.73)$$

We have also seen that the conformal factor, the physical and the conformal extrinsic curvatures can be formally expanded in powers of  $d$  and  $P$  as follows

$$\Phi = \Phi_{(0)} + \Phi_{(2)} d^2 + \Phi_{(3)} d^3 + \mathcal{O}(P^2 d^2, d^4), \quad (6.74)$$

$$\hat{K}_{ij} = Pd \hat{K}_{(1)ij} + Pd^2 \hat{K}_{(2)ij} + \mathcal{O}(Pd^3), \quad (6.75)$$

where  $\hat{K}_{(1)ij}$  and  $\hat{K}_{(2)ij}$  are the coefficients of the terms of order  $Pd$  and  $Pd^2$  respectively in the expansion of  $\hat{K}_{ij}$ . Then, the physical extrinsic curvature,  $K_{ij}$ , given by Eq. (6.3), can be formally expanded in the form

$$K_{ij} = \Phi_{(0)}^{-2} \left( Pd \hat{K}_{(1)ij} + Pd^2 \hat{K}_{(2)ij} \right) + \mathcal{O}(Pd^3), \quad (6.76)$$

which means that in order to obtain the physical extrinsic curvature up to  $\mathcal{O}(Pd^2)$  we only need the zero-th order piece of the conformal factor. The explicit expressions of the coefficients of these expansions are given by equations (6.29), (6.25) and (6.3).

With this in mind, we are going to extract the remaining modes of the initial data. To that end, we use the expression of the separation vector  $\hat{\epsilon}$  in spherical coordinates, namely

$$\hat{\epsilon}^i = \left( \sin \theta \cos \varphi, \frac{\cos \theta \cos \varphi}{R}, -\frac{\sin \varphi}{R \cos \theta} \right). \quad (6.77)$$

Then, the non-zero components of the 3-metric on the initial slice are given by

$$\gamma_{rr} = f^{-1} \left[ 1 + 2 \frac{q}{(1+q)^2} \frac{Md^2}{r^3} \frac{1}{\sigma^5} P_2(\xi) - 2 \frac{q(1-q)}{(1+q)^3} \frac{Md^3}{r^4} \frac{1}{\sigma^7} P_3(\xi) \right] + \mathcal{O}(P^2 d^2, d^4), \quad (6.78)$$

$$\gamma_{ab} = r^2 \Omega_{ab} \left[ 1 + 2 \frac{q}{(1+q)^2} \frac{Md^2}{r^3} \frac{1}{\sigma^5} P_2(\xi) - 2 \frac{q(1-q)}{(1+q)^3} \frac{Md^3}{r^4} \frac{1}{\sigma^7} P_3(\xi) \right] + \mathcal{O}(P^2 d^2, d^4), \quad (6.79)$$

where we have introduced the following definitions

$$\xi = \sin \theta \cos \varphi, \quad \sigma = \frac{1 + \sqrt{f}}{2}. \quad (6.80)$$

We can now rewrite the 3-metric in terms of spherical harmonics as follows

$$\begin{aligned} \gamma_{rr} &= f^{-1} \left\{ 1 - 2\sqrt{\frac{\pi}{5}} \frac{q}{(1+q)^2} \frac{Md^2}{r^3} \frac{1}{\sigma^5} \left[ Y^{2,0} - \sqrt{6} \Re(Y^{2,2}) \right] - 2\sqrt{\frac{\pi}{7}} \frac{q(1-q)}{(1+q)^3} \frac{Md^3}{r^4} \frac{1}{\sigma^7} \right. \\ &\times \left. \left[ \sqrt{3} \Re(Y^{3,1}) - \sqrt{5} \Re(Y^{3,3}) \right] \right\} + \mathcal{O}(P^2 d^2, d^4), \end{aligned} \quad (6.81)$$

$$\begin{aligned} \gamma_{ab} &= r^2 \Omega_{ab} - 2\sqrt{\frac{\pi}{5}} \frac{q}{(1+q)^2} \frac{Md^2}{r} \frac{1}{\sigma^5} \left[ Y_{ab}^{2,0} - \sqrt{6} \Re(Y_{ab}^{2,2}) \right] - 2\sqrt{\frac{\pi}{7}} \frac{q(1-q)}{(1+q)^3} \frac{Md^3}{r^2} \frac{1}{\sigma^7} \\ &\times \left[ \sqrt{3} \Re(Y_{ab}^{3,1}) - \sqrt{5} \Re(Y_{ab}^{3,3}) \right] + \mathcal{O}(P^2 d^2, d^4). \end{aligned} \quad (6.82)$$

In order to repeat this procedure with the extrinsic curvature, we first need to compute the components of the conformal extrinsic curvature with the separation vector  $\hat{\epsilon}$  of Eq. (6.77). The components of the conformal extrinsic curvature are given by

$$\hat{K}_{RR} = 3 \frac{Pd}{R^3} \sin^2 \theta \sin(2\varphi) - 3 \frac{1-q}{1+q} \frac{Pd^2}{R^4} \sin \varphi \sin \theta \left( 5 \sin^2 \theta \cos^2 \varphi - 2 \right) + \mathcal{O}(Pd^3), \quad (6.83)$$

$$\hat{K}_{R\theta} = \frac{3}{4} \frac{1-q}{1+q} \frac{Pd^2}{R^3} \cos \theta \sin \varphi \left( 5 \sin^2 \theta \cos^2 \varphi + 3 \right) + \mathcal{O}(Pd^3), \quad (6.84)$$

$$\hat{K}_{R\varphi} = 3 \frac{Pd}{R^2} \sin^2 \theta + \frac{3}{4} \frac{1-q}{1+q} \frac{Pd^2}{R^3} \sin \theta \cos \varphi \left[ \sin^2 \theta \left( 5 \cos^2 \varphi - 14 \right) + 3 \right] + \mathcal{O}(Pd^3) \quad (6.85)$$

$$\begin{aligned} \hat{K}_{\theta\theta} &= \frac{3}{8} \frac{Pd}{R} \sin(2\varphi) [\cos(2\theta) - 5] - \frac{3}{4} \frac{1-q}{1+q} \frac{Pd^2}{R^2} \sin \theta \sin \varphi \left[ 5 \cos^2 \varphi \left( \cos^2 \theta - 3 \right) + 3 \right] \\ &+ \mathcal{O}(Pd^3), \end{aligned} \quad (6.86)$$

$$\hat{K}_{\theta\varphi} = -\frac{3}{4} \frac{Pd}{R} \sin(\theta) \cos(2\varphi) + \frac{3}{2} \frac{1-q}{1+q} \frac{Pd^2}{R^2} \sin^2 \theta \cos \theta \cos \varphi \left( 5 \cos^2 \varphi - 2 \right) + \mathcal{O}(Pd^3), \quad (6.87)$$

$$\begin{aligned} \hat{K}_{\varphi\varphi} &= \frac{3}{8} \frac{Pd}{R} \sin^2 \theta \sin(2\varphi) [1 + 3 \cos(2\theta)] + \frac{15}{4} \frac{1-q}{1+q} \frac{Pd^2}{R^2} \sin^3 \theta \sin \varphi \\ &\times \left[ \cos^2 \varphi \left( 3 \sin^2 \theta - 2 \right) - 1 \right] + \mathcal{O}(Pd^3). \end{aligned} \quad (6.88)$$

Here we have checked that the terms of  $\mathcal{O}(Pd)$  agree with those in [183] (up to a typo in their value of the  $\{\theta, \varphi\}$  component). The next step is the calculation of the physical extrinsic curvature in terms of spherical harmonics and Schwarzschild coordinates. This

quantity is given by

$$K_{rr} = 4\sqrt{\frac{6\pi}{5}} \frac{Pd}{r^3} \frac{1}{f} \Im(Y^{2,2}) - 2\sqrt{\frac{3\pi}{7}} \frac{1-q}{1+q} \frac{Pd^2}{r^4} \frac{1}{f\sigma^2} \left[ \sqrt{14} \Im(Y^{1,1}) + \Im(Y^{3,1}) - \sqrt{15} \Im(Y^{3,3}) \right] + \mathcal{O}(Pd^3), \quad (6.89)$$

$$K_{ra} = 2\sqrt{3\pi} \frac{Pd}{r^2} \frac{1}{\sqrt{f}} S_a^{1,0} + \frac{1}{2} \sqrt{\frac{\pi}{21}} \frac{1-q}{1+q} \frac{Pd^2}{r^3} \frac{1}{\sqrt{f}\sigma^2} \left[ 6\sqrt{14} \Im(Y_a^{1,1}) + 16\sqrt{\frac{14}{5}} \Re(S_a^{2,1}) + \Im(Y_a^{3,1}) - \sqrt{15} \Im(Y_a^{3,3}) \right] + \mathcal{O}(Pd^3), \quad (6.90)$$

$$K_{ab} = -\sqrt{\frac{6\pi}{5}} \frac{Pd}{r} \left[ 2\Im(Y_{ab}^{2,2}) + \Im(Z_{ab}^{2,2}) \right] + \frac{1}{2} \sqrt{\frac{\pi}{21}} \frac{1-q}{1+q} \frac{Pd^2}{r^2} \frac{1}{\sigma^2} \left\{ 6\sqrt{14} \Im(Y_{ab}^{1,1}) - 8\sqrt{\frac{14}{5}} \Re(S_{ab}^{2,1}) + 6\Im(Y_{ab}^{3,1}) + \Im(Z_{ab}^{3,1}) - \sqrt{15} \left[ 6\Im(Y_{ab}^{3,3}) + \Re(Z_{ab}^{3,3}) \right] \right\} + \mathcal{O}(Pd^3). \quad (6.91)$$

Eqs. (6.81,6.82) and (6.89)-(6.91) give the complete harmonic decomposition of the initial data  $(\gamma_{ij}, K_{ij})$ . We must now extract the initial values of the metric perturbations and their time derivative by comparing these expressions with Eqs. (6.64)-(6.66) and (6.70)-(6.72). To simplify notation, we now drop the truncation error in all equations, since it has already been given in the main expansions. Comparison of Eqs. (6.81,6.82) with Eqs. (6.64)-(6.66) yields the non-vanishing initial metric perturbations, namely

$$K^{2,0} = fh_{rr}^{2,0} = -2\sqrt{\frac{\pi}{5}} \frac{q}{(1+q)^2}, \quad (6.92)$$

$$K^{2,\pm 2} = fh_{rr}^{2,\pm 2} = \sqrt{\frac{6\pi}{5}} \frac{q}{(1+q)^2} \frac{Md^2}{r^3} \frac{1}{\sigma^5}, \quad (6.93)$$

$$K^{3,\pm 1} = fh_{rr}^{3,\pm 1} = \mp \sqrt{\frac{3\pi}{7}} \frac{q(1-q)}{(1+q)^3} \frac{Md^3}{r^4} \frac{1}{\sigma^7}, \quad (6.94)$$

$$K^{3,\pm 3} = fh_{rr}^{3,\pm 3} = \pm \sqrt{\frac{5\pi}{7}} \frac{q(1-q)}{(1+q)^3} \frac{Md^3}{r^4} \frac{1}{\sigma^7}. \quad (6.95)$$

As we can see, all the axial metric perturbations initially vanish. Now, in order to obtain the initial values of the time derivative of the metric perturbations, we must compare Eqs. (6.89)-(6.91) with Eqs. (6.70)-(6.72). It is important to realize that in Eqs. (6.70)-(6.72) there are terms that are associated with the gauge freedom of choosing the slicing, more specifically, terms associated with components of the shift vector [see Eq. (6.68)]. Moreover, there is no unique way of assigning values to the different time derivatives of the metric perturbations and the metric perturbations themselves. This reflects the fact that the values of the metric perturbations are gauge dependent, since in general the components of the metric perturbations (and their time derivatives) are not gauge invariant. Keeping this in mind, we have assigned the following initial values to the time

derivatives of the metric perturbations: the non-vanishing polar modes are

$$\dot{h}_{rr}^{2,\pm 2} = \mp 24i \sqrt{\frac{\pi}{30}} \frac{Pd}{r^3} \frac{1}{\sqrt{f}}, \quad (6.96)$$

$$\dot{h}_{rr}^{3,\pm 1} = 2i \sqrt{\frac{3\pi}{7}} \frac{1-q}{1+q} \frac{Pd^2}{r^4} \frac{1}{\sqrt{f}\sigma^2}, \quad (6.97)$$

$$\dot{h}_{rr}^{3,\pm 3} = -6i \sqrt{\frac{5\pi}{7}} \frac{1-q}{1+q} \frac{Pd^2}{r^4} \frac{1}{\sqrt{f}\sigma^2}, \quad (6.98)$$

$$\dot{p}_r^{3,\pm 1} = -\frac{i}{2} \sqrt{\frac{\pi}{21}} \frac{1-q}{1+q} \frac{Pd^2}{r^3} \frac{1}{\sigma^2}, \quad (6.99)$$

$$\dot{p}_r^{3,\pm 3} = \frac{i}{2} \sqrt{\frac{5\pi}{7}} \frac{1-q}{1+q} \frac{Pd^2}{r^3} \frac{1}{\sigma^2}, \quad (6.100)$$

$$\dot{G}^{2,\pm 2} = \pm i \sqrt{\frac{6\pi}{5}} \frac{Pd}{r^3} \sqrt{f}, \quad (6.101)$$

$$\dot{K}^{2,\pm 2} = \pm 2i \sqrt{\frac{6\pi}{5}} \frac{Pd}{r^3} \sqrt{f}, \quad (6.102)$$

$$\dot{G}^{3,\pm 1} = -\frac{i}{2} \sqrt{\frac{\pi}{21}} \frac{1-q}{1+q} \frac{Pd^2}{r^4} \frac{\sqrt{f}}{\sigma^2}, \quad (6.103)$$

$$\dot{K}^{3,\pm 1} = -i \sqrt{\frac{3\pi}{7}} \frac{1-q}{1+q} \frac{Pd^2}{r^4} \frac{\sqrt{f}}{\sigma^2}, \quad (6.104)$$

$$\dot{G}^{3,\pm 3} = \frac{i}{2} \sqrt{\frac{5\pi}{7}} \frac{1-q}{1+q} \frac{Pd^2}{r^4} \frac{\sqrt{f}}{\sigma^2}, \quad (6.105)$$

$$\dot{K}^{3,\pm 3} = 3i \sqrt{\frac{5\pi}{7}} \frac{1-q}{1+q} \frac{Pd^2}{r^4} \frac{\sqrt{f}}{\sigma^2}; \quad (6.106)$$

and the axial ones are

$$\dot{h}_r^{1,0} = 4\sqrt{3\pi} \frac{Pd}{r^2}, \quad (6.107)$$

$$\dot{h}_r^{2,\pm 1} = \pm 8 \sqrt{\frac{2\pi}{15}} \frac{1-q}{1+q} \frac{Pd^2}{r^3} \frac{1}{\sigma^2}, \quad (6.108)$$

$$\dot{H}^{2,\pm 1} = \mp 4 \sqrt{\frac{2\pi}{15}} \frac{1-q}{1+q} \frac{Pd^2}{r^2} \frac{\sqrt{f}}{\sigma^2}. \quad (6.109)$$

By using the correspondence between our parameterization of the metric perturbations and that of Regge Wheeler [Eqs. (C.1)-(C.5) in Appendix C] we have checked that up to  $\mathcal{O}(d^2)$  and  $\mathcal{O}(Pd)$  our expressions agree with those found in [183] (up to a typo in their  $\dot{h}_r^{1,0}$ ). We have decided to assign values to the time derivatives of the metric perturbations and the metric perturbations themselves by the following usual convention: all modes with  $\ell = 1$  are assigned to metric perturbations associated with the shift vector. These perturbations represent either translations or rotations of the observers associated with the normal to the initial slice with respect to our coordinate system. In our case, these

perturbations are given through the following relationships

$$fh_{tr}^{1,\pm 1'} + \frac{f'}{2}h_{tr}^{1,\pm 1} = -i\sqrt{6\pi} \frac{1-q}{1+q} \frac{Pd^2}{r^4} \frac{\sqrt{f}}{\sigma^2}, \quad (6.110)$$

$$p_t^{1,\pm 1'} - \frac{2}{r}p_t^{1,\pm 1} + h_{tr}^{1,\pm 1} = i\sqrt{6\pi} \frac{Pd^2}{r^3} \frac{1-q}{1+q} \frac{1}{\sigma^2}, \quad (6.111)$$

$$p_t^{1,\pm 1} - rfh_{tr}^{1,\pm 1} = -i\sqrt{\frac{3\pi}{2}} \frac{1-q}{1+q} \frac{Pd^2}{r^2} \frac{\sqrt{f}}{\sigma^2}. \quad (6.112)$$

Here, two comments are in order. First, one can see that these equations are consistent in the sense that the derivative of Eq. (6.112) with respect to  $r$  can be reduced to a trivial identity by using Eqs. (6.110) and (6.111). Second, from these equations we can immediately see that the shift vector is different from zero [see Eq. (6.68)]. A non-zero shift could in principle be a problem if we wanted to place observers at constant  $r$  (in the wave zone), evaluate the linear momentum flux, and then infer a recoil velocity of the final black hole after the merger. If we were to do this, the measured velocity would have a component due to the motion of the observers with respect to the position of the final black hole, as described by the shift vector. This contribution would then have to be subtracted, but it can be seen that the shift vector decays quite fast as  $r$  becomes large and, hence, this effect would be negligible.

#### 6.4.4 Initial data for the master functions

Using the initial data for the metric perturbations [Eqs. (6.92)-(6.95), (6.96)-(6.106), and Eqs. (6.107)-(6.109)] in the master functions [Eqs. (6.46)-(6.48)], we can compute initial data for them:  $(\Psi_{\text{ZM}}^{\ell m}, \dot{\Psi}_{\text{ZM}}^{\ell m})$ ,  $(\Psi_{\text{RW}}^{\ell m}, \dot{\Psi}_{\text{RW}}^{\ell m})$ , and  $(\Psi_{\text{CPM}}^{\ell m}, \dot{\Psi}_{\text{CPM}}^{\ell m})$  on the initial slice  $t = t_o$ .

The results for the Regge-Wheeler master function are:

$$\Psi_{\text{RW}}^{\ell m} = 0, \quad (6.113)$$

$$\dot{\Psi}_{\text{RW}}^{2,\pm 1} = \mp 2\sqrt{\frac{2\pi}{15}} \frac{1-q}{1+q} \frac{Pd^2}{r^4} \frac{\sqrt{f}(1-\sqrt{f})}{\sigma^2} (7\sigma - 3), \quad (6.114)$$

and for the Cunningham-Price-Moncrief master function are

$$\Psi_{\text{CPM}}^{2,\pm 1} = \mp \frac{4}{3} \frac{\sqrt{30\pi}}{5} \frac{1-q}{1+q} \frac{Pd^2}{r^2} \frac{1}{\sigma^2}, \quad (6.115)$$

$$\dot{\Psi}_{\text{CPM}}^{\ell m} = 0. \quad (6.116)$$

In the same way, the non-vanishing initial data for the Zerilli-Moncrief master functions is given by

$$\Psi_{\text{ZM}}^{2,0} = -\frac{2}{3}\sqrt{\frac{\pi}{5}}\frac{q}{(1+q)^2}\frac{Md^2}{r^2}\frac{1+5\sigma}{\Lambda_2\sigma^5}, \quad (6.117)$$

$$\Psi_{\text{ZM}}^{2,\pm 2} = \sqrt{\frac{2\pi}{15}}\frac{q}{(1+q)^2}\frac{Md^2}{r^2}\frac{1+5\sigma}{\Lambda_2\sigma^5}, \quad (6.118)$$

$$\Psi_{\text{ZM}}^{3,\pm 1} = \mp\frac{1}{2}\sqrt{\frac{\pi}{21}}\frac{q(1-q)}{(1+q)^3}\frac{Md^3}{r^3}\frac{3+7\sigma}{\Lambda_3\sigma^7}, \quad (6.119)$$

$$\Psi_{\text{ZM}}^{3,\pm 3} = \pm\frac{1}{6}\sqrt{\frac{5\pi}{7}}\frac{q(1-q)}{(1+q)^3}\frac{Md^3}{r^3}\frac{3+7\sigma}{\Lambda_3\sigma^7}, \quad (6.120)$$

$$\dot{\Psi}_{\text{ZM}}^{2,\pm 2} = \pm i\sqrt{\frac{6\pi}{5}}\frac{Pd}{r^2}\frac{\sqrt{f}}{\Lambda_2}\left(4 + \frac{3M}{r}\right), \quad (6.121)$$

$$\dot{\Psi}_{\text{ZM}}^{3,\pm 1} = -\frac{i}{2}\sqrt{\frac{\pi}{21}}\frac{1-q}{1+q}\frac{Pd^2}{r^3}\frac{\sqrt{f}}{\Lambda_3\sigma^3}\left[10\sigma + (1+3\sigma)\frac{M}{r}\right], \quad (6.122)$$

$$\dot{\Psi}_{\text{ZM}}^{3,\pm 3} = \frac{i}{2}\sqrt{\frac{5\pi}{7}}\frac{1-q}{1+q}\frac{Pd^2}{r^3}\frac{\sqrt{f}}{\Lambda_3\sigma^3}\left[10\sigma + (1+3\sigma)\frac{M}{r}\right]. \quad (6.123)$$

Note that the master equations do not have the same uncontrolled remainders as its derivatives, since they come from different components of the initial data. In the case of unboosted head-on collisions [180], the initial data scales in powers of  $d^N$ . Therefore, one only needs to perform one single numerical evolution of the master functions for some reference value of  $d = d^*$ , and the results for any other value of  $d$  can be found using the scaling relation. For non-time-symmetric data, such as for quasicircular or boosted sets, such scaling does not exist. In our case, for example, although  $\Psi_{\text{ZM}}^{\ell m}$  still scales as  $d^N$ , its time derivative  $\dot{\Psi}_{\text{ZM}}^{\ell m}$  scales as  $Pd^N$ . Therefore, the master functions themselves are not straightforwardly scalable and several runs with different values of the initial parameters must be performed.

## 6.5 Results from the CLA

In this section, we evolve the master functions with the initial data obtained in the previous sections in the CLA scheme and report the results for the main physical quantities, in particular for the gravitational recoil velocities. We first need to choose appropriately the parameters that completely determine the initial data, such that it describes a binary black hole system merging from a quasicircular orbit (subsection 6.5.1).

Then, in subsection 6.5.2, we use a numerical code to evolve the different master equations [Eqs. (6.49)] and compute the relevant physical quantities. We discuss the results and compare with previous ones in the literature when possible.

### 6.5.1 Determining the parameters of the initial data

Our initial data depends on the following parameters:

- The total (ADM) mass of the system,  $M$ ;
- The mass ratio, where one can use either the *bare* mass ratio  $q$  or the *physical* one  $Q$ , related by Eqs. (6.15) and (6.16).
- The initial separation, where again one can use the *bare* separation  $d$  or the *physical* one  $D$ , related by Eq. (6.17);
- The linear momentum parameter  $P$  of each individual hole.

Within the family of initial data spanned by these four parameters, we need to single out the subset that corresponds to configurations in *quasicircular* orbital motion. In numerical relativity this is done by looking at the minimum in the *binding* energy of the system with respect to the distance, while keeping the total ADM angular momentum constant (see, e.g. [18]). We here follow the same procedure without using the *slow motion* approximation. The binding energy that we minimize is

$$E_b = \mathcal{M}_{\text{ADM}} - \mathcal{M}_1 - \mathcal{M}_2. \quad (6.124)$$

where  $\mathcal{M}_{\text{ADM}}$  is the total ADM mass and it is computed in the asymptotically-flat region containing the two holes ( $\Sigma_0$ ). This mass is given by (see, e.g. [201])

$$\mathcal{M}_{\text{ADM}} = M + \frac{5P^2}{8\mu}, \quad (6.125)$$

where  $M$  is given in Eq. (6.12) and  $\mu$  is the reduced *bare* mass, i.e.  $\mu = m_1 m_2 / M$ . Moreover, in Eq. (6.124),  $\mathcal{M}_1$  and  $\mathcal{M}_2$  denote the masses computed in the asymptotically-flat regions  $\Sigma_1$  and  $\Sigma_2$ . These masses are given by (see, e.g. [201])

$$\mathcal{M}_\Lambda = M_\Lambda + \frac{P^2}{8m_\Lambda} \quad (\Lambda = 1, 2), \quad (6.126)$$

where  $M_\Lambda$  is given in Eq. (6.11). Then, the binding energy can be written in the following form

$$E_b = -\frac{m_1 m_2}{d} + \frac{J^2}{2\mu d^2}, \quad (6.127)$$

where  $J$  is the ADM angular momentum, given by  $J = Pd$ . This binding energy is formally the same as the one corresponding to a binary system in Newtonian gravity. One can then minimize this binding energy with respects to  $d$ , while keeping  $J$  fixed, to

obtain the condition for *quasicircular* motion (note that in our context there is no such a thing as an ISCO)

$$d = \frac{J^2}{\mu^2 M}. \quad (6.128)$$

In the same way, one can calculate the associated orbital frequency of such orbital motion by differentiating the binding energy with respect to  $J$ , while keeping  $d$  fixed. The result is

$$\Omega = \frac{J}{\mu d^2}. \quad (6.129)$$

From Eq. (6.128) we can write the linear momentum  $P$  in terms of the other parameters of our initial data as

$$P = \mu \sqrt{\frac{M}{d}}. \quad (6.130)$$

The binding energy and other quantities derived from it have a Newtonian form because of the particular type of initial data that we are using: a conformally-flat 3-metric with a Bowen-York extrinsic curvature and a Brill-Lindquist conformal factor. The PN metric produced by a binary system differs from conformal flatness at  $\mathcal{O}(v^4)$  (see [101, 26] for the argument in the case of time-symmetric initial data), and, hence, the binding energy used above differs from the PN binding energy at that order. Note, however, that although the binding energy, linear and angular momentum used here have a Newtonian form, they are not strictly Newtonian. This is mainly because the distance parameter  $d$  is not the physical distance  $D$ , which is related to the parameter  $d$  via Eq. (6.17).

Adopting Eq. (6.130) for the linear momentum parameter in our initial data and leaving the total mass  $M$  fixed (which defines a system of units), we reduce our initial parameter space to a 2-dimensional one. The final parameter space can be parameterized either by the bare quantities  $(q, d)$  or by the physical quantities  $(Q, D)$ . The range of  $q$ , or  $Q$ , is the obvious one, i.e.  $[0, 1]$ , while the range for the bare distance parameter  $d$  is  $[d_{\min}, d_{\text{CLA}}]$ , where  $d_{\text{CLA}}$  is an estimate of the maximum distance for which the CLA is expected to be valid. For the case of equal-mass head-on collisions, it has been shown [172], by comparing with second-order calculations and with fully numerical relativistic simulations, that  $d_{\text{CLA}} \sim 1.7 M$ , which roughly corresponds to  $D_{\text{CLA}} \sim 4 M$ . On the other hand, in principle  $d_{\min}$  could be just zero however, if we adopt the prescription (6.130) for the linear momentum parameter, then we are limited by the *slow motion* approximation that we are using, which means that  $d_{\min}$  should be bigger than  $qM/(1+q)^2$ . Finally, we should remark that the CLA also is expected to fail in the point-particle limit [202], but, as we will see, the recoil is very small when  $Q \ll 1$ .

In order to study the gravitational recoil in the CLA scheme, we are going to evaluate the recoil velocity for a representative number of (physical) mass ratios for a given fixed physical distance  $D$ . In particular, we study the cases  $D = 3, 3.5, 4 M$  and instead of using  $Q$  we use the physical symmetric mass ratio

$$\eta = \frac{M_1 M_2}{(M_1 + M_2)^2} = \frac{Q}{(1+Q)^2}. \quad (6.131)$$

The inverse relation is given by

$$Q = \frac{1}{2\eta} \left( 1 - \sqrt{1 - 4\eta} \right) - 1. \quad (6.132)$$

However, the parameters that appear in our expressions for the initial data are the bare ones. Then, in order to obtain a plot of the recoil velocity in terms of the physical mass ratio, we need to translate from the set  $(Q, D)$  to  $(q, d)$ . This, however, is not a trivial calculation because the definition of  $D$  [Eq. (6.17)] is quite intricate, involving  $x_1$  and  $x_2$ . These numbers are the values of the coordinate  $x$  in the conformal flat space of the intersections of the extremal surfaces (marginally trapped surfaces or apparent horizons depending on the parameters of each particular configuration) surrounding each individual hole with the  $X$ -axis. The translation has to be done numerically through the following iteration scheme in which the physical distance  $D$  is kept fixed:

1. Given a value of  $\eta$  we pick an initial guess for the bare distance, say  $d_*$ .
2. By solving the equations that determine the extremal surfaces surrounding each individual holes (they are given in Appendix E) we find some intersection points  $x_1^*$  and  $x_2^*$ . This requires another iteration, since we do not know a priori where these surfaces are located. What we do is to start, for each individual hole, with an initial guess for the intersection of the extremal surface at the other end of the  $X$  axis (the intersection more distance to the other hole) and integrate the corresponding ODEs by using an extrapolation Bulirsch-Stoer scheme [203, 204, 205]. Then we study whether the integration ends far away from the  $X$  axis or converges towards it. We repeat the iteration until we find the intersection points  $x_1^*$  and  $x_2^*$  with enough accuracy.
3. Using Eq. (6.17) we compute the physical distance associated with these values of the intersection points and  $(q, d_*)$  [where  $q$  is computed in terms of  $\eta$  and  $d_*$  using expressions (6.132) and (6.16)],  $D_*$ . We compare  $D_*$  and  $D$  and stop the iteration if the absolute difference between them is smaller than  $10^{-4} M$ . Otherwise, we go back to point (i) changing the ansatz depending on whether  $D_*$  is bigger or smaller than  $D$ .

We have carried out this iteration for 101 values of  $\eta$ . The coordinate distance (in the conformally related flat space) from the holes to the intersection points of the extremal surfaces is shown in Figure 6.2. Here, we observe how these distances move from equal values (top right) to the values corresponding to the *point particle* limit,  $M_2 \rightarrow m_2 \rightarrow 0$  (top left). The bare distance as a function of  $\eta$  is shown in Figure 6.3 for the three values of fixed proper separation.

### 6.5.2 Results from the numerical evolution of the master equations

We now have initial data for the master equations and also a method to prescribe the initial data parameters in a meaningful way. Then, the next step is to evolve the

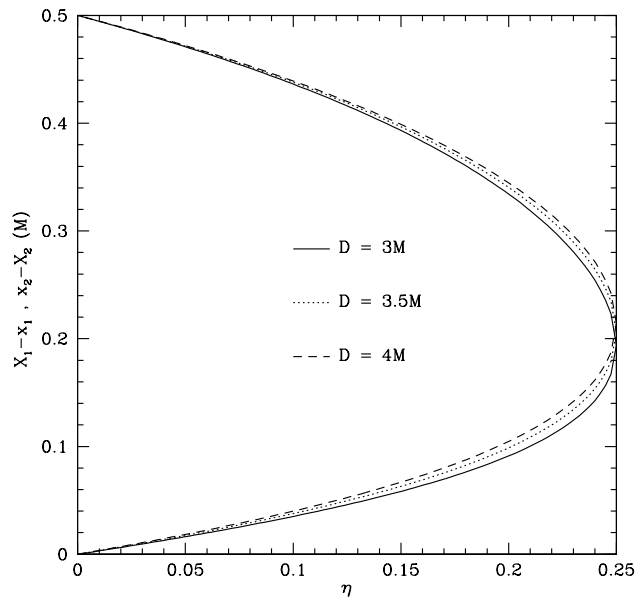


Fig. 6.2. Plot of the coordinate distance between the holes and the intersection points of the extremal surfaces with the  $X$ -axis in terms of the symmetric mass ratio  $\eta$  for three values of the physical distance:  $D = 3, 3.5, 4 M$ .

master equations [Eq. (6.49)]. In this paper we use a numerical code, based on Finite Element methods, that was developed in [206] for calculations of the gravitational radiation emitted by a point particle orbiting a non-rotating black hole. This method is based on linear elements and hence it has a second order convergence rate with respect to the spatial resolution. The time-evolution algorithms that it uses are second-order and unconditionally stable, since they are based on implicit methods. Apart from the tests of the numerical code carried out in [206], we have also done some checks to validate the additional infrastructure added for the gravitational recoil calculations in the CLA scheme. First, we have checked that the energy and angular momentum emitted in an equal-mass grazing collision coincide with the ones found by Khanna *et al* in [183]. Second, we have checked that the recoil velocities that we obtain are consistent with the plots shown by Andrade and Price [180] for the case of head-on collisions from rest of unequal mass black holes using BL initial data.

We have then performed evolutions for 101 equally-spaced values of the symmetric mass ratio  $\eta$  covering the whole range  $[0, 0.25]$  for the three values of the physical distance mentioned above, i.e.  $D = 3, 3.5, 4 M$ . The procedure to calculate the bare distance  $d$  has been described in the previous subsection. Finally, the linear momentum parameter  $P$  is obtained through Eq. (6.130). For each evolution we have computed the fluxes of

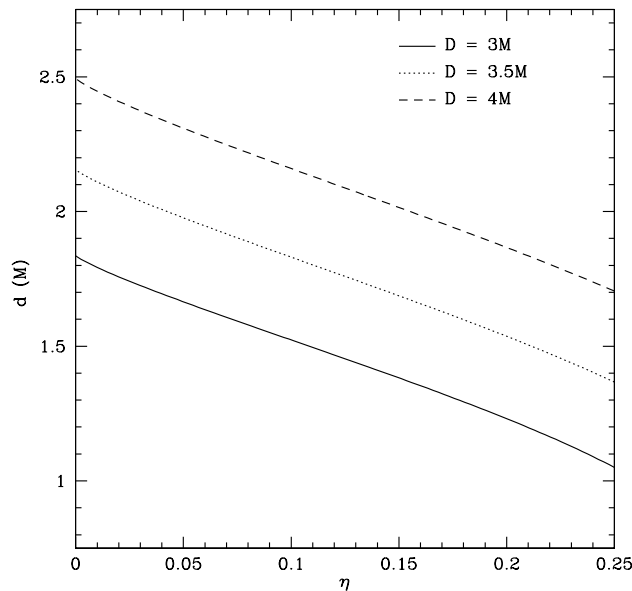


Fig. 6.3. Plot of the bare distance  $d$  in terms of the symmetric mass ratio  $\eta$  for three values of the physical distance:  $D = 3, 3.5, 4 M$ .

energy, angular momentum and linear momentum carried by the gravitational waves to infinity.

Our initial data only has a few non-zero multipoles contributing to the gravitational radiation emitted. Thus, the expressions for the different fluxes simplify dramatically. The energy flux is given by

$$\begin{aligned} \dot{E}_{\text{GW}} &= \frac{3}{8\pi} \left[ (\dot{\Psi}_{\text{ZM}}^{2,0})^2 + 2|\dot{\Psi}_{\text{CPM}}^{2,1}|^2 + 2|\dot{\Psi}_{\text{ZM}}^{2,2}|^2 \right. \\ &\quad \left. + 10 \left( |\dot{\Psi}_{\text{ZM}}^{3,1}|^2 + |\dot{\Psi}_{\text{ZM}}^{3,3}|^2 \right) \right], \end{aligned} \quad (6.133)$$

Figure 6.4 shows the total energy to infinity, given by the integral of Eq. (6.133) over time, as a function of the symmetric mass ratio.

The angular momentum flux also simplifies greatly and becomes

$$\begin{aligned} \dot{L}_{\text{GW}} &= \frac{3}{2\pi} \left\{ \Re(\dot{\Psi}_{\text{ZM}}^{2,2})\Im(\Psi_{\text{ZM}}^{2,2}) - \Im(\dot{\Psi}_{\text{ZM}}^{2,2})\Re(\Psi_{\text{ZM}}^{2,2}) \right. \\ &\quad + \frac{5}{2} \left[ \Re(\dot{\Psi}_{\text{ZM}}^{3,1})\Im(\Psi_{\text{ZM}}^{3,1}) - \Im(\dot{\Psi}_{\text{ZM}}^{3,1})\Re(\Psi_{\text{ZM}}^{3,1}) \right] \\ &\quad \left. + \frac{15}{2} \left[ \Re(\dot{\Psi}_{\text{ZM}}^{3,3})\Im(\Psi_{\text{ZM}}^{3,3}) - \Im(\dot{\Psi}_{\text{ZM}}^{3,3})\Re(\Psi_{\text{ZM}}^{3,3}) \right] \right\}. \end{aligned} \quad (6.134)$$

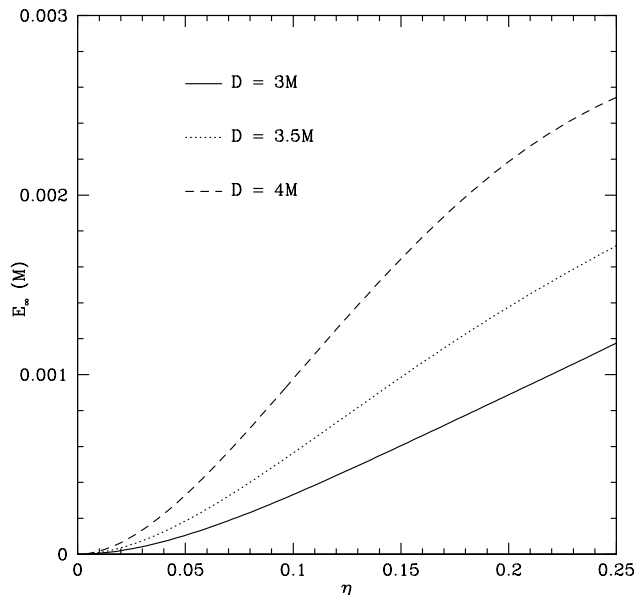


Fig. 6.4. Energy radiated to infinity in terms of the symmetric mass ratio  $\eta$  for three values of the physical distance:  $D = 3, 3.5, 4 M$ .

Note that Eq. (6.134) does not contain any contributions from the axial modes, since the only non-zero axial mode,  $\Psi_{\text{CPM}}^{2,1}$ , is purely real. Figure 6.5 shows the total angular momentum radiated to infinity, given by the integral of Eq. (6.134), as a function of the symmetric mass ratio.

Finally, the gravitational waveform also simplifies, and we obtain

$$\begin{aligned}
 h_+ &= \frac{\sqrt{6}}{r} \left\{ \left[ \Psi_{\text{ZM}}^{2,0} {}_{-2}Y^{2,0} + 2\Re(\Psi_{\text{ZM}}^{2,2}) \Re({}_{-2}Y^{2,2}) - 2\Im(\Psi_{\text{ZM}}^{2,2}) \Im({}_{-2}Y^{2,2}) \right] \right. \\
 &\quad + 2\sqrt{5} \left[ \Re(\Psi_{\text{ZM}}^{3,1}) \Re({}_{-2}Y^{3,1}) - \Im(\Psi_{\text{ZM}}^{3,1}) \Im({}_{-2}Y^{3,1}) \right] \\
 &\quad \left. + \Re(\Psi_{\text{ZM}}^{3,3}) \Re({}_{-2}Y^{3,3}) - \Im(\Psi_{\text{ZM}}^{3,3}) \Im({}_{-2}Y^{3,3}) \right\}, \tag{6.135}
 \end{aligned}$$

$$h_\times = -\frac{2\sqrt{6}}{r} \Re(\Psi_{\text{CPM}}^{2,1}) \Re({}_{-2}Y^{2,1}), \tag{6.136}$$

where the definition and some properties of the spin-weighted spherical harmonics  $Y_s^{\ell m}$  are given in Appendix B.3. Note that the  $\times$ -polarization consists purely of the axial modes, while the  $+$ -polarization contains only polar contributions. Figure 6.6 shows a typical metric waveform, namely  $h_+$  as a function of time, for an observer located at  $\sim 300M$  on the  $Z$ -axis (the cross polarization vanishes on this axis).

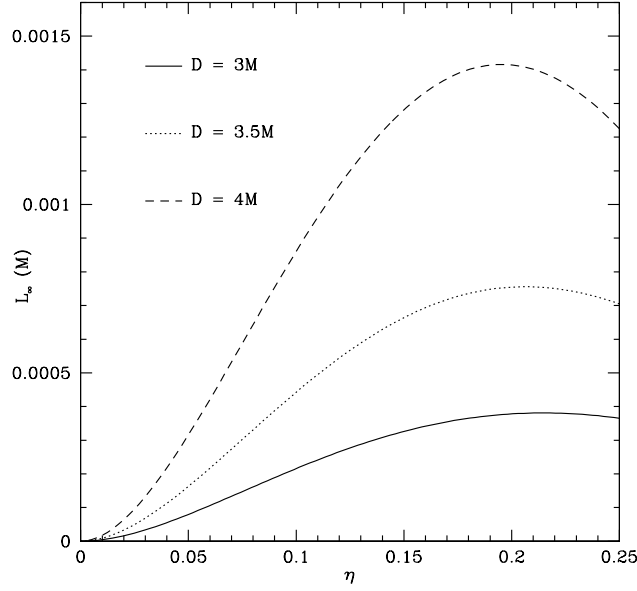


Fig. 6.5. Angular momentum radiated to infinity in terms of the symmetric mass ratio  $\eta$  for three values of the physical distance:  $D = 3, 3.5, 4 M$ .

Let us now concentrate on the main physical quantity of interest, namely the linear momentum flux, given in Eqs. (6.57-6.59). These expressions reduce to

$$\begin{aligned}
 \dot{P}_{\text{GW}}^x &= -\frac{1}{2\pi} \sqrt{\frac{5}{14}} \left\{ \sqrt{6} \dot{\Psi}_{\text{ZM}}^{2,0} \Re(\dot{\Psi}_{\text{ZM}}^{3,1}) \right. \\
 &+ \sqrt{15} \left[ \Re(\dot{\Psi}_{\text{ZM}}^{2,2}) \Re(\dot{\Psi}_{\text{ZM}}^{3,3}) + \Im(\dot{\Psi}_{\text{ZM}}^{2,2}) \Im(\dot{\Psi}_{\text{ZM}}^{3,3}) \right] \\
 &- \left. \left[ \Re(\dot{\Psi}_{\text{ZM}}^{2,2}) \Re(\dot{\Psi}_{\text{ZM}}^{3,1}) + \Im(\dot{\Psi}_{\text{ZM}}^{2,2}) \Im(\dot{\Psi}_{\text{ZM}}^{3,1}) \right] \right\} \\
 &+ \frac{1}{2\pi} \dot{\Psi}_{\text{CPM}}^{2,1} \Im(\dot{\Psi}_{\text{ZM}}^{2,2}), \tag{6.137}
 \end{aligned}$$

$$\begin{aligned}
 \dot{P}_{\text{GW}}^y &= \frac{1}{2\pi} \sqrt{\frac{5}{14}} \left\{ \sqrt{6} \dot{\Psi}_{\text{ZM}}^{2,0} \Im(\dot{\Psi}_{\text{ZM}}^{3,1}) \right. \\
 &+ \sqrt{15} \left[ \Re(\dot{\Psi}_{\text{ZM}}^{2,2}) \Im(\dot{\Psi}_{\text{ZM}}^{3,3}) - \Im(\dot{\Psi}_{\text{ZM}}^{2,2}) \Re(\dot{\Psi}_{\text{ZM}}^{3,3}) \right] \\
 &+ \left. \left[ \Re(\dot{\Psi}_{\text{ZM}}^{2,2}) \Im(\dot{\Psi}_{\text{ZM}}^{3,1}) - \Im(\dot{\Psi}_{\text{ZM}}^{2,2}) \Re(\dot{\Psi}_{\text{ZM}}^{3,1}) \right] \right\} \\
 &+ \frac{1}{2\pi} \dot{\Psi}_{\text{CPM}}^{2,1} \left[ \Re(\dot{\Psi}_{\text{ZM}}^{2,2}) - \sqrt{\frac{3}{2}} \dot{\Psi}_{\text{ZM}}^{2,0} \right], \tag{6.138}
 \end{aligned}$$

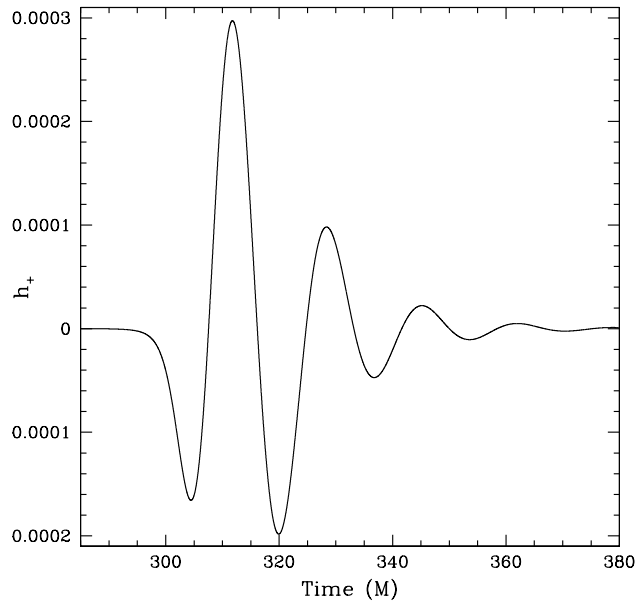


Fig. 6.6. Metric waveform  $h_+$  for the case  $D = 3.5M$  and  $\eta = 0.185$  as a function of time. The observer is located at  $\sim 300M$  on the  $Z$ -axis

$$\dot{P}_{\text{GW}}^z = 0. \quad (6.139)$$

As we can see, there is only contributions from the overlap of polar modes with different  $\ell$  and  $m$ . From this flux, the recoil velocity can be obtained by performing the following integration

$$v_{\text{recoil}}^i = -\frac{1}{M} \int_{t_i}^{t_f} dt \dot{P}^i, \quad (6.140)$$

where the integration times,  $t_i$  and  $t_f$ , are such that the time interval includes essentially all the contribution from the waves to the flux. We can then calculate the magnitude of the recoil velocity simply by

$$v_{\text{recoil}} = \sqrt{(v^x)^2 + (v^y)^2 + (v^z)^2}, \quad (6.141)$$

where  $v^z = 0$  in our case, due to the choices made in the initial setup. Figure 6.7 shows the time derivatives of the master functions that contribute to the recoil velocity for a typical evolution. In this figure, we have separated the real (bottom panel) and the imaginary (top panel) parts of these time derivatives. Observe that the magnitude of the  $\ell = 2$  modes is much bigger than the one of the  $\ell = 3$  modes, as expected. This also gives an indication that the *superposition* of the  $\ell = 2$  modes with  $\ell = 2$  and  $\ell = 3$  modes

is going to be the dominant contribution to the gravitational recoil. The contribution from superpositions involving higher  $\ell$ 's is going to be much smaller.

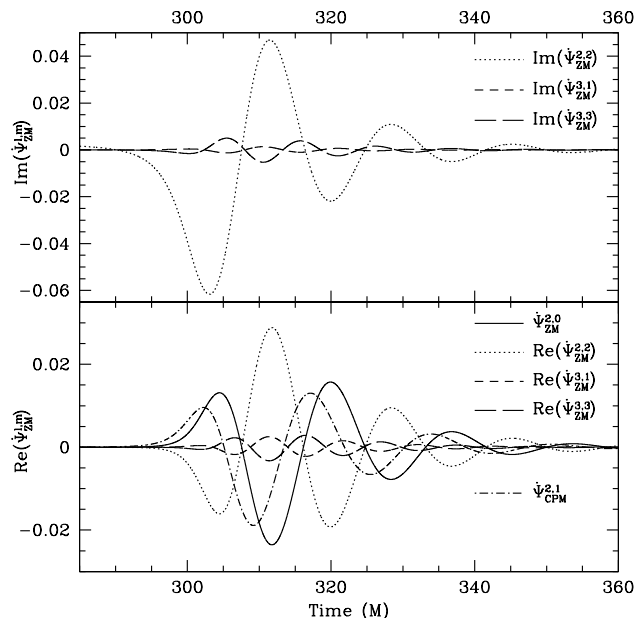


Fig. 6.7. Time derivate of the Zerilli-Moncrief and Cunningham-Price-Moncrief master functions as a function of time, for the case  $D = 3.5M$  and  $\eta = 0.185$ . The plots in the top panel represent the imaginary parts whereas the ones in the bottom panel represent the real parts.

Figure 6.8 shows the the linear momentum flux as a function of time. Observe that the magnitude of the  $x$ -component is bigger than the  $y$ -component, which reflects the fact that our configuration corresponds to the transition from merger to plunge.

Finally, Figure 6.9 presents the magnitude of the recoil velocity as a function of the symmetric mass ratio, for the following initial physical separations:  $D = 3, 3.5, 4M$ . For all cases studied, the maximum velocity is reached for a symmetric mass ratio of  $\eta \sim 0.19$ , which agrees with the value reported in Refs. [49, 57] up to uncontrolled remainders. Observe that this maximum is not a strong peak, but instead resembles a *plateau*, where this maximum is spread out for a number of *etas*, as also seen in other calculations [49, 57].

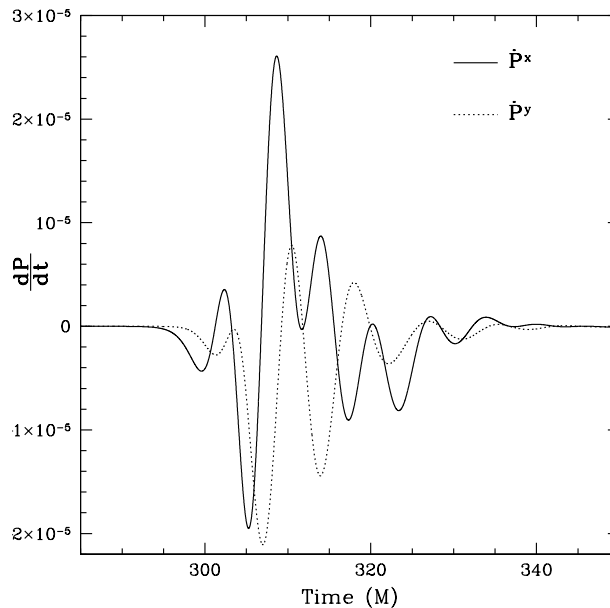


Fig. 6.8. Linear momentum fluxes,  $\dot{P}_{\text{GW}}^x$  and  $\dot{P}_{\text{GW}}^y$ , as a function of time, for the case  $D = 3.5M$  and  $\eta = 0.185$ .

## 6.6 Estimating the total recoil

In this section, we discuss the recoil velocities obtained from the evolution of the master functions and produce lower and upper limits for the total recoil velocity. In particular, we will provide analytic approximations to the data and we will also compare these results to other ones already present in the literature.

One of the limitations, and at the same time an advantage, of the CLA scheme is that the initial separation of the black holes must be *sufficiently* small in some well-defined sense. Apart from numerical relativity, this method is the only known one to be capable of producing accurate estimates of physical quantities near plunge. This advantage, however, is a double-edged sword since the method cannot account for the inspiral phase. Actually, the initial separation must even be smaller than that for which the last ISCO exists. Thus, not only is the inspiral phase neglected but also the beginning part of the merger phase.

Due to these limitations, an approximate value for the *total* recoil velocity cannot be provided by the CLA alone, without supplementing it with some other scheme valid when the system is well separated. The PN scheme is well suited for this task and extensive studies have been recently carried out [49, 57] to estimate the recoil velocity. The approximate recoil velocity accumulated from infinity up to some final separation

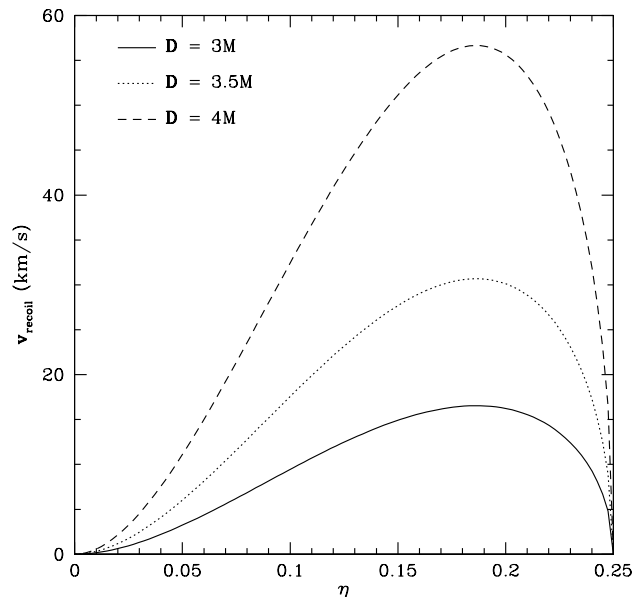


Fig. 6.9. Magnitude of the recoil velocity in terms of the symmetric mass ratio  $\eta$  for three values of the physical distance:  $D = 3, 3.5, 4 M$ .

in the PN scheme is given by [49]

$$\begin{aligned}
 v_{PN} = & \frac{464}{105} \eta^2 \frac{\delta m_{\text{PN}}}{m_{\text{PN}}} x_f^4 \left[ 1 - \left( \frac{452}{87} + \frac{1139}{522} \eta \right) x_f + \frac{309}{58} \pi x_f^{3/2} \right. \\
 & \left. + \left( \frac{71345}{229968} + \frac{36761}{2088} \eta + \frac{147101}{68904} \eta^2 \right) x_f^2 \right], \quad (6.142)
 \end{aligned}$$

with remainders of  $\mathcal{O}(v^5)$ . In Eq. (6.142),  $x_f = (m\omega_f)^{2/3}$  is a PN parameter,  $m_{\text{PN}} = m_{1,\text{PN}} + m_{2,\text{PN}}$  is the total mass,  $m_{1,2,\text{PN}}$  are the masses of the PN point particles,  $\eta = m_1 m_2 / m^2$  is the symmetric mass ratio and  $\delta m_{\text{PN}} = m_{1,\text{PN}} - m_{2,\text{PN}}$  is the mass difference. The PN masses  $m_{1,2,\text{PN}}$  have been shown to agree, within the PN approximation, with the horizon masses  $M_{1,2}$  [101, 26] and we make this identification here. The angular velocity  $\omega$  is given to  $\mathcal{O}(v^4)$  by

$$\omega^2 = \frac{m_{\text{PN}}}{b^3} \left[ 1 + \frac{m_{\text{PN}}}{b} (\eta - 3) + \frac{m_{\text{PN}}^2}{b^2} \left( 6 + \frac{41}{4} \eta + \eta^2 \right) \right]. \quad (6.143)$$

and  $\omega_f$  is the angular velocity evaluated at some final coordinate separation  $b_f$ . Post-Newtonian theory is usually carried out in harmonic coordinates, which are different from the Schwarzschild coordinate system we use in the CLA scheme. However, sufficiently far from the holes,  $D \sim b$ , to  $\mathcal{O}(v^2)$ .

Supplementing the CLA estimate with the PN estimate, we can obtain upper and lower limits on the possible values of the magnitude of the recoil velocity. A lower limit can be obtained via

$$v_{\text{low}} = v_{\text{CLA}}[0, 4M] + v_{\text{PN}}[6M, \infty], \quad (6.144)$$

where  $v_{\text{PN}}[D_2, \infty]$  is the PN estimate for the recoil velocity of Eq. (6.142) evaluated at  $b_f = D_2$ . For this lower limit, we evaluate the PN estimate at the edge of the region of validity of the PN approximation, *i.e.*  $b_f = 6M$ , or equivalently  $x_f = 6^{-3/2}$ , as done in Ref. [49]. This location corresponds to the ISCO of a test particle around a Schwarzschild hole of mass  $M$ . One obtains this value of  $x_f(b_f = 6M)$  by neglecting terms of  $\mathcal{O}(v^2)$  and higher in Eq. (6.143). If we had included these higher order terms in  $\omega_f$  and  $x_f$ , the upper bounds would have decreased by approximately 50 km/s. These higher order terms, however, become large as  $b$  becomes smaller, and thus we choose to neglect them to have a conservative upper bound. In Eq. (6.144),  $v_{\text{CLA}}[0, D_1]$  is the estimate of the recoil velocity in the CLA approximation with an initial proper separation of  $D = D_1$ .

The estimate of  $v_{\text{low}}$  is a lower limit because it does not take into account the contribution to the gravitational recoil in the region  $b \in (4, 6)M$ . In this region neither the CLA, nor the PN scheme, is guaranteed to provide an accurate estimate for the recoil. However, it is possible to construct upper limits by modelling either the entire region or part of it with PN and CLA estimates. Such upper limits are given by

$$v_{\text{up},1} = v_{\text{CLA}}[0, 4M] + v_{\text{PN}}[4M, \infty], \quad (6.145)$$

$$v_{\text{up},2} = v_{\text{CLA}}[0, 5M] + v_{\text{PN}}[5M, \infty]. \quad (6.146)$$

These expressions are upper limits because the contribution to the recoil estimated either with PN theory or the CLA approximation in the region  $b_f \in (4, 6)M$  is monotonically increasing with  $b_f$ .

Equations (6.144), (6.145), and (6.146) require some extra justification and clarification. In general, it is not true that the magnitude of the total recoil can be estimated by adding the magnitude of the integrated momentum flux in the region  $[4M, \infty]$  to that in the region  $[0, 4M]$ . The important point is that the cut is made at a separation  $D = 4M$  in the regime where the main contribution to the recoil comes from. Then, the main contribution to each recoil velocity vector comes from the region near the cut and hence, the error we made by adding the norms will be relatively small. Independent of this argument we have the inequality  $v[0, \infty] \leq v[0, D_{\text{cut}}] + v[D_{\text{cut}}, \infty]$  (with equality when  $v[0, D_{\text{cut}}]$  and  $v[D_{\text{cut}}, \infty]$  are aligned). In this sense, the proposed upper limit is indeed always an upper limit, irrespective of the orientation of the vectors. As for the lower limit, neglecting the accumulated recoil in the region  $[4M, 6M]$  is a very conservative estimate, because there the recoil accumulates greatly. Thus, the issue of

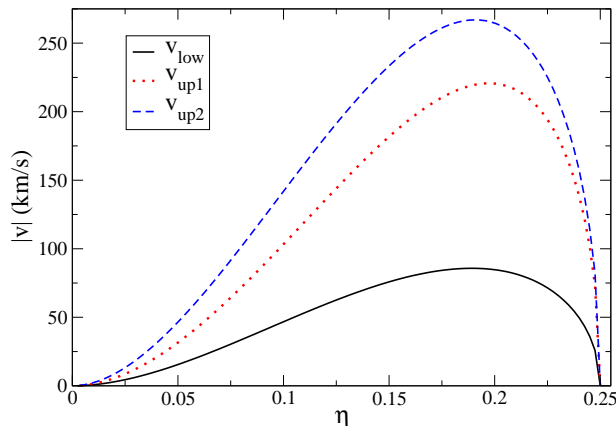


Fig. 6.10. Estimated lower (black solid curve) and upper limits 1 (dotted red line) and 2 (dashed blue line) for the recoil velocity after a binary black hole merger as a function of the physical symmetric mass ratio. Note that the maximum occurs roughly in the same place, namely  $\eta^* \sim \{0.19, 0.2\}$ .

the orientation of the vectors will not affect the fact that this is a lower limit, as other recent estimates in the literature confirm.

Figure 6.10 shows the behavior of these upper limits (red dotted and blue dashed lines respectively) and the lower limit (black solid curve) as a function of  $\eta$ . The maximum in these curves occurs roughly at the same symmetric mass ratio, namely  $\eta \sim \{0.19, 0.2\}$ . The slight disagreement in this maximum is within error bars and rooted in that PN theory predicts it at approximately  $\eta \sim 0.2$ , while the CLA predicts it at  $\eta \sim 0.19$ . We should note that the maximum recoil from  $v_{\text{CLA}}[0, 4M]$  and  $v_{\text{CLA}}[0, 5M]$  is approximately 64 km/s and 215 km/s, while the maximum recoil from  $v_{\text{PN}}[4M, \infty]$ ,  $v_{\text{PN}}[5M, \infty]$  and  $v_{\text{PN}}[6M, \infty]$  is approximately 160 km/s, 50 km/s, and 20 km/s respectively.

A non-linear fit can be performed to these curves via Eq. (6.1)

$$v_{\text{fit}} = a\eta^2 \sqrt{1 - 4\eta} (1 + b\eta + c\eta^2),$$

where the fitting parameters  $a$ ,  $b$  and  $c$  are listed in Table 6.1.

Observe that the mean square error for all cases is small, which is an indication that Eq. (6.1) is a good analytic model for the functional form of the recoil velocity. In this table, we also present the values corresponding to the estimates of Refs. [49] (BQW) and [57] (DG.) Since the predictions of these references are based on analytic formulae, the mean square error can be made arbitrarily small by increasing the number of points in the discretization of the analytic curve.

With the analytic fits to the upper and lower limits, we can construct a curve that is in between these limits with an error given by the distance from the curve to the upper or lower bound. Such a curve is given by Eq. (6.1) with the following fitting

Model	$a$ (km/s)	$b$	$c$	Mean square error
$v_{\text{CLA}}[0, 3M]$	1841	-3.31	3.45	0.001
$v_{\text{CLA}}[0, 3.5M]$	3548	-3.15	3.33	0.003
$v_{\text{CLA}}[0, 4M]$	6576	-2.98	3.21	0.008
$v_{\text{low}}$	7782	-2.51	2.73	0.008
$v_{\text{up},1}$	14802	-1.13	1.48	0.008
$v_{\text{up},2}$	23124	-2.33	2.61	0.06
$v_{\text{BQW}}$	12891	0.25	0	$10^{-8}$
$v_{\text{DG}}$	4483	-0.95	2.68	$10^{-10}$

Table 6.1. Values of the parameter of the non-linear fitting for the following models: the CLA with initial separations of  $D = \{3, 3.5, 4\}M$ ; the lower and upper limits of Eqs. (6.144)-(6.146); Taylor PN (BQW) and EOB PN (DG) calculations [49, 57].

parameters

$$a = \frac{a_{\text{low}} + a_{\text{up}}}{2}, \quad (6.147)$$

$$b = \frac{a_{\text{low}}b_{\text{low}} + a_{\text{up}}b_{\text{up}}}{a_{\text{low}} + a_{\text{up}}}, \quad (6.148)$$

$$c = \frac{a_{\text{low}}c_{\text{low}} + a_{\text{up}}c_{\text{up}}}{a_{\text{low}} + a_{\text{up}}}, \quad (6.149)$$

while the error on this curve is also given by Eq. (6.1) with the following fitting parameters

$$a = \frac{a_{\text{low}} - a_{\text{up}}}{2}, \quad (6.150)$$

$$b = \frac{a_{\text{low}}b_{\text{low}} - a_{\text{up}}b_{\text{up}}}{a_{\text{low}} - a_{\text{up}}}, \quad (6.151)$$

$$c = \frac{a_{\text{low}}c_{\text{low}} - a_{\text{up}}c_{\text{up}}}{a_{\text{low}} - a_{\text{up}}}, \quad (6.152)$$

where the subscript *low* and *up* stand for the fitting parameters of the lower or upper limit respectively. This curve is only an alternative way to visualize the upper and lower limits of Fig. 6.10. The curve is not to be interpreted as the best guess in this work, since in principle, the recoil velocities present in nature could be closer to either upper or lower limit.

We can now compare these estimates of the recoil velocity with those present in the literature. Fig. 6.11 shows the recoil velocity in units of km/s as a function of

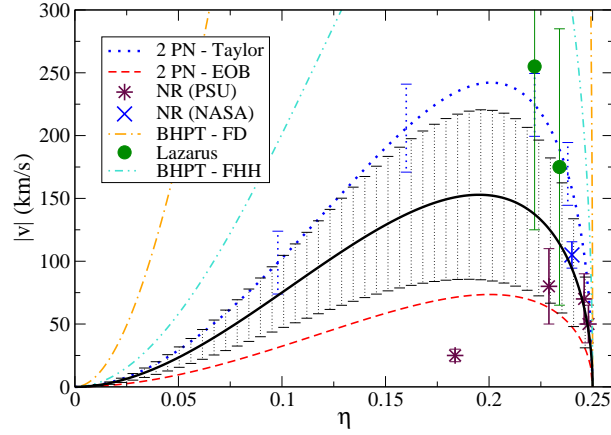


Fig. 6.11. Estimates for the recoil velocity (km/s) of the inspiral and merger of a binary system of compact object as a function of the physical symmetric mass ratio parameter. The symbols used are the following: squares and triangles stand for black hole perturbation theory results [46, 48]; circles stand for Lazarus results [166]; stars and crosses correspond to full numerical relativistic simulation [170, 171]; the dotted line and the dashed line correspond to 2 PN Taylor expansions [49] and 2 PN effective-one-body expansions [57] respectively. The solid black line corresponds to the estimate of this paper, which, together with the error bars, condense both upper and lower limits. Other error bars, when present, correspond to an estimate of some of the error contained in the calculation.

the physical symmetric mass ratio as estimated in the literature and by this paper. As is clear from the figure, there are many approaches to calculate this velocity and not all of them agree. The symbols used are the following: squares and triangles stand for the results obtained using black hole perturbation theory in the extreme-mass ratio approximation in Refs. [46, 48] respectively; circles stand for the calculations carried out via the Lazarus approach [166]; stars and crosses correspond to the results coming from a full numerical relativistic simulation (PSU stands for Ref. [170] and NASA stands for Ref. [171]); the dotted line and the dashed line correspond to the 2 PN Taylor expansion approach [49] and the 2 PN effective-one-body (EOB) approach [57] respectively. The solid line with error bars is the estimate of Eq. (6.149,6.152) that properly condenses the lower and upper limits into one curve. We briefly describe each approach below.

In the PN calculations of Ref. [49], the recoil velocity (dotted line in the figure) and momentum flux are estimated by studying the 2 PN Taylor-expanded radiative moments of a binary system of compact objects, while in Ref. [57] an effective-one-body approach is used (dashed line in the figure.) Post-Newtonian calculations are usually valid only when the binary is weakly gravitating, or equivalently when the orbital separation is greater than the ISCO. In this regime, the recoil velocity (Eq. (6.142) has been found to be small for any mass ratio (usually less than 20 km/s), since, as expected,

most of the contribution to the recoil comes from the merger part of the inspiral. In Ref. [49] the calculation is extended through the merger by integrating the 2 PN Taylor-expanded momentum flux along a geodesic of the Schwarzschild metric. On the other hand, Ref. [57] uses the effective-one-body Hamiltonian to extend the inspiral through the merger. Both of these approaches have inherent errors that are difficult to estimate without calculating the 3 PN contributions to the recoil velocity.

Black hole perturbation theory has also been used to estimate the recoil velocity in Refs. [46, 48]. In these studies, the extreme-mass ratio approximation is adopted (*i.e.*,  $Q \ll 1$ ) and then the system is approximated as a point particle orbiting a black hole. The first study of the recoil velocity using this formalism was performed in Ref. [46] (squares in the figure), but there the gravitational force was treated as Newtonian and only the lowest multipoles were considered. In Ref. [48], these relativistic effects were taken into account, as well as spin, and the velocity estimates were improved (triangles in the figure.) The extreme-mass ratio approximation, however, requires  $Q \ll 1$ , which allows the exploration of a limited section of the  $\eta$ -space.

A combination of black hole perturbation theory and full numerical relativity (the so-called Lazarus approach) has also been implemented to estimate the recoil velocity [166]. In this case, a full numerical relativistic simulation is carried out until the black holes merge and a single perturbed spinning black hole has formed. Then, this spacetime is used as initial data in a Teukolsky evolution to determine the recoil velocity (circles in the figure.) The error in this calculation is rooted in the interpretation of the initial data as that of a perturbed Kerr spacetime. Finally, there have also been recently full numerical relativistic simulations of binary black hole coalescence [170, 171] (shown as stars and crosses respectively in the figure.) In this case, the error shown in the figure is assumed to be given only by finite differencing, while the error due to initial data is neglected.

Even though there has been much work in the calculation of the recoil velocity there is still some disagreement. In Fig. 6.11 we observe that there seem to be three groups of results: one that clusters around the 2 PN Taylor expanded result; another that is close to the 2 PN effective-one-body result; and a third one that is in between the first two. This disagreement, however, is misleading in several ways. First, some estimates of the recoil velocity quote no error bars, as is the case of the first perturbation theory approach [46] and the 2 PN effective-one-body approach [57]. Second, the error bars that do exist in other calculation are only estimates and could very well have been underestimated. A surprising disagreement is between the PN approaches, since when used to calculate other quantities, such as the angular frequency at the ISCO, they do agree. This disagreement seems to be rooted in the fact that the greatest contribution to the recoil velocity comes from the merger part of the inspiral, where neither extension of the PN approach is guaranteed to be accurate.

Our estimates seem to agree with most results if one accounts for error bars. The results of Refs. [46, 166, 48] (squares, triangles and circles in the figure) seem to overestimate the recoil, which is expected in the case of the extreme-mass ratio approximation. The PN results of Refs. [49, 57] seem to overestimate and underestimate the recoil respectively, but they are consistent with our bounds if one takes their error bars (not shown in the figure) into account. The full numerical relativity results seem to overlap

with our bounds, although there are only a few of them. We should note that our bound seems to disagree with the full numerical relativistic result for  $\eta \sim 0.18$ , but that result seems to be an underestimate because of the small initial separation [207].

## 6.7 Conclusions and Discussion

We have calculated the recoil velocity after the merger of an unequal mass binary black hole system using the CLA scheme. This approximation assumes that the black holes are close enough that the system can be approximated by a single perturbed black hole spacetime. In contrast to other approaches, except for full numerical relativity, this approximation allows us to make valid statement about physical process when the system is close to plunge. Therefore, it is of great interest to use this method for the study of gravitational recoil. However, the CLA has the disadvantage that it cannot be used during the beginning of the merger or the inspiral phases.

Initial data for the CLA can be constructed analytically by mapping data suitable for a binary black hole inspiral to that of a single perturbed hole. With such initial data, the Cunningham-Price-Moncrief and the Zerilli-Moncrief master functions can be numerically evolved from some initial proper separation through ringdown. These gauge-invariant master functions contain all the information necessary to evaluate the gravitational metric waveforms and, thus, the energy, angular momentum and linear momentum fluxes carried away from the system.

The results obtained can be summarized as follows. First, the maximum recoil velocity obtained in the CLA scheme is of  $v \sim 64$  km/s for the maximum initial separation allowed by this method ( $D = 4M$ ). This maximum occurs at a symmetric mass ratio of  $\eta \sim 0.19$ . By supplementing this estimate with PN ones valid in the inspiral regime, we obtain lower and upper bounds with maxima of  $v \sim 84$  km/s and  $v \sim 220$  km/s respectively. We have further provided non-linear analytic fit functions that conveniently parameterize these bounds, together with the results from the CLA, and other results in the literature. These results also suggest that there is a region around  $D \sim \{4, 6\}M$  that greatly contributes to the recoil, but can only be poorly modelled by current approximation schemes.

Ultimately, the estimates presented here suffer of the same predicaments as other calculations. Due to its analytical nature, the CLA relies on certain assumptions that do not hold over the entire history of the binary. Such assumptions introduce an error in the estimated recoil that is difficult to quantify. In particular, the assumptions made here are the following: close separations ; slow-motion; simple initial data. The close-limit assumption is essential to allow a mapping of a binary inspiral to a single perturbed spacetime. The slow-motion approximation supplements the close-limit assumption and can, in principle, be improved on in future extensions of this work. The choice of initial data is assumed to represent the gravitational content of some initial slice, although we know that this fails even at large separation because it does not agree with the deviations from conformal flatness predicted by PN theory. Moreover, it does not contain any radiation, which is not what it should be expected for initial data corresponding to a snapshot of the orbital evolution. Due to these assumptions, the estimate of the

recoil velocity will be contaminated by some error. However, experience in CLA calculations indicates that the error made only overestimates the physical quantities calculated, relative to full numerical simulations [175, 208, 183].

Future work will concentrate on extending this approach to second order in  $P$  and to other, more realistic, initial data sets [105, 93]. Ultimately, it would be interesting to compare the CLA approach directly to full numerical relativistic simulations in an attempt to determine the region of validity of the CLA more accurately. Another possibility is to use a multi-parameter perturbation scheme (see [209, 210, 211, 212]) where perturbations in the linear momentum and separation parameters can be cleanly separated at the different perturbative orders.

## Acknowledgments

The authors acknowledge the support of the Center for Gravitational Wave Physics funded by the National Science Foundation under Cooperative Agreement PHY-0114375. This work was partially supported by NSF grants PHY0218750, PHY0244788, PHY0245649, PHY0555436, and PHY0555628. The authors also wish to thank the Information Technology Services at Penn State University for the use of the LION-XO and LION-XM computer clusters in some of the calculations presented in this paper. Other calculations used the computer algebra systems MATHEMATICA and MAPLE (in combination with the GRTensorII package [1]). We would also like to thank Frank Herrmann, Carlos Lousto, Ben Owen and Ulrich Sperhake for enlightening discussions and comments.

**Note added after publication:** After this paper was submitted, full numerical relativity estimates have appeared [58], and a best-bet estimate based on our scheme, which includes some refinements in the PN part with respect to the present paper, has been compared to them in [140]. The agreement between them is remarkable and supports the approach presented in this paper.

## Chapter 7

# Gravitational recoil velocities from eccentric binary black hole mergers

The formation and growth of supermassive black holes is a key issue to unveil the secrets of galaxy formation. In particular, the gravitational recoil produced in the merger of unequal mass black hole binaries could have a number of astrophysical implications, such as the ejection of black holes from the host galaxy or globular cluster. We present estimates of the recoil velocity that include the effect of small eccentricities. The approach is specially suited for the last stage of the merger, where most of the emission of linear momentum in gravitational waves takes place. Supplementing our estimates with post-Newtonian approximations, we obtain lower and upper bounds that constrain previous recoil velocities estimates as well as a best estimate that agrees with numerical simulations in the quasi-circular case. For eccentricities  $e \leq 0.1$ , the maximum recoil is found for a mass ratio of  $M_1/M_2 \sim 0.38$  with velocities in the range  $79 - 216 \text{ km s}^{-1} (1 + e)$  and a best estimate of  $167 \text{ km s}^{-1} (1 + e)$ .

### 7.1 Introduction

In present hierarchical cold dark matter cosmologies, large-scale structures are formed by the merger of small (sub-galactic) structures that originated from small primordial density perturbations<sup>1</sup> [213]. In the case of galaxies, there is evidence that most of the nearby ones host super-massive black holes (SMBH) at their centers [214, 215] with masses in the range  $10^5 - 10^9 M_\odot$ . Moreover, observations have revealed tight relations between the SMBH and the bulge of the host galaxy [216], and indicate also that the SMBH mass may be determined by the mass of the host dark matter halo [217]. This suggests that there must be a deep relation between the formation mechanism of the SMBH and the host galaxy which is not yet completely understood. It has been suggested [218] that SMBHs grow as a combination of gas accretion and mergers with other SMBHs that come together as a result of the merger of their host dark matter halos and dynamical friction [219].

The last stages of the merger of SMBHs will be driven by the emission of gravitational radiation in the low-frequency band. These extremely energetic events will be

---

<sup>1</sup>This chapter is based on the following paper: C. F. Sopuerta, N. Yunes and P. Laguna, *Astrophys. J.* **659**, L9-12 (2006)

observable by the planned space-based gravitational wave antenna LISA [51, 50]. In addition to energy and angular momentum, in the case of unequal mass SMBHs, there is a net flux of linear momentum carried away from the system by the gravitational waves [163, 164]. Then, momentum conservation implies that the final SMBH remnant will experience a recoil. There may be observational evidence of an ejected SMBH from an ongoing galaxy merger [159] either from gravitational recoil or gravitational slingshot of three or more SMBHs in the merger. The knowledge of the magnitude of the recoil velocity is crucial to understand the demography of SMBHs at the centers of galaxies and in the interstellar and intergalactic media, and their apparent absence in dwarf galaxies and stellar clusters [220, 41]. An estimate of the recoil can also be used to constrain theories in which SMBHs grow at the center of dark matter halos [160] and to estimate SMBH merger rates [221].

In this letter, we present the results of a calculation of the recoil velocity based on an approximation scheme which is valid when the black holes (BHs) are very close to each other, that is, in the last stage of the binary merger. During this stage is where most of the recoil accumulates. This contrasts with previous calculations that use approximations valid when the BHs are well-separated, except for recent fully numerical relativistic calculations [171, 170, 58]). We include the effect of eccentricity in the recoil velocity since there are indications that SMBH binaries may have not completely circularized by the time of merger [222, 223, 224].

## 7.2 Recoil velocities and the Close Limit approximation

General relativity predicts that an unequal mass binary system in coalescence produces anisotropic emission of gravitational waves that carry linear momentum away from the binary. As a consequence, the center of mass of the system experiences a recoil velocity  $v_r$  [40]. The first estimates, done by [43] using a quasi-Newtonian approach, yielded a maximum  $v_r \sim 1480 \text{ km s}^{-1} (r_g/r_f)^4$  for a symmetric mass ratio of  $\eta = M_1 M_2 / M^2 \sim 0.2$ , where  $r_g = 2GM/c^2$  is the gravitational radius,  $M_{1,2}$  and  $M$  are the individual and total masses respectively, and  $r_f$  is the orbital separation at which gravitational-wave emission ends. Similar results up to the innermost stable circular orbit (ISCO) were found using a relativistic perturbative method [46]. This velocity estimate is large compared to galactic escape velocities. In contrast, the first post-Newtonian (PN) calculation [40] for neutron star binaries produced a much lower result:  $v_r < 1 \text{ km s}^{-1}$ .

Motivated by the astrophysical impact of the gravitational recoil, there has been recently a number of efforts to obtain better estimates of the recoil velocity. Using a relativistic perturbative scheme for the description of extreme-mass ratio ( $\eta \ll 1$ ) binaries and including gravitational back-reaction, [48] and [41] obtained maximum recoil at  $\eta \sim 0.2$  with  $167 \text{ km s}^{-1} \leq v_r \leq 622 \text{ km s}^{-1}$ , depending on the spin parameter of the massive black hole ( $v_r = 456 \text{ km s}^{-1}$  for the non-spinning case). Recently, [49] used second-order PN approximations up to ISCO, followed by an integration of the 2PN linear-momentum flux along a *plunge* geodesic, to obtain a maximum kick velocity  $v_r = 250 \pm 50 \text{ km s}^{-1}$

for a symmetric mass ratio  $\eta = 0.2$ . On the other hand, estimates with the effective one body approach [57] give a maximum recoil in the range  $49 - 172 \text{ km s}^{-1}$  for the same  $\eta = 0.2$ . Using the hybrid perturbative-fully relativistic Lazarus approach, [166] obtained also that the maximum recoil takes place at  $\eta \sim 0.2$  with a magnitude of  $\sim 250 \text{ km s}^{-1}$ . Currently, there are very few fully general relativistic numerical simulations of kicks. [171] reported  $v_r = 105 \text{ km s}^{-1}$  for a symmetric mass ratio  $\eta = 0.24$ , while [170] obtained  $v_r = 82 \text{ km s}^{-1}$  for  $\eta = 0.23$ . Recently, [58] report a maximum recoil  $v_r = 176 \pm 11 \text{ km s}^{-1}$  for a symmetric mass ratio of  $\eta = 0.195 \pm 0.005$ , where the error bars account only for finite differencing Einstein's equations.

Except for the fully relativistic approaches, which have their own uncertainties (mainly from computational resource limitations), all other approaches become less accurate the closer the BHs get. Motivated by the fact that the main contribution to the recoil comes from the last stage of the merger and plunge, as many of the previously cited studies suggest, in this letter we compute the distribution of kicks using a scheme that works better the closer the orbital separation. This scheme [13], known as the close-limit approximation (CLA), has been shown to provide accurate results for head-on collisions when compared to full numerical relativity [15]. The CLA is based on the idea that the last stages of binary black hole (BBH) mergers can be modeled as a single perturbed BH. Gravitational recoil was studied in the context of the CLA scheme for the case of head-on collisions of BHs starting from rest by [180]. Recently, we [139] extended this analysis to the quasi-circular case and found a maximum recoil of  $v_r \sim 57 \text{ km s}^{-1}$  for  $\eta \sim 0.19$  starting from a separation of  $4GM/c^2$ , the maximum separation at which it has been estimated that the CLA scheme works [172]. This estimate covers the last part of the merger, plunge and ringdown. One can complement this result with PN estimates from the inspiral phase. If we consider the contribution from PN approximations up to ISCO, we obtain a lower bound for the maximum recoil of  $v_r \sim 80 \text{ km s}^{-1}$ , whereas if we push the PN approximations up to the point where we start the CLA scheme, we get an upper limit in the maximum recoil of  $v_r \sim 215 \text{ km s}^{-1}$  (it is known that PN and perturbative schemes overestimate the linear-momentum flux in the strong field region). Alternatively, if, instead of pushing the PN method towards small separations, we push the CLA scheme towards larger separations around  $5GM/c^2$ , we get a slightly larger upper bound.

In this letter, we improve and extend these estimates for initial configurations corresponding to BBHs in eccentric orbits. The most important point in the implementation of the CLA scheme is to establish a correspondence between the initial configuration representing a BBH and a perturbed single BH. This correspondence allows us to identify, in the initial BBH configuration, a background (a non-spinning Schwarzschild BH) and perturbative multipolar gravitational modes [139]. We then evolve these modes by using the machinery of BH perturbation theory and, from the results of the evolution, we can compute the fluxes of energy, angular momentum, and linear momentum ( $\dot{P}_{\text{GW}}^i$ ) emitted

by the BBH system during the merger. Then, the recoil velocity is given by

$$v_r = \|v_r^i\|, \quad v_r^i = -M^{-1} \int_{t_i}^{t_f} dt \dot{P}_{\text{GW}}^i. \quad (7.1)$$

where  $t_i$  is the time corresponding to the initial separation of the BBH, and  $t_f$  is some time after merger, when the gravitational wave emission becomes negligible. In our calculations, we use an initial BBH configuration [22, 21] that has been shown to accurately represent binaries to Newtonian order. They are characterized by four parameters [139]: the total mass of the system ( $M$ ), the symmetric mass ratio of the binary ( $\eta$ ), the initial separation ( $d$ ), and the initial linear momentum ( $P$ ) of each BH.  $M$  and  $\eta$  enter as a scale and input parameters, respectively. Given  $\eta$ , the type of orbit is determined by the pair  $(d, P)$ . For a quasi-circular orbit we find a relation between  $P$  and  $d$  by minimizing the gravitational binding energy of the black hole binary. This relation turns out to be analogous to the Newtonian one, although it has to be interpreted within the framework of general relativity.

In this work, in order to study the effect of eccentricity in the gravitational recoil, we take the distance parameter to be  $d = a(1 - e)$ , where  $a$  is a parameter distance that plays the role of the semi-major axis and  $e$  is the eccentricity. Then, the linear momentum parameter is given by

$$P = P_{\text{qc}}(a) \sqrt{\frac{1+e}{1-e}}, \quad (7.2)$$

where  $P_{\text{qc}}(a)$  is the linear momentum parameter for quasi-circular configurations [139] with radius  $a$ .

For our kick estimates, we have kept the semi-major axis fixed ( $a = 4GM/c^2$ ) and only varied the symmetric mass ratio and eccentricity parameters ( $\eta, e$ ). Figure 7.1 shows the recoil velocity  $v_r$  as a function of the symmetric mass ratio  $\eta$  for several values of the eccentricity:  $e = 0 - 0.25$ . We observe that the maximum recoil occurs at  $\eta \sim 0.19$ , consistent with previous results. As we increase the eccentricity, the recoil velocity also increases by approximately a factor of  $1 + e$  for eccentricities in the range  $e < 0.1$ . This increase can be qualitatively understood by expanding equation (7.2) for small eccentricities, which leads to an increase by a factor  $1 + e$  in the linear momentum parameter. Thus, it seems that an increase in the plunge velocity leads to roughly the same increase in the recoil velocity. If we consider the entire range of eccentricities that we considered, the numerical results can be fitted to the following two-parameter non-linear function

$$v_r^{\text{CLA}}(\eta, e) = \alpha \sqrt{1 - 4\eta} \eta^2 \left(1 + \beta_1 \eta + \beta_2 \eta^2\right) \times \frac{1+e}{1-e} \left(1 + \gamma_1 e + \gamma_2 e^2 + \gamma_3 e^3\right), \quad (7.3)$$

where  $\alpha$  ( $\text{km s}^{-1}$ ),  $\beta_1$ ,  $\beta_2$ ,  $\gamma_1$ ,  $\gamma_2$ , and  $\gamma_3$  are fitting parameters given in Table 7.1 in the CLA row. The fit was performed using numerical results in the range  $\eta = 0 - 0.25$  and

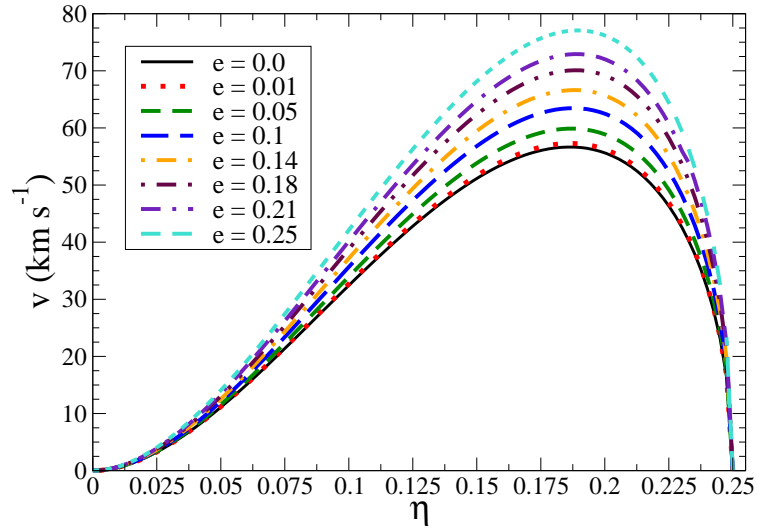


Fig. 7.1. Recoil velocity in  $\text{km s}^{-1}$  as a function of symmetric mass ratio  $\eta$  for eccentricities in the range  $e = 0 - 0.25$ .

$e = 0 - 0.5$  with an average error  $< 1 \text{ km s}^{-1}$ . The fitting function (7.3) can be shown to be functionally equivalent to that presented by [43] for small eccentricities, but with different coefficients that lead to significantly smaller magnitudes for the recoil.

### 7.3 Estimating the total recoil

The estimates of the recoil velocities for BBH mergers provided by equation (7.3) and the first row of Table 7.1 are incomplete because we have not taken into account the contribution from the inspiral ( $\sim 20 \text{ km s}^{-1}$ ) and the beginning of the merger, where fully non-linear computations are needed. In order to obtain an estimate of the total accumulated recoil velocity, we can supplement our calculations with estimates from approximation techniques that are accurate for moderate and large separations. In this letter, we use a PN approximation that provides the accumulated kick up to some minimum separation. For quasi-circular orbits [49] and assuming the angular frequency is given by the Newtonian estimate  $\omega = \sqrt{M/d^3}$ , the accumulated recoil up to some minimum separations of  $4GM/c^2$  and  $6GM/c^2$  respectively can be fitted by Eq. (7.3) with the second and third rows of Table 7.1 respectively. As in [139], upper and lower limits can be obtained by combining these PN estimates with the CLA calculation.

Our best estimate consists in adding to the CLA estimates, obtained by starting at a separation of  $4GM/c^2$ , the PN accumulated recoil from infinity to that separation. However, to compensate for using the PN approximation in a regime where it becomes less accurate, we use a PN expression for the angular velocity with errors of  $\mathcal{O}(v/c)^5$ ,

Model	$\alpha$	$\beta_1$	$\beta_2$	$\gamma_1$	$\gamma_2$	$\gamma_3$
CLA	5232	-2.621	3.199	-0.942	0.808	-0.405
PN ( $r_1^{\min}$ )	8226	0.347	0.083	0	0	0
PN ( $r_2^{\min}$ )	1206	0.1057	0.05	0	0	0

Table 7.1. Non-linear fit parameters for the recoil velocity. Here  $r_1^{\min} = 4GM/c^2$  and  $r_2^{\min} = 6GM/c^2$  are the minimum separations up to which the PN approximation is applied.

instead of the Newtonian value used in [139] to obtain an upper limit. Our results for the quasi-circular case are shown in Fig. 7.2, with error bars derived just from the PN approximate error. In this figure, we also compare our results to the full relativistic results of [58] and find that they agree remarkably well.

The main caveat of supplementing the CLA with a PN approximation is that presently the latter is only available for quasi-circular orbits [49]. However, by comparing the contribution from the CLA scheme with that provided by the PN approximation for the quasi-circular case, we find that the total recoil velocity can be accurately described by the CLA contribution times a factor:

$$v_r^{\text{total}} = v_r^{\text{CLA}} (1 + \mathcal{E}), \quad (7.4)$$

so that  $\mathcal{E}$  can be written in terms of the symmetric mass ratio  $\eta$  as

$$\mathcal{E} = \kappa (1 + \lambda_1 \eta + \lambda_2 \eta^2), \quad (7.5)$$

where the coefficients  $\kappa$ ,  $\lambda_1$ , and  $\lambda_2$  depend on the minimum distance that we use in the PN approximation. When the minimum distance is taken to be  $r_1^{\min} = 4GM/c^2$  we obtain:  $\kappa = 1.357$  (0.648),  $\lambda_1 = 4.418$  (5.612), and  $\lambda_2 = 5.33$  (23.63) [the values in parenthesis correspond to using the 2PN angular velocity instead of the Keplerian one]; whereas when we take it to be  $r_2^{\min} = 6GM/c^2$  the coefficients are:  $\kappa = 0.199$ ,  $\lambda_1 = 4.223$ , and  $\lambda_2 = 3.926$ .

We can then obtain lower and upper bounds as well as a best estimate for the total recoil velocities from eccentric BBH mergers if we assume that expressions (7.4) and (7.5) can be extrapolated to the range of eccentricities under consideration,  $e \leq 0.25$ . When we use  $r_2^{\min} = 6GM/c^2$  and the Keplerian estimate for the angular velocity, the total recoil obtained is a lower limit because we do not account for the contribution in the region  $4-6GM/c^2$ . On the other hand, if we use  $r_1^{\min} = 4GM/c^2$  and the Keplerian angular velocity, Eq. (7.4) provides an upper limit, since it is well-known that the PN approximation overestimate the recoil in the  $4-6GM/c^2$  range. Our best estimate is

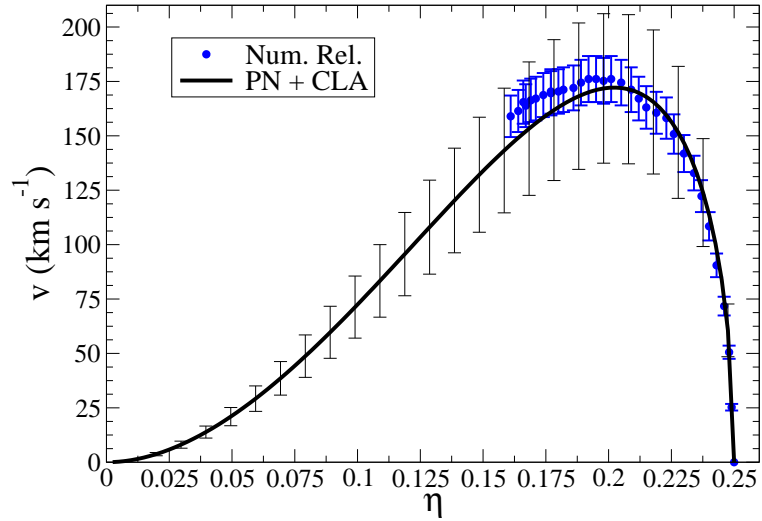


Fig. 7.2. Best estimate of the recoil velocity in  $\text{km s}^{-1}$  as a function of symmetric mass ratio  $\eta$  for the quasi-circular case  $e = 0$ , calculated by combining the CLA calculation with a 2 PN approximation. Also plotted are the results from a full numerical relativistic simulation [58].

obtained with  $r_1^{\min} = 4GM/c^2$  and the 2PN angular velocity. These estimates, lower and upper bounds and best estimate, are shown in Figure 7.3.

#### 7.4 Summary and Discussion

We applied the CLA scheme to the computation of recoil velocities for BBH mergers including the effect of eccentricity. For small eccentricities,  $e < 0.1$ , we find a generic increase in the recoil of the order of 10% with respect to the quasi-circular case. This increase is related to the fact that, for slightly eccentric orbits, the magnitude of the initial velocity of each BH increases roughly by a factor of  $1 + e$ . Since the CLA scheme is valid for separations smaller than the corresponding one for the ISCO, we have supplemented our results with estimates obtained with a 2PN approximation, which work very well for large separations. Combining appropriately both approximation schemes, we have produced lower and upper bounds, as well as a best estimate, for the recoil velocity.

Our calculations indicate that the maximum recoil velocity takes place at a symmetric mass ratio of  $\eta \sim 0.19$  and its magnitude can be as low as  $\sim 79 - 88 \text{ km s}^{-1}$  and as high as  $\sim 216 - 242 \text{ km s}^{-1}$ , with a best estimate in the range  $\sim 167 - 187 \text{ km s}^{-1}$ . The variation in these estimates is due to the eccentricity of the orbit. All our estimates can be fitted by non-linear function of  $\eta$  and  $e$  given by Eq. (7.3). This formula is expected to work well for small eccentricities, and it reduces to the expression given

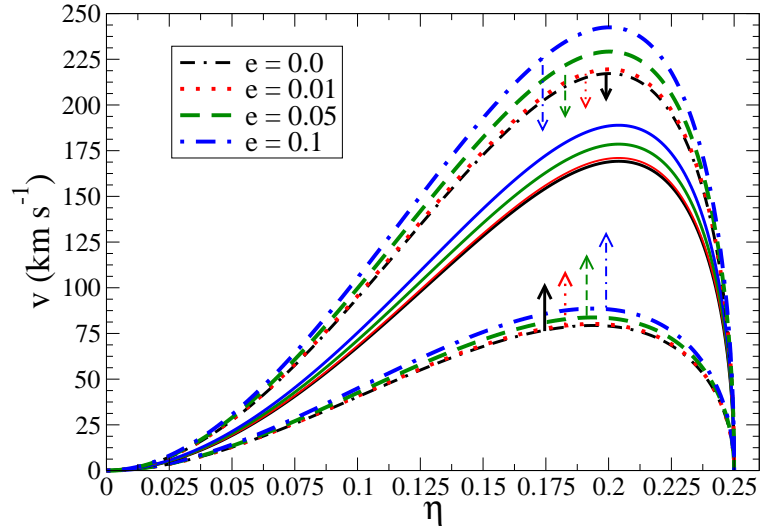


Fig. 7.3. Upper and lower limits (dashed and dotted lines) and best estimate (solid lines) to the total recoil velocity in  $\text{km s}^{-1}$  as a function of symmetric mass ratio  $\eta$  for eccentricities in the range  $e = 0 - 0.1$ .

by [43], with a significantly smaller magnitude, when  $e \ll 1$ . These results also significantly narrow previous calculations [48, 49, 57] and agree remarkably well with full relativistic computations [58] in the quasi-circular case.

One of the main conclusions that can be extracted from our and recent estimates of the gravitational recoil from BBH mergers is that the main contribution to the recoil comes from a narrow interval of separations that include the ISCO. Not surprisingly, this coincides with the non-linear gravitational regime, where perturbative approximation schemes tend to break down. In this sense, the attractive feature of our approach is that it uses an approximation method, the CLA scheme, valid for small separations, and complements the estimate with another approximation, the PN scheme, valid for large to moderate separations.

As mentioned before, SMBH merger recoil velocities are relevant for hierarchical dark matter scenarios for structure formation, as well as in the understanding of the displacement of nuclear structure in dense galaxies and the distortion of X-shaped radio sources. Our results do not significantly alter the astrophysical conclusions obtained previously by [41]. Instead, our results confirm and sharpen these conclusions, by providing a narrower lower and upper bounds for the possible recoil velocities.

Future work can assess the robustness of our estimates by studying their dependence on the initial configuration as well as the inclusion of higher gravitational multipoles in the calculation. In the future, when precise numerical relativistic simulations of eccentric orbits become available, it would then be possible to compare results and to determine with better precision the distribution of recoil velocities in the parameter

space  $(\eta, e)$ . A very important issue is the effect of spins, which has not yet been dealt with enough generality to ascertain what is the impact of the additional scales introduced by spinning BHs.

### **Acknowledgments**

The authors acknowledge the support of the Center for Gravitational Wave Physics funded by the National Science Foundation under Cooperative Agreement PHY0114375, and support from NSF grants PHY0555628, PHY0555436, PHY0218750, PHY0244788, and PHY0245649. CFS was partially supported by the Natural Sciences and Engineering Research Council of Canada. The Information Technology Services at Penn State University is also acknowledged for the use of their computer clusters.

## Chapter 8

# Relativistic Effects in Extreme Mass Ratio Gravitational Wave Bursts

Extreme mass ratio bursts (EMRBs) have been proposed as a possible source for future space-borne gravitational wave detectors, such as the Laser Interferometer Space Antenna (LISA). These events are characterized by long-period, nearly-radial orbits of compact objects around a central massive black hole. The gravitational radiation emitted during such events consists of a short burst, corresponding to periapse passage, followed by a longer, silent interval. In this paper we investigate the impact of including relativistic corrections to the description of the compact object's trajectory via a geodesic treatment, as well as including higher-order multipole corrections in the waveform calculation. The degree to which the relativistic corrections are important depends on the EMRB's orbital parameters. We find that relativistic EMRBs ( $v_{\max}/c > 0.25$ ) are not rare and actually account for approximately half of the events in our astrophysical model. The relativistic corrections tend to significantly change the waveform amplitude and phase relative to a Newtonian description, although some of this dephasing could be mimicked by parameter errors. The dephasing over several bursts could be of particular importance not only to gravitational wave detection, but also to parameter estimation, since it is highly correlated to the spin of the massive black hole. Consequently, we postulate that if a relativistic EMRB is detected, such dephasing might be used to probe the relativistic character of the massive black hole and obtain information about its spin.

### 8.1 Introduction

Low-frequency ( $10^{-5} \lesssim f \lesssim 0.1$  Hz) gravitational wave interferometers, such as the proposed Laser Interferometer Space Antenna (LISA) [225, 226, 227], will open a completely new window to the Universe<sup>1</sup>. Through observations of low-frequency gravitational radiation we will be able to witness the inspiral and merger of massive black hole binaries; the inspiral of compact objects into massive black holes; and millions of quasi-stationary compact galactic binaries. Recently, a new source of low-frequency gravitational radiation has been suggested: extreme mass ratio bursts (EMRBs) [55, 228].

---

<sup>1</sup>This chapter is based on the following paper: N. Yunes, C. F. Sopuerta, L. J. Rubbo and K. Holley-Bockelmann, accepted for publication in the *Astrophys. J.* (2007)

EMRBs consist of a stellar-mass compact object (SCO) orbiting a massive black hole (MBH) of  $10^{4-8} M_{\odot}$  with orbital periods greater than  $T_{\text{cut}} = 3 \times 10^4$  s. The defining orbital period cutoff is derived from LISA's lower frequency limit of  $f_{\text{cut}} = 3 \times 10^{-5}$  Hz. Systems with orbital periods less than  $T_{\text{cut}}$  will radiate continuously inside the LISA band. Such continuous systems are more appropriately categorized as extreme mass ratio inspirals (EMRIs) and have been studied extensively elsewhere: recent estimations of the event rate are given by [229] and [230]; a discussion on a possible EMRI background is given by [231]; accounts on the theoretical description of EMRIs can be found in the reviews by [10] and [53], while the recent review by [54] describes the astrophysical and detection applications.

Although EMRB events are distinct from EMRI events, their evolutionary track could be connected. In the burst scenario, the SCO orbits the MBH emitting a beamed burst of gravitational radiation during pericenter passage. The emitted radiation carries away energy and angular momentum from the system so that after multiple pericenter passages the orbital period decreases, and possibly the system becomes an EMRI. However, this evolutionary track is most likely disrupted by scattering interactions with other stars and/or if the SCO plunges directly into the central MBH on one of its passages.

The EMRB event rate has recently been investigated using simplified galactic models and data analysis techniques [55, 228, 56]. Using a density profile described by an  $\eta$ -model [232], [55, 228] suggested an event rate of  $\sim 15 \text{ yr}^{-1}$  for events with signal-to-noise ratios (SNRs) greater than five out to the Virgo cluster. When mass segregation and different inner cusp models are considered, the predicted rate decreases by an order of magnitude [56]. These preliminary studies were aimed at understanding if EMRB event rates are interesting for low-frequency gravitational wave detectors such as LISA. More work is still needed to improve the predicted event rate in the context of realistic galaxies, where the role of non-equilibrium dynamics, anisotropy, complex star formation histories, substructure, and non-sphericity may act to change the rate from these fiducial estimates by orders of magnitude [233, 55, 228].

In addition to the astrophysical uncertainties, there are no investigations of the impact of relativistic corrections to EMRB dynamics. All EMRB studies have been carried out in a *quasi-Newtonian* framework. In this framework, one uses the Newtonian equations of motion and extracts the gravitational waveforms by means of the *quadrupole formula*. This approximation ignores the black hole nature of the central potential, including the black hole's rotation (spin), and is technically valid only for orbits with non-relativistic velocities. However, a considerable number of EMRBs are characterized by large pericenter velocities ( $v_p \gtrsim 0.25c$ ) and these *relativistic* EMRBs should produce gravitational wave signals with larger SNRs, as we will show later.

In this paper, we shall not consider the issue of EMRB event rates, but instead we shall study the effects of relativistic corrections to such events. For extreme-mass-ratio systems a simple way of introducing relativistic corrections is by using the so-called *semi-relativistic* approximation introduced by [234], and used recently in the context of EMRIs by [235, 236]. In this approximation, the MBH and surrounding area are modeled using the Kerr solution to Einstein's field equations, which describes a stationary spinning black hole (the Schwarzschild solution corresponds to the non-spinning case). The SCO

is considered to be a point-like object (neglecting its own self-gravity) whose trajectory is described by a geodesic of the Kerr spacetime. In other words, relative to previous work, we have replaced the Newtonian equations of motion by relativistic geodesic equations of motion.

The relativistic description introduces effects such as orbital precession and frame dragging, but it does not account for effects due to the gravitational field induced by the SCO. These effects, for example, lead to changes in the (geodesic) constants of motion due to radiation reaction. Even though these effects introduce errors that scale with the system's mass ratio [e.g. see 53], they cannot be neglected for EMRIs. This is because in the late stages of the EMRI the SCO spends a substantial fraction of cycles in the strong-field region of the MBH. On the other hand, in the case of EMRBs, the SCO slingshots around the MBH and its interaction time during pericenter passage is relatively small ( $< 10^5$  s). Radiation reaction effects can then be neglected in EMRBs since the radiation reaction timescale is always much larger than the period of pericenter passage.

In this paper, we also improve on the semi-relativistic approximation by using a more precise gravitational wave extraction procedure. The procedure employed is the multipole-moment wave generation formalism for slow-motion objects with arbitrarily strong internal gravity [59]. We consider terms up to the mass-octopole and current-quadrupole multipoles, thus improving on the mass-quadrupole analysis of [55, 228] and [56]. Higher multipoles will become important if the system becomes even more relativistic, but pericenter velocities for EMRBs are typically small to moderate relative to the speed of light (typically  $0.1 \lesssim v_p/c \lesssim 0.5$ ). Such higher multipolar corrections were taken into account for EMRIs by [237], but for those sources the phase evolution must be tracked very accurately, requiring techniques from black hole perturbation theory [10, 53] that we shall not consider here.

The study of the relativistic corrections considered in this work leads to the following conclusions. First, we find that relativistic effects are significant for approximately 50% of the orbits contained in the EMRB phase space considered by [55, 228]. These relativistic EMRB orbits differ from their Newtonian counterparts in such a way that the associated waveforms present a noticeably different structure. In particular, we find that there is a dephasing relative to Newtonian waveforms that is due to precessional effects and depend strongly on the MBH spin. These findings show that EMRB events are relativistic enough that they should be treated accordingly, as was previously found for EMRIs [53].

Second, we find that the corrections to the trajectories affect the waveforms much more than the corrections in the waveform generation over several bursts. For example, for a given relativistic trajectory, we find that the difference between the SNR of a waveform obtain from the quadrupole formula to that obtained from the quadrupole-octopole formula is of the order of 10% (depending on the location of the observer.) On the other hand, using the same waveform generation formula (quadrupole or quadrupole-octopole), the difference between the SNR of a Newtonian waveform to that of a Kerr waveform is of the order of 100%. These findings show that modeling EMRB waveforms with a quasi-Newtonian treatment might not be sufficient for certain data analysis applications.

Third, we find that the relativistic corrections accumulate with multiple bursts and, thus, they may have an important impact in improving the SNR. It is also conceivable that such corrections might be important for parameter estimation studies and, perhaps, may be used to determine or bound the spin of the MBH if a high SNR event is detected. Along this same lines, if parameters can be determined accurately enough, it might also be possible to use EMRB measurements to test deviations from General Relativity. We must note, however, that changing the orbital parameters in Newtonian waveforms could somewhat mimic some of the relativistic corrections, but a detailed Fisher analysis of such effects is beyond the scope of this paper.

The remainder of this paper is divided as follows: Section 8.2 deals with the dynamics of EMRBs in the semi-relativistic approximation and justifies the use of this approximation for these systems; Section 8.3 reviews the inclusion of higher-order multipolar corrections to the waveform generation formalism; Section 8.4 describes the numerical implementation of the equations of motion and the initial data used; Section 8.5 compares the orbital trajectories and waveforms; Section 8.6 concludes and points to future research.

In this paper, we denote the MBH mass by  $M_{\bullet}$  and its *gravitational radius* by  $R_{\bullet} = 2GM_{\bullet}/c^2$ , where  $c$  is the speed of light and  $G$  the Newtonian gravitational constant. To simplify some expressions we normalize masses with respect to  $M_{\text{MW}} = 4 \times 10^6 M_{\odot}$ , which is of the same magnitude as the mass of the MBH at the center of the Milky Way [238]. The gravitational radius can then be written as:

$$R_{\bullet} = (3.82 \times 10^{-7} \text{ pc}) \frac{M_{\bullet}}{M_{\text{MW}}}. \quad (8.1)$$

## 8.2 EMRB Dynamics

In this section, we discuss the description of the orbital motion. Newtonian dynamics usually provides an adequate description of many astrophysical sources of gravitational waves, at least from a qualitative point of view. However, for certain gravitational wave sources, such a description is insufficient and relativistic effects have to be considered. For EMRB sources with pericenter distances  $r_p > 4R_{\bullet}$  and velocities  $v_p/c < 0.5$ , the semi-relativistic approximation to the equations of motion, in combination with a multipolar description of the gravitational radiation, can adequately model the dynamics and gravitational radiation, as we argue below.

The semi-relativistic approximation treats the motion of the SCO in the point-particle limit as a geodesic of the MBH geometry, which is justified based on the small mass-ratios associated with these systems. In this work, we adopt Cartesian Kerr-Schild coordinates,  $\{t, x^i\}$  ( $i = 1, 2, 3$ ), in which the MBH geometry is time-independent, reflecting its stationary character, and tends to a flat-space geometry in Cartesian coordinates far from the MBH. We denote the geodesic trajectory by  $z^i(t)$ , its spatial velocity by  $v^i(t) = dz^i/dt$ , and its spatial acceleration by  $a^i(t) = dv^i/dt$ . The latter, in such a coordinate system, and by virtue of the geodesic equations of motion, has the following

form [e.g. see 239]:

$$a^i = F^i[v^j; g_{\mu\nu}, \partial_j g_{\mu\nu}], \quad (8.2)$$

where  $g_{\mu\nu}$  ( $\mu, \nu = 0, 1, 2, 3$ ) are the spacetime components of the MBH metric. These equations describe the influence of the spacetime curvature produced by the MBH and approach the Newtonian equations of motion in the regime where  $v/c = |v^i|/c \ll 1$  and  $GM_\bullet/(c^2 r) \ll 1$  ( $r = |x^i|$ ).

The effects from the self-gravity of the SCO can be neglected. To see this, consider the (Keplerian) orbital timescale,  $T_{\text{orb}}$ , in comparison to a characteristic radiation-reaction timescale,  $T_{\text{rr}}$ . For the latter, we can use the timescale associated with the rate of change of the semi-latus rectum,  $p$ , related to the pericenter distance by  $r_p = p/(1+e)$ , namely  $T_{\text{rr}} \sim p/|dp/dt|$ . The radiation-reaction timescales of the other orbital elements are comparable or larger [see, e.g., 53]. The ratio of these timescales is

$$\frac{T_{\text{orb}}}{T_{\text{rr}}} \sim 2\pi\mu \left(\frac{R_\bullet}{2p}\right)^{5/2}, \quad (8.3)$$

where  $\mu = m/M_\bullet$  is the mass ratio of the system and  $m$  the SCO mass. It is evident that the radiation-reaction timescale is much greater than the orbital timescale due to the extreme mass ratio,  $\mu \ll 1$ , and because EMRBs have  $p \gg \mu^{5/2} R_\bullet$ . In the unlikely case that more accuracy is required, one could improve the analysis through the use of ‘‘Kludge’’ waveforms [237], which have been shown to reproduce numerical results in the adiabatic approximation accurately for EMRIs.

Formally, the orbital timescale used is not really the exact timescale of orbital motion. This is because the mass distribution of a MBH-embedded galaxy possesses a non-Keplerian potential that leads to non-Keplerian orbits. However, most EMRBs (by rate) have apocenters that do not extend far into the stellar population, implying that the contribution from the galaxy potential is minimal. The orbits we study in later sections have a contamination from the galactic potential that is less than 2% of the MBH mass. Moreover, [56] rightly argue that the inner region is statistically empty of stars, which is due to finite effects realized at the small scales observed near the MBH.

Certain constraints may be derived on the size of  $p$  and  $r_p$  for EMRB events. The most important constraint is derived from the definition of EMRBs: orbits with sufficiently large orbital period  $T_{\text{orb}} > T_{\text{cut}}$ . Assuming a Keplerian orbit (which is a rough assumption), this constraint translates to pericenter distances as follows

$$r_p > (7.98 \times 10^{-7} \text{ pc}) \frac{(1-e)}{0.1} \left(\frac{M_\bullet}{M_{\text{MW}}}\right)^{1/3} \left(\frac{T}{T_{\text{cut}}}\right)^{2/3}, \quad (8.4)$$

where we have rescaled quantities assuming a typical eccentricity of  $e = 0.9$  [55, 228] and a typical MBH mass of  $M_\bullet = M_{\text{MW}}$ . In terms of geometrized units, such a constraint translates roughly to  $r_p > 2R_\bullet$ .

This constraint can be compared with the requirement that the SCO does not get captured. Any object that enters the black hole event horizon is captured, where the

horizon is located (in Boyer-Lindquist coordinates) at

$$r_{\text{cap}} = (1.91 \times 10^{-7} \text{ pc}) \frac{M_{\bullet}}{M_{\text{MW}}} \left[ 1 + \sqrt{1 - \frac{a_{\bullet}^2}{M_{\bullet}^2}} \right], \quad (8.5)$$

where  $a_{\bullet}$  is the (Kerr) MBH spin parameter, related to its intrinsic angular momentum by  $S_{\bullet} = GM_{\bullet}a_{\bullet}/c$ , and bounded by  $a_{\bullet}/M_{\bullet} \leq 1$ . Thus, for a maximally spinning Kerr MBH ( $a_{\bullet} = M_{\bullet}$ ),  $r_{\text{cap}} = 0.5R_{\bullet}$ , while for a Schwarzschild (non-spinning) MBH it is just  $R_{\bullet}$ . This condition tell us simply that  $r_p > r_{\text{cap}}$ , which is a condition superseded by the constraint on the orbital period given in equation (8.4). One could explore other possible constraints [55, 228] but they are in general superseded by equation (8.4).

These constraints clearly exclude the ergosphere of the MBH ( $r_{\text{cap}} < r \lesssim R_{\bullet}$ ) where frame dragging effects are most pronounced. However, for EMRIs it has been argued [53] that orbits with  $r_p < 10R_{\bullet}$  cannot be considered Keplerian anymore, mainly due to precessional effects. This statement can be made more quantitative by looking at the ratio of first-order post-Newtonian (1 PN) predictions [3] to Newtonian ones (0 PN). For example, for the energy of a circular orbit, this ratio scales as  $7R_{\bullet}/(8r_p)$ , while for the perihelion precession angle, the ratio scales as  $3R_{\bullet}/(2r_p)$ , for extreme-mass ratios. Therefore, for orbits with pericenter passage  $r_p \sim 5R_{\bullet}$ , the 1 PN correction to the energy and the perihelion precession angle is approximately 20% and 30% respectively, relative to the Newtonian value. This indicates that, even for orbits outside the ergosphere, relativistic effects are not necessarily negligible.

The relativistic geodesic equations of motion introduce corrections to the Newtonian motion that can be interpreted in terms of a black hole *effective* potential. By comparing the Newtonian and relativistic potentials one can see that the relativistic corrections dominate over the centrifugal barrier at small distances from the black hole center. In this work we show that these relativistic corrections can be sampled by EMRBs and hence, one should model these systems accordingly. Nevertheless, as we argued above, the relativistic treatment of EMRBs does not need to be as sophisticated as in the case of EMRIs, since radiation-reaction can be neglected.

### 8.3 EMRB Waveforms

In this section we describe how we extract gravitational waveforms once we have integrated the geodesic equations of motion. We use a multipole-moment wave generation formalism for slowly-moving objects with arbitrarily strong internal gravity [59, 240, 53]. In quasi-Newtonian and semi-relativistic treatments, the radiation is modeled by the lowest non-vanishing multipole moment: the mass-quadrupole. To that order, and for the case of a point-like object orbiting a MBH at a fixed coordinate location, the plus and cross polarizations are given by [197, 59]

$$h_{+, \times} = \frac{2Gm}{rc^4} \epsilon_{+, \times}^{ij} \left( a_i z_j + v_i v_j \right), \quad (8.6)$$

where  $r$  is the (flat-space) distance to the observer and  $\epsilon_{+, \times}^{ij}$  are polarization tensors. This expression assumes, based on the slow motion approximation, that the change in the acceleration with respect to time, the *jerk*,  $j^i = da^i/dt$ , is a small quantity. More precisely, we are neglecting terms of order  $(v/c)^3$ , or in other words, since the (quadrupole) leading order terms are of order  $(v/c)^2$ , this implies a relative error of order  $v/c$ .

One can improve on this description for the gravitational radiation by accounting for higher-order multipole moments. In this paper, we consider the mass-octopole and current-quadrupole multipoles, which require the knowledge of one more time derivative of the trajectory, the jerk. Adding these contributions to equation (8.6), the gravitational waveforms are given by [59]

$$\begin{aligned} h_{+, \times} &= \frac{2Gm}{rc^4} \epsilon_{+, \times}^{ij} \left\{ a_i z_j + v_i v_j \right. \\ &+ \frac{1}{c} \left[ (\mathbf{n} \cdot \mathbf{z}) (z_i j_j + 3a_i v_j) + (\mathbf{n} \cdot \mathbf{v}) (a_i z_j + v_i v_j) \right. \\ &\left. \left. - (\mathbf{n} \cdot \mathbf{a}) v_i z_j - \frac{1}{2} (\mathbf{n} \cdot \mathbf{j}) z_i z_j \right] \right\}, \end{aligned} \quad (8.7)$$

where  $n^i = x^i/r$  is a unit vector that points to the observer and the vector product is the flat-space scalar product. In this case, we are neglecting terms of order  $(v/c)^4$  and hence we are making a relative error of order  $(v/c)^2$  with respect to the leading order quadrupole term.

The waveforms of equation (8.7) are a truncated multipole expansion, where we are neglecting the current-octopole, mass-hexadecapole, and higher multipole moments. This expansion is based on a slow-motion approximation which is valid for orbits whose pericenter velocity is small relative to the speed of light. For closed circular orbits, we can use the Virial theorem to argue that this is equivalent to requiring  $r_p > M_\bullet$ . For a relativistic EMRB event with  $v_p/c = 0.4$ , the maximum relative contribution of the octopole to the quadrupole is of the order of 40%, since the octopolar term is of order  $v/c$  smaller than the quadrupolar one. In this paper, we shall study EMRBs from the sample of Milky Way sources studied in [55]. These sources have initial pericenter distances of  $r_p > 8M_\bullet$ , thus justifying the use of a low-multipolar expansion in the wave-generation formalism and the neglect of radiation reaction effects in the orbital motion.

## 8.4 Numerical Simulations

In this section we describe the EMRB simulations that were carried out, including the choice of initial conditions. The simulations involve integrating the equations for geodesic motion around a Kerr black hole, equation (8.2), forward in time. [For a detailed exposition of Kerr geodesics see 241]. Since Cartesian Kerr-Schild coordinates are used, the initial conditions can be denoted by  $(z_0^i, v_0^i)$ . The numerical implementation does not use the Kerr geodesic constants of motion (energy, angular momentum, and Carter constant) in order to reduce the number of variables of the resulting system of ordinary

differential equations. Instead, we have used the constants of motion to monitor the accuracy of the time integration. The integration accuracy is set so that we obtain fractional errors for the constants of motion smaller than one part in  $10^{10}$ . The code uses a Bulirsh-Stoer extrapolation method as the evolution algorithm [see, e.g. 205, 204]. We have also introduced in the code the possibility of switching between Kerr geodesics and Newtonian equations of motion. The gravitational waveforms are then obtained directly by applying expressions (8.6) and (8.7) to the numerically obtained trajectory  $z^i(t)$ .

Comparisons are carried out by choosing a representative relativistic orbit within the allowed phase space for EMRB's. We made the following choices for the test case:

- The central MBH mass is  $M_\bullet = M_{\text{MW}}$  and the SCO mass is  $m = 1 M_\odot$ , such that the mass ratio is  $\mu = m/M_\bullet = 2.5 \times 10^{-7} \ll 1$ .
- The MBH spin parameter is either  $a_\bullet = 0$  (Schwarzschild) or  $a_\bullet = 0.998 M_\bullet$  (Kerr). The angular momentum is aligned along the  $z$ -axis and equal to either  $S^z = 0$  or  $S^z = 0.998GM_\bullet^2/c$ .
- The observer is located at  $r_{\text{obs}} = 8$  kpc along the  $z$ -axis, which corresponds to the approximate distance from Earth to the center of the Milky Way [242].

Furthermore, we make the following choices for the orbital initial conditions:

$$\begin{aligned} z_0^i &= (-1.59, 1.05, -0.185) \times 10^{-5} \text{ pc}, \\ v_0^i &= (1.70, -2.89, 0.510) \times 10^4 \text{ km s}^{-1}. \end{aligned} \quad (8.8)$$

The initial conditions are such that  $r_0 = |z_0^i| = 50R_\bullet = 1.91 \times 10^{-5} \text{ pc}$ , and  $|v_0^i| = 0.11c = 3.39 \times 10^4 \text{ km s}^{-1}$ . The orbital plane is inclined by  $10^\circ$  with respect to the  $x - y$  plane to demonstrate the effects of orbital plane precession, which only occurs for spinning MBHs. Since this paper is concerned with the effect of relativistic corrections to EMRB events, we choose to give all orbits the same initial conditions. The possibility of relaxing this choice and its effect on the conclusions derived in this paper shall be discussed in a later section.

Although the test orbit is in the phase space of EMRB events studied in [55], one might worry that it is too relativistic to actually have a significant probability to occur in nature. In particular, one can think that the SCO may be tidally disrupted. To address this question, let us consider a Newtonian description of the central potential, which leads to the following values of the pericenter distance and velocity:

$$\begin{aligned} r_p &= 6.45 R_\bullet = 2.48 \times 10^{-6} \text{ pc}, \\ |v_p| &= 0.384c = 1.15 \times 10^5 \text{ km s}^{-1}. \end{aligned} \quad (8.9)$$

One might worry that stars might be tidally disrupted with such small pericenters. However, as shown by [56], most SCOs in EMRB scenarios consist of stellar-mass black holes, which cannot be tidally disrupted.

Such relativistic orbits are actually naturally occurring in the phase space of possible EMRBs studied in [55]. Of all orbits in the allowed EMRB phase space considered in [55, 228], 6% is contained within a small 6-dimensional phase space volume centered on the test orbit <sup>2</sup>. Furthermore, the test case shown possesses a short orbital timescale, bursting approximately 150 times per year. Such events with small orbital timescale were shown to dominate the EMRB event rate in [55]. It is in this sense that the test orbit studied here is *typical* or representative of EMRBs.

The relative location of the test orbit in the pericenter distance-eccentricity plane of the phase space of allowed EMRBs [55] is presented in Figure 8.1 (triangle.) The eccentricity was here calculated assuming a Newtonian orbit and the pericenter separation is given in gravitational radii,  $R_\bullet$ . Although the test orbit has a large eccentricity, its apocenter is small enough ( $r_a \lesssim 150R_\bullet \approx 6 \times 10^{-5}$  pc) that the contribution from the surrounding stellar population to the potential can be neglected. In general, the left side of the figure corresponds to highly relativistic orbits with large pericenter velocities and small pericenter distances. Orbits with pericenter velocities  $|v_p| > 0.25c = 3 \times 10^4$  km s<sup>-1</sup> account for approximately 50% of the possible orbits within the phase space studied in [55].

Although the test orbit is a good source to demonstrate the differences between the Newtonian and relativistic treatments, we could have chosen an even more relativistic one. Such an event would still be classified as an EMRB in a Newtonian treatment, but it would border with the definition of a continuous source. An example of such an extreme orbit is shown with a circle in Figure 8.1, to the left of the test orbit (triangle). This extreme orbit possesses the following initial conditions:

$$\begin{aligned} z_0^i &= (-1.81, 0.6, -1.06) \times 10^{-6} \text{ pc}, \\ v_0^i &= (1.72, -1.78, 0.31) \times 10^5 \text{ km s}^{-1}, \end{aligned} \quad (8.10)$$

where  $r_p = 4R_\bullet = 1.53 \times 10^{-6}$  pc and  $|v_p| = 0.49c = 1.46 \times 10^5$  km s<sup>-1</sup> for a Newtonian potential. We will study such an extreme orbit at the end of the next section as an example of a limiting relativistic case.

## 8.5 Comparison of Trajectories and Waveforms

In this section we compare the results obtained for both the orbital motion and the gravitational radiation emitted by an EMRB event using both the Newtonian and relativistic description. Since the *plus* and *cross* polarization waveforms present similar features, we only plot the *plus* polarization waveforms. In the remainder of this section we use the following nomenclature: a quadrupolar (octopolar) Newtonian waveform is one that was calculated using the quadrupole (octopole) formula and Newtonian equations

---

<sup>2</sup>In other words, 6% of the test orbits considered to be EMRBs in [55] are close in phase space to our test orbit. This does not imply that the probability of such a test orbit actually occurring in nature is 6%, since any element of phase space may have small overall probabilities, even down to  $10^{-7}\%$ .

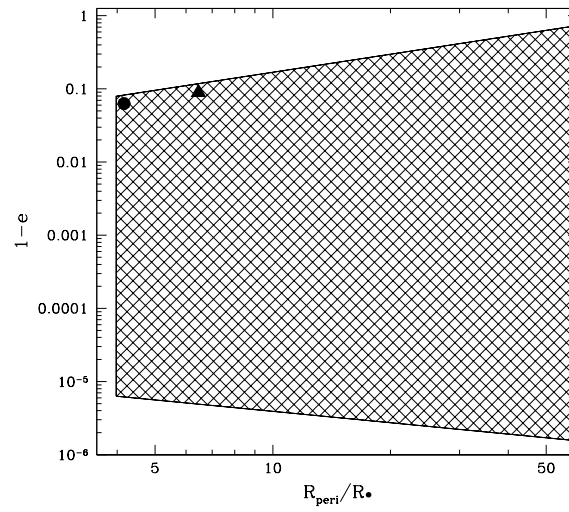


Fig. 8.1. Plot of the set of possible EMRB orbits as computed in [55] in the pericenter distance-eccentricity plane. The pericenter distance is given in units of the gravitational radius  $R_{\bullet}$ . The initial conditions for the test [Eq. (8.8)] and the extreme [Eq. (8.10)] orbits are indicated by a triangle and a circle respectively.

of motion; a quadrupole (octopole) Schwarzschild waveform is one that was calculated using the quadrupole (octopole) formula and the geodesic equations of motion with no spin ( $a_{\bullet} = 0$ ); a quadrupole (octopole) Kerr waveform is one that was calculated using the quadrupole (octopole) formula and the geodesic equations of motion with spin  $a_{\bullet} = 0.998M_{\bullet}$ .

### 8.5.1 Orbital Trajectories

Let us begin by comparing the trajectories obtained in our simulations. In Figure 8.2, we plot the test orbit corresponding to a Newtonian treatment (solid line) and the one corresponding to a relativistic treatment without spin (dashed line) and with spin (dotted line). The dot and arrow indicate the initial location and velocity projected onto the  $x$ - $y$  plane. The MBH is located at the origin of the coordinates, and the vectors denoted by  $L$  and  $S$  describe the direction of the initial orbital angular momentum and the MBH spin respectively. In the relativistic description there are precessional effects in the SCO orbit that can be clearly observed in Figure 8.2. These precessional effects are: pericenter precession about the orbital angular momentum axis, which acts in the initial orbital plane; and frame-dragging precession about the total angular momentum axis, which acts out of the initial orbital plane. While the former always occurs in a relativistic treatment, the latter is present only in the spinning case.

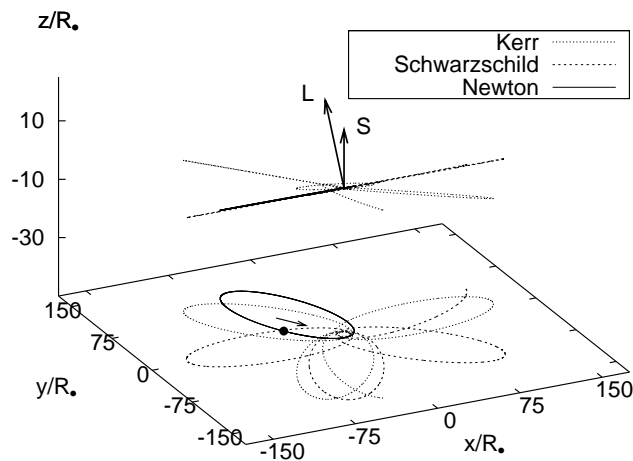


Fig. 8.2. Trajectories for the SCO, with initial conditions given by (8.8), corresponding to a Newtonian description (solid line) and relativistic descriptions with no spin (dashed line) and with spin (dotted line). The MBH is located at the origin and the vectors  $L$  and  $S$  denote the initial orbital angular momentum and the MBH spin respectively.

Different relativistic precessional effects are generally of different magnitude. These effects are usually inversely proportional to the pericenter distance, or equivalently proportional to the pericenter velocity of the SCO. Precession out of the initial orbital plane, however, is smaller than precession in the orbital plane by a relative factor of order  $v_p/c$  and it is directly proportional to the spin of the MBH. In terms of post-Newtonian theory [see, e.g. 3], the pericenter advance is described by 1st-order post-Newtonian corrections to the equations of motion (order  $(v/c)^2$  relative to the Newtonian acceleration), while precession off the orbital plane is due to spin-orbit and spin-spin couplings that correspond to 1.5 and 2-order corrections (order  $(v/c)^3$  and  $(v/c)^4$  relative to the Newtonian acceleration.) Therefore, since EMRBs are characterized as events with small to moderate pericenter velocities, precession out of the initial orbital plane is small to moderate relative to pericenter advance, even for maximally spinning MBHs.

We can estimate the precession rate by comparing the Newtonian and relativistic trajectories. For the test orbit considered, we find that the rate in the orbital plane is roughly  $\pi/3$  radians per orbit for the non-spinning case and  $2\pi/3$  radians per orbit for the spinning one. These precessional effects have been studied extensively in the context of EMRIs [see, e.g. 243] and also specifically for S-stars in the central region of our Galaxy in [244]. Nonetheless, these effects have not been previously analyzed in the context of EMRBs, since previous studies employed a quasi-Newtonian treatment.

### 8.5.2 Waveforms

Let us now analyze how the differences in the SCO trajectories translate into different signatures in the waveforms. In Figure 8.3 we plot the quadrupole Newtonian and Schwarzschild waveforms (solid and dashed lines respectively), while in Figure 8.4 we plot the quadrupole Schwarzschild and Kerr waveforms (dashed and dot-dot-dashed lines respectively.) There are three main differences between the Newtonian and the relativistic waveforms: a modulated phase change, an amplitude change, and a time of arrival change. The changes in amplitude and time of arrival are due to the test particle experiencing a larger “force” of attraction as it approaches the black hole. Quantitatively, this increase in force is due to the presence of  $(r_p^{-n})$ -contributions to the relativistic corrections to the central potential (with  $n$  a real positive number.)

Gravitational wave interferometers are most sensitive to the phase, which is clearly different for Newtonian and relativistic waveforms. The dephasing present in Figures 8.3 and 8.4 parallels the orbital dephasing discussed earlier (the gravitational-wave and orbital frequencies are intimately related) and leads to an amplitude modulation. In terms of the gravitational wave phase, both Figures 8.3 and 8.4 show a dephasing of  $\pi/6$  radians per cycle. This can be seen after the third burst where the waveforms are back in phase. In fact, there is a significant dephasing even between the relativistic waveforms due to the effect of the MBH spin. If a cursory examination by eye can detect the difference in the waveforms due to differences in the nature of the central potential, it stands to reason that strong-field EMRB waveforms might allow us to probe of the spacetime near a MBH. We should note, however, that no work has yet been done to find best-fit parameters for Newtonian waveforms that maximize the correlation with relativistic ones. In other words, it might be possible to mimic some of the relativistic

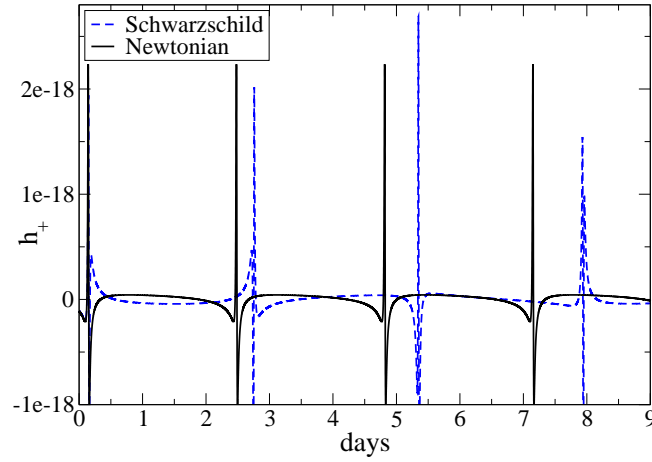


Fig. 8.3. EMRB waveforms (*plus* polarization): The Newtonian waveform corresponds to the solid line and the Schwarzschild one to the dashed line.

corrections by choosing different initial data for the Newtonian waveforms, but such a study is beyond the scope of this paper.

The difference in dephasing can be better studied by calculating the signal overlap,

$$(h_1|h_2) = \frac{\int_0^T h_1(t)h_2(t)dt}{\sqrt{\int_0^T h_1^2(t)dt} \sqrt{\int_0^T h_2^2(t)dt}} . \quad (8.11)$$

The overlap indicates how well a signal  $h_1$  can be extracted via matched filtering with a template  $h_2$ <sup>3</sup>. In Figures 8.5 and 8.6 we plot the normalized integrand as a function of time, with  $h_1$  given by the quadrupole Kerr waveform and  $h_2$  given by either the quadrupole Newtonian or Schwarzschild waveforms. Observe that neither the Newtonian nor the Schwarzschild waveforms match well with the Kerr waveform. Moreover, note that the correlation with the Newtonian waveform deteriorates greatly after only the first cycle. The integral of equation (8.11) gives the correlation between different waveforms over nine days (four bursts): for the Newtonian and Kerr plus-polarized waveforms it is 9.6%; for the Schwarzschild and Kerr plus-polarized waveforms it is  $-6.3\%$ . As a point of comparison, a substantial signal overlap should be  $\gtrsim 95\%$ . As already mentioned, the same initial conditions were chosen for both the Newtonian and relativistic orbits, such that their waveforms would be both initially in-phase and any dephasing due to relativistic effects could be clearly studied. However, such a choice forces the SCO to pass through periapsis at slightly different times, because in the relativistic case this

<sup>3</sup>The overlap is given here in the time domain, but an analogous representation in the frequency domain could also be used. Such an expression in the frequency domain can be derived through Parseval's theorem.

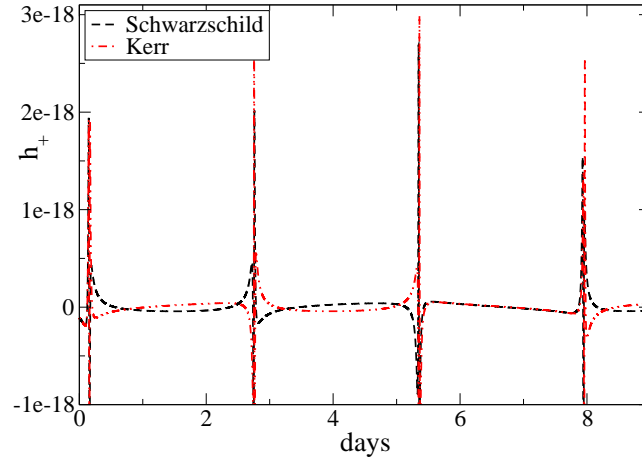


Fig. 8.4. EMRB waveforms (*plus* polarization): The Schwarzschild waveform corresponds to the dashed line and the Kerr one to the dot-dot-dashed line. The dephasing of the waveforms can be best observed during the silent transitions between bursts. For example, in the first silent transition the waveforms are roughly  $\pi$  radians out of phase, while in the third one they are in phase.

object experiences a “deeper” potential. Such a difference in timing degrades the overlap somewhat and could, in principle, be ameliorated by choosing different initial conditions for the Newtonian evolution, *i. e.* by maximizing the overlap over all orbital parameters, but such a study is beyond the scope of this paper.

Figures 8.5 and 8.6 provide some evidence that the use of a relativistic waveform might be required for the data analysis problem of extracting EMRB signals. Such expectations are somewhat confirmed in Table 8.1, where we present the correlation between Newtonian and Kerr plus-polarized waveforms integrated over both a single day (one burst) and nine days of data (several bursts) for a sample of different EMRB orbits<sup>4</sup>. Both a single and several bursts should be studied because, in principle, parameter adjustments might mitigate the between-burst dephasing, but probably not the in-burst dephasing. The orbits chosen were taken directly from the allowed EMRB phase space of [55] and possess different initial positions and velocities, leading to different eccentricities, initial inclination and orbital periods. The orbital period can be used to classify the orbits into highly-bursting (burst more than once per week) and slowly-bursting (burst less than once per week.) For highly-bursting EMRBs, the average correlation is  $\sim 27\%$  when all nine days of data (several bursts) are used, while it is  $\sim 93\%$  when only one day of data (single burst) is used. For the slowly-bursting EMRBs we considered here, there is actually only one burst per week and its correlation is  $\sim 85\%$ . These results

<sup>4</sup>Here we use the frequency representation of the correlation calculation, employing the Fourier transform of the waveforms.

$r_p$ [ $\mu\text{pc}$ ]	$v_p/c$	$P$ [yrs]	$e$	# Bursts	$\frac{ \Delta\rho }{\rho}$	$\frac{ \Delta\rho^{(1)} }{\rho^{(1)}}$	$(h_1 h_2)$	$(h_1 h_2)^{(1)}$
7.8	0.196	0.0042	0.603	6	0.38	0.049	0.27	0.98
7.5	0.207	0.0055	0.684	5	0.13	0.0007	0.20	0.88
7.2	0.217	0.0074	0.749	4	0.22	0.057	0.31	0.90
7.1	0.220	0.0086	0.777	3	0.49	0.061	0.33	0.99
13	0.163	0.0450	0.859	1	.	0.002	.	0.90
8.0	0.217	0.1953	0.968	1	.	0.033	.	0.97
10	0.193	0.7683	0.984	1	.	0.009	.	0.72
12	0.173	3.0407	0.992	1	.	0.015	.	0.80

Table 8.1. SNR and overlap for different EMRB orbits. In this table we present the SNR and correlation computed in the frequency domain between Kerr quadrupole and octopole waveforms for different EMRB orbits. The orbits are separated into two groups: highly-bursting (top) and slowly-bursting (bottom). The first five columns present information about the different orbits, including how many times they burst, their eccentricities and periods, which were chosen directly from the allowed EMRB phase space of [55] and thus represent Milky Way sources. The sixth and seventh columns present the difference in SNR between a Newtonian and Kerr quadrupole waveform relative to the former using the entire data set and only one burst respectively. Similarly, the eighth and ninth columns show the correlation between the plus polarizations using the entire data set four and one burst respectively. Since the slowly-bursting sources burst only once, the sixth and eighth columns are redundant for these sources. All calculations assume the observer is located on the  $z$ -axis and random initial inclination angles.

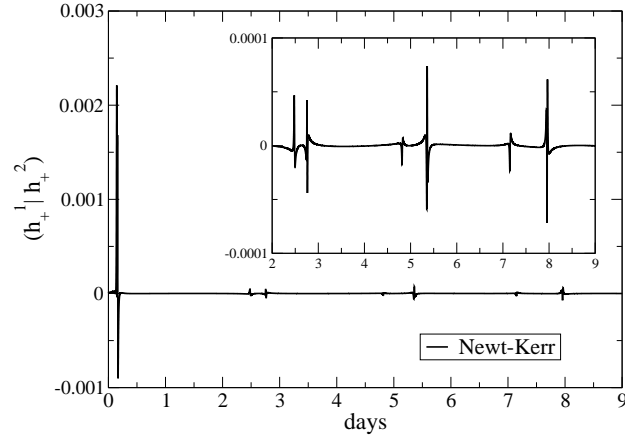


Fig. 8.5. Plot of the overlap integrand of equation (8.11) with  $h_1$  given by the quadrupole Kerr waveform and  $h_2$  by the quadrupole Newtonian one. The inset zooms to a region near the small peaks.

indicate that accumulating precession effects lead to a significant loss of correlation between Newtonian and Kerr waveforms if bursts are to be connected. Moreover, we see that even for a single burst the shape of the relativistic waveforms is sufficiently different from its Newtonian counterpart to lead to a significant mismatch (in-phase dephasing). If one maximizes the correlation over intrinsic orbital parameters it might be possible to increase the correlation somewhat, but again that is to be studied elsewhere.

Let us now focus on the differences in the waveforms when they are calculated with the quadrupolar approximation versus the quadrupolar-octopolar one. In Figure 8.7 we plot the absolute value of the difference between the octopole and quadrupole waveforms as a function of time for a Schwarzschild (upper panel) and a Kerr (lower panel) central potential. The difference is normalized to the maximum of the first peak of the quadrupole waveform, since other peaks have approximately the same maximum. Observe that the inclusion of higher-order multipoles does not affect the phasing of the waveforms, but only the amplitude, which is in general different by roughly 4% relative to the quadrupole waveform for the Kerr test case. At first sight, this result is in disagreement with the expectation that the octopolar correction is at most  $\lesssim 40\%$  of the quadrupolar one. Note, however, that the 40% estimate is an order-of-magnitude *upper limit*, since the octopole correction is dependent on the location of the observer relative to the trajectory, velocity, acceleration and jerk vectors. For the test case, where the observer is located on the  $\hat{z}$ -axis and the orbit is initially inclined by  $10^\circ$ , the octopolar change is reduced by approximately an order of magnitude, since initially  $(\mathbf{n} \cdot \mathbf{z}) \approx (\mathbf{n} \cdot \mathbf{v}) \approx (\mathbf{n} \cdot \mathbf{a}) \approx (\mathbf{n} \cdot \mathbf{j}) \approx 0.1$ . In Table 8.2, we present the approximate maximum difference between octopolar and quadrupolar waveforms as a function of observer location, focusing only on the first burst of radiation. The location of the observer is rotated about the  $\hat{y}$ -axis on the  $\hat{x} - \hat{z}$  plane, always at a fixed radial distance of 8 kpc.

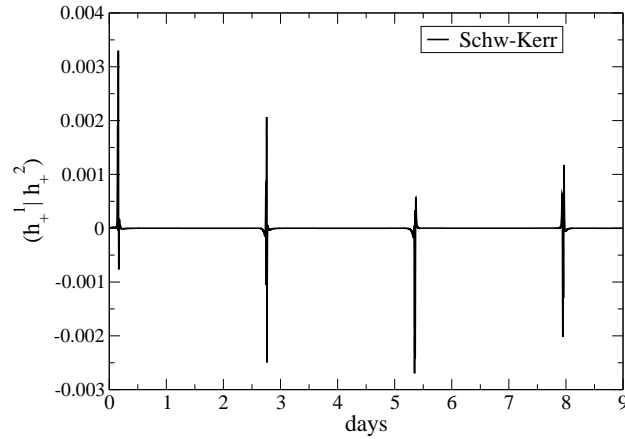


Fig. 8.6. Plot of the overlap integrand of equation (8.11) with  $h_1$  given by the quadrupole Kerr waveform and  $h_2$  by the quadrupole Schwarzschild one.

Note that for some observers the difference is larger and, in fact, of the order of 40%, since the dot products are closer to unity. These results are thus consistent with the expectation that the  $n$ -th multipolar contribution cannot in general be larger than order  $(v/c)^n$  relative to the quadrupolar leading term.

### 8.5.3 Data Analysis

In order to quantify some of our statements about the change in phase and amplitude, we calculated the SNR for the relativistic waveforms via the standard formula

$$\rho^2 = 4 \int_0^\infty \frac{|\tilde{h}(f)|^2}{S_n(f)} df, \quad (8.12)$$

where the tilde denotes the Fourier transform and  $S_n(f)$  is the one-sided power spectral noise density. Here we employ the Online Sensitivity Curve Generator [245] with the standard LISA settings and the inclusion of the white-dwarf background contribution. When calculating SNRs, we set the observation time to roughly nine days, so as to include multiple bursts in our single SNR value.

The inclusion of relativistic corrections in the trajectories has a dramatic impact in the SNR. We find that the Schwarzschild waveform increases the SNR by a factor of approximately 59%, while the Kerr waveform increases it by 162%, relative to the Newtonian SNR. The difference in SNR is because the relativistic orbits experience a deeper effective potential and, thus, the interaction timescale is smaller. Therefore, the inverse of the interaction time,  $f_\star = v_p/r_p$ , is larger for the Schwarzschild and Kerr waveforms relative to the Newtonian one. As a result, the Fourier power is shifted to higher frequencies, where LISA is more sensitive.

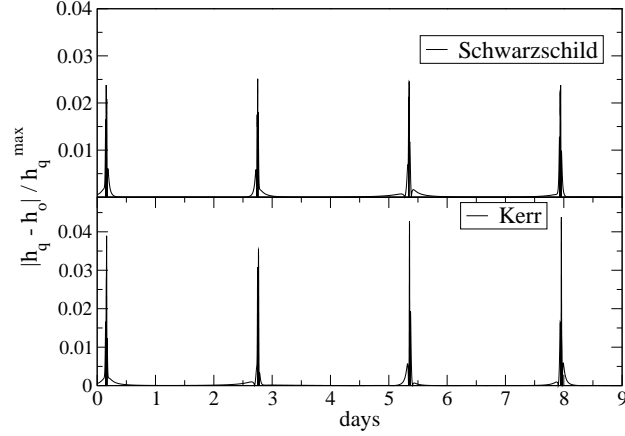


Fig. 8.7. Plot of the absolute magnitude of the difference between the quadrupole and octopole Schwarzschild (upper panel) and Kerr (lower panel) waveforms. The difference is normalized to the maximum value of the first peak of the quadrupole waveform.

Angle [degrees]	$x_{\text{obs}}$ [kpc]	$y_{\text{obs}}$ [kpc]	$z_{\text{obs}}$ [kpc]	Amp. diff.
0	0	0	8	3.9%
20	2.73	0	7.51	3.3%
40	5.14	0	6.12	11.5%
60	6.93	0	4	15.2%
80	7.88	0	1.39	19.7%
100	7.88	0	-1.39	21.6%
120	6.93	0	-4	17.8%
140	5.14	0	-6.13	43.3%
160	2.74	0	-7.52	8.6%

Table 8.2. Comparison between quadrupole and octopole waveforms. Here we present an approximate measure of the amplitude difference between the quadrupole and octopole waveforms. We concentrate only on the first burst of radiation and we normalize the difference to the maximum of the first peak of the quadrupole waveform. The difference is presented as a function of the observer location, which is always at a fixed radial distance of  $r_{\text{obs}} = 8$  kpc, but rotated about the  $\hat{y}$ -axis on  $\hat{x} - \hat{z}$  plane ( $\theta$  is here the usual Euler polar angle.)

The SNR behaves similarly for other EMRB orbits with different orbital periods, eccentricities and pericenter parameters. This can be observed in Table 8.1 where we present the SNR difference between Newtonian and Kerr waveforms for different EMRB orbits for a single and several bursts. Highly-bursting EMRBs lead to a large change in the SNR over a week of data, since they experience the depths of the effective potential several times. Per burst, the change in SNR can range from one, to ten or even ninety percent, depending on the inclination angle of the orbit, the pericenter distance and other orbital parameters. Also note that the orbits presented in the table are not as relativistic as the test case, which is why the SNR difference is smaller. This study seems to indicate that the SNR is in general somewhat larger for relativistic waveforms, specially when several burst are taken into account.<sup>5</sup> Consequently, the event rate calculated in [55, 228], which in particular summed over all bursts in one year of data, is an underestimate for their galaxy model, because some of the systems with a Newtonian SNR  $\lesssim 5$  should have been added to the detectable event rate. However, the uncertainty in the event rate is still probably dominated by astrophysical uncertainties and not by the dynamics modeling.

Conversely, the inclusion of higher multipole moments to the wave generation formalism has little to no effect in the SNR. In the previous section we showed that there was  $\approx 4\%$  difference between the octopole and quadrupole waveforms relative to the maximum of the first peak of the quadrupole waveform. We further showed that this difference depends on the location of the observer (see table 8.2), but for the test case it does not exceed a maximum of 40%, which agrees with the multipole-ordering argument previously described. However, we also pointed out that the amplitude difference is confined to sharp peaks in the time domain. Such a confined change in the waveform amplitude leads to a Fourier power being dispersed over a large frequency region, including outside the LISA band. As a result, there is a correspondingly small change in the SNR: of the order of  $\approx 1\%$  relative to the quadrupolar formalism. Such a result is in agreement with the analysis of [237], which was carried out for EMRIs. Therefore, we see that the change in SNR is primarily dominated by the modifications introduced in the geodesic description of the equations of motion, and not in the octopolar correction to the waveform generation.

The analysis presented in this section, in particular Figure 8.5, makes it clear that relativistic corrections to the waveforms accumulate with multiple bursts. In other words, over a single burst (pericenter passage), a quadrupolar waveform calculation using Newtonian dynamics might be sufficient. However, if one wants to estimate parameters associated with the central MBH, then multiple bursts might be necessary to associate the events to a single SCO trajectory. In terms of data analysis, for a detection search it is simpler to look for a single burst using techniques such as excess power and wavelet decompositions [e.g. see 246, 247, 248, 249]. For estimating MBH parameters, the results

---

<sup>5</sup>Naive intuition might suggest that the change in the SNR should scale like the square root of the number of bursts, but this is not necessarily correct. First, different orbits possess different beaming patterns on the sky due to precession. Second, the starting frequencies of these bursts is very close to the limit of LISA's sensitivity band [ $10^{-5}$  Hz]. As the orbits burst, precession somewhat increases the frequency of the waveform, forcing different bursts to contribute different amounts to the SNR.

of this paper suggest that multiple bursts might have to be connected. For this to occur, a single template may be used, but as our results indicate, the template will need to incorporate the effects of general relativity.<sup>6</sup>

At this juncture, we should comment on some of the caveats in the conclusions derived from the analysis presented here. First, in this paper we have primarily concentrated on the question of characterizing the gravitational waves through the study of the SNR and overlap. In this study, however, we have not maximized these data analysis measures with respect to (intrinsic or extrinsic) orbital parameters. Although it might be possible to improve the SNR and overlap via parameter maximization, our study suggests that the introduction of relativistic effects, such as precession, lead to a clear imprint on the waveform that might be difficult to mimic with a purely Newtonian waveform irrespective of its parameters. Second, in this paper we have only touched the iceberg of the signal characterization and parameter estimation problem. A possible route to study this problem is through a numerical Fisher analysis, with the complications derived from the fact that the waveforms are known only numerically. Furthermore, increasing the complexity of the waveform will also increase the computational cost of these studies and, thus, it might be interesting to investigate whether it is possible or advantageous to search for individual bursts with similar frequency and identify them as belonging to the same physical system. These issues are beyond the scope of this paper, but they should be addressed in future investigations.

Setting these caveats momentarily aside, let us conclude with some discussion of the extreme relativistic case introduced earlier. As we have seen, relativistic corrections can introduce strong modifications to EMRB waveforms, which depend on how relativistic the EMRB event is and, in particular, on the pericenter velocity. The corrections are particularly strong for the class of EMRBs that inhabit the boundary between EMRBs and EMRIs, defined by the  $T_{\text{cut}} = 3 \times 10^4$  s value, corresponding to the period between apocenter passages. An example of such an event is the extreme orbit discussed in Section 8.4, whose waveform is shown in Figure 8.8. Observe that a simplistic Newtonian description misses the rich structure, in which the SCO whirls twice about the black hole before zooming out to apocenter again. This behavior is missed entirely when we evolve the orbit with the Newtonian equations of motion, even though the same initial conditions were used. Even though in the previous cases a Newtonian waveform might be able to extract relativistic events by adjusting intrinsic parameters, such is definitely not the case for the highly-relativistic event of Fig. 8.8, since no choice of parameters in the Newtonian waveform can reproduce its multiple-peak structure.

Due to their whirling behavior, the extreme orbit waveform resembles the zoom-whirl events often mentioned in the EMRI literature [250, 251, 252]. However, the event is still an EMRB and not an EMRI because the period between apocenter passages is too long. For our galactic model, we find the probability of a small region of phase space around this orbit to be rather high, 10%. If this EMRB is detected with sufficiently high

---

<sup>6</sup>A note of caution should be added here, since a detailed study of the maximization of the overlap with respect to orbital parameters in the Newtonian waveform has not yet been carried out. Indeed, it might be possible to mimic some of the relativistic effects with Newtonian waveforms with varying parameters, but such mimicking is most probably not possible for highly relativistic EMRBs.

SNR it seems plausible that a parameter estimation analysis would allow for a determination of the background parameters, such as the black hole spin. [253] have already investigated LISA's ability to measure MBH properties using approximate EMRI signals. They found that, depending on the actual orbital parameters, it will be possible to measure the MBH spin with fractional errors of  $10^{-3}$  to  $10^{-5}$ . This high precision measurement is the result of observing up to  $\sim 10^6$  complete orbits. Conversely, it is very unlikely that EMRB measurements will be able to match the measurement capabilities of EMRI signals, since only a few bursts will probably be available. Whether accurate parameter extraction is possible can only be determined with a more detailed data analysis investigation of EMRBs.

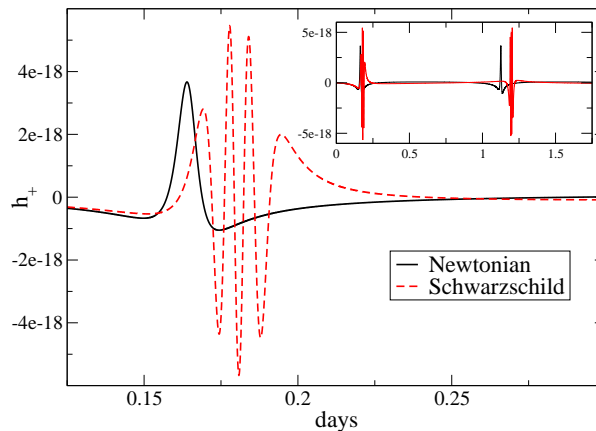


Fig. 8.8. Plot of the quadrupole Newtonian (solid) and Schwarzschild (dashed) gravitational waveform as a function of time.

## 8.6 Conclusions

We have studied the effects of relativistic corrections on the gravitational waves produced by EMRBs. These events originate from long period orbits of a SCO around a MBH, leading to large-amplitude, quasi-periodic gravitational wave bursts. Using a more accurate relativistic treatment of the phenomenon, we have improved on the waveforms and trajectories relative to previous work. The orbital trajectories were corrected by accounting for the spacetime curvature of the system for Schwarzschild and Kerr MBHs. The waveform generation was corrected by accounting for the next order term in the multipolar expansion of gravitational radiation.

We found that relativistic corrections change the waveform shape relative to its Newtonian counterpart. One of the most significant changes was found to be an amplitude-modulated dephasing, produced by the relativistic corrections to the orbital

trajectory and, in particular, by relativistic precessional effects. Other effects included a change in the amplitude of the waveform, partially produced by the inclusion of higher-order terms in the gravitational wave generation scheme.

The magnitude of the relativistic corrections was found to be directly proportional to the pericenter velocity of the orbit, as expected. Surprisingly, we estimated that at least 50% of the orbits analyzed in [55, 228] acquire relativistic velocities and, thus, non-negligible relativistic corrections. We investigated these corrections in detail by choosing a test orbit, that is representative of the kind that dominated the event rate calculation of [55]. We also studied a limiting case of a highly relativistic EMRB and found that it whirls more than once around the MBH before zooming back to apocenter and becoming silent again.

We have also discussed the possible consequences that relativistic effects might have on the detection and parameter estimation of gravitational waves from EMRBs by LISA, namely a change in the SNR and loss of overlap. These changes are mainly due to the relativistic treatment of the equations of motion, while a quadrupolar wave generation formalism seems to suffice. This finding is relevant particularly to match filtering searches, where a Newtonian treatment of the orbit might lead to a deterioration of confidence limits. Furthermore, our study suggests that, given an EMRB gravitational wave detection, it might be plausible to extract or bound the spin of the central potential with a template that takes into account the Kerr character of the MBH. Other astrophysical consequences include a possible increase in the event rate, which implies that the rates of [55, 228] and [56] might be lower limits, although these estimates are still dominated by uncertainties in the astrophysical modeling for the host galaxy.

In addition to the astrophysical modeling, future research should tackle the details of the EMRB data analysis and signal extraction issues put forward above. Based on the results of this paper, one may explore the possibility of testing alternative theories of gravity with EMRBs by performing matched filtering with templates from alternative theories [66, 72, 69, 70, 71]. Another possible avenue for future research is the study of confidence limits with which the spin of the central MBH can be measured.

This research could then be used to examine whether EMRB events can distinguish between a pure Kerr MBH and some other spacetime. Such studies have already begun with the analysis of [254], [145] and [255], where comparisons between a Kerr and other non-Kerr spacetimes were performed. Such studies could be extended to the perturbed Kerr solution found by [104], where the perturbation is parameterized by the Weyl tensor of the external universe and could represent some external accretion disk, planetary system or some other compact object. Ultimately, these investigations will decide whether EMRB events are worth studying in further detail by future gravitational wave observatories.

## Acknowledgments

The authors would like to thank Ben Owen for reading the manuscript and providing useful comments, as well as the anonymous referee for providing insightful suggestions. We would also like to acknowledge the support of the Center for Gravitational Wave Physics funded by the National Science Foundation under Cooperative Agreement

PHY-01-14375, and support from NSF grants PHY 05-55628, PHY 05-55436, PHY 02-18750, PHY 02-44788, PHY 02-45649 and PHY 00-99559. K. H. B. and L. R. also acknowledge the support of NASA NNG04GU99G, NASA NN G05GF71G. C. F. S. acknowledges the support of the Natural Sciences and Engineering Research Council of Canada.

**PART C:**  
**GRAVITATIONAL WAVES AS PROBES**  
**OF QUANTUM GRAVITY**

## Chapter 9

# Parametrized post-Newtonian Expansion of Chern-Simons gravity

We investigate the weak-field, post-Newtonian expansion to the solution of the field equations in Chern-Simmons gravity with a perfect fluid source. In particular, we study the mapping of this solution to the parameterized post-Newtonian formalism to 1 PN order in the metric. We find that the PPN parameters of Chern-Simmons gravity are identical to those of general relativity, with the exception of the inclusion of a new term that is proportional to the Chern-Simmons coupling parameter and the curl of the PPN vector potentials. We also find that the new term is naturally enhanced by the non-linearity of spacetime and we provide a physical interpretation for it. By mapping this correction to the gravito-electro-magnetic framework, we study the corrections that this new term introduces to the acceleration of point particles and the frame-dragging effect in gyroscopic precession. We find that the CS correction to these classical predictions could be used by current and future experiments to place bounds on intrinsic parameters of Chern-Simmons gravity and, thus, string theory.

### 9.1 Introduction

Tests of alternative theories of gravity that modify general relativity (GR) at a fundamental level are essential to the advancement of science<sup>1</sup>. One formalism that has had incredible success in this task is the parameterized post-Newtonian (PPN) framework [256, 80, 257, 81, 258, 82]. In this formalism, the metric of the alternative theory is solved for in the weak-field limit and its deviations from GR are expressed in terms of PPN parameters. Once a metric has been obtained, one can calculate predictions of the alternative theory, such as light deflection and the perihelion shift of Mercury, which shall depend on these PPN parameters. Therefore, experimental measurements of such physical effects directly lead to constraints on the parameters of the alternative theory. This framework, together with the relevant experiments, have already been successfully employed to constrain scalar-tensor theories (Brans-Dicke, Bekenstein) [259], vector-tensor theories (Will-Nordtvedt [260], Hellings-Nordtvedt [261]), bimetric theories (Rosen [262, 263]) and stratified theories (Ni [264]) (see [60] for definitions and an updated review.)

---

<sup>1</sup>This chapter is based on the following papers: S. Alexander and N. Yunes, Phys. Rev. D **75**, 124022 (2007); S. Alexander and N. Yunes, Phys. Rev. Letts. **99**, 241101 (2007)

Only recently has this framework been used to study quantum gravitational and string-theoretical inspired ideas. On the string theoretical side, Kalyana [265] investigated the PPN parameters associated with the graviton-dilaton system in low-energy string theory. More recently, Ivashchuk, *et. al.* [266] studied PPN parameters in the context of general black holes and p-brane spherically symmetric solutions, while Bezerra, *et. al.* [267] considered domain wall spacetimes for low energy effective string theories and derived the corresponding PPN parameters for the metric of a wall. On the quantum gravitational side, Gleiser and Kozameh [268] and more recently Fan, *et. al.* [269] studied the possibility of testing gravitational birefringence induced by quantum gravity, which was proposed by Amelino-Camelia, *et. al.* [270] and Gambini and Pullin [271]. Other non-PPN proposals have been also put forth to test quantum gravity, for example through gravitational waves [66, 67, 72, 68, 69, 70, 71, 272], but we shall not discuss those tests here.

Chern-Simmons (CS) gravity [273, 274] is one such extension of GR, where the gravitational action is modified by the addition of a parity-violating term. This extension is promising because it is required by all 4-dimensional compactifications of string theory [275] for mathematical consistency because it cancels the Green-Schwarz anomaly [276]. CS gravity, however, is not unique to string theory and in fact has its roots in the standard model, where it gives rise to a model independent axion.

Chern-Simmons gravity has been recently studied in the cosmological context. In particular, this framework was used to shed light on the anisotropies of the cosmic microwave background (CMB) [75, 76, 77] and the leptogenesis problem [73, 74, 76]. Parity violation has also been shown to produce birefringent gravitational waves [274, 272], where different polarizations modes acquire varying amplitudes. These modes obey different propagation equations because the imaginary sector of the classical dispersion relation is CS corrected. Different from [271], in CS birefringence the velocity of the gravitational wave remains that of light.

In this paper we study CS gravity in the PPN framework, extending the analysis of [277] and providing some missing details. In particular, we shall consider the effect of the CS correction to the gravitational field of, for instance, a pulsar, a binary system or a star in the weak-field limit. These corrections are obtained by solving the modified field equations in the weak-field limit for post-Newtonian (PN) sources, defined as those that are weakly-gravitating and slowly-moving [3]. Such an expansion requires the calculation of the Ricci and Cotton tensors to second order in the metric perturbation. We then find that CS gravity leads to the same gravitational field as that of classical GR and, thus, the same PPN parameters, except for the inclusion of a new term in the vectorial sector of the metric, namely

$$g_{0i}^{(CS)} = 2\dot{f}(\nabla \times V)_i, \quad (9.1)$$

where  $\dot{f}$  acts as a coupling parameter of CS theory and  $V_i$  is a PPN potential. We also show that this solution can be alternatively obtained by finding a formal solution to the modified field equations and performing a PN expansion, as is done in PN theory. The full solution is further shown to satisfy the additional CS constraint, which leads to equations of motion given only by the divergence of the stress-energy tensor.

The CS correction to the metric found here leads to an interesting interpretation of CS gravity and forces us to consider a new type of coupling. The interpretation consists of thinking of the field that sources the CS correction as a fluid that permeates all of spacetime. Then the CS correction in the metric is due to the “dragging” of such a fluid by the motion of the source. Until now, couplings of the CS correction to the angular momentum of the source had been neglected by the string theory community. Similarly, curl-type terms had also been considered unnecessary in the traditional PPN framework, since previous alternative gravity theories had not required it. As we shall show, in CS gravity and thus in string theory, such a coupling is naturally occurring. Therefore, a proper PPN mapping requires the introduction of a new curl-type term with a corresponding new PPN parameter of the type of Eq. (9.1).

A modification to the gravitational field leads naturally to corrections of the standard predictions of GR. In order to illustrate such a correction, we consider the CS term in the gravito-electro-magnetic analogy [278, 279], where we find that the CS correction accounts for a modification of gravitomagnetism. Furthermore, we calculate the modification to the acceleration of point particles and the frame dragging effect in the precession of gyroscopes. We find that these corrections are given by

$$\begin{aligned}\delta a^i &= -\frac{3\dot{f} G m}{2 r c^2 r^2} \left(\frac{v}{c} \cdot n\right) \left(\frac{v}{c} \times n\right)^i, \\ \delta \Omega^i &= -\frac{\dot{f} G m}{r c^3 r^2} \left[ 3 \left(\frac{v}{c} \cdot n\right) n^i - \frac{v^i}{c} \right],\end{aligned}\tag{9.2}$$

where  $m$  and  $v$  are the mass and velocities of the source, while  $r$  is the distance to the source and  $n^i = x^i/r$  is a unit vector, with  $\cdot$  and  $\times$  the flat-space scalar and cross products. Both corrections are found to be naturally enhanced in regions of high spacetime curvature. We then conclude that experiments that measure the gravitomagnetic sector of the metric either in the weak-field (such as Gravity Probe B [280]) and particularly in the non-linear regime, will lead to a direct constraint on the CS coupling parameter  $\dot{f}$ . In this paper we develop the details of how to calculate these corrections, while the specifics of how to actually impose a constraint, which depend on the experimental setup, are beyond the scope of this paper.

The remainder of this paper deals with the details of the calculations discussed in the previous paragraphs. We have divided the paper as follows: Sec. 9.2 describes the basics of the PPN framework; Sec. 9.3 discusses CS modified gravity, the modified field equations and computes a formal solution; Sec. 9.4 expands the field equations to second order in the metric perturbation; Sec. 9.5 iteratively solves the field equations in the PN approximation and finds the PPN parameters of CS gravity; Sec. 9.6 discusses the correction to the acceleration of point particles and the frame dragging effect; Sec. 9.7 concludes and points to future research.

The conventions that we use throughout this work are the following: Greek letters represent spacetime indices, while Latin letters stand for spatial indices only; semicolons stand for covariant derivatives, while colons stand for partial derivatives; overhead dots stand for derivatives with respects to time. We denote uncontrolled remainders with the symbol  $\mathcal{O}(A)$ , which stands for terms of order  $A$ . We also use the Einstein summation

convention unless otherwise specified. Finally, we use geometrized units, where  $G = c = 1$ , and the metric signature  $(-, +, +, +)$ .

## 9.2 The ABC of PPN

In this section we summarize the basics of the PPN framework, following [82]. This framework was first developed by Eddington, Robertson and Schiff [82, 256], but it came to maturity through the seminal papers of Nordtvedt and Will [80, 257, 81, 258]. In this section, we describe the latter formulation, since it is the most widely used in experimental tests of gravitational theories.

The goal of the PPN formalism is to allow for comparisons of different metric theories of gravity with each other and with experiment. Such comparisons become manageable through a slow-motion, weak-field expansion of the metric and the equations of motion, the so-called PN expansion. When such an expansion is carried out to sufficiently high but finite order, the resultant solution is an accurate approximation to the exact solution in most of the spacetime. This approximation, however, does break down for systems that are not slowly-moving, such as merging binary systems, or weakly gravitating, such as near the apparent horizons of black hole binaries. Nonetheless, as far as solar system tests are concerned, the PN expansion is not only valid but also highly accurate.

The PPN framework employs an order counting-scheme that is similar to that used in multiple-scale analysis [30, 31, 105, 93]. The symbol  $\mathcal{O}(A)$  stands for terms of order  $\epsilon^A$ , where  $\epsilon \ll 1$  is a PN expansion parameter. For convenience, it is customary to associate this parameter with the orbital velocity of the system  $v/c = \mathcal{O}(1)$ , which embodies the slow-motion approximation. By the Virial theorem, this velocity is related to the Newtonian potential  $U$  via  $U \sim v^2$ , which then implies that  $U = \mathcal{O}(2)$  and embodies the weak-gravity approximation. These expansions can be thought of as two independent series: one in inverse powers of the speed of light  $c$  and the other in positive powers of Newton's gravitational constant.

Other quantities, such as matter densities and derivatives, can and should also be classified within this order-counting scheme. Matter density  $\rho$ , pressure  $p$  and specific energy density  $\Pi$ , however, are slightly more complicated to classify because they are not dimensionless. Dimensionlessness can be obtained by comparing the pressure and the energy density to the matter density, which we assume is the largest component of the stress-energy tensor, namely  $p/\rho \sim \Pi/\rho = \mathcal{O}(2)$ . Derivatives can also be classified in this fashion, where we find that  $\partial_t/\partial_x = \mathcal{O}(1)$ . Such a relation can be derived by noting that  $\partial_t \sim v^i \nabla_i$ , which comes from the Euler equations of hydrodynamics to Newtonian order.

With such an order-counting scheme developed, it is instructive to study the action of a single neutral particle. The Lagrangian of this system is given by

$$L = \left( g_{\mu\nu} u^\mu u^\nu \right)^{1/2}, = \left( -g_{00} - 2g_{0i} v^i - g_{ij} v^i v^j \right)^{1/2} \quad (9.3)$$

where  $u^\mu = dx^\mu/dt = (1, v^i)$  is the 4-velocity of the particle and  $v^i$  is its 3-velocity. From Eq. (9.3), note that knowledge of  $L$  to  $\mathcal{O}(A)$  implies knowledge of  $g_{00}$  to  $\mathcal{O}(A)$ ,  $g_{0i}$  to  $\mathcal{O}(A-1)$  and  $g_{ij}$  to  $\mathcal{O}(A-2)$ . Therefore, since the Lagrangian is already known to  $\mathcal{O}(2)$  (the Newtonian solution), the first PN correction to the equations of motion requires  $g_{00}$  to  $\mathcal{O}(4)$ ,  $g_{0i}$  to  $\mathcal{O}(3)$  and  $g_{ij}$  to  $\mathcal{O}(2)$ . Such order counting is the reason for calculating different sectors of the metric perturbation to different PN orders.

A PPN analysis is usually performed in a particular background, which defines a particular coordinate system, and in an specific gauge, called the standard PPN gauge. The background is usually taken to be Minkowski because for solar system experiments deviations due to cosmological effects are negligible and can, in principle, be treated as adiabatic corrections. Moreover, one usually chooses a standard PPN frame, whose outer regions are at rest with respect to the rest frame of the universe. Such a frame, for example, forces the spatial sector of the metric to be diagonal and isotropic [82]. The gauge employed is very similar to the PN expansion of the Lorentz gauge of linearized gravitational wave theory. The differences between the standard PPN and Lorentz gauge are of  $\mathcal{O}(3)$  and they allow for the presence of certain PPN potentials in the vectorial sector of the metric perturbation.

The last ingredient in the PPN recipe is the choice of a stress-energy tensor. The standard choice is that of a perfect fluid, given by

$$T^{\mu\nu} = (\rho + \rho\Pi + p) u^\mu u^\nu + pg^{\mu\nu}. \quad (9.4)$$

Such a stress-energy density suffices to obtain the PN expansion of the gravitational field outside a fluid body, like the Sun, or of compact binary system. One can show that the internal structure of the fluid bodies can be neglected to 1 PN order by the effacement principle [3] in GR. Such effacement principle might actually not hold in modified field theories, but we shall study this subject elsewhere [281].

With all these machinery, on can write down a super-metric [82], namely

$$\begin{aligned} g_{00} &= -1 + 2U - 2\beta U^2 - 2\xi\Phi_W + (2\gamma + 2 + \alpha_3 + \zeta_1 \\ &\quad - 2\xi)\Phi_1 + 2(3\gamma - 2\beta + 1 + \zeta_2 + \xi)\Phi_2 \\ &\quad + 2(1 + \zeta_3)\Phi_3 + 2(3\gamma + 3\zeta_4 - 2\xi)\Phi_4 - (\zeta_1 - 2\xi)\mathcal{A}, \\ g_{0i} &= -\frac{1}{2}(4\gamma + 3 + \alpha_1 - \alpha_2 + \zeta_1 - 2\xi)V_i \\ &\quad - \frac{1}{2}(1 + \alpha_2 - \zeta_1 + 2\xi)W_i, \\ g_{ij} &= (1 + 2\gamma U)\delta_{ij}, \end{aligned} \quad (9.5)$$

where  $\delta_{ij}$  is the Kronecker delta and where the PPN potentials ( $U, \Phi_W, \Phi_1, \Phi_2, \Phi_3, \Phi_4, \mathcal{A}, V_i, W_i$ ) are defined in Appendix F. Equation (9.5) describes a super-metric theory of gravity, because it reduces to different metric theories, such as GR or other alternative theories [82], through the appropriate choice of PPN parameters ( $\gamma, \beta, \xi, \alpha_1, \alpha_2, \alpha_3, \zeta_1, \zeta_2, \zeta_3, \zeta_4$ ). One could obtain a more general form of the PPN metric by performing a post-Galilean transformation on Eq. (9.5), but such a procedure shall not be necessary in this paper.

The super-metric of Eq. (9.5) is parameterized in terms of a specific number of PPN potentials, where one usually employs certain criteria to narrow the space of possible potentials to consider. Some of these restriction include the following: the potentials tend to zero as an inverse power of the distance to the source; the origin of the coordinate system is chosen to coincide with the source, such that the metric does not contain constant terms; and the metric perturbations  $h_{00}$ ,  $h_{0i}$  and  $h_{ij}$  transform as a scalar, vector and tensor. The above restrictions are reasonable, but, in general, an additional subjective condition is usually imposed that is based purely on simplicity: the metric perturbations are not generated by gradients or curls of velocity vectors or other generalized vector functions. As of yet, no reason had arisen for relaxing such a condition, but as we shall see in this paper, such terms are indeed needed for CS modified theories.

What is the physical meaning of all these parameters? One can understand what these parameters mean by calculating the generalized geodesic equations of motion and conservation laws [82]. For example, the parameter  $\gamma$  measures how much space-curvature is produced by a unit rest mass, while the parameter  $\beta$  determines how much “non-linearity” is there in the superposition law of gravity. Similarly, the parameter  $\xi$  determines whether there are preferred-location effects, while  $\alpha_i$  represent preferred-frame effects. Finally, the parameters  $\zeta_i$  measure the amount of violation of conservation of total momentum. In terms of conservation laws, one can interpret these parameters as measuring whether a theory is fully conservative, with linear and angular momentum conserved ( $\zeta_i$  and  $\alpha_i$  vanish), semi-conservative, with linear momentum conserved ( $\zeta_i$  and  $\alpha_3$  vanish), or non-conservative, where only the energy is conserved through lowest Newtonian order. One can verify that in GR,  $\gamma = \beta = 1$  and all other parameters vanish, which implies that there are no preferred-location or frame effects and that the theory is fully conservative.

A PPN analysis of an alternative theory of gravity then reduces to mapping its solutions to Eq. (9.5) and then determining the PPN parameters in terms of intrinsic parameters of the theory. The procedure is simply as follows: expand the modified field equations in the metric perturbation and in the PN approximation; iteratively solve for the metric perturbation to  $\mathcal{O}(4)$  in  $h_{00}$ , to  $\mathcal{O}(3)$  in  $h_{0i}$  and to  $\mathcal{O}(2)$  in  $h_{ij}$ ; compare the solution to the PPN metric of Eq. (9.5) and read off the PPN parameters of the alternative theory. We shall employ this procedure in Sec. 9.5 to obtain the PPN parameters of CS gravity.

### 9.3 CS Gravity in a Nutshell

In this section, we describe the basics of CS gravity, following mainly [273, 274]. In the standard CS formalism, GR is modified by adding a new term to the gravitational action. This term is given by [273]

$$S_{CS} = \frac{m_{pl}^2}{64\pi} \int d^4x f \left( {}^*R R \right), \quad (9.6)$$

where  $m_{pl}$  is the Planck mass,  $f$  is a dynamical field that is prescribed externally<sup>2</sup> with units of squared mass (or squared length in geometrized units),  $R$  is the Ricci scalar and the star stands the dual operation, such that

$$R^* R = \frac{1}{2} R_{\alpha\beta\gamma\delta} \epsilon^{\alpha\beta\mu\nu} R^{\gamma\delta}_{\mu\nu}, \quad (9.7)$$

with  $\epsilon_{\mu\nu\delta\gamma}$  the totally-antisymmetric Levi-Civita tensor and  $R_{\mu\nu\delta\gamma}$  the Riemann tensor.

Such a correction to the gravitational action is interesting because of the unavoidable parity violation that is introduced. Such parity violation is inspired from CP violation in the standard model, where such corrections act as anomaly-canceling terms. A similar scenario occurs in string theory, where the Green-Schwarz anomaly is canceled by precisely such a CS correction [276], although CS gravity is not exclusively tied to string theory. Parity violation in CS gravity inexorably leads to birefringence in gravitational propagation, where here we mean that different polarization modes obey different propagation equations but travel at the same speed, that of light [273, 73, 274, 281]. If CS gravity were to lead to polarization modes that travel at different speeds, then one could use recently proposed experiments [268] to test this effect, but such is not the case in CS gravity. Birefringent gravitational waves, and thus CS gravity, have been proposed as possible explanations to the cosmic-microwave-background (CMB) anisotropies [73], as well as the baryogenesis problem during the inflationary epoch [75].

The magnitude of the CS correction is controlled by the externally-prescribed quantity  $f$ , which depends on the specific theory under consideration. When we consider CS gravity as an effective quantum theory, then the correction is suppressed by some mass scale  $M$ , which could be the electro-weak scale or some other scale, since it is unconstrained. In the context of string theory, the quantity  $f$  has been calculated only in conservative scenarios, where it was found to be suppressed by the Planck mass. In other scenarios, however, enhancements have been proposed, such as in cosmologies where the string coupling vanishes at late times [284, 285, 286, 287, 288, 289, 290, 291, 292, 293, 294], or where the field that generates  $f$  couples to spacetime regions with large curvature [295, 296] or stress-energy density [281, 272]. For simplicity, we here assume that this quantity is spatially homogeneous and its magnitude is small but non-negligible, so that we work to first order in the string-theoretical correction. Therefore, we treat  $\dot{f}$  as an independent perturbation parameter,<sup>3</sup> unrelated to  $\epsilon$ , the PN perturbation parameter.

The field equations of CS modified gravity can be obtained by varying the action with respect to the metric. Doing so, one obtains

$$G_{\mu\nu} + C_{\mu\nu} = 8\pi T_{\mu\nu}, \quad (9.8)$$

---

<sup>2</sup>The quantity  $f$  is a dynamical field that must be determined “externally” [273], within the theoretical framework under consideration. This quantity has been identified with the inflaton field in a cosmological context [282], as well as with a model-independent axion in other contexts [283].

<sup>3</sup>Formally,  $\dot{f}$  by itself is dimensional, so it cannot be treated as an expansion parameter. A dimensionless parameter can, however, be constructed by dividing  $\dot{f}$  by some length scale squared.

where  $G_{\mu\nu}$  is the Einstein tensor,  $T_{\mu\nu}$  is a stress-energy tensor and  $C_{\mu\nu}$  is the Cotton tensor. The latter tensor is defined via

$$C_{\mu\nu} = -\frac{1}{\sqrt{-g}} \left[ f_{,\sigma} \epsilon^{\sigma\alpha\beta} ({}_{(\mu} D_{\alpha} R_{\nu)\beta}) + \left( D_{\sigma} f_{,\tau} \right) {}^* R^{\tau}{}_{(\mu}{}^{\sigma}{}_{\nu)} \right], \quad (9.9)$$

where parenthesis stand for symmetrization,  $g$  is the determinant of the metric,  $D_a$  stands for covariant differentiation and colon subscripts stand for partial differentiation. Here, the factor of  $(-g)^{-1/2}$  could have been absorbed in  $f$ , since  $\epsilon^{\sigma\alpha\beta}{}_{\mu}$  is already a tensor. However, since  $g = 1 + h$ , this term would only contribute to  $\mathcal{O}(h)^2$  and, as we shall show later, the only component that we need to this order in the Cotton tensor actually vanishes.

Formally, the introduction of such a modification to the field equations leads to a new constraint, which is compensated by the introduction of the new scalar field degree of freedom  $f$ . This constraint originates by requiring that the divergence of the field equations vanish, namely

$$D^{\mu} C_{\mu\nu} = \frac{1}{8\sqrt{-g}} D_{\nu} f \left( {}^* R R \right) = 0, \quad (9.10)$$

where the divergence of the Einstein tensor vanished by the Bianchi identities. If this constraint is satisfied, then the equations of motion for the stress-energy  $D_{\mu} T^{\mu\nu}$  are unaffected by CS gravity. A common source of confusion is that Eq. (9.10) is sometimes interpreted as requiring that  $R^* R$  also vanish, which would then force the correction to the action to vanish. However, this is not the case because, in general,  $f$  is an exact form ( $d^2 f = 0$ ) and, thus, Eq. (9.10) only implies an additional constraint that forces all solutions to the field equations to have a vanishing  $R^* R$ .

This new constraint then allows for the use of the stress energy considered discussed above, since it also allows the strong equivalence principle (SEP) to hold in CS gravity [73]. This principle states that the outcome of all local gravitational experiments is independent of the experimenters frame of reference. In other words, the motion of test particles is exclusively governed by the spacetime metric, through the divergence of the particle's stress-energy tensor. In CS gravity, the divergence of the modified field equations leads to Eq. (9.10), where the divergence of the Einstein tensor vanishes by the Bianchi identities, since one can define Riemann normal coordinates where all first derivatives of the metric are zero. The right-hand side of Eq. (9.8) vanishes in vacuum and, thus, the SEP holds provided  $R^* R = 0$ , which is known as the Pontryagin constraint. We shall later see that the solution to the modified field equations found here automatically satisfies this constraint to  $\mathcal{O}(h)^2$  and, thus, the SEP naturally holds without any additional constraints.

The previous success of CS gravity in proposing plausible explanations to important cosmological problems prompts us to consider this extension of GR in the weak-field regime. For this purpose, it is convenient to rewrite the field equations in trace-reversed

form, since this form is most amenable to a PN expansion. Doing so, we find,

$$R_{\mu\nu} + C_{\mu\nu} = 8\pi \left( T_{\mu\nu} - \frac{1}{2} g_{\mu\nu} T \right), \quad (9.11)$$

where the trace of the Cotton tensor vanishes identically and  $T = g_{\mu\nu} T^{\mu\nu}$  is the four dimensional trace of the stress-energy tensor. To linear order, the Ricci and Cotton tensors are given by [273]

$$\begin{aligned} R_{\mu\nu} &= -\frac{1}{2} \square h_{\mu\nu} + \mathcal{O}(h)^2, \\ C_{\mu\nu} &= -\frac{\dot{f}}{2} \tilde{\epsilon}^{0\alpha\beta}{}_{(\mu} \square_{\eta} h_{\nu)\beta,\alpha} + \mathcal{O}(h)^2, \end{aligned} \quad (9.12)$$

where  $\tilde{\epsilon}^{\alpha\beta\gamma\delta}$  is the Levi-Civita symbol, with convention  $\tilde{\epsilon}^{0123} = +1$ , and  $\square_{\eta} = -\partial_t^2 + \eta^{ij} \partial_i \partial_j$  is the flat space D'Alembertian, with  $\eta_{\mu\nu}$  the Minkowski metric. In Eq. (9.12), we have employed the Lorentz gauge condition  $h_{\mu\alpha,}{}^{\alpha} = h_{,\mu}/2$ , where  $h = g^{\mu\nu} h_{\mu\nu}$  is the four dimensional trace of the metric perturbation.

The Cotton tensor changes the characteristic behavior of the Einstein equations by forcing them to become third order instead of second order. Third-order partial differential equations are common in boundary layer theory [30]. However, in CS gravity, the third-order contributions are multiplied by a factor of  $f$  and we shall treat this function as a small independent expansion parameter. Therefore, the change in characteristics in the modified field equations can also be treated perturbatively, which is justified because eventhough  $\dot{f}$  might be enhanced by standard model currents, extra dimensions or a vanishing string coupling, it must still carry some type of mass suppression.

The trace-reversed form of the field equations is useful because it allows us to immediately find a formal solution. Inverting the D'Alembertian operator we obtain

$$\mathcal{H}_{\mu\nu} = -16\pi \square_{\eta}^{-1} \left( T_{\mu\nu} - \frac{1}{2} g_{\mu\nu} T \right) + \mathcal{O}(h)^2, \quad (9.13)$$

where we have defined an effective metric perturbation as

$$\mathcal{H}_{\mu\nu} \equiv h_{\mu\nu} + \dot{f} \tilde{\epsilon}^{0\alpha\beta}{}_{(\mu} h_{\nu)\beta,\alpha}. \quad (9.14)$$

Note that this formal solution is identical to the formal PN solution to the field equations in the limit  $\dot{f} \rightarrow 0$ . Also note that the second term in Eq. (9.14) is in essence a curl operator acting on the metric. This antisymmetric operator naturally forces the trace of the CS correction to vanish, as well as the 00 component and the symmetric spatial part.

From the formal solution to the modified field equations, we immediately identify the *only two possible non-zero CS contributions*: a coupling to the vector component of the metric  $h_{0i}$ ; and coupling to the transverse-traceless part of the spatial metric  $h_{ij}^{TT}$ . The latter has already been studied in the gravitational wave context [273, 274, 281] and it vanishes identically if we require the spatial sector of the metric perturbation to

be conformally flat. The former coupling is a new curl-type contribution to the metric perturbation that, to our knowledge, had so far been neglected both by the string theory and PPN communities. In fact, as we shall see in later sections, terms of this type will force us to introduce a new PPN parameter that is proportional to the curl of certain PPN potentials.

Let us conclude this section by pushing the formal solution to the modified field equations further to obtain a formal solution in terms of the actual metric perturbation  $h_{\mu\nu}$ . Combining Eqs. (9.13) and (9.14) we arrive at the differential equation

$$h_{\mu\nu} + \dot{f}\tilde{\epsilon}^{0\alpha\beta}{}_{(\mu}h_{\nu)\beta,\alpha} = -16\pi\Box_{\eta}^{-1}\left(T_{\mu\nu} - \frac{1}{2}g_{\mu\nu}T\right) + \mathcal{O}(h)^2. \quad (9.15)$$

Since we are searching for perturbations about the general relativistic solution, we shall make the ansatz

$$h_{\mu\nu} = h_{\mu\nu}^{(GR)} + \dot{f}\zeta_{\mu\nu} + \mathcal{O}(h)^2, \quad (9.16)$$

where  $h_{\mu\nu}^{(GR)}$  is the solution predicted by general relativity

$$h_{\mu\nu}^{(GR)} \equiv -16\pi\Box_{\eta}^{-1}\left(T_{\mu\nu} - \frac{1}{2}g_{\mu\nu}T\right), \quad (9.17)$$

and where  $\zeta_{\mu\nu}$  is an unknown function we are solving for. Inserting this ansatz into Eq. (9.15) we obtain

$$\zeta_{\mu\nu} + \dot{f}\tilde{\epsilon}^{0\alpha\beta}{}_{(\mu}\zeta_{\nu)\beta,\alpha} = 16\pi\tilde{\epsilon}^{0\alpha\beta}{}_{(\mu}\partial_{\alpha}\Box_{\eta}^{-1}\left(T_{\nu)\beta} - \frac{1}{2}g_{\nu)\beta}T\right). \quad (9.18)$$

We shall neglect the second term on the left-hand side because it would produce a second order correction. Such conclusion was also reached when studying parity violation in GR to explain certain features of the CMB [77]. We thus obtain the formal solution

$$\zeta_{\mu\nu} = 16\pi\tilde{\epsilon}^{0\alpha\beta}{}_{(\mu}\partial_{\alpha}\Box_{\eta}^{-1}\left(T_{\nu)\beta} - \frac{1}{2}g_{\nu)\beta}T\right) \quad (9.19)$$

and the actual metric perturbation to linear order becomes

$$\begin{aligned} h_{\mu\nu} &= -16\pi\Box_{\eta}^{-1}\left(T_{\mu\nu} - \frac{1}{2}\eta_{\mu\nu}T\right) \\ &+ 16\pi\dot{f}\tilde{\epsilon}^{k\ell i}{}_{\eta}^{-1}\left(\delta_{i(\mu}T_{\nu)\ell,k} - \frac{1}{2}\delta_{i(\mu}\eta_{\nu)\ell}T_{,k}\right) + \mathcal{O}(h)^2, \end{aligned} \quad (9.20)$$

where we have used some properties of the Levi-Civita symbol to simplify this expression. The procedure presented here is general enough that it can be directly applied to study CS gravity in the PPN framework, as well as possibly find PN solutions to CS gravity.

## 9.4 PN expansion of CS Gravity

In this section, we perform a PN expansion of the field equations and obtain a solution in the form of a PN series. This solution then allows us to read off the PPN parameters by comparing it to the standard PPN super-metric [Eq. (9.5)]. In this section we shall follow closely the methods of [82] and [197] and indices shall be manipulated with the Minkowski metric, unless otherwise specified.

Let us begin by expanding the field equations to second order in the metric perturbation. Doing so we find that the Ricci and Cotton tensors are given to second order by

$$\begin{aligned}
R_{\mu\nu} &= -\frac{1}{2} \left[ \square_{\eta} h_{\mu\nu} - 2h_{\sigma(\mu,\nu)}{}^{\sigma} + h_{,\mu\nu} \right] - \frac{1}{2} \left[ h^{\rho\lambda} \left( 2h_{\rho(\mu,\nu)\lambda} - h_{\mu\nu,\rho\lambda} - h_{\rho\lambda,\mu\nu} \right) \right. \\
&\quad \left. - \frac{1}{2} h^{\rho\lambda}{}_{,\mu} h_{\rho\lambda,\nu} + h^{\lambda}{}_{\mu,\rho} h^{\rho}{}_{\nu,\lambda} - h^{\rho}{}_{\mu,\lambda} h_{\rho\nu}{}^{\lambda} + \frac{1}{2} \left( h^{\lambda}{}_{,\rho} - 2h^{\lambda\rho}{}_{,\rho} \right) \left( h_{\mu\nu,\lambda} - 2h_{\lambda(\mu,\nu)} \right) \right] \\
&\quad + \mathcal{O}(h)^3, \\
C_{\mu\nu} &= -\frac{\dot{f}}{2} \tilde{\epsilon}^{0\alpha\beta}{}_{(\mu} \left( \square_{\eta} h_{\nu)\beta,\alpha} - h_{\sigma\beta,\alpha\nu}{}^{\sigma} \right) - \frac{\dot{f}}{2} \tilde{\epsilon}^{0\alpha\beta}{}_{(\mu} \left[ h \left( \square_{\eta} h_{\nu)\beta,\alpha} - h_{\sigma\beta,\alpha\nu}{}^{\sigma} \right) \right. \\
&\quad \left. + \frac{1}{2} \left( 2h_{\nu(\lambda,\alpha)} - h_{\lambda\alpha,\nu} \right) \left( \square_{\eta} h^{\lambda}{}_{\beta} - 2h_{\sigma}{}^{(\lambda}{}_{,\beta)}{}^{\sigma} + h_{,\beta}{}^{\lambda} \right) - 2\hat{Q}R_{\nu)\beta,\alpha} \right] \\
&\quad - \frac{\dot{f}}{4} \tilde{\epsilon}^{\sigma\alpha\beta}{}_{(\mu} \left( 2h^0{}_{(\sigma,\tau)} - h_{\sigma\tau}{}^0 \right) \left( h^{\tau}{}_{[\beta,\alpha]\nu} - h_{\nu[\beta,\alpha]}{}^{\tau} \right) \\
&\quad - \frac{\dot{f}}{2} h_{\mu\lambda} \tilde{\epsilon}^{0\alpha\beta(\lambda} \left( \square_{\eta} h_{\nu)\beta,\alpha} - h_{\sigma\beta,\alpha\nu}{}^{\sigma} \right) - \frac{\dot{f}}{2} \tilde{\epsilon}^{0\alpha\beta(\mu} \left( \square_{\eta} h^{\lambda)}{}_{\beta,\alpha} - h_{\sigma\beta,\alpha}{}^{\sigma\lambda} \right) h_{\nu\lambda} \\
&\quad + \mathcal{O}(h)^3. \tag{9.21}
\end{aligned}$$

where index contraction is carried out with the Minkowski metric and where we have not assumed any gauge condition. The operator  $\hat{Q}(\cdot)$  takes the quadratic part of its operand [of  $\mathcal{O}(h)^2$ ] and it is explained in more detail in Appendix G, where the derivation of the expansion of the Cotton tensor is presented in more detail. In this derivation, we have used the definition of the Levi-Civita tensor

$$\begin{aligned}
\epsilon_{\alpha\beta\gamma\delta} &= (-g)^{1/2} \tilde{\epsilon}_{\alpha\beta\gamma\delta} = \left( 1 - \frac{1}{2}h \right) \tilde{\epsilon}_{\alpha\beta\gamma\delta} + \mathcal{O}(h)^2, \\
\epsilon^{\alpha\beta\gamma\delta} &= -(-g)^{-1/2} \tilde{\epsilon}^{\alpha\beta\gamma\delta} = - \left( 1 + \frac{1}{2}h \right) \tilde{\epsilon}^{\alpha\beta\gamma\delta} + \mathcal{O}(h)^2.
\end{aligned} \tag{9.22}$$

Note that the PN expanded version of the linearized Ricci tensor of Eq. (9.21) agrees with previous results [82]. Also note that if the Lorentz condition is enforced, several terms in both expressions vanish identically and the Cotton tensor to first order reduces to Eq. (9.12), which agrees with previous results [273].

Let us now specialize the analysis to the standard PPN gauge. For this purpose, we shall impose the following gauge conditions

$$\begin{aligned} h_{jk,}{}^k - \frac{1}{2}h_{,j}{}^j &= \mathcal{O}(4), \\ h_{0k,}{}^k - \frac{1}{2}h^k{}_{k,0} &= \mathcal{O}(5), \end{aligned} \tag{9.23}$$

where  $h^k{}_k$  is the spatial trace of the metric perturbation. Note that the first equation is the PN expansion of one of the Lorentz gauge conditions, while the second equation is not. This is the reason why the previous equations were not expanded in the Lorentz gauge. Nonetheless, such a gauge condition does not uniquely fix the coordinate system, since we can still perform an infinitesimal gauge transformation that leaves the modified field equations invariant. One can show that the Lorentz and PPN gauge are related to each other by such a gauge transformation. In the PPN gauge, then, the Ricci tensor takes the usual form

$$\begin{aligned} R_{00} &= -\frac{1}{2}\nabla^2 h_{00} - \frac{1}{2}h_{00,i}h_{00,}{}^i + \frac{1}{2}h^{ij}h_{00,ij} + \mathcal{O}(6), \\ R_{0i} &= -\frac{1}{2}\nabla^2 h_{0i} - \frac{1}{4}h_{00,0i} + \mathcal{O}(5), \\ R_{ij} &= -\frac{1}{2}\nabla^2 h_{ij} + \mathcal{O}(4), \end{aligned} \tag{9.24}$$

which agrees with previous results [82], while the Cotton tensor reduces to

$$\begin{aligned} C_{00} &= \mathcal{O}(6), \\ C_{0i} &= -\frac{1}{4}\dot{f}\epsilon^{0kl}{}_{,i}\nabla^2 h_{0l,k} + \mathcal{O}(5), \\ C_{ij} &= -\frac{1}{2}\dot{f}\epsilon^{0kl}{}_{(i}\nabla^2 h_{j)l,k} + \mathcal{O}(4), \end{aligned} \tag{9.25}$$

where  $\nabla = \eta^{ij}\partial_i\partial_j$  is the Laplacian of flat space [see Appendix G for the derivation of Eq. (9.25).] Note again the explicit appearance of two coupling terms of the Cotton tensor to the metric perturbation: one to the transverse-traceless part of the spatial metric and the other to the vector metric perturbation. The PN expansions of the linearized Ricci and Cotton tensor then allow us to solve the modified field equations in the PPN framework.

## 9.5 PPN Solution of CS gravity

In this section we shall proceed to systematically solve the modified field equation following the standard PPN iterative procedure [82]. We shall begin with the 00 and  $ij$  components of the metric to  $\mathcal{O}(2)$ , and then proceed with the  $0i$  components to  $\mathcal{O}(3)$  and the 00 component to  $\mathcal{O}(4)$ . Once all these components have been solved for in terms of PPN potentials, we shall be able to read off the PPN parameters adequate to CS gravity.

### 9.5.1 $h_{00}$ and $h_{ij}$ to $\mathcal{O}(2)$

Let us begin with the modified field equations for the scalar sector of the metric perturbation. These equations are given to  $\mathcal{O}(2)$  by

$$\nabla^2 h_{00} = -8\pi\rho, \quad (9.26)$$

because  $T = -\rho$ . Eq. (9.26) is the Poisson equation, whose solution in terms of PPN potentials is

$$h_{00} = 2U + \mathcal{O}(4). \quad (9.27)$$

Let us now proceed with the solution to the field equation for the spatial sector of the metric perturbation. This equation to  $\mathcal{O}(2)$  is given by

$$\nabla^2 h_{ij} + \dot{f}\epsilon^{0kl}{}_{(i}\nabla^2 h_{j)l,k} = -8\pi\rho\delta_{ij}, \quad (9.28)$$

where note that this is the first appearance of a Cotton tensor contribution. Since the Levi-Civita symbol is a constant and  $\dot{f}$  is only time-dependent, we can factor out the Laplacian and rewrite this equation in terms of the effective metric  $\mathcal{H}_{ij}$  as

$$\nabla^2 \mathcal{H}_{ij} = -8\pi\rho\delta_{ij}, \quad (9.29)$$

where, as defined in Sec. 9.3,

$$\mathcal{H}_{ij} = h_{ij} + \dot{f}\epsilon^{0kl}{}_{(i}h_{j)l,k}. \quad (9.30)$$

The solution of Eq. (9.29) can be immediately found in terms of PPN potentials as

$$\mathcal{H}_{ij} = 2U\delta_{ij} + \mathcal{O}(4), \quad (9.31)$$

which is nothing but Eq. (9.13). Recall, however, that in Sec. 9.3 we explicitly used the Lorentz gauge to simplify the field equations, whereas here we are using the PPN gauge. The reason why the solutions are the same is that the PPN and Lorentz gauge are indistinguishable to this order.

Once the effective metric has been solved for, we can obtain the actual metric perturbation following the procedure described in Sec. 9.3. Combining Eq. (9.30) with Eq. (9.31), we arrive at the following differential equation

$$h_{ij} + \dot{f}\epsilon^{0kl}{}_{(i}h_{j)l,k} = 2U\delta_{ij}. \quad (9.32)$$

We look for solutions whose zeroth-order result is that predicted by GR and the CS term is a perturbative correction, namely

$$h_{ij} = 2U\delta_{ij} + \dot{f}\zeta_{ij}, \quad (9.33)$$

where  $\zeta$  is assumed to be of  $\mathcal{O}(\dot{f})^0$ . Inserting this ansatz into Eq. (9.32) we arrive at

$$\zeta_{ij} + \dot{f}\tilde{\epsilon}^{0kl}{}_{(i}\zeta_{j)l,k} = 0, \quad (9.34)$$

where the contraction of the Levi-Civita symbol and the Kronecker delta vanished. As in Sec. 9.3, note that the second term on the left hand side is a second order correction and can thus be neglected to discover that  $\zeta_{ij}$  vanishes to this order.

The spatial metric perturbation to  $\mathcal{O}(2)$  is then simply given by the GR prediction without any CS correction, namely

$$h_{ij} = 2U\delta_{ij} + \mathcal{O}(4). \quad (9.35)$$

Physically, the reason why the spatial metric is unaffected by the CS correction is related to the use of a perfect fluid stress-energy tensor, which, together with the PPN gauge condition, forces the metric to be spatially conformally flat. In fact, if the spatial metric were not flat, then the spatial sector of the metric perturbation would be corrected by the CS term. Such would be the case if we had pursued a solution to 2 PN order, where the Landau-Lifshitz pseudo-tensor sources a non-conformal correction to the spatial metric [3], or if we had searched for gravitational wave solutions, whose stress-energy tensor vanishes [73, 274]. In fact, one can check that, in such a scenario, Eq. (9.29) reduces to that found by [273, 73, 274, 281] as  $\rho \rightarrow 0$ . We have then found that the weak-field expansion of the gravitational field outside a fluid body, like the Sun or a compact binary, is unaffected by the CS correction to  $\mathcal{O}(2)$ .

### 9.5.2 $h_{0i}$ to $\mathcal{O}(3)$

Let us now look for solutions to the field equations for the vector sector of the metric perturbation. The field equations to  $\mathcal{O}(3)$  become

$$\nabla^2 h_{0i} + \frac{1}{2}h_{00,0i} + \frac{1}{2}\dot{f}\tilde{\epsilon}^{0kl}{}_{i}\nabla^2 h_{0l,k} = 16\pi\rho v_i, \quad (9.36)$$

where we have used that  $T^{0i} = -T_{0i}$ . Using the lower order solutions and the effective metric, as in Sec. 9.3, we obtain

$$\nabla^2 \mathcal{H}_{0i} + U_{,0i} = 16\pi\rho v_i, \quad (9.37)$$

where the vectorial sector of the effective metric is

$$\mathcal{H}_{0i} = h_{0i} + \frac{1}{2}\dot{f}\tilde{\epsilon}^{0kl}{}_{i}h_{0l,k}. \quad (9.38)$$

We recognize Eq. (9.37) as the standard GR field equation to  $\mathcal{O}(3)$ , except that the dependent function is the effective metric instead of the metric perturbation. We can thus solve this equation in terms of PPN potentials to obtain

$$\mathcal{H}_{0i} = -\frac{7}{2}V_i - \frac{1}{2}W_i, \quad (9.39)$$

where we have used that the superpotential  $X$  satisfies  $X_{,0j} = V_j - W_j$  (see Appendix F for the definitions.) Combining Eq. (9.38) with Eq. (9.39) we arrive at a differential equation for the metric perturbation, namely

$$h_{0i} + \frac{1}{2} \dot{f} \tilde{\epsilon}^{0kl} h_{0l,k} = -\frac{7}{2} V_i - \frac{1}{2} W_i. \quad (9.40)$$

Once more, let us look for solutions that are perturbation about the GR prediction, namely

$$h_{0i} = -\frac{7}{2} V_i - \frac{1}{2} W_i + \dot{f} \zeta_i, \quad (9.41)$$

where we again assume that  $\zeta_i$  is of  $\mathcal{O}(\dot{f})^0$ . The field equation becomes

$$\zeta_i + \frac{1}{2} \dot{f} (\nabla \times \zeta)_i = \frac{1}{2} \left( \frac{7}{2} (\nabla \times V)_i + \frac{1}{2} (\nabla \times W)_i \right), \quad (9.42)$$

where  $(\nabla \times A)^i = \epsilon^{ijk} \partial_j A_k$  is the standard curl operator of flat space. As in Sec. 9.3, note once more that the second term on the left-hand side is again a second order correction and we shall thus neglect it. Also note that the curl of the  $V_i$  potential happens to be equal to the curl of the  $W_i$  potential. The solution for the vectorial sector of the actual gravitational field then simplifies to

$$h_{0i} = -\frac{7}{2} V_i - \frac{1}{2} W_i + 2\dot{f} (\nabla \times V)_i + \mathcal{O}(5). \quad (9.43)$$

We have arrived at the first contribution of CS modified gravity to the metric for a perfect fluid source. Chern-Simons gravity was previously seen to couple to the transverse-traceless sector of the metric perturbation for gravitational wave solutions [273, 73, 274, 281]. The CS correction is also believed to couple to Noether vector currents, such as neutron currents, which partially fueled the idea that this correction could be enhanced. However, to our knowledge, this correction was never thought to couple to vector metric perturbations. From the analysis presented here, we see that in fact CS gravity does couple to such terms, even if the matter source is neutrally charged. The only requirement for such couplings is that the source is not static, *ie.* that the object is either moving or spinning relative to the PPN rest frame so that the PPN vector potential does not vanish. The latter is suppressed by a relative  $\mathcal{O}(1)$  because in the far field the velocity of a compact object produces a term of  $\mathcal{O}(3)$  in  $V_i$ , while the spin produces a term of  $\mathcal{O}(4)$ . In a later section, we shall discuss some of the physical and observational implications of such a modification to the metric.

### 9.5.3 $h_{00}$ to $\mathcal{O}(4)$

A full analysis of the PPN structure of a modified theory of gravity requires that we solve for the 00 component of the metric perturbation to  $\mathcal{O}(4)$ . The field equations

to this order are

$$\begin{aligned}
& - \frac{1}{2} \nabla^2 h_{00} - \frac{1}{2} h_{00,i} h_{00,i} + \frac{1}{2} h_{ij} h_{00,ij} = 4\pi\rho [1 \\
& + 2 \left( v^2 - U + \frac{1}{2} \Pi + \frac{3p}{2\rho} \right) ], \tag{9.44}
\end{aligned}$$

where the CS correction does not contribute at this order (see Appendix G.) Note that the  $h_{0i}$  sector of the metric perturbation to  $\mathcal{O}(3)$  does not feed back into the field equations at this order either. The terms that do come into play are the  $h_{00}$  and  $h_{ij}$  sectors of the metric, which are not modified to lowest order by the CS correction. The field equation, thus, reduce to the standard one of GR, whose solution in terms of PPN potentials is

$$h_{00} = 2U - 2U^2 + 4\Phi_1 + 4\Phi_2 + 2\Phi_3 + 6\Phi_4 + \mathcal{O}(6). \tag{9.45}$$

We have thus solved for all components of the metric perturbation to 1 PN order beyond the Newtonian answer, namely  $g_{00}$  to  $\mathcal{O}(4)$ ,  $g_{0i}$  to  $\mathcal{O}(3)$  and  $g_{ij}$  to  $\mathcal{O}(2)$ .

#### 9.5.4 PPN Parameters for CS Gravity

We now have all the necessary ingredients to read off the PPN parameters of CS modified gravity. Let us begin by writing the full metric with the solutions found in the previous subsections:

$$\begin{aligned}
g_{00} &= -1 + 2U - 2U^2 + 4\Phi_1 + 4\Phi_2 + 2\Phi_3 + 6\Phi_4 + \mathcal{O}(6), \\
g_{0i} &= -\frac{7}{2}V_i - \frac{1}{2}W_i + 2\dot{f}(\nabla \times V)_i + \mathcal{O}(5), \\
g_{ij} &= (1 + 2U)\delta_{ij} + \mathcal{O}(4). \tag{9.46}
\end{aligned}$$

One can verify that this metric is indeed a solution of Eqs. (9.26), (9.28), (9.36) and (9.44) to the appropriate PN order and to first order in the CS coupling parameter. Also note that the solution of Eq. (9.46) automatically satisfies the constraint  ${}^*RR = 0$  to linear order because the contraction of the Levi-Civita symbol with two partial derivatives vanishes. Such a solution is then allowed in CS gravity, just as other classical solutions are [297], and the equations of motion for the fluid can be obtained directly from the covariant derivative of the stress-energy tensor.

We can now read off the PPN parameters of the CS modified theory by comparing Eq. (9.5) to Eq. (9.46). A visual inspection reveals that the CS solution is identical to the classical GR one, which implies that  $\gamma = \beta = 1$ ,  $\zeta = 0$  and  $\alpha_1 = \alpha_2 = \alpha_3 = \xi_1 = \xi_2 = \xi_3 = \xi_4 = 0$  and there are no preferred frame effects. However, Eq. (9.5) contains an extra term that cannot be modeled by the standard PPN metric of Eq. (9.5), namely the curl contribution to  $g_{0i}$ . We then see that the PPN metric must be enhanced by the

addition of a curl-type term to the  $0i$  components of the metric, namely

$$g_{0i} \equiv -\frac{1}{2} (4\gamma + 3 + \alpha_1 - \alpha_2 + \zeta_1 - 2\xi) V_i - \frac{1}{2} (1 + \alpha_2 - \zeta_1 + 2\xi) W_i + \chi M (\nabla \times V)_i, \quad (9.47)$$

where  $\chi$  is a *new* PPN parameter and where  $M$  is a characteristic mass scale of the source inducing the vector potential. Note that there is no need to introduce any additional PPN parameters because the curl of  $W_i$  equals the curl of  $V_i$ . In fact, we could have equally parameterized the new contribution to the PPN metric in terms of the curl of  $W_i$ , but we chose not to because  $V_i$  appears more frequently in PN theory. For the case of CS modified gravity, the new  $\chi$  parameter is simply

$$\chi = 2 \frac{\dot{f}}{M}, \quad (9.48)$$

where  $\dot{f}$  was rescaled by  $M$  to make it dimensionless and coordinate independent. The choice made here to make  $\dot{f}$  dimensionless might seem a bit arbitrary, but if we consider  $\dot{f}$  as some CS mass scale, then  $\chi \propto m_{CS}/M$  is a ratio of masses with a straightforward physical meaning.

## 9.6 Astrophysical Implications

In this section we shall propose a physical interpretation to the CS modification to the PPN metric and we shall calculate some GR predictions that are modified by this correction. This section, however, is by no means a complete study of all the possible consequences of the CS correction, which is beyond the scope of this paper.

Let us begin by considering a system of  $A$  nearly spherical bodies, for which the gravitational vector potentials are simply [82]

$$V^i = \sum_A \frac{m_A}{r_A} v_A^i + \frac{1}{2} \sum_A \left( \frac{J_A}{r_A^2} \times n_A \right)^i, \quad (9.49)$$

$$W^i = \sum_A \frac{m_A}{r_A} (v_A \cdot n_A) n_A^i + \frac{1}{2} \sum_A \left( \frac{J_A}{r_A^2} \times n_A \right)^i,$$

where  $m_A$  is the mass of the  $A$ th body,  $r_A$  is the field point distance to the  $A$ th body,  $n_A^i = x_A^i/r_A$  is a unit vector pointing to the  $A$ th body,  $v_A$  is the velocity of the  $A$ th body and  $J_A^i$  is the spin-angular momentum of the  $A$ th body. For example, the spin angular momentum for a Kerr spacetime is given by  $J^i = m^2 a^i$ , where  $a$  is the dimensionless Kerr spin parameter. Note that if  $A = 2$  then the system being modeled could be a binary of spinning compact objects, while if  $A = 1$  it could represent the field of the sun or that of a rapidly spinning neutron star or pulsar.

In obtaining Eq. (9.49), we have implicitly assumed a point-particle approximation, which in classical GR is justified by the effacement principle. This principle

postulates that the internal structure of bodies contributes to the solution of the field equations to higher PN order. One can verify that this is indeed the case in classical GR, where internal structure contributions appear at 5 PN order. In CS gravity, however, it is a priori unclear whether an analogous effacement principle holds because the CS term is expected to couple with matter current via standard model-like interactions. If such is the case, it is possible that a “mountain” on the surface of a neutron star [298] or an r-mode instability [299, 300, 301] enhances the CS contribution. In this paper, however, we shall neglect these interactions, and relegate such possibilities to future work [281].

With such a vector potential, we can calculate the CS correction to the metric. For this purpose, we define the correction  $\delta g_{0i} \equiv g_{0i} - g_{0i}^{(GR)}$ , where  $g_{0i}^{(GR)}$  is the GR prediction without CS gravity. We then find that the CS corrections is given by

$$\delta g_{0i} = 2 \sum_A \frac{\dot{f}}{r_A} \left[ \frac{m_A}{r_A} (v_A \times n_A)^i - \frac{J_A^i}{2r_A^2} + \frac{3}{2} \frac{(J_A \cdot n_A)}{r_A^2} n_A^i \right], \quad (9.50)$$

where the  $\cdot$  operator is the flat-space inner product and where we have used the identities  $\tilde{\epsilon}_{ijk}\tilde{\epsilon}_{klm} = \delta_{il}\delta_{jm} - \delta_{im}\delta_{jl}$  and  $\tilde{\epsilon}_{ilk}\tilde{\epsilon}_{jlm} = 2\delta_{ij}$ . Note that the first term of Eq. (9.50) is of  $\mathcal{O}(3)$ , while the second and third terms are of  $\mathcal{O}(4)$  as previously anticipated. Also note that  $\dot{f}$  couples both to the spin and orbital angular momentum. Therefore, whether the system under consideration is the Solar system ( $v^i$  of the Sun is zero while  $J^i$  is small), the Crab pulsar ( $v^i$  is again zero but  $J^i$  is large) or a binary system of compact objects (neither  $v^i$  nor  $J^i$  vanish), there will in general be a non-vanishing coupling between the CS correction and the vector potential of the system.

From the above analysis, it is also clear that the CS correction increases with the non-linearity of the spacetime. In other words, the CS term is larger not only for systems with large velocities and spins, but also in regions near the source. For a binary system, this fact implies that the CS correction is naturally enhanced in the last stages of inspiral and during merger. Note that this enhancement is *different* from all previous enhancements proposed, since it does not require the presence of charge [281, 272], a fifth dimension with warped compactifications [295, 296], or a vanishing string coupling [284, 285, 286, 287, 288, 289, 290, 291, 292, 293, 294]. Unfortunately, the end of the inspiral stage coincides with the edge of the PN region of validity and, thus, a complete analysis of such a natural enhancement will have to be carried out through numerical simulations.

In the presence of a source with the vector potentials of Eq. (9.49), we can write the vectorial sector of the metric perturbation in a suggestive way, namely

$$\begin{aligned} g_{0i} &= \sum_A -\frac{7}{2} \frac{m_A}{r_A} v_A^i - \sum_A \frac{m_A}{6r_A^2} \left( v_A - v_A^{(eff)} \right)^i \\ &- \frac{1}{2} \sum_A n_A^i \frac{m_A}{r_A} v_A^{(eff)} \cdot n_A - 2 \sum_A \left[ \frac{J_A^{(eff)}}{r_A^2} \times n_A \right]^i, \end{aligned} \quad (9.51)$$

where we have defined an effective velocity and angular momentum vector via

$$\begin{aligned} v_{A(eff)}^i &= v_A^i - 6\dot{f} \frac{J_A^i}{m_A r_A^2}, \\ J_{A(eff)}^i &= J_A^i - \dot{f} m_A v_A^i, \end{aligned} \quad (9.52)$$

or in terms of the Newtonian orbital angular momentum  $L_{A(N)}^i = r_A \times p_A$  and linear momentum  $p_{A(N)}^i = m_A v_A^i$

$$\begin{aligned} L_{A(eff)}^i &= L_{A(N)}^i - 6\dot{f} (n_A \times J_A)^i, \\ J_{A(eff)}^i &= J_A^i - \dot{f} p_A^i. \end{aligned} \quad (9.53)$$

From this analysis, it is clear that the CS corrections seems to couple to both a quantity that resembles the orbital and the spin angular momentum vector. Note that when the spin angular momentum vanishes the vectorial metric perturbation is identical to that of a spinning moving fluid, but where the spin is induced by the coupling of the orbital angular momentum to the CS term.

The presence of an effective CS spin angular momentum in non-spinning sources leads to an interesting physical interpretation. Let us model the field that sources  $\dot{f}$  as a fluid that permeates all of spacetime. This field could be, for example, a model-independent axion, inspired by the quantity introduced in the standard model to resolve the strong CP problem [302]. In this scenario, then the fluid is naturally “dragged” by the motion of any source and the CS modification to the metric is nothing but such dragging. This analogy is inspired by the ergosphere of the Kerr solution, where inertial frames are dragged with the rotation of the black hole. In fact, one could push this analogy further and try to construct the shear and bulk viscosity of such a fluid, but we shall not attempt this here. Of course, this interpretation is to be understood only qualitatively, since its purpose is only to allow the reader to picture the CS modification to the metric in physical terms.

An alternative interpretation can be given to the CS modification in terms of the gravito-electro-magnetic (GED) analogy [278, 279], which shall allow us to easily construct the predictions of the modified theory. In this analogy, one realizes that the PN solution to the linearized field equations can be written in terms of a potential and vector potential, namely

$$ds^2 = -(1 - 2\Phi) dt^2 - 4(A \cdot dx) dt + (1 + 2\Phi) \delta_{ij} dx^i dx^j, \quad (9.54)$$

where  $\Phi$  reduces to the Newtonian potential  $U$  in the Newtonian limit [279] and  $A^i$  is a vector potential related to the metric via  $A_i = -g_{0i}/4$ . One can then construct GED

fields in analogy to Maxwell's electromagnetic theory via

$$\begin{aligned} E^i &= -(\nabla\Phi)^i - \partial_t \left( \frac{1}{2} A^i \right), \\ B^i &= (\nabla \times A)^i, \end{aligned} \quad (9.55)$$

which in terms of the vectorial sector of the metric perturbation becomes

$$\begin{aligned} E^i &= -(\nabla\Phi)^i + \frac{1}{8} \dot{g}^i, \\ B^i &= -\frac{1}{4} (\nabla \times g)^i, \end{aligned} \quad (9.56)$$

where we have defined the vector  $g^i = g_{0i}$ . The geodesic equations for a test particle then reduce to the Lorentz force law, namely

$$F^i = -mE^i - 2m(v \times B)^i. \quad (9.57)$$

We can now work out the effect of the CS correction on the GED fields and equations of motion. First note that the CS correction only affects  $g$ . We can then write the CS modification to the Lorentz force law by defining  $\delta a^i = a^i - a_{(GR)}^i$ , where  $a_{(GR)}^i$  is the acceleration vector predicted by GR, to obtain,

$$\delta a^i = \frac{1}{8} \delta \dot{g}^i + \frac{1}{2} (v \times \delta \Omega)^i, \quad (9.58)$$

where we have defined the angular velocity

$$\delta \Omega^i = (\nabla \times \delta g)^i. \quad (9.59)$$

The time derivative of the vector  $g^i$  is of  $\mathcal{O}(5)$  and can thus be neglected, but the angular velocity cannot and it is given by

$$\delta \Omega^i = - \sum_A \dot{f} \frac{m_A}{r_A^3} \left[ 3 (v_A \cdot n_A) n_A^i - v_A^i \right], \quad (9.60)$$

which is clearly of  $\mathcal{O}(3)$ . Note that although the first term between square brackets cancels for circular orbits because  $n_A^i$  is perpendicular to  $v_A^i$  to Newtonian order, the second term does not. The angular velocity adds a correction to the acceleration of  $\mathcal{O}(4)$ , namely

$$\delta a^i = -\frac{3}{2} \sum_A \dot{f} \frac{m_A}{r_A^3} (v_A \cdot n_A) (v_A \times n_A)^i, \quad (9.61)$$

which for a system in circular orbit vanishes to Newtonian order. One could use this formalism to find the perturbations in the motion of moving objects by integrating Eq. (9.61) twice. However, for systems in a circular orbit, such as the Earth-Moon system or compact binaries, this correction vanishes to leading order. Therefore, lunar ranging experiments [303] might not be able to constraint  $\dot{f}$ .

Another correction to the predictions of GR is that of the precession of gyroscopes by the so-called Lense-Thirring or frame-dragging effect. In this process, the spin angular momentum of a source twists spacetime in such a way that gyroscopes are dragged with it. The precession angular velocity depends on the vector sector of the metric perturbation via Eq. (9.60). Thus, the full Lense-Thirring term in the precession angular velocity of precessing gyroscopes is

$$\Omega_{LT}^i = -\frac{1}{r_A^3} \sum_A J_{A(eff)}^i - 3n_A^i \left( J_{A(eff)} \cdot n_A \right)^i. \quad (9.62)$$

Note that this angular velocity is identical to the GR prediction, except for the replacement  $J_A^i \rightarrow J_{A(eff)}^i$ . In CS modified gravity, then, the Lense-Thirring effect is not only produced by the spin angular momentum of the gyroscope but also by the orbital angular momentum that couples to the CS correction. Note, however, that this correction vanishes for zero velocities and angular momentum.

If experiments [280] detect frame-dragging and find it in agreement with the GR prediction, we can immediately test CS gravity. In order to place a bound, however, a careful analysis must be performed, using the tools developed in [304] and properly accounting for the experiment's frame. Nonetheless, we can construct a crude, order-of-magnitude estimate of the size of such a bound. In order to do so, we assume the Newtonian limit  $\mathcal{O}(J) \sim \mathcal{O}(mRv)$ , with  $m$  the total mass of the system,  $R$  the distance from the gyroscope to the gravitational source (for GP B,  $R \sim 7000$  km [304]) and  $v$  the orbital velocity, such that we can model the CS correction as  $|\Omega| \sim \Omega^{GR}(1 + \dot{f}/R)^4$ . Then, a one percent accuracy in the frame-dragging measurement relative to the GR prediction (nominal for GP B [304]) translates, roughly, into the bound  $\dot{f} \lesssim 10^{-3}$  seconds.

Are there other experiments that could be performed to measure such a deviation from GR? Any experiment that samples the vectorial sector of the metric would in effect be measuring such a deviation. In this paper, we have only discussed modifications to the frame-dragging effect and the acceleration of bodies through the GED analogy, but this need not be the only corrections to classical GR predictions. In fact, any predictions that depends on  $g_{0i}$  indirectly, for example via Christoffel symbols, will probably also be modified unless the corrections is fortuitously canceled. In this paper, we have laid the theoretical foundations of the weak-field correction to the metric due to CS gravity and studied some possible corrections to classical predictions. A detailed study of other corrections is beyond the scope of this paper.

## 9.7 Conclusion

We have studied the weak-field expansion of the solution to the CS modified field equations in the presence of a perfect fluid PN source in the point particle limit. Such an expansion required that we linearize the Ricci and Cotton tensor to second order in the metric perturbation without any gauge assumption. An iterative PPN formalism was

---

<sup>4</sup>This can be seen by inserting  $\mathcal{O}(J) \sim \mathcal{O}(mRv)$  into Eq. (9.62), with the definition of the effective angular velocity given in Eq. (9.53), and factoring out  $1 + \dot{f}/R$ .

then employed to solve for the metric perturbation in this modified theory of gravity. We have found that CS gravity possesses the same PPN parameters as those of GR, but it also requires the introduction of a new term and PPN parameter that is proportional to the curl of the PPN vector potentials. Such a term is enhanced in non-linear scenarios without requiring the presence of standard model currents, large extra dimensions or a vanishing string coupling.

We have proposed an interpretation for the new term in the metric produced by CS gravity and studied some of the possible consequences it might have on GR predictions. The interpretation consists of picturing the field that sources the CS term as a fluid that permeates all of spacetime. In this scenario, the CS term is nothing but the “dragging” of the fluid by the motion of the source. Irrespective of the validity of such an interpretation, the inclusion of a new term to the weak-field expansion of the metric naturally leads to corrections to the standard GR predictions. We have studied the acceleration of point particles and the Lense-Thirring contribution to the precession of gyroscopes. We have found that both corrections are proportional to the CS coupling parameter and, therefore, experimental measurement of these effects might be used to constraint CS and, possibly, string theory.

Future work could concentrate on studying further the non-linear enhancement of the CS correction and the modifications to the predictions of GR. The PPN analysis performed here breaks down very close to the source due to the use of a point particle approximation in the stress energy tensor. One possible research route could consist of studying the CS correction in a perturbed Kerr background [104]. Another possible route could be to analyze other predictions of the theory, such as the perihelion shift of Mercury or the Nordtvedt effect. Furthermore, in light of the imminent highly-accurate measurement of the Lense-Thirring effect by Gravity Probe B, it might be useful to revisit this correction in a frame better-adapted to the experimental setup. Finally, the CS modification to the weak-field metric might lead to non-conservative effects and the breaking of the effacement principle [281], which could be studied through the evaluation of the gravitational pseudo stress-energy tensor. Ultimately, it will be experiments that will determine the viability of CS modified gravity and string theory.

## Acknowledgments

The authors acknowledge the support of the Center for Gravitational Wave Physics funded by the National Science Foundation under Cooperative Agreement PHY-01-14375, and support from NSF grants PHY-05-55-628. We would also like to thank Cliff Will for encouraging one of us to study the PPN formalism and Pablo Laguna for suggesting one of us to look into the PPN expansion of CS gravity. We would also like to thank R. Jackiw, R. Wagoner and Ben Owen for enlightening discussions and comments.

**Note added after publication:** After submission of this work, another paper appeared, where the analysis presented here is expanded to account for extended sources [83]. After a detailed analysis, it is found that the LAGEOS and GP B experiments can indeed place a bound on the CS coupling parameter of the order predicted in this work.

## Chapter 10

# How do Black Holes Spin in Chern-Simons Modified Gravity?

No Kerr-like exact solution has yet been found in Chern-Simons modified gravity. Intrigued by this absence, we study stationary and axisymmetric metrics that could represent the exterior field of spinning black holes. For the standard choice of the background scalar, the modified field equations decouple into the Einstein equations and additional constraints. These constraints eliminate essentially all solutions except for Schwarzschild. For non-canonical choices of the background scalar, we find several exact solutions of the modified field equations, including mathematical black holes and pp-waves. We show that the ultrarelativistically boosted Kerr metric can satisfy the modified field equations, and we argue that physical spinning black holes may exist in Chern-Simons modified gravity only if the metric breaks stationarity, axisymmetry or energy-momentum conservation.

### 10.1 Introduction

General relativity (GR) is one of physics' most successful theories, passing all experimental tests so far with ever increasing accuracy<sup>1</sup> [305]. Nevertheless, modifications to GR are pursued vigorously for two main reasons: from a theoretical standpoint, we search for an ultraviolet (UV) completion of GR, such as string theory, that would lead to corrections in the action proportional to higher powers of scalar invariants of the Riemann tensor; from an experimental standpoint, observations in the deep infrared (IR) regime suggest the existence of some form of dark energy [306, 307, 308]. One possibility to accommodate dark energy is to consider an action with non-linear couplings to the Ricci scalar [309, 310], similar in spirit to the corrections that we expect from a UV completion of GR.

UV and IR corrections entail higher derivatives of the fundamental degrees of freedom in the equations of motion, which on general grounds tend to have disastrous consequences on the stability of the solutions of the theory<sup>2</sup>: the so-called Ostrogradski instability (for a review cf. e.g. [313]). A few loopholes exist, however, that allow to

---

<sup>1</sup>This chapter is based on the following papers: D. Grumiler and N. Yunes, accepted for publication in the Phys. Rev. D (2007)

<sup>2</sup>If one considers the classical solutions of the non-modified theory (without higher derivatives) and regards additional terms as loop corrections, then no stability issues arise. In that case, additional (unstable) solutions must be considered spurious [311, 312].

bypass this theorem (for example, if the non-linear corrections can be converted into a representation of a scalar-tensor theory). Along these lines, special combinations of scalar invariants that play the role of a topological term, such as the Euler or Pontryagin term, can in general be added safely to the action.

In this paper, we study Chern-Simons (CS) modified gravity [79], where the Einstein-Hilbert action is modified by the addition of a parity-violating Pontryagin term. As described by Jackiw and Pi [79], this correction arises through the embedding of the 3-dimensional CS topological current into a 4-dimensional spacetime manifold. CS gravity is not a random extension of GR, but it has physical roots in particle physics. Namely, if there is an imbalance between left- ( $N_L$ ) and right-handed ( $N_R$ ) fermions, then the fermion number current  $j^\mu$  has a well-known gravitational anomaly [314],  $\partial_\mu j^\mu \propto (N_L - N_R) {}^*RR$ , analogous to the original triangle anomaly [315]. Here  ${}^*RR$  is the Pontryagin term (also known as the gravitational instanton density or Chern-Pontryagin term) to be defined in the next section. CS gravity is also motivated by string theory: it emerges as an anomaly-canceling term through the Green-Schwarz mechanism [276]. Such a correction to the action is indispensable, since it arises as a requirement of all 4-dimensional compactifications of string theory in order to preserve unitarity [74].

CS gravity has been studied in the context of cosmology, gravitational waves, solar system tests and Lorentz invariance. In particular, this framework has been used to explain the anisotropies in the cosmic microwave background [75, 76, 77] and the leptogenesis problem [73, 74] (essentially using the gravitational anomaly described above in the other direction). CS gravity has also been shown to lead to amplitude birefringent gravitational waves [79, 316, 277, 317], possibly allowing for a test of this theory with gravitational-wave detectors [272]. Moreover, CS gravity has been investigated in the far-field of a spinning binary system, leading to a prediction of gyromagnetic precession [277, 317] that differs from GR. This prediction was later improved on and led to a constraint on the magnitude of the CS coupling [83]. Finally, CS gravity has been studied in the context of Lorentz-invariance and -violation [297] and the theory has been found to preserve this symmetry, provided the CS coupling is treated as a dynamical field. For further studies of these and related issues cf. e.g. [79, 318, 319, 316, 320, 321, 322, 323, 324, 325, 77, 326, 282, 297, 317, 327, 83, 328, 329].

CS gravity introduces the following modification to the action [79]:  $S = S_{EH} + S_{\text{mat}} + S_{CS}$ , where  $S_{EH}$  is the Einstein-Hilbert action,  $S_{\text{mat}}$  is some matter action, and the new term is given by

$$S_{CS} \sim \int dV \theta {}^*RR. \quad (10.1)$$

In Eq. (10.1),  $dV$  is a 4-dimensional volume element,  ${}^*RR$  is the Pontryagin term and  $\theta$  is a *background scalar field* (we shall define this action in more detail in the next section). This scalar field, sometimes called a gravitational axion, acts as a *CS coupling function* that can be interpreted either as an external or a dynamical quantity. In the former case, CS gravity is an effective theory that derives from some other, more fundamental gravity theory that physically defines the scalar field. In the latter case, the scalar field

possesses its own equation of motion, which could in principle contain a potential and a kinetic term [83].

The strength of the CS correction clearly depends on the CS coupling function. If we consider CS gravity as an effective theory, the coupling function is suppressed by some mass scale, which could lie between the electro-weak and the Planck scale, but it is mostly unconstrained [83]. In the context of string theory, the coupling constant has been computed in very conservative scenarios, leading to a Planck mass suppression [73]. In less conservative scenarios, there could exist enhancements that elevate the coupling function to the realm of the observable. Some of these scenarios are cosmologies where the string coupling vanishes at late times [284, 285, 286, 287, 288, 289, 290, 291, 292, 293, 294], or where the field that generates  $\theta$  couples to spacetime regions with large curvature [295, 296] or stress-energy density [272].

The CS correction is encoded in the modified field equations, which can be obtained by varying the modified action with respect to the metric. The divergence of the modified field equations establishes the Pontryagin constraint  $*R R = 0$ , through the Bianchi identities for a vacuum or conserved stress-energy tensor. Not only does this constraint have important consequences on the conservation of energy, but it also restricts the space of solutions of the modified theory. For example, although this restriction is not strong enough to eliminate the Schwarzschild solution, it does eliminate the Kerr solution. Since astrophysical observations suggest that supermassive black holes (BHs) at the center of galaxies do have a substantial spin (cf., e. g. [330] and references therein), this raises the interesting question of what replaces the Kerr solution in CS gravity.

In this paper, we search for solutions to the CS modified field equations that could represent the exterior gravitational field of a spinning star or BH. We find that solutions cluster into two different classes: GR solutions that independently satisfy both the vacuum Einstein equations and the modified field equations; non-GR solutions that satisfy the modified field equations but not the vacuum Einstein equations. We carry out an extensive study of solutions by looking at three groups of line elements: spherically symmetric metrics; static and axisymmetric metrics; and stationary and axisymmetric metrics. The first group contains GR solutions only, independently of the choice of the CS scalar field. The second group leads to a decoupling of the modified field equations for 'natural' choices of the scalar field, which again reduces to trivial GR solutions. In fact, we show here that static and axisymmetric line elements are forced to be spatially conformally flat if such a decoupling occurs. The third group also leads to the same decoupling for the canonical choice of the scalar field, and we argue against the existence of non-trivial solutions.

This paper suggests that stationary and axisymmetric line elements in CS gravity probably do not admit solutions of the field equations for the canonical choice of the CS scalar field. However, solutions do exist when more general scalar fields are considered, albeit not representing physical BH configurations <sup>3</sup>. We find two types of solutions,

---

<sup>3</sup>The conclusion that stationary and axisymmetric solutions to the modified field equations do not exist is in agreement with [327]. However, this fact does not lead to the conclusion that spinning BHs cannot exist in the modified theory, as implied in [327]. In fact, an approximate

mathematical BHs and ultrarelativistically boosted BHs, which, to our knowledge, are the first examples of BH and BH-like solutions in CS gravity, besides Schwarzschild and Reissner-Nordström. The first type arises when we consider a subclass of stationary and axisymmetric line elements (the so-called van Stockum class), for which we find both GR and non-GR solutions for non-canonical scalar fields. For instance, we shall demonstrate that the line-element

$$ds^2 = -\rho\left(1 - \frac{2m}{\sqrt{\rho}}\right)dt^2 - 2\rho dt d\phi + \frac{1}{\sqrt{\rho}}(d\rho^2 + dz^2), \quad (10.2)$$

together with the CS scalar field  $\theta = 2\sqrt{\rho}z/3$ , satisfies the modified field equations but does not arise in GR as a vacuum solution. The metric in Eq. (10.2) represents BHs in the mathematical sense only: it exhibits a Killing horizon at  $\sqrt{\rho} = 2m = \text{const.}$ , but it contains unphysical features, such as closed time-like curves that are not screened by a horizon. The second type of solutions with a non-canonical scalar field arises when we consider scalar fields whose divergence is a Killing vector. These fields lead to exact gravitational pp-wave solutions of GR and non-GR type. One particular example that we shall discuss in in this paper is the ultrarelativistically boosted Kerr BH,

$$ds^2 = -2du dv - h_0\delta(u)\ln(x^2 + y^2) du^2 + dx^2 + dy^2, \quad (10.3)$$

with the CS scalar field  $\theta = \lambda v$ , where  $h_0$  and  $\lambda$  are constants.

Although we did not find a Kerr analogue by searching for stationary and axisymmetric solutions, spinning BHs do seem to exist in the theory. This suggestion is fueled by the existence of two different limits of the Kerr spacetime that are still preserved: the Schwarzschild limit and the Aichelburg-Sexl limit, Eq. (10.3), which we shall show persists in CS gravity. These limits, together with the existence of a non-axisymmetric far-field solution [317], indicate that a spinning BH solution must exist, albeit not with the standard symmetries of the Kerr spacetime. Unfortunately, spacetimes with only one or no Killing vector are prohibitively general and their study goes beyond the scope of this work. Nonetheless, the possibility of constructing such solutions by breaking stationarity or axisymmetry is discussed and a better understanding of solutions in CS gravity is developed. Finally, we show how to recover the Kerr solution by postulating, in an ad-hoc manner, a non-conserved energy momentum-tensor and deduce that it violates the classical energy conditions.

This paper is organized as follows: Sec. 10.2 reviews some basic features of CS modified gravity and exploits two alternative formulations of the Pontryagin constraint, one based upon the spinorial decomposition of the Weyl tensor and one based upon its electro-magnetic decomposition, to reveal some physical consequences of this constraint; Sec. 10.3 revisits the Schwarzschild, Friedmann-Robertson-Walker and Reissner-Nordström solutions in CS modified gravity and addresses the sensitivity of these solutions to the choice of CS coupling function; Sec. 10.4 studies static, axisymmetric line elements in great detail, while Sec. 10.5 investigates stationary, axisymmetric metrics and

---

solution that can represent a spinning BH in CS gravity has already been found in the far-field [317, 83].

provides the first non-trivial exact solutions to CS modified gravity, including mathematical BH solutions; Sec. 10.6 addresses metrics that break axisymmetry or stationarity and concentrates on non-trivial solutions for pp-waves and the Aichelburg-Sexl boosted Kerr metric; Sec. 10.7 concludes and points to future research.

We use the following conventions in this paper: we work exclusively in four spacetime dimensions with signature  $(-, +, +, +)$  [197], with Latin letters  $(a, b, \dots, h)$  ranging over all spacetime indices; curvature quantities are defined as given in the MAPLE GRTensorII package [1]; round and square brackets around indices denote symmetrization and anti-symmetrization respectively, namely  $T_{(ab)} := \frac{1}{2}(T_{ab} + T_{ba})$  and  $T_{[ab]} := \frac{1}{2}(T_{ab} - T_{ba})$ ; partial derivatives are sometimes denoted by commas, e.g.  $\partial\theta/\partial r = \partial_r\theta = \theta_{,r}$ . The Einstein summation convention is employed unless otherwise specified, and we use geometrized units where  $G = c = 1$ .

## 10.2 CS modified gravity

### 10.2.1 ABC of CS

In this section, we summarize the basics of CS modified gravity, following the formulation of [79]. Let us begin by defining the full action of the theory <sup>4</sup>:

$$S = \kappa \int d^4x \sqrt{-g} \left( R - \frac{1}{4} \theta {}^*R R \right) + S_{\text{mat}}, \quad (10.4)$$

where  $\kappa = 1/(16\pi)$ ,  $g$  is the determinant of the metric, the integral extends over all spacetime,  $R$  is the Ricci scalar,  $S_{\text{mat}}$  is some unspecified matter action and  ${}^*R R$  is the Pontryagin term. The latter is defined via

$${}^*R R := {}^*R^a{}_b{}^{cd} R^b{}_{acd}, \quad (10.5)$$

where the dual Riemann-tensor is given by

$${}^*R^a{}_b{}^{cd} := \frac{1}{2} \epsilon^{cdef} R^a{}_{bef}, \quad (10.6)$$

with  $\epsilon^{cdef}$  the 4-dimensional Levi-Civita tensor <sup>5</sup>. The Pontryagin term [Eq. (10.5)] can be expressed as the divergence

$$\nabla_a K^a = \frac{1}{4} {}^*R R \quad (10.7)$$

---

<sup>4</sup>There is a relative sign difference in the CS correction to the action compared to [79]. This minus sign is included in order to obtain the same equations of motion as in [79], correcting a minor typo.

<sup>5</sup>We prefer to work with tensors rather than with tensor densities in this paper, so some expressions might appear to differ by factors of  $\sqrt{-g}$  from [79].

of the Chern-Simons topological current ( $\Gamma$  is the Christoffel connection),

$$K^a := \epsilon^{abcd} \left( \Gamma^n{}_{bm} \partial_c \Gamma^m{}_{dn} + \frac{2}{3} \Gamma^n{}_{bm} \Gamma^m{}_{cl} \Gamma^l{}_{dn} \right), \quad (10.8)$$

thus the name ‘‘Chern-Simons modified gravity’’<sup>6</sup>.

The modified field equations can be obtained by varying the action with respect to the metric. Exploiting the well-known relations

$$\delta R^b{}_{acd} = \nabla_c \delta \Gamma^b{}_{ad} - \nabla_d \delta \Gamma^b{}_{ac} \quad (10.9)$$

and

$$\delta \Gamma^b{}_{ac} = \frac{1}{2} g^{bd} (\nabla_a \delta g_{dc} + \nabla_c \delta g_{ad} - \nabla_d \delta g_{ac}), \quad (10.10)$$

the variation of the geometric part of the action leads to

$$\begin{aligned} \delta S - \delta S_{\text{mat}} &= \kappa \int d^4 x \sqrt{-g} \left( R_{ab} - \frac{1}{2} g_{ab} R + C_{ab} \right) \delta g^{ab} \\ &- \frac{\kappa}{4} \int d^4 x \sqrt{-g} {}^* R R \delta \theta \\ &+ \Sigma_{EH} + \Sigma_{CS}. \end{aligned} \quad (10.11)$$

Here, the tensor  $C_{ab}$  stands for a 4-dimensional Cotton-like tensor, which we shall refer to as the C-tensor<sup>7</sup>, given by

$$C^{ab} := v_c \epsilon^{cde(a} \nabla_e R^b){}_d + v_{cd} {}^* R^{d(ab)c}, \quad (10.12)$$

where

$$v_a := \nabla_a \theta, \quad v_{ab} := \nabla_a \nabla_b \theta = \nabla_{(a} \nabla_{b)} \theta \quad (10.13)$$

are the velocity and covariant acceleration of  $\theta$ , respectively<sup>8</sup>. We shall always assume that  $v_a$  does not vanish identically, because otherwise the model reduces to GR<sup>9</sup>.

Surface terms are collected in the third line of Eq. (10.11) and arise due to repeated integration by parts and application of Stokes’ theorem. In particular,  $\Sigma_{EH}$  and  $\Sigma_{CS}$  arise from variation of the Einstein-Hilbert and CS sector of the action, respectively.

<sup>6</sup>If  $\nabla_a K^a$  is converted into  $1/\sqrt{g} \partial_a (\sqrt{g} K^a)$  the results (2.4) and (2.5) of [79] are recovered.

<sup>7</sup>In the original work of [79], this tensor was called ‘Cotton tensor’ because it shares similarities with the 3-dimensional Cotton-tensor. However, the notion of a higher-dimensional Cotton tensor already exists [331] and differs from the definition of  $C_{ab}$ , which is why we refer to Eq. (10.12) as a ‘‘C-tensor’’.

<sup>8</sup>The quantity  $v_a$  is sometimes referred to as an *embedding coordinate* since it embeds the 3-dimensional CS theory into a 4-dimensional spacetime.

<sup>9</sup>When  $v_a = 0$  then  $\theta$  is constant and the Pontryagin term becomes a topological term not contributing to the field equations.

The former expression is well-known, while the latter contains a term with  $\delta\Gamma$ ,

$$\Sigma_{CS} = \kappa \int d^4x \sqrt{-g} \nabla_d \left( \theta {}^*R^{abcd} \delta\Gamma_{bac} \right) + \dots \quad (10.14)$$

It is worthwhile pointing out that one cannot just impose Dirichlet boundary conditions on the induced metric at the boundary by adding the Gibbons-Hawking-York term, as it is the case in GR [185, 332]. There is no obvious way to cancel the term containing the variation of the connection,  $\delta\Gamma$ , in Eq. (10.14), except by imposing suitable fall-off conditions on the scalar field  $\theta$  or Dirichlet boundary conditions on the connection. Even though we shall neglect boundary issues henceforth, we emphasize that these considerations are relevant in many applications, such as BH thermodynamics.

The modified field equations are then given by the first line of Eq. (10.11), provided the second line vanishes. The vanishing of  ${}^*RR$  is the so-called Pontryagin constraint and we shall study it in Sec. 10.2.2. The modified field equations in the presence of matter sources are then given by

$$G_{ab} + C_{ab} = 8\pi T_{ab}, \quad (10.15)$$

where  $G_{ab} = R_{ab} - \frac{1}{2}g_{ab}R$  is the Einstein tensor and  $T_{ab}$  is the stress-energy tensor of the source. In this paper, we are primarily concerned with the vacuum case,  $T_{ab} = 0$ , for which the modified field equations reduce to

$$R_{ab} + C_{ab} = 0, \quad (10.16)$$

due to the tracelessness of the C-tensor,  $C^a_a = 0$ . Like in GR, vacuum solutions in CS gravity satisfy

$$R = 0. \quad (10.17)$$

## 10.2.2 Pontryagin Constraint

Let us now discuss the Pontryagin constraint

$${}^*RR = 0, \quad (10.18)$$

which then forces the second line in Eq. (10.11) to vanish. One route to obtain the Pontryagin constraint is to treat  $\theta$  as a dynamical field (or rather a Lagrange multiplier). By varying the action with respect to  $\theta$ , we obtain the equations of motion for the scalar field that dynamically enforce the Pontryagin constraint.

Another route to obtain the Pontryagin constraint is to treat  $\theta$  as an external quantity. In this case, there are no equations of motion for the scalar field. Nonetheless, by taking the covariant divergence of the equations of motion and using the contracted Bianchi identities, one obtains

$$\nabla_a C^{ab} = \frac{1}{8} v^b {}^*RR = 8\pi \nabla_a T^{ab}. \quad (10.19)$$

Usually, it is desirable to require that the stress-energy be covariantly conserved. However, in CS modified gravity this need not be the case because a non-vanishing covariant divergence  $\nabla_a T^{ab} \neq 0$  could be balanced by a non-vanishing Pontryagin term – this is, in fact, how the term arises in some approaches in the first place, cf. [322]. We shall come back to this issue at the end of Sec. 10.6, but for the time being we shall set  $T^{ab} = 0$ , which then leads to the Pontryagin constraint.

The Pontryagin constraint is a necessary condition for any vacuum spacetime that solves the modified field equations, but what does it mean physically? We shall attempt to answer this question by providing two alternative formulations of this constraint, but before doing so, let us discuss some general properties and consequences of Eq. (10.18). First, notice that setting the  ${}^*RR$  term to zero leads to the conserved current  $K^a$  [Eqs. (10.7) and (10.8)], which is topological in nature, and thus implies this quantity is intrinsically different from typical conserved quantities, such as energy or angular momentum. Second, when the CS action is studied on-shell [Eq. (10.4) with  ${}^*RR = 0$ ] it reduces to the GR action, an issue that is of relevance for stability considerations, e.g. thermodynamic stability in BH mechanics.

The first physical interpretation of the Pontryagin constraint can be obtained by considering a spinorial decomposition. Let us then consider the useful relation

$${}^*RR = {}^*CC, \quad (10.20)$$

which we prove in appendix H. In Eq. (10.20),  $C$  is the Weyl tensor defined in (H.2) and  ${}^*C$  its dual, defined in (H.3). This identity allows us to use powerful spinorial methods to map the Weyl tensor into the Weyl spinor [333], which in turn can be characterized by the Newman-Penrose (NP) scalars  $(\Psi_0, \Psi_1, \Psi_2, \Psi_3, \Psi_4)$ . In the notation of [334], the Pontryagin constraint translates into a reality condition on a quadratic invariant of the Weyl spinor,  $\mathcal{I}$ ,

$$\Im(\mathcal{I}) = \Im(\Psi_0\Psi_4 + 3\Psi_2^2 - 3\Psi_1\Psi_3) = 0. \quad (10.21)$$

Such a reality condition is particularly useful for the consideration of algebraically special spacetimes. For instance, it follows immediately from Eq. (10.21) that spacetimes of Petrov types *III*, *N* and *O* obey the Pontryagin constraint, since in the latter case all NP scalars vanish, while in the former cases (in an adapted frame) only  $\Psi_3$  or  $\Psi_4$  are non-vanishing. Moreover, all spacetimes of Petrov types *D*, *II* and *I* are capable of violating Eq. (10.21). For example, for spacetimes of Petrov type *II* one can choose an adapted tetrad such that  $\Psi_0 = \Psi_1 = \Psi_3 = 0$ , which then reduces Eq. (10.21) to the condition that either the real part or the imaginary part of  $\Psi_2$  has to vanish.

The reality condition of Eq. (10.21) can also be useful in applications of BH perturbation theory. For instance, in the metric reconstruction of the perturbed Kerr spacetime [104], the NP scalars  $\Psi_1 = \Psi_3 = 0$  vanish. In this context gravitational waves are characterized by  $\Psi_{4,0}$ , while  $\Psi_2$  is in general non-vanishing. In a tetrad that represents a transverse-traceless frame, these scalars are given by

$$\Psi_{4,0} = \ddot{h}_+ \mp i\ddot{h}_\times, \quad (10.22)$$

where  $h_{+,\times}$  are the plus/cross polarization of the waveform, and the overhead dot stands for partial time derivative [335]. Obviously,  $\Psi_0\Psi_4 = (\ddot{h}_+)^2 + (\ddot{h}_\times)^2$  is real, which again reduces Eq. (10.21) to the condition that either the real part or the imaginary part of  $\Psi_2$  has to vanish. Neither of these possibilities is the case for the Kerr BH or perturbations of it [104].

Another interpretation of the Pontryagin constraint can be obtained by exploiting the split of the Weyl tensor into electric and magnetic parts (cf. e.g. [336]). Given some time-like vector field  $u^a$ , normalized so that  $u_a u^a = -1$ , one can define the electric and magnetic parts of the Weyl tensor as

$$(C_{abcd} + \frac{i}{2}\epsilon_{abef}C^{ef}_{cd})u^b u^d = E_{ac} + iB_{ac}. \quad (10.23)$$

Then, the Pontryagin constraint is equivalent to the condition <sup>10</sup>

$$E_{ab}B^{ab} = 0. \quad (10.24)$$

This leads to three possibilities: either the spacetime is purely electric ( $B_{ab} = 0$ ) or purely magnetic ( $E_{ab} = 0$ ) or orthogonal, in the sense that Eq. (10.24) holds. Equation (10.24) is a perfect analogue to the condition  ${}^*F F \propto \mathbf{E} \cdot \mathbf{B} = 0$ , which holds for specific configurations in electro-dynamics, including purely electric ( $\mathbf{B} = 0$ ), purely magnetic ( $\mathbf{E} = 0$ ) and electromagnetic wave configurations ( $\mathbf{E} \neq 0 \neq \mathbf{B}$ ,  $\mathbf{E} \cdot \mathbf{B} = 0$ ). This suggests that there could be single shock-wave solutions in CS gravity compatible with Eq. (10.24), which we shall indeed encounter in Sec. 10.6. In light of this electro-magnetic analogy, the Pontryagin constraint can be rephrased as “the gravitational instanton density must vanish,” since the quantity  ${}^*F F$  is sometimes referred to as the “instanton density.”

The electromagnetic decomposition of the Pontryagin constraint also allows for a physical interpretation in terms of perturbations of the Schwarzschild solution. In BH perturbation theory (cf. e.g. [135]), the metric perturbation is also decomposed through the electromagnetic Weyl tensor. The electric and magnetic parts can then be related to the flux of mass and angular momentum across the horizon. Suffice it to say that for a binary BH system in the slow-motion/small-hole approximation [135], these tensors are of order  $E_{ab} \sim \mathcal{O}(\Phi)$  and  $B_{ab} \sim \mathcal{O}(v\Phi)$ , where the Newtonian potential  $\Phi$  is of  $\mathcal{O}(v^2)$  via the Virial theorem, with  $v \ll 1$  the orbital velocity. In this case, the Pontryagin constraint is satisfied *automatically* up to terms of  $\mathcal{O}(v^5)$ . Within the post-Newtonian (PN) approximation [3], these conclusions imply that the PN metric for non-spinning point-particles in the quasi-circular approximation violates the Pontryagin constraint at 2.5 PN order [ $\mathcal{O}(v/c)^5$ ], which is precisely the order at which gravitational waves appear.

Even for non-canonical choices of the scalar field, such as  $\theta = z$  proposed in [327], the far field expansion of the Kerr metric does not satisfy the Pontryagin constraint to all orders. This is so because obviously  ${}^*R R$  is independent of  $\theta$ . In fact, one can

---

<sup>10</sup>One can show that Eq. (10.24) is related to the vanishing of certain derivatives of the Regge-Wheeler function in the Regge-Wheeler [189] decomposition of the metric perturbation. We are currently studying how such a condition impacts the ringing of CS BHs elsewhere [337]. The equivalence between Eqs. (10.21) and (10.24) was shown for the first time in [338].

show that violations of the constraint for the metric considered in [327] occur already at second order in the metric perturbation, which renders this metric hopeless as an exact CS solution. This observation is concurrent with the role the Pontryagin constraint may play for gravitational waves [339].

Finally, we can employ the electromagnetic analogy to anticipate the answer to the question we pose in the title of this paper. Namely, we are looking for a “rotating charge” configuration (where  $\mathbf{E} \neq 0 \neq \mathbf{B}$ ), which simultaneously is an “electromagnetic wave” configuration (where  $\mathbf{E} \cdot \mathbf{B} = 0$ ). We know that no such solutions exist in electrodynamics, except for two limits<sup>11</sup>: if the rotation (and thus  $\mathbf{B}$ ) approaches zero or if the charge is infinitely boosted (and thus  $\mathbf{B}$  becomes orthogonal to  $\mathbf{E}$ ). The first case corresponds to a static configuration, while the second one to an ultrarelativistic limit. We shall indeed find below both analogues as solutions of CS modified gravity, but we stress that the naive analogy with electrodynamics does not yet rule out other possible spinning configurations in CS modified gravity.

### 10.2.3 Space of Solutions

Before discussing some specific solutions to the CS modified field equations, let us classify the space of solutions. Figure 10.1 presents a 2-dimensional depiction of this space. The set  $\mathcal{E}$  denotes the Einstein space of solutions, whose members have a vanishing Ricci tensor, while  $\mathcal{CS}$  denotes the CS space of solutions, whose members satisfy the CS modified field equations [Eq. (10.16)], without necessarily being Ricci flat. The intersection of the Einstein and the CS space defines the Pontryagin space, denoted by  $\mathcal{P} := \mathcal{E} \cap \mathcal{CS}$ , whose members satisfy both the Einstein and the modified field equations independently. Therefore, solutions that live in  $\mathcal{P}$  possess a vanishing C-tensor and automatically satisfy the Pontryagin constraint, while those living in  $\mathcal{E} \setminus \mathcal{P}$  satisfy the vacuum Einstein equations but not the Pontryagin constraint. Moreover, solutions that live in  $\mathcal{CS} \setminus \mathcal{P}$  are not Ricci-flat but do satisfy the Pontryagin constraint because they solve the modified field equations. Solutions of class  $\mathcal{P}$  shall be referred to as GR solutions, while solutions of class  $\mathcal{CS} \setminus \mathcal{P}$  shall be referred to as non-GR solutions.

To date, only one non-GR solution has been found perturbatively [317] by assuming a far field expansion for point-particle sources in the PN weak-field/slow-motion approximation. We shall show in the next sections that non-GR solutions exist only in scenarios with a sufficient degree of generality, but not in highly symmetric cases. In the language of dynamical systems theory, the  $\mathcal{P}$  space acts as an “attractor” of highly symmetric solutions, emptying out the  $\mathcal{CS}$  space.

In view of this, let us discuss some properties of solutions that live in the  $\mathcal{P}$  space. In this space, the C-tensor simplifies to

$$C^{ab}|_{R_{ab}=0} = v_{cd} {}^*R^{d(ab)c} = v_{cd} {}^*C^{d(ab)c} = 0, \quad (10.25)$$

---

<sup>11</sup>Actually there is a third limit,  $\mathbf{E} = 0$ , which is either trivial (if also  $\mathbf{B}$  vanishes) or a magnetic monopole.

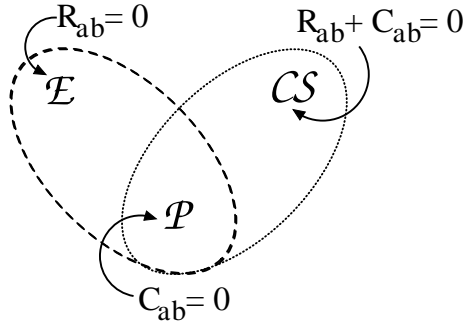


Fig. 10.1. Space of solutions of Einstein gravity  $\mathcal{E}$  and CS modified gravity  $\mathcal{CS}$ .

where  $C_{abcd}$  is the Weyl tensor and  ${}^*C$  its dual, defined in Eqs. (H.2) and (H.3). Equation (10.25) leads to three distinct possibilities:

1. The (dual) Weyl tensor vanishes. However, since class  $\mathcal{P}$  members also have a vanishing Ricci tensor, this condition reduces all possible solutions to Minkowski space.
2. The covariant acceleration of  $\theta$  vanishes. This condition imposes a strong restriction on the geometry (cf. e.g. [334]), which leads to spacetimes that are either flat or exhibit a null Killing vector.
3. Only the contraction of the covariant acceleration with the dual Weyl tensor vanishes.

Moreover, for solutions in  $\mathcal{P}$ , the vanishing of the Ricci tensor forces the Weyl tensor to be divergenceless, via the contracted Bianchi identities. These observations are a clear indication that the solutions inhabiting  $\mathcal{P}$  must be special – for instance, exhibit a certain number of Killing vectors. Conversely, one may expect that solutions inhabiting  $\mathcal{CS} \setminus \mathcal{P}$  cannot be “too special.” We shall put these expectations on a solid basis and confirm them in the next sections.

### 10.3 Persistence of GR solutions

In this section, we study some solutions of GR that are known to persist in CS gravity [79, 297], using the insight on the Pontryagin constraint gained so far. In the language of Sec. 10.2.3 we look for solutions that inhabit  $\mathcal{P}$ , cf. Fig. 10.1.

#### 10.3.1 Schwarzschild Solution

The Schwarzschild solution,

$$ds^2 = -\left(1 - \frac{2M}{r}\right) dt^2 + \left(1 - \frac{2M}{r}\right)^{-1} dr^2 + r^2 \left(d\Theta^2 + \sin^2(\Theta) d\phi^2\right), \quad (10.26)$$

is also a solution of the CS modified field equations if [79]

$$\theta = \frac{t}{\mu} \quad \rightarrow \quad v_\mu = [1/\mu, 0, 0, 0]. \quad (10.27)$$

We refer to Eq. (10.27) as the canonical choice of the CS scalar field [79]. In that case, the C-tensor can be interpreted as a 4-dimensional generalization of the ordinary 3-dimensional Cotton tensor. Moreover, spacetime-dependent reparameterization of the spatial variables and time translation remain symmetries of the modified action [79].

We investigate now the most general form of  $\theta = \theta(t, r, \Theta, \phi)$  that will leave the Schwarzschild metric a solution of the modified theory. The Pontryagin constraint always holds, regardless of  $\theta$ , because the spacetime is spherically symmetric, but  $C_{ab} = 0$  yields non-trivial equations. Since we have chosen the Schwarzschild line element, we cannot force the (dual) Weyl tensor to vanish (option 1 in Sec. 10.2.3), where the only linearly independent component is

$${}^*C_{tr\Theta\phi} = \frac{2M}{r} \sin \Theta. \quad (10.28)$$

Another possibility is to force the scalar field to have a vanishing covariant acceleration (option 2 in Sec. 10.2.3). This condition then yields an over-constrained system of partial differential equations (PDEs), whose only solution for  $M \neq 0$  is the trivial one: constant  $\theta$ . We are thus left with the remaining possibility (option 3 in Sec. 10.2.3), namely that only the contraction of the covariant acceleration with the dual Weyl tensor vanishes. This possibility yields the following set of PDEs

$$\theta_{,t\Theta} = \theta_{,t\phi} = \frac{\partial}{\partial r} \left( \frac{\theta_{,\Theta}}{r} \right) = \frac{\partial}{\partial r} \left( \frac{\theta_{,\phi}}{r} \right) = 0, \quad (10.29)$$

the solution of which is given by

$$\theta = F(t, r) + rG(\Theta, \phi). \quad (10.30)$$

Note that this scalar field possesses a non-vanishing covariant acceleration, namely  $v_{tt}$ ,  $v_{tr}$ ,  $v_{rr}$ ,  $v_{\Theta\Theta}$ ,  $v_{\Theta\phi}$  and  $v_{\phi\phi}$  are non-vanishing, e.g.

$$v_{tt} = \partial_{rr} F - \frac{M}{r^2} \left( 1 - \frac{2M}{r} \right) (\partial_r F + G). \quad (10.31)$$

For the choice of  $\theta$  given in Eq. (10.30) the Schwarzschild solution is always a solution of the modified theory. Note that Eq. (10.30) reduces to the canonical choice for  $G = 0$  and  $F = t/\mu$ , for which the only non-vanishing component of the covariant acceleration is  $v_{tr} = -M/(r^2 f \mu)$ .

This simple calculation of the most general form of the scalar field that respects the Schwarzschild solution leads to two important consequences:

- The existence of specific solutions depends sensitively on the choice of the scalar field.

- The satisfaction of the Pontryagin constraint is a necessary but not a sufficient condition for the C-tensor to vanish.

In order to illustrate the second point, let us consider the scalar field  $\theta = m_{CS} \sin \Theta$ , with  $m_{CS}$  a constant. Then the Pontryagin constraint is still satisfied, but the C-tensor has one non-vanishing component,

$$C_{t\phi} = \frac{3Mm_{CS}}{r^4} \sin^2 \Theta \left( 1 - \frac{2M}{r} \right), \quad (10.32)$$

and the Schwarzschild line element [Eq. (10.26)] is no longer a solution to the modified field equations [Eq. (10.16)].

### 10.3.2 Spherically symmetric metrics

Let us now pose the question whether there can be non-GR solutions in CS modified gravity that preserve spherical symmetry. Any line element respecting this symmetry must be diffeomorphic to (cf. e.g. [340])

$$ds^2 = g_{\alpha\beta}(x^\gamma) dx^\alpha dx^\beta + \Phi^2(x^\gamma) d\Omega_{S^2}^2, \quad (10.33)$$

where  $g_{\alpha\beta}(x^\gamma)$  is a Lorentzian 2-dimensional metric with some coordinates  $x^\gamma$ ,  $\Phi(x^\gamma)$  is a scalar field (often called “dilaton” or “surface radius”) and  $d\Omega_{S^2}^2$  is a line element of the round 2-sphere, with some coordinates  $x^i$ . For such a line element, one can show straightforwardly that the Pontryagin constraint is always satisfied (cf. e.g. appendix A of [341]), and that the only non-vanishing components of the Ricci tensor are  $R_{\alpha\beta}$  and  $R_{ij}$ . On the other hand, for the most general scalar field  $\theta$ , the only non-vanishing components of the C-tensor are of the form  $C_{\alpha i}$ . Remarkably, the C-tensor and the Ricci tensor decouple and both have to vanish independently as a consequence of the modified field equations. In other words, for spherically symmetric line elements there cannot be solutions that live in  $\mathcal{CS} \setminus \mathcal{P}$ . Instead all solutions are pushed to  $\mathcal{P}$ , which then uniquely leads to the Schwarzschild solution by virtue of the Birkhoff theorem<sup>12</sup>.

We have just shown that for all spherically symmetric situations the vacuum solutions to the CS modified field equations live in  $\mathcal{P}$ , and therefore are given uniquely by the Schwarzschild solution. For non-vacuum solutions with the same symmetries, similar conclusions hold, since the field equations still decouple into non-vacuum Einstein equations and the vanishing of the C-tensor. Therefore, all solutions are again pushed to  $\mathcal{P}$  and spherically symmetric solutions of GR (such as the Reissner-Nordström BH or Friedmann-Robertson-Walker spacetimes) persist in CS modified gravity, provided  $\theta$  is of the form

$$\theta = F(x^\gamma) + \Phi(x^\gamma) G(x^i). \quad (10.34)$$

---

<sup>12</sup>The persistence of Birkhoff’s theorem in CS modified gravity was first proved by one of us (NY) in collaboration with C. Sopena [337].

This result is completely analog to Eq. (10.30). In all spherically symmetric scenarios, the solutions to the CS modified field equations live in  $\mathcal{P}$  and the expectations of Sec. 10.2.3 hold.

### 10.3.3 Losing the Kerr solution

As an example of a relevant GR solution that does not persist in the modified theory we consider the Kerr solution. The Kerr metric yields a non-vanishing Pontryagin term<sup>13</sup>, which in Boyer-Lindquist coordinates

$$ds^2 = -\frac{\Delta - a^2 \sin^2 \Theta}{\Sigma} dt^2 - \frac{4aMr \sin^2 \Theta}{\Sigma} dt d\phi \quad (10.35)$$

$$+ \frac{(r^2 + a^2)^2 - a^2 \Delta \sin^2 \Theta}{\Sigma} \sin^2 \Theta d\phi^2 + \frac{\Sigma}{\Delta} dr^2 + \Sigma d\Theta^2 \quad (10.36)$$

can be written as

$${}^*RR = 96 \frac{aM^2 r}{\Sigma^6} \cos \Theta \left( r^2 - 3a^2 \cos^2 \Theta \right) \left( 3r^2 - a^2 \cos^2 \Theta \right), \quad (10.37)$$

with  $\Sigma = r^2 + a^2 \cos^2 \Theta$  and  $\Delta = r^2 + a^2 - 2Mr$ . In light of the physical interpretations of Sec. 10.2.2, one would expect this result since the Kerr spacetime possesses a complex Newman-Penrose scalar  $\Psi_2$ .

The Pontryagin constraint is satisfied in certain limits. For example, as the Kerr parameter goes to zero,  $a \rightarrow 0$ , the Schwarzschild solution is recovered and the right-hand side of Eq. (10.37) vanishes. Similarly, in the limit as the mass goes to zero,  $M \rightarrow 0$ , the right-hand side of Eq. (10.37) also vanishes. However, for any finite  $a$  and  $M$  the Pontryagin term is non-vanishing and, thus, the Kerr spacetime cannot be a solution to the CS modified field equations [327].

What line element then replaces the Kerr solution in the modified theory? A reasonable attempt to construct a spinning BH in CS gravity is to consider axisymmetric and either static or stationary line elements, which we shall investigate in the next sections.

## 10.4 Static, axisymmetric solutions

Before embarking on a *tour de force* through stationary and axisymmetric<sup>14</sup> solutions, we shall first consider the simpler case of static and axisymmetric solutions. Following [342], the most general static and axisymmetric line element is diffeomorphic

<sup>13</sup>Similar conclusions hold for the Kerr-Newman and Kerr-NUT spacetimes.

<sup>14</sup>Stationarity and axisymmetry require not only the existence of two Killing vectors, but also additional conditions, some of which can be considered optional. In the present work we employ stationarity and axisymmetry in the strictest sense possible. In particular, we always impose the integrability conditions  $\xi^a R_{a[b\xi_c\psi_d]} = \psi^a R_{a[b\xi_c\psi_d]} = 0$ . For further discussion of these issues cf. e.g. [334].

to

$$ds^2 = -Vdt^2 + V^{-1}\rho^2 d\phi^2 + \Omega^2 (d\rho^2 + \Lambda dz^2), \quad (10.38)$$

where we have three undetermined functions of two coordinates:  $V(\rho, z)$ ,  $\Omega(\rho, z)$  and  $\Lambda(\rho, z)$ . The two commuting Killing fields,  $\xi^a = (\partial_t)^a$  and  $\psi^a = (\partial_\phi)^a$ , are associated with stationarity and axisymmetry respectively. However, since there is no cross-term  $dt d\phi$ , the line element of Eq. (10.38) is not just stationary but also static. The components of its Ricci tensor are given by

$$R_{t\phi} = R_{t\rho} = R_{tz} = R_{\phi\rho} = R_{\phi z} = 0, \quad (10.39)$$

$$R_{tt} = \frac{1}{2\Omega^2} \left[ V_{,\rho\rho} + \frac{V_{,zz}}{\Lambda} + \frac{V_{,\rho}}{\rho} - \frac{V^2}{V} - \frac{V^2}{V\Lambda} + \frac{V_{,\rho}\Lambda_{,\rho}}{2\Lambda} - \frac{V_{,z}\Lambda_{,z}}{2\Lambda^2} \right], \quad (10.40)$$

$$R_{\phi\phi} = \frac{1}{2\Omega^2} \left[ \frac{\rho^2 V_{,\rho\rho}}{V^2} + \frac{\rho^2 V_{,zz}}{V^2 \Lambda} + \frac{\rho V_{,\rho}}{V^2} - \frac{\rho^2 V^2}{V^3} - \frac{\rho^2 V^2}{V^3 \Lambda} - \frac{\rho \Lambda_{,\rho}}{V\Lambda} + \frac{\rho^2 \Lambda_{,\rho} V_{,\rho}}{2V^2 \Lambda} - \frac{\rho^2 \Lambda_{,z} V_{,z}}{2V^2} \right], \quad (10.41)$$

$$R_{\rho\rho} = \frac{V_{,\rho}}{\rho V} - \frac{V^2}{2V^2} - \frac{\Omega_{,\rho\rho}}{\Omega} - \frac{\Omega_{,zz}}{\Lambda\Omega} + \frac{\Omega_{,\rho}}{\rho\Omega} + \frac{\Omega^2}{\Omega^2} + \frac{\Omega^2}{\Lambda\Omega^2} - \frac{\Lambda_{,\rho\rho}}{2\Lambda} + \frac{\Lambda^2}{4\Lambda^2} - \frac{\Omega_{,\rho}\Lambda_{,\rho}}{2\Lambda\Omega} + \frac{\Omega_{,z}\Lambda_{,z}}{2\Lambda^2\Omega}, \quad (10.42)$$

$$R_{zz} = -\frac{V^2}{2V^2} - \frac{\Lambda\Omega_{,\rho\rho}}{\Omega} - \frac{\Omega_{,zz}}{\Omega} - \frac{\Omega_{,\rho}\Lambda}{\rho\Omega} + \frac{\Omega^2\Lambda}{\Omega^2} + \frac{\Omega^2}{\Omega^2} - \frac{\Lambda_{,\rho\rho}}{2} - \frac{\Lambda_{,\rho}}{2\rho} + \frac{\Lambda^2}{4\Lambda} - \frac{\Omega_{,\rho}\Lambda_{,\rho}}{2\Omega} + \frac{\Omega_{,z}\Lambda_{,z}}{2\Omega\Lambda}, \quad (10.43)$$

$$R_{\rho z} = -\frac{V_{,z}V_{,\rho}}{2V^2} + \frac{V_{,z}}{2\rho V} + \frac{\Omega_{,z}}{\rho\Omega}, \quad (10.44)$$

and exhibit only five non-vanishing components. With the canonical choice of the CS scalar field [Eq. (10.27)] it is now straightforward to check that the five corresponding components of the C-tensor vanish,

$$C_{tt} = C_{\phi\phi} = C_{\rho\rho} = C_{zz} = C_{\rho z} = 0. \quad (10.45)$$

As in the spherically symmetric case, we are faced with the remarkable consequence that the field equations [Eq. (10.16)] decouple into the vacuum Einstein equations plus the

vanishing of the C-tensor, viz.

$$R_{ab} = 0, \quad C_{ab} = 0. \quad (10.46)$$

In other words, using the classification of Sec. 10.2.3, all static and axisymmetric solutions live in  $\mathcal{P}$ , which again confirms previous expectations.

With these considerations in mind, we can now simplify the line element of Eq. (10.38). From [342], the function  $\Lambda$  can be chosen to be constant, e.g.  $\Lambda = 1$ , and therefore the line-element reduces to the Weyl class,

$$ds^2 = -e^{2U} dt^2 + e^{-2U} \left[ e^{2k} (d\rho^2 + dz^2) + \rho^2 d\phi^2 \right]. \quad (10.47)$$

The vacuum Einstein equations then simplify to

$$\Delta U = 0, \quad k_{,\rho} = \rho(U_{,\rho}^2 - U_{,z}^2), \quad k_{,z} = 2\rho U_{,\rho} U_{,z}, \quad (10.48)$$

where  $\Delta = \partial^2/\partial\rho^2 + 1/\rho\partial/\partial\rho + \partial^2/\partial z^2$  is the flat space Laplacian in cylindrical coordinates. The function  $U$  thus solves a Laplace equation, and for any such solution the function  $k$  can be determined by a line integral [334].

The Pontryagin constraint is fulfilled automatically for all line elements diffeomorphic to Eq. (10.47), but as we have seen in the previous sections, this is not sufficient to achieve  $C_{ab} = 0$ . For example, with the choices [343, 344] ( $m$  is constant)

$$U = -\frac{m}{\sqrt{\rho^2 + z^2}}, \quad k = -\frac{m^2 \rho^2}{2(\rho^2 + z^2)^2}, \quad (10.49)$$

the vacuum Einstein equations hold and the Pontryagin constraint is fulfilled, but the C-tensor has the non-vanishing components

$$C_{\rho\phi} = \frac{2m^4 \rho^3 z}{\mu (\rho^2 + z^2)^5} \exp \left[ \frac{m^2 \rho^2}{(\rho^2 + z^2)^2} \right], \quad C_{z\phi} = \frac{1}{2\rho z} C_{\rho\phi}. \quad (10.50)$$

Since the C-tensor must vanish independently from the Einstein equations, once more we are faced with three distinct possibilities, identical to those described in Sec. 10.2.3. The first possibility (option 1 in Sec. 10.2.3) is to demand that the Weyl tensor vanishes, but since also the Ricci tensor vanishes, the spacetime would have to be flat. The second possibility (option 2 in Sec. 10.2.3) is to demand that the covariant acceleration of  $\theta$  vanishes, *i.e.*,  $\nabla_a \theta$  is a covariantly constant vector. However, as we have mentioned already, a vacuum solution with a covariantly constant vector field must be either flat, or the vector must be a null-vector. The first alternative is trivial, while the second one is not particularly interesting in the context of static axisymmetric spacetimes. We shall discuss the latter possibility further in Sec. 10.6.1.

The only remaining possibility (option 3 in Sec. 10.2.3) is for the contraction of the covariant acceleration and the dual Weyl tensor to vanish. The C-tensor can then

be simplified to

$$C^{ab} \propto \Gamma_{\rho t}^t * C^{t(ab)\rho} + \Gamma_{zt}^t * C^{t(ab)z} = 0, \quad (10.51)$$

which has only two non-vanishing components. Using the Einstein equations to simplify these expressions we obtain a set of nonlinear PDEs,

$$\begin{aligned} U_{,\rho z} U_{,\rho} + U_{,zz} U_{,z} &= 2\rho \left( U_{,z}^3 U_{,\rho} + U_{,\rho}^3 U_{,z} \right) - \frac{2}{\rho} U_{,\rho} U_{,z}, \\ U_{,\rho z} U_{,z} - U_{,zz} U_{,\rho} &= \rho \left( U_{,\rho}^4 - U_{,z}^4 \right) - \frac{1}{\rho} U_{,\rho}^2. \end{aligned} \quad (10.52)$$

We used Maple to obtain some solutions to these PDEs. The Schwarzschild solution

$$U = \frac{1}{2} \ln \frac{\sqrt{\rho^2 + (z+M)^2} + \sqrt{\rho^2 + (z-M)^2} - 2M}{\sqrt{\rho^2 + (z+M)^2} + \sqrt{\rho^2 + (z-M)^2} + 2M} \quad (10.53)$$

of course solves these PDEs. Some other simple solutions are  $U = U_0$ ,  $U = U_0 \pm \ln \rho$  and  $U = U_0 + \ln(\sqrt{\rho^2 + z^2} + z)/2$ , where  $U_0$  is a constant. Not only do these solution yield a vanishing Ricci tensor, but they also yield a vanishing Riemann tensor, which shows they are Minkowski spacetime in disguise. In addition to these trivial solutions, there exist exactly two more:

$$ds^2 = -\frac{1}{z} dt^2 + z dz^2 + z^2 (d\rho^2 + \rho^2 d\phi^2) \quad (10.54)$$

and

$$\begin{aligned} ds^2 &= -\left(\frac{2m}{z} - 1\right) dt^2 + \left(\frac{2m}{z} - 1\right)^{-1} dz^2 \\ &+ z^2 (d\rho^2 + \sinh^2 \rho d\phi^2) \end{aligned} \quad (10.55)$$

While these solutions certainly are non-trivial, neither the first [Eq. (10.54)] nor the second [Eq. (10.55)] solution is physically relevant. The former has a naked singularity at  $z = 0$ , while the latter, whose singularity at  $z = 0$  is screened by a Killing horizon at  $z = 2m = \text{const.}$ , possesses a Killing vector  $k^a = (\partial_t)^a$  that is spacelike in the “outside” region  $z > 2m$ , *i.e.*  $g_{ab} k^a k^b = 1 - 2m/z > 0$ .

Let us now prove that these are the only solutions to the modified field equations. The crucial observation is that the spatial part of the C-tensor for static, axisymmetric spacetimes reduces to the 3-dimensional Cotton tensor [79]. This tensor vanishes if and only if the corresponding 3-dimensional space (spatial sector of the 4-dimensional metric) is conformally flat, *i.e.*  $g_{ij} = \Phi \delta_{ij}$ , where the conformal factor  $\Phi$  is a function of the coordinates and  $\delta_{ij}$  is the spatial part of the Minkowski metric. We may then exploit a result by Lukács and Perjés [345] that the line elements of Eqs. (10.54), (10.55) and (10.26) are the only static and axisymmetric solutions that are spatially conformally flat. Therefore, it follows that these equations are the only solutions to the modified field equations.

The above considerations also apply to more general CS scalar fields. All simplifications hinge on the decoupling of the modified field equations, which occurs if and only if  $\theta_{,t\phi} = 0$ . We can solve this PDE to obtain

$$\theta = \theta_1(t, \rho, z) + \theta_2(\rho, z, \phi). \quad (10.56)$$

For all scalar fields of this form, the modified field equations decouple and the C-tensor has five non-vanishing components, which define a system of PDEs for one of the two arbitrary functions  $k$  or  $U$ . However, we do not expect more solutions to arise in this way, since this case leads to the same constraints as the canonical one, plus three extra PDEs, which essentially compensate the freedom to tinker with the two arbitrary functions in Eq. (10.56).

The most general CS scalar field, however, does not allow for a decoupling of the type described above. If the scalar field has  $\theta_{,t\phi} \neq 0$ , then the  $(\rho, \rho)$ ,  $(\rho, z)$  and  $(z, z)$  components of the modified field equations do not decouple. However, the  $(t, t)$  and  $(\phi, \phi)$  components still do decouple because the corresponding C-tensor components vanish. The equation

$$R^t_t + R^\phi_\phi = -\frac{1}{2} \frac{\Lambda_{, \rho}}{\Lambda \rho^2 \Omega^2} = 0, \quad (10.57)$$

forces  $\Lambda$  to be a function of  $z$  alone. Through a diffeomorphism, this function can be set to unity, as argued in [342].

The modified field equations are too difficult to solve analytically with Maple, so in order to study solutions that do not lead to a decoupling of the modified field equations, we shall assume for simplicity  $\theta = \tilde{\theta}(t, \phi)$ . From the Ricci sector of the field equations ( $R_{tt} = 0 = R_{\phi\phi}$ ) we find that  $U$  is again a solution of  $\Delta U = 0$ . We can use this relation to simplify the C-tensor, and the ensuing equations  $C_{t\phi} = C_{t\rho} = C_{tz} = C_{\phi\rho} = C_{\phi z} = 0$  lead to a system of second order PDEs for  $\theta$  and  $k$ . We investigated this system with Maple and found that solutions exist if and only if  $\theta$  is a function of only one variable, *i.e.*  $\theta = \theta(t)$  or  $\theta = \theta(\phi)$ . These results indicate that there are no solutions of the modified field equations if  $\theta$  is bivariate.

In summary, we have shown in this section that the field equations decouple if the CS scalar field solves  $\theta_{,t\phi} = 0$ , and their solution is the Schwarzschild BH and two additional (unphysical) solutions [Eqs. (10.54) and (10.55)]. For CS fields that satisfy  $\theta_{,t\phi} \neq 0$ , the modified field equations do not seem to have a solution. Therefore, there are no static and axisymmetric solutions in CS gravity, apart from the Schwarzschild BH and some unphysical solutions, irrespective of the CS scalar field.

## 10.5 Stationary, axisymmetric solutions

### 10.5.1 General line elements

Equipped with the tools from the previous section, we drop the requirement of staticity and replace it by the weaker one of stationarity. In essence, this means that we shall allow the gravitomagnetic sector of the metric to be different from zero. The most

general, stationary and axisymmetric line-element is diffeomorphic to [334]

$$ds^2 = -V(dt - wd\phi)^2 + V^{-1}\rho^2 d\phi^2 + \Omega^2(d\rho^2 + \Lambda dz^2), \quad (10.58)$$

where the functions  $V$ ,  $w$ ,  $\Omega$  and  $\Lambda$  depend on  $\rho$  and  $z$ , only. This line element is identical to Eq. (10.38) as  $w \rightarrow 0$ . In GR, the function  $w$  can be identified with the angular velocity. The Ricci tensor for this line element is similar to  $R_{ab}^{\text{static}}$  [Eqs. (10.39)-(10.44)] and its components are

$$R_{t\rho} = R_{tz} = R_{\phi\rho} = R_{\phi z} = 0, \quad (10.59)$$

$$R_{tt} = R_{tt}^{\text{static}} + \left(w_{,\rho}^2 + \frac{w_{,z}^2}{\Lambda}\right) \frac{V^3}{2\rho^2\Omega^2}, \quad (10.60)$$

$$\begin{aligned} R_{t\phi} = \frac{w}{2\Omega^2} & \left[ -V_{,\rho\rho} - \frac{V_{,zz}}{\Lambda} - \frac{V_{,\rho}}{\rho} + \frac{V^2}{V} + \frac{V^2}{V\Lambda} - 2\frac{V_{,\rho}w_{,\rho}}{w} - 2\frac{V_{,z}w_{,z}}{w\Lambda} - \frac{w_{,\rho\rho}V}{w} \right. \\ & - \frac{w_{,zz}V}{w\Lambda} + \frac{w_{,\rho}V}{\rho w} - \frac{w^2 V^3}{\rho^2} - \frac{w^2 V^3}{\rho^2\Lambda} - \frac{\Lambda_{,\rho}V_{,\rho}}{2\Lambda} + \frac{\Lambda_{,z}V_{,z}}{2\Lambda^2} - \frac{\Lambda_{,\rho}w_{,\rho}V}{2w\Lambda} \\ & \left. + \frac{\Lambda_{,z}w_{,z}V}{2w\Lambda^2} \right], \quad (10.61) \end{aligned}$$

$$R_{\rho\rho} = R_{\rho\rho}^{\text{static}} + w_{,\rho}^2 \frac{V^2}{2\rho^2}, \quad (10.62)$$

$$R_{zz} = R_{zz}^{\text{static}} + w_{,z}^2 \frac{V^2}{2\rho^2}, \quad (10.63)$$

$$R_{\rho z} = R_{\rho z}^{\text{static}} + w_{,\rho}w_{,z} \frac{V^2}{2\rho^2}, \quad (10.64)$$

$$R = R^{\text{static}} + \left(w_{,\rho}^2 + \frac{1}{\Lambda}w_{,z}^2\right) \frac{V^2}{2\rho^2\Omega^2}. \quad (10.65)$$

The somewhat lengthy component  $R_{\phi\phi}$  can be deduced from  $R$  and the other components. The quantity  $R^{\text{static}}$ ,

$$\begin{aligned} R^{\text{static}} = \frac{1}{2\Omega^2} & \left[ 2\frac{V_{,\rho}}{V\Lambda} - \frac{V^2}{V^2} - \frac{V^2}{V^2\Lambda} - 4\frac{\Omega_{,\rho\rho}}{\Omega} - 4\frac{\Omega_{,zz}}{\Lambda\Omega} + 4\frac{\Omega_{,\rho}^2}{\Omega^2} + 4\frac{\Omega_{,z}^2}{\Lambda\Omega^2} \right. \\ & \left. - 2\frac{\Lambda_{,\rho\rho}}{\Lambda} - 2\frac{\Lambda_{,\rho}}{\rho\Lambda} + \frac{\Lambda^2}{\Lambda^2} - 2\frac{\Lambda_{,\rho}\Omega_{,\rho}}{\Lambda\Omega} + 2\frac{\Lambda_{,z}\Omega_{,z}}{\Lambda^2\Omega} \right], \quad (10.66) \end{aligned}$$

is the trace of Eqs. (10.39)-(10.44).

As before, let us begin with the canonical choice for the CS scalar field, namely Eq. (10.27). Then the only non-zero components of the C-tensor are  $C_{\rho t}$ ,  $C_{zt}$ ,  $C_{\rho\phi}$  and

$C_{z\phi}$ . As in the previous cases, there is a decoupling of the field equations that allows us to set  $\Lambda = 1$  and to consider the slightly simpler line element (Lewis-Papapetrou-Weyl metric)

$$ds^2 = -e^{2U}(dt - wd\phi)^2 + e^{-2U} \left[ e^{2k}(d\rho^2 + dz^2) + \rho^2 d\phi^2 \right], \quad (10.67)$$

where again the functions  $U$ ,  $k$  and  $w$  depend on the coordinates  $\rho$  and  $z$  only. With this line element, the last lines vanish in the multi-line expressions for the Ricci tensor, Eqs. (10.40)-(10.43), (10.61) and (10.66), because  $\Lambda = 1$ . The vacuum Einstein equations simplify considerably with  $\Lambda = 1$ . Essentially, they are similar to Eq. (10.48) but with a complicated source and an additional equation for  $w$ . Even within GR, explicit solution to this set of PDEs can only be found in certain special cases [334].

The Pontryagin constraint for the line element of Eq. (10.67) is not satisfied in general. This constraint yields a complicated second order PDE for  $w$ ,  $U$  and  $k$ , presented in appendix I, which of course is trivially satisfied as  $w \rightarrow 0$ . Certain solutions to the PDE in appendix I can be obtained, e.g. ( $\bar{w} := e^{2U} w$ )

$$k = k(\rho, z), \bar{w} = c_1 e^{2U}, U = U(\rho, z), \quad (10.68a)$$

$$k = k(\rho, z), \bar{w} = \pm \rho, U = U(\rho, z), \quad (10.68b)$$

$$k = \ln(\rho) + \tilde{k}(z), \bar{w} = \tilde{w}(z)\rho, U = \frac{1}{2} \ln(\rho) + c_1, \quad (10.68c)$$

$$k = k(\rho), \bar{w} = \bar{w}(\rho), U = U(\rho), \quad (10.68d)$$

where  $c_1$  is a constant. The first line reduces to static solutions upon redefining  $t' = t - c_1 \phi$ . The second line leads to metrics of Petrov type *II*, the so-called van Stockum class, which we shall discuss in Sec. 10.5.2. The third line of Eq. (10.68) cannot be made to solve the modified field equations. The last line implies cylindrical symmetry, which again via the field equations leads to flat spacetime. We have thus been unable to find non-trivial solutions either by hand or using symbolic manipulation software<sup>15</sup>.

Unlike the previous section, we cannot provide here a truly exhaustive discussion of all solutions of the decoupled field equations. This is because  $C_{ab} = 0$  does not necessarily imply spatial conformal flatness for the stationary case. Based on the evidence found so far, it seems unlikely that there are other non-trivial and physically interesting solutions besides the static ones. This is because the vacuum Einstein equations [ $R_{ab} = 0$ ] already determine the function  $k$  uniquely up to an integration constant, and also impose strong restrictions on the functions  $U$  and  $w$  [334]. The constraints  $C_{ab} = 0$  impose four additional conditions on these functions that can be found in [346]. Since the system of partial differential equations is over-constrained, it is unlikely that additional solutions exist. Therefore, whenever the field equations decouple into  $R_{ab} = 0 = C_{ab}$  we do not expect physically relevant solutions besides the Schwarzschild one and its flat space limit.

The decoupling exhibited by the modified field equations does not occur only for the canonical choice of the CS scalar field. In order for such a decoupling to occur, the

---

<sup>15</sup>We were able to find additional solutions with Maple, but upon imposing the field equations they reduced to previously studied or trivial spacetimes.

following system of PDEs must be satisfied:

$$\theta_{,tt} = \theta_{,\phi\phi} = \theta_{,t\phi} = \theta_{,\rho} = \theta_{,z} = 0, \quad (10.69)$$

which yields the solution

$$\theta = \frac{t}{\mu} + \frac{\phi}{\nu}, \quad (10.70)$$

with constant  $\mu, \nu$ . The canonical choice is recovered as  $\nu \rightarrow \infty$ .

But what if the scalar field is not of the form of Eq. (10.70)? In this case, the field equations do not decouple and solving the entire system is much more complicated. However, we can deduce from Eq. (10.59) that still the four C-tensor components  $C_{\rho t}$ ,  $C_{zt}$ ,  $C_{\rho\phi}$  and  $C_{z\phi}$  have to vanish. Therefore, even though no decoupling occurs, the same issue of an over-constrained system of equations does arise, analogous to the one in Sec. 10.5.1. Even with this generalization, it is still quite difficult to find solutions to the coupled system. In general, one might be able to find solutions both of class  $\mathcal{P}$  and class  $\mathcal{CS} \setminus \mathcal{P}$  because non-canonical CS fields allow for general  $\theta$ , which entails a new degree of freedom. We shall see in Sec. 10.5.2 that for a simplified subclass of stationary and axisymmetric line elements, which automatically satisfy the Pontryagin constraint, solutions can indeed be found, including mathematical BHs.

### 10.5.2 Van Stockum line element

We study now a slightly less general line element that still is stationary and axisymmetric, namely the van Stockum line element [334]

$$ds^2 = \rho\Omega dt^2 - 2\rho dt d\phi + \frac{1}{\sqrt{\rho}} (d\rho^2 + dz^2), \quad (10.71)$$

where the only arbitrary function is  $\Omega = \Omega(\rho, z)$ . The metric is different from that considered in Eq. (10.67) since it does not possess a  $d\phi^2$  component. The only non-vanishing component of the Ricci tensor for such a spacetime is

$$R_{tt} = -\frac{\rho^{3/2}}{2} \Delta\Omega, \quad (10.72)$$

where again  $\Delta$  is the flat space Laplacian in cylindrical coordinates.

The Pontryagin constraint is automatically satisfied for the van Stockum line element even though it is of Petrov type *II*, precisely because of the vanishing  $d\phi^2$  term. The *tt* component of the modified equations then determines  $\Omega$ , and this forces all other components of the C-tensor to vanish, except for  $C_{t\phi}$  and  $C_{\phi\phi}$  that are automatically zero. These constraints act as a system of PDEs for the scalar field, whose unique solution is  $\theta = \theta(\rho, z)$ . Note that the canonical choice for  $\theta$  is not compatible with the van Stockum line element. The remaining PDE  $R_{tt} + C_{tt} = 0$  can be solved for  $\theta$  and  $\Omega$ ,

where  $C_{tt}$  now simplifies to

$$C_{tt} = \frac{\rho^2}{2} \left[ (\theta_{,\rho\rho} - \theta_{,zz})(\Omega_{,\rho z} + \frac{3}{4\rho}\Omega_{,z}) + \theta_{,\rho}(\Omega_{,zzz} + \Omega_{,\rho\rho z} + \frac{3}{2\rho}\Omega_{,\rho z} + \frac{3}{8\rho^2}\Omega_{,z}) \right. \\ \left. - \theta_{,z}(\Omega_{,\rho\rho\rho} + \Omega_{,\rho z z} + \frac{9}{4\rho}\Omega_{,\rho\rho} + \frac{3}{4\rho}\Omega_{,zz} + \frac{3}{8\rho^2}\Omega_{,\rho}) - \theta_{,\rho z}(\Omega_{,\rho\rho} - \Omega_{,zz} + \frac{3}{2\rho}\Omega_{,\rho}) \right]. \quad (10.73)$$

Combining this with  $R_{tt}$  from Eq. (10.72) we find two simple solutions of Eq. (10.16):

$$\Omega = c, \quad \theta = \theta(\rho, z), \quad (10.74)$$

where  $c$  is a constant and

$$\Omega = c + \frac{d}{\sqrt{\rho}}, \quad \theta = \frac{2}{3}\sqrt{\rho}z + \tilde{\theta}(\rho), \quad (10.75)$$

where  $c$  and  $d$  are constants<sup>16</sup>. Equation (10.74) leads to zero Ricci and C-tensor separately and it is thus a GR solution that belongs to the subspace  $\mathcal{P}$ . The ensuing metric is exceptional in that it has a third Killing vector,  $t\partial_t - \phi\partial_\phi + ct\partial_\phi$ . Some of the non-vanishing Riemann tensor components for this geometry are

$$R_{t\rho t\rho} = \frac{c}{8\rho}, \quad R_{t\rho\rho\phi} = \frac{1}{8\rho}, \quad R_{t\phi t\phi} = \frac{1}{4}\sqrt{\rho}. \quad (10.76)$$

On the other hand, Eq. (10.75) is perhaps even more interesting since it is not Ricci-flat, but has one non-vanishing component of the Ricci tensor,

$$R_{tt} = -\frac{d}{8\rho} = -C_{tt}. \quad (10.77)$$

This solution is thus a non-GR solution and it belongs to the subspace  $\mathcal{CS} \setminus \mathcal{P}$ . Some of the non-vanishing components of the Riemann tensor for this solution are

$$R_{t\rho t\rho} = \frac{d + 2c\sqrt{\rho}}{16\rho^{3/2}}, \quad R_{t\rho\rho\phi} = \frac{1}{8\rho}, \quad R_{t\phi t\phi} = \frac{1}{4}\sqrt{\rho}. \quad (10.78)$$

Notice that such a solution can represent a mathematical BH, provided  $\Omega$  vanishes for some  $\rho$ , *i.e.* a Killing horizon emerges. We call these configurations “mathematical BHs” because they are physically not very relevant: the Killing vector generating axial symmetry is light-like, as evident from (10.71), and the spacetime admits closed timelike curves which are not screened by a horizon [334]. For  $c = 1$  and  $d = -2m$  we recover (10.2).

---

<sup>16</sup>There is a straightforward generalization of Eq. (10.75), namely  $\Omega = c + d/\rho^\alpha$ ,  $\theta = \beta\sqrt{\rho}z$ , where  $\alpha$  is an arbitrary constant and  $\beta = 8\alpha/(8\alpha^2 + 2\alpha + 3)$ .

Let us then summarize the most important conclusions of this section. We have investigated stationary and axisymmetric solutions to the modified field equations. We found that, for the canonical choice of  $\theta$ , it is unlikely that solutions can be found that differ from Minkowski and Schwarzschild. Nonetheless, for non-canonical choices of this scalar, solutions must exist. This conclusion derives from the investigation of a slightly less general stationary and axisymmetric metric, namely that of van Stockum. For this line element we found a solution to the modified field equations that lives in  $\mathcal{P}$  and a family of solutions that live in  $\mathcal{CS} \setminus \mathcal{P}$ , both with non-canonical CS scalar fields. To our knowledge, this is the first time an exact non-GR solution is found for CS modified gravity, which in particular can represent mathematical BH configurations.

## 10.6 Beyond the canon

We have failed in finding an exact, stationary and axisymmetric solution to the CS modified field equations representing a physical spinning BH. A solution, however, already exists for a similar line element, albeit in a perturbative sense. In [317] and later in [83], a far-field solution to the CS modified field equations with a canonical CS scalar field was found in the weak-field/slow-motion approximation. This solution is identical to the far-field expansion of the Kerr solution, except for the addition of two new components in the gravitomagnetic sector of the metric  $g_{0i}$ . These components vanish in GR, since only one component is required and it is aligned with the angular momentum of the spinning source. In CS gravity, the remaining components of  $g_{0i}$  are proportional to the curl of the spin angular momentum, thus breaking axisymmetry but preserving stationarity. Such a stationary, but non-axisymmetric BH will not emit gravitational waves, but it might possess a non-trivial multipolar structure, with probably more than just two non-vanishing multipoles. Such a far-field structure suggests that perhaps the only way to obtain an analog to the Kerr solution in CS gravity is to relax either the assumption of axisymmetry or stationarity or to drop the integrability conditions mentioned in footnote [99].

Alternatively, the van Stockum example suggests that another possibility is to allow for a general CS scalar field. In this case, however, the line element must significantly differ from the Kerr metric such that it satisfies the Pontryagin constraint<sup>17</sup>. We shall explore these possibilities in this section.

### 10.6.1 Killing embedding

We study now the possibility that the 'embedding coordinate', *i.e.*, the velocity of the CS scalar field  $\theta$ , is a Killing vector. Then,  $v_a$  is covariantly conserved because of the Killing equation ( $\nabla_{(a} v_{b)} = 0$ ) and the fact that the connection is torsion-free

---

<sup>17</sup>We attempted to solve the modified field equations with a line element equal to Kerr plus a stationary and axisymmetric contribution and an arbitrary CS scalar field. No solution could be found exactly, while perturbatively such an Ansatz leads to non-asymptotically flat solutions [327].

( $\nabla_{[a}v_{b]} = \nabla_{[a}\nabla_{b]}\theta = 0$ ). This puts a strong restriction on spacetime, which for a timelike  $v_a$  yields line elements that are diffeomorphic to

$$ds^2 = -dt^2 + g_{ij}(x^k)dx^i dx^j, \quad (10.79)$$

where  $i$  and  $j$  range over all coordinates except time. Actually, Eq. (10.79) describes a special class of static spacetimes. When studying static solutions to the CS modified field equations with timelike  $v_a$  in Sec. 10.4, we found no physically relevant solution besides Schwarzschild. The same conclusions hold here, except that we do not even recover Schwarzschild, so this route is not a promising one. A similar discussion applies to spacelike Killing vectors.

A more interesting situation arises if the vector field  $v^a$  is a null Killing vector,  $v^a v_a = \nabla_{(a}v_{b)} = 0$ . In this case, we get in an adapted coordinate system the line element

$$ds^2 = -2dvdx^1 + g_{ij}(x^k)dx^i dx^j \quad (10.80)$$

Once again, the Pontryagin constraint is immediately satisfied, the Ricci tensor has non-vanishing  $R_{ij}$  components, but no components of the C-tensor vanish. Even when we pick a simple null Killing embedding, e.g.  $v_a = (0, \chi, 0, 0)$  with  $\chi = \text{const.}$ , the C-tensor has complicated spatial non-vanishing components and the modified field equations are too difficult to solve in full generality. Therefore, we focus instead on an interesting special case in the next subsection.

### 10.6.2 pp-waves and boosted black holes

As suggested at the end of Sec. 10.2.2, it might be possible to find solutions to the modified field equations if one considers line elements that represent exact gravitational wave solutions (pp-waves [347]). The line element for these waves is

$$ds^2 = -2dvdu - H(u, x, y)du^2 + dx^2 + dy^2, \quad (10.81)$$

which is simply a special case of the line elements considered in the previous subsection [Eq. (10.80)]. Particular examples of physical scenarios that are well-represented by Eq. (10.81) are the Aichelburg-Sexl limits [348] of various BHs. In essence, this limit is an ultrarelativistic boost that keeps the energy of the BH finite by taking a limit where its mass vanishes while the boost velocity approaches the speed of light. In particular, Eq. (10.81) can be used to represent ultrarelativistic boosts of the Kerr BH [349, 350].

Is it conceivable that a Kerr BH that moves ultrarelativistically solves the modified field equations, even though the Kerr BH does not? One of the main problems with the Kerr metric is that it does not satisfy the Pontryagin constraint, cf. Eq. (10.37), but that constraint is trivially satisfied as  $M \rightarrow 0$ . Nonetheless, the satisfaction of the Pontryagin constraint is only a necessary condition, but not a sufficient one, to guarantee that the modified field equations are also satisfied.

In order to study this issue, let us find the appropriate expressions for the Ricci and C-tensors. The only non-vanishing component of the Ricci tensor for the line element

of Eq. (10.81) is given by

$$R_{uu} = \Delta H, \quad \Delta := \frac{\partial^2}{\partial x^2} + \frac{\partial^2}{\partial y^2}. \quad (10.82)$$

In general, the components  $C_{ux}$ ,  $C_{uy}$ ,  $C_{xx}$ ,  $C_{yy}$ ,  $C_{xy}$  are all non-vanishing and form a system of PDEs for  $H$  and  $\theta$ . The  $C_{xx}$ ,  $C_{yy}$  and  $C_{xy}$  components are given by

$$C_{yy} = -C_{xx} = \theta_{,vv} H_{,xy}, \quad C_{xy} = \frac{1}{2} \theta_{,vv} (H_{,xx} - H_{,yy}). \quad (10.83)$$

Let us first look for GR-solutions of class  $\mathcal{P}$ , such that  $R_{ab} = 0$  and  $C_{ab} = 0$  independently. Since  $C_{ab} = 0$ , there are two possibilities here: either  $\theta_{,vv} = 0$  or  $H_{,xy} = 0 = H_{,xx} - H_{,yy}$ . In the latter case,  $H$  is constrained to

$$H = \frac{1}{2} (x^2 + y^2) A(u) + x B(u) + y C(u) + D(u), \quad (10.84)$$

which also forces  $C_{ux}$  and  $C_{uy}$  to vanish. The only component of the field equations left is  $(u, u)$ , which upon simplification with Eq. (10.84) yields  $C_{uu} = 0$  and  $R_{uu} = 2A(u)$ , so that  $A(u) = 0$ . We have then found the solution

$$H = x B(u) + y C(u) + D(u), \quad \theta = \theta(u, v, x, y), \quad (10.85)$$

to the modified field equations. However, this solution is nothing but flat space in disguise.

Another possibility to find GR-solutions is to pick  $\theta$  such that  $C_{xx}$ ,  $C_{yy}$  and  $C_{xy}$  vanish, *i.e.*  $\theta_{,vv} = 0$ . This condition leads to

$$\theta = \lambda(u, x, y)v + \tilde{\theta}(u, x, y), \quad (10.86)$$

The remaining non- $(u, u)$  components of the C-tensor lead to

$$C_{ux} = 0 \quad \rightarrow \quad \lambda_{,x} H_{,xy} = \lambda_{,y} H_{,yy} \quad (10.87)$$

$$C_{uy} = 0 \quad \rightarrow \quad \lambda_{,x} H_{,yy} = \lambda_{,y} H_{,xx} \quad (10.88)$$

where we have used  $R_{uu} = 0$ . The solution to this system of PDEs leads either to flat spacetime or to

$$\lambda(u, x, y) = \lambda(u). \quad (10.89)$$

Choosing Eq. (10.89), the remaining modified field equation [the  $(u, u)$  component] becomes

$$\Delta H = 0, \quad (10.90)$$

$$2H_{,yy} \tilde{\theta}_{,xy} = H_{,xy} (\tilde{\theta}_{,yy} - \tilde{\theta}_{,xx}). \quad (10.91)$$

For some  $H$  that solves the Einstein equations [*i.e.* the Laplace equation in Eq. (10.90)], the C-tensor yields a PDE for  $\tilde{\theta}$  [Eq. (10.91)]. Thus we conclude that we can lift any

pp-wave solution of the vacuum Einstein equations to a pp-wave solution of CS modified gravity (of class  $\mathcal{P}$ ) by choosing  $\theta$  such that Eqs. (10.86), (10.89)-(10.91) hold.

Let us give an example of this method to generate CS solutions by studying ultrarelativistically boosted Kerr BHs, for which

$$H = h_0 \delta(u) \ln(x^2 + y^2) \quad (10.92)$$

satisfies Eq. (10.90). In Eq. (10.92),  $\delta(u)$  is the Dirac delta function and  $h_0$  is a constant. Inserting this  $H$  into Eq. (10.91) we find

$$\tilde{\theta} = x\alpha\left(\frac{y}{x}\right) + \beta\left(x^2 + y^2\right), \quad (10.93)$$

where  $\alpha$  and  $\beta$  are arbitrary functions of their respective arguments  $(y/x)$  and  $(x^2 + y^2)$ . Equation (10.93), together with Eq. (10.86) and (10.89), give the full solution for the CS scalar field. We have therefore lifted the boosted Kerr BH to a solution of the modified field equations of class  $\mathcal{P}$  by choosing the CS scalar field appropriately. For  $\theta = \lambda v$  we recover Eq. (10.3).

Let us now search for non-GR solutions to the modified field equations. Since all equations decouple except for the  $(u, u)$  component, we must enforce that the non  $(u, u)$ -components of the C-tensor vanish, *i.e.*  $\theta_{,v} = 0$ , which leads to

$$\theta = \tilde{\theta}(u, x, y). \quad (10.94)$$

With Eq. (10.94), the only component of the modified field equations left is again the  $(u, u)$  one, which simplifies to a linear third order PDE:

$$(1 + \tilde{\theta}_{,y}\tilde{\theta}_{,x} - \tilde{\theta}_{,x}\tilde{\theta}_{,y})\Delta H = (\tilde{\theta}_{,xx} - \tilde{\theta}_{,yy})H_{,xy} - (H_{,xx} - H_{,yy})\tilde{\theta}_{,xy}. \quad (10.95)$$

For simplicity, we choose

$$\tilde{\theta} = a(u)x + b(u)y + c(u), \quad (10.96)$$

and Eq. (10.95) reduces to the poisson equation

$$\Delta H = f. \quad (10.97)$$

The source term  $f$  solves a linear first order PDE

$$bf_{,x} - af_{,y} - f = 0, \quad (10.98)$$

whose general solution [assuming  $b(u) \neq 0$ ]

$$f(u, x, y) = e^{x/b(u)} \phi[a(u)x + b(u)y] \quad (10.99)$$

contains one arbitrary function  $\phi$  of the argument  $a(u)x + b(u)y$ . We shall assume this function to be non-vanishing so that  $R_{ab} \neq 0$ . We can now insert Eq. (10.99) into the poisson equation and solve for  $H(x, y, u)$ . We need two boundary conditions to determine  $H$  from the poisson equation [Eq. (10.97)] and another one to determine the arbitrary

function  $\phi$  in Eq. (10.99). Let us then provide an example by assuming that  $b(u) < 0$  and  $\phi$  remains bounded. In this case, we must restrict the range of the coordinates to the half-plane,  $0 \leq x < \infty$ ,  $-\infty < y < \infty$ . We impose a boundary condition  $H_0(u, y) := H(u, 0, y)$  and appropriate fall-off behavior for  $|y| \rightarrow \infty$ . We then obtain the particular solution

$$\begin{aligned}
 H(u, x, y) &= \frac{1}{\pi} \int_{-\infty}^{\infty} \frac{x H_0(u, \eta) d\eta}{x^2 + (y - \eta)^2} - \frac{1}{4\pi} \int_0^{\infty} \int_{-\infty}^{\infty} e^{-\xi/|b(u)|} \phi [a(u)\xi + b(u)\eta] \\
 &\quad \times \ln \left[ \frac{(x + \xi)^2 + (y - \eta)^2}{(x - \xi)^2 + (y - \eta)^2} \right] d\xi d\eta
 \end{aligned} \tag{10.100}$$

where the double integral extends over the half-plane.

The exponential behavior in Eq. (10.99) is particularly interesting, since it resembles the gravitational wave solutions found in Refs. [79, 316, 277, 272]. Moreover, as  $x \rightarrow \pm\infty$  [depending on the sign of  $b(u)$ ] the source term in Eq. (10.97) diverges, indicating a possible instability. Since we were mainly concerned with the existence of solutions we have not attempted to construct solutions for more general  $\theta$  than Eq. (10.96).

### 10.6.3 Weakening axisymmetry/stationarity

From the analysis so far, it is clear that stationary and axisymmetric solutions in CS gravity do not seem to be capable of describing physical spinning BHs. The far-field solution has guided us to weaken some of the requirements necessary for axisymmetry and stationarity. One possibility is to keep two Killing vectors (one time-like and one space-like), but to drop all additional requirements (in particular the integrability conditions mentioned in footnote [99]). The most general line-element compatible with two Killing vectors

$$ds^2 = g_{\alpha\beta} dx^\alpha dx^\beta + A_{\alpha i} dx^\alpha dx^i + g_{ij} dx^i dx^j \tag{10.101}$$

contains two 2-metrics,  $g_{\alpha\beta}(x^k)$  and  $g_{ij}(x^k)$ , and cross-terms parameterized by  $A_{\alpha i}(x^k)$ . Here  $\{\alpha, \beta\} = \{0, 1\}$  are the Killing coordinates and  $\{i, j, k\} = \{2, 3\}$  are the non-Killing coordinates. Alternatively we could conceive of losing stationarity or axisymmetry by dropping the  $(\partial_t)^a$  or  $\partial_\phi^a$  Killing vector, respectively. The general idea is then that by losing one Killing vector we gain new undetermined metric components that could allow for a physical spinning BH solution in CS gravity. However, our attempts have not revealed any interesting exact solution corresponding to a spinning BH, so we confine ourselves to a couple of general remarks.

Spinning BHs that break axisymmetry or stationarity would be radically different from those considered in GR. On the one hand, non-axisymmetric spinning objects would have an intrinsic precession rate that would not allow the identification of an axis of rotation. Such precession would possibly also lead to solutions with more than two non-zero multipole moments, thus violating the no-hair theorem. On the other hand, non-stationary spinning objects would unavoidably lead to the emission of gravitational radiation, even if the BH is isolated. These considerations could be flipped if we take

them as predictions of the theory, thus leading to new possible tests of CS gravity. Work along these lines is currently underway. The results of [351] for the Pontryagin constraint may be helpful here.

#### 10.6.4 Adding matter

The inclusion of matter sources is of relevance in the present context for several reasons. First, the Kerr BH has a distributional energy momentum tensor [352], so we need not set the stress-energy tensor strictly to zero to construct a Kerr-like solution. Second, in Ref. [73] the Pontryagin-term in the action arises from matter currents, so the inclusion of the latter would actually be mandatory within that framework.

Two conceptually different approaches are possible to the problem of finding exact solutions of the modified field equations in the presence of matter. These approaches essentially depend on whether we require the energy-momentum tensor to be covariantly conserved,  $\nabla_a T^{ab} = 0$ , or not. If this tensor is conserved, then the Pontryagin constraint must be satisfied and the Kerr BH cannot be a solution. Basically, this route leads to only a slight generalization of the discussion presented so far, with solutions of class  $\mathcal{P}$ ,

$$R_{ab} - \frac{1}{2}g_{ab}R = 8\pi T_{ab}, \quad C_{ab} = 0, \quad (10.102)$$

and solutions of class  $\mathcal{CS} \setminus \mathcal{P}$  that solve Eq. (10.15). Relaxing covariant conservation of the stress-energy tensor, we can promote the Kerr BH to a solution of the modified field equations, provided that

$$R_{ab} - \frac{1}{2}g_{ab}R = 8\pi T_{ab}^{\text{dist}}, \quad C_{ab} = 8\pi T_{ab}^{\text{ind}}. \quad (10.103)$$

Here  $T_{ab}^{\text{dist}} = 0$  except for the usual distributional contributions for Kerr [352], while  $T_{ab}^{\text{ind}}$  provides the non-conserved matter flux. The induced matter fluxes for the Kerr BH are given by

$$\begin{aligned} T_{tr}^{\text{ind}} &= \frac{am^2}{4\pi\mu\Sigma^5\Delta} \cos\Theta \left( r^2 - a^2 \cos^2\Theta \right) \\ &\times \left[ a^2 \cos^2\Theta \left( 11r^2 - a^2 \right) + r^2 \left( 3r^2 - 9a^2 \right) \right], \end{aligned} \quad (10.104)$$

$$\begin{aligned} T_{t\Theta}^{\text{ind}} &= -\frac{am^2r}{4\pi\mu\Sigma^5} \sin\Theta \\ &\times \left[ 3r^4 - 12r^2a^2 \cos^2\Theta + a^4 \cos^4\Theta \right], \end{aligned} \quad (10.105)$$

$$\begin{aligned} T_{\phi r}^{\text{ind}} &= -\frac{a^2m^2}{4\pi\mu\Sigma^5\Delta} \sin^2\Theta \cos\Theta \left[ \cos^4\Theta a^4 \left( a^2 - r^2 \right) \right. \\ &\left. + \cos^2\Theta r^2 a^2 \left( 8a^2 + 12r^2 \right) - 9r^4 a^2 - 3r^6 \right], \end{aligned} \quad (10.106)$$

$$T_{\phi\Theta}^{\text{ind}} = -a \sin^2\Theta T_{t\Theta}^{\text{ind}}. \quad (10.107)$$

Of course, with such a method any GR solution can be promoted to a solution of the modified field equations.

The crucial issue here is whether or not the induced matter flux can be regarded as physically acceptable. In order to shed light on this issue, we analyzed if the induced stress-energy given by Eqs. (10.104)-(10.107) obeys the energy conditions of GR [353]. Because  $T_{ab}^{\text{ind}}$  is always traceless, the strong and weak energy conditions are equivalent and reduce to the statement that  $T_{ab}^{\text{ind}}\xi^a\xi^b \geq 0$  for any timelike vector  $\xi^a$ . This, however, is not the case, as we can show by considering for instance  $\xi^t = \sqrt{2}$ ,  $\xi^r = 1$ , which is timelike for sufficiently large  $r$ :  $\xi^a\xi^b g_{ab} = -1 + 6m/r + \mathcal{O}(m/r)^2$ . The only relevant component of  $T_{ab}^{\text{ind}}$  is given by Eq. (10.104), but since  $T_{tr}^{\text{ind}}$  is proportional to  $\cos\Theta$ , this quantity is negative in half of the spacetime, and thus the weak energy condition is violated. While this might be tolerated close to the horizon, we stress that this violation arises also in the asymptotic region. This violation is somewhat attenuated by the fall-off behavior of  $T_{ab}^{\text{ind}}$ , where its components decay at least as  $1/r^5$  and the scalar invariant  $T_{ab}^{\text{ind}}T^{ab \text{ind}}$  as  $1/r^{12}$  as  $r \rightarrow \infty$ . Thus, if ordinary matter is added then the induced exotic fluxes might not be detectable after all for a far-field observer.

There is another approach capable of circumventing the Pontryagin constraint that also relies on new matter sources. Namely, if the field  $\theta$  is considered a dynamical field, instead of an external field, it is natural to study more general actions than Eq. (10.4) with  $S_{\text{mat}} = 0$ , such as [83]

$$S = \kappa \int d^4x \sqrt{-g} \left( R + \frac{1}{2}(\nabla\theta)^2 - V(\theta) - \frac{1}{\alpha}\theta {}^*RR \right). \quad (10.108)$$

Then the Pontryagin constraint (10.18) is replaced by

$${}^*RR = -\alpha[\square\theta + V'(\theta)], \quad (10.109)$$

where  $\alpha$  is a constant. This provides a natural generalization of the model considered in our paper. However, it also introduces an amount of arbitrariness, since  $V$  is a free function and, in fact, more general couplings between  $\theta$  and curvature might be considered.

We conclude that allowing GR solutions to be also CS solutions by inducing a stress-energy tensor via Eq. (10.103) can lead to unphysical energy distributions. In particular, the Kerr solution induces an energy momentum tensor given by Eqs. (10.104)-(10.107), which violates all energy conditions, even in the asymptotic region. The alternative approach described above lifts  $\theta$  to a genuine dynamical field with a kinetic term and possibly self-interactions, at the cost of introducing an arbitrary potential.

## 10.7 Conclusions and discussion

No exact solution has yet been found that could possibly represent a spinning BH in CS modified gravity. In particular, the Kerr solution is found to be incompatible with the constraints imposed by the modified field equations. Previously, only perturbative

solutions of CS gravity had been considered, which might represent the exterior of a BH. The first study was carried out by Alexander and Yunes [277, 317], who performed a weak-field parameterized post-Newtonian analysis to find a non-axisymmetric Kerr-like solution. This study was later extended by Smith, et. al. [83] to non-point like sources, finding that the Israel junction conditions are effectively modified by the C-tensor. Another study was carried out by Konno, et. al. [327], but this analysis was restricted to a limited class of perturbations that did not allow for the breakage of stationarity or axisymmetry. Within that restricted perturbative framework, a Kerr-like solution was found only for non-canonical choices of  $\theta$ , concluding that BHs cannot rotate in the modified theory for canonical  $\theta$ . This conclusion of Konno et. al. is at odds with both the results of Alexander and Yunes and Smith et. al.

In order to address these issues, in the current paper we attempted to determine what replaces the Kerr solution in CS modified gravity. We thus studied exact solutions of the modified theory, comprising spherically symmetric, static-axisymmetric, and stationary-axisymmetric vacuum configurations, as well as some generalizations thereof.

We began our analysis in Sec. 10.2.1 by considering the CS action in detail and rederiving the equations of motion, together with the resultant surface integral terms. We continued in Sec. 10.2.2 by rederiving the Pontryagin constraint from the equations of motion and providing two alternative interpretations of it. One of them [Eq. (10.21)] is a reality condition on a quadratic curvature invariant of the Weyl tensor, while the other [Eq. (10.24)] is a null condition on the contraction of the electric and magnetic parts of the Weyl tensor. Before considering specific line elements, in Sec. 10.2.3 we classified all solutions into two groups: GR-type (class  $\mathcal{P}$ ), which contains solutions of both the vacuum Einstein equations and the modified field equations; non-GR type (class  $\mathcal{CS} \setminus \mathcal{P}$ ), which contains solutions of CS gravity that are not solutions of the vacuum Einstein equations (cf. Fig. 10.1).

After these general considerations, we began a systematic study of line elements, starting with general spherically symmetric metrics in Sec. 10.3. This class of line elements [Eq. (10.33)] is particularly important since it contains the Schwarzschild, Friedmann-Robertson-Walker and Reissner-Nordström solutions. We showed that, for the canonical choice of the CS scalar field [Eq. (10.27)] and more general choices [Eq. (10.34)], the modified field equations decouple and any possible solution is forced to be of class  $\mathcal{P}$ .

We continued in Sec. 10.4 with an analysis of static and axisymmetric metrics [Eq. (10.38)]. We showed that, for the canonical choice of the CS scalar field and more general choices [Eq. (10.56)], the modified equations decouple once more. We also showed that any static and axisymmetric line element is forced to become spatially conformally flat, provided the field equations decouple. Exploiting this result, we found three different solutions [Eqs. (10.26), (10.54) and (10.55)], only one of which was physically relevant, namely the Schwarzschild solution. For the most general CS scalar field, however, the field equations do not decouple, but we have shown that fields with such generality do not seem to allow for a solution to the field equations apart from trivial ones. Thus, we may conclude that CS gravity does not allow for static and axisymmetric solutions, apart from flat space, the Schwarzschild solution and two additional (unphysical) solutions, irrespective of the choice of the CS scalar field.

Static line elements then gave way to the central point of this paper: stationary and axisymmetric solutions of CS gravity, discussed in Sec. 10.5. As in the previous cases, we showed that, for the canonical choice of the CS scalar field and slightly more general choices [Eq. (10.70)], the field equations again decouple. In this case, however, the Pontryagin constraint does not hold automatically and we used it to constrain the class of possible metric functions, cf. appendix I. In essence, the decoupling requires not only that solutions must obey the Einstein equations, but also the fulfillment of additional constraints (cf. Ref. [346]), which leads to an overdetermined system of PDEs. Therefore, we concluded that non-trivial stationary and axisymmetric solutions do not seem to exist for canonical CS fields.

When a completely generic CS scalar field is considered, the modified field equations do not decouple and solutions are not easy to find, even with the simplifications derived from the Pontryagin constraint. However, generic CS fields increase the degrees of freedom of the problem and thus might allow for stationary and axisymmetric solutions. We proved this statement by providing an example in Sec. 10.5.2, through a sub-class of stationary and axisymmetric metrics [Eq. (10.71)], belonging to the van Stockum class. In that case, we showed that the only possible CS field compatible with the field equations excludes the canonical choice. Moreover, we found both, non-flat solutions of class  $\mathcal{P}$  [Eq. (10.74)] as well as non-flat solutions of class  $\mathcal{CS} \setminus \mathcal{P}$  [Eq. (10.75)] To the best of our knowledge, this is the first time an exact solution in CS modified gravity is constructed that is not also a solution of GR. One of these solutions [Eq. (10.75)] represents mathematical BHs, in the sense that although they exhibit a Killing horizon, they are not physically relevant, because the Killing vector generating the 'axial' symmetry is light-like and closed timelike curves arise. We concluded that it is unlikely that stationary, axisymmetric solutions exist that represent a spinning physical BH.

Finally, in Sec. 10.6 we considered the possibility of constructing solutions beyond the set of stationary and axisymmetric spacetimes. We began in Sec. 10.6.1 by considering CS scalar fields whose velocity is a Killing vector of the spacetime and found that the only interesting case arises if that vector is null. Naturally, such considerations led to exact gravitational shock-wave spacetimes [Eq. (10.81)]. Within this pp-wave scenario, in Sec. 10.6.2 we constructed a generating method through which any pp-wave solution of GR can be lifted to a solution of CS modified gravity with an appropriate choice of the CS scalar field. We also built a solution of class  $\mathcal{CS} \setminus \mathcal{P}$  [Eq. (10.100)] that is not a GR pp-wave solution but does satisfy the CS modified field equations.

Through this detailed study of solutions in CS gravity we have ascertained that at least two different limits of the Kerr BH are solutions to the modified field equations, even though the Kerr BH is not: the Schwarzschild limit and the Aichelburg-Sexl limit. The former was already known to be a solution to the CS modified field equations, but the latter, which includes ultrarelativistically boosted BHs, was not. The existence of these solutions concurs with the naive expectations expressed at the end of Sec. 10.2.2. Moreover, such expectations, together with the input from the far-field solution, point to the existence of a physical spinning BH solution in CS gravity, provided the conditions of stationarity and/or axisymmetry are weakened. We addressed this possibility briefly in Sec. 10.6.3, but unfortunately such spacetimes are so general that the modified field

equations become prohibitively difficult, even with the use of symbolic manipulation software.

Other possibilities of bypassing the Pontryagin constraint were discussed in Sec. 10.6.4, since this constraint is in essence responsible for the absence of interesting stationary and axisymmetric solutions. First, we stated that obviously any (GR or non-GR) solution formally can be lifted to a solution of the modified field equations by allowing for arbitrary matter sources, and we demonstrated the nature of these matter sources for the Kerr BH. We found that the induced energy momentum tensor [Eqs. (10.104)-(10.107)] is exotic even in the asymptotic region, but drops off rapidly with the radial coordinate. Second, we mentioned the possibility that the CS scalar field  $\theta$  might acquire a kinetic term and self-interactions. In this case, the Pontryagin constraint ceases to hold and is replaced by a dynamical condition [Eq. (10.109)], relating the gravitational instanton density to the (generalized) Klein-Gordon operator acting on  $\theta$ .

We now conclude with a list of possible directions for future research to which our current work may provide the basis.

- The number of physical degrees of freedom in CS modified gravity is not known yet. Various considerations appear to lead to contradictory expectations. On the one hand, the appearance of higher order derivatives in the action [Eq. (10.1)] suggests that additional degrees of freedom should emerge. On the other hand, the appearance of an additional constraint [Eq. (10.68)] suggests that fewer degrees of freedom should arise. Actually, the linearization procedure suggests that these competing effects cancel each other and that there are two polarizations of gravitons, just like in GR, albeit with properties that differ from GR [79, 272].
- The role of boundary terms induced in CS gravity for BH thermodynamics could be investigated more thoroughly [354]. Also here general considerations lead to contradictory expectations. On the one hand, new boundary terms that arise in CS gravity [Eq. (10.14)] differ qualitatively from those that arise in GR or in scalar tensor theories. Such boundary terms suggest modifications of BH thermodynamics, even for solutions whose line elements coincide with GR solutions, like the Schwarzschild spacetime. On the other hand, the Pontryagin constraint eliminates the CS contribution [Eq. (10.1)] to the on-shell action, which suggests that BH thermodynamics is left unchanged, at least in the classical approximation.
- Both previous issues can be addressed by a thorough Hamiltonian analysis, which is also of interest by itself and for exhibiting the canonical structure as well as the classical constraint algebra. Such a study would also be useful for numerical evolutions of BH binary spacetimes in CS gravity, which is currently being carried out [355].
- While our discussion of stationary and axisymmetric solutions was quite comprehensive, a few issues are still open, which may be an interesting topic for mathematical relativists. For instance, while we were able to provide a proof that there are only three types of solutions for static and axisymmetric spacetimes (with the canonical choice for the CS scalar field), we could only provide good evidence,

but no mathematical proof, that no further solutions exist for spacetimes that are stationary and axisymmetric.

- Combining the evidence found in this paper with the far field solutions found previously, we concluded that spinning BHs should weaken the requirements of stationarity and/or axisymmetry in CS modified gravity. Perturbations away from axisymmetry were neglected in [327], although non-axisymmetric solutions can still represent spinning BHs, albeit with an inherent precession induced by the CS modification. Therefore, future work could focus on finding exact spacetimes with a smaller amount of symmetries or dropping the integrability conditions starting from (10.101).
- A manageable implementation of the Pontryagin constraint could be useful in many CS gravity applications. The brute force methods that led us to the formulas in appendix I will render any generalization unintelligible. The considerations presented in Ref. [351] provide such an implementation, but it has not been exploited so far in the construction of explicit solutions.
- Far-field solutions of CS gravity that break stationarity could also be studied. These solutions could then be used as tests of the modified theory, through comparisons with gravitational-wave and astrophysical observations [356].
- Perhaps it is feasible to apply the method of matched asymptotic expansion for caged BHs [357, 358] to the construction of spinning BH solutions in the present context. To this end, one would need an asymptotic expansion and a near horizon expansion of that BH. The former exists already, so it remains to construct the latter and perform the asymptotic matching.
- Finally, it is worthwhile to consider not just vacuum solutions, but also solutions with matter sources, as outlined briefly in Sec. 10.6.4.

Certainly the range of issues that can be addressed has been extended in a non-negligible way. Only through a better understanding of the consequences and predictions of CS gravity will we be able to determine the viability of the modified theory.

## Acknowledgments

We are grateful to Stephon Alexander and Roman Jackiw for encouraging us to study this problem in the first place and for enlightening discussions. We would also like to thank Abhay Ashtekar, Henriette Elvang, Alexander Hariton, Scott Hughes, Ralf Lehnert, Ben Owen, Richard O’Shaughnessy, Tristan Smith, Carlos Sopena, Max Tegmark and Richard Woodard for discussions and comments. Most of our calculations used the computer algebra systems MAPLE v.11 in combination with the GRTensorII package [1].

DG is supported in part by funds provided by the U.S. Department of Energy (DoE) under the cooperative research agreement DEFG02-05ER41360. DG has been supported by the project MC-OIF 021421 of the European Commission under the Sixth EU Framework Programme for Research and Technological Development (FP6).

NY acknowledges the support of the Center for Gravitational Wave Physics funded by the National Science Foundation under Cooperative Agreement PHY-01-14375 and support from NSF grant PHY-05-55-628.

## Chapter 11

# Perturbations of Schwarzschild Black Holes in Chern-Simons Modified Gravity

We study perturbations of a Schwarzschild black hole in Chern-Simons modified gravity. We begin by showing that Birkhoff's theorem holds for a wide family of Chern-Simons *coupling* functions, a scalar field present in the theory that controls the strength of the Chern-Simons correction to the Einstein-Hilbert action. After decomposing the perturbations in spherical harmonics, we study the linearized modified field equations and find that axial and polar modes are coupled, in contrast to general relativity. The divergence of the modified equations leads to the *Pontryagin constraint*, which forces the vanishing of the Cunningham-Price-Moncrief master function associated with axial modes. We analyze the structure of these equations and find that the appearance of the Pontryagin constraint yields an overconstrained system that does not allow for generic black hole oscillations. We illustrate this situation by studying the case characterized by a canonical choice of the coupling function and pure-parity perturbative modes. We end with a discussion of how to extend Chern-Simons modified gravity to bypass the Pontryagin constraint and the suppression of perturbations.

### 11.1 Introduction

Extensions of general relativity (GR) are inherently interesting because they hold the promise to address unresolved problems in cosmology and astrophysics<sup>1</sup>. One such extension is Chern-Simons (CS) modified gravity [273], which has recently been used to propose an explanation to the cosmic baryon asymmetry [73] and polarization in the cosmic microwave background (CMB) [75]. This extension has also attracted some recent interest because it might allow for a test of a wide class of string theories [272].

CS modified gravity introduces a well-motivated correction to the Einstein-Hilbert action: the product of a parity-violating, *Pontryagin term*<sup>2</sup> and a scalar field or *CS coupling function* that controls the strength of the correction. Such a modification has deep roots in the standard model, since chiral, gauge and gravitational anomalies possess Pontryagin-like structures. CS modified gravity is also motivated by string theory and

---

<sup>1</sup>This chapter is based on the following papers: N. Yunes and C. F. Sopuerta, submitted to Phys. Rev. D (2007)

<sup>2</sup>See [359] for a discussion of this term and some physical interpretations

loop quantum gravity [360]. In the former, it arises through the Green-Schwarz mechanism [276], as an anomaly-canceling term. In fact, the CS term is a requirement of all model-independent extension of 4-dimensional compactifications of string theory [275].

Some theoretical aspects of CS modified gravity have recently been investigated. Cosmological studies have been carried out in [75, 76, 77] in connection with the Cosmic Microwave Background radiation and in [73, 74] in the context of leptogenesis. Gravitational wave solutions have also been studied in [273, 316, 277, 317], where they were found to possess amplitude birefringence, possibly leading to a test of the theory [272]. Weak-field solutions for spinning objects in CS modified gravity have been studied in [277, 317], leading to a prediction of gyromagnetic precession that differs from GR, and later to a constraint on the magnitude of the CS correction [83]. Further discussion on these issues and others related can be found in [318, 319, 316, 320, 321, 323, 324, 325, 77, 326, 282, 297, 317, 327, 83, 328, 329, 351] and references therein.

Solutions to the CS modified field equations that represent interesting physical configurations have also attracted attention. Apart from first formalizing the theory, Jackiw and Pi [273] also showed that the Schwarzschild and gravitational plane-wave spacetimes remain solutions in CS modified gravity. The Reissner-Nordstrom and Friedman-Robertson-Walker metrics were also found to persist in the theory [297]. On the perturbative front, [277, 317] found a weak-field solution for orbiting, spinning objects, while [327] showed that the weak-field limit of the Kerr metric remained a CS solution to first order in the metric perturbation for a specific choice non-canonical of the CS coupling. Exact solutions that represent spinning objects in CS modified gravity have so far only been studied in [359], where it was suggested that these exist provided the gravitomagnetic sector of the metric is non-vanishing or that stationarity is broken.

In this paper, we study perturbations of a Schwarzschild black hole (BH) in CS modified gravity<sup>3</sup>. We begin by showing that Birkhoff's theorem –the statement that the Schwarzschild solution is the only vacuum, spherically-symmetric solution of the theory–persists in the modified theory for a wide class of coupling functions. After decomposing the metric perturbations in spherical harmonics, we find equations that govern the behaviour of each harmonic. In GR, the divergence of the field equations (both at the perturbative and non-perturbative levels) implies energy-momentum conservation and, in the absence of matter, it becomes an identity that ensures diffeomorphism invariance. In CS gravity, however, the divergence of the field equations (again at the perturbative and non-perturbative levels) leads to a constraint, the so-called Pontryagin constraint, which ensures that the theory remains diffeomorphic invariant and that the Strong Equivalence Principle holds. This constraint imposes a restriction on the class of metrics that can be solutions of the theory, specially in vacuum [359]. At the perturbative level, the Pontryagin constraint is automatically satisfied for a flat background, but we show that for a BH background it forces the Cunningham-Price-Moncrief (CPM) master function, associated with axial perturbations (perturbations of odd parity), to

---

<sup>3</sup>The term “CS modified gravity” stands for the formulation introduced in [273]. Extensions of this formulation have been considered in [83, 359] and we shall discuss how these affect the analysis of this paper in the last section.

vanish. Such a strong restriction on the possible perturbative modes a BH is allowed to possess is a distinctive feature of CS gravity.

After investigating these preliminary issues, we concentrate on the study of general perturbations of a Schwarzschild spacetime<sup>4</sup>. We find that the CS modification introduces new terms into the field equations that results in a mixing of polar and axial parity modes. Therefore, in CS modified gravity modes with different parity do not decouple, as is the case in GR. Moreover, the new terms contain third-order derivatives that change the basic structure of the partial differential equations that describe the behavior of the metric perturbations. In particular, the Pontryagin constraint constitutes a new equation for the metric perturbations, which in general leads to an overdetermined system. A priori, it remains unclear whether this system has non-trivial solutions, *i.e.* whether the entire set of field equations is compatible. This paper shows that at least a wide class of BH oscillation modes are forbidden in the modified theory for a large family of CS coupling functions. More specifically, we show that it is not possible to have either pure axial or pure polar oscillations of a BH in CS gravity for a wide class of coupling functions.

We end with a discussion of possible routes to extend CS modified gravity such that generic BH oscillations are allowed. A promising route is to allow the CS coupling function to be a dynamical quantity. In this case, the Pontryagin constraint is balanced by the equation of motion of the scalar field, thus preventing the CPM function to identically vanish. Moreover, the field equations are modified by the introduction of a stress-energy tensor for the CS scalar field and by terms describing perturbations of the scalar field. The extended set of field equations, which has a certain ambiguity encoded in the potential of the CS scalar field, is no longer overdetermined, and hence, it provides a suitable framework to study the modified dynamics of BH oscillations.

This paper is divided as follows: Sec. 11.2 describes the basics of CS modified gravity; Sec. 11.3 establishes Birkhoff's theorem for a family of CS coupling functions; Sec. 11.4 begins by describing the basics of Schwarzschild BH perturbation theory, and then discusses the consequences of the linearized Pontryagin constraint and the structure of the modified field equations; Sec. 11.5 investigates perturbations of canonical CS gravity, including the impossibility of having either purely polar or purely axial perturbative modes; Sec. 11.6 points to directions in which the theory could be extended to bypass the Pontryagin constraint and allow for generic oscillations of a Schwarzschild BH; Sec. 11.7 concludes and points to future work.

We use the following conventions throughout this work. Greek letters and a semicolon are used to denote indices and covariant differentiation respectively on the 4-dimensional spacetime. In some cases, we denote covariant differentiation with respect to a Schwarzschild background metric by  $\bar{\nabla}_\mu$ . Partial differentiation of a quantity  $Q$  with respect to the coordinate  $x^\mu$  is denoted as  $\partial_{x^\mu} Q$  or  $Q_{,\mu}$ . Symmetrization and antisymmetrization is denoted with parenthesis and square brackets around the indices

---

<sup>4</sup>BH perturbations were previously studied in [327], but only perturbative modes that resemble the weak-field limit of the Kerr metric were considered. In this paper, we consider the most general perturbations in a Schwarzschild background.

respectively, such as  $A_{(ab)} := [A_{ab} + A_{ba}]/2$  and  $A_{[ab]} := [A_{ab} - A_{ba}]/2$ . We use the metric signature  $(-, +, +, +)$  and geometric units in which  $G = c = 1$ .

## 11.2 Introduction to Chern-Simons Modified Gravity

In this section we describe the basics of CS modified gravity as it was introduced by Jackiw and Pi [273]. (more details can be found in [273, 73, 359] and references therein). In this paper, we shall be mainly concerned with this formulation [273], but we will also discuss possible extensions later on.

The CS extension of the GR action is given by [83]

$$S_{\text{CS}} := \kappa \int d^4x \sqrt{-g} \left[ R + \mathcal{L}_{\text{mat}} - \frac{1}{4} \theta {}^*R R \right], \quad (11.1)$$

where  $\kappa = 1/(16\pi)$ ,  $g$  is the determinant of the spacetime metric  $g_{\mu\nu}$ ,  $R$  stands for the Ricci scalar and  $\mathcal{L}_{\text{mat}}$  is the Lagrangian density of the matter fields. We recognize the first two terms as the Einstein-Hilbert action in the presence of matter, while the last term is the CS modification, defined via

$${}^*R R := R_{\alpha\beta\gamma\delta} {}^*R^{\alpha\beta\gamma\delta} = \frac{1}{2} R_{\alpha\beta\gamma\delta} \eta^{\alpha\beta\mu\nu} R_{\mu\nu}^{\gamma\delta}, \quad (11.2)$$

where the asterisk denotes the dual tensor, constructed using the 4-dimensional Levi-Civita tensor  $\eta^{\alpha\beta\mu\nu}$ <sup>5</sup>. The strength of the CS correction is controlled by the scalar field  $\theta$ , which we shall refer to as the *CS coupling function* or *CS scalar field*. The so-called *canonical* choice of  $\theta$  corresponds to [273]

$$\theta_{\text{can}} := [t/\mu, 0, 0, 0], \quad (11.3)$$

where  $\mu$  is a dimensional parameter.

As usual, we obtain the (modified) field equations by varying the action with respect to the metric, yielding

$$G_{\mu\nu} + C_{\mu\nu} = 8\pi T_{\mu\nu}^{\text{mat}}, \quad (11.4)$$

where  $T_{\mu\nu}^{\text{mat}}$  is the matter stress-energy tensor. We shall refer to the quantity  $C_{\mu\nu}$  as the C-tensor, defined as

$$C_{\mu\nu} := C_{\mu\nu}^{(1)} + C_{\mu\nu}^{(2)}, \quad (11.5)$$

---

<sup>5</sup>In non-vacuum spacetimes, the dual of the Riemann tensor with respect to the first pair of indices does not coincide with the dual with respect to the second pair of indices. In this paper we use the second type of dual, but the results of this paper are independent of this choice. This can also be seen from the condition  ${}^*R R = {}^*C C$  [361]

where

$$C_{\mu\nu}^{(1)} := \theta_{;\sigma} \eta^{\sigma\alpha\beta} R_{\nu\beta;\alpha}, \quad (11.6)$$

$$C_{\mu\nu}^{(2)} = \theta_{;\sigma\tau} {}^*R^{\sigma\tau}{}_{(\mu\nu)}. \quad (11.7)$$

The spatial sector of the C-tensor reduces to the 3-dimensional Cotton tensor in some symmetric cases<sup>6</sup>. For this reason, the quantity  $v_{\mu} := \theta_{;\mu}$  is sometimes referred to as the embedding coordinate, since it embeds the 3-dimensional CS theory into a 4-dimensional spacetime.

Diffeomorphism invariance is preserved provided an additional equation is satisfied. This equation can be obtained by computing the covariant divergence of the modified field equations

$$C_{\mu\nu}{}^{;\mu} = \frac{1}{8} v_{\nu} {}^*R R = 8\pi T_{\mu\nu}^{\text{mat};\mu} \quad (11.8)$$

In vacuum,  $T_{\mu\nu}^{\text{mat}} = 0$  and thus we are left with the so-called Pontryagin constraint

$${}^*R R = 0, \quad (11.9)$$

which is an additional equation that the metric tensor has to satisfy.

### 11.3 Birkhoff's Theorem in Chern-Simons Modified Gravity

Birkhoff's theorem states that the most general, spherically symmetric solution to the vacuum Einstein equations is the Schwarzschild metric. In CS modified gravity, this is not necessarily the case because the C-tensor modifies the field equations. In [273] it was shown that the Schwarzschild solution persists in CS modified gravity, but this does not necessarily imply that Birkhoff's theorem holds. Let us then study Birkhoff's theorem in CS modified gravity in more detail.

The line element of a general, spherically-symmetric spacetime can be written as a warped product of two 2-dimensional metrics [181, 182]: a Lorentzian one,  $g_{AB}$  ( $A, B, \dots, H = t, r$ ), and the unit two-sphere metric,  $\Omega_{ab}$  ( $a, b, \dots, h = \theta, \phi$ ). This line element takes the following 2 + 2 form:

$$g_{\mu\nu} dx^{\mu} dx^{\nu} = g_{AB} (x^C) dx^A dx^B + r^2 (x^A) \Omega_{ab} (x^c) dx^a dx^b, \quad (11.10)$$

where the warped factor is the square of the area radial coordinate  $r$ . Covariant differentiation on the Lorentzian manifold is denoted by a bar while on the 2-sphere is denoted by a colon. The case of the Schwarzschild metric in Schwarzschild coordinates is given

---

<sup>6</sup>In [273],  $C_{\mu\nu}$  was identified with the 'Cotton tensor' because it reduces to its 3-dimensional counterpart in certain symmetric cases. However, a higher-dimensional Cotton tensor already exists [331], and its definition is different from that of Eq. (11.5). To avoid confusion, we refer to  $C_{\mu\nu}$  as the C-tensor instead of the Cotton tensor.

by:

$$g_{AB} dx^A dx^B = -f dt^2 + f^{-1} dr^2, \quad f = 1 - \frac{2M}{r}, \quad (11.11)$$

where  $M$  is the BH mass.

The Cotton tensor associated with this metric vanishes identically if the scalar field has the following form <sup>7</sup>:

$$\theta = \bar{\theta}(x^A) + r(x^A) \Theta(x^a). \quad (11.12)$$

This functional form is invariant under coordinate changes that leave the 2+2 structure of the metric [Eq. (11.10)] invariant, i.e. coordinate transformations:  $x^A \rightarrow \tilde{x}^A = \tilde{x}^A(x^B)$ ,  $x^a \rightarrow \tilde{x}^a = \tilde{x}^a(x^b)$ , and transformations on the unit two-sphere. Moreover, one can show that the two pieces of the C-tensor shown in Eqs. (11.6) and (11.7) vanish independently for the family of scalar fields given in Eq. (11.12). For most of this paper, we will consider the particular case in which the scalar field also respects the spherical symmetry of the background:

$$\theta = \bar{\theta}(x^A). \quad (11.13)$$

Let us comment some more on this result and place it in context. The CS scalar field  $\theta$  is usually assumed to depend only on *cosmic* time,  $\theta = \theta(t)$ . This assumption has its roots in the work of Jackiw and Pi [273], who further imposed that  $\dot{\theta} = d\theta/dt$  be constant, such that time-translation symmetry and space-time reparameterization of the spatial variables be preserved. With these assumptions, they showed that CS gravity can be interpreted as a 4-dimensional generalization of 3-dimensional Cotton gravity, and that the Schwarzschild and Friedman-Robertson-Walker solutions persist in the modified theory. Later on, Smith, *et. al.* [83] argued that the CS scalar field could represent some quintessence field that enforces the arrow of time associated with cosmic expansion. In this paper we have considered the most general spherically-symmetric spacetime and we have written its line element in the 2 + 2 form that follows from its warped geometric structure. This form of the metric is invariant under general coordinate transformations in the two 2-dimensional manifolds, associated with this 2 + 2 structure. Therefore, it is not too surprising that if Birkhoff's theorem is satisfied for the canonical choice of CS scalar field, it is also satisfied for fields that depend arbitrarily on  $t$  and  $r$ .

## 11.4 Perturbations of a Schwarzschild Black Hole

### 11.4.1 Basics

We begin with a short summary of the basics of metric perturbations about a Schwarzschild background. The spacetime metric of a perturbed BH can be written in the form

$$g_{\mu\nu} = \bar{g}_{\mu\nu} + h_{\mu\nu}, \quad (11.14)$$

---

<sup>7</sup>A similar result is found in [359]

where  $\bar{g}_{\mu\nu}$  is the background Schwarzschild metric (geometric objects associated with it will have an overbar) and  $h_{\mu\nu}$  is a generic metric perturbation. Thanks to the spherical symmetry of the background, we can expand the metric perturbations in (tensor) spherical harmonics. In this way, we can separate the angular dependence in the perturbative equations, which yields a much more simple system of equations: a system of 1+1 partial differential equations (PDEs) in time and in the radial area coordinate  $r$ . In addition, we can distinguish between harmonics with polar and axial parity<sup>8</sup>, also called even and odd parity modes respectively. In GR, the perturbative field equations decouple for modes of different parity, but this may not be the case for alternative theories.

Let us then split the metric perturbation  $h_{\mu\nu}$  into polar and axial perturbations,  $h_{\mu\nu} = h_{\mu\nu}^{\text{a}} + h_{\mu\nu}^{\text{p}}$ , and each of these into (tensor) spherical harmonics via

$$h_{\mu\nu}^{\text{a}} = \sum_{\ell,m} h_{\mu\nu}^{\text{a},\ell m}, \quad h_{\mu\nu}^{\text{p}} = \sum_{\ell,m} h_{\mu\nu}^{\text{p},\ell m}, \quad (11.15)$$

where

$$h_{\mu\nu}^{\text{a},\ell m} = \begin{pmatrix} 0 & h_A^{\ell m} S_a^{\ell m} \\ * & H^{\ell m} S_{ab}^{\ell m} \end{pmatrix}, \quad (11.16)$$

$$h_{\mu\nu}^{\text{p},\ell m} = \begin{pmatrix} h_{AB}^{\ell m} Y^{\ell m} & p_A^{\ell m} Y_a^{\ell m} \\ * & r^2 (K^{\ell m} Y_{ab}^{\ell m} + G^{\ell m} Z_{ab}^{\ell m}) \end{pmatrix}, \quad (11.17)$$

and where asterisks denote components given by symmetry. The quantity  $Y^{\ell m}$  refers to the standard scalar spherical harmonics [see [139] for conventions], while  $Y_a^{\ell m}$  and  $S_a^{\ell m}$  are polar and axial, vector spherical harmonics, defined only for  $\ell \geq 1$  via

$$Y_a^{\ell m} \equiv Y_{:a}^{\ell m}, \quad S_a^{\ell m} \equiv \eta_a^b Y_b^{\ell m}. \quad (11.18)$$

Similarly,  $Y_{ab}^{\ell m}$  and  $Z_{ab}^{\ell m}$  are polar, and  $S_{ab}^{\ell m}$  axial, symmetric tensor spherical harmonics, defined only for  $\ell \geq 2$  via

$$Y_{ab}^{\ell m} \equiv Y^{\ell m} \Omega_{ab}, \quad Z_{ab}^{\ell m} \equiv Y_{:ab}^{\ell m} + \frac{\ell(\ell+1)}{2} Y^{\ell m} \Omega_{ab}, \quad (11.19)$$

$$S_{ab}^{\ell m} \equiv S_{(a;b)}^{\ell m}. \quad (11.20)$$

---

<sup>8</sup>Polar and axial modes as those which, under a parity transformation, acquire a factor of  $(-1)^\ell$  and  $(-1)^{\ell+1}$  respectively.

The sign convention for the Levi-Civita tensor of the 2-sphere is:  $\eta_{\theta\varphi} = \sin\theta$ . All metric perturbations, scalar ( $h_{AB}^{\ell m}$ ), vectorial ( $p_A^{\ell m}$  and  $q_A^{\ell m}$ ), and tensorial ( $K^{\ell m}$ ,  $G^{\ell m}$ , and  $q_2^{\ell m}$ ), are functions of  $t$  and  $r$  only.

In GR, the Einstein equations can be decoupled in terms of complex master functions that obey wave-like master equations. Once the master functions are constructed we can recover all remaining metric perturbations from them. For axial modes, we can use the Cunningham-Price-Moncrief (CPM) master function [193], defined by

$$\Psi_{\text{CPM}}^{\ell m} = -\frac{r}{\lambda_\ell} \left( h_{r,t}^{\ell m} - h_{t,r}^{\ell m} + \frac{2}{r} h_t^{\ell m} \right), \quad (11.21)$$

whereas for polar modes we can use the Zerilli-Moncrief (ZM) master function [190, 191]

$$\begin{aligned} \Psi_{\text{ZM}}^{\ell m} &= \frac{r}{1 + \lambda_\ell} \left\{ K^{\ell m} + (1 + \lambda_\ell) G^{\ell m} \right. \\ &\quad \left. + \frac{f}{\Lambda_\ell} \left[ f h_{rr}^{\ell m} - r K_{,r}^{\ell m} - \frac{2}{r} (1 + \lambda_\ell) p_r^{\ell m} \right] \right\}, \end{aligned} \quad (11.22)$$

where  $\lambda_\ell = (\ell + 2)(\ell - 1)/2$  and  $\Lambda_\ell = \lambda_\ell + 3M/r$ . These two complex master functions are gauge invariant. In order to simplify our analysis we shall here fix the gauge by setting the following metric perturbations to zero (Regge-Wheeler gauge):

$$H^{\ell m} = 0, \quad (11.23)$$

$$G^{\ell m} = p_t^{\ell m} = p_r^{\ell m} = 0. \quad (11.24)$$

The master equations for the master functions, in the case of perturbations without matter sources, have the following wave-like structure:

$$\left[ -\partial_{t^2}^2 + \partial_{r_\star^2}^2 - V_\ell^{\text{Polar/Axial}}(r) \right] \Psi_{\text{CPM/ZM}}^{\ell m} = 0, \quad (11.25)$$

where  $r_\star$  is the *tortoise* coordinate  $r_\star = r + 2M \ln[r/(2M) - 1]$ . The quantity  $V_\ell^{\text{Polar/Axial}}(r)$  is a potential that depends on the parity and harmonic number  $\ell$  (its precise form can be found elsewhere. To follow our notation, see [139]).

When the master functions are known, one can use them to construct the plus and cross-polarized gravitational waveforms via

$$h_+ - ih_\times = \frac{1}{2r} \sum_{\ell \geq 2, m} \sqrt{\frac{(\ell + 2)!}{(\ell - 2)!}} \left( \Psi_{\text{ZM}}^{\ell m} + i\Psi_{\text{CPM}}^{\ell m} \right) {}_{-2}Y^{\ell m}, \quad (11.26)$$

where  ${}_{-2}Y^{\ell m}$  denotes spherical harmonics of spin weight  $-2$  [198]. One can also compute the fluxes of energy and angular momentum emitted toward infinity and also into the

BH horizon in terms of the master functions. These fluxes are evaluated using a short-wavelength approximation in the *radiation zone*, where we can introduce a well-defined gauge-invariant energy-momentum tensor for gravitational radiation [195, 196, 197]. However, the expression for this effective energy-momentum tensor depends on the structure of the field equations. In the case of CS modified gravity, given that the modification in the field equations is additive, the form of these fluxes will be the same as in GR but with extra terms proportional to the CS scalar field and its derivatives. That is,

$$\begin{aligned} \dot{E}_{\text{GW}} &= \frac{1}{64\pi} \sum_{\ell \geq 2, m} \frac{(\ell+2)!}{(\ell-2)!} \left( |\dot{\Psi}_{\text{CPM}}^{\ell m}|^2 + |\dot{\Psi}_{\text{ZM}}^{\ell m}|^2 \right) \\ &+ \mathcal{O}(\partial\theta, \partial^2\theta), \end{aligned} \quad (11.27)$$

$$\begin{aligned} \dot{L}_{\text{GW}} &= \frac{1}{64\pi} \sum_{\ell \geq 2, m} im \frac{(\ell+2)!}{(\ell-2)!} \left( \bar{\Psi}_{\text{CPM}}^{\ell m} \dot{\Psi}_{\text{CPM}}^{\ell m} + \bar{\Psi}_{\text{ZM}}^{\ell m} \dot{\Psi}_{\text{ZM}}^{\ell m} \right) \\ &+ \mathcal{O}(\partial\theta, \partial^2\theta), \end{aligned} \quad (11.28)$$

where the dots here denote time differentiation.

#### 11.4.2 Pontryagin Constraint

We have seen that diffeomorphism invariance requires an extra condition, the Pontryagin constraint [Eqs. (11.2)-(11.9)]. This condition is automatically satisfied not only by the most general spherically symmetric metric (its C-tensor vanishes), but also for linear perturbations of Minkowski spacetime. Nonetheless, this condition is not satisfied for generic perturbations of a Schwarzschild BH. In this case, at first-order, the Pontryagin constraint becomes

$${}^*R R = \frac{96M}{r^6} \left[ h_t^{\ell m} + \frac{r}{2} \left( h_{r,t}^{\ell m} - h_{t,r}^{\ell m} \right) \right] \ell(\ell+1) Y^{\ell m}. \quad (11.29)$$

Remarkably, the Pontryagin constraint involves only axial modes, which is a consequence of the appearance of the Levi-Civita tensor (a completely antisymmetric tensor) in the modification of the gravitational sector of the action. Perhaps even more remarkably, this specific combination of axial modes corresponds exactly to the Cunningham-Price-Moncrief master function [193] [eq. (11.21)], which appears in the metric waveforms [Eq. (11.26)] and in the fluxes of energy and angular momentum [Eq. (11.27) and (11.28)]. We can thus rewrite Eq. (11.29) as

$${}^*R R = -\frac{24M}{r^6} \frac{(\ell+2)!}{(\ell-2)!} \Psi_{\text{CPM}}^{\ell m} Y^{\ell m}. \quad (11.30)$$

Then, the Pontryagin constraint forces the CPM function to vanish for all harmonics with  $\ell \geq 2$ . Such a restriction does not imply that all axial perturbations necessarily

vanish in CS modified gravity, but it does require that these modes satisfy the relation

$$h_{r,t}^{\ell m} = h_{t,r}^{\ell m} - \frac{2}{r} h_t^{\ell m}. \quad (11.31)$$

Such a condition seems to reduce the set of possible solutions of the perturbative vacuum field equations, which might lead to an overconstrained system. For the choice of  $\theta$  in Eq. (11.13), we shall see in Sec. 11.5.1 that this is indeed the case.

### 11.4.3 Structure of the Modified Field Equations

The CS modified dynamics of linear perturbations about a Schwarzschild background can be studied by expanding the metric perturbations into spherical harmonics, Eqs. (11.15)-(11.17). After introducing these expansions into the field equations

$$G_{\mu\nu} = -C_{\mu\nu}. \quad (11.32)$$

we can extract individual evolution equations for each harmonic.

The choice of the CS scalar field will determine the form of the right-hand side in Eq. (11.32). Since we are considering perturbations about a Schwarzschild spacetime, we must choose  $\theta$  such that Birkhoff's theorem holds. In Sec. 11.3, we determined that scalar fields of the form of Eq. (11.12) would indeed allow Birkhoff's theorem to persist in CS modified gravity. We shall here choose  $\theta$  as in Eq. (11.13), such that this field agrees with the symmetries of the background, namely

$$\theta = \bar{\theta}(t, r), \quad (11.33)$$

where  $t$  and  $r$  are here the Schwarzschild time and radial coordinates. This family of CS coupling functions encompasses the canonical choice:  $\bar{\theta} = t/\mu$ .

The structure of the linearized field equations is analyzed by first looking at the harmonic decomposition of the Einstein tensor and the C-tensor. The structure of the former is well-known from the study of perturbations of non-rotating BHs in GR, and is given by

$$G_{AB}^{\ell m} = \mathcal{G}_{AB}^{\ell m}[\mathbf{U}_{\text{Polar}}^{\ell m}] Y^{\ell m}, \quad (11.34)$$

$$G_{Aa}^{\ell m} = \mathcal{G}_A^{\ell m}[\mathbf{U}_{\text{Polar}}^{\ell m}] Y_a^{\ell m} + \mathcal{H}_A^{\ell m}[\mathbf{U}_{\text{Axial}}^{\ell m}] S_a^{\ell m}, \quad (11.35)$$

$$G_{ab}^{\ell m} = \mathcal{G}_{ab}^{\ell m}[\mathbf{U}_{\text{Polar}}^{\ell m}] Y_{ab}^{\ell m} + \mathcal{H}^{\ell m}[\mathbf{U}_{\text{Polar}}^{\ell m}] Z_{ab}^{\ell m} + \mathcal{I}^{\ell m}[\mathbf{U}_{\text{Axial}}^{\ell m}] S_{ab}^{\ell m}, \quad (11.36)$$

where  $\mathbf{U}_{\text{Polar}}^{\ell m}$  denotes the set of  $(\ell, m)$ -polar perturbations

$$\mathbf{U}_{\text{Polar}}^{\ell m} = (h_{AB}^{\ell m}, p_A^{\ell m}, K^{\ell m}, G^{\ell m}), \quad (11.37)$$

and  $\mathbf{U}_{\text{Axial}}^{\ell m}$  denotes the set of  $(\ell, m)$ -axial perturbations

$$\mathbf{U}_{\text{Axial}}^{\ell m} = (h_A^{\ell m}, H^{\ell m}). \quad (11.38)$$

Expressions for the coefficients  $\mathcal{G}_{AB}^{\ell m}$ ,  $\mathcal{G}_A^{\ell m}$ ,  $\mathcal{G}^{\ell m}$ ,  $\mathcal{H}_A^{\ell m}$ ,  $\mathcal{H}^{\ell m}$ , and  $\mathcal{I}^{\ell m}$  are given in Appendix J. Clearly, polar spherical harmonics have functional coefficients that depend only on polar metric perturbations, while axial spherical harmonics have functional coefficients that depend only on axial metric perturbations. On the other hand, the harmonic structure of the C-tensor is given by

$$C_{AB}^{\ell m} = C_{AB}^{\ell m} [U_{\text{Axial}}^{\ell m}] Y^{\ell m}, \quad (11.39)$$

$$C_{Aa}^{\ell m} = C_A^{\ell m} [U_{\text{Axial}}^{\ell m}] Y_a^{\ell m} + \mathcal{D}_A^{\ell m} [U_{\text{Polar}}^{\ell m}] S_a^{\ell m}, \quad (11.40)$$

$$C_{ab}^{\ell m} = C^{\ell m} [U_{\text{Axial}}^{\ell m}] Y_{ab}^{\ell m} + \mathcal{D}^{\ell m} [U_{\text{Axial}}^{\ell m}] Z_{ab}^{\ell m} + \mathcal{E}^{\ell m} [U_{\text{Polar}}^{\ell m}] S_{ab}^{\ell m}, \quad (11.41)$$

where explicit expressions for the coefficients  $C_{AB}^{\ell m}$ ,  $C_A^{\ell m}$ ,  $C^{\ell m}$ ,  $\mathcal{D}_A^{\ell m}$ ,  $\mathcal{D}^{\ell m}$ , and  $\mathcal{E}^{\ell m}$  are also given in Appendix J. In this case, polar spherical harmonics have functional coefficients that depend on axial perturbations, while axial spherical harmonics have functional coefficients that depend on polar perturbations. The main consequence of this fact is that in CS modified gravity modes with different parity are coupled, and hence, in general they cannot be treated separately.

The linearized field equations, after harmonic decomposition, become

$$\mathcal{G}_{AB}^{\ell m} = -C_{AB}^{\ell m}, \quad \mathcal{G}_A^{\ell m} = -C_A^{\ell m}, \quad (11.42)$$

$$\mathcal{G}^{\ell m} = -C^{\ell m}, \quad \mathcal{H}^{\ell m} = -\mathcal{D}^{\ell m}, \quad (11.43)$$

$$\mathcal{H}_A^{\ell m} = -\mathcal{D}_A^{\ell m}, \quad \mathcal{I}^{\ell m} = -\mathcal{E}^{\ell m}. \quad (11.44)$$

We can view these equations as the standard Einstein equations, linearized about a Schwarzschild background, with “source terms” that depend linearly on metric perturbations of opposite parity and their derivatives. Such a coupling between different parity modes is analogous to what occurs to gravitational-wave perturbations about a Minkowski background, where left- and right-polarized perturbations mix [273, 73, 274]. The intrinsic decoupling of the modified field equations into polar and axial sectors is thus lost.

## 11.5 Black Hole Perturbation Theory with a Canonical Embedding

In order to understand the dynamics of the perturbations that derives from this theory and, in particular, the role and consequences of the Pontryagin constraint, we shall concentrate on the special case of a canonical CS coupling function, *i.e.*  $\bar{\theta} = t/\mu$ . This canonical coupling function leads to the canonical timelike embedding  $v_\mu = [1/\mu, 0, 0, 0]$  and its acceleration  $v_{\mu;\nu} = \Gamma_{\mu\nu}^\sigma v_\sigma$ .

### 11.5.1 One-handed Perturbations

To begin with, we concentrate on perturbations with a single handedness, *i.e.* purely polar or purely axial perturbations. We shall analyze these cases separately.

### 11.5.1.1 Pure Axial Perturbations

We begin with pure axial metric perturbations, that is

$$h_{AB}^{\ell m} = p_A^{\ell m} = K^{\ell m} = G^{\ell m} = 0. \quad (11.45)$$

This conditions imply

$$\mathcal{G}_{AB}^{\ell m} = \mathcal{G}_A^{\ell m} = \mathcal{G}^{\ell m} = \mathcal{H}^{\ell m} = 0, \quad (11.46)$$

$$\mathcal{D}_A^{\ell m} = \mathcal{E}^{\ell m} = 0, \quad (11.47)$$

and hence the field equations reduce to:

$$\mathcal{H}_A^{\ell m} = 0, \quad \mathcal{I}^{\ell m} = 0, \quad (11.48)$$

$$\mathcal{C}_{AB}^{\ell m} = 0, \quad \mathcal{C}_A^{\ell m} = 0, \quad (11.49)$$

$$\mathcal{C}^{\ell m} = 0, \quad \mathcal{D}^{\ell m} = 0. \quad (11.50)$$

Looking at the expressions of  $\mathcal{C}^{\ell m}$  and  $\mathcal{C}_{rr}^{\ell m}$  (see Appendix J) we see that both of them are proportional to the metric perturbation  $h_r^{\ell m}$ . Therefore, using Eqs. (11.49)-(11.50) we conclude that

$$h_r^{\ell m} = 0. \quad (11.51)$$

Similarly,  $\mathcal{C}_{tr}^{\ell m}$  is proportional to  $h_t^{\ell m}$ , and thus, using Eq. (11.50)

$$h_t^{\ell m} = 0. \quad (11.52)$$

Since  $H^{\ell m}$  is zero in the Regge-Wheeler gauge, we conclude that all axial perturbations must vanish. In summary, the Pontryagin constraint together with the coupling of opposite parity modes in the modified field equations, forbids the existence of purely axial oscillations of a Schwarzschild BH in CS modified gravity with a canonical embedding.

### 11.5.1.2 Pure Polar Perturbations

Let us now study pure polar perturbations by setting all axial modes to zero:

$$h_A^{\ell m} = 0. \quad (11.53)$$

The immediate consequences are

$$\mathcal{H}_A^{\ell m} = \mathcal{I}^{\ell m} = 0, \quad (11.54)$$

$$\mathcal{C}_{AB}^{\ell m} = \mathcal{C}_A^{\ell m} = \mathcal{C}^{\ell m} = \mathcal{D}^{\ell m} = 0, \quad (11.55)$$

and the field equations become

$$\mathcal{G}_{AB}^{\ell m} = \mathcal{G}_A^{\ell m} = \mathcal{G}^{\ell m} = \mathcal{H}^{\ell m} = 0, \quad (11.56)$$

$$\mathcal{D}_A^{\ell m} = \mathcal{E}^{\ell m} = 0. \quad (11.57)$$

From  $\mathcal{H}^{\ell m} = 0$  we find that (see Appendix J)

$$h_{tt}^{\ell m} = f^2 h_{rr}^{\ell m}, \quad (11.58)$$

while, from equations  $\mathcal{G}_A^{\ell m} = 0 = \mathcal{G}_{AB}^{\ell m}$  we find expressions for all first and second derivatives of  $K^{\ell m}$  in terms of  $h_{rr}^{\ell m}$ ,  $h_{tr}^{\ell m}$  and its derivatives. Substituting these expressions into  $\mathcal{E}^{\ell m} = 0$  leads to

$$h_{rr}^{\ell m} = 0, \quad (11.59)$$

which combined with Eq. (11.58) implies

$$h_{tt}^{\ell m} = 0. \quad (11.60)$$

There are now only two non-zero metric perturbations:  $K^{\ell m}$  and  $h_{tr}^{\ell m}$ . Inserting the expressions for the derivatives of  $K^{\ell m}$  into  $\mathcal{D}_A^{\ell m} = 0$ , we can solve the resulting equations for  $h_{tr,rr}^{\ell m}$  and  $h_{tr,tr}^{\ell m}$ . Using all the information we have collected so far in  $\mathcal{G}^{\ell m} = 0$ , one can show by direct evaluation that this equation requires that  $h_{tr,t}^{\ell m} = 0$ . Such a result, in combination with the previously found expression for  $h_{tr,tr}^{\ell m}$ , leads to

$$K^{\ell m} = 0. \quad (11.61)$$

Returning to the previous expressions for derivatives of  $K^{\ell m}$  we obtain

$$h_{tr}^{\ell m} = 0. \quad (11.62)$$

We have then found that all polar perturbations vanish. We conclude that purely polar oscillations of a Schwarzschild BH are not allowed in CS modified gravity with a canonical embedding.

The results obtained for single-parity oscillations are quite surprising and raise questions about its robustness. In other words, can we expect the same conclusion if we repeat the analysis for other CS coupling functions? We have repeated this analysis for different CS coupling functions within the class  $\theta = \bar{\theta}(t, r)$ . The algebra involved is significantly more complicated and it requires intensive use of symbolic manipulation software [1]. In all studied cases, we have arrived at the same conclusion: CS modified gravity does not allow for single-parity BH oscillations.

### 11.5.1.3 General Perturbations

General perturbations are significantly more difficult to analyze, since we cannot separately study the components of the Einstein and C-tensors, as was the case for single parity oscillations, due to the particular structure of these tensors [Eqs. (11.42)-(11.44)]. Nonetheless, we can still make some general comments about the consequences of the Pontryagin constraint on general oscillations and the extent to which these are restricted.

The Pontryagin constraint unavoidably adds an extra equation to the modified field equations, *i.e.* Eq. (11.31). Since this equation only involves axial perturbations, one may *a priori* think that polar modes are unaffected. The modified field equations, however, mix polar and axial modes, and thus, polar modes are also affected and restricted by the Pontryagin constraint. This situation has been clearly illustrated by the study of single-parity oscillations in the previous subsection.

The coupling of polar and axial metric perturbations in the modified field equations, together with the extra condition imposed by the Pontryagin constraint, lead to new conditions on the metric perturbations. In other words, these new conditions constitute new equations for the metric perturbations that are independent of the previous ones. For example, the components of  $C_{AB}^{\ell m}$  in Eq. (11.39) are linear combinations of the axial metric perturbations  $h_A^{\ell m}$  (see Appendix J), which can be combined to reconstruct the CPM master function, leading to an additional equation for polar modes. Similarly, the components of  $\mathcal{H}_A^{\ell m}$  [Eq. (11.35)] can also be combined to construct the CPM master function, and hence find another constraint on polar modes. Again, due to the mixing of different parity modes, these constraints on polar modes can in turn produce new constraints on axial modes. It is unclear where this chain of new constraints on the metric perturbations ends, but it is very likely that they will severely restrict the set of allowed BH oscillations.

One may think that choosing the CS coupling function  $\theta$  appropriately, namely choosing  $\bar{\theta}(x^A)$  and  $\Theta(x^a)$  in Eq. (11.12), may end this chain of new constraints through cancellations in the generation of new equations. In the case  $\theta = \bar{\theta}(x^A)$ , if such cancellations were to occur for a certain harmonic number  $\ell$ , they could not happen for other  $\ell$ , as the equations depend on the harmonic number. Moreover, such cancellations would have to occur in different ways, associated with the different combinations of equations that produce new constraints, discussed in the previous paragraph. Adding the term  $\Theta(x^a)$  to the CS scalar field only complicates the field equations further by inducing a coupling between perturbations with different harmonic number. Even in this case, given that the functional coefficient of  $\Theta(x^a)$  is fixed (it is just  $r$ ) and  $\ell$ -independent, it seems unlikely that the coupling of harmonic modes will lead to the cancellations necessary to avoid new equations for the metric perturbations.

Our analysis suggests that the present structure of CS modified gravity does not seem to allow for generic BH oscillations. In particular, we have shown that for certain choices of the CS scalar field, single-parity perturbations are not allowed. For general perturbations, and with the help of computer algebra, we have analyzed the equations as discussed above and found that cancellations in the generation of new conditions on the metric perturbations are very unlikely. Therefore, the present set up for CS modified gravity does not seem to allow for the study of generic oscillations of non-rotating BHs.

Such a result is reminiscent to that found in GR when additional restrictions are imposed on the metric tensor. An example of this can be found in the study of relativistic cosmological dynamics [362, 363]

Although the modified theory seems too restrictive, it is possible to develop an extension where the aforementioned constraints are avoided, while keeping the main characteristics of the modified theory untouched. Two distinctive features of the non-extended theory are the coupling of different parity modes and the Pontryagin constraint. While the former can be preserved by extensions of the modified theory, the latter must be relaxed to prevent the vanishing of the CPM master function. Since, by assumption, any extension should introduce small modifications to CS gravity, the CPM master function would be forced to be small but not quite zero. If this is the case, such extensions would have strong implications in the energy flux and, in particular, in the angular momentum flux of gravitational waves [Eqs. (11.27) and (11.28)]. These arguments motivate the study of BH oscillations in extensions of CS modified gravity, which we shall explore in the next section.

## 11.6 Beyond the Cannon

The strong restrictions obtained on the dynamics of BH oscillations thus far can be bypassed provided we considered extensions of CS modified gravity beyond the canon. One such possibility is to consider a more general CS coupling function that, for example, is not spherically symmetric. However, as we have argued before, it does not seem likely that such a modification would avoid the generation of new restrictions on the metric perturbations. Another more interesting possibility is to extend the action of Eq. (11.1) to allow for the dynamical evolution of the CS scalar field. Such a route is particularly promising because it weakens the Pontryagin constraint, as we shall see in this section. However, a certain amount of arbitrariness is inherent to such a route, encoded in the choice of the scalar field action and, in particular, its potential. We shall discuss this and other issues in the remaining of this section.

### 11.6.1 Extended CS Modified Gravity

Until now, we have treated the CS coupling function as a non-dynamical quantity. Recently, Smith, et. al. [83] added a kinetic and a potential term to the action, which they found did not contribute to their weak-field analysis. These additional terms are of the form

$$S_{\text{ext}} = S_{\text{CS}} + \kappa \int d^4x \sqrt{-g} \left[ \frac{1}{2} \theta_{,\mu} \theta^{,\mu} - V(\theta) \right], \quad (11.63)$$

where  $V(\theta)$  is some potential for the CS scalar field.

The variation of the extended action with respect to the metric and scalar field yields the equations of motion of the extended theory

$$G_{\mu\nu} + C_{\mu\nu} = 8\pi \left( T_{\mu\nu}^{\text{mat}} + T_{\mu\nu}^{\theta} \right), \quad (11.64)$$

$$\square\theta = -\frac{dV}{d\theta} - \frac{1}{4} {}^*R R, \quad (11.65)$$

where the D’Alambertian of any scalar can be computed from

$$\square\theta = \frac{1}{\sqrt{-g}} \left[ \sqrt{-g} g^{\mu\nu} \theta_{,\nu} \right]_{,\mu}, \quad (11.66)$$

and where the stress-energy tensor of the scalar field is [364]

$$T_{\mu\nu}^{\theta} = \theta_{,\mu} \theta_{,\nu} - \frac{1}{2} g_{\mu\nu} \theta_{;\sigma} \theta^{;\sigma} - g_{\mu\nu} V(\theta). \quad (11.67)$$

In this extension of CS modified gravity, the Pontryagin constraint is replaced by an equation of motion for the CS scalar field, Eq. (11.65), where the quadratic curvature scalar  ${}^*R R$  plays the role of a driving force. Moreover, looking at the field equations for the metric, we realize that they are not only sourced by the matter fields but also by the CS scalar field through its energy-momentum content. In the next subsection we shall study what consequences this modification imposes on the satisfaction of Birkhoff’s theorem and the Pontryagin constraint.

### 11.6.2 Birkhoff’s Theorem in the Extended Theory

The simple derivation of Birkhoff’s theorem in Sec. 11.3 is now modified by the extended action. For a CS scalar field of the form of Eq. (11.12) and the line element of Eq. (11.10), the C-tensor vanishes, which now leads to

$$G_{\mu\nu} = 8\pi T_{\mu\nu}^{\theta}. \quad (11.68)$$

If the metric of Eq. (11.10) is a solution to Einstein’s equations, as is the case for the Schwarzschild metric, the stress-energy tensor of the scalar field must vanish. For the choice of  $\theta$  in Eq. (11.33) and the Schwarzschild metric, this implies the following conditions:

$$\begin{aligned} 0 &= \theta_{,t} \theta_{,r}, \\ 0 &= \frac{1}{2} \theta_{,t}^2 + \frac{f^2}{2} \theta_{,r}^2 \pm fV(\theta), \end{aligned} \quad (11.69)$$

where  $f$  is given in Eq. (11.11). The only solution to this system is the trivial one:  $V = 0$  and  $\theta = \text{const.}$ , which reduces CS theory to GR. However, if we treat  $\theta$  as a small quantity, as it is suggested by the different physical scenarios that motivate CS modified gravity, then Birkhoff’s theorem holds to  $\mathcal{O}(\theta^2)$  provided  $V$  is at least of the same order. An example of such a potential is a mass term  $V = m\theta^2$ , typical of scalar interactions.

The results of this subsection also apply to more general CS coupling functions and background metrics. In fact, these results hold for any line element that represents a general, spherically symmetric spacetime, *i.e.* Eq. (11.10). Moreover, they also hold for the most general CS field that leads to a vanishing C-tensor, *i.e.* Eq. (11.12), because the kinetic sector of  $T_{\mu\nu}^{(\theta)}$  is always quadratic in  $\theta$ .

### 11.6.3 BH perturbations in the Extended Theory and the Pontryagin constraint

In the extended theory, the Pontryagin constraint is replaced by a dynamical equation for the CS scalar field with a purely gravitational driving term. Since now there is no Pontryagin constraint, there is no *a priori* reason for the equations to disallow general BH oscillations. In fact, as we shall see in this subsection, the extended theory leads to a system of 11 PDEs for 11 dynamical variables  $(\theta, h_{\mu\nu})$ .

But can we treat  $\theta$  as a perturbation? As we have just seen, Birkhoff's theorem holds only to linear order in  $\theta$ , for a wide class of potentials  $V(\theta)$ . On the one hand, in most string-theory scenarios that necessitate the CS correction [74, 282, 83], the scalar field  $\theta$  is proportional to the string scale. In such cases,  $\theta$  is much smaller than any metric perturbation and Birkhoff's theorem holds. Nonetheless, even within such frameworks, the CS correction could be enhanced by couplings to non-perturbative, string theoretical degrees of freedom (*i.e.* gravitational instantons) [283]. Moreover, there are some theoretical frameworks where the string coupling  $g_s$  vanishes at late times [284, 285, 286, 287, 288, 290, 291, 292, 293, 294], in which case a larger coupling is permissible.

From this discussion, we cannot necessarily assume that the magnitude of the scalar field is smaller or of the same order as the metric perturbations. In fact, these perturbations and the scalar field act on completely independent scales. Therefore, all we can assume is that  $\theta$  and  $|h_{ab}|$  are both *independently* smaller than the background, which is enough to justify the use of perturbation theory.

We shall thus consider a two-parameter (bivariate) perturbative expansion of CS gravity. One perturbative parameter shall be associated with the metric perturbations,  $\epsilon$ , and the other with the scalar field,  $\tau$ . The metric in Eq. (11.14) and the scalar field can then be rewritten as

$$g_{\mu\nu} = \bar{g}_{\mu\nu} + \epsilon h_{\mu\nu}, \quad (11.70)$$

$$\theta = \tau(\bar{\theta} + \epsilon \delta\theta) = \tau\bar{\theta} + \tau\epsilon \sum_{\ell \geq 1, m} \tilde{\theta}^{\ell m} Y^{\ell m}, \quad (11.71)$$

where  $\bar{\theta}$  satisfies Birkhoff's theorem [Eq. (11.12)] and respects the spherical symmetry of the background. The quantities  $\tilde{\theta}^{\ell m} = \tilde{\theta}^{\ell m}(x^A)$  are harmonic coefficients of the scalar field perturbations, associated with the BH oscillations. There are no  $\ell = 0$  modes in the sum of Eq. (11.71) because they can always be absorbed in the monopole term  $\bar{\theta}$ .

The equations of motion for the metric perturbation and the scalar field now become formal bivariate expansions in  $\epsilon \ll 1$  as well as  $\tau \ll 1$ . The modified field equations to zeroth order in  $\epsilon$  are simply equations for the background metric, which are automatically satisfied to this order by Birkhoff's theorem. The equation of motion for the scalar field to the same order becomes

$$\tau \bar{\square}\theta = \tau \bar{g}^{\mu\nu} \bar{\nabla}_\mu \bar{\nabla}_\nu \theta = 0. \quad (11.72)$$

In Eq. (11.72), and in all remaining equations, the overhead bars on any quantity are to remind us that these quantities are to be evaluated with respect to the background metric  $\bar{g}_{\mu\nu}$ . Moreover, in Eq. (11.72) and henceforth, we shall neglect the contribution of the potential, by assuming that it is at least of  $\mathcal{O}(\tau^2)$ . As discussed earlier, the potential encodes a certain arbitrariness in the extension of the CS modification, which is why we have chosen to neglect it.

The first-order equations govern the dynamics of the metric perturbation and the perturbations of the scalar field. The equation of motion for the scalar field to  $\mathcal{O}(\epsilon)$  is given by

$$\begin{aligned} \epsilon \frac{1}{4} \delta({}^*R R) &= \epsilon \tau \left\{ \bar{\square} \delta \theta - \left[ \bar{\theta}_{,\mu\nu} + (\ln \sqrt{-\bar{g}})_{,\mu} \bar{\theta}_{,\nu} \right] h^{\mu\nu} \right. \\ &\quad \left. - \bar{\theta}_{,\mu} h^{\mu\nu}_{,\nu} + \frac{1}{2} h_{,\mu} \bar{g}^{\mu\nu} \bar{\theta}_{,\nu} \right\}. \end{aligned} \quad (11.73)$$

In Eq. (11.73),  $\delta({}^*R R)$  is the functional coefficient of  ${}^*R R$  to  $\mathcal{O}(\epsilon)$  [Eq. (11.30)] and  $h = g^{\mu\nu} h_{\mu\nu} = \bar{g}^{\mu\nu} h_{\mu\nu}$ . Equation (11.73) is harmonically decomposed in the Regge-Wheeler gauge in Eq. (K.3) of Appendix K.

Similarly, the equations of motion for the metric perturbation to  $\mathcal{O}(\epsilon)$  reduce to

$$\begin{aligned} \mathcal{O}(\tau^2) &= \epsilon \delta G_{\mu\nu} + \epsilon \tau \left[ \bar{\theta}_{,\sigma} \bar{\eta}^{\sigma\alpha\beta} \bar{\nabla}_{(\mu} \delta R_{\nu)\beta} \right. \\ &\quad + \left( \bar{\nabla}_{\tau} \bar{\theta}_{,\sigma} \right) \delta {}^*R^{\sigma}{}_{(\mu}{}^{\tau}{}_{\nu)} + \left( \bar{\nabla}_{\tau} \delta \theta_{,\sigma} \right. \\ &\quad \left. - \bar{\theta}_{,\rho} \delta \Gamma^{\rho}{}_{\sigma\tau} \right) {}^*R^{\sigma}{}_{(\mu}{}^{\tau}{}_{\nu)} \left. \right]. \end{aligned} \quad (11.74)$$

In Eq. (11.74),  $\delta G_{\mu\nu}$  is the functional coefficient of  $G_{\mu\nu}$  to  $\mathcal{O}(\epsilon)$  (see Appendix J), and all other  $\delta A^{\alpha\beta\dots}_{\chi\zeta\dots}$  stands for the coefficient to  $\mathcal{O}(\epsilon)$  of any tensor  $A^{\alpha\beta\dots}_{\chi\zeta\dots}$ . In fact, Eq. (11.74) is the formal covariant expression of the perturbation of the Einstein and C-tensors to  $\mathcal{O}(\epsilon)$ , which we computed in Appendix J for the CS coupling function in Eq. (11.33), with the exception of the term proportional to  $\delta\theta$ . The quadratic terms on the right-hand side of Eq. (11.74) come from the energy-momentum tensor of the scalar field  $\theta$  [see Eq. (11.64)]. When taking the divergence of this equation, we recover Eq. (11.73) only when quadratic terms in  $\tau$  are taken into account because functional differentiation with respect to  $\theta$  reduces the order in  $\tau$  of the resulting expression by unity.

Equations (11.73) and (11.74) govern the dynamics of BH oscillations in this extended version of CS modified gravity, but how do we solve them? Although it would be useful to decouple these equations in terms of master functions as done in GR, this is not an easy task. In addition to the mixing of parity modes and the fact that the Pontryagin constraint can no longer be used to simplify equations, there is now additional terms in the modified field equations due to the perturbations of the scalar field. Moreover, these perturbations possess their own dynamics, and hence, any decoupling should involve the whole set of perturbative variables, *i.e.*  $(\tilde{\theta}^{\ell m}, h^{\ell m}_{\mu\nu})$ .

Nonetheless, it should be possible to numerically solve the perturbative field equations of the extended modified theory in an iterative way with  $\tau \ll 1$ . One such possible iterative procedure is as follows. To zeroth order in  $\tau$ , the equations reduce to those of GR, which can be decoupled and solved numerically with standard methods. The numerical result can then be reinserted in the field equations to first order in  $\tau$ . These equations can now be decoupled in exactly the same way and will contain source terms determined by the zeroth order solution. This problem will be tackled in a future publication.

Before concluding, let us make some general remarks about the consequences of extending CS modified gravity through such kinetic terms. Equation (11.73) shows that the Pontryagin constraint has become an evolution equation for the perturbations of the scalar field,  $\delta\theta$ . Together with Eq. (11.74), this evolution equation constitutes a system of PDEs for the perturbative variables  $(\tilde{\theta}^{\ell m}, h_{\mu\nu}^{\ell m})$  that could in principle allow for generic oscillations. However, since  $\tau \ll 1$ , the magnitude of the CPM master function is forced to be small [of  $\mathcal{O}(\tau)$ ]. Otherwise, the scalar field would lead to an amplification of the CS correction to levels forbidden by solar system tests [83]. The extended theory thus relaxes the vanishing of the CPM function and replaces it by somewhat of a suppression of radiative axial modes.

Such an effect may lead to important observational consequences. In particular, the dynamics of astrophysical systems, where axial modes contribute significantly to the gravitational-wave emission, would be greatly modified. In such cases, Eqs. (11.27) and (11.28) suggest that the flux of energy emitted would be dominated by polar modes and the flux of angular momentum would be very small, since it would be linear in  $\tau$ . Such a flux suppression is in contrast to predictions of GR, where the gravitational wave emission of angular momentum is known to be large (approximately 14% of the initial ADM angular momentum for quasi-circular BH mergers [36]). Consequently, the dynamics of gravitational wave sources in the radiation-reaction dominated phase should be quite different in CS modified gravity relative to GR, thus allowing for gravitational wave tests of the extended theory.

## 11.7 Conclusions

We have studied Schwarzschild BH perturbation theory in CS modified gravity. We began by showing that Birkhoff's theorem (the statement that the Schwarzschild solution is the only vacuum, spherically-symmetric solution of the theory) holds in the modified theory for a wide class of CS coupling functions. We then decomposed the metric perturbations into tensor spherical harmonics and found the linearized modified field equations that determine their behavior. The divergence of these equations led to the linearized Pontryagin constraint, which imposes a restriction on axial metric perturbations—the CPM master function has to vanish.

Once these preliminary issues were studied, we focused on the general structure of the metric perturbations in CS modified gravity. We found that the modified theory adds new terms to the field equations that couple perturbations with polar and axial parity. Moreover, due to the restrictions imposed by the Pontryagin constraint, we find that in general the system of equations is overdetermined. Whether the entire set of equations is compatible remains unclear, but for a wide class of initial physical conditions, we

found that linear BH oscillations are not allowed in CS modified gravity. Specifically, we showed that pure axial or pure polar oscillations are disallowed for a wide class of coupling functions.

Possible extensions of the modified theory that would allow for generic BH oscillations were also discussed. In particular, we investigated the possibility of providing the CS coupling function with dynamics. In other words, the inclusion of a kinetic and potential term in the action led to the replacement of the Pontryagin constraint with an equation of motion for the coupling function. This route then lifts the vanishing restriction of the Pontryagin constraint and imposes a smallness condition on the CPM function.

The extended CS modified framework thus allows for generic BH oscillations but it imposes an important smallness restriction on axial perturbation that could lead to astrophysical observables. In particular, we saw that such a suppression of axial modes would lead to a significant decrease in the magnitude of energy, linear and angular momentum carried by gravitational radiation relative to GR. Such a decrease in gravitational wave intensity would have important consequences in the dynamics of compact object inspirals, specially in the radiation-reaction dominated phase.

Future observations of the ringdown signal in binary BH mergers could be used to test and constrain CS modified gravity. For such studies, the results found in this paper would be critical in order to determine the quasi-normal frequency spectrum of perturbations. Future work could concentrate on such a spectrum, by numerically studying the linearized and harmonically-decoupled field equations presented here. Moreover, semi-analytic studies might also be possible through the close-limit approximation. Only through detailed studies of all aspects of the modified theory and its links to experimental observations will we be able to determine its viability.

## Acknowledgments

We would like to thank Eric Poisson and Jorge Pullin for encouragement to study perturbations of black holes in the context of CS gravity. We would also like to thank Ted Jacobson, Stephon Alexander, Daniel Grumiller, Ben Owen, and Richard O'Shaughnessy for discussions. Most of our calculations used the computer algebra systems MAPLE v.11 in combination with the GRTensorII package [1].

NY would also like to thank Ben Owen for his ongoing support. CFS acknowledges support from the Natural Sciences and Engineering Research Council of Canada during the first stages of this work. Presently, he is supported by the Ramon y Cajal Programme of the Ministry of Education and Science of Spain and by a Marie Curie International Reintegration Grant (MIRG-CT-2007-205005/PHY) within the 7th European Community Framework Programme. NY acknowledges the support of the Center for Gravitational Wave Physics funded by the National Science Foundation under Cooperative Agreement PHY-01-14375, support from NSF grant PHY-05-55-628, and the University of Guelph for hospitality during a visit in which this work was started.

## Chapter 12

### A gravitational-wave probe of effective quantum gravity

The Green-Schwarz anomaly-cancelling mechanism in string theories requires a Chern-Simons term in the Einstein-Hilbert action, which leads to an amplitude birefringence of spacetime for the propagation of gravitational waves. While the degree of birefringence may be intrinsically small, its effects on a gravitational wave will accumulate as the wave propagates. The proposed Laser Interferometer Space Antenna (LISA) will be sensitive enough to observe the gravitational waves from sources at cosmological distances great enough that interesting bounds on the Chern-Simons may be found. Here we evaluate the effect of a Chern-Simons induced spacetime birefringence to the propagation of gravitational waves from such systems. We find that gravitational waves from in coalescing binary black hole system are imprinted with a signature of Chern-Simons gravity. This signature appears as a time-dependent change in the apparent orientation of the binary's orbital angular momentum with respect to the observer line-of-sight, with the change magnitude reflecting the integrated history of the Chern-Simons coupling over the worldline of a radiation wavefront. While spin-orbit coupling in the binary system will also lead to an evolution of the system's orbital angular momentum, the time dependence and other details of this *real* effect are different than the *apparent* effect produced by Chern-Simons birefringence, allowing the two effects to be separately identified. In this way gravitational wave observations with LISA may thus provide our first and only opportunity to probe the quantum structure of spacetime over cosmological distances.

#### 12.1 Introduction

“Gravitational wave” is the name we give to a short-wavelength feature of the structure of spacetime, the arena within which all other phenomena play-out their roles<sup>1</sup>. As such, the direct observation of gravitational waves offers an unprecedented opportunity to explore the environment that both enables and constrains the action of the broader phenomena of nature. Here we describe an observational probe of quantum gravity made possible by the forthcoming generation of space-based gravitational wave detectors.

---

<sup>1</sup>This chapter is based on the following papers: S. Alexander, L. S. Finn and N. Yunes, submitted to Phys. Rev. D (2007)

In most corners of the perturbative string theory moduli space (*i.e.* Type IIB, I, Heterotic) in four-dimensional compactifications, the addition of a parity-violating Chern-Simons term to the Einstein-Hilbert is required for mathematical consistency<sup>2</sup>. Furthermore in the presence of the Ramond-Ramond scalar (D-instanton charge), the Chern-Simons term is induced in *all* string theories due to duality symmetries [275, 74]. The Chern-Simons term is not unique to string theory, but in fact it could also arise in Loop Quantum Gravity, where the coupling is not necessarily limited to small values. In the strong gravity sector of this framework, this term arises to ensure invariance under large gauge transformations of the Ashtekar connection variables [78]. This correction plays the same role in string theory that an analogous anomaly-canceling correction to the quantum-chromodynamics path integral plays in the Standard Model [314]. While the anomaly-cancelling field in the Standard Model case interacts with photons, leading to significant observational constraints on its coupling, the anomaly canceling term considered here only affects the gravitational sector of the theory and is mostly unconstrained by observation [277, 317, 83].

The Chern-Simons correction to the Einstein-Hilbert action, Chern-Simons gravity [273], has been recently studied in connection with tests both in the cosmological [75, 76, 77, 74] and the weak-gravitational contexts [277, 317, 83]. In the context of gravitational wave theory, Chern-Simons gravity leads to an *amplitude birefringence* of spacetime for gravitational wave propagation [273, 74, 274]: *i.e.*, a polarization dependent amplification/attenuation of wave amplitude with distance propagated. Observation of gravitational waves that have propagated over cosmological distances, such as will be possible with the Laser Interferometer Gravitational Wave Observatory (LISA) [365, 366, 367], provide the opportunity to measure or bound the magnitude of the birefringence and, correspondingly, provide the first experimental constraints on string theory models of gravity.

Gravitational wave observations have long been recognized as a tool for testing our understanding of gravity (see [60] for a recent review). Eardley and collaborators [61, 62] first proposed a far-field test of all metric theories of gravity through gravitational wave observations. Finn [63], and later Cutler and Lindblom [64], proposed a means of realizing these measurements using a space-based detector in a circumsolar orbit observing solar oscillations in the far-zone field. Ryan [65] argued that observations of the phase evolution of the gravitational waves emitted during the gravitational-wave driven inspiral of, *e.g.*, a neutron star or stellar mass black hole into a supermassive black hole could be used to “map-out” the spacetime metric in the vicinity of the black hole horizon, testing the predictions of general relativity in the regime of strong-fields. There have been several proposals describing different ways in which gravitational wave observations could be used to place bounds on the graviton Compton-wavelength [66, 67, 68, 69, 70, 71], the existence of a scalar component to the gravitational interaction [72, 69, 70, 71], and the existence of other corrections to general relativity as manifest in some fundamental,

---

<sup>2</sup>In the case of string theory, the absence of a Chern-Simons term leads to the Green-Schwarz anomaly. Quantum consistency requires cancellation of this anomaly. In order to eliminate the anomaly, the introduction of a Chern-Simons term is essential. Heterotic M-theory makes use of an anomaly inflow, which also leads to the same requirement.

dimensionful length scale [368, 369]. The measurements we propose here are, we believe, the first example of a direct model-independent probe of string theory and quantum gravity with gravitational waves.

In section 12.2 we review Chern-Simons modified gravity, focusing attention on the scale of the Chern-Simons term and its effect on the propagation of gravitational waves in a cosmological background. In section 12.3 we evaluate the observational consequences of the Chern-Simons term in the context of ground- and space-based gravitational wave detectors. In section 12.5 we summarize our conclusions and discuss avenues of future research.

Conventions used in relativity work and conventions used in quantum field theory work are often at odds. We follow the relativity conventions Misner, Thorne and Wheeler [197] in this work: in particular,

- Our metric has signature  $- + + +$ ;
- We label indices on spacetime tensors with greek characters and use latin indices to label indices on tensors defined on spacelike slices;
- We use a semicolon in an index list to denote a covariant derivative (i.e.,  $\nabla_{\mathbf{V}}\mathbf{U}$  becomes  $V^\nu U_{\mu;\nu}$ ) and a comma to denote ordinary partial derivatives;
- Except where explicitly noted we work in *geometric units*, wherein  $G = c = 1$  for Newtonian gravitational constant  $G$  speed of light  $c$ .

Note that in geometric units, units of mass and length are interchangeable (i.e.,  $G/c^2$  has units of (length)/(mass)). This is in contrast to Planck units ( $\hbar = c = 1$ ), where units of mass and units of inverse length are interchangeable (i.e.,  $\hbar/c$  has units of (mass)  $\times$  (length)).

## 12.2 Chern-Simons Modified Gravity

### 12.2.1 Brief Review

In this subsection we review the modification to classical General Relativity by the inclusion of a Chern-Simons term, based on [273, 274]. All four dimensional compactifications of string theory lead, via the Green-Schwarz anomaly canceling mechanism, to the presence of a four dimensional gravitational Chern-Simons term [275]. Chern-Simons forms are formally defined for odd dimensions, with the 3-form of particular interest for gauge theories. By introducing an embedding coordinate, which may be dynamical, Jackiw and Yi [273] described a Chern-Simons correction to the Einstein-Hilbert action:

$$S_{\text{CS}} = \frac{1}{64\pi} \int d^4x \theta R^* R \quad (12.1)$$

where  $\theta$  is (a functional of) the embedding coordinate,

$$R^* R = \frac{1}{2} R_{\alpha\beta\gamma\delta} \epsilon^{\alpha\beta\mu\nu} R^{\gamma\delta}_{\mu\nu}, \quad (12.2)$$

and  $\epsilon^{\alpha\beta\gamma\delta}$  is the Levi-Civita tensor density. The variation with respect to the metric of this contribution to the total action (which includes the Einstein-Hilbert action plus the action corresponding to any additional matter fields) yields [273]

$$\delta S_{\text{CS}} = -\frac{1}{16\pi} \int d^4x \sqrt{-g} C_{\alpha\beta} \delta g^{\alpha\beta}, \quad (12.3)$$

where  $g$  is the determinant of the metric and  $C^{ab}$  is the C-tensor<sup>3</sup>,

$$C^{\alpha\beta} = -\frac{1}{\sqrt{-g}} \left[ \theta_{,\epsilon} \epsilon^{\epsilon\gamma\delta(\alpha} \nabla_{\gamma} R^{\beta)}_{\delta} - \nabla_{\delta} \theta_{,\gamma} \epsilon^{\mu\nu\gamma(\alpha} R^{\beta)\delta}_{\mu\nu} \right], \quad (12.4)$$

and the parenthesis in the superscript stand for symmetrization. The variation of  $S_{\text{CS}}$ , the usual Einstein-Hilbert action, and the action of other matter fields leads to the equations of motion of Chern-Simons modified gravity:

$$G_{\alpha\beta} + C_{\alpha\beta} = 8\pi T_{\alpha\beta}, \quad (12.5)$$

where  $G_{ab}$  is the Einstein tensor (i.e., the trace-reversed Ricci tensor) and  $T_{ab}$  is the stress-energy tensor of the matter fields.

By construction the divergence of the Einstein tensor  $G_{\alpha\beta}$  vanishes. If  $\theta$  is treated as a fixed, external quantity then general covariance, which requires  $\nabla \cdot \mathbf{T} = 0$ , leads to the constraint  $\nabla \cdot \mathbf{C} = 0$ , which is shown in [273] to be equivalent to  $R^*R = 0$ . Alternatively, if  $\theta$  is a dynamical field, then variation of the action with respect to  $\theta$  will lead to the same constraint on  $R^*R$ . Here we are interested in the propagation of gravitational waves in vacuum, where  $\mathbf{T} = 0$  and the constraint  $\nabla \cdot \mathbf{C} = 0$  is satisfied regardless of whether we view  $\theta$  as a dynamical field or a fixed, externally-specified quantity.

### 12.2.2 Linearized Chern-Simons gravitational waves

Focus attention on gravitational wave perturbations to a Friedmann-Robertson-Walker (FRW) cosmological background in Chern-Simons gravity. Following [274], we can write the perturbed FRW line element as

$$ds^2 = a^2(\eta) \left[ -d\eta^2 + \left( \delta_{ij} + h_{ij} \right) d\chi^i d\chi^j \right] \quad (12.6)$$

where  $\eta$  is conformal time,  $\chi^i$  are comoving spatial coordinates,  $\delta_{ij}$  is the Euclidean metric, and  $h_{ij}$  is the metric perturbation, which — for gravitational wave solutions — we can take to be transverse and traceless<sup>4</sup>. Introducing this perturbation into the field

<sup>3</sup>In [273],  $C_{ab}$  was defined as a 4-dimensional generalization of the 3-dimensional Cotton tensor. However, such a generalization already exists [331] and differs from that introduced in [273]. Therefore, we shall here refer to this quantity as the C-tensor.

<sup>4</sup>One can show that a transverse-traceless gauge exists in Chern-Simons gravity, following the same steps as in classical general relativity [197]

equations [Eq. (12.5)] leads to

$$\square_g h^j{}_i = -\frac{1}{a^2} \epsilon^{pj k} \left[ (\theta'' - 2\mathcal{H}\theta') \partial_p h'_{ki} + \theta' \partial_p \square_g h_{ki} \right], \quad (12.7)$$

where we have introduced the notation

$$' = \partial_\eta \quad (12.8)$$

$$\square_g = \partial_\eta^2 - \partial_i \partial_j \gamma^{ij} + 2\mathcal{H}\partial_\eta \quad (12.9)$$

$$\mathcal{H} = a'/a. \quad (12.10)$$

Conformal time  $\eta$  is related to proper time measured by an observer at rest with respect to the cosmological fluid via

$$dt = a(\eta)d\eta; \quad (12.11)$$

correspondingly, the conformal Hubble function  $\mathcal{H}$  is related to the Hubble function  $H$  measured by an observer at rest with respect to slices of homogeneity via

$$H \equiv \frac{\dot{a}}{a} = \frac{1}{a} \mathcal{H}, \quad (12.12)$$

where we have use dots to stand for derivatives with respect to cosmic time  $t$ .

Focus attention on plane-wave solutions to the wave equation [Eq. (12.7)]. With the ansatz

$$h_{lm}(\eta, \chi^l) = \frac{\mathcal{A}_{lm}}{a(\eta)} e^{-i[\phi(\eta) - \kappa n_k \chi^k]}, \quad (12.13)$$

where the amplitude  $\mathcal{A}_{lm}$ , the unit vector in the direction of wave propagation  $n_k$  and the conformal wavenumber  $\kappa > 0$  are all constant, we find that  $\phi$ ,  $\kappa$  and  $\mathcal{A}_{ij}$  must satisfy

$$\mathcal{D}\mathcal{A}_{ij} = -a^{-2} \epsilon^{pj k} n_p \mathcal{A}_{ki} \left[ (\theta'' - 2\mathcal{H}\theta') (\phi' - i\mathcal{H}) \kappa + i\theta' \kappa \mathcal{D} \right] \quad (12.14)$$

where

$$\mathcal{D} = -i\phi'' - (\phi')^2 - \mathcal{H}' - \mathcal{H}^2 + \kappa^2. \quad (12.15)$$

Since the Chern-Simons correction breaks parity, it is convenient to resolve  $\mathcal{A}_{ij}$  into definite parity states, corresponding to radiation amplitude in the right- and left-handed polarizations  $e_{ij}^R$  and  $e_{ij}^L$ :

$$\mathcal{A}_{ij} = \mathcal{A}_R e_{ij}^R + \mathcal{A}_L e_{ij}^L \quad (12.16a)$$

where

$$e_{kl}^R = \frac{1}{\sqrt{2}} (e_{kl}^+ + i e_{kl}^\times) \quad (12.16b)$$

$$e_{kl}^L = \frac{1}{\sqrt{2}} (e_{kl}^+ - i e_{kl}^\times) \quad (12.16c)$$

and  $e_{kl}^{+, \times}$  are the usual linear polarization tensors [197]. It is straightforward to show that

$$n_i \epsilon^{ijk} e_{kl}^{\text{R,L}} = i \lambda_{\text{R,L}} \left( e^j_l \right)^{\text{R,L}}, \quad (12.17a)$$

where

$$\lambda_{\text{R}} = +1 \quad (12.17b)$$

$$\lambda_{\text{L}} = -1. \quad (12.17c)$$

With this substitution equation (12.14) becomes two decoupled equations, one for right-hand polarized waves and one for left-hand polarized waves:

$$i \phi''_{\text{R,L}} + \left( \phi'_{\text{R,L}} \right)^2 + \mathcal{H}' + \mathcal{H}^2 - \kappa^2 = \frac{i \lambda_{\text{R,L}} \left( \theta'' - 2\mathcal{H}\theta' \right) \left( \phi' - i\mathcal{H} \right) \kappa / a^2}{\left( 1 - \lambda_{\text{R,L}} \kappa \theta' / a^2 \right)} \quad (12.18)$$

The terms on the right-hand side of equation (12.18) are the Chern-Simons corrections to gravitational plane-wave propagation in a FRW spacetime. To understand the relative scale of these terms, we rewrite the equation in terms of the ratio  $\phi'/\kappa$ :

$$\frac{y'}{\kappa} + i \left( 1 - \gamma^2 \Gamma^2 - \delta \Delta - y^2 \right) = \frac{\lambda_{\text{R,L}} (\epsilon E - 2\gamma \zeta \Gamma Z)}{1 - \lambda_{\text{R,L}} \zeta Z} (y - i\gamma \Gamma) \quad (12.19a)$$

where

$$y = \frac{\phi'}{\kappa} \quad (12.19b)$$

$$\gamma = \frac{\mathcal{H}_0}{\kappa} \quad \text{and} \quad \Gamma = \frac{\mathcal{H}}{\mathcal{H}_0} \quad (12.19c)$$

$$\delta = \frac{\mathcal{H}'_0}{\kappa^2} \quad \text{and} \quad \Delta = \frac{\mathcal{H}'}{\mathcal{H}'_0} \quad (12.19d)$$

$$\epsilon = \frac{\theta''}{a_0^2} \quad \text{and} \quad E = \frac{\theta''}{a^2 \epsilon} \quad (12.19e)$$

$$\zeta = \frac{\kappa \theta'_0}{a_0^2} \quad \text{and} \quad Z = \frac{\kappa \theta'}{a^2 \zeta} \quad (12.19f)$$

and a subscript 0 indicates the present-day value of the functions  $\theta'$ ,  $\theta''$ ,  $\mathcal{H}$ ,  $\mathcal{H}'$  and  $a$ .

If we assume that  $\theta$  and  $\mathcal{H}$  evolve on cosmological timescales (i.e.,  $f' \sim \mathcal{H}f$ ) then

$$\epsilon^2 \sim (\gamma \zeta)^2 \ll \gamma^2 \sim |\delta|. \quad (12.20)$$

Treating the terms in  $\epsilon$  and  $\gamma \zeta$  as perturbations, write the solution to equation (12.19a) as

$$y = y_0 + \epsilon y_{0,1} + \gamma \zeta y_{1,0} + \dots \quad (12.21)$$

where  $y_0 = \phi'_0/\kappa$  is the solution to the unperturbed equation [i.e., the dispersion relation in an FRW cosmology, given by equation (12.19a) with vanishing right-hand side]. The first corrections  $y_{0,1}$  and  $y_{1,0}$  owing to the Chern-Simons terms satisfy

$$y'_{0,1} - 2i\kappa y_0 y_{0,1} = \lambda_{\text{R,L}} \kappa E y_0 \quad (12.22\text{a})$$

$$y'_{1,0} - 2i\kappa y_0 y_{1,0} = -2\lambda_{\text{R,L}} \kappa \Gamma Z y_0. \quad (12.22\text{b})$$

Requiring that the perturbation vanish at some initial (conformal) time  $\eta_i$  the perturbations  $y_{0,1}$  and  $y_{1,0}$  satisfy

$$y_{0,1}(\eta) = \lambda_{\text{R,L}} \mathcal{Y}[E](\eta) \quad (12.23\text{a})$$

$$y_{1,0}(\eta) = -2\lambda_{\text{R,L}} \mathcal{Y}[\Gamma Z](\eta) \quad (12.23\text{b})$$

where

$$\mathcal{Y}[g](\eta) = \kappa e^{2i\phi_0(\eta)} \int_{\eta_i}^{\eta} dx e^{-2i\phi_0(x)} y_0(x) g(x). \quad (12.23\text{c})$$

Finally, the Chern-Simons correction to the accumulated phase as the plane-wave propagates from  $\eta_i$  to  $\eta$  is

$$\delta\phi_{\text{R,L}} = \kappa \lambda_{\text{R,L}} \int_{\eta_i}^{\eta} d\eta \{ \epsilon \mathcal{Y}[E](\eta) - 2\gamma \zeta \mathcal{Y}[\Gamma Z](\eta) \} \quad (12.24)$$

When  $\gamma \ll 1$ , i.e.,  $k_0$  is very much greater than the Hubble constant  $H_0$ , the rescaled frequency  $|y_0| \sim 1$ . In this limit we can use integration by parts to find an asymptotic expansion for  $\mathcal{Y}[g]$ :

$$\mathcal{Y}[g](\eta) \sim \frac{i\epsilon^{2i\phi_0(\eta)}}{2} \left[ e^{-2i\phi_0} \sum_{\ell=0}^n \left( \frac{1}{2i\kappa} \right)^\ell \left( \frac{1}{y_0} \frac{d}{d\eta} \right)^\ell g \right]_{\eta_i}^{\eta} + \mathcal{O} \left( \frac{1}{2i\kappa} \right)^{n+1} \quad (12.25)$$

In the next section we explore the observational consequences of gravitational wave propagation in Chern-Simons gravity.

## 12.3 Observational consequences

### 12.3.1 Birefringence in a Matter-Dominated Cosmology

Current and proposed ground-based gravitational wave detectors are sensitive to gravitational waves in the 10 Hz – 1 KHz band [370, 371, 372, 373]. Detectable sources in this band are expected to have redshifts  $z \lesssim 1$ . Space-based gravitational wave detectors like LISA [365] will be sensitive to gravitational waves in the 0.1 – 100 mHz band and, in this band, be sensitive enough to observe the gravitational waves from the inspiral of several  $\sim 10^6 M_\odot$  black hole binary systems at  $z \lesssim 30$ : i.e., anywhere in the universe

they are expected [374, 366]. For sources in the band of these detectors

$$\gamma = 3.7 \times 10^{-19} \left( \frac{h_{100}}{0.72} \right) \left( \frac{1 \text{ Hz}}{kc/2\pi} \right) \ll 1 \quad (12.26)$$

where

$$h_{100} = \frac{H_0}{100 \text{ km s}^{-1} \text{ Mpc}^{-1}}. \quad (12.27)$$

Additionally, for redshifts  $z \lesssim 30$  the universe is well described by a matter-dominated FRW cosmological model. In this section we evaluate the effect that the Chern-Simons corrections described above have on propagation of gravitational plane-waves through a matter-dominated FRW model.

In a matter-dominated FRW model the scale factor  $a(t)$  satisfies [197]

$$\frac{a(\eta)}{a_0} = \eta^2 = \frac{1}{1+z} \quad (12.28a)$$

where, by convention,  $\eta = 1$  at the present epoch. In this model and with this convention

$$\mathcal{H} = \frac{2}{\eta} = 2\sqrt{1+z} \quad \text{and} \quad \mathcal{H}_0 = 2, \quad (12.28b)$$

$$\gamma = \frac{2}{\kappa} \quad \text{and} \quad \Gamma = \eta^{-1} = \sqrt{1+z}, \quad (12.28c)$$

$$\delta = -\frac{2}{\kappa^2} \quad \text{and} \quad \Delta = \eta^{-2} = 1+z, \quad (12.28d)$$

$$\epsilon = \frac{H_0^2}{4} \theta_0'' \quad \text{and} \quad E = \frac{1}{\eta^4} \theta_0'', \quad (12.28e)$$

$$\zeta = \frac{H_0 k}{2} \theta_0' \quad \text{and} \quad Z = \frac{1}{\eta^4} \theta_0', \quad (12.28f)$$

$$(12.28g)$$

Additionally,

$$E = \frac{1}{\eta^4} \theta_0'' \quad (12.28h)$$

$$Z = \frac{1}{\eta^4} \theta_0' \quad (12.28i)$$

$$a_0 = \frac{\mathcal{H}_0}{H_0} = \frac{2}{H_0}. \quad (12.28j)$$

With the  $\gamma$  and  $\Gamma$  parameters for a matter-dominated FRW cosmological model, the unperturbed equation for  $y_0$  has solutions of the form

$$y_0 = -\frac{i}{\kappa\eta} \frac{\left(1 + C\kappa\eta - \kappa^2\eta^2\right) \cos(\kappa\eta) - \left(C - \kappa\eta - C\kappa^2\eta^2\right) \sin(\kappa\eta)}{(1 + C\kappa\eta) \cos(\kappa\eta) - (C - \kappa\eta) \sin(\kappa\eta)}, \quad (12.29)$$

where  $C$  is a constant of the integration. In the limit of large  $\kappa$  the evolution of  $\kappa$  should decouple from the universal expansion; thus, we are led to choose  $C = \pm i$ , which eliminates the oscillatory terms in our general solution for  $y_0$ :

$$y_0 = \frac{\pm\kappa^3\eta^3 - i}{\kappa\eta(1 + \kappa^2\eta^2)} \quad (12.30)$$

Consistent with our ansatz [cf. Eq. (12.13)] we choose the solution with positive  $\Re(y_0)$ : i.e.,  $C = +i$ . Solving this equation for the phase  $\phi'_0 = \kappa y_0$  we find

$$\Delta\phi_0(\eta) = \phi_0(1) - \phi_0(\eta) \quad (12.31a)$$

$$= \left[ \kappa(1 - \eta) - \arctan \frac{\kappa(1 - \eta)}{1 + \kappa^2\eta} \right] - \frac{i}{2} \ln \left[ \frac{1 + \kappa^2\eta^2}{\eta^2(1 + \kappa^2)} \right] \quad (12.31b)$$

$$= \left[ \frac{2}{\gamma} \frac{\sqrt{1+z}-1}{\sqrt{1+z}} - \arctan \frac{2\gamma(\sqrt{1+z}-1)}{4 + \gamma^2\sqrt{1+z}} \right] - \frac{i}{2} \ln \left[ 1 + \frac{\gamma^2 z}{4 + \gamma^2} \right] \quad (12.31c)$$

In the absence of the Chern-Simons correction an observer at rest with respect to slices of (cosmological) homogeneity will observe a passing gravitational plane-wave to undergo a change in phase  $\Delta\phi_0(\eta)$  between cosmological time  $\eta$  and the present epoch.

With  $y_0$  and equations (12.23) we can evaluate the Chern-Simons contribution to the phase change owing to propagation from cosmological time  $\eta_0$ . Making use of the asymptotic expansions for  $y_{0,1}$  and  $y_{1,0}$  [Eq. (12.25)] we find

$$y_{0,1(R,L)} \sim \frac{i\lambda_{R,L}}{2} \left[ E(\eta) - E(\eta_0)e^{-2i[\Delta\phi_0(\eta_0) - \Delta\phi_0(\eta)]} \right] + \mathcal{O}(\gamma) \quad (12.32a)$$

$$y_{1,0(R,L)} \sim -i\lambda_{R,L} \left[ \Gamma(\eta)Z(\eta) - \Gamma(\eta_0)Z(\eta_0)e^{-2i[\Delta\phi_0(\eta_0) - \Delta\phi_0(\eta)]} \right] + \mathcal{O}(\gamma), \quad (12.32b)$$

which may be integrated to find  $\Delta\phi_{1(R,L)}$ :

$$\Delta\phi_{1(R,L)} = i\lambda_{R,L} \frac{\kappa}{2} \int_{\eta_0}^1 \left[ \epsilon \frac{1}{\eta^4} \frac{\theta''(\eta)}{\theta''_0} - 2\gamma\zeta \frac{1}{\eta^5} \frac{\theta'(\eta)}{\theta'_0} \right] d\eta + \mathcal{O}(\gamma), \quad (12.33a)$$

$$= i\lambda_{R,L} \frac{k_0}{H_0} \xi(\eta). \quad (12.33b)$$

It is convenient to rewrite  $\xi$  as a function of  $z$ :

$$\xi(z) = \alpha A(z) + \beta B(z), \quad (12.33c)$$

where

$$A(z) = \int_0^z dz (1+z)^{5/2} \frac{d\theta/dz}{(d\theta/dz)_0} \quad (12.33d)$$

$$B(z) = \int_0^z dz (1+z)^{7/2} \frac{d^2\theta/dz^2}{(d^2\theta/dz^2)_0} \quad (12.33e)$$

$$\alpha = -\gamma\zeta + \frac{3\epsilon}{2} \frac{(d\theta/dz)_0}{2(d^2\theta/dz^2)_0 + 3(d\theta/dz)_0}, \quad (12.33f)$$

$$\beta = \frac{\epsilon (d^2\theta/dz^2)_0}{2(d^2\theta/dz^2)_0 + 3(d\theta/dz)_0}, \quad (12.33g)$$

and the subscript zero denotes present-day values of the subscripted quantities. The leading order Chern-Simons correction to the accumulated phase is thus pure imaginary, corresponding to an attenuation of one circular polarization state and an equal amplification of the other. The attenuation/amplification is linearly dependent on the wavenumber. The function  $\xi(z)$  may be thought of as a “form-factor” that probes the past history of the coupling  $\theta$ .

### 12.3.2 Binary Inspiral at Cosmological Distances

The proposed LISA gravitational wave detector is capable of observing coalescing binary black hole systems at cosmological distances: for example, the gravitational waves associated with a pair of  $10^6 M_\odot$  black holes will be observable at redshifts  $z$  approaching 30. Over the year leading up to the merger of two such black holes the binary’s period will decrease by two orders of magnitude, leading to a corresponding decrease in the radiation wavelength and increase in the magnitude of the Chern-Simons correction. The time-dependent relationship between the radiation amplitude in the two polarization states thus carries with it the signature of Chern-Simons gravity and can be used to characterize the functional  $\theta$  that describes the Chern-Simons correction to classical General Relativity.

To calculate the signature left by the Chern-Simons correction on the gravitational waves from a coalescing binary system at redshift  $z$ , we begin with the radiation near the source. Treating, as before, the Chern-Simons correction as a perturbation, the quadrupole approximation to the radiation from the binary system in the neighborhood

of the source is given by

$$\hat{\mathbf{h}} = \Re \left[ \hat{h}_+ e_+ + \hat{h}_\times e_\times \right] \quad (12.34a)$$

$$\hat{h}_+ = \frac{2\widehat{\mathcal{M}}}{d} \left[ 1 + \hat{\chi}^2 \right] \left[ \widehat{\mathcal{M}}\hat{k}(\hat{t})/2 \right]^{2/3} \exp \left[ -i \left( \hat{\Phi}(\hat{t}) - \hat{k}(\hat{t})d \right) \right], \quad (12.34b)$$

$$\hat{h}_\times = \frac{4i\widehat{\mathcal{M}}}{d} \hat{\chi} \left[ \widehat{\mathcal{M}}\hat{k}(\hat{t})/2 \right]^{2/3} \exp \left[ -i \left( \hat{\Phi}(\hat{t}) - \hat{k}(\hat{t})d \right) \right], \quad (12.34c)$$

where  $d$  is the proper distance to the source and

$$\hat{\Phi}(\hat{t}) = -2 \left( \frac{\hat{T} - \hat{t}}{5\widehat{\mathcal{M}}} \right)^{5/8} + \hat{\delta}, \quad (12.35)$$

$$\hat{k}(\hat{t}) = \frac{2}{\widehat{\mathcal{M}}} \left( \frac{5}{256} \frac{\widehat{\mathcal{M}}}{\hat{T} - \hat{t}} \right)^{3/8}. \quad (12.36)$$

The constants  $\hat{T}$  and  $\hat{\delta}$ , which determine when coalescence occurs and the phase of the gravitational wave signal at some fiducial instant, are set by initial conditions. The quantities  $\widehat{\mathcal{M}}$  and  $\hat{\chi}$  are constants that depend on the binary system's component masses ( $m_1, m_2$ ) and orientation with respect to the observer:

$$\hat{\chi} = \left( \begin{array}{l} \text{cosine-angle between the orbital angular} \\ \text{momentum and the observer line-of-sight} \end{array} \right) \quad (12.37a)$$

$$\widehat{\mathcal{M}} = \frac{m_1^{3/5} m_2^{3/5}}{(m_1 + m_2)^{1/5}} = (\text{“chirp” mass}). \quad (12.37b)$$

We “hat” all these quantities to remind us that, as expressed above, they are appropriate descriptions only in the neighborhood of the source where the Chern-Simons and cosmological corrections to the propagation of the waves may be neglected.

To describe the radiation after it has propagated to the detector we first describe the near-source radiation in terms of circular polarization states

$$\hat{\mathbf{h}} = \Re \left[ \hat{h}_R e_R + \hat{h}_L e_L \right], \quad (12.38a)$$

$$\hat{h}_{R,L} = \sqrt{2} \frac{\widehat{\mathcal{M}}}{d} \left( \frac{\widehat{\mathcal{M}}\hat{k}}{2} \right)^{2/3} \left( 1 + \lambda_{R,L} \hat{\chi} \right)^2 \exp \left[ -i \left( \hat{\Phi}(\hat{t}) - \hat{k}(\hat{t})d \right) \right]. \quad (12.38b)$$

We are interested in the radiation incident on our detector today ( $z = 0, \eta = 1$ ) from a source at redshift  $z$ . Matching the near-source description of the radiation [Eq. (12.38)] to our ansatz [Eq. (12.13)] we find the description of the radiation after propagating to

the detector from a redshift  $z$ :

$$\mathbf{h} = \Re \left[ \hat{h}_R e_R + \hat{h}_L e_L \right], \quad (12.39a)$$

$$\begin{aligned} h_{R,L} = & \sqrt{2} \frac{\mathcal{M}}{d_L} \left( \frac{\mathcal{M}k_0}{2} \right)^{2/3} \left( 1 + \lambda_{R,L} \hat{\chi} \right)^2 \exp \left[ -i \left( \Phi_0(t) - \kappa(1 - \eta) \right. \right. \\ & \left. \left. + \Delta\phi_0(t) + \Delta\phi_{1(R,L)}(t) \right) \right] \end{aligned} \quad (12.39b)$$

where

$$\Phi_0(t) = -2 \left( \frac{T-t}{5\mathcal{M}} \right)^{5/8} + \delta, \quad (12.39c)$$

$$k_0(t) = \frac{2}{\mathcal{M}} \left( \frac{5}{256} \frac{\mathcal{M}}{T-t} \right)^{3/8} \quad (12.39d)$$

$$d_L = a_0 \eta (1+z) = (\text{Luminosity distance to source}) \quad (12.39e)$$

$$\mathcal{M} = (1+z) \hat{\mathcal{M}} \quad (12.39f)$$

$$\begin{aligned} \Delta\phi_0 = & \frac{2(\sqrt{1+z}-1)}{H_0\sqrt{1+z}} k_0(t) - \arctan 2\gamma(t) \frac{\sqrt{1+z}-1}{4+\sqrt{1+z}\gamma^2(t)} \\ & - \frac{i}{2} \ln \left[ 1 + \gamma^2(t) \frac{z}{4+\gamma^2(t)} \right] \end{aligned} \quad (12.39g)$$

$$\gamma(t) = \frac{H_0}{k_0(t)}, \quad (12.39h)$$

and  $\Delta\phi_{1(R,L)}$  given by equations (12.33) above. Here  $t$  is proper time as measured by a detector at rest with respect to the cosmological fluid at the present epoch ( $\eta = 1$ ),  $k_0(t)$  is the instantaneous wavenumber of the wavefront passing the detector at observer time  $t$ , and  $T$  and  $\delta$  are, as before, constants of the integration. The correction  $\Delta\phi_0$ , which is the same for all polarizations, embodies  $\mathcal{O}(k_0/H_0)$  corrections to the wave phase owing to the wave propagation through the time-dependent cosmological background. The correction  $\Delta\phi_{1(R,L)}$  is of opposite character for the two polarization states and embodies the (first-order) corrections to wave propagation owing to the Chern-Simons corrections to the Einstein Field Equations.

Focus attention on the argument of the exponential in equation (12.39b). The term  $\kappa(1 - \eta)$  cancels the first term in equation (12.39g) for  $\Delta\phi_0$ , leading to

$$\begin{aligned} h_{R,L} = & \sqrt{2} \frac{\mathcal{M}}{d_L} \left( \frac{\mathcal{M}k_0}{2} \right)^{2/3} \left( 1 + \lambda_{R,L} \hat{\chi} \right)^2 \exp \left[ -i \left( \Phi_0(t) \right. \right. \\ & \left. \left. - \frac{\gamma(t)}{2} (\sqrt{1+z}-1) + \Delta\phi_{1(R,L)}(t) \right) \right] \end{aligned} \quad (12.40)$$

The observational effect of the Chern-Simons is readily identified by looking at the ratio of the polarization amplitudes  $h_R$  and  $h_L$ :

$$\frac{h_R}{h_L} = \frac{(1 + \hat{\chi})}{(1 - \hat{\chi})} \exp \left[ \frac{2k(t)\xi(z)}{H_0} \right] \quad (12.41)$$

$$= \frac{1 + x}{1 - x} \quad (12.42)$$

where  $\xi$  is given by equations (12.33) and  $x$  may be interpreted as the *apparent* inclination cosine-angle. The effect of the Chern-Simons correction on gravitational wave propagation is to confound the identification between polarization amplitude ratios and binary orbit inclination cosine-angle. *In the same way that we say that the curvature of spacetime “bends” light passing close to strongly gravitating body we may say that the effect of the Chern-Simons correction is to “rotate” the apparent inclination angle of the binary system’s orbital angular momentum axis either toward or away from us.*

## 12.4 Discussion

### 12.4.1 What can be measured?

Over the course of a year-long observation the LISA spacecraft constellation will measure the radiation in both polarizations of an incident gravitational wave train associated with an inspiraling coalescing binary system. The relative amplitude of the two polarizations will be determined by the orientation of the binary systems orbital plane to the observer line-of-sight and the form factor  $\xi(z)$ . A non-vanishing  $\xi$  leads to a time-varying apparent inclination angle that, by nature of its time dependence, can (in principle) be measured directly from the apparent inclination angle’s time variation.

Other properties of an inspiraling binary can lead to an evolution of the (apparent) inclination cos-angle. Spin-orbit coupling leads to a real precession of the binary’s orbital plane and a corresponding time-dependence in the actual inclination cos-angle  $\hat{\chi}$ . Referring to equation (12.39b), it is apparent that for small  $|\hat{\chi}| \sim 0$  an incremental change  $\mu$  in  $\hat{\chi}$  will lead to changes in  $h_{R,L}$  that are indistinguishable from an increment in  $x$  associated with  $\xi$ . Following Vecchio [375, eq. 27–31] we note that, at first non-vanishing post-Newtonian order, spin-orbit interactions in an inspiraling binary system lead to

$$\left( \frac{d\hat{\chi}}{dt} \right)_{\text{so}} \propto k_0^{2/3}(t). \quad (12.43)$$

This is a different dependence on  $k_0$  than the  $\mathcal{O}(k_0)$  dependence associated with  $\xi$ . Thus, it remains in principle possible to distinguish the signature of Chern-Simons gravity in the signal from cosmologically distant coalescing binary black hole systems. The accuracy with which such a measurement can be made is the topic of the next subsection.

### 12.4.2 How accurately can $\xi$ be measured?

The most general astrophysical black hole binary system can be described by eleven independent parameters, which may be counted as two component masses; component spins and their orientation (six parameters); orbital eccentricity; orbital phase; and a reference time when the phase, spins and eccentricity are measured. The gravitational wave signal in any particular polarization will depend on the description of the binary and six additional parameters that describe the binary's orientation with respect to the detector. These six additional parameters may be counted as orbital plane orientation (two angles); source location with respect to the detector (distance and two position angles); orbit orientation in orbital plane (one angle)<sup>5</sup>. To these seventeen parameters we now add  $\xi$ , which describes the effect of propagation through the birefringent Chern-Simons spacetime, for a total of eighteen parameters that are required to describe the signal from a coalescing binary system.

To-date, all analyses of expected parameter estimation errors have been made with under a set of approximations that focus attention on the measurement of component masses, source location (both distance and angular position), and the expected time of binary coalescence. Even the most sophisticated of these analysis ignore all but the leading-order contribution to the gravitational wave signal *amplitude* at twice the orbital frequency<sup>6</sup> and assume that the orbital eccentricity is *known* to vanish. These approximations are quite appropriate for their purpose (estimation of component masses, source location and expected time of coalescence); however, by ignoring all but the leading order contribution to the signal magnitude they are inadequate starting points for exploring the accuracy with which  $\xi$ , which affects only the signal amplitude in the different polarizations, can be bounded<sup>7</sup>. Evaluating and presenting the errors associated with the measurement of  $\xi$  via a full co-variance matrix analysis is thus a formidable enterprise, to be addressed in a future work.

Nevertheless, through a series of plausible approximations it is possible to make a crude estimate of the accuracy with which  $\xi$  can be determined. To begin, assume we have two gravitational wave detectors such that, via a linear combination of observations made at each, we can synthesize two other detectors with one exclusively sensitive to  $h_R$  and one exclusively sensitive to  $h_L$ . Write the scalar detector response of each of these detectors as

$$m_{R,L}(t) = \exp \left[ \mu_{R,L}(t) + i\psi_{R,L}(t) \right], \quad (12.44)$$

for real  $\mu_{R,L}$  and  $\psi_{R,L}$ . Next, note that the parameters that describe a coalescing binary system can be divided into two groups: those that principally affect only the signal amplitude (i.e.,  $\mu(t)$ ) and those that affect only or principally the real part of the signal

---

<sup>5</sup>This parameterization, while convenient for counting, is not the most appropriate for describing a coalescing binary, where spins, eccentricity, and orbital plane orientation all evolve with time.

<sup>6</sup>See [376] for an analysis that relaxes this approximation

<sup>7</sup>This applies also to the assumption of zero eccentricity: if, as is likely, the estimation errors associated with eccentricity and  $\xi$  are correlated it will be necessary to include an eccentricity-like parameter in the analysis in order to avoid under-estimating the errors associated with the measurement of  $\xi$ .

phase (i.e.,  $\psi(t)$ ). The first group includes distance, source orientation with respect to the observer line-of-sight, and  $\xi$ . The second group includes the orbital phase, sky location (through its affect on the Doppler correction to the signal phase as the detector orbits about the sun), the instantaneous binary period at some fiducial moment, and the parameters associated with spin and orbital angular momentum <sup>8</sup>. If we approximate each detectors' noise as white with one-sided noise power spectral density  $S_0$  then the elements of the inverse covariance matrix  $\mathbf{\Gamma}$  — the so-called Fisher matrix — are given by [378, 4]

$$\Gamma_{ij} = \sum_{k=R,L} \frac{2}{S_0} \int_{t_i}^{t_f} \Re \left( \frac{\partial m_k}{\partial x^i} \right) \Re \left( \frac{\partial m_k}{\partial x^j} \right) dt \quad (12.45)$$

where the integration is over the observation period  $(t_i, t_f)$  and the  $x^i$  are the parameters that characterize the incident gravitational wave, which we have divided into two groups. Matrix elements  $\Gamma_{ij}$  where  $x^i$  and  $x^j$  belong to different groups will be much smaller than elements where  $x^i$  and  $x^j$  belong to the same group. Setting the cross-group elements to zero we obtain an approximate  $\mathbf{\Gamma}$  that is block diagonal, with one block corresponding to  $\Gamma_{ij}$  with  $(x^i, x^j)$  drawn from the first group and the other block corresponding to  $\Gamma_{ij}$  with  $(x^i, x^j)$  drawn from the second group. Estimation uncertainties of parameters in either group can now be determined independently of the parameters in the other group.

Focus attention now on those parameters that affect only  $\mu(t)$ , the signals amplitude evolution. The leading order dependence of the amplitude  $|h_{R,L}|$  on the binary systems parameters is given by

$$A_{R,L} = |h_{R,L}| = \left(1 + \lambda_{R,L} \hat{\chi}_0\right)^2 \frac{2\mathcal{M}}{d_L} \left[ \frac{k_0(t)\mathcal{M}}{2} \right]^{2/3} \exp \left( \lambda_{R,L} \xi \frac{k_0(t)}{H_0} \right) \quad (12.46)$$

where  $\mathcal{M}$  is assumed known. Setting aside the antenna pattern factors associated with the projection of the signal onto the LISA detector (which depend only on the known source sky position and the LISA orbital ephemeris), assuming that there is no real precession in the binary system under observation (i.e.,  $\hat{\chi}_0$ ), and that  $k(t)$  is given by equation (12.36) the inverse of the covariance matrix — the so-called Fisher matrix,  $\mathbf{\Gamma}$  —

---

<sup>8</sup>This approximation is weakest for the spin and orbital angular momentum parameters: see [377].

associated with the amplitude measurements is a symmetric  $3 \times 3$  matrix with elements

$$\Gamma_{\mathcal{D}\mathcal{D}} = \frac{1}{S_0} \int_{t_i}^{t_f} (A_R^2 + A_L^2) dt \simeq 8 \left(1 + 6\hat{\chi}_0^2 + \hat{\chi}_0^4\right) \left(\frac{\mathcal{M}}{d_L}\right)^2 \mathcal{I} + \mathcal{O}(\xi) \quad (12.47a)$$

$$\Gamma_{\mathcal{D}\hat{\chi}_0} = \frac{1}{S_0} \int_{t_i}^{t_f} \left[ \frac{2}{1 - \hat{\chi}_0} A_L^2 - \frac{2}{1 + \hat{\chi}_0} A_R^2 \right] dt \simeq -16\hat{\chi}_0 \left(3 + \hat{\chi}_0^2\right) \left(\frac{\mathcal{M}}{d_L}\right)^2 \mathcal{I} + \mathcal{O}(\xi) \quad (12.47b)$$

$$\Gamma_{\mathcal{D}\xi} = \frac{1}{S_0} \int_{t_i}^{t_f} \frac{k_0(t)}{H_0} (A_L^2 - A_R^2) dt \simeq -\frac{64\hat{\chi}_0 (1 + \hat{\chi}_0^2)}{\mathcal{M}H_0} \left(\frac{\mathcal{M}}{d_L}\right)^2 \mathcal{J} + \mathcal{O}(\xi) \quad (12.47c)$$

$$\Gamma_{\hat{\chi}_0\hat{\chi}_0} = \frac{1}{S_0} \int_{t_i}^{t_f} \left[ \frac{4A_R^2}{(1 + \hat{\chi}_0)^2} + \frac{4A_L^2}{(1 - \hat{\chi}_0)^2} \right] dt \simeq 32 \left(1 + \hat{\chi}_0^2\right) \left(\frac{\mathcal{M}}{d_L}\right)^2 \mathcal{I} + \mathcal{O}(\xi) \quad (12.47d)$$

$$\Gamma_{\hat{\chi}_0\xi} = \frac{1}{S_0} \int_{t_i}^{t_f} \frac{2k_0(t)}{H_0} \left[ \frac{A_R^2}{1 + \hat{\chi}_0} + \frac{A_L^2}{1 - \hat{\chi}_0} \right] dt \simeq \frac{32 \left(1 + 3\hat{\chi}_0^2\right)}{\mathcal{M}H_0} \left(\frac{\mathcal{M}}{d_L}\right)^2 \mathcal{J} + \mathcal{O}(\xi) \quad (12.47e)$$

$$\Gamma_{\xi\xi} = \frac{1}{S_0} \int_{t_i}^{t_f} \frac{k_0^2(t)}{H_0^2} (A_R^2 + A_L^2) dt \simeq \frac{32 \left(1 + 6\hat{\chi}_0^2 + \hat{\chi}_0^4\right)}{(\mathcal{M}H_0)^2} \left(\frac{\mathcal{M}}{d_L}\right)^2 \mathcal{K} + \mathcal{O}(\xi) \quad (12.47f)$$

where

$$\mathcal{D} = \ln d_L \quad (12.47g)$$

$$\begin{aligned} \mathcal{I} &= \int_{t_i}^{t_f} \left(\frac{k_0(t)\mathcal{M}}{2}\right)^{4/3} \frac{dt}{S_0} = \frac{5}{192} \int_{k_{\min}}^{k_{\max}} \left(\frac{k\mathcal{M}}{2}\right)^{-7/3} \frac{\mathcal{M}^2 dk}{S_0} \\ &= -\frac{2^{1/3}\mathcal{M}}{S_0} \frac{5}{64} (k\mathcal{M})^{-4/3} \Big|_{k_{\min}}^{k_{\max}} \end{aligned} \quad (12.47h)$$

$$\begin{aligned} \mathcal{J} &= \int_{t_i}^{t_f} \left(\frac{k_0(t)\mathcal{M}}{2}\right)^{7/3} \frac{dt}{S_0} = \frac{5}{192} \int_{k_{\min}}^{k_{\max}} \left(\frac{k\mathcal{M}}{2}\right)^{-4/3} \frac{\mathcal{M}^2 dk}{S_0} \\ &= -\frac{2^{1/3}\mathcal{M}}{S_0} \frac{5}{32} (k\mathcal{M})^{-1/3} \Big|_{k_{\min}}^{k_{\max}} \end{aligned} \quad (12.47i)$$

$$\begin{aligned} \mathcal{K} &= \int_{t_i}^{t_f} \left(\frac{k_0(t)\mathcal{M}}{2}\right)^{10/3} \frac{dt}{S_0} = \frac{5}{192} \int_{k_{\min}}^{k_{\max}} \left(\frac{k\mathcal{M}}{2}\right)^{-1/3} \frac{\mathcal{M}^2 dk}{S_0} \\ &= \frac{2^{1/3}\mathcal{M}}{S_0} \frac{5}{128} (k\mathcal{M})^{2/3} \Big|_{k_{\min}}^{k_{\max}}. \end{aligned} \quad (12.47j)$$

and we have taken advantage of the fact that for inspiraling compact binary systems in the quadrupole approximation  $k(t)$  is monotonic in  $t$  to re-express the integrals over the

interval  $(t_i, t_f)$  as integrals over  $[k(t_i), k(t_f)] = (k_{\min}, k_{\max})$ . In the particular case of a binary seen plane-on ( $\hat{\chi}_0 = 0$ ), the  $(\mathcal{D}\hat{\chi}_0)$  and  $(\mathcal{D}\xi)$  blocks of  $\mathbf{\Gamma}$  are diagonal, leading to

$$\nu_{\hat{\chi}_0\hat{\chi}_0} = \frac{1}{4\rho^2} \frac{\mathcal{K}\mathcal{I}}{\mathcal{I}\mathcal{K} - \mathcal{J}^2} \quad (12.48a)$$

$$\nu_{\xi\xi} = \frac{(\mathcal{M}H_0)^2}{4\rho^2} \frac{\mathcal{I}^2}{\mathcal{I}\mathcal{K} - \mathcal{J}^2} \quad (12.48b)$$

where  $\nu_{ij}$  is the ensemble average co-variance

$$\nu_{ij} = \overline{(x^i - \bar{x}_i)(x^j - \bar{x}_j)} = (\mathbf{\Gamma}^{-1})_{ij} \quad (12.48c)$$

and we have expressed the  $\nu_{ij}$  in terms of the ensemble average amplitude-squared signal-to-noise ratio  $\rho^2$

$$\rho^2 = \frac{1}{S_0} \int_{t_i}^{t_f} dt (A_R^2 + A_L^2) \quad (12.48d)$$

Focus attention on a binary system of two black holes at redshift  $z$ , each with mass  $M = 10^6 M_\odot (1+z)^{-1}$ . Over the final year before coalescence the radiation wavelength  $2\pi/k$  observed at the detector will range from  $c(10^{-4} \text{ Hz})^{-1}$  to  $c(10^{-2} \text{ Hz})^{-1}$ . For such a system,

$$\rho = \frac{10^5 h_{100}}{1+z - \sqrt{1+z}} \left( \frac{10^{-40} \text{ Hz}^{-1}}{S_0} \right)^{1/2} \quad (12.49)$$

$$\nu_{\xi\xi} = 3.1 \times 10^{-40} \left( \frac{S_0}{10^{-40} \text{ Hz}^{-1}} \right) (1+z - \sqrt{1+z})^2 \quad (12.50)$$

Observation of binary systems like these at  $z = 15$  by LISA will be capable of placing a “1-sigma” upper bound on  $\xi$  of order  $10^{-19}$ .

### 12.4.3 How large might $\xi$ be?

To estimate  $\xi$  [cf. Eq. (12.33c)] we must invoke a theoretical model for the functional  $\theta[\phi(z)]$ . As described in the introduction, perturbative string theory requires a Chern-Simons correction to the Einstein-Hilbert action<sup>9</sup>. Here we describe a different mechanism, that can also lead to the presence of a Chern-Simons correction. Consider the back-reaction of a  $\mathcal{N} = 1$  supersymmetric Yang-Mills theory in a curved background (cf. [282, Appendix A]) with action

$$S_{\text{CS}} = \frac{1}{16\pi} \int d^4x \mathcal{F}_1(S) (\mathbf{R}^* \mathbf{R}), \quad (12.51)$$

<sup>9</sup>Other theories, such as loop quantum gravity, may also possess a similar correction in the low-energy limit; however, no effective Hamiltonian has yet been found in the full theory of loop quantum gravity and cosmology, which prevents further speculation as to whether such an extension of general relativity requires a Chern-Simons modification.

where  $S$  is the glueball superfield and  $\mathcal{F}_1(S)$ , which plays the role of  $\theta$  in equation (12.1), can be exactly evaluated by using perturbative matrix model technology developed in [379]. Within this Yang-Mills framework,  $\theta$  is a functional  $\theta[\varphi]$  of some pseudo-scalar field  $\varphi$ , the gravitational axion, that depends only on conformal time [274]. The functional  $\theta[\varphi]$  can be expressed as

$$\theta[\varphi] = \frac{\mathcal{N} \ell_{\text{Pl}}^2}{2\pi} \frac{\varphi}{M_{\text{Pl}}}, \quad (12.52)$$

where  $\ell_{\text{Pl}} = (\hbar G/c^3)^{1/2}$  is the Planck length,  $M_{\text{Pl}} = (\ell_{\text{Pl}} \sqrt{8\pi})^{-1}$  is the reduced Planck mass and  $\mathcal{N}$  is a dimensionless constant. Through use of the low-energy effective 4-dimensional heterotic string action the constant  $\mathcal{N}$  can be evaluated in terms of the ten-dimensional fundamental string energy scale  $M_s$  and the dimensionless string coupling  $g_s$ ,

$$\mathcal{N} = \left( \frac{M_{\text{Pl}}}{M_s} \right)^2 \frac{1}{\sqrt{g_s}}, \quad (12.53)$$

leading to

$$\theta[\varphi] = \frac{1}{16\pi^2 M_{\text{Pl}}^2} \frac{\varphi}{M_s} \frac{M_{\text{Pl}}}{M_s \sqrt{g_s}}. \quad (12.54)$$

Assuming that  $\varphi$ , which has units of inverse length, evolves with the Hubble parameter  $H \propto \eta^{-3}$  we have

$$A(z) = B(z) = -\frac{2}{11} \left[ (1+z)^{11/2} - 1 \right] \quad (12.55)$$

and

$$\xi = -\frac{1}{11} \left[ (1+z)^{11/2} - 1 \right] (\epsilon - 2\gamma\zeta) \quad (12.56)$$

with  $(\epsilon - \gamma\zeta)$  of the order of

$$\epsilon - 2\gamma\zeta \simeq \frac{(1.8 + 3.5h_{100}^2) \times 10^{-120}}{\sqrt{g_s}} \left( \frac{\varphi_0}{M_s} \right) \left( \frac{10^{16} \text{ GeV}}{M_s} \right). \quad (12.57a)$$

The size of  $\xi$  thus depends on the present value of the field  $\varphi_0$ , the fundamental string energy scale  $M_s$  and the string coupling  $g_s$ , none of which are constrained by present-day theory.

The lesson to draw from the discussion of this scenario is that the magnitude of any Chern-Simons correction depends strongly on the external theoretical framework that prescribes the functional  $\theta[\varphi]$ . For non-vanishing string coupling in the perturbative string theory scenario the Chern-Simons correction seems undetectable owing to the Planck scale suppression of the decay constant of the universal gravitational axion field  $\varphi$ . However, this model and the associated expected scale of  $\epsilon - 2\gamma\zeta$  applies only to the *perturbative* sector of string theory and, in particular, when Ramond-Ramond charges are turned off. If present these additional degrees of freedom do couple and source the Chern-Simons correction, leading to a larger decay constant (e.g. D3 branes always excite the

Chern-Simons interaction in four dimensions). In a recent work, Svrcek [380] noted that, due to non-perturbative gravitational instanton corrections, the Chern-Simons coupling in the non-perturbative sector is currently incalculable. Even within the perturbative framework there are theoretical frameworks where  $\xi$  could become significant: e.g., if the string coupling  $g_s$  vanishes at late times [284, 285, 286, 287, 288, 289, 290, 291, 292, 293, 294]. Therefore, within the full string theory framework, a larger coupling, which would push the stringy Chern-Simons correction into the observational window, is not excluded and bounding it places a constraint on string theory motivated corrections to classical general relativity.

Setting aside string theory for a moment, other theoretical frameworks lead to a Chern-Simons correction to the Einstein-Hilbert action. Jackiw and Pi [273] showed that the embedding of the 3-dimensional Chern-Simons action into 4-dimensional General Relativity leads to Chern-Simons gravity as described by equation (12.1). Quantum mechanically, the Chern-Simons correction encodes information about the Immirzi parameter in loop quantum gravity and is also related to torsion. In this case, the Chern-Simons term is *required* to ensure invariance under large gauge transformations [78]. In both these classical and quantum mechanical scenarios the coupling of the Chern-Simons term to the Einstein-Hilbert action is theoretically unconstrained and is consistent with a coupling of order unity. Observations of gravitational waves from inspiraling binary black hole systems can thus be used to probe the strong gravity sector of quantum gravity.

## 12.5 Conclusions

Chern-Simons type corrections to the Einstein-Hilbert action are strongly motivated by string theory, loop quantum gravity, and other scenarios. In all cases these corrections lead to an amplitude birefringence for gravitational wave propagating through space time. We have evaluated the correction to the gravitational wave amplitude for waves propagating over cosmological distances in a matter-dominated Friedmann-Robertson-Walker cosmology. In the case of the gravitational waves from inspiraling binary black hole systems the effect of the spacetime birefringence is an *apparent* time-dependent change in the inclination angle between the binary system's orbital angular momentum and the line-of-sight to the detector. (This change is apparent in the same sense that light is "bent" upon passage nearby a strongly gravitating object.) Sufficiently long observations of a binary system will enable this apparent rotation to be distinguished from the real rotation caused by spin-orbit and spin-spin angular momentum interactions in the binary system. Observations of just this kind will be possible using the LISA gravitational wave detector [365, 366, 367], which will be able to observe the inspiral of massive black hole binaries at redshifts approaching 30 for periods of a year or more. Gravitational wave observations of these systems with LISA may thus provide the first test of string theory or other quantum theories of gravity: yet another way in which gravitational wave observations can act a unique tool for probing the fundamental nature of the universe.

## Acknowledgments

We are grateful to S. James Gates Jr. for encouraging us to look into the possibility of testing string theories with the Green-Schwarz term. We also thank Lubos Motl, Benjamin Owen, Michael Peskin, Andy Strominger, Emanuele Berti, Clifford Will, Carlos Sopena, Eric Poisson and Scott Hughes for enlightening discussions and comments.

SA acknowledges the support of the Eberly College of Science. NY acknowledges support from National Science Foundation awards PHY 05-55628 and PHY 02-45649. LSF acknowledges the support of NSF awards PHY 06-53462 and PHY 05-55615, and NASA award NNG05GF71G. Lastly, we acknowledge the support of the Center for Gravitational Wave Physics, which is funded by the National Science Foundation under Cooperative Agreement PHY 01-14375.

## Appendix A

### Coordinate transformation from Kerr to Kerr-Schild

In this appendix we provide explicit formula for the transformation from Kerr coordinates to Kerr-Schild coordinate. This transformation can be found in Refs. [118, 364, 381] and is given by

$$\begin{aligned}x &= \sin \theta (r \cos \phi - a \sin \phi), \\y &= \sin \theta (r \sin \phi + a \cos \phi). \\z &= r \cos \theta.\end{aligned}\tag{A.1}$$

The inverse transformation is given by

$$\begin{aligned}r &= \sqrt{\frac{R^2 - a^2 + w}{2}}, \\w &= \sqrt{(R^2 - a^2)^2 + 4a^2 z^2}, \\ \theta &= \arccos \frac{z}{r}, \\ \phi &= \arctan \frac{ry - ax}{rx + ay}.\end{aligned}\tag{A.2}$$

Other useful relations are

$$\begin{aligned}\sin \theta &= \left( \frac{x^2 + y^2}{r^2 + a^2} \right)^{1/2}, \\ \sin \phi &= \frac{ry - ax}{[(r^2 + a^2)(x^2 + y^2)]^{1/2}}, \\ \cos \phi &= \frac{rx + ay}{[(r^2 + a^2)(x^2 + y^2)]^{1/2}}.\end{aligned}\tag{A.3}$$

Note that these transformation reduce to the usual transformation from spherical polar coordinates to Cartesian coordinates in the limit  $a \rightarrow 0$ .

The Jacobian of the transformation,  $\Lambda^a_b = \partial x^a / \partial x^b$ , is given explicitly by

$$\begin{aligned}
\Lambda^r_x &= \frac{x}{2r} \left( 1 + \frac{R^2 - a^2}{w} \right), \\
\Lambda^r_y &= \frac{y}{2r} \left( 1 + \frac{R^2 - a^2}{w} \right), \\
\Lambda^r_z &= \frac{z}{2r} \left( 1 + \frac{R^2 + a^2}{w} \right), \\
\Lambda^\theta_x &= \frac{zx}{2r^2} \left( 1 + \frac{R^2 - a^2}{w} \right) (r^2 - z^2)^{-1/2}, \\
\Lambda^\theta_y &= \frac{zy}{2r^2} \left( 1 + \frac{R^2 - a^2}{w} \right) (r^2 - z^2)^{-1/2}, \\
\Lambda^\theta_z &= - (r^2 - z^2)^{-1/2} \left[ 1 - \frac{z^2}{2r^2} \left( 1 + \frac{R^2 + a^2}{w} \right) \right], \\
\Lambda^\phi_x &= \frac{rx + ay}{(r^2 + a^2)(x^2 + y^2)} \left[ \left( y - x \frac{ry - ax}{rx + ay} \right) \left( 1 + \frac{R^2 - a^2}{w} \right) \frac{x}{2r} - a - r \frac{ry - ax}{rx + ay} \right], \\
\Lambda^\phi_y &= \frac{rx + ay}{(r^2 + a^2)(x^2 + y^2)} \left[ \left( y - x \frac{ry - ax}{rx + ay} \right) \left( 1 + \frac{R^2 - a^2}{w} \right) \frac{y}{2r} + r - a \frac{ry - ax}{rx + ay} \right], \\
\Lambda^\phi_z &= \frac{rx + ay}{(r^2 + a^2)(x^2 + y^2)} \left[ \left( y - x \frac{ry - ax}{rx + ay} \right) \left( 1 + \frac{R^2 + a^2}{w} \right) \frac{z}{2r} \right].
\end{aligned}$$

(A.4)

Note that this Jacobian reduces to the standard Jacobian of the transformation between spherical polar and Cartesian coordinates in the limit  $a \rightarrow 0$ . There is a more elegant

way to write this Jacobian in tensor notation as

$$\begin{aligned}
 \Lambda^r_a &= \frac{1}{2r} \left\{ \delta_{ai} x^i + \frac{1}{w} \left[ \delta_{ia} x^i (R^2 - a^2) + 2a^2 z \delta_{az} \right] \right\}, \\
 \Lambda^\theta_a &= \frac{z}{r (r^2 - a^2)^{1/2}} \Lambda^r_a, \\
 \Lambda^\phi_a &= \frac{rx + ay}{(r^2 + a^2)(x^2 + y^2)} \left[ \Lambda^r_a \left( y - \frac{ry - ax}{rx + ay} x \right) \right. \\
 &\quad \left. + \left( r - \frac{ry - ax}{rx + ay} a \right) \delta_{ya} - \left( a + \frac{ry - ax}{rx + ay} r \right) \delta_{xa} \right].
 \end{aligned} \tag{A.5}$$

With this Jacobian, the metric in Kerr-Schild coordinates is given by

$$g_{ab} = g_{a'b'} \Lambda^{a'}_a \Lambda^{b'}_b, \tag{A.6}$$

where here the primed indices refer to spherical coordinates and the unprimed indices to Cartesian coordinates.

## Appendix B

### Conventions for special functions

In this appendix, we describe the conventions we use for the special functions presented in this paper, and we also present some important properties of such functions.

#### B.1 Special polynomials

The expression for the associated Legendre polynomials that we are using in this paper is the following

$$P_{\ell}^m(x) = \frac{(-1)^{\ell+m}}{2^{\ell} \ell!} (1-x^2)^{m/2} \frac{d^{\ell+m}}{dx^{\ell+m}} (1-x^2)^{\ell}, \quad (\text{B.1})$$

where  $\ell$  is a non-negative integer and  $m$  is an integer restricted to the following range:  $m \in (-\ell, -(\ell-1), \dots, \ell-1, \ell)$ .

Gegenbauer polynomials, also known as ultraspherical harmonics [188], are generalization of Legendre polynomial for higher dimensional spaces. They can be written in terms of other special functions, as in

$$C_n^{(\lambda)} = \frac{\Gamma(\lambda+1/2)}{\Gamma(2\lambda)} \frac{\Gamma(n+2\lambda)}{\Gamma(n+\lambda+1/2)} P_n^{(\lambda-1/2, \lambda-1/2)}, \quad (\text{B.2})$$

where  $\lambda$  is a real number,  $n$  is a positive integer,  $\Gamma$  is the Gamma function, and  $P_n^{(\lambda_1, \lambda_2)}$  are the Jacobi polynomials [188]. There are also recursion relations for these polynomials, but we will not present them here. Instead, we will provide the first few Gegenbauer polynomials

$$C_0^{(\lambda)}(x) = 1, \quad (\text{B.3})$$

$$C_1^{(\lambda)}(x) = 2\lambda x, \quad (\text{B.4})$$

$$C_2^{(\lambda)}(x) = -\lambda \left[ 1 - 2(1+\lambda)x^2 \right], \quad (\text{B.5})$$

$$C_3^{(\lambda)}(x) = -2\lambda(1+\lambda)x \left[ 1 - \frac{2}{3}(2+\lambda)x^2 \right]. \quad (\text{B.6})$$

These polynomials allow for the far field expansion of potentials that scale as  $|\vec{x} - \vec{x}_0|^{-\alpha}$  to arbitrary order.

## B.2 Spherical harmonics

The scalar spherical harmonics are solutions of the eigenvalue problem described by the following equation

$$\Omega^{ab} Y_{:ab}^{\ell m} + \ell(\ell + 1) Y^{\ell m} = 0, \quad (\text{B.7})$$

where  $(\ell, m)$  have the same range of values as in the associated Legendre polynomials above. In this paper we use the conventions of [382, 205] to define specify the solutions of Eq. (B.7). The precise expression is given by

$$Y^{\ell m}(\theta, \varphi) = \sqrt{\frac{2\ell + 1}{4\pi} \frac{(\ell - m)!}{(\ell + m)!}} P_{\ell}^m(\cos \theta) e^{im\varphi}. \quad (\text{B.8})$$

The scalar spherical harmonics form an orthonormal basis on the two-sphere, that is

$$\int_{S^2} d\Omega Y^{\ell m} \bar{Y}^{\ell' m'} = \delta^{\ell\ell'} \delta^{mm'}, \quad (\text{B.9})$$

where  $\delta^{ab}$  denotes the Kronecker delta. The vector spherical harmonics are defined in terms of the scalar ones as in Eq. (6.37), and from this definition we can derive the following orthogonality relations:

$$\int_{S^2} d\Omega \Omega^{ab} Y_a^{\ell m} \bar{Y}_b^{\ell' m'} = \ell(\ell + 1) \delta^{\ell\ell'} \delta^{mm'}, \quad (\text{B.10})$$

$$\int_{S^2} d\Omega \Omega^{ab} S_a^{\ell m} \bar{S}_b^{\ell' m'} = \ell(\ell + 1) \delta^{\ell\ell'} \delta^{mm'}, \quad (\text{B.11})$$

$$\int_{S^2} d\Omega \Omega^{ab} Y_a^{\ell m} \bar{S}_b^{\ell' m'} = 0. \quad (\text{B.12})$$

The (symmetric) tensor spherical harmonics used in this paper are also constructed from the scalar ones by means of Eqs. (6.38) and (6.39), from where the following orthogonality relations can be deduced:

$$\int_{S^2} d\Omega \Omega^{ac} \Omega^{bd} Y_{ab}^{\ell m} \bar{Y}_{cd}^{\ell' m'} = 2\delta^{\ell\ell'} \delta^{mm'}, \quad (\text{B.13})$$

$$\int_{S^2} d\Omega \Omega^{ac} \Omega^{bd} Z_{ab}^{\ell m} \bar{Z}_{cd}^{\ell' m'} = \frac{(\ell + 2)!}{2(\ell - 2)!} \delta^{\ell\ell'} \delta^{mm'}, \quad (\text{B.14})$$

$$\int_{S^2} d\Omega \Omega^{ac} \Omega^{bd} S_{ab}^{\ell m} \bar{S}_{cd}^{\ell' m'} = \frac{(\ell + 2)!}{2(\ell - 2)!} \delta^{\ell\ell'} \delta^{mm'}, \quad (\text{B.15})$$

$$\int_{S^2} d\Omega \Omega^{ac} \Omega^{bd} Z_{ab}^{\ell m} \bar{S}_{cd}^{\ell' m'} = 0, \quad (\text{B.16})$$

and

$$\Omega^{ac} \Omega^{bd} Z_{ab}^{\ell m} Y_{cd}^{\ell' m'} = \Omega^{ac} \Omega^{bd} S_{ab}^{\ell m} Y_{cd}^{\ell' m'} = 0. \quad (\text{B.17})$$

### B.3 Spin-weighted scalar spherical harmonics

Spin-weighted scalar spherical harmonics are another basis to expand functions on the 2-sphere. They can be defined by the following general formula [383]

$${}_s Y^{lm}(\theta, \varphi) = \begin{cases} \left[ \frac{(l-s)!}{(l+s)!} \right]^{1/2} \hat{\partial}^s Y^{lm}, & 0 < s < l, \\ (-1)^s \left[ \frac{(l+s)!}{(l-s)!} \right]^{1/2} \check{\partial}^{-s} Y^{lm}, & -l < s < 0, \\ 0, & l < |s|, \end{cases} \quad (\text{B.18})$$

where  $\hat{\partial}$  ( $\check{\partial}$ ) is a ladder operator, usually called the edth operator, that raises (lowers) in a unity the spin weight of any quantity. Its action on a scalar  $Q$  can be expressed in the following way [383, 384]

$$\hat{\partial} Q = m^a \partial_a Q - \frac{s}{2} (\bar{m}^a m^b \nabla_b m_a) Q, \quad (\text{B.19})$$

$$\check{\partial} Q = \bar{m}^a \partial_a Q + \frac{s}{2} (m^a \bar{m}^b \nabla_b \bar{m}_a) Q, \quad (\text{B.20})$$

where  $s$  is the spin weight of  $Q$  and  $(m^a, \bar{m}^a)$  is a null complex basis on the 2-sphere ( $\Omega_{ab} m^a m^b = 0$ ,  $\Omega_{ab} m^a \bar{m}^b = 1$ ). It is worth noting that the action of the edth depends explicitly on the spin weight of the quantity on which it acts. Taking  $m^a = \frac{1}{\sqrt{2}} [1, \frac{i}{\sin \theta}]$ , we can write the edth-operator as [384]

$$\hat{\partial} = \frac{1}{\sqrt{2}} \left[ \partial_\theta + \frac{i}{\sin \theta} \partial_\varphi - \frac{s \cos \theta}{2 \sin \theta} \right] \quad (\text{B.21})$$

$$\check{\partial} = \frac{1}{\sqrt{2}} \left[ \partial_\theta - \frac{i}{\sin \theta} \partial_\varphi + \frac{s \cos \theta}{2 \sin \theta} \right] \quad (\text{B.22})$$

It is important to mention that these definitions are applicable only to integer powers of the spin-weight. A generalized definition for half-integer powers of  $s$  exists but will not be discussed here (see [383]).

In this paper we are interested in the  $s = -2$  case, for which the definition of the spin-weighted spherical harmonics reduces to [385]

$${}_{-2} Y^{\ell m} = 2 \sqrt{\frac{(\ell-2)!}{(\ell+2)!}} Z_{ab}^{\ell m} \bar{m}^a \bar{m}^b. \quad (\text{B.23})$$

## Appendix C

### Regge-Wheeler parameterization

For the sake of completeness, we give here the relations between our parameterization of the metric perturbations and the one used by Regge and Wheeler [189]. For polar modes (our notation is on the left column and the one of Regge and Wheeler is on the right one) we have

$$(h_{AB}^{\ell m}) \leftrightarrow \begin{pmatrix} fH_0^{\ell m} & H_1^{\ell m} \\ * & f^{-1}H_2^{\ell m} \end{pmatrix}, \quad (\text{C.1})$$

$$p_A^{\ell m} \leftrightarrow (h_t^{\ell m}, h_r^{\ell m}), \quad (\text{C.2})$$

$$K^{\ell m} \leftrightarrow K^{\ell m} - \frac{\ell(\ell+1)}{2}G^{\ell m}, \quad (\text{C.3})$$

$$G^{\ell m} \leftrightarrow G^{\ell m}. \quad (\text{C.4})$$

and for axial modes

$$(h_A^{\ell m}) \leftrightarrow -(h_0^{\ell m}, h_1^{\ell m}), \quad (\text{C.5})$$

$$H^{\ell m} \leftrightarrow -h_2^{\ell m}. \quad (\text{C.6})$$

The expressions for the master functions, in Schwarzschild coordinates, in terms of the parameterization of Regge and Wheeler are:

$$\begin{aligned} \Psi_{\text{ZM}}^{\ell m} &= \frac{r}{1+\lambda_\ell} \left[ K^{\ell m} + \frac{f}{\Lambda_\ell} \left( H_2^{\ell m} - r \partial_r K^{\ell m} \right) \right] \\ &\quad - \frac{2f}{\Lambda_\ell} \left( h_1^{\ell m} - \frac{r^2}{2} \partial_r G^{\ell m} \right), \end{aligned} \quad (\text{C.7})$$

$$\Psi_{\text{RW}}^{\ell m} = \frac{f}{r} \left( h_1^{\ell m} - \frac{1}{2} \partial_r h_2^{\ell m} + \frac{1}{r} h_2^{\ell m} \right), \quad (\text{C.8})$$

$$\Psi_{\text{CPM}}^{\ell m} = \frac{r}{\lambda_\ell} \left( h_1^{\ell m} - \partial_r h_0^{\ell m} + \frac{2}{r} h_0^{\ell m} \right). \quad (\text{C.9})$$

## Appendix D

### Derivation of the linear momentum flux

In order to obtain Eqs. (6.57)-(6.59) from Eq. (6.55) we need to use the decompositions of products of spherical harmonics in single harmonics typical of problems that deal with angular momentum coupling (for accounts dealing with this problem see [59], where multipole expansions of gravitational radiation in different sets of harmonics are described; see [386] for a recent systematic treatment of higher-order perturbation theory where these issues are also treated).

Introducing Eq. (6.54) into Eq. (6.55), using that any spherical harmonic  $\mathcal{S}^{\ell m}$  has the property  $\mathcal{S}^{\ell, -m} = (-1)^m \bar{\mathcal{S}}^{\ell m}$ , and the fact that  $Z_{ab}^{\ell m}$  is symmetric and traceless we get

$$\begin{aligned} \dot{P}_{GW}^k &= \frac{1}{32\pi} \sum_{\substack{\ell \geq 2, m \\ \ell' \geq 2, m'}} \left( \dot{\Psi}_{ZM}^{\ell m} \dot{\Psi}_{ZM}^{\ell' m'} + \dot{\Psi}_{CPM}^{\ell m} \dot{\Psi}_{CPM}^{\ell' m'} \right) \int_{S^2} d\Omega \hat{r}_{obs}^k Z_{ab}^{\ell m} \bar{Z}_{cd}^{\ell' m'} \Omega^{ac} \Omega^{bd} \\ &\quad - \frac{1}{32\pi} \sum_{\substack{\ell \geq 2, m \\ \ell' \geq 2, m'}} \left( \dot{\Psi}_{CPM}^{\ell m} \dot{\Psi}_{ZM}^{\ell' m'} - \dot{\Psi}_{ZM}^{\ell m} \dot{\Psi}_{CPM}^{\ell' m'} \right) \int_{S^2} d\Omega \hat{r}_{obs}^k Z_{ab}^{\ell m} \bar{Z}_{cd}^{\ell' m'} \Omega^{ac} \epsilon^{bd} \end{aligned} \quad (\text{D.1})$$

At this point everything reduces to evaluating the integrals on the 2-sphere. To that end, the starting point is the well-known formula [387]

$$Y^{\ell m} Y^{\ell' m'} = \sum_{L, M} \sqrt{\frac{(2\ell+1)(2\ell'+1)(2L+1)}{4\pi}} \begin{pmatrix} \ell & \ell' & L \\ m & m' & M \end{pmatrix} \begin{pmatrix} \ell & \ell' & L \\ 0 & 0 & 0 \end{pmatrix} \bar{Y}^{LM} \quad (\text{D.2})$$

where the objects with the round brackets are the 3j-Wigner symbols, which are related to the Clebsch-Gordon coefficients. They are subject to certain *selection* rules, namely,  $(\ell, m)$ ,  $(\ell', m')$ , and  $(L, M)$  are integers with the usual ranges of values;  $m + m' + M = 0$ ; and the triangular inequality  $|\ell - \ell'| \leq L \leq \ell + \ell'$ . By using (D.2) and the definition of  $Z_{ab}^{\ell m}$  [Eq. (6.38)] we find the following relationship

$$\begin{aligned} Z_{ab}^{\ell m} \bar{Z}_{cd}^{\ell' m'} \Omega^{ac} \Omega^{bd} &= \sum_{L, M} C(\ell, \ell', L) \sqrt{\frac{(2\ell+1)(2\ell'+1)(2L+1)}{4\pi}} \begin{pmatrix} \ell & \ell' & L \\ m & m' & M \end{pmatrix} \\ &\quad \times \begin{pmatrix} \ell & \ell' & L \\ 0 & 0 & 0 \end{pmatrix} \bar{Y}^{LM}. \end{aligned} \quad (\text{D.3})$$

where  $C(\ell, \ell', L)$  is a constant given by

$$C(\ell, \ell', L) = \frac{1}{4} \left\{ L^2(L+1)^2 + \ell^2(\ell+1)^2 + \ell'^2(\ell'+1)^2 + 2L(L+1) - 2 \left[ \ell(\ell+1) + \ell'(\ell'+1) \right] [L(L+1) + 1] \right\}. \quad (\text{D.4})$$

A similar formula can be found for the second term in (D.1). Then, since the components of  $r_{obs}^k$  are linear in  $Y^{1,m}$ , the integral that appears in Eq. (D.1) is now straightforward. In order to get Eqs. (6.57)-(6.59) we just need to use the selection rules of the  $3-j$  Wigner symbols and the following additional properties:

$$\begin{aligned} \begin{pmatrix} j_1 & j_2 & j_1 + j_2 \\ m_1 & m_2 & -M \end{pmatrix} &= (-1)^{j_1 - j_2 + M} \left[ \frac{(2j_1)!(2j_2)!}{(2j_1 + 2j_2 + 1)!} \right. \\ &\quad \left. \times \frac{(j_1 + j_2 + M)!(j_1 + j_2 - M)!}{(j_1 + m_1)!(j_1 - m_1)!(j_2 + m_2)!(j_2 - m_2)!} \right]^{1/2}, \end{aligned} \quad (\text{D.5})$$

$$\begin{aligned} \begin{pmatrix} j_1 & j_2 & j \\ 0 & 0 & 0 \end{pmatrix} &= \begin{cases} (-1)^g \left[ \frac{(2g-2j_1)!(2g-2j_2)!(2g-2j)!}{(2g+1)!} \right]^{1/2} \\ \quad \times \frac{g!}{(g-j_1)!(g-j_2)!(g-j)!}, & \text{if } J = 2g, \\ 0, & \text{if } J = 2g + 1, \end{cases} \end{aligned} \quad (\text{D.6})$$

where  $J = j_1 + j_2 + j$ .

Alternatively, one can use the following relation for the integral of three spin-weighted spherical harmonics:

$$\begin{aligned} \int_{S^2} d\Omega \, Y_S^{LM} Y_s^{\ell m} Y_{s'}^{\ell' m'} &= \sqrt{\frac{(2L+1)(2\ell+1)(2\ell'+1)}{4\pi}} \begin{pmatrix} L & \ell & \ell' \\ -S & -s & -s' \end{pmatrix} \\ &\quad \times \begin{pmatrix} L & \ell & \ell' \\ M & m & m' \end{pmatrix}. \end{aligned} \quad (\text{D.7})$$

## Appendix E

### Extremal surfaces in Brill-Lindquist data

We are interested in finding the location of the extremal surfaces that surround the individual holes in the BL binary black hole initial data that we are using in this paper. When the holes are separated enough these surfaces form the apparent horizon of the initial data (since we are neglecting the extrinsic curvature the data is time symmetric). If we put the two holes close enough, another maximal surface enclosing the two holes appears and becomes the apparent horizon, and then, the two individual maximal surfaces are called marginally trapped surfaces.

Following Bishop [388, 389], in order to look for maximal surfaces in the BL data it is very convenient to exploit the cylindrical symmetry of the configuration by expressing the metric in cylindrical coordinates (for coherence with the conventions of the paper we choose the axis of symmetry to be the  $X$  axis):  $x = x$ ,  $y = \rho \cos \vartheta$ ,  $z = \rho \sin \vartheta$ . Then, the line element of Eq. (6.2) becomes:

$$ds^2 = \Phi^4(\rho, x) \left( d\rho^2 + \rho^2 d\vartheta^2 + dx^2 \right), \quad (\text{E.1})$$

where now

$$\Phi = 1 + \frac{m_1}{2\sqrt{\rho^2 + (x - X_1)^2}} + \frac{m_2}{2\sqrt{\rho^2 + (x - X_2)^2}}. \quad (\text{E.2})$$

Moreover, the problem of finding the extremal surfaces reduces to that of finding a path  $(\rho(\lambda), x(\lambda))$  in the subspace  $(\rho, x)$ . The area of a surface with cylindrical symmetry can be written as

$$\mathcal{A} = 2\pi \int_{\lambda_1}^{\lambda_2} \rho \Phi^4 \sqrt{\dot{\rho}^2 + \dot{x}^2} d\lambda, \quad (\text{E.3})$$

where the dots denote differentiation along the path, that is  $d/d\lambda$ , and  $(\lambda_1, \lambda_2)$  are the intersections of the surface with the symmetry axis  $X$ . The equations for the path  $(\rho(\lambda), x(\lambda))$  is found by extremizing the area,  $\delta\mathcal{A} = 0$ , Bishop [388, 389] took  $\lambda$  to be an affine parameter, that is, such that  $\mathcal{A} = 2\pi(\lambda_2 - \lambda_1)$ . We have fixed  $\lambda$  in such a way the ordinary differential equations for  $(\rho(\lambda), x(\lambda))$  are simple and amenable for numerical computations. In particular, we have chosen  $\lambda$  so that

$$\sqrt{\dot{\rho}^2 + \dot{x}^2} = \rho \Phi^4, \quad (\text{E.4})$$

which is a constraint preserved by the Euler-Lagrange equations that we obtain from  $\delta\mathcal{A} = 0$ :

$$\ddot{\rho} = -\partial_{\rho} \mathcal{V}, \quad (\text{E.5})$$

$$\ddot{x} = -\partial_x \mathcal{V}, \quad (\text{E.6})$$

where the *potential*  $\mathcal{V}$  is given by

$$\mathcal{V}(\rho, x) = \frac{1}{2}\rho^2 \Phi^8. \quad (\text{E.7})$$

## Appendix F

### PPN Potentials

In this appendix, we present explicit expressions for the PPN potentials used to parameterize the metric in Eq. (9.5). These potentials are the following:

$$\begin{aligned}
U &\equiv \int \frac{\rho}{|\mathbf{x} - \mathbf{x}'|} d^3 x', \\
V_i &\equiv \int \frac{\rho' v'_i}{|\mathbf{x} - \mathbf{x}'|} d^3 x', \\
W_i &\equiv \int \frac{\rho' v'_j (x - x')^j (x - x')_i}{|\mathbf{x} - \mathbf{x}'|^3} d^3 x', \\
\Phi_W &\equiv \int \rho' \rho'' \frac{(x - x')^i}{|\mathbf{x} - \mathbf{x}'|^3} \left( \frac{(x' - x'')_i}{|\mathbf{x} - \mathbf{x}'|} - \frac{(x - x'')_i}{|\mathbf{x}' - \mathbf{x}''|} \right) d^3 x' d^3 x'', \\
\Phi_1 &\equiv \int \frac{\rho' v'^2}{|\mathbf{x} - \mathbf{x}'|} d^3 x', & \Phi_2 &\equiv \int \frac{\rho' U'}{|\mathbf{x} - \mathbf{x}'|} d^3 x', \\
\Phi_3 &\equiv \int \frac{\rho' \Pi'}{|\mathbf{x} - \mathbf{x}'|} d^3 x', & \Phi_4 &\equiv \int \frac{p'}{|\mathbf{x} - \mathbf{x}'|} d^3 x', \\
\mathcal{A} &\equiv \int \frac{\rho' [v'_i (x - x')^i]^2}{|\mathbf{x} - \mathbf{x}'|} d^3 x', \\
X &\equiv \int \rho' |\mathbf{x} - \mathbf{x}'| d^3 x'.
\end{aligned} \tag{F.1}$$

These potentials satisfy the following relations

$$\begin{aligned}
\nabla^2 U &= -4\pi\rho, & \nabla^2 V_i &= -4\pi\rho v_i, \\
\nabla^2 \Phi_1 &= -4\pi\rho v^2, & \nabla^2 \Phi_2 &= -4\pi\rho U, \\
\nabla^2 \Phi_3 &= -4\pi\rho\Pi, & \nabla^2 \Phi_4 &= -4\pi p, \\
\nabla^2 X &= -2U
\end{aligned} \tag{F.2}$$

The potential  $X$  is sometimes referred to as the super-potential because it acts as a potential for the Newtonian potential.

## Appendix G

### Linearization of the Cotton Tensor

In this appendix, we present some more details on the derivation of the linearized Cotton tensor to second order. We begin with the definition of the Cotton tensor [273] in terms of the symmetrization operator, namely

$$C^{\mu\nu} = -\frac{1}{\sqrt{-g}} \left[ (D_\sigma f) \epsilon^{\sigma\alpha\beta(\mu} D_\alpha R^{\nu)}_{\beta} + (D_{\sigma\tau} f)^* R^{\tau(\mu|\sigma|\nu)} \right]. \quad (\text{G.1})$$

Using the symmetries of the Levi-Civita and Riemann tensor, as well as the fact that  $f$  depends only on time, we can simplify the Cotton tensor to

$$\begin{aligned} C^{\mu\nu} &= (-g)^{-1} \dot{f} \left[ \tilde{\epsilon}^{0\alpha\beta(\mu} R^{\nu)}_{\beta,\alpha} + \tilde{\epsilon}^{0\alpha\beta(\mu} \Gamma^{\nu)}_{\lambda\alpha} R^\lambda_{\beta} \right. \\ &\quad \left. + \frac{1}{2} \Gamma^0_{\sigma\tau} \tilde{\epsilon}^{\sigma\alpha\beta(\mu} R^{\nu)\tau}_{\alpha\beta} \right]. \end{aligned} \quad (\text{G.2})$$

Noting that the determinant of the metric is simply  $g = -1 + h$ , so that  $(-g)^{-1} = 1 + h$ , we can identify four terms in the Cotton tensor

$$\begin{aligned} C_A^{\mu\nu} &= \dot{f} \tilde{\epsilon}^{0\alpha\beta(\mu} \left[ \hat{L} R^{\nu)}_{\beta,\alpha} \right], \\ C_B^{\mu\nu} &= \dot{f} \tilde{\epsilon}^{0\alpha\beta(\mu} h_{\rho\rho} \left[ \hat{L} R^{\nu)}_{\beta,\alpha} \right], \\ C_C^{\mu\nu} &= \dot{f} \tilde{\epsilon}^{0\alpha\beta(\mu} \left[ \hat{L} \Gamma^{\nu)}_{\lambda\alpha} \right] \left[ \hat{L} R^\lambda_{\beta} \right], \\ C_D^{\mu\nu} &= \frac{\dot{f}}{2} \tilde{\epsilon}^{\sigma\alpha\beta(\mu} \left[ \hat{L} \Gamma^0_{\sigma\tau} \right] \left[ \hat{L} R^{\nu)\tau}_{\alpha\beta} \right], \\ C_E^{\mu\nu} &= \dot{f} \tilde{\epsilon}^{0\alpha\beta(\mu} \left[ \hat{Q} R^{\nu)}_{\beta,\alpha} \right], \end{aligned} \quad (\text{G.3})$$

where the  $\hat{L}$  operator stands for the linear part of its operand, while the  $\hat{Q}$  operator isolates the quadratic part of its operand. For example, if we act  $\hat{L}$  and  $\hat{Q}$  on  $(1 + h)^n$ , where  $n$  is some integer, we obtain

$$\left[ \hat{L}(1 + h)^n \right] = nh, \quad \left[ \hat{Q}(1 + h)^n \right] = \frac{n(n-1)}{2} h^2. \quad (\text{G.4})$$

Let us now compute each of these terms separately. The first four terms are given by

$$\begin{aligned}
C_A^{\mu\nu} &= -\frac{\dot{f}}{2}\tilde{\epsilon}^{0\alpha\beta(\mu} \left( \square_\eta h^\nu{}_{\beta,\alpha} - h_{\sigma\beta, \alpha\sigma}{}^\nu \right), \\
C_B^{\mu\nu} &= -\frac{\dot{f}}{2}h\tilde{\epsilon}^{0\alpha\beta(\mu} \left( \square_\eta h^\nu{}_{\beta,\alpha} - h_{\sigma\beta, \alpha\sigma}{}^\nu \right), \\
C_C^{\mu\nu} &= -\frac{\dot{f}}{4}\tilde{\epsilon}^{0\alpha\beta(\mu} \left( h^\nu{}_{\lambda,\alpha} + h^\nu{}_{\alpha,\lambda} - h_{\lambda\alpha, \nu}{}^\nu \right) \\
&\quad \times \left( \square_\eta h^\lambda{}_\beta - h_{\sigma, \beta}{}^\lambda{}^\sigma - h_{\sigma\beta, \lambda\sigma} + h_{, \beta}{}^\lambda{}^\sigma \right), \\
C_D^{\mu\nu} &= \frac{\dot{f}}{4}\tilde{\epsilon}^{\sigma\alpha\beta(\mu} \left( 2h^0{}_{(\sigma,\tau)} - h_{\sigma\tau,}{}^0 \right) \left( h^\tau{}_{[\beta,\alpha]}{}^\nu - h^\nu{}_{[\beta,\alpha]}{}^\tau \right).
\end{aligned} \tag{G.5}$$

The last term of the Cotton tensor is simply the derivative of the Ricci tensor which we already calculated to second order in Eq. (9.21). In order to avoid notation clutter, we shall not present it again here, but instead we combine all the Cotton tensor pieces to obtain

$$\begin{aligned}
C^{\mu\nu} &= -\frac{\dot{f}}{2}\tilde{\epsilon}^{0\alpha\beta(\mu} \left( \square_\eta h^\nu{}_{\beta,\alpha} - h_{\sigma\beta,\alpha}{}^{\sigma\nu} \right) - \frac{\dot{f}}{2}\tilde{\epsilon}^{0\alpha\beta(\mu} \left[ h \left( \square_\eta h^\nu{}_{\beta,\alpha} - h_{\sigma\beta,\alpha}{}^{\sigma\nu} \right) \right. \\
&\quad \left. + \frac{1}{2} \left( 2h^\nu{}_{(\lambda,\alpha)} - h_{\lambda\alpha, \nu}{}^\nu \right) \left( \square_\eta h^\lambda{}_\beta - 2h_{\sigma, \beta}{}^{(\lambda}{}^\sigma + h_{,\beta}{}^\lambda) \right) - 2\hat{Q}R^\nu{}_{\beta,\alpha} \right] \\
&\quad + \frac{\dot{f}}{4}\tilde{\epsilon}^{\sigma\alpha\beta(\mu} \left( 2h^0{}_{(\sigma,\tau)} - h_{\sigma\tau,}{}^0 \right) \left( h^\tau{}_{[\beta,\alpha]}{}^\nu - h^\nu{}_{[\beta,\alpha]}{}^\tau \right) + \mathcal{O}(h)^3
\end{aligned} \tag{G.6}$$

where its covariant form is

$$\begin{aligned}
C_{\mu\nu} &= -\frac{\dot{f}}{2}\tilde{\epsilon}^{0\alpha\beta}{}_{(\mu} \left( \square_\eta h_{\nu)\beta,\alpha} - h_{\sigma\beta,\alpha\nu}{}^\sigma \right) - \frac{\dot{f}}{2}\tilde{\epsilon}^{0\alpha\beta}{}_{(\mu} \left[ h \left( \square_\eta h_{\nu)\beta,\alpha} - h_{\sigma\beta,\alpha\nu}{}^\sigma \right) \right. \\
&\quad \left. + \frac{1}{2} \left( 2h_{\nu(\lambda,\alpha)} - h_{\lambda\alpha,\nu} \right) \left( \square_\eta h^\lambda{}_\beta - 2h_{\sigma, \beta}{}^{(\lambda}{}^\sigma + h_{,\beta}{}^\lambda) \right) - 2\hat{Q}R_{\nu)\beta,\alpha} + h_{\nu\lambda} \right. \\
&\quad \left. \times \left( \square_\eta h^\lambda{}_{\beta,\alpha} - h_{\sigma\beta,\alpha}{}^{\sigma\lambda} \right) \right] + \frac{\dot{f}}{4}\tilde{\epsilon}^{\sigma\alpha\beta}{}_{(\mu} \left( 2h^0{}_{(\sigma,\tau)} - h_{\sigma\tau,}{}^0 \right) \left( h^\tau{}_{[\beta,\alpha]\nu} - h_{\nu)[\beta,\alpha]}{}^\tau \right) \\
&\quad - \frac{\dot{f}}{2}h_{\mu\lambda}\tilde{\epsilon}^{0\alpha\beta(\lambda} \left( \square_\eta h_{\nu)\beta,\alpha} - h_{\sigma\beta,\alpha\nu}{}^\sigma \right) + \mathcal{O}(h)^3.
\end{aligned} \tag{G.8}$$

For the PPN mapping of CS modified gravity, only the 00 component of the metric is needed to second order, which implies we only need  $C_{00}$  to  $\mathcal{O}(h)^2$ . This component is given by

$$\begin{aligned}
C_{00} &= \frac{\dot{f}}{4}\tilde{\epsilon}^{ijk}{}_0 \left( 2h^0{}_{(i,\ell)} - h_{i\ell,}{}^0 \right) \left( h^\ell{}_{[k,j]0} - h_{0[k,j]}{}^\ell \right) \\
&\quad - \frac{\dot{f}}{2}h_{0\ell}\tilde{\epsilon}^{0jk(\ell} \left( \square_\eta h_{0k,j} - h_{ik,j0}{}^i \right) + \mathcal{O}(h)^3,
\end{aligned} \tag{G.9}$$

where in fact the last term vanishes due to the PPN gauge condition. Note that this term is automatically of  $\mathcal{O}(6)$ , which is well beyond the required order we need in  $h_{00}$ .

## Appendix H

### Proof of ${}^*R R = {}^*C C$

The equality

$${}^*R R = {}^*C C \tag{H.1}$$

relates the Pontryagin term expressed as in Eq. (10.5) to the Weyl tensor

$$C^{ab}{}_{cd} := R^{ab}{}_{cd} - 2\delta_{[c}^{[a} R_{d]}^{b]} + \frac{1}{3}\delta_{[c}^a \delta_{d]}^b R \tag{H.2}$$

and its dual

$${}^*C^a{}_{b cd} := \frac{1}{2}\epsilon^{cdef} C^a{}_{bef}. \tag{H.3}$$

Equation (H.1) is quite simple to prove, but not entirely obvious. Indeed, we were not able to find it in any of the standard textbooks, review articles or papers on CS modified gravity. Therefore, we provide here a proof by straightforward calculation.

Let us begin by inserting the definitions (10.5), (H.2) and (H.3) into (H.1),

$${}^*R R = {}^*R^a{}_{b cd} R^b{}_{acd} = {}^*C^a{}_{b cd} C^b{}_{acd} + \Delta. \tag{H.4}$$

where  $\Delta$  is precisely the violation of Eq. (H.1). Thus, if we can show that  $\Delta$  vanishes in Eq. (H.4) we have proven Eq. (H.1). The quantity  $\Delta$  contains eight terms. Four of them are linear in the Weyl tensor. Two of these terms are proportional to  $C_{cdef}$  and two are proportional to  $C_{cdeb}$ . Since

$$\epsilon^{cdef} C_{cdef} = \epsilon^{cdef} C_{cdeb} = 0, \tag{H.5}$$

these terms vanish. Each of the remaining four terms contains at least two Kronecker  $\delta$ . These terms always lead to a contraction of the Levi-Civita tensor, e.g. of the form  $\epsilon^{cd}{}^f{}_c = 0$ . Therefore, also these four terms vanish and establish

$$\Delta = 0. \tag{H.6}$$

q. e. d.

## Appendix I

## Pontryagin constraint

For the line element Eq. (10.67) the Pontryagin constraint Eq. (10.18) is given by  
 $(\bar{w} := e^{-2U} w)$

$$0 = A_0 \bar{w} + A_1 \bar{w}^3 + A_2 \bar{w}_{,\rho} + A_3 \bar{w}^2 \bar{w}_{,\rho} + A_4 \bar{w}^2_{,\rho} + A_5 \bar{w}_{,z} + A_6 \bar{w}^2 \bar{w}_{,z} + A_7 \bar{w}^2_{,z} \\ + A_8 \bar{w}_{,\rho} \bar{w}_{,z} + A_9 \bar{w}_{,\rho z} + A_{10} (\bar{w}_{,\rho\rho} - \bar{w}_{,zz}), \quad (\text{I.1})$$

with

$$A_0 = -\rho^2 A_1 + 2\rho^2 [2U_{,\rho z} k_{,\rho} - (U_{,\rho\rho} - U_{,zz}) k_{,z} - 2U_{,\rho\rho} U_{,z} + 2U_{,\rho z} U_{,\rho} \\ + 4U_{,z} (U_{,\rho}^2 + U_{,z}^2) + U_{,z} (k_{,\rho\rho} + k_{,zz}) + 8U_{,\rho} U_{,z} k_{,\rho} - 6U_{,\rho}^2 k_{,z} + 2U_{,z}^2 k_{,z} \\ - 2U_{,z} (k_{,\rho}^2 + k_{,z}^2)] + 2\rho (U_{,\rho} k_{,z} - U_{,z} k_{,\rho} + 2U_{,z} U_{,\rho}) \quad (\text{I.2})$$

$$A_1 = 8\rho [U_{,\rho} U_{,z} (U_{,zz} - U_{,\rho\rho}) + U_{,\rho z} (U_{,\rho}^2 - U_{,z}^2) - U_{,\rho}^3 k_{,z} + U_{,z}^3 k_{,\rho} \\ + U_{,\rho} U_{,z} (U_{,\rho} k_{,\rho} - U_{,z} k_{,z})] + 8U_{,z} (U_{,\rho}^2 + U_{,z}^2) \quad (\text{I.3})$$

$$A_2 = 2\rho^3 [2U_{,zz} U_{,z} + 2U_{,\rho z} U_{,\rho} + 4U_{,\rho}^2 U_{,z} + 4U_{,z}^3 + (U_{,\rho\rho} - U_{,zz}) k_{,z} - U_{,z} (k_{,\rho\rho} + k_{,zz}) \\ - 2U_{,\rho z} k_{,\rho} - 4U_{,\rho} U_{,z} k_{,\rho} + 2U_{,z} k_{,\rho}^2 + 2U_{,z} k_{,z}^2 - 4U_{,z}^2 k_{,z}] \\ - 2\rho^2 (U_{,\rho z} + 4U_{,z} U_{,\rho} - 2U_{,\rho} k_{,z}) - \rho k_{,z} \quad (\text{I.4})$$

$$A_3 = 4\rho (3U_{,\rho}^2 k_{,z} + U_{,z}^2 k_{,z} - 2U_{,\rho} U_{,z} k_{,\rho} - 4U_{,\rho}^2 U_{,z} + (U_{,\rho\rho} - U_{,zz}) U_{,z} \\ - 2U_{,\rho} U_{,\rho z} - 4U_{,z}^3) - 8U_{,\rho} U_{,z} \quad (\text{I.5})$$

$$A_4 = 2\bar{w} (\rho U_{,z} k_{,\rho} - 3\rho U_{,\rho} k_{,z} + U_{,z} + 6\rho U_{,\rho} U_{,z} + \rho U_{,\rho z}) - \bar{w}_{,\rho} \rho (2U_{,z} - k_{,z}) \quad (\text{I.6})$$

$$A_5 = 2\rho^3 [-2U_{,\rho\rho} U_{,\rho} - 2U_{,\rho z} U_{,z} - 4U_{,z}^2 U_{,\rho} - 4U_{,\rho}^3 + (U_{,\rho\rho} - U_{,zz}) k_{,\rho} + U_{,\rho} (k_{,zz} + k_{,\rho\rho}) \\ + 2U_{,\rho z} k_{,z} + 4U_{,z} U_{,\rho} k_{,z} - 2U_{,\rho} (k_{,\rho}^2 + k_{,z}^2) + 4U_{,\rho}^2 k_{,\rho}] + 2\rho^2 (U_{,\rho\rho} + 4U_{,\rho}^2 - 2U_{,\rho} k_{,\rho}) \\ + \rho^2 (2k_{,\rho}^2 + 2k_{,z}^2 - k_{,\rho\rho} - k_{,zz}) - \rho (2U_{,\rho} - k_{,\rho}) \quad (\text{I.7})$$

$$\begin{aligned}
A_6 &= 4\rho U_{,\rho}(U_{,\rho\rho} - U_{,zz}) + 8\rho U_{,z}U_{,\rho z} - 4U_{,\rho}^2 - 12U_{,z}^2 + 4\rho[4U_{,\rho}(U_{,\rho}^2 + U_{,z}^2) \\
&\quad - U_{,\rho}^2 k_{,\rho} + 2U_{,z}U_{,\rho}k_{,z} - 3U_{,z}^2 k_{,\rho}] \tag{I.8}
\end{aligned}$$

$$\begin{aligned}
A_7 &= \bar{w}(6U_{,z} - 2\rho U_{,\rho z} - 12\rho U_{,z}U_{,\rho} - 2\rho U_{,\rho}k_{,z} + 6\rho U_{,z}k_{,\rho}) \\
&\quad + \bar{w}_{,z}\rho(2U_{,\rho} - k_{,\rho}) - \bar{w}_{,z} \tag{I.9}
\end{aligned}$$

$$\begin{aligned}
A_8 &= 2\bar{w}\rho(U_{,zz} - U_{,\rho\rho} + 6U_{,z}^2 - 6U_{,\rho}^2 - 2U_{,z}k_{,z} + 2U_{,\rho}k_{,\rho}) + 4\bar{w}U_{,\rho} \\
&\quad + \bar{w}_{,z}\rho(2U_{,\rho} - k_{,\rho}) - \bar{w}_{,\rho} - \bar{w}_{,z}\rho(2U_{,z} - k_{,z}) \tag{I.10}
\end{aligned}$$

$$\begin{aligned}
A_9 &= 2\rho^3(U_{,zz} - U_{,\rho\rho} + 2U_{,z}^2 - 2U_{,\rho}^2 + 2U_{,\rho}k_{,\rho} - 2U_{,z}k_{,z}) - 2\rho^2 k_{,\rho} - 4\bar{w}^2\rho(U_{,\rho}^2 - U_{,z}^2) \\
&\quad + 4\bar{w}\rho(\bar{w}_{,\rho}U_{,\rho} - \bar{w}_{,z}U_{,z}) - (\bar{w}_{,\rho}^2 - \bar{w}_{,z}^2)\rho \tag{I.11}
\end{aligned}$$

$$\begin{aligned}
A_{10} &= 2\rho^3(U_{,\rho z} + 2U_{,\rho}U_{,z} - U_{,\rho}k_{,z} - U_{,z}k_{,\rho}) + \rho^2 k_{,z} + 4\bar{w}^2\rho U_{,\rho}U_{,z} \\
&\quad - 2\bar{w}\bar{w}_{,\rho}\rho U_{,z} - 2\bar{w}\bar{w}_{,z}\rho U_{,\rho} + \bar{w}_{,\rho}\bar{w}_{,z}\rho. \tag{I.12}
\end{aligned}$$

## Appendix J

### Explicit expressions for the perturbed C- and Einstein tensors

Here we provide explicit expressions in Schwarzschild coordinates for the coefficients of the expansion in spherical harmonics of the Einstein and C-tensors. In these expressions, the Pontryagin constraint [Eq. (11.9)] has been used. For simplicity we omit the superscripts  $(\ell, m)$ . The components of the harmonically decomposed Einstein tensor read

$$\begin{aligned} \mathcal{G}_{tt} &= -f^2 K_{,rr} - f \left( \frac{f'}{2} + \frac{3f}{r} \right) K_{,r} + \frac{(\ell+2)(\ell-1)f}{2r^2} K + \frac{f^3}{r} h_{rr,r} \\ &+ \frac{f^2}{r^2} \left[ \frac{\ell(\ell+1)}{2} + f + 2rf' \right] h_{rr}, \end{aligned} \quad (\text{J.1})$$

$$\mathcal{G}_{tr} = -K_{,tr} + \frac{1}{2f} \left( f' - \frac{2f}{r} \right) K_{,t} + \frac{f}{r} h_{rr,t} + \frac{\ell(\ell+1)}{2r^2} h_{tr}, \quad (\text{J.2})$$

$$\begin{aligned} \mathcal{G}_{rr} &= -\frac{1}{f^2} K_{,tt} + \frac{1}{2f} \left( f' + \frac{2f}{r} \right) K_{,r} - \frac{(\ell+2)(\ell-1)}{2r^2 f} K - \frac{1}{rf} h_{tt,r} \\ &+ \frac{1}{r^2 f^2} \left[ \frac{\ell(\ell+1)}{2} + rf' \right] h_{tt} + \frac{2}{rf} h_{tr,t} - \frac{1}{r^2} h_{rr}, \end{aligned} \quad (\text{J.3})$$

$$\mathcal{G}_t = -\frac{1}{2} K_{,t} + \frac{f}{2} h_{tr,r} - \frac{f}{2} h_{rr,t} + \frac{f'}{2} h_{tr}, \quad (\text{J.4})$$

$$\mathcal{G}_r = -\frac{1}{2} K_{,r} + \frac{1}{2f} h_{tt,r} - \frac{1}{4f^2} \left( f' + \frac{2f}{r} \right) h_{tt} - \frac{1}{2f} h_{tr,t} + \frac{1}{4} \left( f' + \frac{2f}{r} \right) h_{rr}, \quad (\text{J.5})$$

$$\mathcal{H}_t = \frac{(\ell+2)(\ell-1)}{2r^2} h_t, \quad (\text{J.6})$$

$$\mathcal{H}_r = \frac{(\ell+2)(\ell-1)}{2r^2} h_r, \quad (\text{J.7})$$

$$\begin{aligned}
\mathcal{G} &= -\frac{r^2}{2f}K_{,tt} + \frac{r^2f}{2}K_{,rr} + \frac{r^2}{2}\left(f' + \frac{2f}{r}\right)K_{,r} - \frac{r^2}{2}h_{tt,rr} + \frac{r^2}{4f}\left(f' - \frac{2f}{r}\right)h_{tt,r} \\
&+ \frac{r^2}{2f}\left[\frac{\ell(\ell+1)}{2r^2} + f'' + \frac{f'}{r} - \frac{f'^2}{2f}\right]h_{tt} + r^2h_{tr,tr} + \frac{r^2}{2f}\left(f' + \frac{2f}{r}\right)h_{tr,t} - \frac{r^2}{2}h_{rr,tt} \\
&- \frac{r^2f}{4}\left(f' + \frac{2f}{r}\right)h_{rr,r} - \frac{r^2f}{2}\left[\frac{\ell(\ell+1)}{2r^2} + f'' + \frac{3f'}{r} + \frac{f'^2}{2f}\right]h_{rr}, \tag{J.8}
\end{aligned}$$

$$\mathcal{H} = \frac{1}{2f}\left(h_{tt} - f^2h_{rr}\right), \tag{J.9}$$

$$\mathcal{I} = -\frac{1}{f}\left(h_{t,t} - f^2h_{r,r} - ff'h_r\right). \tag{J.10}$$

while the components of the harmonically decomposed C-tensor read

$$\mathcal{C}_{tt} = -\frac{(\ell+2)!}{(\ell-2)!}\frac{f}{2r^4}\bar{\theta}_{,r}h_t, \tag{J.11}$$

$$\mathcal{C}_{tr} = -\frac{(\ell+2)!}{(\ell-2)!}\frac{1}{4r^4f}\left(\bar{\theta}_{,t}h_t + f^2\bar{\theta}_{,r}h_r\right), \tag{J.12}$$

$$\mathcal{C}_{rr} = -\frac{(\ell+2)!}{(\ell-2)!}\frac{\bar{\theta}_{,t}}{2r^4f}h_r, \tag{J.13}$$

$$\begin{aligned}
\mathcal{C}_t &= -\frac{(\ell+2)(\ell-1)}{4r^2}\left\{\bar{\theta}_{,t}\left(h_{t,r} - \frac{2h_t}{r}\right) + f^2\bar{\theta}_{,r}\left[h_{r,r} - \frac{2h_r}{rf}\left(1 - \frac{4M}{r}\right) - \frac{2h_{t,t}}{f^2}\right]\right. \\
&+ \left.f^2\bar{\theta}_{,rr}h_r - \bar{\theta}_{,tr}h_t\right\}, \tag{J.14}
\end{aligned}$$

$$\begin{aligned}
\mathcal{C}_r &= -\frac{(\ell+2)(\ell-1)}{4r^3f^2}\left[\bar{\theta}_{,t}\left(-rh_{t,t} + 2rf^2h_{r,r} + rff'h_r - 2f^2h_r\right)\right. \\
&- \left.\bar{\theta}_{,r}\left(-rf^2h_{t,r} + rff'h_t\right) - \bar{\theta}_{,tt}rh_t + \bar{\theta}_{,tr}f^2rh_r\right], \tag{J.15}
\end{aligned}$$

$$\begin{aligned}
\mathcal{D}_t &= \bar{\theta}_{,t} \left( \frac{1}{4} K_{,tr} - \frac{1}{4f} \left( f' - \frac{2f}{r} \right) K_{,t} + \frac{f}{4} h_{tr,rr} + \frac{f'}{4} h_{tr,r} - \frac{f}{2r} h_{rr,t} \right. \\
&\quad \left. - \frac{1}{4} \left\{ -f'' + \frac{f'^2}{f} + \frac{2}{r^2} \left[ \frac{\ell}{2} (\ell + 1) + f - 1 - r f' \right] \right\} h_{tr} - \frac{f}{4} h_{rr,tr} \right) \\
&\quad + \bar{\theta}_{,r} \left\{ \frac{Kf}{4r^2} (\ell + 2) (\ell - 1) + \frac{h_{tt}}{8r^2 f} \left[ 2f\ell(\ell + 1) - 1 - 2f + f^2 \right] - \frac{h_{rr}f}{8r^2} (1 - 6f + 3f^2) \right. \\
&\quad \left. - \frac{1 - 3f}{8r} (f^2 h_{rr,r} - h_{tt,r}) - \frac{f}{4} \left( h_{tt,rr} - \frac{2}{r} h_{tr,t} - h_{tr,tr} + f K_{,rr} \right) - \frac{f}{4r} K_{,r} (1 + f) \right\} \\
&\quad + \bar{\theta}_{,rr} \left\{ \frac{1}{8r} \left[ (3f - 1) h_{rr} f^2 + (1 + f) h_{tt} \right] - \frac{f}{4} (h_{tt,r} - h_{tr,t} + f K_{,r}) \right\} \\
&\quad + \bar{\theta}_{,tr} \left[ \frac{1}{4} K_{,t} - \frac{f}{4} h_{rr,t} + \frac{f}{4} h_{tr,r} - \frac{h_{tr}}{4r} (3f - 1) \right] - \frac{f f'''}{4} \tilde{\theta} + \frac{3M}{r^3} f \tilde{\theta}_{,r}, \tag{J.16}
\end{aligned}$$

$$\begin{aligned}
\mathcal{D}_r &= \frac{\bar{\theta}_{,t}}{4f} \left\{ -h_{rr,tt} + \frac{1}{r^2} [\ell(\ell + 1) - 2] (K - f h_{rr}) + h_{tr,t} \left( -\frac{2}{r} + \frac{f'}{f} \right) + h_{tr,tr} + \frac{1}{f} K_{,tt} \right\} \\
&\quad + \bar{\theta}_{,r} \left[ -\frac{1}{8r} (f'r - 2f) h_{rr,t} + \frac{1}{8f^2 r} (f'r + 2f) h_{tt,t} + \frac{1}{4f} (h_{tr,tt} - h_{tt,tr} - f K_{,tr}) \right. \\
&\quad \left. + \frac{(\ell + 2)(\ell - 1)}{4r^2} h_{tr} \right] - \frac{\bar{\theta}_{,tt}}{4r f^2} (-r f h_{tr,r} + 2h_{tr} f + r f h_{rr,t} - r f' h_{tr} - r K_{,t}) \tag{J.17} \\
&\quad + \bar{\theta}_{,tr} \left[ \frac{1}{4f} (h_{tr,t} - f K_{,r} - h_{tt,r}) + \frac{h_{tt}}{8r f^2} (r f' + 2f) - \frac{h_{rr}}{8r} (r f' - 2f) \right] + \frac{3M}{f r^3} \tilde{\theta}_{,t},
\end{aligned}$$

$$\mathcal{C} = \frac{(\ell + 2)!}{(\ell - 2)! 4r^2} (\bar{\theta}_{,t} h_r - \bar{\theta}_{,r} h_t), \tag{J.18}$$

$$\begin{aligned}
\mathcal{D} &= \bar{\theta}_{,t} \left\{ -f h_{r,rr} - \left( \frac{3}{2} f' - \frac{f}{r} \right) h_{r,r} + \frac{1}{2} \left[ \frac{\ell(\ell + 1)}{r^2} - f'' + \frac{2}{r} \left( f' - \frac{f}{r} \right) \right] h_r + \frac{1}{f} h_{t,tr} \right. \\
&\quad \left. - \frac{1}{2f^2} \left( f' + \frac{2f}{r} \right) h_{t,t} \right\} + \bar{\theta}_{,r} \left\{ -\frac{1}{f} (h_{t,tt} - f^2 h_{t,rr}) - \frac{h_t}{2r^2} [4f'r + f''r^2 - 6f + \ell(\ell + 1)] \right. \\
&\quad \left. + \frac{1}{r} (f'r - 2f) h_{t,r} \right\} + \left( \bar{\theta}_{,rr} + \frac{\bar{\theta}_{,tt}}{f^2} \right) \left[ -\frac{h_t}{2r} (2f + f'r) + f h_{t,r} \right] - \bar{\theta}_{,tr} \left( f h_{r,r} + \frac{h_{t,t}}{f} \right), \tag{J.19}
\end{aligned}$$

$$\begin{aligned}
\mathcal{E} &= \bar{\theta}_{,t} \left[ \frac{1}{2} K_{,r} + \frac{1}{2f} h_{tr,t} - \frac{f}{2} h_{rr,r} - \frac{f'}{2} h_{rr} \right] + \frac{\bar{\theta}_{,r}}{2f} (f^2 h_{tr,r} - f K_{,t} - h_{tt,t} + f f' h_{tr}) \\
&\quad + \frac{f}{2} h_{tr} \left( \bar{\theta}_{,rr} + \frac{\bar{\theta}_{,tt}}{f^2} \right) - \frac{\bar{\theta}_{,tr}}{2f} (h_{tt} + f^2 h_{rr}). \tag{J.20}
\end{aligned}$$

## Appendix K

### Equations of the extended CS theory in the Regge-Wheeler gauge

The equation for the background component of the scalar field, Eq. (11.72), is

$$\left(-\partial_{t^2}^2 + \partial_{r_*^2}^2 - \frac{2Mf}{r^3}\right)(r\bar{\theta}) = 0, \quad (\text{K.1})$$

The divergence of the field equations, which in the non-extended theory leads to the Pontryagin constraint, now leads to the equations of motion for the scalar field. To leading order in  $\epsilon$ , this equation reduces to Eq. (11.73), which when harmonically decomposed becomes

$$\begin{aligned} & \left[ f\tilde{\theta}_{,rr}^{\ell m} - \frac{1}{f}\tilde{\theta}_{,tt}^{\ell m} + \frac{2}{r}\left(1 - \frac{M}{r}\right)\tilde{\theta}_{,r}^{\ell m} - \frac{\tilde{\theta}^{\ell m}}{r^2}\ell(\ell+1) \right] - \left[ f^2 h_{rr}^{\ell m}\bar{\theta}_{,rr} + \frac{1}{f^2}h_{tt}^{\ell m}\bar{\theta}_{,tt} \right] \\ + & \left( -\frac{1}{2f^2}h_{tt,t}^{\ell m} - \frac{1}{2}h_{rr,t}^{\ell m} + h_{tr,r}^{\ell m} + \frac{2}{r}h_{tr}^{\ell m} \right)\bar{\theta}_{,t} + \left[ -\frac{f^2}{2}h_{rr,r}^{\ell m} - \frac{1}{2}h_{tt,r}^{\ell m} \right. \\ + & \left. h_{tr,t}^{\ell m} + \frac{M}{r^2f}h_{tt}^{\ell m} - \frac{f}{2r}(3+f)h_{rr}^{\ell m} \right]\bar{\theta}_{,r} + fK_{,r}^{\ell m}\bar{\theta}_{,r} - \frac{K_{,t}^{\ell m}}{f}\bar{\theta}_{,t} = \frac{6M}{r^6}\frac{(\ell+2)!}{(\ell-2)!}\Psi_{\text{CPM}}^{\ell m}. \end{aligned} \quad (\text{K.2})$$

## Bibliography

- [1] *Grtensorii*, this is a package which runs within Maple but distinct from packages distributed with Maple. It is distributed freely on the World-Wide-Web from the address: <http://grtensor.org>.
- [2] C. Cutler and K. S. Thorne (2002), [gr-qc/0204090](#).
- [3] L. Blanchet, Living Rev. Rel. **9**, 4 (2006), and references therein, [gr-qc/0202016](#).
- [4] L. S. Finn and D. F. Chernoff, Phys. Rev. **D47**, 2198 (1993), [gr-qc/9301003](#).
- [5] LIGO, IIGO - <http://www.ligo.caltech.edu/>.
- [6] VIRGO, vIRGO - <http://www.virgo.infn.it/>.
- [7] GEO, gEO600 - <http://g/www.geo600.uni-hannover.de/>.
- [8] TAMA, tAMA - <http://tamago.mtk.nao.ac.jp/>.
- [9] T. W. Baumgarte and S. L. Shapiro, Phys. Rept. **376**, 41 (2003), and references therein, [gr-qc/0211028](#).
- [10] E. Poisson, Living Rev. Relativity **7**, 6 (2004), [gr-qc/0306052](#), URL <http://www.livingreviews.org/lrr-2004-6>.
- [11] L. Blanchet, T. Damour, and G. Esposito-Farese, Phys. Rev. **D69**, 124007 (2004), [gr-qc/0311052](#).
- [12] L. Blanchet, T. Damour, G. Esposito-Farese, and B. R. Iyer, Phys. Rev. Lett. **93**, 091101 (2004), [gr-qc/0406012](#).
- [13] R. H. Price and J. Pullin, Phys. Rev. Lett. **72**, 3297 (1994), [gr-qc/9402039](#).
- [14] P. Anninos, D. Hobill, E. Seidel, L. Smarr, and W.-M. Suen, Phys. Rev. Lett. **71**, 2851 (1993), [gr-qc/9309016](#).
- [15] P. Anninos, R. H. Price, J. Pullin, E. Seidel, and W.-M. Suen, Phys. Rev. **D52**, 4462 (1995), [gr-qc/9505042](#).
- [16] W. Tichy, B. Brügmann, M. Campanelli, and P. Diener, Phys. Rev. **D67**, 064008 (2003), [gr-qc/0207011](#).
- [17] S. Brandt and B. Brügmann, Phys. Rev. Lett. **78**, 3606 (1997), [gr-qc/9703066](#).
- [18] G. B. Cook, Living Rev. Rel. **3**, 5 (2000), [gr-qc/0007085](#).
- [19] J. York, Jr., Phys. Rev. Lett. **26**, 1656 (1971).
- [20] J. York, Jr., J. Math. Phys. **14**, 456 (1973).

- [21] J. M. Bowen and J. W. York, *Phys. Rev.* **D21**, 2047 (1980).
- [22] D. R. Brill and R. W. Lindquist, *Phys. Rev.* **131**, 471 (1963).
- [23] R. A. Matzner, M. F. Huq, and D. Shoemaker, *Phys. Rev. D* **59**, 024015 (1999).
- [24] P. Marronetti and R. A. Matzner, *Phys. Rev. Lett.* **85**, 5500 (2000), [gr-qc/0009044](#).
- [25] E. Bonning, P. Marronetti, D. Neilsen, and R. Matzner, *Phys. Rev.* **D68**, 044019 (2003), [gr-qc/0305071](#).
- [26] L. Blanchet, *Phys. Rev.* **D68**, 084002 (2003), [gr-qc/0304080](#).
- [27] S. Nissanke, *Phys. Rev.* **D73**, 124002 (2006), [gr-qc/0509128](#).
- [28] K. Alvi, *Phys. Rev.* **D61**, 124013 (2000), [gr-qc/9912113](#).
- [29] K. Alvi, *Phys. Rev.* **D67**, 104006 (2003), [gr-qc/0302061](#).
- [30] C. M. Bender and S. A. Orszag, *Advanced mathematical methods for scientists and engineers 1, Asymptotic methods and perturbation theory* (Springer, New York, 1999).
- [31] J. Kevorkian and J. D. Cole, *Multiple scale and singular perturbation methods* (Springer, New York, 1991), and references therein.
- [32] N. Jansen and B. Brügmann (2002), unpublished.
- [33] H. Tagoshi, A. Ohashi, and B. J. Owen, *Phys. Rev.* **D63**, 044006 (2001), [gr-qc/0010014](#).
- [34] E. Poisson, *Phys. Rev.* **D70**, 084044 (2004), [gr-qc/0407050](#).
- [35] F. Pretorius, *Phys. Rev. Lett.* **95**, 121101 (2005), [gr-qc/0507014](#).
- [36] M. Campanelli, C. O. Lousto, P. Marronetti, and Y. Zlochower, *Phys. Rev. Lett.* **96**, 111101 (2006), [gr-qc/0511048](#).
- [37] J. G. Baker, J. Centrella, D.-I. Choi, M. Koppitz, and J. van Meter, *Phys. Rev.* **D73**, 104002 (2006), [gr-qc/0602026](#).
- [38] L. Lindblom and B. Owen, *private communication*.
- [39] N. K. Johnson-McDaniel, N. Yunes, W. Tichy, and B. Owen (2008), in progress.
- [40] A. G. Wiseman, *Phys. Rev.* **D46**, 1517 (1992).
- [41] D. Merritt, M. Milosavljevic, M. Favata, S. A. Hughes, and D. E. Holz, *ApJ* **607**, L9 (2004), [astro-ph/0402057](#).
- [42] K. Holley-Bockelmann, K. Gultekin, D. Shoemaker, and N. Yunes (2007), [arXiv:0707.1334\[astro-ph\]](#).

- [43] M. J. Fitchett, *MNRAS* **203**, 1049 (1983).
- [44] K. I. Oohara and T. Nakamura, *Physics Letters A* **94**, 349 (1983).
- [45] T. Nakamura and M. P. Haugan, *ApJ* **269**, 292 (1983).
- [46] M. J. Fitchett and S. Detweiler, *MNRAS* **211**, 933 (1984).
- [47] I. H. Redmount and M. J. Rees, *Comments on Astrophysics* **14**, 165 (1989).
- [48] M. Favata, S. A. Hughes, and D. E. Holz, *ApJ* **607**, L5 (2004), [astro-ph/0402056](#).
- [49] L. Blanchet, M. S. S. Qusailah, and C. M. Will, *ApJ* **635**, 508 (2005), [astro-ph/0507692](#).
- [50] T. Prince, American Astronomical Society Meeting **202**, 3701 (2003).
- [51] K. Danzmann, *Advances in Space Research* **32**, 1233 (2003).
- [52] J. R. Gair, L. Barack, T. Creighton, C. Cutler, S. L. Larson, E. S. Phinney, and M. Vallisneri, *Class. Quant. Grav.* **21**, S1595 (2004).
- [53] K. Glampedakis, *Class. Quantum Grav.* **22**, S605 (2005), [gr-qc/0509024](#).
- [54] P. Amaro-Seoane, J. R. Gair, M. Freitag, M. C. Miller, I. Mandel, C. J. Cutler, and S. Babak, *ArXiv Astrophysics e-prints* (2007), [astro-ph/0703495](#).
- [55] L. J. Rubbo, K. Holley-Bockelmann, and L. S. Finn, *Astrophys. J.* **649**, L25 (2006).
- [56] C. Hopman, M. Freitag, and S. L. Larson, *Mon. Not. Roy. Astron. Soc.* **378**, 129 (2007), [astro-ph/0612337](#).
- [57] T. Damour and A. Gopakumar, *Phys. Rev.* **D73**, 124006 (2006), [gr-qc/0602117](#).
- [58] J. A. Gonzalez, U. Sperhake, B. Bruegmann, M. Hannam, and S. Husa, *Phys. Rev. Lett.* **98**, 091101 (2007), [gr-qc/0610154](#).
- [59] K. S. Thorne, *Rev. Mod. Phys.* **52**, 299 (1980).
- [60] C. M. Will, *Living Reviews in Relativity* **9** (2006).
- [61] D. M. Eardley, D. L. Lee, and A. P. Lightman, *Phys. Rev. D* **8**, 3308 (1973).
- [62] D. M. Eardley, D. L. Lee, A. P. Lightman, R. V. Wagoner, and C. M. Will, *Phys. Rev. Lett.* **30**, 884 (1973).
- [63] L. S. Finn, *Class. Quantum Grav.* **2**, 381 (1985).
- [64] C. Cutler and L. Lindblom, *Phys. Rev. D* **54**, 1287 (1996), [gr-qc/9601047](#).
- [65] F. D. Ryan, *Phys. Rev. D* **56**, 1845 (1997).
- [66] C. M. Will, *Phys. Rev. D* **57**, 2061 (1998), [gr-qc/9709011](#).

- [67] L. S. Finn and P. J. Sutton, *Phys. Rev. D* **65**, 044022 (2002).
- [68] P. J. Sutton and L. S. Finn, *Class. Quantum Grav.* **19**, 1355 (2002), [gr-qc/0112018](#).
- [69] C. M. Will and N. Yunes, *Class. Quantum Grav.* **21**, 4367 (2004), [gr-qc/0403100](#).
- [70] E. Berti, A. Buonanno, and C. M. Will, *Class. Quantum Grav.* **22**, S943 (2005), [gr-qc/0504017](#).
- [71] E. Berti, A. Buonanno, and C. M. Will, *Phys. Rev.* **D71**, 084025 (2005), [gr-qc/0411129](#).
- [72] P. D. Scharre and C. M. Will, *Phys. Rev. D* **65**, 042002 (2002), [gr-qc/0109044](#).
- [73] S. H. S. Alexander, M. E. Peskin, and M. M. Sheik-Jabbari, *Phys. Rev. Lett.* **96**, 081301 (2006), [hep-th/0403069](#).
- [74] S. H. S. Alexander and J. Gates, S. James, *JCAP* **0606**, 018 (2006), [hep-th/0409014](#).
- [75] A. Lue, L.-M. Wang, and M. Kamionkowski, *Phys. Rev. Lett.* **83**, 1506 (1999), [astro-ph/9812088](#).
- [76] M. Li, J.-Q. Xia, H. Li, and X. Zhang, *Phys. Lett.* **B651**, 357 (2007), [hep-ph/0611192](#).
- [77] S. H. S. Alexander (2006), [hep-th/0601034](#).
- [78] A. Ashtekar, A. P. Balachandran, and S. Jo, *Int. J. Mod. Phys.* **A4**, 1493 (1989).
- [79] R. Jackiw and S. Y. Pi, *Phys. Rev.* **D68**, 104012 (2003), [gr-qc/0308071](#).
- [80] K. Nordtvedt, *Phys. Rev.* **169**, 1017 (1968).
- [81] C. M. Will, *ApJ* **163**, 611 (1971).
- [82] C. M. Will, *Theory and experiment in gravitational physics* (Cambridge University Press, Cambridge, UK, 1993).
- [83] T. L. Smith, A. L. Erickcek, R. R. Caldwell, and M. Kamionkowski, *Phys. Rev.* **D77**, 024015 (2008), [arXiv:0708.0001\[astro-ph\]](#).
- [84] G. B. Cook, *Phys. Rev. D* **50**, 5025 (1994).
- [85] T. W. Baumgarte, *Phys. Rev. D* **62**, 024018 (2000), [gr-qc/0004050](#).
- [86] P. Grandclément, E. Gourgoulhon, and S. Bonazzola, *Phys. Rev. D* **65**, 044021 (2002), [gr-qc/0106016](#).
- [87] H. P. Pfeiffer, G. B. Cook, and S. A. Teukolsky, *Phys. Rev.* **D66**, 024047 (2002), [gr-qc/0203085](#).

- [88] B. D. Baker (2002), [gr-qc/0205082](#).
- [89] W. Tichy, B. Brügmann, and P. Laguna, *Phys. Rev. D* **68**, 064008 (2003), [gr-qc/0306020](#).
- [90] W. Tichy and B. Brügmann, *Phys. Rev. D* **69**, 024006 (2004), [gr-qc/0307027](#).
- [91] H.-J. Yo, J. N. Cook, S. L. Shapiro, and T. W. Baumgarte, *Phys. Rev. D* **70**, 084033 (2004), [gr-qc/0406020](#).
- [92] G. B. Cook and H. P. Pfeiffer, *Phys. Rev.* **D70**, 104016 (2004), [gr-qc/0407078](#).
- [93] N. Yunes and W. Tichy, *Phys. Rev.* **D74**, 064013 (2006), [gr-qc/0601046](#).
- [94] K. S. Thorne and J. B. Hartle, *Phys. Rev.* **D31**, 1815 (1985).
- [95] E. Poisson, *Phys. Rev. Lett.* **94**, 161103 (2005), [gr-qc/0501032](#).
- [96] C. M. Will and A. G. Wiseman, *Phys. Rev.* **D54**, 4813 (1996), [gr-qc/9608012](#).
- [97] W. L. Burke and K. S. Thorne, in *Relativity*, edited by M. Carmeli, S. I. Fickler, and L. Witten (Plenum Press, 1970), pp. 209–228.
- [98] W. L. Burke, *J. Math. Phys.* **12**, 401 (1971).
- [99] P. D. D’Eath, *Phys. Rev.* **D12**, 2183 (1975).
- [100] P. D. D’Eath, *Phys. Rev.* **D11**, 1387 (1975).
- [101] L. Blanchet, G. Faye, and B. Ponsot, *Phys. Rev.* **D58**, 124002 (1998), [gr-qc/9804079](#).
- [102] M. Visser and N. Yunes, *Int. J. Mod. Phys.* **A18**, 3433 (2003), [gr-qc/0211001](#).
- [103] P. Jaranowski and G. Schafer, *Phys. Rev.* **D57**, 7274 (1998), [gr-qc/9712075](#).
- [104] N. Yunes and J. A. Gonzalez, *Phys. Rev.* **D73**, 024010 (2006), [gr-qc/0510076](#).
- [105] N. Yunes, W. Tichy, B. J. Owen, and B. Bruegmann, *Phys. Rev.* **D74**, 104011 (2006), [gr-qc/0503011](#).
- [106] B. Schutz, *Class. Quantum Grav.* **16**, A131 (1999).
- [107] M. A. Miller, *Phys. Rev.* **D71**, 104016 (2005), [gr-qc/0502087](#).
- [108] J. York, James W., *Phys. Rev. Lett.* **82**, 1350 (1999), [gr-qc/9810051](#).
- [109] P. Marronetti, M. F. Huq, P. Laguna, L. Lehner, R. A. Matzner, and D. Shoemaker, *Phys. Rev. D* **62**, 024017 (2000), [gr-qc/0001077](#).
- [110] P. Grandclement, E. Gourgoulhon, and S. Bonazzola, *Phys. Rev.* **D65**, 044021 (2002), [gr-qc/0106016](#).

- [111] M. D. Hannam, C. R. Evans, G. B. Cook, and T. W. Baumgarte, *Phys. Rev.* **D68**, 064003 (2003), [gr-qc/0306028](#).
- [112] M. Holst et al., *Phys. Rev.* **D70**, 084017 (2004), [gr-qc/0407011](#).
- [113] M. Ansorg, B. Bruggmann, and W. Tichy, *Phys. Rev.* **D70**, 064011 (2004), [gr-qc/0404056](#).
- [114] M. D. Hannam, *Phys. Rev.* **D72**, 044025 (2005), [gr-qc/0505120](#).
- [115] J. M. Aguirregabiria, L. Bel, J. Martin, A. Molina, and E. Ruiz, *Gen. Rel. Grav.* **33**, 1809 (2001), [gr-qc/0104019](#).
- [116] G. Schafer, *Annals Phys.* **161**, 81 (1985).
- [117] P. Jaranowski and G. Schäfer, *Phys. Rev. D* **55**, 4712 (1997).
- [118] M. Misner, Charles, K. S. Thorne, and J. A. Wheeler, *Gravitation* (Freeman, New York, 1970).
- [119] A. Abramovici et al., *Science* **256**, 325 (1992).
- [120] B. Willke et al., *Class. Quant. Grav.* **19**, 1377 (2002).
- [121] A. Giazotto, *Nucl. Instrum. Meth.* **A289**, 518 (1990).
- [122] M. Ando (TAMA), *Class. Quant. Grav.* **19**, 1409 (2002).
- [123] K. Danzmann, *Class. Quant. Grav.* **14**, 1399 (1997).
- [124] *Lisa*, [lisa.jpl.nasa.gov](#).
- [125] A. Buonanno and T. Damour, *Phys. Rev.* **D62**, 064015 (2000), [gr-qc/0001013](#).
- [126] A. Buonanno, Y. Chen, and T. Damour, *Phys. Rev.* **D74**, 104005 (2006), [gr-qc/0508067](#).
- [127] Y. Mino, M. Sasaki, and T. Tanaka, *Prog. Theor. Phys. Suppl.* **128**, 373 (1997), [gr-qc/9712056](#).
- [128] C. Lanczos, *Phys. Zeits.* **23**, 539 (1922).
- [129] C. Lanczos, *Ann der Phys.* **74**, 528 (1924).
- [130] G. Darrois, *Les équations de la gravitation einsteinienne* (in *Mémorial des sciences mathématiques XXV*, Gauthier-Villars, Paris, 1927).
- [131] A. Lichnerowicz, *Theories relativistes de la gravitation et de l'électromagnétisme. Relativité générale et théories unitaires* (Collection d'Ouvrages de Mathématiques à l'Usage des Physiciens, Paris: Masson, 1955, 1955).
- [132] C. W. Misner and D. H. Sharp, *Phys. Rev.* **B136**, 571 (1964).

- [133] C. Barrabes and W. Israel, Phys. Rev. **D43**, 1129 (1991).
- [134] W. Israel, Nuovo Cimento **B44**, 1 (1966).
- [135] E. Poisson, *A Relativist's Toolkit: The mathematics of black-hole mechanics* (Cambridge, New York, United States, 2004), and references therein.
- [136] O. Poujade and L. Blanchet, Phys. Rev. **D65**, 124020 (2002), [gr-qc/0112057](#).
- [137] H. Tagoshi, A. Ohashi, and B. J. Owen, Phys. Rev. **D 63**, 440006 (2001).
- [138] S. A. Hughes, Phys. Rev. **D64**, 064004 (2001), [gr-qc/0104041](#).
- [139] C. F. Sopuerta, N. Yunes, and P. Laguna, Phys. Rev. **D74**, 124010 (2006), [astro-ph/0608600](#).
- [140] C. F. Sopuerta, N. Yunes, and P. Laguna, Astrophys. J. **656**, L9 (2007), [astro-ph/0611110](#).
- [141] E. Poisson and M. Sasaki, Phys. Rev. **D51**, 5753 (1995), [gr-qc/9412027](#).
- [142] H. Tagoshi, S. Mano, and E. Takasugi (1997), prepared for APCTP Workshop: Pacific Particle Physics Phenomenology (P4 97), Seoul, Korea, 31 Oct - 2 Nov 1997.
- [143] K. Alvi, Phys. Rev. **D64**, 104020 (2001), [gr-qc/0107080](#).
- [144] K. Martel, Phys. Rev. **D69**, 044025 (2004), [gr-qc/0311017](#).
- [145] K. Glampedakis and S. Babak, Class. Quant. Grav. **23**, 4167 (2006), [gr-qc/0510057](#).
- [146] P. D. D'Eath, *Black holes: Gravitational interactions* (Clarendon Press, Oxford, 1996).
- [147] T. Regge and J. Wheeler, Phys. Rev. **108**, 1063 (1957).
- [148] P. L. Chrzanowski, *Phys. Rev. D* **11**, 2042 (1975).
- [149] A. Ori, Phys. Rev. **D67**, 124010 (2003), [gr-qc/0207045](#).
- [150] R. M. Wald, Phys. Rev. Lett. **41**, 203 (1978).
- [151] L. S. Kegeles and J. M. Cohen, Phys. Rev. **D19**, 1641 (1979).
- [152] M. Campanelli and C. O. Lousto, Phys. Rev. **D59**, 124022 (1999), [gr-qc/9811019](#).
- [153] M. Ansorg and D. Petroff, Phys. Rev. **D72**, 024019 (2005), [gr-qc/0505060](#).
- [154] W. H. Press and S. A. Teukolsky, Astrophys. J. **185**, 649 (1973).
- [155] C. O. Lousto and B. F. Whiting, Phys. Rev. **D66**, 024026 (2002), [gr-qc/0203061](#).

- [156] S. Chandrasekhar, *The Mathematical Theory of Black Holes* (Clarendon Press, Oxford, 2000).
- [157] B. Binggeli and H. Jerjen, *A&A* **333**, 17 (1998), [astro-ph/9704027](#).
- [158] B. Binggeli, F. Barazza, and H. Jerjen, *A&A* **359**, 447 (2000).
- [159] M. G. Haehnelt, M. B. Davies, and M. J. Rees, *Mon. Not. Roy. Astron. Soc. Lett.* **366**, L22 (2006), [astro-ph/0511245](#).
- [160] Z. Haiman, *Astrophys. J.* **613**, 36 (2004), [astro-ph/0404196](#).
- [161] W. Bonnor and M. Rotenberg, *Proc. R. Soc. London* **A265**, 109 (1961).
- [162] A. Papapetrou, *Ann. Inst. Henri Poincare* **14**, 79 (1962).
- [163] A. Peres, *Physical Review* **128**, 2471 (1962).
- [164] J. D. Bekenstein, *ApJ* **183**, 657 (1973).
- [165] S. A. Hughes, M. Favata, and D. E. Holz, in *Growing Black Holes: Accretion in a Cosmological Context*, edited by A. Merloni, S. Nayakshin, and R. A. Sunyaev (2005), pp. 333–339.
- [166] M. Campanelli, *Class. Quant. Grav.* **22**, S387 (2005), [astro-ph/0411744](#).
- [167] P. Anninos and S. Brandt, *Phys. Rev. Lett.* **81**, 508 (1998), [gr-qc/9806031](#).
- [168] S. Brandt and P. Anninos, *Phys. Rev.* **D60**, 084005 (1999), [astro-ph/9907075](#).
- [169] J. G. Baker, J. Centrella, D.-I. Choi, M. Koppitz, and J. van Meter, *Phys. Rev. Lett.* **96**, 111102 (2006), [gr-qc/0511103](#).
- [170] F. Herrmann, I. Hinder, D. Shoemaker, and P. Laguna, *Class. Quant. Grav.* **24**, S33 (2007).
- [171] J. G. Baker et al., *Astrophys. J.* **653**, L93 (2006), [astro-ph/0603204](#).
- [172] R. J. Gleiser, C. O. Nicasio, R. H. Price, and J. Pullin, *Phys. Rev. Lett.* **77**, 4483 (1996), [gr-qc/9609022](#).
- [173] R. J. Gleiser, C. O. Nicasio, R. H. Price, and J. Pullin, *Phys. Rept.* **325**, 41 (2000), [gr-qc/9807077](#).
- [174] W. Krivan and R. H. Price, *Phys. Rev. Lett.* **82**, 1358 (1999), [gr-qc/9810080](#).
- [175] C. O. Nicasio, R. J. Gleiser, R. H. Price, and J. Pullin, *Phys. Rev.* **D59**, 044024 (1999), [gr-qc/9802063](#).
- [176] R. J. Gleiser and E. A. Dominguez, *Phys. Rev.* **D65**, 064018 (2002), [gr-qc/0109018](#).
- [177] G. Khanna, *Phys. Rev.* **D63**, 124007 (2001), [gr-qc/0101015](#).

- [178] O. Sarbach, M. Tiglio, and J. Pullin, Phys. Rev. **D65**, 064026 (2002), [gr-qc/0110085](#).
- [179] G. Khanna, Phys. Rev. **D66**, 064004 (2002), [gr-qc/0206010](#).
- [180] Z. Andrade and R. H. Price, Phys. Rev. **D56**, 6336 (1997), [gr-qc/9611022](#).
- [181] U. H. Gerlach and U. K. Sengupta, Phys. Rev. **D19**, 2268 (1979).
- [182] U. H. Gerlach and U. K. Sengupta, Phys. Rev. **D22**, 1300 (1980).
- [183] G. Khanna, R. Gleiser, R. Price, and J. Pullin, New J. Phys. **2**, 3 (2000), [gr-qc/0003003](#).
- [184] A. Lichnerowicz, J. Math. Pures et Appl. **23**, 37 (1944).
- [185] J. York, Jr., Phys. Rev. Lett. **28**, 1082 (1972).
- [186] C. W. Misner, Phys. Rev. **118**, 1110 (1960).
- [187] E. U. Condon and G. H. Shortley, *The Theory of Atomic Spectra* (Cambridge University Press, Cambridge, 1970).
- [188] Arfken and Weber, *Mathematical Methods for Physicists* (Academic Press, California, 2001).
- [189] T. Regge and J. A. Wheeler, Phys. Rev. **108**, 1063 (1957).
- [190] F. J. Zerilli, *Phys. Rev. Lett.* **24**, 737 (1970).
- [191] V. Moncrief, Ann. Phys. (N.Y.) **88**, 323 (1974).
- [192] K. Martel and E. Poisson, Phys. Rev. **D71**, 104003 (2005), [gr-qc/0502028](#).
- [193] C. T. Cunningham, R. H. Price, and V. Moncrief, *ApJ* **224**, 643 (1978).
- [194] S. Jhingan and T. Tanaka, Phys. Rev. **D67**, 104018 (2003), [gr-qc/0211060](#).
- [195] R. A. Isaacson, Phys. Rev. **166**, 1263 (1968).
- [196] R. A. Isaacson, Phys. Rev. **166**, 1272 (1968).
- [197] C. W. Misner, K. Thorne, and J. A. Wheeler, *Gravitation* (W. H. Freeman & Co., San Francisco, 1973).
- [198] J. N. Goldberg, A. J. Macfarlane, E. T. Newman, F. Rohrlich, and E. C. G. Sudarshan, J. Math. Phys. **8**, 2155 (1967).
- [199] R. Arnowitt, S. Deser, and C. W. Misner, in *Gravitation: An introduction to current research*, edited by L. Witten (Wiley, New York, 1962), pp. 227–265.
- [200] A. M. Abrahams and R. H. Price, Phys. Rev. **D53**, 1963 (1996), [gr-qc/9508059](#).

- [201] R. Beig (2000), [gr-qc/0005043](#).
- [202] C. O. Lousto and R. H. Price, *Phys. Rev.* **D55**, 2124 (1997), [gr-qc/9609012](#).
- [203] R. Bulirsch and J. Stoer, *Num. Math.* **8**, 1 (1966).
- [204] J. Stoer and R. Bulirsch, *Introduction to Numerical Analysis* (Springer-Verlag, New York, 1993).
- [205] W. H. Press, B. P. Flannery, S. A. Teukolsky, and W. T. Vetterling, *Numerical Recipes: The Art of Scientific Computing* (Cambridge University Press, Cambridge (UK) and New York, 1992).
- [206] C. F. Sopuerta and P. Laguna, *Phys. Rev.* **D73**, 044028 (2006), [gr-qc/0512028](#).
- [207] F. Herrmann, *private communication*.
- [208] G. Khanna et al., *Phys. Rev. Lett.* **83**, 3581 (1999), [gr-qc/9905081](#).
- [209] M. Bruni, L. Gualtieri, and C. F. Sopuerta, *Class. Quant. Grav.* **20**, 535 (2003), [gr-qc/0207105](#).
- [210] C. F. Sopuerta, M. Bruni, and L. Gualtieri, *Phys. Rev.* **D70**, 064002 (2004), [gr-qc/0306027](#).
- [211] A. Passamonti, M. Bruni, L. Gualtieri, and C. F. Sopuerta, *Phys. Rev.* **D71**, 024022 (2005), [gr-qc/0407108](#).
- [212] A. Passamonti, M. Bruni, L. Gualtieri, A. Nagar, and C. F. Sopuerta, *Phys. Rev.* **D73**, 084010 (2006), [gr-qc/0601001](#).
- [213] W. H. Press and P. Schechter, *ApJ* **187**, 425 (1974).
- [214] D. Richstone et al., *Nature* **395**, 14 (1998), [astro-ph/9810378](#).
- [215] J. Magorrian et al., *Astrophys. J.* **115**, 2285 (1998), [astro-ph/9708072](#).
- [216] L. Ferrarese and D. Merritt, *ApJ* **539**, L9 (2000), [astro-ph/0006053](#).
- [217] L. Ferrarese, *ApJ* **578**, 90 (2002), [astro-ph/0203469](#).
- [218] M. Volonteri, F. Haardt, and P. Madau, *ApJ* **582**, 559 (2003), [astro-ph/0207276](#).
- [219] M. C. Begelman, R. D. Blandford, and M. J. Rees, *Nature* **287**, 307 (1980).
- [220] P. Madau and E. Quataert, *ApJ* **606**, L17 (2004), [astro-ph/0403295](#).
- [221] M. Micic, T. Abel, and S. Sigurdsson, preprint ([astro-ph/0609443](#)) (2006).
- [222] S. J. Aarseth, *ApJSS* **285**, 367 (2003), [astro-ph/0210116](#).
- [223] P. J. Armitage and P. Natarajan, *ApJ* **634**, 921 (2005), [astro-ph/0508493](#).

- [224] M. Dotti, M. Colpi, and F. Haardt, *MNRAS* **367**, 103 (2006).
- [225] P. Bender et al., LISA Pre-Phase A Report, Max-Planck-Institut für Quantenoptik, Garching (1998), mPQ 233.
- [226] K. Danzmann and A. Rüdiger, *Class. Quantum Grav.* **20**, S1 (2003).
- [227] T. J. Sumner and D. N. A. Shaul, *MPLA* **19**, 785 (2004).
- [228] L. J. Rubbo, K. Holley-Bockelmann, and L. S. Finn, in *Laser Interferometer Space Antenna: 6th International LISA Symposium*, edited by S. M. Merkowitz and J. C. Livas (AIP Conference Proceedings, 2007), vol. 873, pp. 284–288.
- [229] J. R. Gair et al., *Class. Quantum Grav.* **21**, S1595 (2004), [gr-qc/0405137](#).
- [230] C. Hopman and T. Alexander, *Astrophys. J.* **645**, L133 (2006), [astro-ph/0603324](#).
- [231] L. Barack and C. Cutler, *Phys. Rev. D* **70**, 122002 (2004).
- [232] S. Tremaine et al., *AJ* **107**, 634 (1994).
- [233] K. Holley-Bockelmann and S. Sigurdsson, ArXiv e-print [astro-ph/0601520](#) (2006), [astro-ph/0601520](#).
- [234] R. Ruffini and M. Sasaki, *Prog. Theor. Phys.* **66**, 1627 (1981).
- [235] J. R. Gair, D. J. Kennefick, and S. L. Larson, *Phys. Rev. D* **72**, 084009 (2005), [gr-qc/0508049](#).
- [236] J. R. Gair, D. J. Kennefick, and S. L. Larson, *Astrophys. J.* **639**, 999 (2006), [astro-ph/0508275](#).
- [237] S. Babak, H. Fang, J. R. Gair, K. Glampedakis, and S. A. Hughes, *Phys. Rev. D* **75**, 024005 (2007), [gr-qc/0607007](#).
- [238] A. M. Ghez et al., *Astrophys. J.* **620**, 744 (2005).
- [239] J.-A. Marck, *Class. Quant. Grav.* **13**, 393 (1996), [gr-qc/9505010](#).
- [240] E. E. Flanagan and S. A. Hughes, *New J. Phys.* **7**, 204 (2005), [gr-qc/0501041](#).
- [241] S. Chandrasekhar, *The mathematical theory of black holes* (Oxford University Press, New York, 1992).
- [242] F. Eisenhauer et al., *Astrophys. J.* **628**, 246 (2005).
- [243] W. Schmidt, *Class. Quantum Grav.* **19**, 2743 (2002).
- [244] G. V. Kraniotis, *Class. Quantum Grav.* **24**, 1775 (2007).
- [245] S. L. Larson, W. A. Hiscock, and R. W. Hellings, *Phys. Rev. D* **62**, 062001 (2000), <http://www.srl.caltech.edu/~shane/sensitivity/index.html>.

- [246] W. G. Anderson, P. R. Brady, J. D. E. Creighton, and E. E. Flanagan, *Phys. Rev. D* **D63**, 042003 (2001), [gr-qc/0008066](#).
- [247] S. Klimenko, I. Yakushin, and G. Mitselmakher, *Class. Quantum Grav.* **21**, S1685 (2004).
- [248] A. L. Stuver and L. S. Finn, *Class. Quantum Grav.* **23**, S733 (2006).
- [249] M. Camarda and A. Ortolan, *Phys. Rev. D* **74**, 062001 (2006).
- [250] S. A. Hughes, *Phys. Rev. D* **64**, 064004 (2001).
- [251] S. A. Hughes, *Class. Quantum Grav.* **18**, 4067 (2001).
- [252] K. Glampedakis and D. Kennefick, *Phys. Rev. D* **66**, 044002 (2002).
- [253] L. Barack and C. Cutler, *Phys. Rev. D* **69**, 082005 (2004).
- [254] N. A. Collins and S. A. Hughes, *Phys. Rev. D* **D69**, 124022 (2004), [gr-qc/0402063](#).
- [255] E. Barausse, L. Rezzolla, D. Petroff, and M. Ansorg, *Phys. Rev. D* **D75**, 064026 (2007), [gr-qc/0612123](#).
- [256] L. I. Schiff, *Proc. Nat. Acad. Sci.* **46**, 871 (1960).
- [257] K. J. Nordtvedt and C. M. Will, *ApJ* **177**, 775 (1972).
- [258] C. M. Will, *ApJ* **185**, 31 (1973).
- [259] R. V. Wagoner, *Phys. Rev.* **D1**, 3209 (1970).
- [260] C. M. Will and K. J. Nordtvedt, *ApJ* **177**, 757 (1972).
- [261] R. W. Hellings and K. Nordtvedt, *Phys. Rev. D* **7**, 3593 (1973).
- [262] N. Rosen, *Annals Phys.* **84**, 455 (1974).
- [263] D. L. Lee, W.-T. Ni, C. M. Caves, and C. M. Will, *ApJ* **206**, 555 (1976).
- [264] D. L. Lee, A. P. Lightman, and W. T. Ni, *Phys. Rev. D* **D10**, 1685 (1974).
- [265] S. Kalyana Rama, *ArXiv High Energy Physics - Theory e-prints* (1994), [hep-th/9411076](#).
- [266] V. D. Ivashchuk, V. S. Manko, and V. N. Melnikov, *ArXiv General Relativity and Quantum Cosmology e-prints* (2001), [gr-qc/0101044](#).
- [267] V. B. Bezerra, L. P. Colatto, M. E. Guimarães, and R. M. Teixeira Filho, *Phys. Rev. D* **65**, 104027 (2002), [gr-qc/0104038](#).
- [268] R. J. Gleiser and C. N. Kozameh, *Phys. Rev. D* **64**, 083007 (2001), [gr-qc/0102093](#).
- [269] Y.-Z. Fan, D.-M. Wei, and D. Xu, *Mon. Not. Roy. Astron. Soc.* **376**, 1857 (2006), [astro-ph/0702006](#).

- [270] G. Amelino-Camelia, J. Ellis, N. E. Mavromatos, D. V. Nanopoulos, and S. Sarkar, *Nature* **393**, 763 (1998), [astro-ph/9712103](#).
- [271] R. Gambini and J. Pullin, *Phys. Rev.* **D59**, 124021 (1999), [gr-qc/9809038](#).
- [272] S. Alexander, L. S. Finn, and N. Yunes (2007), [arXiv:0712.2542\[gr-qc\]](#).
- [273] R. Jackiw and S. Y. Pi, *Phys. Rev.* **D68**, 104012 (2003), [gr-qc/0308071](#).
- [274] S. Alexander and J. Martin, *Phys. Rev.* **D71**, 063526 (2005), [hep-th/0410230](#).
- [275] J. Polchinski, *String theory. Vol. 2: Superstring theory and beyond* (Cambridge University Press, Cambridge, UK, 1998).
- [276] M. B. Green, J. H. Schwarz, and E. Witten, *Superstring theory. Vol. 2: Loop and amplitudes, anomalies and phenomenology* (Cambridge University Press (Cambridge Monographs On Mathematical Physics), Cambridge, Uk, 1987).
- [277] S. Alexander and N. Yunes, *Phys. Rev. Lett.* **99**, 241101 (2007), [hep-th/0703265](#).
- [278] K. S. Thorne, R. H. Price, and D. A. MacDonald, *Black holes: The membrane paradigm* (Black Holes: The Membrane Paradigm, 1986).
- [279] B. Mashhoon (2003), [gr-qc/0311030](#).
- [280] A discussion of the history, technology and physics of Gravity Probe B can be found at <http://einstein.standfod.edu>.
- [281] S. Alexander, B. Owen, and N. Yunes, *work in progress*.
- [282] S. H. Alexander, M. E. Peskin, and M. M. Sheikh-Jabbari (2007), [hep-ph/0701139](#).
- [283] P. Svrcek and E. Witten, *JHEP* **06**, 051 (2006), [hep-th/0605206](#).
- [284] R. H. Brandenberger and C. Vafa, *Nucl. Phys.* **B316**, 391 (1989).
- [285] A. A. Tseytlin and C. Vafa, *Nucl. Phys.* **B372**, 443 (1992), [hep-th/9109048](#).
- [286] A. Nayeri, R. H. Brandenberger, and C. Vafa, *Phys. Rev. Lett.* **97**, 021302 (2006), [hep-th/0511140](#).
- [287] C.-Y. Sun and D.-H. Zhang (2006), [hep-th/0611101](#).
- [288] D. H. Wesley, P. J. Steinhardt, and N. Turok, *Phys. Rev.* **D72**, 063513 (2005), [hep-th/0502108](#).
- [289] S. Alexander, R. H. Brandenberger, and D. Easson, *Phys. Rev.* **D62**, 103509 (2000), [hep-th/0005212](#).
- [290] R. Brandenberger, D. A. Easson, and D. Kimberly, *Nucl. Phys.* **B623**, 421 (2002), [hep-th/0109165](#).
- [291] T. Battefeld and S. Watson, *Rev. Mod. Phys.* **78**, 435 (2006), [hep-th/0510022](#).

- [292] R. H. Brandenberger, A. Nayeri, S. P. Patil, and C. Vafa, *Int. J. Mod. Phys.* **A22**, 3621 (2007), [hep-th/0608121](#).
- [293] R. H. Brandenberger, *Mod. Phys. Lett.* **A22**, 1875 (2007), [hep-th/0702001](#).
- [294] P. Brax, C. van de Bruck, and A.-C. Davis, *Rept. Prog. Phys.* **67**, 2183 (2004), [hep-th/0404011](#).
- [295] L. Randall and R. Sundrum, *Phys. Rev. Lett.* **83**, 3370 (1999), [hep-ph/9905221](#).
- [296] L. Randall and R. Sundrum, *Phys. Rev. Lett.* **83**, 4690 (1999), [hep-th/9906064](#).
- [297] D. Guarrera and A. J. Hariton, *Phys. Rev.* **D76**, 044011 (2007), [gr-qc/0702029](#).
- [298] B. J. Owen, *Phys. Rev. Lett.* **95**, 211101 (2005), [astro-ph/0503399](#).
- [299] S. Chandrasekhar, *Phys. Rev. Lett.* **24**, 611 (1970).
- [300] J. L. Friedman and B. F. Schutz, *Astrophys. J.* **222**, 281 (1978).
- [301] L. Lindblom, B. J. Owen, and S. M. Morsink, *Phys. Rev. Lett.* **80**, 4843 (1998), [gr-qc/9803053](#).
- [302] M. Dine, W. Fischler, and M. Srednicki, *Phys. Lett.* **B104**, 199 (1981).
- [303] J. Murphy, T. W., K. Nordtvedt, and S. G. Turyshev, *Phys. Rev. Lett.* **98**, 071102 (2007), [gr-qc/0702028](#).
- [304] C. M. Will, *Phys. Rev.* **D67**, 062003 (2003), [gr-qc/0212069](#).
- [305] C. M. Will, *Living Rev. Relativity* **9**, 3 (2005), [gr-qc/0510072](#).
- [306] A. G. Riess et al. (Supernova Search Team), *Astron. J.* **116**, 1009 (1998), [astro-ph/9805201](#).
- [307] S. Perlmutter et al. (Supernova Cosmology Project), *Astrophys. J.* **517**, 565 (1999), [arXiv:astro-ph/9812133](#).
- [308] M. Tegmark et al., *Phys. Rev.* **D74**, 123507 (2006), [astro-ph/0608632](#).
- [309] P. Jordan, *Z. Phys.* **157**, 112 (1959).
- [310] C. Brans and R. H. Dicke, *Phys. Rev.* **124**, 925 (1961).
- [311] J. Z. Simon, *Phys. Rev.* **D41**, 3720 (1990).
- [312] J. Z. Simon, *Phys. Rev.* **D43**, 3308 (1991).
- [313] R. P. Woodard, *Lect. Notes Phys.* **720**, 403 (2007), [astro-ph/0601672](#).
- [314] L. Alvarez-Gaume and E. Witten, *Nucl. Phys.* **B234**, 269 (1984).
- [315] J. S. Bell and R. Jackiw, *Nuovo Cim.* **A60**, 47 (1969).

- [316] S. Alexander and J. Martin, Phys. Rev. **D71**, 063526 (2005), [hep-th/0410230](#).
- [317] S. Alexander and N. Yunes, Phys. Rev. **D75**, 124022 (2007), [arXiv:0704.0299\[hep-th\]](#).
- [318] V. A. Kostelecky, Phys. Rev. **D69**, 105009 (2004), [hep-th/0312310](#).
- [319] T. Mariz, J. R. Nascimento, E. Passos, and R. F. Ribeiro, Phys. Rev. **D70**, 024014 (2004), [hep-th/0403205](#).
- [320] R. Bluhm and V. A. Kostelecky, Phys. Rev. **D71**, 065008 (2005), [hep-th/0412320](#).
- [321] C. Eling, T. Jacobson, and D. Mattingly (2004), [gr-qc/0410001](#).
- [322] S. H. S. Alexander, M. E. Peskin, and M. M. Sheikh-Jabbari, Phys. Rev. Lett. **96**, 081301 (2006), [hep-th/0403069](#).
- [323] D. H. Lyth, C. Quimbay, and Y. Rodriguez, JHEP **03**, 016 (2005), [hep-th/0501153](#).
- [324] D. Mattingly, Living Rev. Rel. **8**, 5 (2005), [gr-qc/0502097](#).
- [325] R. Lehnert (2006), [gr-qc/0602073](#).
- [326] A. J. Hariton and R. Lehnert, Phys. Lett. **A367**, 11 (2007), [hep-th/0612167](#).
- [327] K. Konno, T. Matsuyama, and S. Tanda, Phys. Rev. **D76**, 024009 (2007), [arXiv:0706.3080\[gr-qc\]](#).
- [328] W. Fischler and S. Paban, JHEP **10**, 066 (2007), [arXiv:0708.3828\[hep-th\]](#).
- [329] B. Tekin, Phys. Rev. **D77**, 024005 (2008), [arXiv:0710.2528\[gr-qc\]](#).
- [330] B. Aschenbach (2007), [arXiv:0710.3454\[astro-ph\]](#).
- [331] A. Garcia, F. W. Hehl, C. Heinicke, and A. Macias, Class. Quant. Grav. **21**, 1099 (2004), [gr-qc/0309008](#).
- [332] G. W. Gibbons and S. W. Hawking, Phys. Rev. **D15**, 2752 (1977).
- [333] R. Penrose and W. Rindler, *Spinors and Space-Time II* (Cambridge University Press, 1986).
- [334] H. Stephani, D. Kramer, M. MacCallum, C. Hoenselaers, and E. Herlt, *Exact solutions of Einstein's field equations* (Cambridge University Press, Cambridge, 2003).
- [335] A. Buonanno, G. B. Cook, and F. Pretorius, Phys. Rev. **D75**, 124018 (2007), [gr-qc/0610122](#).
- [336] C. Cherubini, D. Bini, S. Capozziello, and R. Ruffini, Int. J. Mod. Phys. **D11**, 827 (2002), [gr-qc/0302095](#).

- [337] N. Yunes and C. F. Sopuerta (2007), [arXiv:0712.1028\[gr-qc\]](#).
- [338] A. Matte, *Ca. J. Math.* **5**, 1 (1953).
- [339] R. Lehnert, private communication.
- [340] H. Balasin, C. G. Boehmer, and D. Grumiller, *Gen. Rel. Grav.* **37**, 1435 (2005), [gr-qc/0412098](#).
- [341] D. Grumiller, W. Kummer, and D. V. Vassilevich, *Phys. Rept.* **369**, 327 (2002), [hep-th/0204253](#).
- [342] R. M. Wald, *General Relativity* (The University of Chicago Press, 1984).
- [343] J. Chazy, *Bull. Soc. Math. France* **52**, 17 (1924).
- [344] H. E. J. Curzon, *Proc. London Math. Soc.* **23**, 477 (1924).
- [345] B. Lukács and Z. Perjés, *Phys. Lett.* **A88**, 267 (1982).
- [346] <http://www.gravity.psu.edu/yunes/public.html> The Maple scripts that generate these quantities are available upon request.
- [347] P. Jordan, J. Ehlers, and W. Kundt, *Akad. Wiss. Lit. (Mainz) Abhandl. Math.-Nat. Kl.* **2**, 21 (1960).
- [348] P. C. Aichelburg and R. U. Sexl, *Gen. Rel. Grav.* **2**, 303 (1971).
- [349] C. O. Lousto and N. G. Sanchez, *Nucl. Phys.* **B383**, 377 (1992).
- [350] H. Balasin and H. Nachbagauer, *Class. Quant. Grav.* **12**, 707 (1995), [gr-qc/9405053](#).
- [351] D. Grumiller and R. Jackiw (2007), [arXiv:0711.0181\[math-ph\]](#).
- [352] H. Balasin and H. Nachbagauer, *Class. Quant. Grav.* **11**, 1453 (1994), [gr-qc/9312028](#).
- [353] S. Hawking and G. Ellis, *The Large Scale Structure of Space-Time* (Cambridge University Press, 1973).
- [354] S. Alexander, D. Grumiller, and N. Yunes, in progress (2008).
- [355] S. Wood, in preparation.
- [356] N. Yunes, in preparation.
- [357] D. Gorbonos and B. Kol, *JHEP* **06**, 053 (2004), [hep-th/0406002](#).
- [358] D. Gorbonos and B. Kol, *Class. Quant. Grav.* **22**, 3935 (2005), [hep-th/0505009](#).
- [359] D. Grumiller and N. Yunes (2007), [arXiv:0711.1868\[gr-qc\]](#).

- [360] S. Alexander, in progress (2008).
- [361] D. Grumiller, *private communication*.
- [362] C. F. Sopuerta, Phys. Rev. **D55**, 5936 (1997).
- [363] C. F. Sopuerta, R. Maartens, G. F. R. Ellis, and W. M. Lesame, Phys. Rev. **D60**, 024006 (1999), [gr-qc/9809085](#).
- [364] S. M. Carrol, *An introduction to general relativity, Spacetime and Geometry* (Pearson - Benjamin Cummings, San Francisco, 2003).
- [365] e. . Merkowitz, S. M. and e. . Livas, J. C. (2006), prepared for 6th International LISA Symposium, Greenbelt, Maryland, 19-23 Jun 2006.
- [366] J. Baker, P. Bender, Binetruy, P., J. Centrella, Creighton, T., J. Crowder, C. Cutler, K. Danzmann, et al. (2007), <http://www.lisa-science.org/resources/talks-articles/science>.
- [367] *Committee on nasa's beyond einstein program: An architecture for implementation* (2007), Space Studies Board, Board on Physics and Astronomy, and Division on Engineering and Physical Sciences of the National Research Council.
- [368] O. Dreyer et al., Class. Quant. Grav. **21**, 787 (2004), [gr-qc/0309007](#).
- [369] E. Berti, V. Cardoso, and C. M. Will, Phys. Rev. D **73**, 064030 (2006), ISSN 1550-7998, times Cited: 2, [gr-qc/0512160](#).
- [370] Waldman and T. L. S. Collaboration (The LIGO Scientific Collaboration), Class. Quant. Grav. **23**, S653 (2006).
- [371] F. Acernese et al., Class. Quant. Grav. **23**, S635 (2006).
- [372] B. Willke, P. Ajith, B. Allen, P. Aufmuth, C. Aulbert, S. Babak, R. Balasubramanian, B. W. Barr, S. Berukoff, and A. Bunkowski, Class. Quant. Grav. **23**, 207 (2006).
- [373] H. Lück, M. Hewitson, P. Ajith, B. Allen, P. Aufmuth, C. Aulbert, S. Babak, R. Balasubramanian, B. W. Barr, and S. Berukoff, Class. Quant. Grav. **23**, 71 (2006).
- [374] P. Bender, P. Binetruy, S. Buchman, J. Centrella, M. Cerdonio, N. Cornish, M. Cruise, C. Cutler, K. Danzmann, L. S. Finn, et al. (2007).
- [375] A. Vecchio, *Phys. Rev. D* **70**, 042001 (2004).
- [376] K. G. Arun, B. R. Iyer, B. S. Sathyaprakash, S. Sinha, and C. V. D. Broeck, Phys. Rev. **D76**, 104016 (2007), [arXiv:0707.3920\[astro-ph\]](#).
- [377] C. Van Den Broeck and A. S. Sengupta, Class. Quant. Grav. **24**, 1089 (2007), [gr-qc/0610126](#).

- [378] L. S. Finn, Phys. Rev. D **46**, 5236 (1992).
- [379] R. Dijkgraaf, A. Sinkovics, and M. Temurhan, Adv. Theor. Math. Phys. **7**, 1155 (2004), [hep-th/0211241](#).
- [380] P. Svrcek and E. Witten, JHEP **06**, 051 (2006).
- [381] R. D’Inverno, *Introducing Einstein’s Relativity* (Oxford University Press, Oxford, 1992).
- [382] M. Abramowitz and I. A. Stegun, *Handbook of Mathematical Functions with Formulas, Graphs, and Mathematical Tables* (Dover, New York, 1972).
- [383] J. Stewart, *Advanced General Relativity* (Cambridge University Press, New York, 1990).
- [384] T. Dray, J. Math. Phys. **26**, 1030 (1985).
- [385] K. Martel, Ph.D. thesis, The University of Guelph (2003).
- [386] D. Brizuela, J. M. Martin-Garcia, and G. A. Mena Marugan, Phys. Rev. **D74**, 044039 (2006), [gr-qc/0607025](#).
- [387] A. Messiah, *Quantum Mechanics, Vol. 2* (North-Holland, Amsterdam, 1962).
- [388] N. T. Bishop, Gen. Rel. Grav. **14**, 717 (1982).
- [389] N. T. Bishop, Gen. Rel. Grav. **16**, 589 (1984).

## Vita

Nicolas Yunes was born in Buenos Aires, Argentina on July 17, 1980. He obtained a B. S. in physics from Washington University in Saint Louis in 2003. Since then, he has been a Ph. D. student at the Pennsylvania State University. His honors include the Mebus, Duncan and Downsborough Fellowships and the Excellence in Teaching Award from the Pennsylvania State University, as well as the Blue Apple Award from the General Relativity and Gravitation Topical Group of the American Physical Association. He has presented invited and contributed talks, both in the United States and internationally, such as at the Massachusetts Institute of Technology, at Cornell University and Institute of Astrophysics in Paris. Some of his publications are presented below:

- S. Alexander, L. S. Finn and N. Yunes, *A gravitational-wave probe of effective quantum gravity*, submitted to Phys. Rev. D (2007)
- D. Grumiller and N. Yunes, *How do black holes spin in Chern-Simons gravity?*, accepted for publication in Phys. Rev. D (2007)
- N. Yunes and C. F. Sopuerta, *Perturbations of Schwarzschild Black Holes in Chern-Simons Modified Gravity*, submitted to Phys. Rev. D (2007)
- S. Alexander and N. Yunes, *A new PPN parameter to test Chern-Simons gravity*, Phys. Rev. Letters **99**, 241101 (2007)
- S. Alexander and N. Yunes, *Parameterized post-Newtonian expansion of Chern-Simons gravity*, Phys. Rev. D **75**, 124022 (2007)
- N. Yunes, C. F. Sopuerta, L. J. Rubbo and K. Holley-Bockelmann, *Relativistic effects in extreme mass ratio gravitational wave bursts*, accepted for publication in the Astrophys. J. (2007)
- C. F. Sopuerta, N. Yunes and P. Laguna, *Gravitational recoil velocities from eccentric binary black hole mergers*, Astrophys. J. **659**, L9-L12 (2007)
- C. F. Sopuerta, N. Yunes and P. Laguna, *Gravitational recoil from binary black hole mergers: The Close-Limit Approximation*, Phys. Rev. D **74**, 124010 (2006)
- N. Yunes, *Frankenstein's glue: Transition functions for approximate solutions*, Class. Quant. Grav. **24**, 4313-4336 (2007)
- N. Yunes and J. González, *Metric of a tidally perturbed spinning black hole*, Phys. Rev. D **73**, 024010 (2006)
- N. Yunes and W. Tichy, *Improved initial data for black hole binaries by asymptotic matching of post-Newtonian and perturbed black hole solutions*, Phys. Rev. D **74**, 064013 (2006)
- N. Yunes, W. Tichy, B. J. Owen and B. Bruegmann, *Binary black hole initial data from matched asymptotic expansions*, Phys. Rev. D **74**, 104011 (2006)